Analysis of Thin Concrete Shells Revisited:

Opportunities due to Innovations in Materials and Analysis Methods

Delft University of Technology
Faculty of Civil Engineering and Geosciences
Structural and Building Engineering
Concrete Structures
Stevinweg 1, Delft, the Netherlands

Master's thesis committee

Prof.dr.ir. J.C. Walraven	Concrete Structures
Ir. W.J.M. Peperkamp	Concrete Structures
Prof.dr.ir. J.G.Rots	Structural Mechanics
Dr.ir. P.C.J. Hoogenboom	Structural Mechanics
Ir. L.J.M. Houben	Graduation coordinator

Preface

This is the final report of my Master's thesis performed at the department of Structural and Building Engineering, part of the faculty of Civil Engineering and Geosciences of Delft University of Technology. The subject of this thesis is "Analysis of Thin Concrete Shells Revisited: Opportunities due to Innovations in Materials and Analysis Methods".

The subject of the thesis associates with today's renewed interest in free-form shells by the society. The construction of thin concrete shells ended abruptly at the end of the 1970s, mainly caused by the high costs in compare to other structural systems. However, uncertainties in the structural behaviour of shells did not help either. Contemporary progress in finite element software discards these uncertainties as it allows the engineer to closely approach the actual behaviour of thin concrete shells by performing geometrically and physically nonlinear finite element analyses. In addition, recent developments in concrete technology have led to ultra high performance fibre reinforced concrete with revolutionary performance in tension and compression. In fact, ultra high performance fibre reinforced concrete can be seen as a completely new construction material and its possibilities are still to be revealed. The combination of advanced finite element analyses and ultra high performance fibre reinforced concrete may lead to shells with even greater spans and thinner thicknesses than achieved so far. In the following, this hypothesis is tested on a case study. The thesis' report describes the activities undertaken and the results found, supplemented with historical, practical and theoretical background.

I would like to thank my graduation committee, Prof.dr.ir. J.C. Walraven, Ir. W.J.M. Peperkamp, Prof.dr.ir. J.G.Rots, Dr.ir. P.C.J. Hoogenboom and Ir. L.J.M. Houben for their guidance and ideas during the project. Special thanks to Dr.ir. M.A.N. Hendriks and Ir. R.A. Burgers, for their support and advice on finite element analyses. Furthermore, I would like to thank the other graduates in room 0.72 for their inspirational conversations during coffee breaks. Last but not least, I would like to thank my parents for giving me the opportunity to develop myself both professionally and socially during my years in Delft.

Bart Peerdeman

Delft, June 2008

Summary

Shell structures have been constructed since ancient times. The Pantheon in Rome and the Hagia Sophia in Istanbul are well-known examples. After the Roman times the traditions of domes continued up to the 17th century. Since then they seemed forgotten. Stimulated by the newly developed reinforced concrete and the demand to cover long-spans economically and column free the shell made a comeback in the early 20th century. Franz Dischinger and Ulrich Finsterwalder designed in 1925 the first thin concrete shell of the modern era, the Zeiss planetarium in Germany. The modern era of shell construction is recognised by the trend towards greater spans and thinner shells. Guided by well-known engineers as Pier Luigi Nervi, Eduardo Torroja, Anton Tedesko, Nicolas Esquillan, Felix Candela and Heinz Isler a blooming period of widespread shell construction took place between 1950 and 1970. Shell construction suddenly vanished at the end of the 1970s, mainly caused by the high costs in compare to other structural systems. Moreover, inflexible usability and uncertainties in the structural behaviour of shells and difficulty of proper analysis methods did not help neither did the stylistic identification with the *1950s* and *1960s*. Today the great era of thin shells is over, however, nowadays natural free-form shapes and blobs attract more and more attention. In addition, recent developments in concrete technology have led to ultra high performance fibre reinforced concrete with revolutionary performance in tension and compression. Eventually this may lead to a revival of the thin concrete shell.

Shells are constructed from concrete, profoundable due to the combination of filling and load carrying capacities. They are being built as 'thin shells', with a radius-to-thickness ratio starting at *200* reaching up to *800* and higher. The low consumption of material follows from the profound that shells are very efficient in carrying loads acting perpendicular to their surface by in-plane membrane stresses. In fact, the preference for membrane action arises as a consequence of being thin. Bending moments eventually arise only to satisfy specific equilibrium or deformation requirements. They do not carry loads and have a local character.

Concrete shells include single and double curved surfaces which are either synclastic, monoclastic or anticlastic. The surface can be generated by mathematical functions or by form-finding methods such as hanging membranes or pneumatic models. Contemporary computational advancement launched (real-time) computer based shell generation techniques such as the particle-spring systems. To calculate the membrane stresses of a given geometry quantitative information can be obtained by constructing a polygon of forces (for simple geometries), by using the Kirchhoffean based classical thin shell theory or by computer software such as finite element programs. For qualitative information over the force flow the rainflow analysis or model tests can be performed. The geometry forms a structural effective shell if the shell is able to develop a prevalent membrane stress field up to the highest degree. Optimisation techniques, such as shape optimisation by minimising strain energy, may lead to a design which is much more efficient from a

structural point of view. Optimisation may be enhanced by computation optimisation algorithms such as ESO or ACO. In general the design will lead to a shell with a rise to span ratio between *1/10* and *1/6* with an opening angle between *60* and *90* degrees. The shell thickness is practically bounded by *60* to *80 mm* for one- or two-layers of traditional steel reinforcing bars, respectively. Fibre reinforced structures may be even thinner. The reinforcement percentages are rather low, approximately *0.15* to *0.4%*. Possible prestressing may be applied in the edge (ring) beam or even in the shell surface itself. Finally, for a sound shell structure extra attention must be paid to the shell edge design in case of free edges. In general, forces flowing away from the edge prevent large edge beams which may cause problems such as shear off.

Most shells are constructed in a conventional manner: pouring concrete on a formwork. Other possibilities are the use of airform moulds or stressed membranes combined with sprayed concrete. Although the number of repetition is often not very high, prefabricated elements may be used. After hydratation, the concrete is predominantly left blank, allowing the climate freely attack the concrete skin.

In case of a failure, the shell may fail due to large deformations (buckling) or due to material nonlinearity (cracking and crushing) or by a combination of both (so-called inelastic or plastic buckling). The buckling behaviour of shells is a complicated phenomenon. Opposite to columns and plates, shells experience a sudden decrease in load carrying capacity after the bifurcation point (which can be obtained by a simple linear buckling analysis). The fall-back is caused by the phenomenon of compound buckling which refers to several buckling modes associated with the same critical load. In the postbuckling range the modes, which were orthogonal in the linear prebuckling range, start to interact resulting in a significantly reduced load carrying capacity. As discovered by Koiter, the major problem of the shell buckling behaviour is the accompanied imperfection sensitivity. Initial geometrical imperfections in the shell cause the bifurcation point never to be reached and lead to limit point buckling at a considerably lower load. The size of the imperfections determines the limit load at which the shell fails. In case of plastic buckling, the fall-back is further intensified by material nonlinearity.

From the foregoing two primary research questions can be formulated:

What is for a shell of hemispherical geometry, with given material properties, given support conditions, and subjected to a given load, the knock-down factor which indicates the difference between the linear critical buckling load and the actual critical buckling load taking into account imperfections and geometrical and physical nonlinearities?

And

Can high strength fibre reinforced concrete add to the trend towards greater spans and thinner shells with possibilities for even more slender structures?

To obtain an answer to the research questions a series of analyses (linear elastic, stability, geometrically nonlinear and geometrically and physically nonlinear) is performed on a given hemispherical shell: the Zeiss planetarium shell. The shell has a radius of curvature of *12500 mm* and a thickness of *60 mm*. Thereby, the

R/t ratio is equal to *200*. The shell is reinforced with one layer of low quality reinforcement FeB220 and assumed to be made from a C20/25 low quality concrete mixture to ally with the early 20th century concrete technology. For this research the shell is modelled with an axisymmetric curved line model and a three-dimensional model subjected to uniform spherical or vertical load. During analyses, the *R/t ratio* is ranged from *200* up to *1000* (stepsize *200*). Additionally, the possibilities of even more slender structures by using high strength fibre reinforced concrete are investigated by comparing the original C20/25 shell to a C180/210 ultra high performance fibre reinforced concrete mixture. To investigate the influence of initial geometrical imperfections a local top imperfection is modelled with an imperfection amplitude ranging from $w_0/t = 0.0$ to 1.0 (stepsize 0.2). Moreover, the influence of four boundary conditions is investigated, i.e. roller, inclined-roller, hinged and clamped support.

The linear elastic analysis proved to be in fair agreement with the (benchmark) analytical results for the three-dimensional model. The axisymmetric model is found to be less accurate and reliable, in particular with respect to the bending moments caused by restrained deformation at the supports. In both models disturbances in the stress and bending moment distribution were caused by the numerical imperfections. They appeared to be negligible on the linear solution. The disturbances are more apparent in the stability analysis, as they cause premature buckling modes preceding the actual shell buckling shape. Membrane supported shells with spherical load show a global buckling pattern of small local waves. The critical buckling load is significantly lower for membrane incompatible support conditions and/or vertical load. Shells subjected to vertical load, by definition, buckle in the boundary layer. The three-dimensional buckling results reveal the occurrence of compound buckling as adjacent critical loads are very close to each other. In general, thinner shells experience compound buckling up to a higher degree than thicker shells. The results of the axisymmetric shell model are poor, as compound buckling is not predicted correctly. Moreover, the axisymmetry causes the tendency to buckle at the top and the buckling loads are disturbed by the incorrect bending moments in case of a hinged and clamped support.

The geometrically nonlinear results demonstrate the imperfection sensitivity of shells as even small imperfection amplitudes already cause a significant decrease in load carrying capacity. The results appear to be in reasonable correlation to the Koiter half-power law and the relation as proposed by the IASS Recommendations, Kollar and Dulacska [54]. The inclined-roller supported shell subjected to spherical load provides an upper bound solution. The shell, by definition, fails at the imperfection. Variations in boundary and load conditions may lead to a shell failure insensitive to the top imperfection until the imperfection progresses to a certain size. The introduction of material nonlinearity leads to a further decrease in load-carrying capacity and the transformation to a strength failure rather than a buckling failure in case of shells subjected to uniform vertical load. Buckling eventually takes place after significant cracking, responsible for the major part of the knock-down factor, has occurred. In the considered hemispherical shells cracking, crushing and buckling strongly interact before and during failure. This is influenced by loading, shell thickness, material properties and geometrical imperfections. For the considered C20/25 hemispherical shell the knock-down factor is much smaller than the knock-down factor as derived using the IASS recommendations, which apparently are very conservative. The use of high strength fibre reinforced concrete appeared to be advantageous, in particular the higher axial and flexural tensile strength give the engineer opportunities to design thinner shells. Furthermore, high strength concrete is advantageous in compression as it excludes premature compressive crushing failure before the critical buckling load is reached. Opposed to fibre reinforced beams in bending, the significant ductility (postcracking plateau) of high strength fibre reinforced concrete does not influence the ultimate load carrying capacity of hemispherical shells. This might be caused by the buckling which occurs simultaneously with significant cracking.

From the results it can be concluded that it is impossible to derive a general expression for the knock-down factor, unless high factors of uncertainty are taken into consideration. However, contemporary finite element software makes possible to determine the structural behaviour of an imperfect shell and to compute its fall-back in load carrying capacity conveniently within a small amount of time by performing a geometrically and physically nonlinear analysis. In fact, it is this conclusion that is the most salient.

Contents at a Glance

Preface	I
Summary	III
Contents at a Glance	VII
Contents	IX
Chapter 1: Introduction and Aim of Thesis	1
PART I. Background	
Chapter 2: History of Thin Concrete Shell	6
Chapter 3: Shell Design	36
Chapter 4: Shell Construction	70
PART II. Theory	
Chapter 5: Theory of Shells	86
Chapter 6: Structural Failure	116
PART III. Case Study	
Chapter 7: Zeiss Planetarium	167
Chapter 8: Material	169
Chapter 9: Loading	189
Chapter 10: Hemispherical Example	197
PART IV. Finite Element Analysis	
Chapter 11: Finite Element Method	220
Chapter 12: Linear Elastic Finite Element Analysis	274
Chapter 13: Stability Finite Element Analysis	306
Chapter 14: Geometrically Nonlinear Finite Element Analysis	330
Chapter 15: Geometrically and Physically Nonlinear Finite Element Analysis	348
Chapter 16: Conclusions	381
Chapter 17: Recommendations	391
References	XVIII

Contents

Preface	I
Summary	III
Contents at a Glance	VII
Contents	IX
Chapter 1. Introduction and Aim of Thesis	1
1.1 Context of Thesis	2
1.2 Aim of Thesis	3
1.2.1 Problem Description	3
1.2.2 Objective	3
1.2.3 Process	4
1.3 Approach of Thesis Aim	4
PART I. Background	
Chapter 2. History of Thin Concrete Shells	6
2.1 Precursors	7
2.2 Start of Modern Era	8
2.3 World War II	15
2.4 Blooming Period, Sudden Death	16
2.5 Contemporary Shells	30
2.6 Future History	33
2.7 National Schools	34
2.8 Shell Dimensions	35
Chapter 3. Shell Design	36
3.1 Preliminaries of Shell Design and Analysis	38
3.1.1 Membrane Behaviour	38
3.1.2 Bending Behaviour	38
3.1.3 Material Effects on Shell Behaviour	39
3.1.4 In-extensional Deformation	39
3.1.5 Structural Failure	40
3.2 Classification of Shell Surfaces	40
3.2.1 Synclastic	41

3.2.2 Monoclastic 41
3.2.3 Anticlastic 41
3.3 Geometrical Surface Generation 42
3.3.1 Surfaces of Revolution 42
3.3.2 Translational Surfaces 42
3.3.3 Ruled Surfaces 42
3.3.4 Free-Form Surfaces 43
3.4 Non-Geometrical Surface Generation 43
3.4.1 Physical Modelling 44
3.4.2 Computational Modelling 45
3.5 Mechanical Behaviour 46
3.5.1 Balance Calculation 47
3.5.2 Polygon of Forces 47
3.5.3 Classical Shell Theory 48
3.5.4 Model Tests 49
3.5.5 Computational Numerical Analysis 50
3.5.6 Rainflow Analysis 51
3.6 Structural Optimisation 52
3.6.1 Size Optimisation 53
3.6.2 Material Optimisation 53
3.6.3 Topology Optimisation 54
3.6.4 Shape Optimisation 54
3.6.5 Computational Optimisation Algorithms 55
3.7 Design Codes 57
3.8 Design Considerations 58
3.8.1 Span/Rise/Radius of Curvature 58
3.8.2 Thickness 58
3.8.3 Ribbed Shells 59
3.8.4 Reinforcement 61
3.8.5 Prestressing 64
3.8.6 Material 65
3.8.7 Supports 65
3.8.8 Edge Design/Free Edges 66
3.8.9 Loading 68
3.8.10 Economics 69
3.9 Conclusions 69

Chapter 4. Shell Construction 70
4.1 Formwork 71
4.1.1 Conventional Formwork 72
4.1.2 Prefabricated Moulds 73
4.1.3 Airform Shells 74

4.1.4 Stresses Membranes 76
4.2 Reinforcement 77
4.3 Placement of Concrete 79
4.3.1 Conventional Placement 80
4.3.2 Sprayed Concrete 81
4.4 Finishing 82
4.4.1 Prestressing 82
4.4.2 Surface Treatment 82
4.5 Prefabrication 83
4.6 Conclusions 85

PART II. Theory
Chapter 5. Theory of Shells 86
5.1 General 87
5.1.1 History 87
5.1.2 Basic Relations 88
5.1.3 Assumptions 89
5.2 Theory of Bars 90
5.2.1 Extension 90
5.2.2 Bending 91
5.2.3 Combined Extension and Bending 94
5.3 Theory of Plates 94
5.3.1 Extension 95
5.3.2 Bending 98
5.3.3 Combined Extension and Bending 101
5.4 Theory of Shells 101
5.4.1 Extension 102
5.4.2 Bending 107
5.4.3 Combined Extension and Bending 110
5.5 Solve Methods 111
5.5.1 Direct Methods 111
5.5.2 Indirect Methods 112

Chapter 6. Structural Failure 116
6.1 Strength Failure 117
6.2 Buckling Failure 117
6.2.1 Stability and Instability 119
6.2.2 Form of Buckling 119
6.2.3 Koiter Initial Postbuckling Theory 122
6.2.4 Path of Equilibrium 123
6.3 Elastic Column Buckling 125
6.3.1 Ideal Linear Elastic Column 125

6.3.2 Ideal Nonlinear Elastic Column 127

6.3.3 Imperfect Elastic Column 128

6.3.4 Imperfections (I) 129

6.4 Elastic Place Buckling 130

6.4.1 Ideal Linear Elastic Plate 130

6.4.2 Ideal Nonlinear Elastic Plate 133

6.4.3 Imperfect Elastic Plate 135

6.4.4 Imperfections (II) 135

6.5 Elastic Shell Buckling 135

6.5.1 General Buckling Equation 136

6.5.2 Axially Compressed Circular Cylindrical Shells 139

6.5.3 Spherical Shells under External Pressure 148

6.5.4 Imperfections (III) 156

6.6 Inelastic Shell Buckling 157

6.7 Initial Geometrical Imperfections 158

6.8 Knock-Down Factor Approach 160

6.9 Buckling Recommendations 161

6.9.1 Linear Buckling Load 161

6.9.2 Postbuckling Category 161

6.9.3 Large Deflections and Geometric Imperfections 162

6.9.4 Modification for Material Properties 163

6.9.5 Total Reduction Factor and Safety Factor 165

6.9.6 Conclusion IASS Recommendations 165

6.10 Conclusions 166

PART III. Case Study

Chapter 7. Zeiss Planetarium 167

7.1 Geometry 168

7.2 Material 168

7.3 Support 168

7.4 Loading 168

Chapter 8. Material 169

8.1 Conventional Concrete 170

8.1.1 Compressive Behaviour 170

8.1.2 Tensile Behaviour 172

8.1.3 C20/25 Mixture Design 173

8.2 High Strength Fibre Reinforced Concrete 175

8.2.1 High Compression Strength 175

8.2.2 Fibre Reinforcement 176

8.2.3 UHPFRC in Practice 182

8.2.4 Compressive Behaviour 182

8.2.5 Tensile Behaviour 183
8.2.6 C180/210 Mixture Design 184
8.3 Conclusions 187

Chapter 9. Loading 189
9.1 Permanent Loads 190
9.2 Variable Loads 190
9.2.1 Wind Load 190
9.2.2 Snow Load 193
9.3 Accidental Loads 196
9.4 Load Cases 196
9.5 Conclusions 196

Chapter 10. Hemispherical Example 197
10.1 Shell Parameters 198
10.1.1 Geometry 198
10.1.2 Material 198
10.1.3 Support 198
10.1.4 Loading 198
10.2 Analysis Scheme 198
10.3 Linear Analysis 199
10.3.1 Membrane Behaviour 199
10.3.2 Membrane Stress Resultants 202
10.3.3 Membrane Strains 204
10.3.4 Membrane Displacements 204
10.3.5 Bending Behaviour 206
10.3.6 Bending Solution 208
10.3.7 Total Solution 212
10.4 Geometrical and Material Influences 214
10.4.1 Geometrical Influences 214
10.4.2 Material Influences 215
10.5 Linear (Euler) Buckling Analysis 215
10.6 Postbuckling Analysis 216
10.7 Inelastic Buckling Analysis on Imperfect Shells 217
10.8 Conclusions 218

PART IV. Finite Element Analysis
Chapter 11. Finite Element Method 220
11.1 Mathematical Fundamentals 221
11.11.1 Matrices and Vectors 221
11.11.2 Tensors 223
11.2 Generalised Finite Element Procedure 223

11.2.1 Global Formulation 223
11.2.2 Displacements 224
11.2.3 Strains and Stresses 226
11.2.4 Equilibrium Relations 227
11.2.5 Strong Form – Weak Form 227
11.2.6 Numerical Integration 231
11.2.7 System Stiffness Matrix 232
11.2.8 Right Hand Side Vector 233
11.3 Linear Finite Element Procedure 233
11.3.1 Virtual Work Formulation 233
11.3.2 Stiffness Matrix Formulation 235
11.3.3 Assembling RHS Vector 235
11.3.4 Equilibrium 236
11.4 Nonlinear Finite Element Procedure 236
11.4.1 Physical Nonlinearity 237
11.4.2 Geometrical Nonlinearity 238
11.5 Solution Procedures for Static Linear Analysis 239
11.5.1 Direct Procedures 239
11.5.2 Iterative Procedures 240
11.5.3 General Remarks 241
11.6 Solution Procedures for Static Nonlinear Analysis 241
11.6.1 Iterative Procedures 241
11.6.2 Incremental Procedures 243
11.6.3 General Remarks 246
11.7 Stability Analysis 246
11.7.1 Euler Stability (Linear Buckling) 247
11.7.2 Generalised Eigenproblem 248
11.7.3 Shifting 249
11.7.4 Postbuckling Analysis 249
11.8 Solution Methods for Eigenproblems 250
11.9 Finite Element Software 252
11.10 Geometrical Modelling 253
11.10.1 Geometry 253
11.10.2 Mesh Generation 253
11.10.3 Element Types 256
11.10.4 Integration Schemes 260
11.11 Material Modelling 262
11.11.1 Tensile Cracking 263
11.11.2 Compressive Behaviour 268
11.11.3 Modelling Conclusions 273
11.12 Conclusions and Comments 273

Chapter 12. Linear Elastic Finite Element Analysis 274
12.1 Shell Parameters 275
12.1.1 Geometry 275
12.1.2 Material Properties 275
12.1.3 Boundary Conditions 275
12.1.4 Loading 275
12.1.5 Analysis Scheme 275
12.2 Axisymmetric Shell Model 276
12.2.1 FE Model 276
12.2.2 Support Reactions 276
12.2.3 Stresses 277
12.2.4 Strains 285
12.2.5 Displacements 286
12.3 Three-Dimensional Model 288
12.3.1 FE Model 288
12.3.2 Support Reactions 289
12.3.3 Stresses 290
12.3.4 Strains 296
12.3.5 Displacements 296
12.4 Geometrical Influences 299
12.5 Material Influences 300
12.6 Load Influences 301
12.7 Conclusions 303

Chapter 13. Stability Finite Element Analysis 306
13.1 Shell Parameters 307
13.1.1 Geometry 307
13.1.2 Material 307
13.1.3 Boundary Conditions 307
13.1.4 Loading 307
13.1.5 Analysis Scheme 307
13.2 Linear Buckling Analysis 307
13.2.1 Axisymmetric Shell Model 307
13.2.2 Three-Dimensional Shell Model 315
13.3 Geometrical Influences 323
13.4 Material Influences 323
13.5 Perturbation and Continuation Analysis 324
13.6 Conclusions 326

Chapter 14. Geometrically Nonlinear Finite Element Analysis 330
14.1 Shell Parameters 331
14.1.1 Geometry 331

14.1.2 Initial Geometrical Imperfections 331
14.1.3 Material 332
14.1.4 Boundary Conditions 332
14.1.5 Loading 332
14.1.6 Analysis Scheme 332
14.1.7 FEA Settings 332
14.2 Perfect Shell 333
14.2.1 Results and Findings 333
14.2.2 Axisymmetric Comparison 334
14.3 Imperfect Shell 335
14.3.1 Results and Findings 335
14.4 Effect of Imperfections 339
14.4.1 Theoretical Comparison 340
14.4.2 Axisymmetric Comparison 341
14.5 Support and Load Influences 341
14.6 Geometrical Influences 344
14.7 Material Influences 344
14.8 Knock-Down Factor Approach 344
14.9 Conclusions 345

Chapter 15. Geometrically and Physically Nonlinear Finite Element Analysis 348
15.1 Shell Parameters 349
15.1.1 Geometry 349
15.1.2 Initial Geometrical Imperfections 349
15.1.3 Material Modelling 349
15.1.4 Boundary Conditions 352
15.1.5 Loading 352
15.1.6 Analysis Scheme 352
15.1.7 FEA Settings 352
15.2 Results UHPFRC Shell under Spherical Load 352
15.2.1 Zeiss 2 353
15.2.2 Zeiss 1, 3 and 4 359
15.3 Results UHPFRC Shell under Vertical Load 360
15.3.1 Zeiss 1, 2, 3 and 4 360
15.4 Results C20/25 Shell under Spherical Load 364
15.4.1 Zeiss 2 364
15.4.2 Zeiss 1, 3 and 4 369
15.5 Results C20/25 Shell under Vertical Load 370
15.5.1 Zeiss 1, 2, 3 and 4 370
15.6 Practical Considerations 374
15.7 Material Influences 375
15.8 Knock-Down Factor Approach 376

15.9 Conclusions 377

Chapter 16. Conclusions 381
16.1 Part I Conclusions 381
16.2 Part II Conclusions 382
16.3 Part III Conclusions 383
16.4 Part IV Conclusions 384
16.4.1 Linear Elastic Analysis 384
16.4.2 Stability Analysis 384
16.4.3 Geometrically Nonlinear Analysis 385
16.4.4 Geometrically and Physically Nonlinear Analysis 387
16.5 Principal Conclusions 389

Chapter 17. Recommendations 391
17.1 Part I Recommendations 391
17.2 Part II Recommendations 391
17.3 Part III Recommendations 391
17.4 Part IV Recommendations 392

References XVIII

1 Introduction and Aim of Thesis

Appearing first in the early 20th century, *thin concrete shell structures* were frequently used for long-span roof structures throughout Europe and beyond during the period between 1920 and 1970. The development stemmed from the need to cover medium to large spans economically and from a fascination with a new material: *reinforced concrete*. Concrete shells include single curved shapes such as cylinders and cones and double curved geometries such as domes which are either *synclastic* (curves running in the same direction) or *anticlastic* (curves running in opposite directions). Most shells are constructed in a conventional matter: pouring concrete on a formwork. Concrete shells are built as 'thin shells'. There is referred to a thin shell as the *radius-to-thickness ratio* of *200* puts the shell in the range of being 'thin'. Thin shells provide in an advantageous low consumption of material.

The low consumption of material in shell structures follows from the unique character of the shell: the curvature in spatial form. This unique character is responsible for the profound that shell structures are very efficient in carrying loads acting perpendicular to their surface by so-called *membrane action*, a general state of stress which consists of in-plane normal and shear stress resultants only, whereas other structural forms carry the applied load mostly by *bending action*, the least efficient load carrying method. This membrane action results in (low) in-plane membrane stresses which can be absorbed by only a small thickness of the shell. As a consequence shell structures can be very thin and still span great distances. Radius-to-thickness ratios of *400* or *500* are not uncommon. Bending moments eventually arise to satisfy specific equilibrium or deformation requirements. Because bending moments are confined to a small region the rest of the shell is virtually free from bending actions and still behaves as a true membrane. It is this salient feature of shells that is responsible for the most profound and efficient structural performance!

Historically, shell structures have been developed since ancient times. The *Pantheon* in Rome and the *Hagia Sophia* in Istanbul are two well-known examples, respectively constructed in the 2nd and 6th century A.C. After the Roman times the tradition of domes continued up to the 17th century, however, in the 18th/19th century, the art of designing concrete shell structures seemed forgotten. Guided by German designers Franz Dischinger and Ulrich Finsterwalder, the concrete shell made a come-back in the early 20th century. The first shell of the modern era is the *Zeiss planetarium* in Germany built in 1925.

The Zeiss planetarium was the start of a new tradition of thin concrete shell structures. Besides Dischinger and Finsterwalder, Eduardo Torroja in Spain, Pier Luigi Nervi in Italy and Anton Tedesko in the United States were among the pioneer shell builders. The inception of the Second World War caused an interruption in shell development. The post-war period, however, created exactly those conditions needed for flourishing shell construction: low labour costs and construction material (in particular steel) being in short supply. That launched the blooming period of shell construction which spans approximately *20* years between the *1950s* and *1970s* and can be characterised by wide spread shell construction throughout the entire world. The post-war thin shell tradition was carried forward by engineers such as Felix Candela, Mircea Mihailescu and Nicolas Esquillan. In particular the shells of Candela are spectacular and attracted the attention of architects like Saarinen which became involved in shell design.

The blooming period ended abruptly in the *1970s*. Already since the *1960s* the emphasis of concrete shell building has moved to developing countries as shells in Europe became too expensive in compare to other structural systems, mainly due to labour and formwork costs. However, from the *1970s* almost no shells were built, except for those of Swiss Heinz Isler who used inventive reusable formwork and standardised shell sizes. Isler is, however, most famous for his elegant free-form shells derived from form-finding methods which are the basis of much contemporary research.

Today the great era of thin concrete shells is over. However, stimulated by the search towards new architectural boundaries and stemming from the fascination of contemporary computational design as well as the availability of high tech construction materials such as carbons and ultra high performance concrete, nowadays more natural *free-form shapes* and *blobs* attract attention of architects (and engineers) and are accepted and liked by the society. So far these structures do not behave like shells but with more architectural and engineering interaction these structures may be turned into *form active structural surfaces* in time.

1.1 Context of Thesis

The modern era of shell construction is recognised by the trend towards greater spans and thinner shells. Modern shell structures span larger column-free areas (up to *200 m* and more) and, more important, with thinner thicknesses than the traditional domes. The desire to reduce the thickness is understandable as the dead weight of the shell represents the major portion of the total load. Moreover, the preference for membrane action arises as a consequence of being thin. For engineers, the significance of the ever growing span in combination with a larger radius-to-thickness ratio lies in the realisation that the shell contains less strength reserve and, more important, *buckling* becomes dominant for failure.

Similar to the stability theory of centrally compressed bars (Euler), the *critical load* for shells can be found by looking for the load at which, besides the original, unbuckled state, another neighbouring shape, infinitely close to the first one, also becomes possible. This was successfully done for the first time by Zoëlly as he derived the equation for the linear critical buckling load of a sphere under radial pressure in 1915. However, opposite to bars (and plates) significant discrepancies were found between theory and experiment. The answer to the great discrepancy between theory and experiment laid in the *geometrically nonlinear theories* and the influence of *initial geometric imperfections*. The introduction of geometrical nonlinearities (large deformations) enabled investigation to the postbuckling behaviour of shells. It was found that after the bifurcation point the shell experiences a significant decrease in load carrying capacity caused by the phenomenon of *compound buckling*. Compound buckling refers to the situation in which several buckling modes are associated with the same critical load. Within the linear range the modes are orthogonal; however, they start to interact in the postbuckling regime causing the load to fall down. Moreover, it was discovered that shells are very sensitive to initial geometric imperfections which cause the bifurcation point never to be reached and premature *limit point failure* is detected. Furthermore, the differences are not only the result of the nonlinear behaviour due to large deflections and imperfections in geometry, but also the result of *material nonlinearities* such as *cracking* and *crushing*.

Extensive research to the shell buckling behaviour has resulted in a *qualitative* explanation of the phenomenon. It is clear that shells by no means can be designed on the basis of the linear critical buckling load. Engineers solved this by using (very) high safety factors for their shells. However, this is not very accurate and reliable. Hence, there is a need for usable *design aids* to determine the (*quantitative*) buckling response of thin concrete shell structures.

1.2 Aim of Thesis

1.2.1 Problem Description

Modern era shell design is recognised by the trend toward greater spans and thinner shells. Recent development of high strength fibre reinforced concrete can add to this trend with possibilities for even more slender shell structures. However, in correlation with high slenderness, shells become very sensitive for initial geometrical imperfections which may lead to a buckling failure at substantially lower load than follows from the linear theory. The need at this time is to extend the understanding in concrete shell buckling and to provide shell designers and analysts with reliable design aids to determine the fall-back in load carrying capacity, easily understood and used.

1.2.2 Objective

The objective of this master thesis is to verify the expectation of constructing shells with an even higher slenderness than is reached today using high strength fibre reinforced concrete. Furthermore, the research must contribute to a better understanding of the buckling phenomenon, in particular, a better understanding of the decrease in load carrying capacity caused by initial geometrical imperfections and geometrical and material nonlinearities. As the structural engineer prefers general methods of calculation with a limited amount of computational work, a procedure is proposed for which the actual buckling load is determined by multiplying the linear critical buckling load (which can easily be obtained from a linear stability analysis) with a so-called *knock-down factor*. Perhaps, a reliable design aid can be obtained to determine the knock-down factor using simple design formulae.

The objective leads to two research questions which can be formulated as;

1. *What is for a shell of hemispherical geometry, with given material properties, given support conditions, and subjected to a given load, the knock-down factor which indicates the difference between the linear critical buckling load and the actual critical buckling load taking into account imperfections and geometrical and physical nonlinearities?*
2. *Can high strength fibre reinforced concrete add to the trend towards greater spans and thinner shells with possibilities for even more slender structures?*

1.2.3 Process

To obtain an answer to the research questions, a shell with given geometry is introduced: the 1925 Zeiss planetarium in Jena, Germany. The Zeiss planetarium shell is analysed with the finite element program DIANA. For the research the base shell is modelled by conventional and high strength fibre reinforced concrete. In order to gain insight in the structural behaviour first a linear elastic analysis is performed and compared to a benchmark hand calculation determined using the *classical shell theory*. Afterwards the linear critical buckling load and the actual critical buckling load taking into account for imperfections and geometrical and physical nonlinearities are computed in a stepwise approach. First the effect of initial geometrical imperfections and geometrical nonlinearities is considered while additional material nonlinearities are introduced in succession. By varying the load conditions, support conditions and the radius-to-thickness ratio the general response may be found. The results are compared to buckling theories.

1.3 Approach of Thesis Aim

The aim of the thesis is reached through four parts with, in total, 14 chapters;

Part I – Background

Chapter 2	History of Thin Concrete Shells
Chapter 3	Shell Design
Chapter 4	Shell Construction

Part II – Theory

Chapter 5	Theory of Shells
Chapter 6	Structural Failure

Part III – Case Study

Chapter 7	Zeiss Planetarium

Chapter 8	Material
Chapter 9	Loading
Chapter 10	Hemispherical Example

Part IV – Finite Element Analysis

Chapter 11	Finite Element Method
Chapter 12	Linear Elastic Finite Element Analysis
Chapter 13	Stability Finite Element Analysis
Chapter 14	Geometrically Nonlinear Finite Element Analysis
Chapter 15	Fully Nonlinear Finite Element Analysis

Part I discusses general background information. Chapter 2 covers the historical development in modern era shell construction from the Zeiss planetarium in Jena up to contemporary free-form designs. In Chapter 3 the design process is studied by means of structural behaviour, surface generation and classification, optimisation techniques and important design considerations. Chapter 4 discusses the shell construction process.

Part II represents the theoretical part. In Chapter 5, the classical shell theory as formulated by Love is derived using a stepwise approach starting with the theory of bars and plates. In Chapter 6 the structural failure, mainly governed by the phenomenon of buckling, is extensively reported. Similar to Chapter 5, the bar and plate are discussed first.

Part III includes the elaboration of a case study of a hemispherical shell; the Zeiss planetarium in Germany. The case study is prepared by setting the geometry in Chapter 7, the material properties in Chapter 8 and the load conditions using the *Eurocode 2* in Chapter 9. In Chapter 10, the linear elastic behaviour of the hemispherical shell is determined and a buckling calculation is performed.

Part IV discusses the finite element analysis. Some theoretical background is provided in Chapter 11. In Chapter 12, 13, 14 and 15, the finite element analysis is performed in the case study shell described in Part III. The results of the linear elastic finite element analyses are presented in Chapter 12 while the buckling response is reported in Chapter 13. Chapter 14 covers limit point buckling caused by large deformations and initial geometrical imperfections and Chapter 15 approaches the actual behaviour with the inclusion of material nonlinearity such as cracking and crushing.

The thesis concludes in Chapter 16 and 17 with the Conclusion and Recommendations.

part I

Background

2 History of Thin Concrete Shells

The Roman Pantheon, as it stands today in the centre of the city of Rome, really is a remarkable and imposing structure. The Pantheon is a masterpiece of ancient shell construction and has withstood for almost two-thousand years. Today, the span of *43 m* still impresses the engineering profession. The Pantheon, built in the early 2nd century A.C., approximately 125, is the largest unreinforced dome in the history, Croci [26]. It can be seen in Figure 2.1.

The Hagia Sophia is a second example of the structural capacity of the classical builders. It is built in the 6th century, however, damages from earthquakes and fires have drastically altered the structure giving the building the appearance that it has today. The Hagia Sophia features some important differences with the Pantheon because of the fact that the dome is supported by four huge columns on the corners of a *32* by *32 m* square. The problems how to resists the circumferential tensile stresses of the lower part of the dome and how to transfer the vertical meridian forces to the pillars are solved by the introduction of hemidomes and abutments (to balance the thrust) and pendentives associated with arches (to transfer the vertical load). The dome, which rises up to *54 m*, has a diameter of *32 m*, Croci [26]. Cronogically it is the second biggest dome in the ancient times, after the Pantheon. It is also seen in Figure 2.1.

Long before the Pantheon and the Hagia Sophia, classical builders constructed pseudo vaults in early aged beehive houses (2500 B.C.) and Egyptian and Assyrian cultures used barrel vaults for tombs and covered canals, Hanselaar [44]. The widespread arch construction for aqueducts and amphitheatres in the Roman Empire leaded to the domes of the Pantheon and Hagia Sophia. After the Roman times the tradition of vaults and domes continued in Byzantium, the Romanesque, the Gothic, the Renaissance and the Baroque. However, in the 18th and 19th century, the art of designing shell structures seemed forgotten, Popov and Medwadowski [62].

Guided by German designers Franz Dischinger and Ulrich Finsterwalder and the newly developed reinforced concrete, the shell made a come-back in the *1920s*. The modern era of shell design, which started with the completion of the Zeiss planetarium in Germany, is recognised by the trend toward greater spans and thinner shells. Furthermore, theoretical progression and state-of-the-art computational features enabled more and more architectural freedom, leading to the contemporary free-form and blob structures.

The modern era of shell history is discussed in this chapter. Therefore, the era is divided into four periods. A period of *precursors* before the Second World War (1925-1940), the *War years* (1940-1945), the *blooming period* with widespread shell construction which ended suddenly in the *70s* (1945-1970) and the *contemporary period* with pioneering construction techniques, modern architecture and computational advancement. The historical perception is guided by the important shell structures and designers of the 20th century.

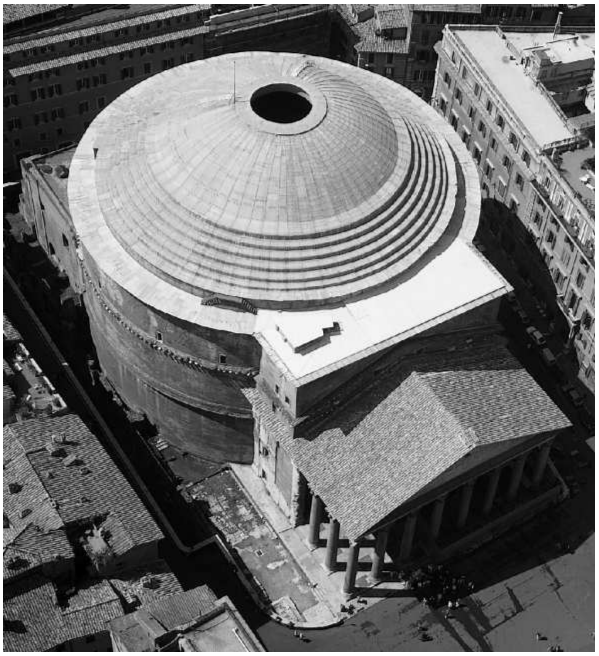


Figure 2.1. Aerial view of the Pantheon (125) in Rome, http.nl.wikipedia.org, and the interior of the Hagia Sophia (537) in Istanbul, http://folk.uio.no

While reading, one must keep in mind that, however in reality different historical events coincide, it is not possible to write like that. Therefore, and because of the relationship between certain events, occasionally there are made small steps (forward and backward) in time.

2.1 **Precursors** (1900-1925)

The modern era of shell structures started in 1925 with the completion of the first thin reinforced concrete shell covering the Zeiss planetarium in Jena, Germany. It was, however, a few years earlier, in the beginning of the 20th century that throughout Europe several reinforced concrete shell structures arise, inspired by the new material reinforced concrete, patented and promoted by Joseph Monier, a French gardener, Billington [7]. These early 'thick' shells are mostly documented in national literature only, and, therefore, less accessible for historical research. An example is the dome of the 1914 Cenakel church by J.G. Wiebenga, constructed in Nijmegen in the east of the Netherlands. The church, presented in Figure 2.2, was most probably the largest reinforced concrete dome in Europe at that time with a diameter of *14.5 m* and a thickness of *100 mm*, Haas [42]. The thickness to span ratio is *1/73* (hence, the shell is referred to a thick shell as a thickness to span ratio of *1/200* puts the shell in the range of being 'thin').

Figure 2.2. Cenakel church (1914) Nijmegen by J.G. Wiebenga, http.nl.wikipedia.org

Nine years later French engineer Eugene Freyssinet (1870-1947) did pioneering work and constructed two celebrated cylindrical vaults at the military airfield in Orly, presented in Figure 2.3. The corrugated airship hangars are a fine example of an early folded slab, where Freyssinet used the folding to stiffen the hangar avoiding heavy material use. They span *86 m* with a height of *50 m*, Billington [7]. The structures were demolished at the end of the Second World War. In 1924 Freyssinet applied the same principle for the construction of two airplane hangars spanning *55 m* at Velizy-Villacoublay airport. Unfortunately, also these hangers did not survive; however, there still is an international subsidiary of the modern civil engineering Freyssinet Company in the village near Paris.

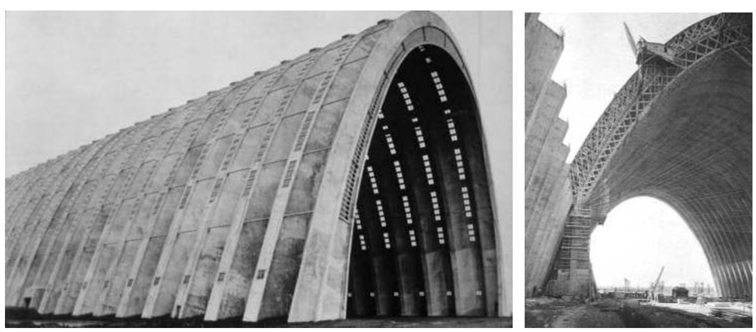

Figure 2.3. Freysinnet's Airship hangar (1923) Orly, www.essential-architecture.com

2.2 Start of Modern Era (1925-1940)

The pioneering work of early 20th century engineers like Freyssinet raised the fascination of the new reinforced concrete of Germans Franz Dischinger (1887-1953) and Ulrich Finsterwalder (1897-1988), engineers at Dyckerhoff & Widmann AG. They recognised that the combination of concrete and steel would enable them to overcome the tension problems of ancient domes which forced large cross-sections and limited spans. Dischinger and Finsterwalder became involved in designing a reinforced concrete shell structure for the Carl Zeiss Optical Industries in Jena in the east of Germany. Walter Bauersfeld (1879-1959), an engineer of the Carl Zeiss Company, wanted to build a planetarium and needed a large hemisphere for the projection of the starry sky. He had developed a triangular steel grid as stay-in-place framework and reinforcement (and with that he became the inventor of the so-called *geodesic dome*, later developed to its full potential by Buckminster Fuller). Before designing the planetarium Dischinger and Finsterwalder experienced with the steel framework and constructed several small-scale models which eventually leaded to a small, but very thin, canopy with a span of *16 m* and a thickness of only *30 mm* on top of the Zeiss factory seen in Figure 2.4, Günschel [40].

Figure 2.4. The experimental canopy on the Zeiss factory, http://ke.arch.rwth-aachen.de

The success of the canopy resulted in the construction of the shell for the planetarium in 1925, the first thin reinforced concrete shell structure in the world. The planetarium shell has a span of *25 m* and a thickness of just *60 mm*. The Zeiss planetarium shell has a height of *12.5 m* and spans a circular room with *500* seats. The shell and the triangular steel framework can be seen on Figure 2.5. The reinforcement grid is encased with concrete using the so-called Torkret method in which concrete is sprayed with air pressure on a wooden formwork. Eventually the concrete was covered by sheet metal. The planetarium is supported by a continuous tension ring capable of absorbing the circumferential tensile stresses rising in the lower part of the shell, Günschel [40]. The planetarium is still in use today and scheduled to become a historic monument.

Figure 2.5. Zeiss Planetarium (1925) by Dischinger, Finsterwalder and Bauersfeld, www.structurae.co.uk

The realisation of the Zeiss planetarium shell became a huge success for Dyckerhoff & Widmann AG in shell construction. Dyckerhoff & Widmann AG and in particular Dischinger and Finsterwalder earned world wide recognition. Following their success of the planetarium construction and the successful cooperation with Walter Bauersfeld, the construction system with the stay-in-place steel network system encased by concrete was patented the Zeiss-Dywidag system, Billington [7].

From 1925 to 1931, the year in which Dischinger became lecturer for reinforced concrete construction at the Berlin University of Technology, Dischinger and Finsterwalder engineered several impressive Zeiss-Dywidag shell structures, such as market halls in Hanover, Frankfurt, Leipzig and Basel. In particular, the structures in Frankfurt and Leipzig where milestones in early reinforced concrete shell construction, as both structures showed the enormous potential of shell structures covering large areas with less material, Billington [7]. Martin Elsässer's design for the market hall in Frankfurt, Figure 2.6, consists of *15* cylindrical shells of *14 m* wide and *37 m* long which lay side-by-side forming a column-free area of *11000 m²*. The thickness of a shell is just *70 mm* and it is reinforced by a double layer of the Zeiss-Dywidag triangular steel network.

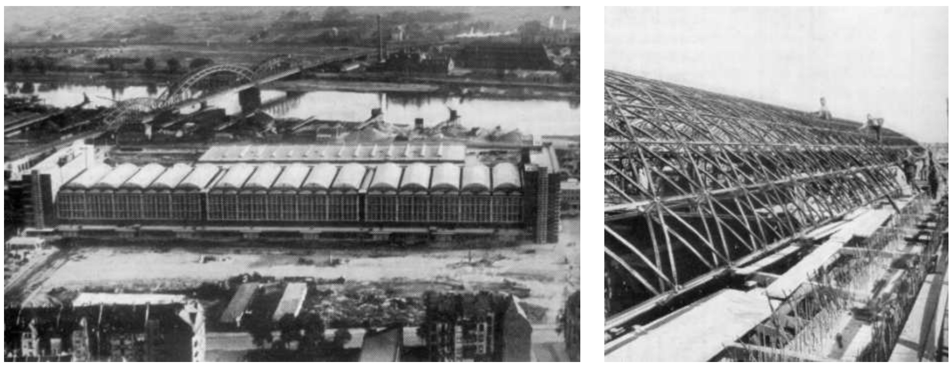

Figure 2.6. Frankfurter market hall (1927) with the Zeiss-Dywidag steel reinforcement, Joedicke 1962

The Leipzig hall, Figure 2.7, is designed by H. Ritter and is covered by two elliptical segmental shells with a thickness of *90 mm*. The shell segments are stiffened at the corners by *8* arch-shaped beams and span *74 m*. At the base of the shell structure, the tensile stresses are absorbed by a tension ring which is practically continuous supported by a system of columns and arches. The upper part of the shell is replaced by a glass façade through which natural light enters the building, Joedicke [52].

Figure 2.7. Leipzig market hall (1929) by Dischinger and Finsterwalder, www.structurae.co.uk

The German construction firm Dyckerhoff & Widmann AG played a major role in early shell construction and distribution with their patented Zeiss-Dywidag system. First in Germany and neighbouring countries as The Netherlands, Switzerland and Hungary and later further throughout Europe and in the United States of America, Billington [7]. The company had a remarkable group of structural engineers developing their new reinforced thin concrete shells in the early *1930s*. Besides head engineer Franz Dischinger and his assistant (and later successor) Ulrich Finsterwalder, there were young promising engineers as Hubert Rüsch (1904-1979), Wilhelm Flügge (1904-1990) and Anton Tedesko (1903-1994).

The name of Anton Tedesko is directly related to the history of shells in the USA. In 1932 Dyckerhoff and Widmann AG decided to send young engineer Anton Tedesko and their patent to Roberts & Schaefer in Chicago to promote their Zeiss-Dywidag shell systems in the United States. Hence, not without success, the rise of thin concrete shell structures in the USA can completely be attributed to Tedesko. At the age of *33* he constructed the first shell of America in 1936, the Hersheypark Arena in Hershey, Pennsylvania. The Hersheypark shell is a cylindrical barrel vault shell, see Figure 2.8. As he did with most of his shell structures, Tedesko designed the Arena as a shell with stiffening ribs. The Hersheypark shell has a square plan of *70* by *110 m* and a height of *30 m*. The thickness of the shell is just *90 mm* which slightly increases near the supports. The shell, which covers an ice-hockey rink and *7228* seats, was financed by the Hershey Chocolate Company, Weingardt [84].

Figure 2.8. Hersheypark Arena (1936) with inside stiffening ribs by Anton Tedesko, www.hersheyarchives.org

Although Tedesko had made many designs before 1936, none of them where built. However, the publicity relating to the Hersheypark Arena opened doors and more shell structures followed. Also other engineers came involved in shell construction. Besides Anton Tedesko, the names of Richard Bradshaw, Norwegian Frederick Severud (also of the St. Louis Gateway Arch) and the Ammann & Whitney Company must be mentioned. Their contribution to the American shell history is, however, post-war and thus discussed later.

Where the construction of the Zeiss planetarium first only served as catalyst for thin reinforced concrete shells in Germany and neighbouring countries, it did not last for long until the shell experiences distributed throughout entire Europe. Besides Franz Dischinger and Ulrich Finsterwalder in Germany, Eugene Freyssinet and Bernard Laffaille (1900-1955) in France, Pier Luigi Nervi (1891-1979) and Giorgio Baroni in Italy and Eduardo Torroja (1899-1961) in Spain where among the first shell builders.

Pier Luigi Nervi completed Italy's first shell structure in 1932. The shell covered the grandstand of the new municipal stadium in Florence, a single curved shell structure which cantilevers *17 m* and is supported every *4.7 m* by cantilever frames. The design was the winner of a competition, largely because of the relatively low costs involved in realisation (!). The shell for the municipal stadium turned out to be a presage of Nervi's imposing career involving shells. Immediately after Nervi finished the Florence project he won another competition written by the Italian Air Force. They needed housing for their air fleet at the military airports of Orvieto, Orbetello and Torre del Lago. Inspired by nature, Nervi constructed large ribbed cylindrical hangars of intense beautiness as can be seen in Figure 2.9. The structures are designed as a geodetic framework and span *100* by *40 m*. They were built in 1935 using wooden formwork and reinforced concrete. The application of ribs to stiffen the shell would return in later shell designs, becoming his trademark. To Nervi, the problems that arise during construction provided an illustration of the disadvantages of wooden formwork wherever the concrete work goes beyond the simple shape. When Nervi got commission to build another series of airplane hangars in 1940, he made a second design to overcome the disadvantages, Desideri [28].

He came with the pioneering idea of replacing the poured-in-place concrete beams with beams constructed of prefabricated parts. Nervi designed the ribs of the new hangar as lattice ribs making the construction lighter and suitable for prefabrication. Only at the points of greatest stress Nervi used poured-in-place concrete beams. The connections between the prefabricated parts where done by welding the steel and using high strength concrete in the space left at the junction. The difference between the first and second hangar designs can be seen on Figure 2.9. The left imagine shows the original design and both righter imagines the new shell with the prefabricated lattice ribs. The precasting and erection was simple and fast and when the Germans dynamited his airplane hangars at the end of the war, the majority of the joints stayed intact. Nervi had proved that the monolithic qualities of the construction were not disturbed by dividing the structure into precast elements, Desideri [28].

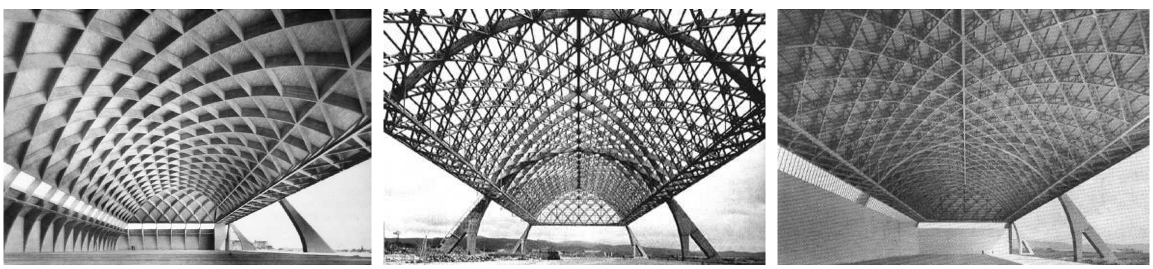

Figure 2.9. The two Airplane Hangar designs at Orvieto, Orbetello and Torre del Lago (1935, 1940), www.structurae.co.uk

In Spain the first engineer to construct thin reinforced concrete shells was Eduardo Torroja, one of the greatest engineers of the *20th* century and the founder of the International Association of Shell Structures (IASS) in 1959, a platform organisation for scientists, architects and engineers, IASS [93]. Torroja followed Antonio Gaudi in his search for expressing the structural idea of thinness. Torroja showed how the identity of form and architecture achieved by Gaudi in masonry (e.g. a saddle-shaped roof for a school alongside the church of the Sagrada Familia) could be realised in concrete, Billington [7]. The shell structures of Torroja are a combination of structural efficiency and aesthetical assessment. The first shell he constructed was a market hall in Algeciras in the southern region Andalusia in 1933, by the time of completion the largest shell in the world. The shell, seen in Figure 2.10, is a lowered semi-spherical dome with an octagonal plan and a diameter span of *47.6 m*. The radius of curvature is *44 m* and the shell has a predominant thickness of *90 mm*. At the supports the thickness is increased to *500 mm*. At each corner point the shell is supported by a column which only transfers vertical load. The horizontal tension stress is absorbed by a hoop tension cord. When the shell was finished, the tension cord was used to bring compression into the shell causing an upward movement. This enabled a fast and easy removal of the formwork. Torroja was a smart engineer; he confined the shell to the compression zone and used curvature from cylindrical cantilevering vaults to obtain sufficient rigidity between the supporting columns. An inventive solution, which later would be used by several other shell engineers like Nervi and Isler. Because the low rising shell is in complete compression, there is no cladding needed to obtain water tightness. At the top of the shell there is an oculus of *9 m* diameter that consists of a triangulated area to provide for daylight in the shell, Fernandez Ordonez and NavarroVera [35]

Figure 2.10. Algeciras market hall (1933) by Eduardo Torroja, www.structurae.co.uk

Three years after finishing the market hall, Torroja constructed the Fronton Recoletos in Madrid in 1936. The Fronton Recoletos, seen Figure 2.11, consists of two large intersecting cylindrical vaults, only supported at the two end facades. The structure was built as a basketball stadium (in contrast to the often impute function of concert hall). The cylindrical shells have a radius of *6.4* and *12.2 m* and together span an area of *55* by *32.6 m*. The thickness of the shell is only *85 mm*, except in the region in which both cylindrical shells meet each other. For placement of extra reinforcement to absorb the large tension forces, the shell is thickened there. Daylight enters through large triangular sections in both cylinders. Unfortunately, the Fronton Recoletos was destroyed in 1936 in the Spanish Civil War (1936-1939), Fernandez Ordonez and NavarroVera [35].

Figure 2.11. Fronton Recoletos (1936) by Eduardo Torroja, Fernandez Ordonez and Navarro Vera 1999

In the same year as Torroja completed the Fronton Recoletos he also completed the much celebrated grandstand of the hippodrome La Zarzuela in Madrid. The structure consists of neighbouring *12.8 m* cantilevering hyperboloid umbrella shells. The shells are only *50 mm* thick and. The shells are supported by a mechanism of compression studs and tension rods to compensate the cantilever. Torroja used an overhanging base structure to raise tension forces needed for balancing the cantilevering shell, resulting in a cunning ensemble of compensating forces. Also the Zarzuela shell was under attack during the Spanish Civil War, but withstood several impacts, Fernandez Ordonez and Navarro Vera [35]. The structure is illustrated in Figure 2.12.

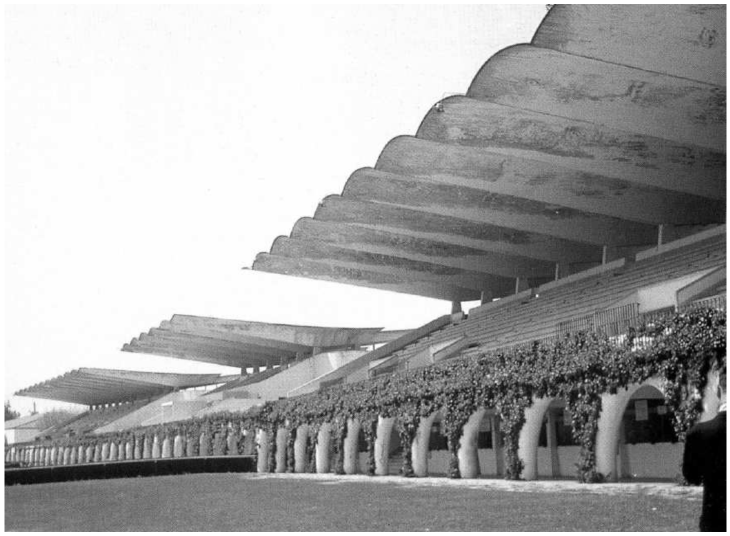

Figure 2.12. Hippodrome La Zarzuela (1936) by Eduardo Torroja, Fernandez Ordonez and Navarro Vera 1999

Near the end of the *1930s* the shell structures of Freyssinet, Dischinger, Finsterwalder, Tedesko, Torroja and Nervi attracted the attention of other great engineers of that time, like Robert Maillart (1872-1940). They where beginning to see that thin concrete shell structures can cover the roofs of various buildings efficiently and aesthetically. Swiss innovating engineer Robert Maillart, famous for his reinforced concrete arch bridges of high slenderness, designed his first shell structure in 1939. Maillart constructed an exposition hall in Zurich, a hyperbolic curved shell of *16 m* height, *12 m* span and a thickness of *60 mm*, seen in Figure 2.13. Remarkable, the main vertical load is carried only by four tapered columns, Billington [7]. His positive experiences would probably have leaded to more shell structures if he had not suddenly died shortly after completion in 1940 at the age of *68*.

Figure 2.13. Zurich Exposition Hall (1939) by Robert Maillart, Giovannardi 2007

The history of concrete shells in the UK, closely related to influential engineer Ove Arup (1895-1988), shows a slower initial progress than the rest of Europe, with the first reinforced concrete shells appearing in the late *1930s*, just before the inception of the Second World War. Also the shell construction in The Netherlands and Belgium is largely a post-war event.

2.3 World War II (1939-1945)

The inception of the Second World War caused an interruption in shell development. Throughout entire Europe the construction of new shell structures vanished as proposals for new shells were rejected. For example in Germany where two designs of Finsterwalder, a large dome of *280 m* span for a stadium in Munich in 1939 and a *250 m* span shell for a congress hall in Berlin, were not realised as the German leader Hitler rejected concrete shell architecture, Dicleli [30]. Furthermore, during the war several existing shell structures, such as the airplane hangars of Nervi, were demolished.

Although shell construction in Europe was disturbed during the war, the construction of shell structures in the USA continued and started in South America. Brazilian Architect Oscar Niemeyer (1907-) may be seen as the founder of the Brazilian thin shell structures, Underwood [75]. Oscar Niemeyer is considered to be one of the most important architects in international modern architecture and was a pioneer in constructing with reinforced concrete. Making use of the favourable reinforced concrete characteristics he constructed several thin shell structures. The 1943 Pampulha Church of Sao Francisco de Assis near the village of Belo Horizonte was the first shell of Niemeyer as it was of Brazil and South America. The Church is seen in Figure 2.14. It immediately caused controversy as the conservative church authorities refused to inaugurate the building due to the unorthodox shape and external paintings of Candido Portinari, Underwood [75].

Figure 2.14. Pampulha Church of Sao Francisco de Assis (1943) by Oscar Niemeyer, http://pt.trekearth.com

Following the Pampulha project Niemeyer would design several shells receiving orders from Juscelino Kubitschek, first major of the city of Belo Horizonte and later president of Brazil. Niemeyer is most famous for his architectural contribution to the new capital Brasilia, founded by Kubitschek in 1960, in which he constructed all buildings of importance as the Nation Congress and the Cathedral of Brasilia, Figure 2.15, Underwood [75]. Although, Oscar Niemeyer introduced thin shells in Brazil, he did not have much following. It would last until 1951 before Felix Candela promoted shell construction throughout the entire continent and beyond.

Figure 2.15. The 1960 shell structures of Oscar Niemeyer in Brasilia, the national congress (left) and the national museum (right), http://en.wikipedia.org

2.4 Blooming Period, Sudden Death (1945-1970)

However, the Second World War had a catastrophic and destructive effect throughout entire Europe; the consequences of the war for shells were two sided. Besides disturbed shell construction and shell demolishing, the post-war reconstruction period created exactly those conditions that are needed for flourishing shell construction. Low labour costs and the need for many new buildings and (as a consequence) the construction material, and in particular steel, being in short supply. Hence, the need for structures which offer economical material use: shells. The post-war reconstruction consequently served as main catalyst for the start of a blooming period of shell construction. The labour intensive construction of the complex shape could be economically justified through the significant savings in materials. Thus, the economy in construction was the key to the popularity of thin concrete shells at that time.

Figure 2.16. Cruise Terminal (1949) Rotterdam, www.locaties.nl

Throughout entire Europe, shell construction gained high interest. Many industrial shells were built in Italy. In France, new engineers as Rene Sarger and Nicolas Esquillan contributed to the revival by building market halls, while in Germany Dyckerhoff & Widmann AG constructed many shells with their Zeiss-Dywidag system. The Zeiss-Dywidag system was also used a number of times in the Netherlands for cylindrical shells, such as storehouses in Hilversum and Amsterdam and the 1949 Cruise Terminal in Rotterdam, seen in Figure 2.16, Garcia [37]. Although it is often assumed that shell structures are quite unknown in the Netherlands, a report carried out by the Dutch magazine *Cement* [43] in the year 1961, recorded *131* shell structures by then, mainly domes (*14*), cylindrical shells (*35*) and shed frames (*41*). Most of them are for industrial purposes, which might be the reason of unknowingness. A major contribution to the Dutch shell history was delivered by Prof. A.M. Haas, the successor of Eduardo Torroja as the second President of the IASS. Haas contributed as researcher (buckling research on cylindrical shells together with Van Koten during the *1960s*), designer (e.g. ANWB Building, The Hague) and Professor (Delft University of Technology). Furthermore, he wrote a series of books on shells (e.g. Design of Thin Concrete Shells [42]).

Also in Belgium, shell construction commenced in the early post-war years. The key Figure in design, construction and popularisation was English born André Paduart (1914-1985), Espion et al. [32]. In particular the 1948 shells at the Antwerp harbour attained international attention, as specialist designers noticed the originality of the construction as the cylindrical shells were constructed one after another by reusing the same formwork and balancing the outward thrust with temporary ties. A total of $50000\ m^2$ was covered by large cylindrical shells with spans of $15\ m$ and a thickness of 80 to $120\ mm$. Paduart worked as engineer for the SETRA Company and did pioneering work for the Comité Européen du Béton (CEB) and in 1971 he was elected as the third president of the IASS, after Torroja and Haas. Paduart remained president until 1980.

Besides continental Europe, the post-war scarcity gave an enormous boost to the use of shell roofing in Britain. The shells were designed by known UK specialist designers like Ove Arup and Felix Samuely. Moreover the construction of thin reinforced shells extended to the Eastern part of Europe and Russia. The names of Czech Konrad Hruben, Romanian Mircea Mihailescu and later Bulgarian Ilia Doganoff must be mentioned as important shell builders.

The sudden surge of popularity of shells was further stimulated in the mid 1950s by the work of Felix Candela (1910-1997) in Mexico. Felix Candela, a Spanish-Mexican engineer, is most famous for his hypar shaped shell structures. He can claim on constructing an impressive series of exciting and beautiful hypar shells, inspiring many new (shell) engineers and architects.

Candela decided to practice shell engineer as he was inspired by Eduardo Torroja's Fronton Recoletos, but an attempt to go to Germany and benefit from German engineers Dischinger and Finsterwalder failed because of the sudden inception of the Spanish civil war in 1936. Candela stayed in Spain and fight, sided with the republic, against Franco. After imprisoned in France, liberation came by a ship to Mexico chartered by fellow republicans and there Candela would design his renowned hypar shells, Colin [23]. The first attempts on hypar shells were done by French engineers Bernard Laffaille and Fernand Aimond who committed theoretical investigations in 1933-36. Moreover, Italian engineer Giorgio Baroni constructed a few hypar shells at the end of the *1940s* in Milan and Ferrara, Popov and Medwadowski [62]. The hypar shape remained unknown until Candela started experimenting with hypar shells in Mexico in 1951 and, however Felix Candela did not invent the hypar shell shape, he is solely responsible for the wide popularisation of the form in the early *1950s*. The success of the form rests for the architect in its appealing aspect, for the structural engineer in its simple structural analysis (under the oversimplifying assumptions of membrane behaviour) and for the contractor in its economical formwork consisting in a system of straight planks supported by another system of straight lines, Bradshaw et al. [18].

Candela constructed his first hypar shell for a laboratory building for the University of Mexico. The University needed a laboratory for measuring neutrons and the roof had to be thin enough to admit cosmic rays. Candela designed and constructed a double curvature shell, his first hyperbolic paraboloid, seen in Figure 2.17. The very thin hypar shell, local as thin as *15 mm*, spans an almost square area of *132 m²*. Despite the double curvature of the shell Candela did not fully trusted the stability, given the fact that he assumed a safety factor of *9* against buckling, Colin [23].

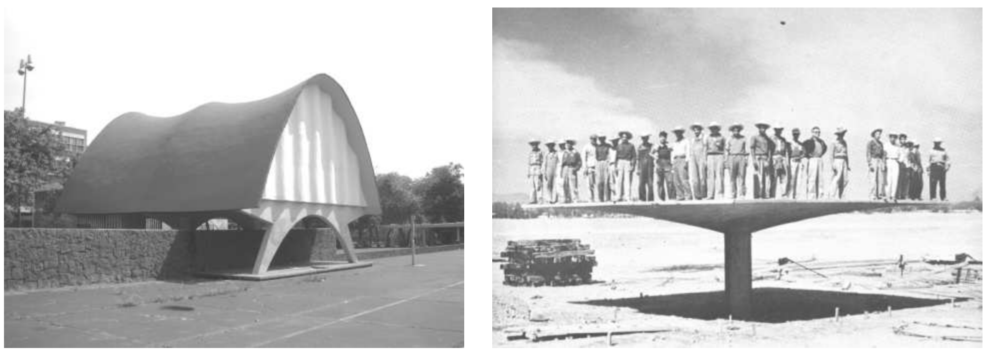

Figure 2.17. Cosmic Rays Pavilion (1951), http://bloggers.ja.bz, and umbrella shell experiment by Candela, Colin 1963

In 1952 Candela started experimenting with hypar umbrella prototypes, a shell geometry which Candela would widely used for factories, warehouses and statues. During experimenting he found the proper rise of the slab to decrease the deflections at the edges and learned about the tendency of flutter in the wind. Candela developed an appropriate and economical footing solution, to overcome the problem of the low bearing capacity of the Mexican subsoil. The footing has the same, but inverted, shape as the umbrella shell. The umbrella shell was as a Candela trademark for low-cost industrial construction, building about *30* umbrellas per week at that time. Mostly designed in groups, the formwork could be used several times and the final structure could be built in a very short period, Colin [23].

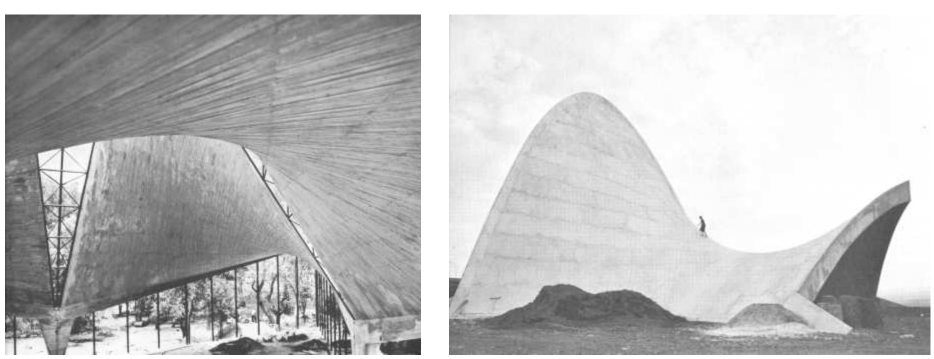

Figure 2.18. Church of San Jose Obrero (1959) near Monterrey and the church of San Felipe de Jesus y la Ascencion del Senor (1959) in Morelos, Mexico, Colin 1963

Candela constructed all (*over 300*) his shells in just two decades. He constructed his most celebrated shells at the end of the 1950s. From 1956 the edge beams disappeared out of the shells designs and the curvy free edges of the structures showed great slenderness and elegance. Candela realised his best known structures which include the 1959 Church San Jose Obrero near Monterrey, seen in Figure 2.18, and the famous 1957 Los Manantiales restaurant in Xochimilco in this period.

If one shell has to be chosen as being the inspiration for a complete generation of new shell engineers, it must be the Los Manantiales Restaurant in Xochimilco, Mexico. Felix Candela completed the shell in 1957 and the design was that much of a success that, at the present day, it has been copied several times. Jorg Schlaich designed a Xochimilco-like shell in 1977 in Stuttgart, Ulrich Muther constructed the Seerose in 1983 in Potsdam and in just recently in 2002 in Valencia another look-a-like has been constructed by Santiago Calatrava: the new l'Oceanografic. Furthermore, famous shell builder Heinz Isler was inspired by the slenderness of the Manantiales restaurant. The original Xochimilco shell, seen on Figure 2.19, is an octagonal groined vault composed of four intersecting hypars.

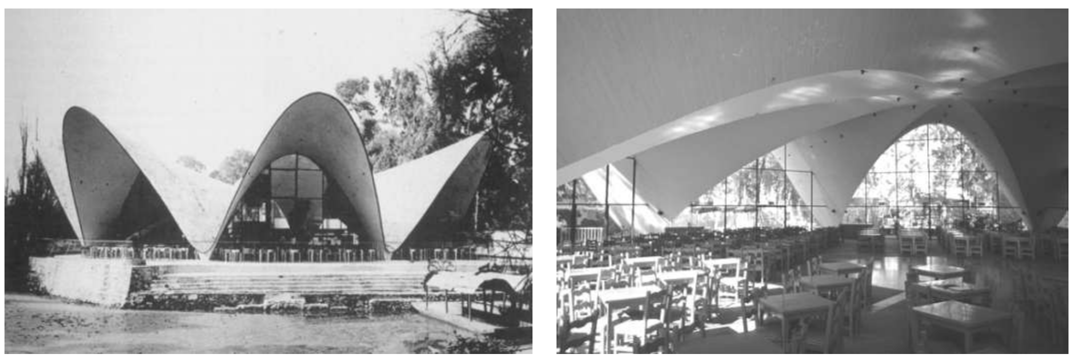

Figure 2.19. Los Manantiales Restaurant (1957) in Xochimilco, Mexico by Felix Candela, www.structurae.co.uk

The efficient structural system and the upward direction of the edges results in a very slender shell structure with a thickness of just *40 mm* and an internal span of *30 m*. In the middle part the shell has a height of *5.8 m* and the edges rise up to *9.9 m*. The supports are connected to each other by a tension rod beneath the floor construction of the shell, capable of compensating the horizontal stress resultants at the supports. The Xochimilco shell is a light, simple and graceful shell and Candela himself considers the shell to be his most significant work, Colin [23].

The shells of Felix Candela are spectacular both for engineering as for appearance. It was an article in *Progressive Architecture* in 1955 on the shells of Candela that launched the modern shell era by attracting the attention of architects, Bradshaw et al. [18]. Until then, the shell industry mainly had build vaults and domes for industrial or military services of little architectural value. Candela showed architects the possibilities of extravagant and fancy shell geometries which they started to use for concert halls, sport buildings, auditoria and even houses. The architectural profession got interested in the apparent 'free forms' of shell constructions and famous architects like Eero Saarinen, Jørn Utzon and Bernard Zehrfuss started to design spatial structures with more luxury shapes and less emphasis on the force flow. The involvement of architects in shell construction was, however, not only beneficial as architects tended to forget that not all curved surfaces are appropriate for thin-shell construction, resulting in shell-like structures in which the curvature is not of any structural use. Therefore, many of the most prominent thin shell constructions designed during the *1950s* by architects were not thin, far overran cost estimates and often performed badly, Billington [7]. Famous examples are the Berlin Congress Hall, the Sydney Opera House, the Kresge Auditorium and the TWA Terminal, seen in Figure 2.20.

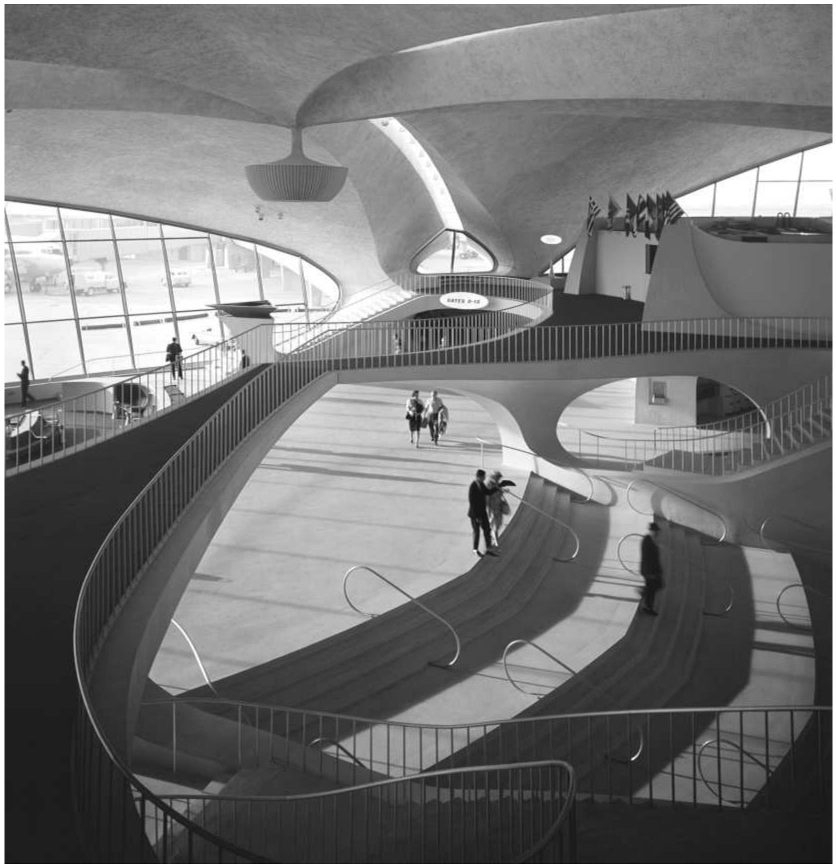

Figure 2.20. Interior of the TWA Terminal (1962) at JFK International Airport by Eero Saarinen, www.mfa.fi

Probably the best example of a bad conditioned shell structure is the Kresge Auditorium on the campus of the Massachusetts Institute of Technology, Figure 2.21. The shell covering the Kresge Auditorium is designed by Finnish architect Eero Saarinen and completed in 1955. The shape of the Auditorium is diverted from the top one-eight part of a hemisphere sliced to a triangular base shape. The shell spans *49 m* at each side and rises up to *15 m*. The thickness of the shell is *650 mm* and the radius of curvature of the hemisphere is *34 m*. The total weight is only *1200 ton*. The Auditorium houses a concert hall with *1226* seats, a theatre with *204* seats and several rehearsal rooms and offices.

The reason for the bad condition of the shell is found in the misunderstanding of the importance of edge effects in shell structures. The shape of the shell implied the use of (large) edge beams to transfer the forces which reach the edge of the shell to the supports. After removal of the scaffolding the edge beam had considerable larger settlement in compare to the thin, flexible shell. Hence, the shell surface was pulled down and the large deformation caused bending and cracking, Ramm and Wall [65]. Due to the cracks the shell lost it water tightness and the problem was not solved until a copper cladding was put on top of the concrete surface. The problems did not end with the structural problems, it was difficult and unusual to construct and significant difficulties were encountered in concrete placement and protection of the reinforcing steel. The repair of the problems was annoying, costly and forced the closure for a few months.

Figure 2.21. Kresge Auditorium (1955) by Eero Saarinen, www.structurae.co.uk

A second example of a bad conditioned shell is the hyper shell of the Berlin Congress Hall constructed in 1957 and designed by American architect Hugh Stubbins, Figure 2.22. The shell was the American contribution to the International Building Exhibition in Berlin. In 1980 the shell partly collapsed after a portion of the prestressing ties failed by corrosion, Ramm and Wall [65]. However, actually, the poor design was responsible for the collapse. Although it looked like a real surface oriented shell, the structure did not allow the shell to exhibit its two dimensional membrane behaviour as the main reinforcement by the already mentioned ties was only unidirectional. After the collapse the shell was rebuilt by a membrane design.

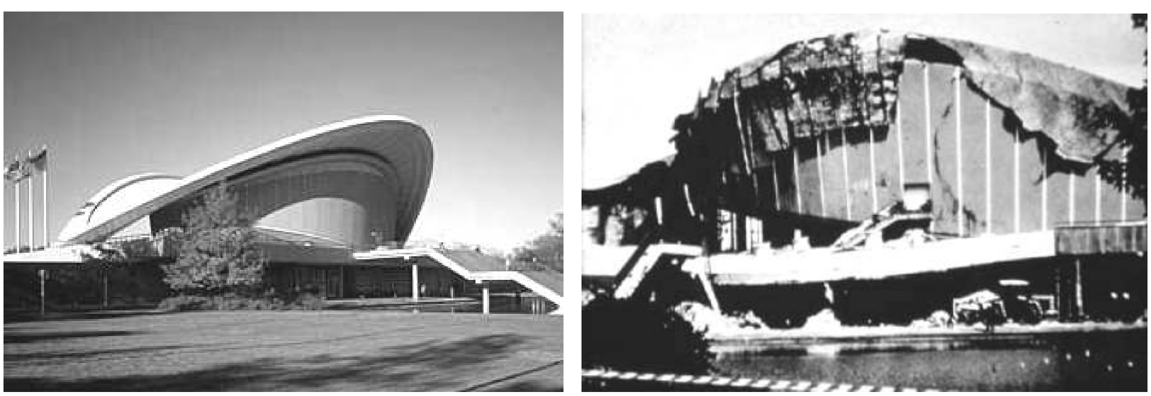

Figure 2.22. Berlin Congress Hall (1957) by Hugh Stubbins, www.archrecord.construction.com

Besides architectural attention, the post-war shell period can be characterised by the search toward greater spans and thinner thicknesses. The short supply of construction materials urged to material economic construction which forced shell engineers to utilise larger spans with the same or even less amount of material. Furthermore, during the cold war, military purposes required long-span shell structures. Where the largest span before the war was *74 m*, in the late *1940s* the spans of shells where already slightly exceeding *100 m*. The search for greater spans led to radically different solutions in the USA and Europe, Espion et al. [32]. The record span at that time in the USA, *103 m*, was achieved by two hangars of the Roberts & Schaefer Company of Anton Tedesko and completed in 1949, see Figure 2.23. The hangars were based at a major military base in Limestone, Maine, and Rapid City, South Dakota. The span was reached by a *130 mm* thick cylindrical shell stiffened with external ribs. The thickness is only slightly increased to *180 mm* at the base. In Europe the record span of *101.5 m* was held by the Marignane hangar which consists of *6* neighbouring double curved *60 mm* thick shells, see Figure 2.23 (the Figure is rather misleading, in reality the span is larger than the supporting wall). The shell is equilibrated by prestressing ties resulting in a much more delicate and appealing structure. It was designed by French engineer Nicolas Esquillan in 1942 but not built before 1952, Espion et al. [32].


Figure 2.23. Airplane hangar (1949) Limestone, Weingardt 2007, and the Marignane hangar (1952), www.structurae.co.uk

Besides the ever growing spans the radii of curvature to thickness ratio increased rapidly. Though, before the war already amazing large ratios where up to *500* obtained, the post-war development advanced to ratios of 800 and even more. The record ratio is hold by the abov e Marignane hall with a ratio of *1470*, however, achieved by placing a series of stiffening ribs in each individual shell lane. The record ratio for single surface shells is kept by the 1957 shopping centre in Kaneohe, Hawaii, with a ratio of *1000*, Popov and Medwadowski [62]. The shell is designed by Richard Bradshaw and illustrated in Figure 2.24.

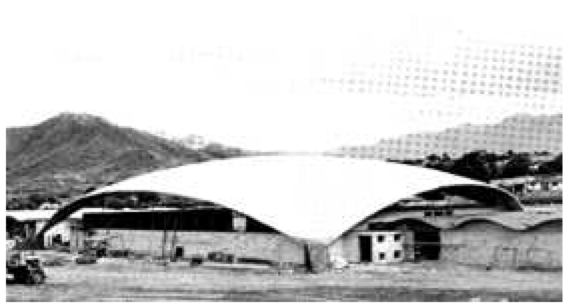

Figure 2.24. Kaneohe Shopping Centre (1957), Joedicke 1962

French engineer Nicolas Esquillan can be seen as the record span builder. Besides the aforementioned Marignane hangar he constructed many long-span shells in the *1950s* and *1960s*, along them the CNIT shell in Paris (1958), the Exposition Palace in Turin (1961) and the Olympic Ice Stadium in Grenoble (1967). At the present day, the Centre des Nouvelles Industries et Technologies (CNIT) in Paris holds the record span for shell structures with a span of *219 m*. The largest shell structure of the world, seen in Figure 2.25, is designed by Bernard Zehrfuss. Zehrfuss designed a triangular ground plan, covered by a large curved surface. The first designs for the cover came from renowned engineers as Nervi and Freyssinet. Their ideas, however, appear to be impracticable due to various reasons. Finally, Esquillan, head engineer of the constructor Entreprises Boussiron, came with the design as it is built today, Caquot [21].

Figure 2.25. CNIT shell (1958) Paris by Nicolas Esquillan, www.insecula.com

The shell of the CNIT is a groined vault, formed from the intersection of three parabolic cylinder segments rising up to *50 m*. The shell has a radius of curvature changing from *90 m* to *420 m* and covers an area of $900000\ m^2$. Buckling considerations forced Esquillan to construct the skin of the shell out of two thin surface layers, connected by cellular shear transferring diaphragms, see Figure 2.26. The thickness of both surface layers is only *170* to *240 mm* and the total thickness of the cross-section develops from *1910 mm* at the top to *2740 mm* at the support, Caquot [21]. Therefore, the thickness to radii ratio of the shell is rather large, *1:47* to *1:153*, but misleading. During construction a movable framework was used and many parts were prefabricated to save costs.

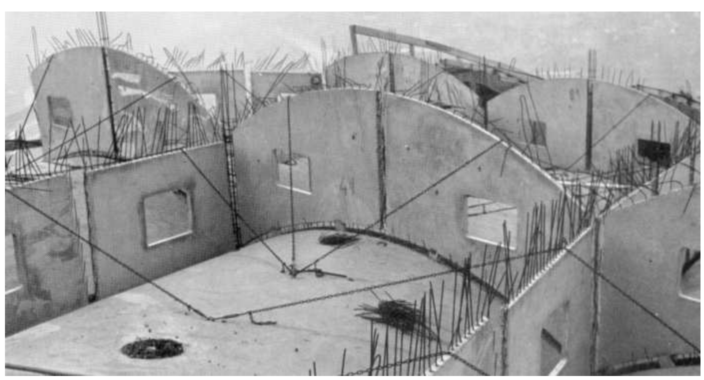

Figure 2.26. The double skin of the CNIT shell in Paris with prefabricated shear transferring diaphragms, Joedicke 1962

A remarkable part of the shell structure forms the tensile cord which is applied beneath the ground surface to counteract the pointing outward thrust forces at each support. Due to underground entrance and service shafts, the cord needed to be lowered in the middle part forming a trapezoidal shape with two bending points. To ensure the cable stays in place, the bending points are fixed in place with *8* vertical and *8* horizontal tensile cords each, anchored in the ground, Caquot [21].

Esquillan's other long span shells, the Turin Exposition Palace and the Grenoble Stadium, may not be the largest in the world, they still are special as they served as Olympic Stadium. However shells are par excellence suitable for covering sport halls, shells have played only a minor role for the most important sport event in the world; the Olympic Games. The only two shell engineers having a special connection with the Olympic Games are Nicolas Esquillan and Pier Luigi Nervi. In fact, Nervi is probably most famous for his contribution to the 1960 Olympic Games sport facilities in Rome, the Olympic Games which gave Rome the possibility to show the world its re-birth from the ruins of the Second World War, Desideri [28].

Figure 2.27. Palazzetto dello Sport (1960) Rome, www.structurae.co.uk

For the 1960 Olympic Games, Nervi designed the Olympic Stadium, which is nowadays in use as a football stadium (Lazio and AS Roma), and two domed sport arenas, the Palazzetto dello Sport (small sport palace), Figure 2.27, and the larger Palazzo dello Sport. Both arenas have a double curved shell roof construction which is built using prefabricated aced shaped ferrocement elements filled with poured-in-place concrete. Ferrocement, a material composed of several layers of steel mesh sprayed with cement mortar requiring no formwork, was developed by Nervi a view years earlier for moulds of clean surface to save time and costs in the construction of the Turin exhibition hall, Desideri [28]. The dome with webbed ceiling of the Palazzetto dello Sport covers a basketball field and a stand of *5000* seats, which Nervi also designed in reinforced concrete. At the top, daylight enters via a compression ring and a cupola. The base of the shell is supported by exterior Y-shaped buttresses which rest on a pre-stressed reinforced concrete ring. The Palazzo dello Sport seats *16000* people under the webbed ceiling which is stabilised by a tension ring, Desideri [28]. Unfortunately, the impressive construction is not seen on the outside, due to the peripheral gallery surrounding the structure.

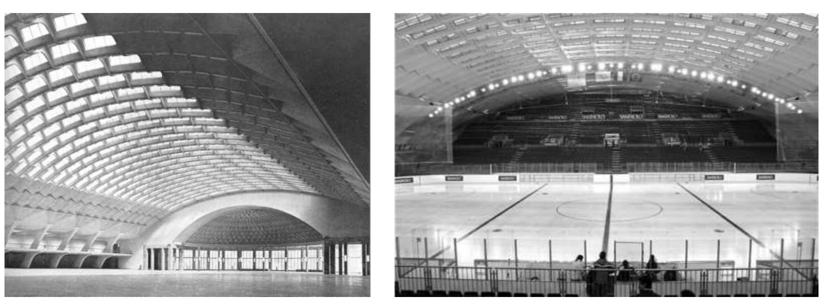

Figure 2.28. Turin Exhibition hall (1949) after construction and during the 2006 Olympic Games, www.structurae.co.uk

The 1960 Olympics where not the only Olympic Games at which Nervi contributed. However, the second time was without his consciousness. When to Olympic committee needed housing for the Ice-hockey tournament of the 2006 Olympic Games in Turin they found the Turin exhibition hall which Nervi constructed in 1949. The shell is illustrated in Figure 2.28. The 2006 Olympic Games did not only reuse Nervi's Exhibition hall in Turin. The committee also decided to give the Turin Exposition Palace of Nicolas Esquillan an Olympic rebirth as being the home of the Ice-dancing event. The Turin Exposition Palace, one of the long-span shells that French engineer Nicolas Esquillan constructed, is a large groined vault shell with a span of *130 m* between the supports and has a rise of *29 m*. The shell has a hexagonal plan which is created by the overhang of the free edges of three intersecting cylinders. As with the CNIT shell, buckling considerations forced Esquillan to design a double skin cellular shell surface, Scordelis [69]. The shell cross-section consists of two layers of *60 mm* which are coupled by a *1300 mm* diaphragm. Esquillan finished the structure in 1961, and just before the Games in 2006, a complete Ice-hall was built under the shell, indicating its immense proportions. The shell is seen in Figure 2.29.

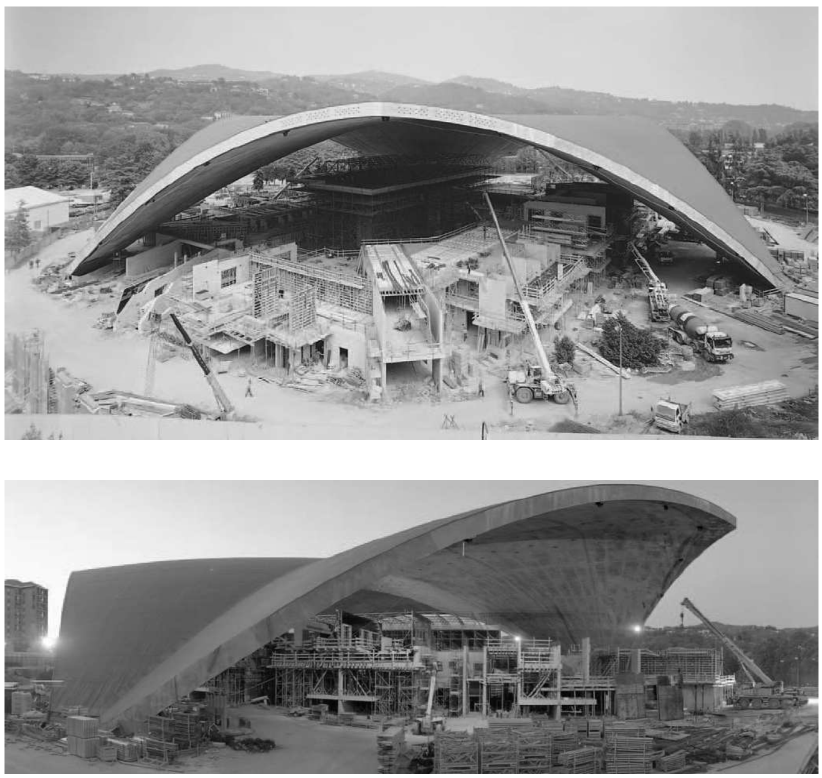

Figure 2.29. The new Olympic facility beneath the Turin Exposition Palace (1961) of Nicolas Esquillan, Salardi 2006

It was not the first time a shell of Esquillan was used as sport facility for the Olympic Games. For the Olympic Games in 1968 in Grenoble, Esquillan designed a long-span groined vault which was based on the same principles as the double-skinned CNIT and Turin shells. The Grenoble shell consists of two intersecting cylindrical vaults with approximate spans of *91* and *61 m*. The shell has a double skin with two layers of *60 mm* and a diaphragm of *1300 mm* and raises up to *18.9* and *13.7 m*.

The emphasis of shell construction lay in the years between 1950 and 1970. Under the leading of the great engineers, many shells were built throughout Europe and the United States. Along them Dyckerhoff & Widmann and Fred Severud in Germany, Freyssinet, Sarger, Hereng and Esquillan in France, Ammann &

Whitney, Anton Tedesko, Richard Bradshaw in the USA, Felix Candela in Mexico, Giorgio Baroni and Pier Luigi Nervi in Italy and later the USA, Torroja in Spain, Arup and Samuely in the UK, and Mircea Mihailescu, Konrad Hruben and Ilja Doganoff in East Europe.

Figure 2.30. St. Louis Airport by Tedesko, www.ketchum.org, and the Auditorium in Hamburg by Dyckerhoff & Widmann, http://en.wikipedia.org

During this period many famous shell structures were constructed, such as the aforementioned Kresge Auditorium, the Palazzetto dello Sport, the shells of Candela including the Xochimilco restaurant, the Hamburg University Auditorium, the Kaneohe Shopping centre, the TWA Terminal, the St. Louis airport shell, the long span shells of Esquillan, etc. Some shells of this period are seen in Figure 2.30 and 2.31.

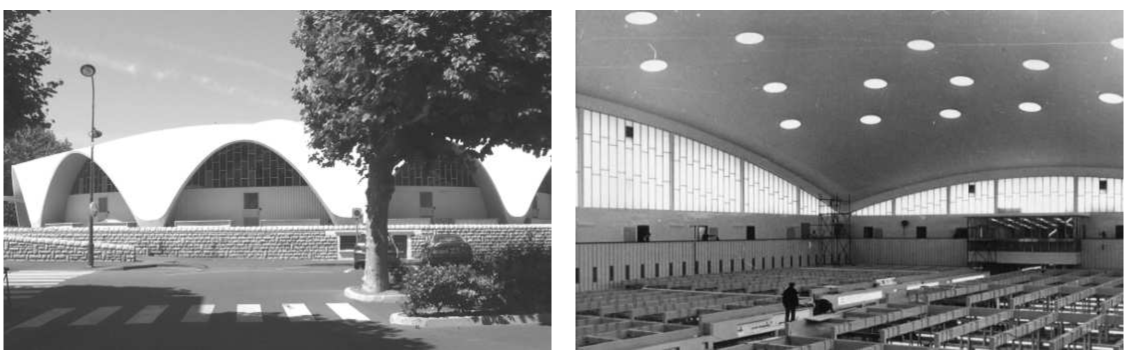

Figure 2.31. The Royan Market hall (1956) by Sarger, www.structurae.co.uk, and the Smithfield Poultry Market (1963) in London by Arup, www.viewimages.com

In the blooming period also a few shells have been constructed in Africa, for example Torroja's Fedala reservoir in Mohamedia near the west coast of Morocco in 1957, the 1968 University of Constantine in Algeria by Niemeyer, both seen in Figure 2.32, and a sports hall in Pretoria, South Africa. However, bad economical, constructural and climatological circumstances have prevented shell success.

By the late *1960s*, a curious paradox became evident. Although more and more articles appeared on thin shell analysis and construction, fewer and fewer shells were being built, Billington [7]. The costs of labour increased and shell engineers were forced to start their search for, simpler, faster and more economical, construction techniques. The conventional construction method of spatial curved wooden formwork supported on steel framework became too expensive and time consuming for shells to compete with other structural systems. The first attempts to new construction techniques were already done by Pier Luigi Nervi, first with prefabricated lattice beams and later with the ferrocement moulds (as well stay behind as re-usable) in combination with poured-in-place concrete. These small prefabricated parts eventually evolved to the large prefabricated shell elements seen today, e.g. the 1977 Stuttgart Federal Garden Fair shell of Jörg Schlaich, fabricated from 8 parts, and the 2003 Shawnessy LRT Station in Calgary. Aforementioned, alongside with Nervi, Nicolas Esquillan used prefabricated elements for the construction of his long-span shells in which he also saved costs by using a movable framework; the skin was poured in place on a moveable frame which each time moved outwards for realisation of neighbouring segments.


Figure 2.32. University of Constantine (1968) by Niemeyer, www.arcspace.com, and the Fedala Reservoir (1957) of Torroja, www.structurae.co.uk

An engineer that contributed major to new construction techniques is Heinz Isler (1926-). The innovation in construction of Heinz Isler provide in large scale re-use of formwork. Isler reused special formwork for standard sized bubble shells, developed in collaboration with the Bösiger Construction Company. The economical, fast and simple construction method enabled Isler to build several shells until the *1990s*, despite the ever increasing labour costs. Isler showed that shells where still wanted and still economically viable.

Heinz Isler can be considered as the most important shell engineer at the present day and the founder of modern free-form design and shape optimisation. However, Isler started designing shell structures at the end of the *1950s*, at a time in which increasing labour costs in Europe became a growing threat for shells, he was still able to make career by developing an economical construction method based on standardised bubble shells, Chilton [22]. He developed in the early *1950s* the bubble shell from his observations of a pumped-up pillow. The bubble shell appeared to be the answer to the growing labour costs as it was suitable for a standardised construction method. Because of the rigid strong curved corner ribs bubble shells transfer about *90%* of their total load directly to the corner supports. This enabled Isler to make a standard type of bubble shell on four supports mainly used for small industrial units, garages and warehouses. By prestressing the edge beams the supporting columns only had to transfer vertical load. Heinz Isler developed in combination with the Bösiger Construction Company standard sizes and re-usable formwork and falsework to economise the construction. Most of them were *80* to *100 mm* with spans of ranging in size from 14×20 m to 25×25 m. For daylight and ventilation, they are executed with domed roof lights. The standard shell can be seen in Figure 2.33.

The bubble shell is the most commonly constructed shell of Heinz Isler. Between 1956 and 1985 a total of *749* shells of this type, generally arranged in groups, were constructed. The largest bubble shell of Heinz Isler was constructed in 1960 as a distribution facility for railway wagons. The shell spans $54.6 \times 58.8\ m$ with a centre rise of $9\ m$ and contained *17* circular roof lights. The edge of the shell is supported by six intermediate supports resulting in a column free area of over $3200\ m^2$. Isler was concerned about the buckling behaviour due to the fact that parts of the shell were close to cylindrical in form, a shape with a much lower buckling resistance. He thickened the shell to $150\ mm$ in critical areas. Concreting took three consecutive days and night, using around $1000\ m^3$ of concrete, Chilton [22].

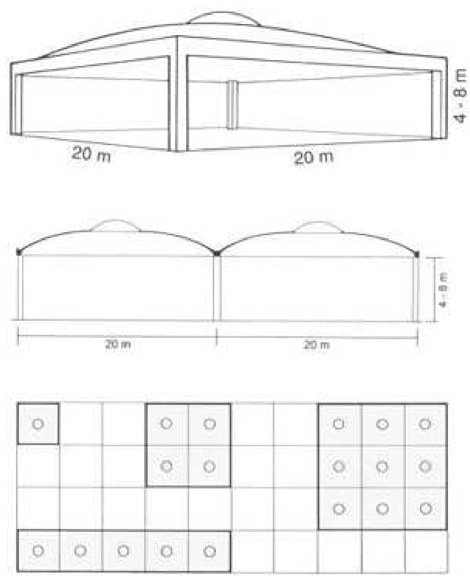

Figure 2.33. The 1950 standard Bubbleshell from the Bösiger Construction Company, www.boesiger-ag.ch

While the bubble shell is Isler's most commonly constructed shell, Isler obtained world-wide fame with his pioneering experimental free-form shells. When Isler recognised a plumped-up pillow on his bed as the continuously curved shape he searched for a roof of a concert hall at the hotel Kreuz in Langental, he realised that a physical model was the solution for designing free-formed shells, Chilton [22]. Isler started to construct numerous shells by finding the most efficient form and then perform small-scale model tests to verify their performance. The shells can be classified on the way their efficient form is determined, the aforementioned 'Bubble' shells, free form expansion shells and free-form shells from hanging membranes.

Figure 2.34. The Wyss Garden Centre (1962) and the Bellinzona Supermarket (1964) by Heinz Isler, Chilton 2000

Isler's first free-expansion form shell was realised in 1962, the Wyss Garden Centre in Solothurn, and ended in 1973 with the Bürgi Garden Centre in Camorino. However these shells are free form in the sense that they are not consisting of a regular geometry, they are based on combinations of circular curves, Chilton [22]. This was the reason for the lack of efficiency in shape, which resulted in problems like tensile stresses in the shell surface (Wyss Garden Centre) or the need for vertical prestressing to pull-down the free edge near the supported corners (Bellinzona shell). In Figure 2.34 the painted Wyss Garden Centre and the rather forced shape of the Bellinzona shell can be seen.

Figure 2.35. Deitingen Service Station (1968) and the Sicli shell (1969) in Geneva by Heinz Isler, Chilton 2000

Free-form shells from hanging membranes solved the problems encountered by the expansion formed shells. Furthermore, the inverted hanging membranes helped Isler to fulfil his wish to show the slender character of the thin concrete shell as he had seen by Felix Candela's Manantiales restaurant in Xochimilco. According to Isler, the shell shapes derived with hanging models give the best performance, due to the fact that they are almost pure compression structures, Chilton [22]. Form follows force. The first shell of Isler being built following the hanging membrane technique is the shell over a service station near Deitingen, built in 1968. Two shells are symmetrically situated on each side of an amenity building, which houses the facilities of the service station, see Figure 2.35. The *31.6 m* long and *26.0 m* wide shells rise up to *11.5 m* above the ground and have a thickness of *90 mm*. Prestressed ties in the subsoil connect the outer supports with the base of the amenity building, so that the outward thrust is balanced. The slab of the amenity building transmits the inward horizontal thrust. During construction the shells where balanced with temporary ties. This made it possible to construct both shells separately and, more important, to make use of the formwork twice. To introduce compressive stresses into the shell surface, the two outer supports were moved *12 mm* towards the central building, Chilton [22]. The concrete of both shells has a white external protection and is still, after 39 years, in perfect condition. However, Isler's most impressive job is that he realised the shell without the need for edge beams.

Isler's most complex prestressed concrete shell distracted from a hanging membrane is probably the shell being built for a factory of Sicli in Geneva in 1969, also seen in Figure 2.35. The seven-point supported irregular surface has spans of *35 m* and a general thickness of *100 mm*. There are no edge beams required as the forces flow away of the slightly curved up edges. Due to its complexity, Isler has measured the behaviour of the shell over almost *20* years.

Isler presented his innovative method of form-finding of shells for the first time to the engineering and architectural establishment in 1959 in Madrid at the First Congress of the International Association for Shell Structures, founded and at that time also presided by Eduardo Torroja. He discussed three methods of form-finding, 'the freely shaped hill, the membrane under pressure and the hanging cloth reversed'. The presentation had an enormous impact and eminent engineers, like Ove Arup, Eduardo Torroja and Nicolas Esquillan, where somewhat sceptical of the ideas proposed by Isler. Today Heinz Isler has designed nearly 1000 thin concrete shell structures, most of them in Switzerland. He returned to the *20th* Anniversary Congress of IASS in 1979 as a keynote speaker and is now member of the IASS Executive Council, Chilton [22]. As Felix Candela was the undisputed shell master builder, is difficult to believe that his shells could be surpassed in elegance. But Isler's shells are even better. His wish to intervene gently in nature leaves us some exceptional light and extreme thin shell structures, see Figure 2.36.

Figure 2.36. Aichtal Outdoor Theatre (1977) by Heinz Isler, Flury 2002

After the immense success of shell construction in the *1950s* and *1960s* there was a sudden death in shell construction in the early *1970s*. The sudden death can be clarified by the changes in the society. Aforementioned, where, at first, the labour intensive construction of the complex shape was economically justified through significant savings in materials, the high rise of European and American labour costs made that shells became very expensive in compare to other structural systems. This was already the reason that during the *1960s* the emphasis of shell construction moved to developing countries in South America, where labour is often cheap and material still costly. Moreover, inflexible usability and uncertainties in the behaviour of shells and difficulty of proper analysis methods did not help and neither did the stylistic identification with the *50s* and *60s*. All these circumstances urged the end of large-scale shell construction in Europe and the USA. The only shells constructed were possible through inventive solutions to reduce costs, as the bubble-shell of Isler, or shells for industrial purposes, as cooling towers.

2.5 Contemporary Shells (1970-2008)

During the golden years the first shell builders where succeed by a new generation of spatial engineers. It was Isler in Switzerland, Ulrich Müther (1934-), Jörg Schlaich (1934-) and Frei Otto (1925-) in Germany, several engineers such as Jack Christiansen in the USA and Eladio Dieste (1917-2000) in Uruguay. The new generation of spatial designers continued the concrete shell voyage as it was developed by the first shell engineers, however, obliged by increasing labour costs (among other things), they also searched for new types of spatial structures. Engineers like Müther remained active in conventional concrete shell structures. Müther constructed many shell structures in Germany from 1965. He can be considered the most important shell builder in Germany after Dischinger and Finsterwalder, Dechau [27]. Several Americans engineers constructed concrete shells for churches and large sport arenas, a typical American tradition. Jack Christiansen is one of them and known from his contribution to the Seattle Kingdome, a large sport arena which was built in 1975. The Seattle Kingdome was the world's largest thin shell concrete dome with a span of *202 m* until demolished in March 2000.

Figure 2.37. Teepott restaurant (1968) by Ulrich Müther, www.structurae.co.uk and the Seattle Kingdome (1976) by Jack Christiansen, http://www.arche.psu.edu

The search for new spatial structures resulted in widespread pioneering with new types of shells. Jörg Schlaich constructed a few concrete shells before he started experimenting with glass reinforced concrete shells and later with grid shells, a shell where the continuous surface is replaced by linear or curvilinear interconnected members. By constructing the grid shells from triangular elements or quadrilaterals with internal tie rods the spatial grid acts like a real shell structure, if the curvature allows for membrane stresses to develop. The grid shell was originally developed by Frei Otto in the late *60s* and is mostly built with steel or timber (but sometimes even concrete, see Figure 2.38). In that period Otto also developed the tensioned membranes as spatial structure, e.g. the 1957 Dance Pavilion at the Federal Garden Exhibition. From the same period is the geodesic dome for the Montreal Expo in 1967 by Richard Buckminster Fuller, Holgate [46]. Besides the new grid shells, Eladio Dieste in Uruguay became famous with his reinforced brick shells which show large similarities with reinforced concrete shells, see Figure 2.38.

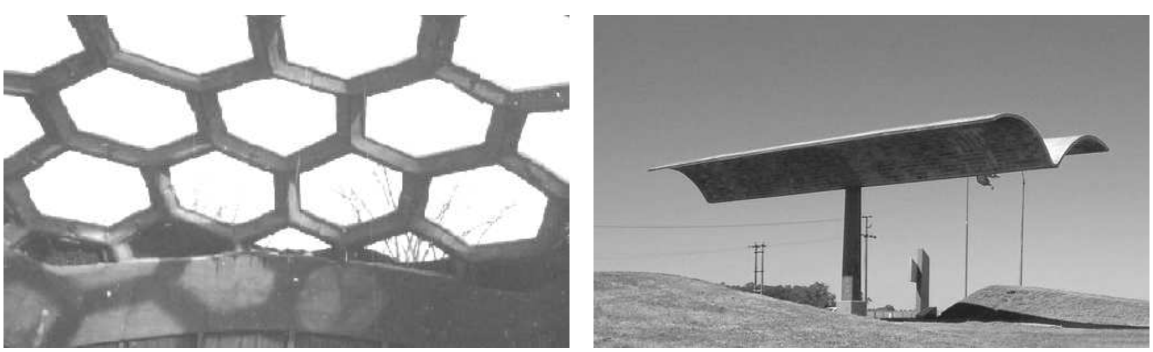

Figure 2.38. Unknown concrete honeycomb grid shell and a reinforced brick shell of Eladio Dieste, http.nl.wikipedia.org

An important development for fast and more economical shell construction was the concept of the air inflated membranes as formwork for concrete shells. The concept, that came from the search of new, more economical, construction techniques, was already developed by Wallace Neff in the *1940s* (he received a patent in the system in 1942). However, it did not find much application until the late *1970s*. Wallace Neff's patent involved an inflated membrane to the shape of a shell structure and subsequently placing reinforcement and shotcrete on the exterior to form the final shell. Later, Dante Bini developed and patented (BINI 1986) the BINI Shell, which is also based on an inflated airform, however, the reinforcement and concrete are placed in the exterior before inflation. Dante Bini constructed the first shell houses in 1954 in Florida. Alternatively, Lloyd Turner inverted the principle and applied a foam structural layer on the internal airform. He achieved a patent in 1972. A breakthrough to long-span airform shell was the development of the Monolithic Dome by the South brothers, Figure 2.39. The monolithic dome concept involves, besides a polyurethane foam layer, reinforcement and shotcrete to construct a thin concrete shell. The practicality and workability of the process was first proven in 1975 for the construction of a potato storage facility of a height of *9 m* and a diameter of *26 m*. For that project the patent was earned in 1979, Monolithic Dome [94].

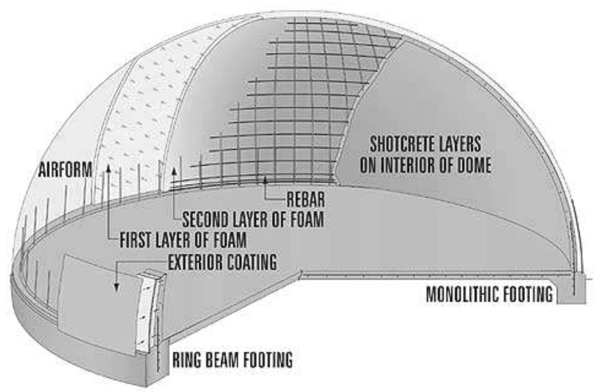

Figure 2.39. The Monolithic Dome concept, www.monolithic.com

Since 1976 the Monolithic Dome concept is used for the construction of houses, schools, churches, sport and commercial facilities in *45* states and many countries over the world. At the present day, the innovative construction method is still gaining popularity for as well long-span shells up to *300 m* as for small houses in developing countries (Solid House Foundation). However their aesthetical appearance is questioned, the domes are wanted due to the advantages of low costs, energy efficiency, low maintenance requirements, their strength and stiffness and their relative simple construction, Monolithic Dome [94].

Despite the new construction techniques, today, reinforced concrete shells find only minor application and are mostly built using conventional formwork. The shells which are constructed, however, can be of high architectural and structural value. Due to the computational advancement, architects are more and more able to construct highly esthetical free-form shapes and so-called blobs. Blobs refer to organic, amoeba, multi curved shaped buildings which first appeared in the mid *1990s* and completely redefined the look of buildings, Bechthold [5]. A designer much involved in contemporary concrete shell designs is Santiago Calatrava. Two of his latest shells, the l'Oceanografic in Valencia and the Tenerife Opera House are illustrated in Figure 2.43. The aforementioned similarity of the l'Oceanografic with the Xochimilco restaurant of Felix Candela is clearly seen. The l'Oceanografic shell and the shell for the Tenerife Opera House are fine examples of the sculpterous capabilities of modern concrete structures.

Figure 2.40. l'Oceanografic (2002) Valencia, www.fundacioncac.es, and the Tenerife Opera House (2003) by Calatrava, http://www.arch.mcgill.ca

In this historical reflection, shells in Asia (in particular Japan and China), Australia and the Middle East are not mentioned. Almost no information on their shell history was found, although several shells are known to be constructed in these continents. Nowadays, thin concrete shells encounter increasing interest in Asia and the Middle East. Examples of recent shell structures are seen in Figure 2.41.

Figure 2.41. The Baha'I House of Worship (1986) in Delhi by architect Fariburz Sahba, www.melburns.com, and Abu Dhabi Conference Centre, www.academie-des-beaux-arts.fr

2.6 Future History (2008-)

Future architecture seems to continue the recent revival of double curved shapes with undefined free-form shapes (*Deconstructivism*), as mentioned, in particular in the Middle East and Asia. Besides their ambition to built sky high, they have increasing interest to curvy shaped landmark buildings. However, also in Europe there seem to be interest to develop special shapes counteracting the rectangular environments which have realised over the last few decades. Two contemporary designs using concrete as base material are illustrated in Figure 2.42. The design of Tadao Ando foresees in a large concrete shell covering a boat housing basin under and above which the museum is situated. The architects of SANAA designed a very shallow thin concrete shell-like landscape for the EPFL Learning Centre in Lausanne, currently in engineering stage.

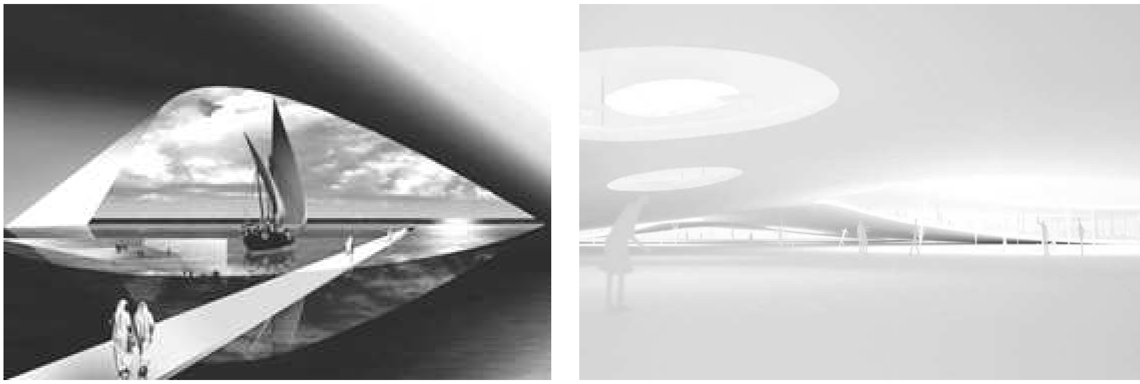

Figure 2.42. Design for the Abu Dhabi Maritime Museum by Tadao Ando, www.tdic.ae, and the design for the EPFL Learning Centre in Lausanne by SANAA, www.normale.net

The curiosity to free-form curved shapes is also seen in the popularity of the designs of architect Zaha Hadid, who won the Pritzker-Price in 2004. In Figure 2.43 her designs for the Sardinia museum in Cagliari and the Opera House in Dubai are seen. Although her designs are not based on concrete as primary construction material, it is not unthinkable they end up (in slightly adapted shapes) as thin concrete shells.

Figure 2.43. Zaha Hadid's designs for the Sardinia Museum in Cagliari and the Dubai Opera House, www.zaha-hadid.com

2.7 National Schools

With the great shell engineers coming from Germany, Italy and Spain, Billington [7] describes three prominent '*national schools*' of thin shell construction. According to Billington distinction can be made in the *German school*, the *Italian school* and the *Spanish school*. Each school has their own traditions encompassing several decades and, more important, their own skilled designers. The German school is pioneered by Dischinger and Finsterwalder and carried forward by Anton Tedesko in the USA. The school, mathematical and scientific, characterise itself by the reliance on basic geometrical forms amenable for mathematical treatment, e.g. cylindrical shells or shells of revolution. The Italian school, historic and artistic, is propagated by Nervi and characterised by a more intuitive than mathematical structural design. The shell shapes are derived from ancient arches, vaults and domes and re-designed in reinforced concrete and ferrocement, i.e. the ribbed Nervi shells are in fact based on the Italian tradition of coffering domes like the Pantheon. These shell structures are much less constrained than those of the German school. The Spanish school, rooted in an artisan building traditions such as the designs of Gaudi, stands for shell shapes primarily motivated by aesthetics. Carried forward by Torroja and Candela, the Spanish school tends to use double curved shapes, as hyperbolic paraboloids, instead of stiffening ribs. Since the late *1950s*, it may be fair to add a fourth school, the Swiss school of free-form shells, founded by Heinz Isler.

2.8 Shell Dimensions

Shell dimensions and thickness to span ratios have increased significantly since the 1925 Zeiss planetarium, first shell of the modern era. Some of the shells constructed since then are shown in the table below, together with the ancient Pantheon and Hagia Sophia. Moreover, the enormous structural capacity of human engineers can be seen by comparing thickness-to-span ratios of modern concrete shells with a hen's egg.

Year	Shell	Geometry	Dimensions	Radius R	Thickness	t/R
-	Hen's Egg	Surface of revolution		20 mm	0.2 to 0.4 mm	1:100 to 1:50
100	Pantheon	Hemisphere	43.3 m (dia)	21.6 m	1.2 m at top	1:24
537	Hagia Sophia	Hemisphere	31 m	15.5 m	0.6 m at top	1:26
1926	Jena Planetarium	Hemisphere	25 m (dia)	12.5 m	60 mm	1:200
1928	Leipzig Market Hall	Segmented shell of revolution	74 m	46 m	90 mm	1:500
1934	Algeciras Market Hall	Spherical cap	47.6 m (dia)	44.1 m	90 mm	1:490
1936	Fronton Recoletos	Cylindrical combination	32.5 m	12.2 m (largest)	85 mm	1: 150
1936	Hershey Arena	Cylindrical vault	70m span	35 m	90 mm	1:390
1955	Auditorium MIT	Segment of a sphere	48.0 m between supports	34.0m	65 mm	1:520
1955	Royan Market Hall	Axisymmetric hypars	52,4 m (dia)	6 m, single hypar 65 m span	80 mm	1:75 1:812
1957	Kaneohe Shopping	Groined Vault	39 x 39 between supports	78m	76mm	1:1000
1957	Palazzetto dello Sport	Spherical cap	58.5 m (dia)	30.9 m	335 m (rib)	1:92
1959	Hamburg Auditorium	Segment of a sphere	50 m between supports	65 m	130mm	1:500

3 Shell Design

Structural design refers to the iterative process of designing an efficient structural system which transfers loads on a structure to the supports. For most building structures the structural design differs from the geometrical design, hence, the distinction between architect and engineer. For shell structures, however, the structural design and the geometrical form converge in the three-dimensional curved shell surface. The shell needs the spatial curvature to develop the profound membrane behaviour and the geometrical shape has major influence on how the shell behaves and how the shell fails. Obviously, the expression 'form active structural surface' finds its origin here. To design an efficient shell structure, it is thus important to provide in an extensive study of the geometrical and structural interaction. There is often referred to the term 'structural morphology'. An optimal shell design provides in an advantageous geometrical and structural interaction which results in a prevalent membrane stress field.

A prevalent membrane stress field forms an efficient load-carrying system without the need for bending moments. Bending moments normally arise when the line of thrust, determined by the loading and supporting conditions, does not coincide with the system line of the structure. In shells, however, circumferential stresses are able to 'correct' the deviating line of thrust back into the system line. By this principle, the surface of a properly designed shell can give rise to quite large shape deviations form the line of thrust while staying in a membrane stress state. Provided that there is sufficient curvature in the other direction, even back curvature is possible. Hence, the geometry and structural behaviour can benefit from each other, giving the designer more architectural freedom.

The important geometrical and structural interaction was already concerning classical master builders. Ancient engineers were well aware of the force flow in shell structures as can be seen in the construction of old domes and churches, for example the famous Pantheon in Rome. The Pantheon in Rome can practically be seen as a combination between an arch and a shell. The upper part of the Pantheon is in compression and acts like a real shell structure. In the lower part, however, tensile stresses arise in circumferential direction. Because their low quality concrete was unable to absorb these tension forces, the lower part of the pantheon acts like an arch. The ancient engineers must have been aware of the tension forces and even must have known the location where the circumferential stresses transform from compression into tension, providing the increase in cross-sectional thickness at the turning point. The larger cross-section makes sure the line of thrust stays inside the system line. In other ancient structures tension is absorbed by the wooded ties placed along the parallel circles of the dome or prevented by constructing domes confined to the compression zone, Farshad [34].

It is presumed that the classical engineers used graphical methods and physical models, like the hanging chain, to construct their arch and shell structures. Although these principles made them conscious about the relation between force and form, they were restricted by their limited constructional possibilities. Therefore, modern shells achieve longer spans with a thickness which is much smaller than the thickness of traditional domes. Not only the higher quality contemporary construction materials capable of resisting tension forces contributed to this development, but also the theoretical knowledge gained from the late 19th century up to the present day. The first basic shell equations which describe the behaviour of thin elastic shell structures were derived in 1888 by Love. The elastic theory he proposed was based on the Kirchhoffean thin plate assumptions. The theory can be described as an extension of the plate theory to structures with surface-like geometries. In 1912 Reissner discovered that the membrane and bending solution can be obtained separately and that superposition of both yields the total solution. This relative simple but effective calculation method handed the early shell builders of the modern era quantitative information about the stresses in shells.

The early shell builders employed only simple geometrical shapes for their shells as stresses in an irregular shape where impossible to determine by hand calculation. Intrigued by the hanging models of the early shell builders, it was Swiss engineer Heinz Isler who developed a new concept for designing shells in the *1950s*. He derived the shell shape from experiments with physical models such as inflatable rubber membranes or hanging fabric. These Isler shells are equilibrium shapes, their shape balances loads through membrane stresses. At the same time, researches at the Frei Otto's Institute of Lightweight Construction at Stuttgart University experimented with form-finding methods for tensile systems by studying minimal surfaces using soap bubbles and other methods.

Up to the present day the theory of shells and the physical models of Isler and Otto are extended by computational design and analysis methods. Numerical analyses facilitate engineers in determining stresses and techniques as form-finding and shape optimisation are automised. These new techniques offer innovative design possibilities to determine membrane supporting shapes, for example for the contemporary free-form blob architecture. Hereby, it must be mentioned that, however often assumed, not all curved surfaces are useful as primary structural elements. Referring back to the first lines of this introduction, surface curvature forms a structural effective shell only if the shell is able to develop membrane stresses. The curvature present in the flowing shapes of the blob architecture seldom allows membrane stresses to develop. The shape algorithms are optimised for visualisation purposes and not for structural membrane behaviour. In practice the free-form of the blob structure is therefore often achieved by conventional structural systems which carry a non-structural building skin or they rely on a hybride structural system in which there is a supporting frame and a supporting skin (like a car). These systems, however, often rely heavily on bending, the least efficient basic load carrying system, while in a sound shell the shell surface itself is the primary structural element and carries the load with the more efficient in-plane membrane stresses. Thus, although, the blob architecture reminds us of thin concrete shells, the structural elegance of the shell often contrasts with the relative clumsiness of the supporting systems of the irregular shapes. Hence, the transformation of the form-active designed blobs to surface-active structures is an area of ongoing research.

3.1 Preliminaries of Shell Design and Analysis

Before determining the structural design of a shell one has to know about the structural behaviour that is observed in shell structures. Especially with shell structures, the structural design is of great importance in developing the advantageous membrane stress field and to prevent uninvited deformations and failure. The most important aspects of the structural behaviour are discussed below.

3.1.1 Membrane Behaviour

The membrane behaviour of shell structures refers to the general state of stress in a shell element that consists of in-plane normal and shear stress resultants which transfer loads to the supports, illustrated in Figure 3.1. In thin shells, the component of stress normal to the shell surface is negligible in comparison to the other internal stress components and therefore neglected in the classical thin shell theories. The initial curvature of the shell surface enables the shell to carry even load perpendicular to the surface by in-plane stresses only.

The carrying of load only by in-plane extensional stresses is closely related to the way in which membranes carry their load. Because the flexural rigidity is much smaller than the extensional rigidity, a membrane under external load mainly produces in-plane stresses. In case of shells, the external load also causes stretching or contraction of the shell as a membrane, without producing significant bending or local curvature changes. Hence, there is referred to the membrane behaviour of shells, described by the membrane theory.

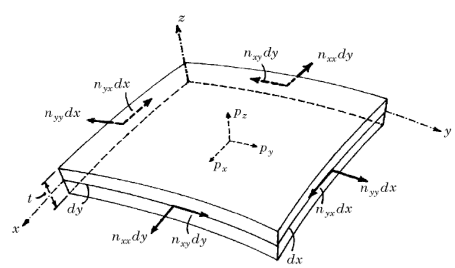

Figure 3.1. Membrane stress field of a shell element, Hoefakker and Blaauwendraad 2003

Carrying the load by in-plane membranes stresses is far more efficient than the mechanism of bending which is often seen by other structural elements such as beams. Consequently, it is possible to construct very thin shell structures. Thin shell structures are unable to resist significant bending moments and, therefore, their design must allow and aim for a predominant membrane state. Bending stresses eventually arise when the membrane stress field is insufficient to satisfy specific equilibrium or deformation requirements.

3.1.2 Bending Behaviour

In regions where the membrane solution is not sufficient for describing the equilibrium and/or deformations requirements, bending moments arise to compensate for the shortcoming of the membrane behaviour. For example at the supports, by local concentrated load (thin shell structures are exceptionally suited to carrying distributed loads, however, they are unsuited to carrying concentrated loads) or a sudden change in geometry the membrane state is disturbed causing bending action, see Figure 3.2. Bending moments only compensate the membrane solution and do not carry loads. Hence, there is often referred to compatibility moments. Due to their compensating character, bending moments are confined to a small region; the major part of the shell still behaves as a true membrane. It is this salient feature of shells that is responsible for the most profound and efficient structural performance!

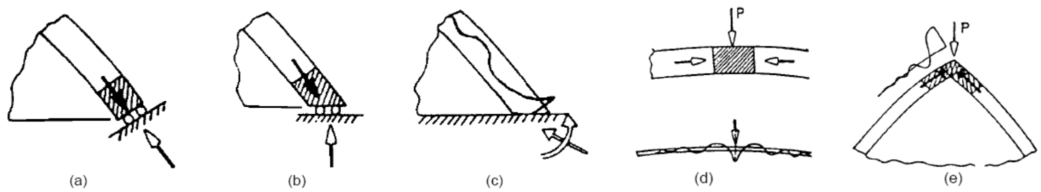

Figure 3.2. Bending moments to compensate the shortcomings of the membrane behaviour, Hoefakker and Blaauwendraad 2003

The preference for membrane action arises as a consequence of being thin. In thicker shells the preference is not so notorious and eventually it may reverse. According to Farshad [34], shells can be categorisation into *membrane-dominated*, *bending dominated* and *mixed shell problems*. The category can be made more specific by considering the asymptotic behaviour of shells.

3.1.3 Material Effects on Shell Behaviour

Reinforced concrete shells have complicated nonlinear material behaviour with strong influence on the structural behaviour. Significant tensile stresses in the shell will cause cracking and with that weakening of the shell cross-section. Micro-cracking at the surface is caused by the evaporation of water. Due to the high amount of surface exposed the micro-cracking in the shell surface may exceed the allowable value. Furthermore, creep of concrete will cause flattening of the shell surface, resulting in less curvature and possible bending stresses to occur. Additionally, shrinkage may lead to unwanted residual stresses. The material behaviour is discussed in detail in Chapter 8.

3.1.4 In-extensional Deformation

An *in-extensional deformation* is a deformation of a shell surface in which only bending moments arise, without producing membrane extension and contraction. Thus, the strains of the middle surface are equal to zero. This special deformation mode is highly undesirable as the shell is unable to produce significant resistance against such deformations. A thin shell has very high in-plane stiffness but the perpendicular direction has very low flexural stiffness. Hence, a shell will have a strong preference for such deformations. Figure 3.3 shows an in-extensional deformation of a circular cylindrical shell due to settlement of the foundation. Consequently, the *ovalisation* of the upper part of the shell produces no strains. A remarkable property of an in-extensional deformation is that the product of the minimal and maximal curvature (*Gaussian curvature*) is equal to the undeformed state.

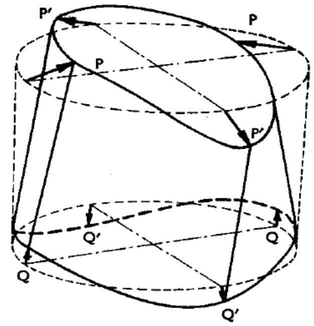

Figure 3.3. In-extensional deformation of a circular cylindrical shell, Hoefakker and Blaauwendraad 2003

A shell is only a shell when it remains it shape when it is loaded. Otherwise in-extensional deformation occurs. Shells sometimes are referred to as form resistant structures.

3.1.5 Structural Failure

Shell structures are remarkable thin structures with the radius to thickness ratio varying between *200* up to *800* and more. Such high slenderness immediately concerns the engineer of the possible occurrence of the premature failure of the structure due to buckling instability. In case of thin concrete shells, the shell may also fail because of material degradation such as cracking and crushing. Furthermore, professor E. Ramm [66] of the University of Stuttgart argues that the highly nonlinear behaviour of reinforced concrete, e.g. cracking, creep, shrinkage, yielding of reinforcement, may have a severe influence on the structural failure of shells, referring to so-called inelastic or plastic buckling. According to professor Ramm a failure can be addressed as a buckling failure when finite deformations cause the collapse of the shell and a strength failure when the nonlinear material behaviour is responsible. The classification can be seen in Figure 3.4.

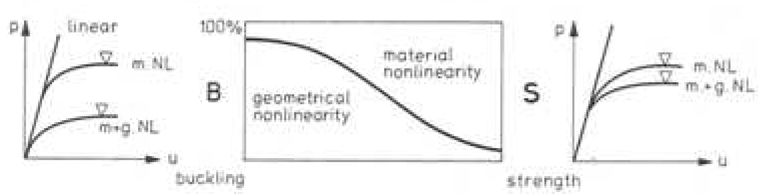

Figure 3.4. Structural failure due to buckling or strength, Ramm 1987

Unfortunately the type of failure cannot be determined in advance. In Chapter 6 the structural failure of shells will be discussed in more detail.

3.2 Classification of Shell Surfaces

The spatially curved surfaces of shell structures can be classified in several ways. For shell structures it is convenient to make a classification according the *Gaussian curvature*. The Gaussian curvature of a three-dimensional surface is the product of the *principal curvatures*, which are defined as the maximum and minimum curvature of a certain surface. The principal curvatures can be found by intersecting a shell by an infinite number of planes normal to the shell surface at an arbitrary point and determining the two planes for which the secant with the surface has a maximum curvature and a minimum curvature. The principal curvatures are, by definition, orthogonal to each other. The product of the principal curvatures is either positive, zero or negative. Classification in Gaussian curvature therefore means a classification in surfaces with positive Gaussian curvature (*synclastic*), zero Gaussian curvature (*monoclastic*) or negative Gaussian curvature (*anticlastic*), visualised in Figure 3.5.

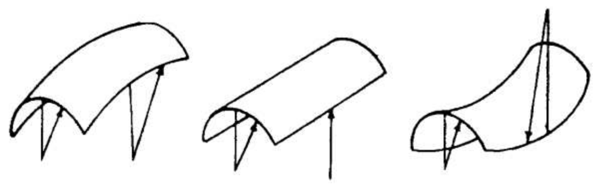

Figure 3.5 a. positive Gaussian curvature, b. zero Gaussian curvature and c. negative Gaussian curvature, Hoefakker and Blaauwendraad 2003

3.2.1 Synclastic

The Gaussian curvature of synclastic shells is positive; both principal curvatures have the same sign. A synclastic surface is non-developable. A shell surface is either *developable* or *non-developable*. If it is possible to develop a surface it can, in contrast with non-developable surfaces, be changed into a plane form without cutting and/or stretching the middle surface. Therefore, surfaces which are non-developable are stronger. An example of a synclastic structure is the dome. Synclastic surfaces carry their load by meridional and circumferential in-plane stresses. Except for the elpar (hemisphere sliced to a square base shape) which carries forces with in-plane shear

3.2.2 Monoclastic

An example of a developable surface is a monoclastic surface. The Gaussian curvature of monoclastic surfaces equals zero. Zero Gaussian curvature refers also to structures with zero curvature in both directions, as plates; however, these structures are named *zeroclastic*. Monoclastic shells do have curvature in one direction but zero in the orthogonal direction. An example of monoclastic surfaces are cylindrical shells such as barrel vaults. Cylindrical shells, probably the most used form of concrete shells, are widely used to cover e.g. airplane hangars or train stations. The membrane behaviour of cylindrical shells loaded perpendicular to their surface consists of an interaction of two behavioural components: beam action and arch action. Whether the cylindrical shell has mostly the beam action or the arch action depends on the shell geometry and the edge conditions. Long cylindrical shells resting on end supports act like simply supported beams.

3.2.3 Anticlastic

A surface with negative Gaussian curvature is called anticlastic and is, like synclastic surfaces, non-developable. The two principal curvatures have opposite signs, which make the product negative. The characteristic feature of having a positive curvature in one direction and a negative curvature in the perpendicular direction makes the shell act as a combination of a compression and tension arch when loaded perpendicular to its surface. Examples of anticlastic shell are the hyperbolic paraboloid (hypar) shells of Felix Candela. The hypar carries forces with in-plane shear like elpar shells.

3.3 Geometrical Surface Generation

The generation of three-dimensional surfaces like shells, with either positive, zero or negative Gaussian curvature, can be done by *geometrical* or *non-geometrical* methods. Geometrical generation is based on defining surfaces by mathematical functions. It can be recognised that most of the early twentieth century shells consist of analytically defined regular shapes. Typical design practice was to experiment with standard geometries, like sphere, cones and cylinders, and adjust the final shape to the prescribed plan by cutting out segments or different shell types are put together. In this way the shape stayed in range of the classical shell theory. Generated surfaces can be divided into *surfaces of revolution, translational surfaces*, *ruled surfaces* and *free-form surfaces* which are defined by a series of *NURBS*. Non-geometrical generation refers to methods which define shapes by a more natural process as *form-finding*, discussed in the next section.

3.3.1 Surfaces of Revolution

Surfaces of revolution (Figure 3.6.a) are created by rotating a plane, two-dimensional, curve (meridional curve) around an axis (*axis of revolution*). The surface that is created using the revolution method is a synclastic surface.

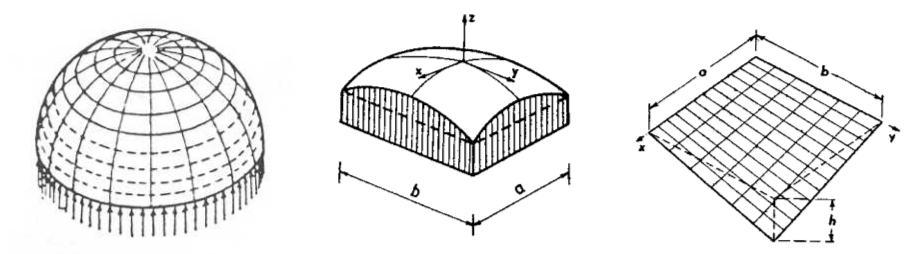

Figure 3.6 a. Surface of revolution, b. translational surface and c. ruled surface, Hoefakker and Blaauwendraad 2003

3.3.2 Translational Surfaces

Translational surfaces (Figure 3.6.b) are formed by sliding a plane curve (*generator*) along another plane curve (*directrix*). During this process the orientation of the sliding curve remains constant. Surfaces generated can be either synclastic, anticlastic or monoclastic, depending on the curvatures of the generator and the directrix.

3.3.3 Ruled Surfaces

Ruled surfaces (Figure 3.6.c) are generated by sliding the two ends of a straight line on their own curve, while remaining parallel to a prescribed direction or plane. Ruled surfaces are generated by straight lines only. Hence, from a practical point of view, ruled surfaces can be more easily and economically made for concrete shells. A ruled surface is anticlastic.

3.3.4 Free-Form Surfaces

The shape used, however, need not be restricted to those easily described in mathematical terms. Free-form shapes may provide a viable solution to many structural problems. A special group of geometrical generated surfaces are free-form surfaces generated by NURBS. NURBS stands for Non-Uniform Rational B-Spline and makes possible to present almost all imaginable shapes or free-forms by a combination of mathematical objects, formulas and procedures. The NURBS technique forms a curve of a certain degree between control points. Usually, the first and last control points coincide with the start and end of the curve. The points in between have certain weights which determines how the curve is influenced by that particular point, Vambersky et al. [76]. Thus, unlike other geometrical generated surfaces, the free-forms are not described by fixed equations. Generating free-form surfaces with NURBS-techniques is particularly suitable for computer implementation (CAD software). Architects make use of the free-form NURBS surfaces when designing the blob structures mentioned in the introduction. A famous example of a free-form shell is the TWA Terminal at the New York JFK Airport designed by Eero Saarinen, Figure 2.20.

3.4 Non-Geometrical Surface Generation

It can be stated that, ideally, the type of load determines the shape of a shell. A technique that is based on this hypothesis is form-finding, a non-geometrical surface generation technique. Form-finding refers to a technique that determines the shape of a structure by equilibrium with the applied load, form follows force.

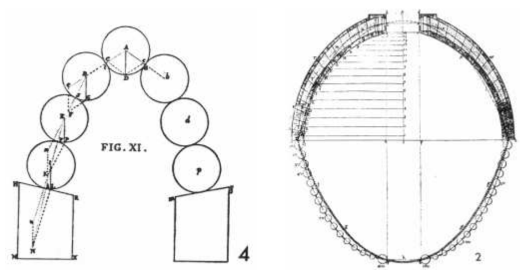

Figure 3.7. The inverted hanging model phrase from Robert Hooke and the principle applied by Poleni for finding the thrust-line of the St. Peter in Rome, Ramm and Wall 2002

In the year 1675 the basis of the form finding principle was established by Robert Hooke (1635-1703), famous for his elastic law which relates strains to stresses. Robert Hooke asked his contemporaries about the optimum shape of a masonry arch. Their explanation poses that how the flexible chain hangs, the inverted arch stays, Ramm and Wall [65]. Later, in 1691, Johann Bernoulli generated the exact equation for the catenary. The hanging model concept of Robert Hooke has been of great importance as it has been the basic ingredient for designing spatial structures up to the present time. A famous example of application is the hanging model of the Sagrada Familia Church of Antonio Gaudi, under construction since 1882.

Form-finding techniques in structural design were re-introduced by Heinz Isler and Frei Otto. The shapes derived from standard geometries did not lead to optimal membrane oriented designs (as less bending as possible). In fact, the cutting out of segments or put together of regular shapes often leads to high bending regions and large displacements which were usually avoided by additional stiffening elements. For shells, the principle of inverting hanging models reduced the form-finding of a shell to a natural process, leading to bending free shapes in pure compression.

Form-finding surfaces can be achieved by *physical modelling* and/or *computation modelling*.

3.4.1 Physical Modelling

Form-finding for shells by physical modelling became famous due to the pioneering work of Antonio Gaudi and, for shells, Heinz Isler. Isler's experimental work with hanging membranes resulted in the advantageous stress flow for shells, no tensile stresses and bending free. The hanging models can for example be made from a chain net or a textile fabric. The materials cannot absorb bending moments and therefore are in complete tension due to the gravity load. The structure that is achieved by inverting the hanging model, thus, contains only compression. The hanging membrane is an example of an equilibrium shape; the basis of the hanging model experiment is that one characteristic load case is used to generate the final shape by large deflections of a given membrane.

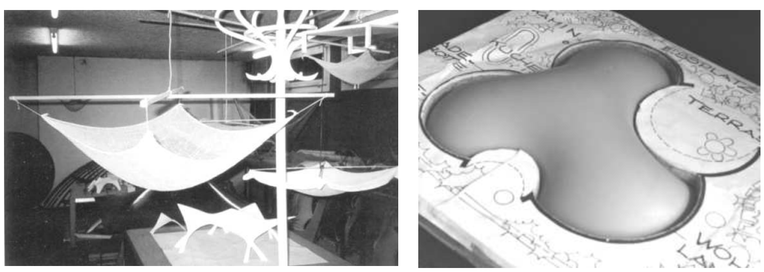

Figure 3.8. A hanging model from Heinz Isler and a pneumatic model of a shell structure, Chilton 2000

The procedure has the drawback that when different load cases are dominant, it is not possible to find a compromise. Furthermore, it is not possible to consider criteria for the genesis of shapes not based on elastic deformations. Before Isler used hanging models, he derived the shape of his shells from pneumatic models where a membrane is deformed under influence of air pressure.

Form-finding with a pneumatic model is based on the homogeneous stress state; everywhere in the surface yields the same stress. The pneumatic shapes therefore fit extremely well with 'pressure like' loading (water), but develop a less favourable stress field when applied in other circumstances with different load (dead weight or wind). Therefore, their application is less desirable for concrete shell structures.

For the determination of minimal surfaces between predefined boundaries, use can be made of soap film modelling. A minimal surface can be described as the smallest possible surface area between given boundaries. The minimal surface has zero mean curvature and a constant surface stress. Soap bubbles automatically find the minimal surface for membrane structures and shells and by applying internal pressure the minimal surface is found for pneumatic structures. The minimal surface can be captured by photographing.

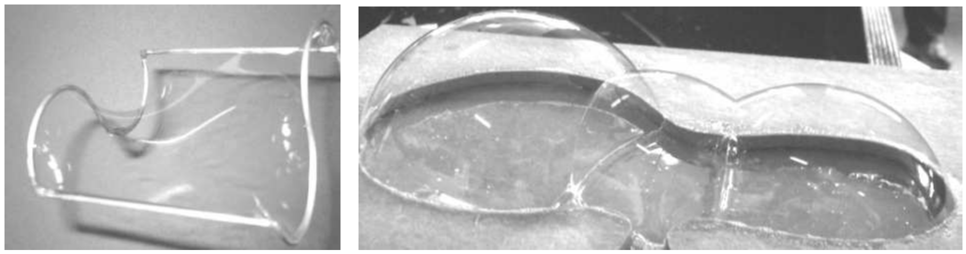

Figure 3.9. A minimal surface (left) and a pneumatic soap film model (right), Vambersky, Wagemans and Coenders 2006

The form-finding methods described before refer to human models. However, structural shapes can also be obtained by close investigation of nature. The theory of Charles Darwin, survival of the fittest, and gravity forces nature to develop and optimise its own structures like trees, spider webs, leafs and honey combs. Considering a simple example of a tree, it can be observed that its trunk is optimised to resist wind load. The thickness of the trunk increases with the magnitude of internal bending moment. Furthermore, everything in nature, whatever you find is organic shape, is double curvature, nothing plane. Shell engineers and architects may take profit by using the structural intelligence of nature to construct their own spatial curved surfaces as several shapes appearing in nature show similarities with thin concrete shells, e.g. the shell of an egg, shells of fruits, etc. A variety of information on this subject can be found in the books of Gibson and Ashby (1997) and D'Arcy Thompson (1942) in which several of nature's structures are described and analysed.

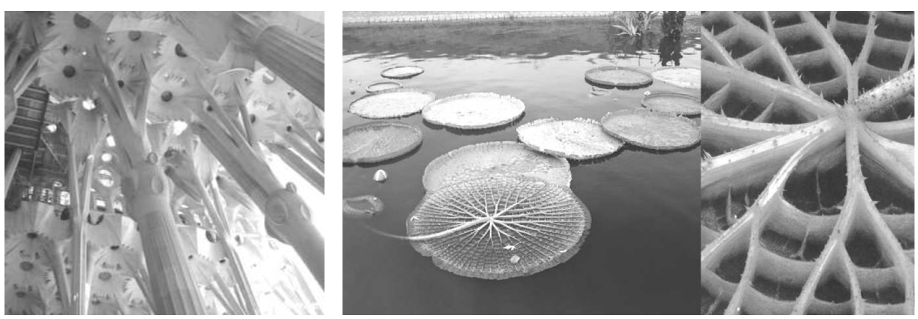

Figure 3.10. Structure inspired by nature designed by Gaudi for the Sagrada Familia (left) and leafs on water (right),

The form-finding methods give designers a powerful tool in designing structures. However, it must be mentioned that it is impossible to design efficient structures by simple scaling of the form-finding shapes to real dimensions.

3.4.2 Computational Modelling

Modern computer software enables designers to define an efficient structural shape by means of mathematical form-finding without using physical models. Computational modelling can be seen as the numerical equivalent of physical modelling. They provide in an additional form-finding method, thus not replacing the physical one. The underlying mathematical theory in computational modelling defines shapes on the basis of minimal surface by solving the weak form of the equation of virtual work for a prescribed stress. In other words, they aim for finding the equilibrium position of a structural network with a desired level of internal force. Two conventional computational methods are the *Dynamic Relaxation Method* and the *Force Density Method*. Dynamic relaxation is based on a step-by-step small time increment traced motion of the nodes in the structure. The nodes are set for motion by an imposed stress or force and their behaviour is determined by equating the geometrical nonlinear problem to a dynamic problem. To ensure convergence the structures damping properties must be specified. The Force Density Method differs from the Dynamic Relaxation Method as it is specially developed for tension structures. The Force Density Method finds the minimal surface by levelling the force densities for each node. Force densities ratios, the force in a cable divided by the cable length, defined for each element in the net, linearise the form-finding equation. The method is independent of the material properties of the structure and, thus, can be used for membrane structures if they are discretised in cable-net elements.

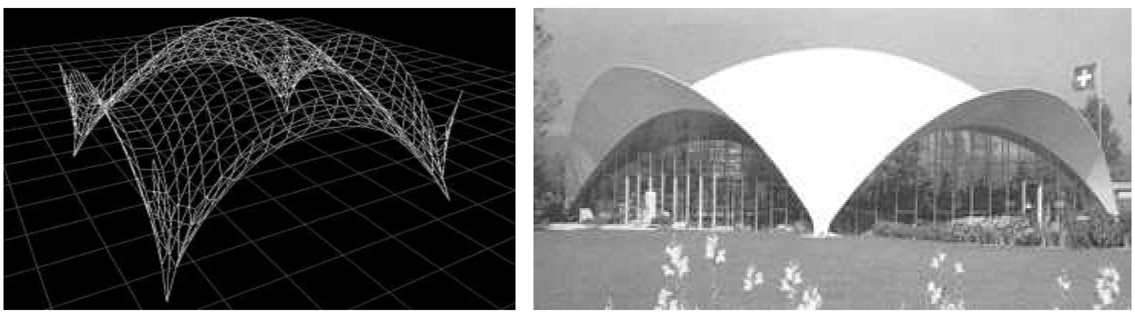

Figure 3.11. Square shell formed by a particle-spring network supported near the corners, Kilian and Ochsendorf 2005, and the Wyss Garden Centre that Isler constructed using a hanging model, Chilton 2000

A novel approach for the exploration of funicular involves *Particle-spring systems*. Particle-spring systems are based on lumped masses, particles, which are connected by linear elastic springs used for finding structural forms composing only axial forces. Each spring is assigned a constant axial stiffness, an initial length, and a damping coefficient. External forces such as gravitational acceleration can be applied to the particles and subsequently equilibrium is found using an implicit iterative Runge-Kutta solver, Kilian and Ochsendorf [53]. Allowing large deformations and real-time discovery of structural form they provide in a powerful tool for form finding. In Figure 3.11 an example of a square shell formed by a three-dimensional particle-spring network supported near the corners is illustrated, together with a shell designed by Isler using physical (hanging) models.

3.5 Mechanical Behaviour

To determine the mechanical behaviour of the shell surfaces, generated with techniques as described in the previous section, there are several methods, each of them having their own favours and restrictions. The mechanical behaviour of shell structures refers to the stresses, strains and displacements which arise in the shell due to the applied load. This section discusses several techniques which are often used in shell analysis.

3.5.1 Balance Calculation

A very practical method is to determine stresses by a simple balance calculation. Tests from Isler show that for shells with a square base plan only *10%* of the weight of the shell goes to the walls. *90%* of the weight arrives directly at the four corners. A simple calculation of the stresses in a shell can be carried out. Every corner carries about *25%* of the total vertical load on the shell. The horizontal forces are in the middle across surface of the shell the same as at the support. This means that when the total of load is known and the angle by which the shell enters the support is known, the horizontal load can be calculated. Dividing the horizontal load through the stressed area (across distance times the thickness) gives the horizontal stress in the shell.

3.5.2 Polygon of Forces

The polygon of forces is a graphical method to determine the forces in a structure, Bogart [13]. It is presumed that the ancient engineers used the graphical method as it is a simple and useful method to obtain and understand the membrane forces in shells. The application of the method is most likely a result of the discovery that the line of a hanging chain can be described by constructing a polygon of forces for each point in a discretized chain line. As they used the inverted hanging chain principle for form-finding, they used the polygon method for determining the forces.

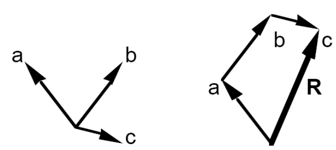

Figure 3.12. Determining the resultant force R for a point by considering the forces a, b and c in cyclic order

The polygon of forces method is based on the first law of Newton which states that a body is in equilibrium and can remain stationary if there is no force acting on the body or, alternatively, if there are several forces which balance each other. When forces acting through a single point are in equilibrium the magnitudes and directions of these forces can be represented on a vector diagram which forms the sides of a polygon. All the forces must lie in one plane and must be considered in cyclic order.

For an arch, the polygon of forces can be used to construct the line of thrust. In case of an arch with irregular shaped blocks, the line of thrust can be constructed by assuming the weights of the blocks as a lumped mass applied at their centre of gravity, given that the magnitude of the forces must be proportional to the weights of the blocks. The constructed polygon of forces shows the relation of the horizontal resultant with the line of thrust and the summed weights. In practice, the weights of the blocks and maximum supporting horizontal force are predefined and by assuming the supports on the same horizontal level the polygon of forces and, thus, the line of thrust is fixed. If the line of thrust does not coincide within the middle third of the arch cross-section, tensile stresses occur and bending moments are needed to compensate.

For shells, as mentioned in the introduction, bending is prevented by the circumferential stresses which correct the line of thrust back into the system line of the shell. These circumferential stresses can be found using the polygon of forces. This is shown in Figure 3.13 below.

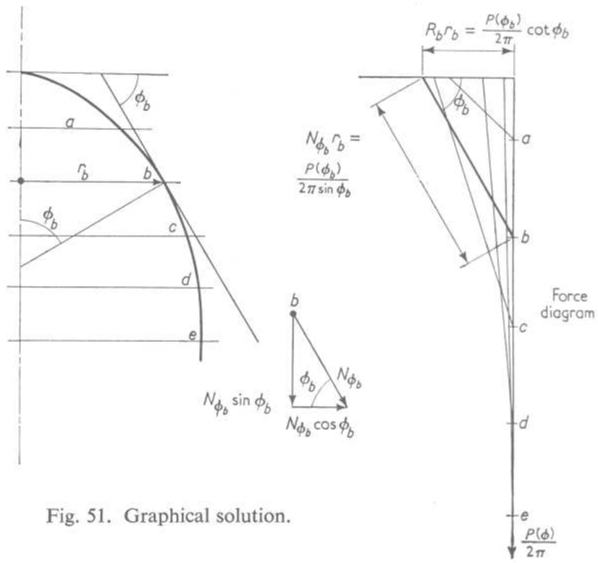

Figure 3.13. Graphical solution of a shell of revolution, Haas 1962

The graphical method is a useful method to understand the behaviour of shell geometries. It is however restricted to simple shell geometries and linear behaviour.

3.5.3 Classical Shell Theory

Founded by Augustus Edward Hough Love in 1888, the classical shell theory was the first shell theory and is often referred to as Love's first approximation. The theory was an extension of the plate theory to structures with surface-like geometries using the same assumptions as the Kirchhoffean theory of plates. Hence, the approximation of Love essentially is a thin shell theory. The most important part of the approximation of Love is the reduction of the three-dimensional problem to a two-dimensional surface problem, i.e. stresses or strains in normal direction are of no significance to the solution. Furthermore, Love identified that the shell behaviour can be approached by a membrane field in combination with plate bending that compensates for the shortcomings of the membrane solution. The classical shell theory is further discussed in Chapter 5.

Although the approximation of Love is restricted to thin shells, it must be mentioned that the approximation still appeared to be sufficient for conceptualising the behaviour of older three-dimensional shapes as masonry domes, which are considerably thicker relative to their span and cannot be exactly characterised as carrying loads by in-plane axial or shear stresses (more bending exits and final stresses are not uniform).

The emphasis of pre-war shell investigations laid on theoretical description of the linear elastic behaviour. By exception Zoëlly, Von Karman and Tsien did investigations to the buckling phenomenon of shells. After the war the research on buckling failure predominated. The trend towards greater spans and thinner shells leaded to buckling sensitive structures with less strength reserve. However, modern designers where aware of these disadvantages and fully realised the need to protect shells for buckling failure, they could not predict the buckling load due to their limited understanding of the phenomenon. At first, mathematicians tried to capture the buckling problem in the same linear manner as Euler did with the buckling of a column. The shell buckling problem is, however, far more complicated and those attempts failed as they resulted in large deviations with the experimental obtained critical loads.

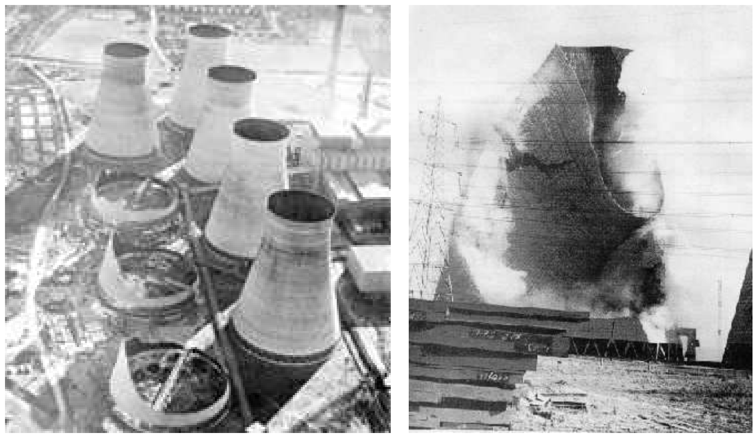

Figure 3.14. The collapse of the Ferrybridge cooling towers on the 1st November 1965

From the year 1965 the research on shell buckling was further stimulated by a collapse of three large cooling towers of 115 m height at Ferrybridge, UK. The collapse is subscribed to insufficient study on wind loading as mistakes in assumptions of wind speeds as well as the non-investigated effect of turbulence due to grouping of the towers caused unforeseen dynamic wind loads. The single layered reinforced concrete towers could not resist these loads and failed. Luckily, no one got injured. The collapse is seen in Figure 3.14.

It was found that the lack of correlation between theory and practice finds its origin in the initial geometrical imperfections of the small-scale models which caused deviation from the linear path of equilibrium to the nonlinear post-buckling path. It appeared that the linear bifurcation point is never reached as the shell fails due to the reduced post-buckling load carrying capacity. A significant step in the direction of providing this answer was made by Dutch professor Koiter who investigated the post-buckling behaviour of shells in the vicinity of the bifurcation point: the Koiter initial post-buckling theory. Koiter permits in a study of the slope and curvature of the secondary path of equilibrium in the immediate vicinity of the bifurcation point on the basis of linearised formulation. The conclusions of Koiter are discussed in Chapter 6.

3.5.4 Model Tests

Until recent progress of computational numerical analysis, experimental tests on small-scale models did provide in a very practical and convenient method to determine stresses in a shell which goes beyond the simple shape. The shells of Heinz Isler are a famous example of shells designed using small-scale models. Besides his form-finding models Heinz Isler used small-scale models to determine stresses and to observe the possible full-scale performance. He used the experimental results to optimise his shell designs.

Before performing experimental tests the intention must be discussed, whether it is to confirm a mathematical theory, to verify a specific design or for observation of full-scale performance. For using small-scale model tests in determining the full-scale mechanical behaviour it is important to approach the reality as close as possible. For example, small-scale models made of metals or plastics are not representative for concrete shells in the situation where pre-buckling cracking is known to be present. The high tensile strength of metals and plastics in relation to concrete will give misleading results. Because of the importance of cracking in structural behaviour of shells, time effects as creep and shrinkage and local effects such as bond slip and aggregate interlock, small-scale models should in be made from micro-concrete or other cementitious model material. The loading which can be expected in reality can be modelled by hanging weights, hydrostatic pressure, air pressure or partial vacuum.

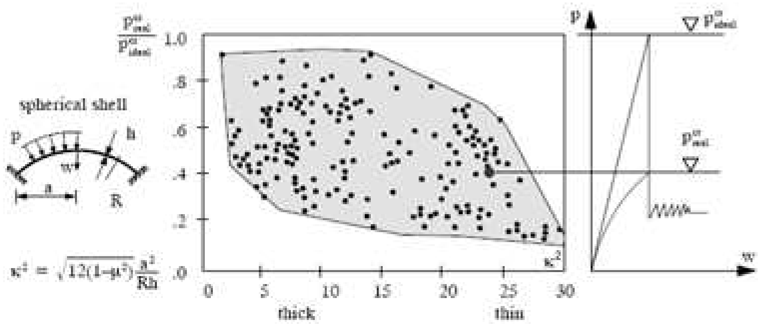

Figure 3.15. Experiments on buckling of spherical caps under uniform pressure

Because of the long-time absent of mathematical answers, much research on different types of shell phenomena has been done by experimental tests on small-scale models. Scientists as Csonka, Klöppel and Jungbluth, Von Karman and Tsien and Vandenpitte have done numerous small-scale experiments on as well concrete as metal or plastic shells. At the TU Delft during the *1960s* experiments on several concrete cylindrical shells have been performed by Van Koten and Haas.

A lot of these experiments where done to obtain information about the buckling behaviour of thin shells, the field of the aforementioned Koiter initial post-buckling theory. In particular the tests performed at the University of Ghent of Vandenpitte provide in an extensive experimental studies on concrete dome buckling. The research on the buckling phenomenon resulted in an enormous scatter in experimental results as can be seen in Figure 3.15. This scatter is ascribed to the effects of initial imperfections in the shell surface.

3.5.5 Computational Numerical Analysis

Late shell designs are largely influenced by the advent of the computer. The importance of nonlinear features (large deformations) in shell design raised a huge barrier for designers to find an analytical solution. The advent of the computer made it possible to solve the nonlinear shell equations by numerical approximation methods. A classical method is the numerical integration of the shell equations with methods such as Runge-Kutta or predictor-corrector techniques. The method is only applicable to shell problems which can be reduced to a system of ordinary differential equations, primarily the problems of shells of revolution.

A powerful method for numerical computer analysis is the finite element method, essentially an approximation method for calculating the real behaviour of a structure by performing a solution of a set of equations describing an idealised situation. The finite element method discretises the structural domain into elements bounded by nodes. The methods work like a spider web. The movement of a point forces other surrounding points also to make a movement. The movement of the nodal points is connected to the rise of strains and stresses in the elements. By energy formulation and boundary conditions the response of the structure to certain loads is determined.

The finite element method (FEM) has revolutionised the analysis of structures and is widely available in computer software programs as ADINA, DIANA and ANSYS. It is difficult to quote a date of invention, but the roots of the finite element method is both mathematicians, physicists and engineers. The name 'finite element' first appeared in the paper of R.W. Clough (1960). Important early contributions are linked to the names of Argyris, Zienkiewicz and Cheung. Since the *1960s* a large amount of research and publications was devoted to the technique, Bathe [3]. Commercial software producers embraced the method and have developed it into very advanced analysis programs. The finite element method is discussed in Chapter 11.

It must be mentioned that the computer software based on numerical analysis must not be confused with the frame analysis programs as MATRIX FRAME and ESA PT. Frame analysis programs are based on the exact solution of a linear elastic formulation. Finite element programs are able to give a far better approximation of the nonlinear reality. However, the producers of frame analysis programs are trying to close the gap (ESA PT includes the possibility of a plate analysis with finite elements) they are by no means applicable for the more advance structural problems with large influences of nonlinear behaviour.

3.5.6 Rainflow Analysis

A relative new method is the rainflow analysis which is based on the way how rainwater runs off the surface. Like the rain flow loads will flow. The problem of modern computational numerical analysis, as the finite element method, is that only quantitative information is obtained. The designer does not know how the applied load is transferred from the loading point to the supports. In particular for designing irregular surfaces and/or supporting conditions, the undefined force flow gives raise to questions whether the shell has a sufficient structural surface. In order to obtain qualitative information about the force flow the rainflow analysis is developed, Bogart [14].

The rainflow analysis is derived from the study to the way in which plates carry their load. A plate carries load perpendicular to their surface by bending and out-of-plane shear. From the equations for plates engineers know that, when there is no torsional load, the second equilibrium equation yields that the shear force is equal to the derivative of the sum of the bending moments (see Chapter 5). The maximum shear force in a plate is a vector equal to the value of the applied load and points in the direction of the shear flow to the support. Hence, the maximum shear vector can be found by making a gradient plot of the deflection curvature. The deflection curved surface also represents an air inflated membrane and, analogous to this hypothesis, the flow of shear forces represents the way in which the rainwater flows from the inflated membrane, with the largest run-off at the curves with the steepest ascent and thus the largest shear.

In the case of shell structures, the deflection curvature is replaced by the initial curvature of the shell surface. In this case the rainflow represents the force flow and qualitative information can be obtained. Drain curves indicate the membrane force flow. Slow flow means little slope causing a distortion of the membrane behaviour by out-of-plane shear and bending. Fast flow, thus, represent a sound structural surface. Bending can also be expected at regions with water accumulation or when loads are acting perpendicular to the drain curves (for example at the edges). Furthermore, a rapid change in the slope of a drain curve is sign of large circumferential stresses (and even can lead to bending as well), Bogart [14].

3.6 Structural Optimisation

Structural optimisation can be regarded as the search for a better solution to a structural problem by generating additional sensitivities with respect to non-considered parameters. The optimised structure is thus better and more efficient than the initial structure. However this seems to be a very simple principle, the question how to define the optimisation problem and to which extend it is executed is not.

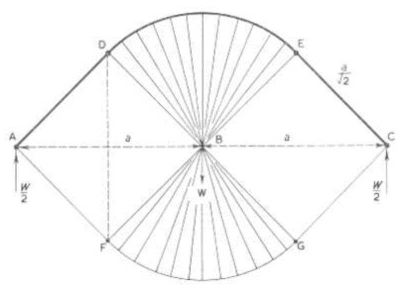

Figure 3.16. The most efficient Michell structure for carrying a point load

The preliminary stage of structural optimisation were the structures of A.G.M. Michell which he developed at the beginning of the 20th century, see Figure 3.16. Michell structures carry the load with the least possible weight. The structural system follows the force trajectories and each member is either in compression or tension. Despite their efficiency, Michell structures are of little practical use due to their specific structural scheme.

Structural optimisation is a synthesis of various individual disciplines, design modelling, structural analysis, behaviour-sensitivity analysis and mathematical programming with special emphasis on the modelling stage. It is one of the most significant processes obtained from nature. An example is the aforementioned tapered trunk of a tree and the constant stress distribution in the stem and branches of a tree. This principle of constant surface stress, also seen in the minimal surface of a soap-film, may be applied to the optimisation of engineering components.

Structural optimisation deals with maximising the performance of a structure for certain objectives and constraints. The choice of the objectives and constraints can lead to a large diversion of solutions to the optimisation question. Think of the differences in optimisation results when optimised with respect to construction costs, weight, or natural frequencies. In a so-called multi criterion optimisation these (conflicting) objectives can be considered simultaneously to obtain an optimal compromise of structural design. Moreover, limitations of the optimisation process give rise to questions whether a local or global optimum is obtained.

The basic idea of the optimisation process is much related to the engineer approach. At first a shape is chosen for which the structural behaviour according to the given load cases and support conditions is evaluated. After the stresses, displacements, buckling loads and other safety requirements are checked a new and better design can be proposed by means of a sensitivity analysis. The process is repeated until the desired optimum is obtained.

Shape-sensitive structures like shells require high quality design to obtain an optimal membrane design. Since in many situations this optimal shape is not obvious, the need for optimisation techniques is evident. To fulfil the basic membrane oriented design rules, a modification of the original design could substantially improve the structural behaviour reaching the ideal of a pure membrane stress in compression for all loading conditions. Optimisation for shells results in a highly nonlinear optimisation problem. This means that, in order to generate a reliable design by structural optimisation, the nonlinear structural response, e.g. buckling or plasticity must be considered.

With respect to optimisation shells are known to be extremely parameter sensitive because they are already optimised structures. This means that the danger of over-optimisation is very close. In fact, shells often show typical characteristics of 'over-optimised' specialisations with high sensitivity with respect to small changes of certain parameters such as the reduction of the buckling load due to only small initial imperfections. On the other hand an optimisation may contribute to a better design with more safety.

The difference between optimisation objectives has resulted in various classifications over the years, none of them having reached global usage. In this thesis the categorisation which can be made according to Ramm and Wall [65] is used. Ramm and Wall argue that distinction can be made between *size optimisation*, *material optimisation*, *topology optimisation* and *shape optimisation*, even though these optimisation techniques may have a lot of overlapping.

3.6.1 Size Optimisation

Size optimisation refers to the optimisation of the size of structural elements in a structure. The initial geometry is not changed. Size optimisation leads to an optimal structure with respect to the weight and overall stiffness or strength satisfying the equilibrium condition and the boundary constraints. It results in structures with modified cross-sections of structural elements.

3.6.2 Material Optimisation

Material optimisation is everyday practice for engineers. Material optimisation is namely related to the optimal use of material in the structure, e.g. reinforcement dimensions. The goal is to achieve an optimum in material usage and stress distribution. In fact, the shell itself is already a material optimisation by covering a long-span with minimum of material use.

3.6.3 Topology Optimisation

The topology of a structure is defined as a spatial arrangement of structural members and joints. Consequently, topology optimisation means varying the connectivity between structural members of discrete structures or between domains of continuum structures. For discrete structures, such as trusses, the variation of connectivity means to generate or to eliminate structural members between existing joints. Analogously, for continuum structures the variation of connectivity means to separate or to join together structural domains and to generate or to reduce structural domains. In other words, in case of continuum structures, topology optimisation transforms the design space in an optimal stressed space by removal or addition of elements. Low stressed elements are removed and areas of high stress are facilitated by the addition of elements. At first, the support conditions and applied loads are the only determined parameters as is a block of structural material. By defining the stresses in each element, the low stress and high stress elements are found and subsequently elements can be removed or added. Consecutive execution finally leads to a more optimal distribution of material in the design space, Veenendaal [77]. In Figure 3.17 a topology optimisation applied as maximum stiffness problem to a four point supported spherical shell under a concentrated load is visualised.

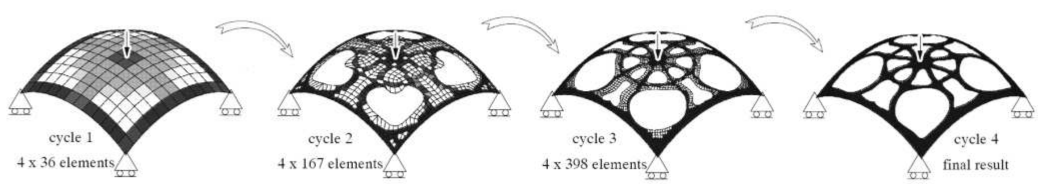

Figure 3.17. Topology optimisation of a spherical shell

The application fits extremely well to computer implementation. Nowadays, topology optimisation can be used to identify a potential good design and as starting point and improved by further design tools, such as shape optimisation techniques, discussed later. This is called adaptive topology optimisation.

In the case of continuum structures it is not sufficient to only indicate where cuts must be made to change the structural topology. In addition, the shapes of the cuts must be determined to define the new structural layout. Therefore, optimising the topology of continuum structures is sometimes called generalised shape optimisation, Maute and Ramm [58].

3.6.4 Shape Optimisation

Shape optimisation refers to a technique in which the shape and thickness of a structure are optimised. The shape optimisation method leads by the aim of minimum of the total strain energy (sum of bending strain energy and membrane strain energy) during form modification to a membrane oriented design. By shape optimisation the original design can be adapted in order to lower tension and bending stresses and progress to a more advantageous membrane state. An example of shape optimisation by minimising the strain energy is seen in Figure 3.18 where the optimised shell provides in significant lower bending moments, Bletzinger and Ramm [12]. In Figure 3.19, the tennis hall shells of Isler are presented. Obviously, they show great similarity with the optimal shell of Figure 3.18.b.

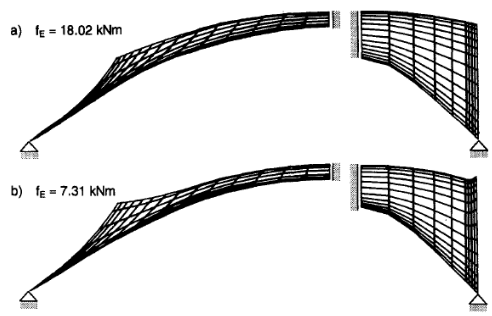

Figure 3.18. Shape optimisation of a shell with, a, the initial shell and b. the optimised shell

Shape optimisation reminds us of the form-finding technique as presented in section 3.4. Indeed, form-finding may be addressed as a surface generation tool and optimisation technique in one. Shape optimisation, however, is more than that. Shape optimisation is more general and differs from the form-finding principle where the generating rule itself is already the criterion for optimality. E.g. in shape optimisation, the non-considered load other than dead weight changes the initial design. Moreover, shape optimisation can also refer to optimisation with respect to deflection, buckling, stress levelling, flexibility etc.

Figure 3.19. The shell as built by Isler for a tennis hall in Düdingen (1978)

3.6.5 Computational Optimisation Algorithms

As the optimisation of structures becomes dependent of an increasing amount of criteria, finding the best solution becomes a very complicated mission. Hence, multi-criteria optimisation fits well to computer implementation. The development of optimisation computational algorithms has advanced spectacular over the last decades. This final section deals with optimisation algorithms.

Computational algorithms are developed since 1988, as the Homogenization method by Bendsøe & Kikuchi was the first structural optimisation method developed for computer implementation, Veenendaal [77]. Since then scientists have searched for various optimisation algorithms with all kinds of application fields which results today in a wide variety of algorithms. Computational optimisation algorithms are not restricted to the classification as presented above, but often use a combination between different types of optimisation, for example an integrated shape and topology optimisation. Roughly, they can be categorised in *specific* or *tailored algorithms* and *general algorithms*, Veenendaal [77].

The most popular specific algorithm for structural optimisation is, by far, Evolutionary Structural Optimisation (ESO). ESO is a topology optimisation method and thus involves consecutive removal of low stresses material until the maximum stress in the remaining material part is reached. Computational software based on ESO is, for example, OPTFRAME or EVOLVE97. The software makes use of finite element techniques to determine stresses. The algorithm of ESO is further refined to Additive ESO (AESO), Bi-directional ESO (BESO) and Extended ESO (XESO) which are equipped with more extensive and efficient optimisation techniques, for example the possibility of as well removal as adding of material and faster removal methods.

Other specific algorithms are the aforementioned Homogenization method and the Metamorphic Development (MD) method.

Genetic algorithms are the most used general algorithms. The Darwinian based method (survival of the fittest) generates every iteration new solutions by selection and crossover of previous obtained solutions in order to end up with a higher fitness generation. Random mutation of the new generation increases the change of reaching a global optimum. The process is repeated several times, keeping the size of the population constant. One can imagine that the large amount of work that has to be done results in a long optimisation time.

Other general algorithms are the Differential Evolution (DE) method, the Simulated Annealing (SA) method and the rather eccentric named Ant Colony Optimisation (ACO) method. The latter optimisation is based on the fact that ants, by leaving behind the chemical pheromone on their followed path, find the most optimum (the shortest) way from their nest to a food source. Think of two paths, short and long, from their nest to a food source. Ants at the short path reach the food earlier and go back in the way with the most pheromone. Eventually all ants use the way with the most pheromone which is the shortest way. ACO uses this to find an optimum solution for a given problem. A disadvantage of ACO is its sensitivity to local optima. Therefore, the optimalisation algorithm must be programmed not to converge to one solution immediately, but to allow for more solutions for a longer period of time.

Optimisation software, however, must still be further developed as the bulk of investigations are devoted towards cross-sectional optimisation, 2D shape optimisation and the, for shell important, nonlinear behaviour is usually not taken into account as it greatly increases the complexity of the problem. Hence, the application of computation optimisation algorithms seems to be far away from designing a sound shell structure. Ongoing progression may foresee in sufficient optimising shell software in the future.

3.7 Design Codes

Two design codes that contain recommendations for the analysis of concrete shells are the codes of the *American Concrete Institute* (ACI) and the *International Association for Shell and Spatial Structures* (IASS). According to Farshad [34] the *German Norm* (DIN), the *British Standards* (BS) and the *Indian Standards* (IS) also offer general design guidelines for shells. The guidelines mainly focus on buckling.

The ACI Committee 334 on concrete shells was formed in 1959 under the chairmanship of Anton Tedesko. The committee published two reports on shell design in 1964. The first report '*Criteria*' covered general design considerations and the second report '*Commentary*' discussed data of general interest to shell designers. The discussion of stability is mainly governed by the second report. In the 'Commentary' the relative importance of post-buckling behaviour and the significant reduction in the buckling load when both principal in-plane stresses are compressive is mentioned. The report states that for anticlastic shells it is possible to use the linear buckling theory. For synclastic shells the ACI report assumes that information on buckling of ideal shells for cylinders and spheres may be used as starting point of the analysis for the considered shell. The report recommends that the combined apparent safety factor F based on the apparent safety factors calculated for an ideal shell in the direction of the principal radii of curvature, using an analogous sphere of cylinder in each direction, however, not less than *5*. The rather large value was intended to allow for uncertainties of the various effects not included in the calculation. The effect of creep was allowed for by assuming a reduced value of E or a tangent value divided by a value not less than *2*. Finally, it is mentioned that a shell with two layers of reinforcement has greater buckling load than a shell with only one layer.

In general, the report reflects the concern and imperfect state of knowledge on buckling at its time of publication. When the report was implemented in the ACI Standard, the problem of stability of concrete shells was confined to the point where almost no information of the use to a shell designer survived.

The IASS recommendations on shell design where developed by a working group in 1969. The text intended to serve as recommended practice in the design, analysis and construction of concrete shells. However, shells such as cooling towers where excluded. The recommendation was published in 1979. The discussion on stability of shells was largely based on Kollar and Dulacska [54]. After the qualitative discussion on buckling, including the mentioning of the importance of post-buckling behaviour, the report offers a five step approach to calculate the safety factor to be used. The IASS recommendations provides in a rational approach by covering all the effects which might influence the buckling in a shell. Throughout a conservative approach is taken. According to Popov and Medwadowski [62] the critical load may be as little as 1 or 2% of the linear buckling load, if all of the cumulative effects are taken into account. Since the safety factor is yet to be applied, the allowable load is even less.

A more detailed discussion concerning the application of the IASS recommendations is found in Chapter 6.

3.8 Design Considerations

The numerous of shell structures built up to the present day give an enormous amount of information for new shell designs. The information which has been achieved may provide the new shell engineer a guideline and a series of do's and don'ts when designing a sound shell structure. This section tries to formulate the things learned in design considerations.

3.8.1 Span/Rise/Radius of Curvature

The span of the shell is determined by its final usage. Shells can span up to *200 m* and more. The main concern of long span shells is the question of stability of the shell structure. Today, the largest span of a shell is the *218 m* span of the CNIT in Paris, Figure 2.25

When the span is known, the rise and radii of curvature must be set. According to ACI Committee 344 domes usually give rise to span ratios of *1/10* to *1/6* while Scordelis [69] reports on shells with rise to span ratios of *1/7.46* to *1/4.82* and radius of curvature to span ratios of *1* to *0.707*. The ideal rise-to-span ratio for arches, *1/7*, is considered to be reasonable for shells as well. Shells with lower ratios than *1/7* are considered to be flat shells. It is generally suggested that the rise should be larger than *1/10*. The rise to span ratio also fixes the radius of curvature. The central angle of shells is usually selected between *60* to *90 degrees*, Scordelis [69]. Higher central angles would result in shell geometries with steeper slopes. Placing of concrete on these slopes would then require double forming.

Candela believes that every shell has an optimum span, keeping in mind structural, practical and economical parameters. Spans which exceed *30 m* makes the shell rise greater giving it tremendous cubage, which requires costly formwork. Large span improper shells, like folded slabs or barrel vaults, need extra thickness which causes high dead weight and increasing reinforcement. At this point transverse bending ceases to be secondary and becomes critical. In short cylinders stiffening arches get so big with large spans that the advantages natural to the shell are nullified.

3.8.2 Thickness

The thickness of the shell is an important parameter in shell design. Because the dead weight of the shell often represents the major portion of the total load, there is a desire to reduce the thickness. Secondly, thinner shells approach more closely to the profoundable membrane state. However a reduced shell thickness is less favourable of resisting bending moments. Fortunately, the edge disturbances have only local character and can be compensated by local increase of thickness.

The thickness of the shell surface is prescribed by either practical or structural purposes, depending on the span and the construction material of the shell. For long-span shells structural considerations as failure due to buckling or surpassing material strength demand a certain shell thickness. Usually dimensioning the shell thickness is based on buckling considerations rather than material strength criteria. However, for short span shells the thickness is determined by practical considerations as the concrete cover for preventing corrosion of the reinforcement or concrete placement. The turning point whether the shell thickness is determined by practical or structural factors is not a fixed parameter.

Determining the thickness with respect to practical considerations means providing enough space for the reinforcement (in combination with the concrete cover) and the maximum grain size. As a general rule it can be said that the thickness should at least equal three to four times the maximum aggregate dimensions, Haas [42]. By this it is possible to overcome imperfections as gravel pockets or separation of the concrete mixture. For the concrete cover climatological considerations play a large role. Because the surface of the shell often remains untreated the concrete cover must avoid water reaching the reinforcement to prevent corrosion. In general a concrete cover of *30 mm* will be sufficient for maritime regions. The thickness is further influenced by the application of one or two layers of reinforcement. The practical thickness of a shell is also influenced by the placing method of the concrete and placing difficulties. Using common placing methods the thickness of slabs can be controlled up to about *19 mm*. With extreme care *6 mm* can be obtained. The curvature of the shell will have a negative effect and the designer must take account for larger deviations. Special fabrication methods as prefabrication may reduce surface deviations. As a rule, the thinner the shell is as compared to its radius of curvature, the less accurately it can be built. A common practical thickness of conventional concrete shells varies between *60* to *80 mm*.

The practical thickness is the minimum thickness of the conventional concrete shell. Structural considerations may, however, force the designer to increase the thickness. Most shells have an increased thickness near the supports to prevent stress concentrations and to facilitate the force flow to the supports. Long-span shell structures may take this increase thickness to be necessary over the complete shell surface. Although, the shell thickness has no influence on the membrane stresses (the thickness parameter falls out of the equations) and only minor influence on the bending stress (double thickness increase the bending moment just 26%!) the thickness is important for buckling considerations. Aforementioned, as increasing spans become more and more vulnerable for buckling, long-span shells may need a thickness which is larger than the practical thickness.

3.8.3 Ribbed Shells

Instead of increasing the thickness of a shell, several shell designers such as Nervi and Tedesko used ribs to stiffen their shells in order to obtain a larger resistance against buckling. Ribs came in order to find a modification in the way the material is distributed throughout the surface of the shell. They are applied to increase the effective depth of the shell greater than if the material were evenly distributed. Though ribbed shells are not thoroughly discussed in this thesis, their principle and influence on the buckling behaviour is outlined here.

The functioning of ribs can be simply explained. Due to the rib-stiffening the buckling is represented by the local buckling of the skin between the ribs, conditionally that the ribs distances are chosen inferior to the buckling lengths of the unstiffened shell (if the distance between neighbouring ribs is larger than the buckling length of the unstiffened shell, they have, off course, no influence). When the rib design is known, the rib shell can be replaced by a continuous surface for the analysis. The continuous surface must include the effective width of the skin with respect to the bending of the ribs, possible eccentricity of the ribs and the role of Poisson's ratio. After that, the rigidity characteristics of the equivalent orthotropic shell can be established and an overall buckling analysis can be performed.

The latter explanation leads to some questions. First of all, the dimensions of the buckle must be known in order to determine the rib distances. A safe choice is the linear buckling lengths of the unstiffened shell as the imperfect buckling lengths are larger, see Chapter 6. For example, when assuming rectangular buckles, the half buckling wavelengths of a spherical shell subjected to radial pressure cannot be shorter than $1.72\sqrt{(Rt)}$. This means that if the rib distances are shorter than $1.72\sqrt{(Rt)}$ they lead to an increased critical load. According to Kollar and Dulacska [54], in general, ribs can certainly be considered as practically effective if the distance of the ribs is not greater than 0.7 times the buckling length of the unstiffened shell. In that case the critical load of the shell panel between the ribs is approximately twice the value of the unstiffened shell.

The second problem that may arise is the question to what is the necessary stiffness of the ribs to allow us to consider the ribs as rigid supports of the skin during buckling. As this question is not generally been answered yet, Kollar and Dulacska introduced the following analogy. If we want to stiffen a weak simple frame, we can add a sufficient rigid structure according to Figure 3.20.

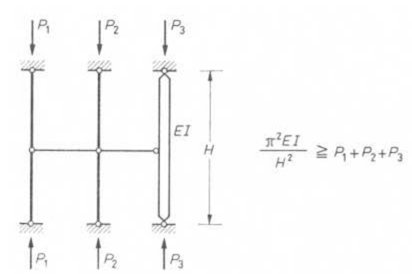

Figure 3.20. The basic principle of the necessary rib rigidity, Kollar and Dulacska 1984

The rigidity of the added part can be taken as sufficient if its critical load, computed assuming infinitely elastic material, is not less than the sum of all loads on the stiffened frame. When this is projected to our shell, we have to demand that the ribs be capable of carrying all the load acting on the shell surface and on the ribs, assuming infinitely elastic behaviour. In this computation an effective width of the skin, as valid before skin buckling can be assumed as part of the rib.

The shell surface can be stiffened in two ways: the ribs can be arranged on both sides of the skin, symmetrically to its middle surface, or eccentric stiffening on one side only. For symmetrical positioned ribs, the rigidity can be smeared out and the orthotropic shell equations can be applied. This is, however, much more difficult to construct and is less economical to eccentric ribs which foresee in a considerable higher bending rigidity with the same amount cross-sectional area. However, eccentric ribs can be described by the orthotropic shell equations much more difficult. Like symmetrical rib-stiffeners, eccentrically ribbed shells cause increase in rigidity. However, as discovered by Van der Neut in 1947, it does make a difference whether the ribs are positioned on the outer (e.g. the St. Louis airport shell, Figure 2.30) or on the inner (Palazzetto dello Sport, Figure 2.27) side of the shell surface. This is caused by so-called primary (phenomenon of twist due to varying amplitude of outward and inward buckles which cause shearing deformation in the shell surface) and secondary (outward buckling waves in longitudinal direction cause tension in ring direction due to Poisson's ratio) effects which act in opposite sense. Unfortunately, it cannot be decided without a detailed analysis which effect, and thus which eccentric arrangement, prevails.

To draw a conclusion, the following comments must be made. The difference in primary behaviour of outer and inner stiffeners only appears if the buckling deformation contains some twist. The secondary effect is present, however, ceases when the Poisson's ratio is chosen equal to zero which also benefits the safety. Furthermore, as concluded by Hutchinson and Amazigo (1967), the favourable effect of outside stiffeners is greatly reduced as it is partially counterbalanced by its sensitivity to initial imperfections. Therefore, Kollar and Dulacska propose to neglect the 'warping rigidity' and the primary and secondary effects caused by the eccentricity of the stiffening ribs. Hence, the analysis of ribbed stiffened shells can be reduced to that of simple orthotropic shells with a higher stiffness.

3.8.4 Reinforcement

Modern shell structures are reinforced concrete structural surfaces. Reinforcement in shells is applied for four requirements. At first, reinforcement is the reason that modern shell structures are capable of transferring tensile stresses resulting from the membrane and bending action as well as the tensile stresses due to transverse and membrane shear. Secondly, reinforcement provides in a distribution net for local concentrated loads and, thirdly, the application of a reinforcement grid enables the shell to control shrinkage and temperature effects. The final reason for applying reinforcement is the reduction of deformations due to local bending and thereby decreasing the likelihood of instability due to buckling of the shell. Thus, the reinforcement has an important role in preventing buckling.

Figure 3.21. Welded wire mesh reinforcement for the Jena Planetarium, Joedicke 1962

Ordinary reinforcement in a concrete shell consists of conventional steel rebars or a welded wire mesh, Figure 3.21. Wire mesh is recommended where possible. It is very suitable for developable surfaces as it can be obtained in flat sheets and easily bended in the right shape. For doubly curved shells wire mesh is less useful as it is difficult to obtain the double curved shape. Mild steel reinforcement is commonly applied for such surfaces. A small amount of shells has been built using high-tech reinforcement. An example is the shell of Jorg Schlaich which was built for the Federal Garden Fair in Stuttgart in 1977 using glass reinforced concrete. However, this is not common practice due to the higher costs. The research within this thesis on the applicability of fibre reinforcement may open new ways.

Using conventional rebars or welded mesh reinforcement, usually a percentage between *0.15* and *0.4%* is applied for single layer reinforced shells, although, due to their extreme thinness, the shells of Candela may reach higher percentages. The reinforcement of a series of concrete shells is illustrated in Table 3.1. To compare, beam reinforcement is approximately between *0.8* and *1.2 %*. The shell can be executed with one or two layers of reinforcement. Generally, engineers as Heinz Isler prefer two layers of reinforcement, mostly to give more resistant against buckling. However, two layers also provide more resistant to the previously described negative effects as shrinkage, temperature gradients and local concentrated loads. The application of single layer reinforcement is therefore restricted to shells with small dimensions or sometimes when prestressing is applied.

Shell	Thickness (mm)	Ø (mm)	Spacing (mm)	%
Shopping Centre Hawaii, Bradshaw	76	9.5	300 (max)*	0.37 (min)
Markethall Algeciras, Torroja	85	12	300 (max)*	0.40 (min)
Church Monterrey, Candela	40	9.5	150	1.24
Restaurant Xochimilco, Candela	40	8	100	1.25
Factory Tacuba, Candela	40	9.5	200	0.89
Swimming pool Norwich, Isler	80	6	100	0.57**

* Reinforcement is placed in circumferential direction; ** Two layers of reinforcement

Table 3.1. Reinforcement in concrete shell structures

Shells with combined reinforcement, one layer in the compression zone and two layers near its base, are often seen in practice. Candela makes his shell surface such thin (*40 mm*) that there is only space for one layer. While in the majority of the shell surface only one layer is applied, the reinforcement ratio is increased by supports. The table below shows the reinforcement ratios of different shells. The values are surface values which hold for the majority of the shell surface without taken into account extra reinforcement near the edge or at supports.

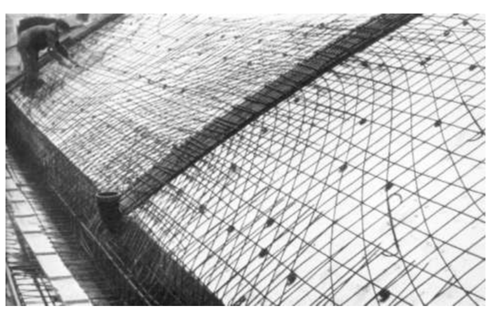

Figure 3.22. Rebars aligned with the stress trajectories, Joedicke 1962

The reinforcement can be placed in different patterns. Initially, shells where reinforced with the bars parallel to the stress trajectories, Figure 3.22. However technical and academic, this consumes much labour and is thus of little practical value. Nowadays a straight perpendicular reinforcement is applied, sufficient to withstand effects of shrinkage and temperature and able of proper distribution of local concentrated loads. For areas of larger diagonal tensile stresses supplementary diagonal reinforcement is applied, see Figure 3.23. At the edges of the shell, stirrups are placed for absorbing out-of-plane shear forces (which e.g. can be determined with the so-called Kirchhoff boundary condition, see Chapter 5).

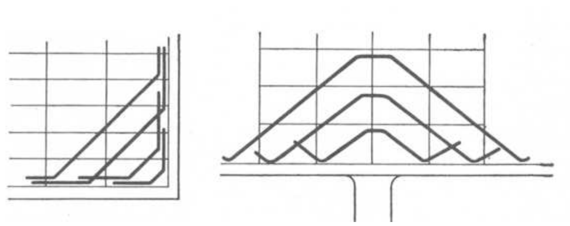

Figure 3.23. Supplementary diagonal reinforcement, Haas 1962

The diameter of conventional reinforcement should be kept small. However small bars have the disadvantage of high flexibility and are easy bent out of place by the shell builders, they are easier to handle. A fine net is preferred above a coarse net as it better distributes disturbances. According to the standard of the American Concrete Institute (ACI) the spacing between deformed rebars should be limited up to five times the shell thickness but not exceed *450 mm*. For a welded mesh the spacing should not exceed *300 mm*. European codes limit the spacing to not more than twice the slab thickness for plates. For shells it can be said that the spacing in most cases should be between two and three times the thickness.

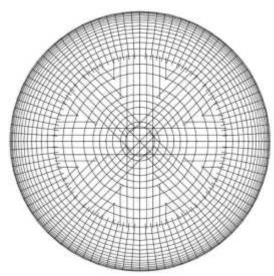

Figure 3.24. Possible reinforcement of a Monolithic Dome spherical shell

If fibre reinforced concrete is used, fibres can reduce the amount of reinforcement or even totally substitute the reinforcement. An example is the reinforcement in the l'Oceanografic shell in Valencia. The shell contains combined reinforcement for which *50 kg/m3* DRAMIX fibres are combined with a reinforcement mesh of *Ø8-150 mm*. The shell has a thickness of only *60-120 mm* and is seen in Figure 3.25.

Figure 3.25. Shell l'Oceanografic in Valencia constructed from as well fibres as a reinforcement mesh, www. structurae.co.uk

3.8.5 Prestressing

Prestressing in concrete shells is, as with other structures, applied for the aim of reduction or even prevention of tensile stresses by introduction of compressive stresses. For example to ensure that long-span shells are in compression prestressing may be applied. A practical rule states that shells up to *30 m* can be made of non-prestressed reinforced concrete. For longer spans prestressing must be applied. However, prestressing can also be included in short-span shells as it may cause the edge beams to be superfluous.

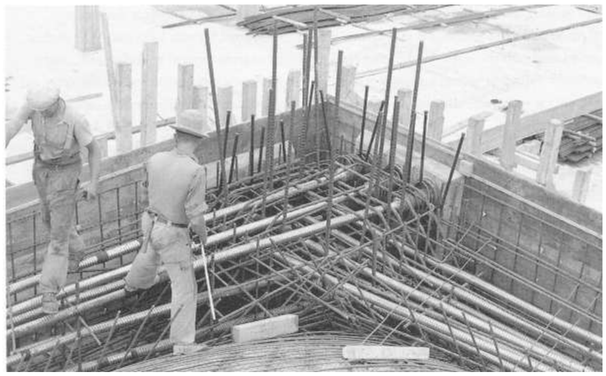

Figure 3.26. Prestressing canals in the edge beams of an Isler shell, Chilton 2000

Prestressing was first applied in shells to balance the outward thrust of a dome by bringing into compression a tension ring, or to contain the compression state in the shell surface under all possible loading conditions. Initially, the prestressing ties where accommodated into the edge beams of shells as is seen in Figure 3.26. Isler used prestressing to control the size of the edge beams. He applies prestressing if the span exceeds *30 m*. Later, shell designers also placed the prestressing ties inside the shell surface or outside the basic structure, as tension cord within the foundation or across the diagonals (hypars). An example of a prestressed shell with prestressing in the shell surface is the 1982 Olympic Swimming Pool in Kirchberg, Luxembourg City, designed by French architect Roger Taillibert, seen in Figure 3.27.

Figure 3.27. The 1982 Kirchberg Olympic Pool in Luxembourg City by architect Roger Taillibert, www.academie-des-beaux-arts.fr

The shell of Isler at the Deitingen Service Station is an example of prestressing outside the basic structure as the prestressing cords are placed beneath the ground surface and connects the outer support of the shell with an embankment structure which supports the two inner supports. By pulling the support points slightly inwards using the pre-tensioning cables the shell is brought into compression.

The use of prestressing in shells also has the advantage of improving crack control. Furthermore, with prestressing the influences of shrinkage and temperature is kept in check and the bending moments can be better controlled. The prestressing ties are also used for simple removal of the formwork. The tensioning of the ties after hardening not only brings the shell in compression, but also causes an up-lift of the shell surface. The shell moves free from the formwork which easily can be removed.

3.8.6 Material

The shells discussed here are constructed from (fibre) reinforced concrete. Stresses in concrete shells are often a small proportion of those permitted by the strength of the material. From experience, in a shell of *20* or *30 m* span the stresses vary from *1.5* to *3.0* N/mm^2, including the effect of pre-stressing, Chilton [22]. The foot of the shell is the only point where the stresses go above *50%* of the allowable concrete strength. Therefore, durability of the concrete is probably more important than strength.

After placement, attention must be paid to the surface treatment of the concrete, as the majority of shells do not have cladding or painting. A smooth surface improves the appearance and reflection of light. Furthermore, a smooth surface shows higher resistance against degeneration due to climate attacks. Measurements of Heinz Isler at some of his shell structures have shown that the shells lose *1* or *2 mm* of their surface in the first ten years. Over *35* years the erosion does usually not exceed *2* to *4 mm*. During a similar period of about *35* years the concrete will suffer carbonation to a depth of less than *10 mm*, Chilton [22]. However, the durability largely depends on the climatological circumstances. For example, in South Africa, which is largely sub-tropical, the temperature differential can vary *30 degrees* and thin concrete shells suffer large expansion variations. For increased durability, or visual reasons, the concrete cover may be coated, painted or cladded.

3.8.7 Supports

With respect to the supports, it is most important that they are fixed in place. Possible movement of the supports may lead to a disturbed membrane stress field, significantly increased deflections and/or in-extensional deformations such as seen in Figure 3.3. For self balancing shells (e.g. hemispherical shells) the supports only have to carry the dead weight of the shell. However, in case of more shallow shells, the supports sometimes also must absorb the outward thrust of the shell. In these situations the supports may be connected to each other by tensile cords or they are balanced by piles and/or (grouted) anchors.

The shell support design is closely related to the shell design as the membrane stress field is locally disturbed by suppressed deformations. A choice for a particular support condition, thus, influences the shell edge design, discussed hereafter. Commonly, shells are clamped supported, e.g. encased in concrete beams, or membrane compatible supported, e.g. ball-and-socket hinges. An example of a (rare) hinged support is seen in Figure 3.28 in which the hinge is approximated by a series of pendulums, with the horizontal thrust absorbed by a prestressed edge ring, Haas [42].

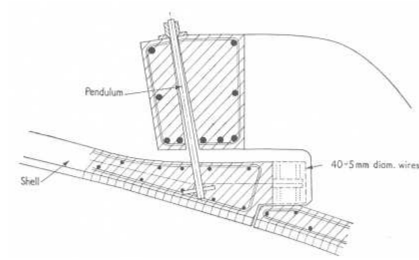

Figure 3.28. Support detail of a hinged support for a dome in Zürich, Haas 1962

3.8.8 Edge Design/Free Edges

The first shells of the early twentieth century were fully supported along their boundaries. However, when the architectural profession got interested, they wanted to show the spectacular thin cross-sections of shells by building shells with unsupported boundaries. If shells are unsupported at their edges, there is referred to shells with free edges. Obviously, shells with free edges are more appealing as they appear to be more graceful.

Discontinuously supported shells, e.g. Nervi's Palazzetto dello Sport in Rome, experience a significant change in the principal stress directions, simply as a consequence of transferring the weight of the shell to a small portion of the edge, illustrated in Figure 3.29. Moreover, in case of structures such as the Palazzetto dello Sport with columns tangential to the meridian, also the outward thrust contributes to the change of the stress trajectories.

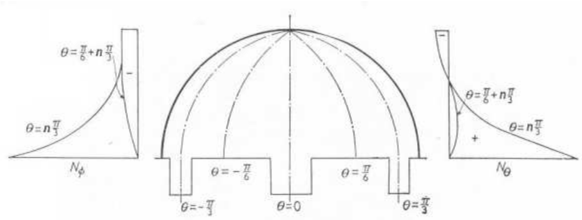

Figure 3.29. Stress distribution in a hemispherical dome on six supports, Haas 1962

In Figure 3.29 it can be seen that the meridional and circumferential stresses must vanish at the unsupported edge part while at the supports the stresses show high peaks. Furthermore, it can be seen that the edge disturbance caused by the discontinuous support stretches up to about halfway the shell surface. To counteract the change of stress trajectories a possible solution is to introduce a stiff ring girder. The ring girder is also beneficial as it simplifies the calculation, i.e. the shell above the ring girder can be analysed as a uniformly supported shell. A more aesthetical solution is the aforementioned feathered shell in which the unbalanced forces are fluently transferred to the (tangential) columns by arch action, Haas [42]. Basically, the feathered shell is an example of a shell with a free edge.

Although the possible thrust from the dome is usually taken by an edge ring beam or tension cord which is commonly prestressed, in some cases the edge ring beam is replaced by a thickening of the shell near its supports or by a feathered upturned shell, in case of a discontinuous support, Scordelis [69].

The membrane stress state of shells, however, seldom allows for totally free edges. In general, longitudinal edge beams must be applied to carry the applied loads, which have been transferred to them by the mechanism of internal shear force, and transfer them in turn to the supports of the shell structure. Furthermore, due to their free edges, these shells generally do not buckle locally, but the combined shell-edge system buckles as a whole. In other words, the shell-like buckling merges to arch-like buckling of the complete structure. This phenomenon is seen in Figure 3.30. The Figure shows a buckling analysis of an elpar shaped shell in DIANA with increasing edge beam stiffness. The most left picture (no edge beam) shows typical arch-like buckling while the most right picture (fully supported) has shell buckling with *5%* accuracy with respect to the theoretical value of a radially pressed sphere (see Chapter 6). The problem is that the arch-like buckling load is considerably lower than the load necessary to cause shell buckling. Thus, besides carrying load, the edge beams must also provide additional stiffness for buckling instability.

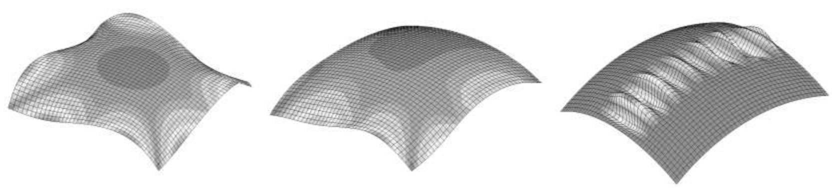

Figure 3.30. A series of shell buckling analyses with increasing edge stiffness

Edge members are found in various sizes and shapes. Distinction is made between edge beams and curved edges. Curved edges are essentially curved edge beams with open cross sections, while edge beams have rectangular closed cross-sections. The size of the edge members is determined by the magnitude of the load which they must transfer or buckling considerations. A possible height of an edge beam to shell length is somewhere between *1/25* and *1/20*, Farshad [34].

Figure 3.31. A shell of Heinz Isler in Switzerland and the shell at the Deitingen Service Station by Isler

The main problem of shell designers is the fact that the cross section of an edge beam, under influence of load transfer or buckling, becomes so large that they cause deformation problems. Large edge beams tend to shear-off easily from the shell or prescribe the shell deformation due to their own deformation.

Aforementioned in Chapter 2, the Kresge Auditorium on the MIT campus had major problems with watertighness due to the shear-off of the edge beam from the shell.

The problem can be solved by designing a more sound shell structure in which the membrane stress resultants do not run out of the edge. Think of the rainflow analysis mentioned before. If the rainwater flows over the edge, the shell often needs (large) edge beams. To prevent large edge beams the shell can be provided with curved-up edges, which obviously leads to forces running away from the edge. An example is shown in Figure 3.31. The graceful curved edge solution is used many times by great designers such as Candela and Isler. In particular, Isler was the master of edge design, as he was able to construct the famous shell at the Deitingen service station without edge members, Figure 3.31.

Concluding, a good shell design has a proper designed edge. Most important is that forces flow away from the edge in order not to have large discrepancies at the edge. Curved edges work like edge beams, but better, and may lead to the elegant and stylish shells as desired by architects.

3.8.9 Loading

Loads on the shell can be classified by their variation in time into permanent variable accidental and time dependent loads. For shell roofs, as dealt with here, the predominant loading is often the dead weight of the shell structure. Hence, in case of shell walls, cooling towers, the primary wall loading is wind and the distribution of the load is of major significance. The climatological conditions determine the variable loads such as wind and snow. Wind and snow load may cause the meridional curves and parallel circles do no longer present the principal directions of the internal stresses as there is a nonzero membrane shear force field, as well as normal membrane forces. Thus, the so-called stress trajectories transform under the influence of wind or snow load.

Time depended loading refers to effects such as creep, shrinkage and temperature gradients. Creep and shrinkage cause flattening of the shell, which in turn has major influence on the load carrying capacity, especially in case of a shallow shell. An example of a shell for which creep and shrinkage are dominant is the new EPFL Learning Centre shell in Lausanne, illustrated in Figure 2.42. Furthermore, due to the large exposed area with respect to the concrete volume, high temperature gradients can be critical. Aforementioned, in South Africa, temperature differences of *30 degrees* cause large expansion variations. A parabolic shell structure for a sports hall in Pretoria was constructed in the *1960s* using a *250 mm* higher thickness than structurally needed to provide sufficient mass to resists the climate attacks. Still it was plagued with maintenance problems. Furthermore, a recent example of cracks due to temperature gradients, are the cracks in the dome houses of the solid house foundation in El Alto, Bolivia, constructed in 2004.

In Chapter 9 the loading will be further discussed.

3.8.10 Economics

The economics of shells is not of interest for this thesis. However, in general it can be said that if the ultimate overall object is economics, do not build a shell structure. As shell construction techniques traditionally rely heavily on labour, their construction is hampered by today's high labour costs. According to Martin Bechthold [5], Professor at Harvard University Graduate School of Design, labour costs increased with the factor eight to eleven (unskilled labour and manufacturing labour) between the golden years of shell construction around 1960 and 2002 whereas the costs of construction materials increased only 4.8 in the same period. Less labour-intensive construction techniques need to be found as the formwork and falsework accounts for the major part of the costs, about *50%*. Cheaper alternatives may lead to a shell revival. Until then, the construction of new shells is dependent on the feeling for fine engineering art and structural honesty of the client.

3.9 Conclusions

From this Chapter it can be concluded that to design a sound shell structure, the designer must ensure firm support, allow for membrane stresses to develop, add sufficient curvature everywhere, and take care of edge effects by designing proper curved edges. Subsequently, the designer should optimise the shape and thickness of the shell for buckling and membrane dominant behaviour (minimising strain energy). Furthermore, a shell is only a shell when it remains it shape when it is loaded (shells sometimes are referred to as form resistant structures). Thus, in-extensional deformation must be prevented.

4 Shell Construction

After the historical reflection of the modern shell era in Chapter 2 and the discussion concerning the structural design of shell structures in Chapter 3, one may wonder how the three-dimensional curved surface of the thin concrete shell can be realised in practice. In this chapter the theoretical and practical considerations affecting the construction of shells are discussed.

Historically, shells are constructed using conventional timber formwork and supporting framework. However, as mentioned in Chapter 3, the conventional formwork had traditionally relied heavily on labour as forming the spatial curvature of the shell by timber formwork consisting of curved boards and beams is labour intensive. With increasing labour costs came the search to new construction techniques. A few of those new construction methods and applications were already mentioned in Chapter 2, such as the prefabricated elements of Nervi and the airform shells.

Besides developments in less labour intensive and inexpensive formwork there is the search for high quality materials and improved placement methods. At first, progress was searched in the position and quantity of rebar or mesh reinforcement, depending on the size and shape of the shell and the application of prestressing. Today, research extends towards the application of high strength mixtures and the possible addition of fibres which may reduce or even totally replace the conventional reinforcement. Furthermore, common concrete placement evolves to faster and better controlled processes and, in addition, new techniques as the vacuum method are introduced.

After the concrete is hardened and the possible prestressing activated, the formwork can be removed. What results is the free standing, bare shell, Figure 4.1.

Figure 4.1. Bürgi Garden Centre (1973), Camorino, Switzerland by Heinz Isler, Flury 2002

4.1 Formwork

The formwork of the shell, in combination with the framework, is a dominant factor in shell construction. The formwork gives the shell its final shape, is of main importance for the costs of the shell and the choice for a certain type of formwork may influence the design. Hence, the relevance of careful selecting and manufacturing of formwork.

The main purpose of the formwork is to support the reinforcement and to provide in a mould for the wet concrete until it has reached sufficient strength. As mentioned, the formwork gives the shell its final shape and because of the structural importance of correctness in shape, possible shape deviations such as dents or local loss of curvature may lead to a significant decrease in load bearing capacity (Chapter 3), the formwork, and the workman, must meet high standards. I.e. forming the three-dimensional curved shell requires craftsmanship as the spatial curvature must be applied over a large amount of surface with a minimum of shape deviations. Moreover, it is pointed out by Haas [42], that a shell usually attracts attention and every blemish of unevenness, for example a displaced board or mould, will immediately become apparent.

A well-proportioned formwork is, however, of no use if the supporting framework fails at its job. A framework must provide in a continuous supporting frame in which by no means (local) settlements may occur. This irrevocably will lead to the much unwanted imperfections in the shell surface. In order to prevent possible settlements, conventional shell construction may start with the realisation of a concrete slab, providing in a sound foundation for the framework and the shell structure in a later stage.

Besides the technological requirements, the formwork must meet economical demands. The cost of formwork and framework is perhaps the major constraint on widespread shell construction. Already for simple geometries, intensive labour is needed to obtain a well lined formwork with a smooth surface. The restriction in costs becomes even more pertinent where free-form shells are involved. Because there is neither a considerable element of repetition or symmetry nor a simple geometrical shape, forming the spatial curvature is time consuming and, thus, expensive. Furthermore, costs are negatively influenced by the possible need for double formwork. The need for double forms is primarily governed by the aperture of the shell. At maximum, the inclination of the shell surface cannot exceed *30* to *45 degrees*, depending on the consistency of the concrete mixture. Besides the economical drawback, a double formwork also has a negative influence on the quality of the concrete due to the higher water content required for the placement within the double form. Hence, when designing a shell, double forms should be avoided, Haas [42].

To reduce formwork costs several shell engineers have tried (and still do) to overcome the disadvantages of the conventional construction method in roughly three ways. At first, there is the search for improvement of the conventional timber formwork, secondly, the introduction of standardised shell dimensions for re-use of moulds. Thirdly, up to the present day, widespread pioneering with new construction techniques is done. In this paragraph three techniques most used for shell construction are discussed in combination with a rather new technique showing large potential. The sequence of discussion may in short be named as conventional formwork, prefabricated moulds, airform techniques and stressed membranes. In practice, when constructing a shell structure, there are also combinations possible.

4.1.1 Conventional Formwork

Conventional formwork can be divided into the mould itself and a supporting framework. The supporting framework builds up the skeleton of the shell. In general, the relative thin layer of concrete of a shell does not need scaffolding designed to carry heavy load. The major question forming the double curvature of the shell formwork is to *fill* or to *shape*. The double-curved shape predominantly is achieved using lines of curved glued-laminated timber beams (*shape*) supported by adjustable height metal trestles or metal frames, like the Brügg shell (1981) seen in Figure 4.2. If necessary, the number of supporting metal frames can be reduced using curved trusses of timber, e.g. for the Wyss Garden Centre (1962). Another option to construct a double curved shape is to add a form layer (*fill*) between straight beams and the timber board mould.

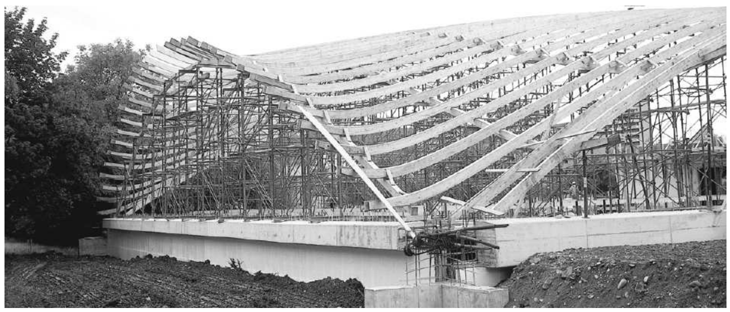

Figure 4.2. Framework of the Swimming Pool shell in Brügg (1981) by Isler, Flury 2002

The centres between the beams are such that thin timber boards placed across them take up the appropriate spatial curvature. Regular timber boards of sizes of *2.4 × 1.2 m* with a thickness of *18 mm* may be used. Steel boards are rarely used. Possibly, the timber boards are used to support a layer of insulation used as permanent shuttering, such as wood-wool slabs with a final topping of sprayed polyurethane. On top of the insulation layer (or the timber boards) the steel reinforcement is placed. To guarantee detachment of the insulation to the concrete, plastic fixings connect the insulation to the reinforcement with the least amount of cold bridging. For seamless clean concrete surfaces a hybrid plastic coating may be used, Haas [42].

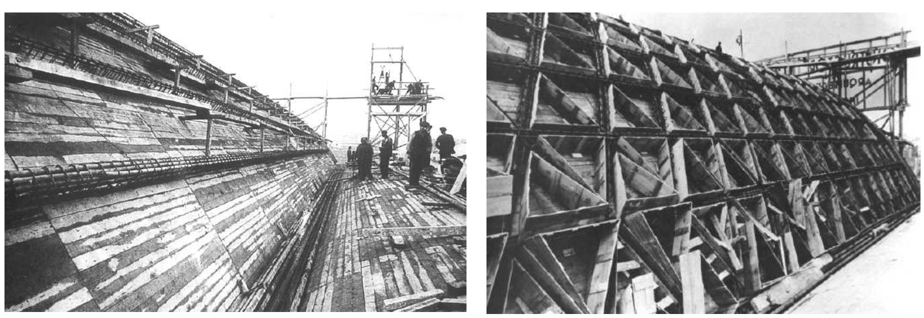

Figure 4.3. Formwork of the Fronton Recoletos (1936) in Madrid by Torroja, Fernandez Ordonez and NavarroVera 1999

Regardless of the fact that there may be some symmetry in the shell design, each beam in the framework slightly differs from its neighbour. For doubly curved shells, the timber boards and insulation must be cut exactly to measure and placed well lined. Additionally, shells may have daylight openings or points of intersecting curvatures which are extremely labour intensive, see Figure 4.3. The shape of the shell may be that complex that prefabrication of the timber formwork in a factory using more advanced construction techniques is required. Hence, forming (and designing) the conventional formwork is extremely time consuming and, thus, expensive (an exception form the hypar shaped shells, because the formwork can be made mainly from straight beams and boards). Despite the disadvantages, the great advantage of the conventional formwork is that every possible shape of a shell can be constructed. This is the reason that Swiss engineer Heinz Isler used conventional formwork for his shells. Isler solved the economical problem by cooperation with the Bösiger Construction Company. He designed his shells using standard sizes and shapes. This made possible the development of re-usable formwork and framework. Because of that, Heinz Isler was able to construct shells even after the sudden death in the early *1970s*, Chilton [22].

The first shells of the modern era are constructed using plates and boards. However, at highly double curved areas seams are visible indicating small deviations from the pure shape and highly curved sections were impossible to achieve with sufficient accuracy. Therefore, new techniques were developed and used to construct the contemporary, highly curved, free-form shells and blobs with amorphous shapes. Foamed plastic (polystyrene) formwork fabricated with a computer numerical controlled (CNC) milling cutter is a popular but expensive type of formwork. It can be combined with conventional timber boards for less curved areas. To prevent seams both surfaces are treated afterwards with a hybrid plastic coating, Dingsté [31].

4.1.2 Prefabricated Moulds

The first attempts to save costs and time in shell construction were made by Italian Pier Luigi Nervi. He was the first to use prefabricated elements in shell construction (discussed later in Section 4.5) and the first to use prefabricated Ferrocement moulds of clean surface. Prefabricated moulds are used in shell construction as permanent formwork. Commonly, the units are small, while combined they form a structural element or complete shell. Placed on conventional scaffolding (or self supporting) and topped with a layer of reinforcement they can be filled with concrete. The final shell consists of a composite structure of in-situ placed concrete and permanent (Ferrocement) formwork.

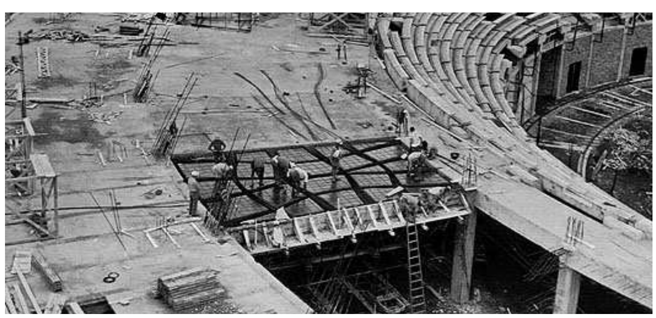

Figure 4.4. Prefabricated floor elements in Nervi's Palazzo dello Sport (1960) in Rome, www.uniroma1.it

Using prefabricated moulds, it is important that the permanent mould interacts with the poured-in-place concrete. Therefore, it is desirable that the material chosen for mould fabrication matches the concrete and/or additional facilities (e.g. reinforcement) fixed to the mould make connection. Nervi used the material Ferrocement, a material which consists of several layers of steel mesh sprayed with a cement mortar easily fabricated in several shapes, for the fabrication of the moulds. He first used Ferrocement for the construction of the Turin exposition hall (1949), saving time and costs successfully, see Figure 2.28. This leaded to several other applications in shells and floors, for example the floor elements used for the Palazzo dello Sport (1960) in Rome, Figure 4.4. A modern type of a prefabricated mould is the Comshell roof system for monoclastic shells, a steel-concrete composite shell roof formed by pouring concrete on a thin stiffened steel base shell which serves as both the permanent formwork and the tensile steel reinforcement. The steel base shell is constructed by bolting together modular steel units in the form of an open-topped box consisting of a flat or slightly curved base plate surrounded by edge plates. The edge plates serves as barriers to prevent concrete from flowing, shear connectors, stiffeners and spacers for positioning additional reinforcing bars. They may have lip stiffeners for enhanced local buckling resistance.

The prefabricated moulds are beneficial mainly due to the reduced construction time as is the easiness with which complex geometry can be made and the small units can be handled. The elimination of much of the labour intensive temporary formwork, and sometimes framework, results in a further reduction of costs. Prefabricated moulds allow for long-span structures of great sophistication to be built relatively economically.

4.1.3 Airform Shells

From the pioneering work of Wallace Neff in 1942 to widespread inflated dome construction today, airform shells have made their mark in shell construction. Aforementioned in Chapter 2, the airform immediately became popular in the USA and several successive developments have resulted in a wide offer of commercial systems at the present day. Well-known are the BINI shell and the Monolithic Dome techniques.

The airform construction technique uses air inflated membranes as formwork. The fabric for airforms must be selected to meet requirements of strength, elongation, ruggedness, durability and desired surface characteristics. Strength requirements are dictated by inflation pressures and the shape and size of the structure. In general, the limitation of the shell diameter is the pressure withstanding of the allowable stresses in the fabric and the welds. Durability for withstanding degradation from ultraviolet and weather exposure is only important when the fabric serves as permanent cladding, like the Monolithic Dome concept. A common choice for the fabric is PVC coated nylon or polyester fabrics with thicknesses of *0.7* to *0.8 mm*. The shape of the shell is created by welding pieces of fabric together at high temperature (*>500°C*). By using cable net patterns it is possible to form ribs. In this way a ribbed shell can be realised, Monolithic Dome [94].

Before the airform can be inflated, the foundation of the shell must be realised. Subsequently, the membrane is connected to the foundation by requirement of airtightness. Inflating the membrane using blower fans usually takes *1* to *1.3* hour for a hemispherical dome with a diameter of *50 m* (approximately $200\ m^3$ per minute). Since the airform is most vulnerable when partially inflated, inflation must stop at strong winds (no more than *16-24 km/h*). When inflated, it is recommended to let the membrane stand for at least *12* hours, providing time to stretch (at normal air pressures the fabrics may stretch *10%*). After sufficient air pressure is present, the structural surface can be formed against the inflated membrane. During this process the pressure must be accurately controlled; a change in air pressure will affect the stress and the geometry of the final shell. For the placement of an internal structural surface the airform is provided with an airlock entrance whereas a small opening in the fabric allows for healthy airflow, Monolithic Dome [94].

For the placement of the reinforcement and concrete, distinction can be made in three different techniques: (1) the reinforcement and concrete are placed on the exterior of the membrane, (2) the reinforcement and concrete are put in between two layers of membrane or (3) the reinforcement and concrete are placed on the interior of an inflated membrane. With respect to alternative 1 and 2, distinction can be made between techniques in which the reinforcement and concrete are placed before inflation of the membrane and techniques in which this is done after inflation. They will be denoted (a) and (b), respectively.

Figure 4.5. The MINI Shell concept, www.binisystems.com

The different types of systems each have their own benefits and restrictions. System 1.a is commercially available as the MINI shell concept, developed as addition to the BINI shell. Reinforcement and wet concrete are placed on top of the membrane which subsequently is inflated to form the shell. The shell can be erected in just *30* to *40* minutes but is restricted to small dimensions. When the shell dimensions become too large (diameter exceeds *10 m*), correct placement of reinforcement and appropriate thickness of concrete cannot be guaranteed, BINI Shell [90]. The MINI system can be seen in Figure 4.5.

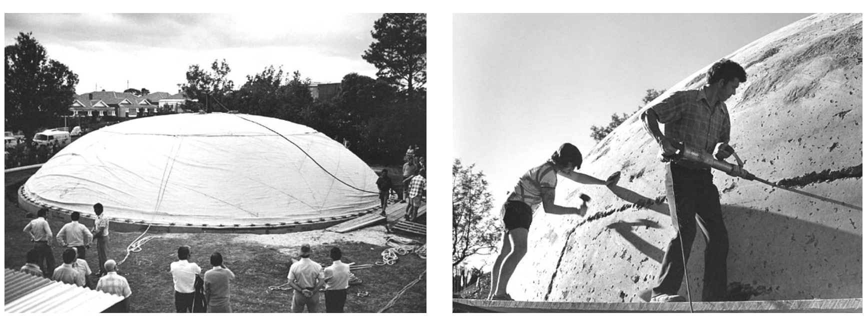

Figure 4.6. The BINI Shell system inflating and making a gap, www.binisystems.com

System 1.b is closely related to the patent of Wallace Neff and the Solid House Foundation which constructs small houses in developing countries. After inflation of the membrane the reinforcement and concrete are placed. Prefabrication of the reinforcement may shorten construction time. An appropriate dry concrete mixture must be applied to prevent it from sliding down. For larger dimensioned shells, system 2.a is available as the BINI shell, see Figure 4.6. The construction process is very much similar to the MINI shell concept. However, before inflation the concrete is covered by a second layer of fabric. By this, the correctness of the concrete thickness and placement of the reinforcement is secured, even for diameters up to *40 m*. The BINI shell can be erected in just *60* to *120* minutes, BINI Shell [90].

System 2.b is relative new as the concrete is by vacuum leaded into an inflated, double layered membrane. It is rarely used as it is difficult to assure proper concrete distribution and not discussed further. The largest shells are constructed with technique 3, e.g. the Monolithic Dome system. The Monolithic Dome starts as a concrete ring foundation reinforced with steel rebar. Vertical steel bars are embedded in the ring to attach the steel reinforcing of the dome itself later. For small domes an integrated floor/ring foundation is often applied whereas the floor is poured after completion of the dome in case of larger sizes. Then, an airform is placed on the ring base which is inflated. After the membrane is inflated, the shape is fixed by a layer of *80 mm* of polyurethane foam on the interior. The foaming takes place at roughly *500 Pa* air pressure, significant lower than needed for a direct placement of concrete. Hence, because of the limitation of shell diameter by the strength of the fabric, this concept enables much larger shell dimensions. The polyurethane foam serves as permanent insulation as well as formwork and temporary base for the reinforcement. After placement of reinforcement the structural concrete is sprayed onto the foam in layers of *20 mm*. Depending on the type of commercial system, the membrane is removed or serves as permanent outer surface. Therefore, the fabric is available in several styles, colours, and finishes, Monolithic Dome [94].

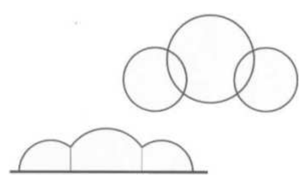

Figure 4.7. Combination of inflated membranes, Pronk et al. 2003

The airform technique offers fast, simple and efficient shell construction. The fabric saves the need for expensive and labour intensive formwork. It forms a proper mould of high correctness and, when damaged, the fabric can usually be repaired on the construction site. The biggest disadvantage of the airform shell is the lack of variety in shape. Because the flexible membrane buckles when the skin stress is equal or less than zero, the use of air pressure only allows for construction of synclastic spherical shapes. The only variation possible is to slice down part of the sphere, or to construct a membrane which consists out of a combination of several spherical shapes (of different sizes). However, the architectural freedom for free-form shell structures remains limited.

4.1.4 Stressed Membranes

A new technique showing large potential is the use of stressed membranes for shell construction. Similar to the airform shells, a fabric is used as formwork for the reinforced concrete. However, instead of air pressure, prestressing is used to stress the membrane into a desired shape. The most advantageous property lies in the fact that stressed membranes enable anticlastic shapes, Figure 4.8, and, combined with airform shapes, even free-forms, Figure 4.9, Pronk et al. [63]. The construction technique is recently tested at the University of Eindhoven in The Netherlands. A fabric was stressed between three points into an anticlastic shape. Subsequently, the shape was transformed into a structural surface by spraying it with *20 mm* layers of fibre reinforced concrete. Because of the large self-weight of the concrete, the fibre mixture was enhanced with plasticizers and accelerators to speed up the hardening of the concrete, preventing hydrostatical pressure to develop, Pronk [64]. The test model is seen in Figure 4.8.

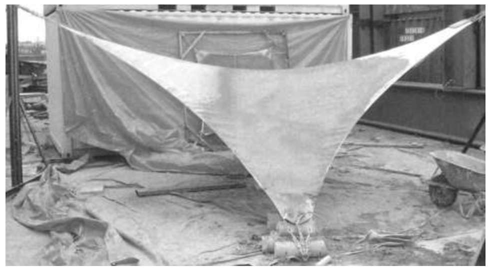

Figure 4.8. Stressed membrane with concrete, Cement 2006

From the tests, it can be concluded that it is possible to construct structural surfaces by the use of stressed membranes. The deformations of the membrane sprayed with concrete are within reasonable limits. However, during construction, one must take into account the larger deformations of the middle surface in compare to the corner points in order to arrive at the correct shape. Furthermore, the tests also included a successful application of conventional reinforcement. The method allows for prefabrication, as parts of the shell can be constructed independently before combined at the construction site, Pronk [64].

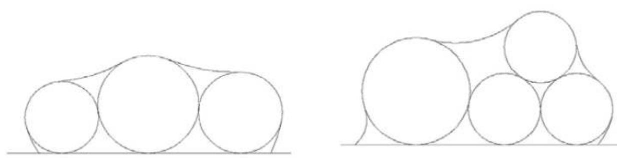

Figure 4.9. Free form shells out of several inflatable membranes, Pronk et al. 2003

The application may provide in a good alternative for conventional formwork in the construction of all types of shell shapes. However, there are no applications of this method on large dimensioned shells yet, so their use and effectiveness needs further research.

4.2 Reinforcement

In Chapter 3 the dimensioning of reinforcement in the design stage is discussed. This paragraph gives a reflection of the placement of reinforcement in practice. Due to the fact that shells are mainly constructed using conventional formwork or by airform technique, the placement of reinforcement at both will be considered.

Typical shell reinforcement consists of one or two layers of steel rebar or wire mesh. Usually, the reinforcement consists of relatively small diameters, which is beneficial for placement. A small bar is easy to carry and bent in the correct curvature. For conventional formwork the reinforcement is put in place by crane and workman. A single layer of reinforcement consists of bars in perpendicular directions wired attached or by welding. To ensure the concrete cover, distance controllers are used between the mould and the reinforcement. If a second layer is applied, supporting frames are placed on top of the first layer. Finally, distance controllers are placed for the outer concrete cover. When placed correctly, they provide in a helpful visual tool for 'measuring' the thickness of the shell during concreting. Using wire mesh reinforcement for a double-curved shell may require bending before placement to prevent residual stresses. As pointed out in Chapter 3, the reinforcement is placed in the most straight perpendicular manner possible. The points of greatest interest (and care) are the corner points of the shell near the supports. These points of high stress need large amounts of reinforcement and may include anchorages of prestressing cables. The curvature of the shell is not necessarily a problem for placement of reinforcement. Practically disadvantageous roll-off of rebars or easily bended out of place bars by workman are only of minor importance, Haas [42]. It may happen that the shape of a shell is that steep and complex that difficulties for the placement of reinforcement between double formwork are introduced. A possible solution is to prefabricate a steel or concrete frame to which the reinforcement can be attached before the formwork is placed. In case of a steel frame the frame itself already serves as part of the reinforcement. A steel frame technique is, for example, used for the construction of the University Music Theatre in Graz, Austria, Dingsté [31].

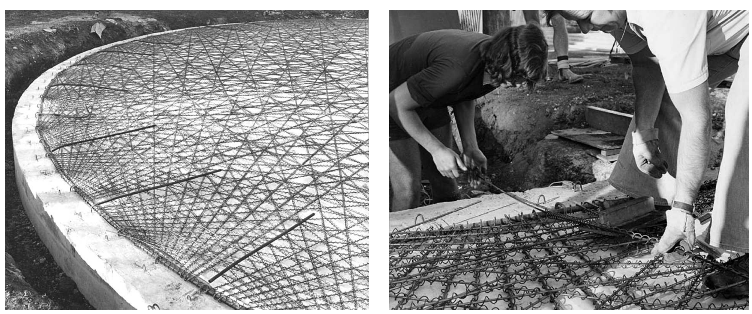

Figure 4.10. Steel spring reinforcement for a BINI Shell structure just before inflation, www.binisystems.com

The placement of reinforcement in airform shells varies for different types of construction method. Using the MINI shell or BINI shell system, great care is needed to ensure the reinforcement is at the right position after inflation. As can be seen in Figure 4.10, the before inflation arrangement is chaotic. The reinforcement may consist of a square mesh or steel springs capable of stretching so as to become automatically positioned on the curved surface when the membrane is inflated. Analogously, a wire mesh, which lays bunched on the membrane, is autopositioned because of the articulations at the joints of the mesh. The wire mesh reaches a particular shape while the spring mesh adapts itself to a variety of shapes, BINI Shell [90].

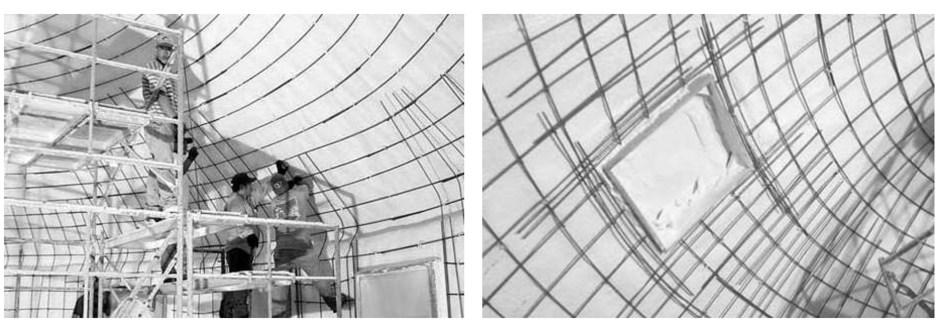

Figure 4.11. The placement of reinforcement on the foam of a Monolithic Dome, www.monolithic.com

Different placement techniques are involved when the reinforcement is added after the inflation of the membrane. An exterior concreted shell makes possible to just lay over a (prefabricated) wire mesh or rebar network. For internal shell construction, such as the Monolithic Dome, the rebars are fixed to the foam by hangers. Rebar hangers are *50 mm* square thin steel base plates with a wire welded perpendicular in the center and barbs protruding the opposite side. The barbs are pressed into the initial *40 mm* of foam, before the additional layers of foam are applied. After that, steel reinforcing rebars can be attached to the hangers using a specially engineered layout of hoop (horizontal) and vertical steel rebar. Small domes need small diameter bars with wide spacing. Large domes require larger bars with closer spacing. Placing the reinforcement into the hangers takes effort, see Figure 4.11. A continual tugging of workman pulling hoop reinforcement inside when attaching vertical reinforcement uninvitingly move the bars outward of the foam. Hence, careful treatment is needed. Furthermore, one must think of possibilities to transport the reinforcement and scaffolding, or other supporting material, through the airlock into the internal airform, Monolithic Dome [94].

4.3 Placement of Concrete

The placement of concrete of shells is a rigorous job. The large surface has to be of the correct thickness and needs to be properly compacted with an accurately smooth finish. Added to that, the placement introduces difficulties as the shell often has double curvature and quite steeply inclined locations. Therefore, it takes time and care to form the correct concrete profile, Haas [42].

Concreting starts when formwork is finished and reinforcement put into position. In general, shells are constructed using sprayed concrete or placed from a skip using a tower crane with a jib. The latter will be referred to as conventional placement, even though the first modern shell was constructed using the spray technique. Other techniques, as the vacuum method, only find minor application and are not considered. The placement technique to choose is mainly governed by the type of formwork. In general, the choice between sprayed and skipped concrete may said to be as follows: inflated airform moulds and stressed membranes require sprayed concrete whereas economical considerations imply for the use of skipped concrete in all other situations.

The choice for the type of concrete mixture is governed by strength and durability demands. As mentioned, the durability of the concrete is probably more important than strength, except for the possible high stressed regions near the supports. It is, thus, of great importance that the hardened concrete reaches sufficient quality. To reach high quality concrete, the mixture composition differs for each placement method. Sprayed concrete needs self-compacting properties and fast hardening. Conversely, concrete placed by skip needs heavy retardation to remain the concrete workable for periods longer than normal as forming of the shell by skipped concrete is a time-consuming process. Sometimes the mixture composition even varies for different locations in the shell, Chilton [22]. For example, a drier mix needed to prevent flow down from steep slopes. In this paragraph, the placement, compacting and finishing techniques are discussed as well as the required accompanying concrete mixture characteristics.

4.3.1 Conventional Placement

The conventional placement technique refers (in this thesis) to placement from a skip using a tower crane with a jib long enough to cover the whole plan area of the shell. For placement a special designed skip for easy placing of concrete with low water content is used. Usually, concrete takes place starting at one corner, filling the thickest part of the shell containing heavy reinforcement (and prestressing anchorages). Once the anchor block is full, concrete is placed on the sloping shuttering. When reaching about one third of the way to the top, first the other three corners are filled. The remainder of the shell is finished later, which is the reason for the heavy retardation of the concrete setting time at the joint, Chilton [22]. Besides heavy retardation, the concrete mixture composition must contain enough plasticizers to permit a drier mix which does not flow down steep slopes. Furthermore, plasticizers must assist in compaction around the network of reinforcement and prestressing ducts. A tricky part of the operation occurs at the end as the concreting progresses towards the middle of the shell. All workers and equipment ends up at the top and have to be removed by crane. The final area of concrete has to be placed and finished from a platform suspended from the jib of the crane.

Figure 4.12. The placement of concrete at the Kresge Auditorium (1955), www.arche.psu.edu

During placement and spreading, see Figure 4.12, the thickness of the concrete is assessed by gauging whether the correct cover is being provided to the top reinforcement. Careful concrete compaction of the thickest part is done by poker (or needle) vibrators. The steeply corner slopes of the shell are compacted using a flat vibrating plate and a rotating vibrating plate which looks like an electric floor polishing machine. For the remainder of the surface, fast compaction by flat vibrating plates only, is sufficient to obtain an acceptable surface finish. For the largest part of the shell surface, the common used poker vibrators are not suitable because of the small thickness of the shell. Besides the vibrating plate, compaction may be reached by vibration of the reinforcement or supporting framework. Vibrating the reinforcement is only satisfactory with rigid reinforcement grids. When vibrating the framework, the vibrators are attached directly to the supporting steel beams as to set the entire formwork in vibration. Usually the damping of the formwork will be sufficient to provide only a low energy level for compaction. No matter which compaction method is chosen, for satisfactory results the equipment used should be designed to operate on the principle of small energy dissipation with normal vibration amplitude; the danger of segregation is ever present, Haas [42].

Aforementioned, the final surface may be finished by vibrating plate or, for small shells, by screeding of the surface using suitable curved guides. If the finishing leaves a smooth surface, little surface-treatment is required and maintenance can be limited to occasional whitewashing or treatment with cement paint.

Sometimes even plasterers are used, e.g. to mould a rim along the edges. Because of the form of the shell is such that the rainwater run-off converges on the corners and water cascade off the edge looks careless, a rim is needed to channel the rainwater into the drainage system. Over the years it has been found that forming these channels is more easily carried out by hand by skilled craftsmen, Chilton [22].

4.3.2 Sprayed Concrete

Sprayed concrete or pneumatic concrete, also known as the Torkret method in Germany or the Gunite method (only for dry-mix process) in the UK, consists of spraying a mortar or concrete mixture with air pressure on a mall or an existing structure. The process is seen in Figure 4.13. The method finds its origin in the USA and is invented by American Carl Akeley. Akeley developed a system to strengthen plaster models. He used a dry plaster which he transported through a tube by air pressure before mixing it with water and spraying it onto the models. The technique for spraying concrete used today is actually quite similar to the one from Akeley; however, sometimes the water is added before transportation by tube, Speelman [71].

Figure 4.13. Spraying the concrete inside the airform of a Monolithic Dome, www.monolithic.com

In 1919 the method was first introduced in Europe by Carl Weber and the Torkret Company in Germany to repair damaged concrete. Obviously, the term Torkretieren finds its origin here. The success leaded to widespread usage in repairing operations for damaged concrete structures during and after the war. For the Zeiss planetarium in Jena in 1925, designers Dischinger and Finsterwalder came up with the idea to use the Torkret method for the construction, spraying the concrete against timber formwork. Spraying concrete means transporting a dry mixture of structural concrete by tube to the desired place where it is mixed with water, deposited and compacted. The dry mixture, consisting of sand, gravel and cement, is mixed at a special designed nozzle with water, just before it is sprayed. Advantageous of the dry mixture is the possible transportation over large distances and heights with relatively little energy. Spraying is done by workman or robot arms (less scaffolding, higher capacity). The chemical reaction starts when the mix is deposited. Using pneumatic sprayed concrete limits the grain size and modification by plasticizers and accelerators to achieve a low water-cement ratio and fast hardening. Today, to control shrinkage and thermical cracking and enlarge the tension capacity, fibre reinforcement is often applied. The mixture is sprayed in layers of $20\ mm$ thickness, and as the layers builds up, the coarser pieces can embed themselves and are firmly compacted therein. During initial application the coarser particles bounce back until the surface is covered with a thin coating of cement paste in which at first only the finer aggregate is retained. The amount of bounced back particles can be influenced by adapting the air pressure while keeping in mind the decrease of compaction. Sprayed concrete with dry mixture has a capacity of 4 to $10\ m^3$ per hour, Speelman [71].

From the middle *1940s*, also wet mixtures were transported through tubes before spraying. The technique is based on premature water mixing with only little air addition at the nozzle. Wet mixtures had been rarely used, as the large water amount needed badly influenced the concrete quality. However, after World War II, new developments made it possible to reduce the water cement ratio while increasing the quality of the concrete. Today, the method is used ever more for its higher capacity of *7* to *12* m^3 each hour, Speelman [71].

Using sprayed concrete, the final reached mixture has good density and bonding character with relatively high standard compression strength of *30* to *50* N/mm^2. The concrete shows high water tightness and little shrinkage, as a result of the low water cement ratio. The disadvantage is the higher costs involved in compare to conventional placement and the dust formation when using the dry method, Speelman [71].

4.4 Finishing

After hydration of the concrete, the shell construction can be finished. The formwork and framework can be removed and possible surface treatment applied. The finishing may also include bringing into compression of the shell by pulling inward its supports (so-called precompressing) or activating the prestressing ties.

4.4.1 Prestressing

The procedure of bringing the shell into compression differs for each shell design. Therefore, as an example, the stressing procedure of the Aquapark shell of Heinz Isler in Norwich (1991), as described by Chilton [22], is listed here. The Aquapark shell has a thickness of *100 mm* and a square ground plan with sides of *35 m*. The reinforcement consists of two layers of *6 mm* diameter steel bars at *100 mm* centres on a square grid. In the foundation beams prestressing ties are positioned. The first stage of prestressing initiated once the pour was completed and the concrete had developed strength for approximately three days. The initial prestress applied was more or less *25%* of the final force. This was achieved by stressing the foundation beams along each side, which had the effect of pulling the corners slightly towards each other and the precompressed shell lifted up from the formwork. The supporting trestles curved beams and light boards were then dismantled and stored for future reuse. After *21* days the remaining part of the prestress was applied using the same method.

4.4.2 Surface Treatment

Uncracked, well compacted concrete with appropriate cement content often is durable and impermeable enough to apply no surface protection, allowing the climate freely attack the concrete skin. This is generally the case, as the majority of the shell surfaces remain untreated. Maintenance can be limited to occasional whitewashing if, however, the skin is smooth enough, Chilton [22]. If not, for visual reasons or in case of tensile cracking, a surface treatment is applied. Several surface treatments are available, from simple cement paint to complete copper claddings similar to the skin of the Kresge Auditorium. In case of the Monolithic Dome concept shells, the fabric serves as surface protection. Surface protection or periodical surface treatment is a straight ahead operation which can be carried out on the hardened concrete surface.

4.5 Prefabrication

An increasing number of shell structures are constructed using prefabricated elements. Prefabricated elements in conventional structures have the advantage of faster erection time and save costs on formwork. For shells, the relative cost of formwork and staging are even greater than for more conventional concrete structures. Besides that, the use of prefabricated elements also offers advantages as reduced independency of the weather conditions, greater flexibility in construction methods and schedules and the possibility to standardisation and automation.

The use of prefabricated elements in shell construction goes back to 1940, when Pier Luigi Nervi used prefabricated lattice ribs for his airplane hangars in Italy. Later, in 1958, Nicolas Esquillan used prefabricated internal shear walls for his long span shells in Paris, Grenoble and Turin. Just before, in 1957, Ilia Doganoff constructed a fully prefab shell in Bulgaria. The shell of Doganoff consisted of a series of conoid shells, each of them formed out of four prefab elements which rest on prefabricated beams. The elements had a thickness varying from *30* to *60 mm*. A second example is the shell of Heinz Hossdorft in Switzerland, a storage hall built in 1961. The shell consisted of small (*1.39 m*) neighbouring curved panels which were prestressed afterwards, Joedicke [52]. Recently prefabricated shells appeared in Duxford and Millau.

Figure 4.14. A concept of a prefabricated shell out of many small elements by the BINI shell company, www.binisystems.com

With respect to shell construction, the question is how to apply prefabrication and which are the problems that arise. A shell can be prefabricated as a whole, in large parts, or in very small parts. In general, the choice is determined by the aim of prefabrication, namely, to obtain a maximum of repetition with a minimum of joints and work on site. Furthermore, prefabrication introduces three basic problems: transportation and erection, question of tolerances and the joints to be used. Obviously, they have a close relationship with each other. To obtain a proper prefabricated shell, the geometrical (subdivision) and practical (joints, placement) based problem must be solved to an optimum with a minimum of costs.

The transportation and erection of prefab elements limits the weight and dimensions of the shell elements. Even though they can be very thin (thicknesses of only *30 mm*) due to the low compressive stresses in shells and the accurate construction possible, the hoisting of complete shells is only possible for small shells and therefore finds minor application. The assembly of a large number of small shell elements is also possible, similar to the Duxford Imperial War Museum (1997) by Ove Arup and Partners and the prefabricated shell concept seen in Figure 4.14. This offers the possibility of standardisation and re-useable formwork, simplification of concreting and transportation and handling as desired in prefabrication. The advantages of small components are, however, offset by the problem of supporting the many individual parts during erection and the problem of joining the pieces into a monolithic shell. This can be solved by using smart framework, e.g. an inflatable membrane, see Figure 4.14. This is, however, only applicable for small spans.

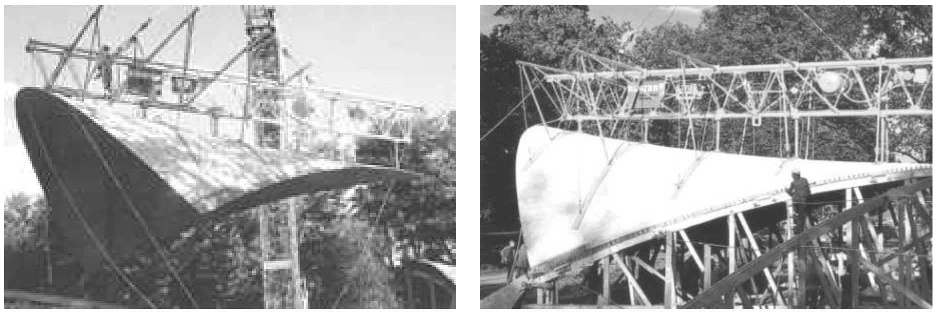

Figure 4.15. A prefabricated segment of the Stuttgart Federal Garden Fair shell (1977) by Jorg Schlaich, Holgate 1997

Besides the problem of framework, there are many joints. Joints are labour consuming and therefore expensive to apply. The more there are, the less the advantage is of prefabrication. Furthermore, the guiding principle should be that the joints are in areas where compression and/or shear will prevail, which forms a limitation to the structural design. There is a difference in wet and dry joints, referring to the use of filler material at the site. For example, cast in place concrete. Other possibilities are for bolded welded or glued connections. Joints may be unreinforced, simply reinforced or prestressed. The joints in Figure 4.14 are to be filled with poured-in-place concrete.

Figure 4.16. Placement of the prefabricated elements on temporary scaffolding of the Millau shell (2005), Servant 2006

A compromise solution is to construct the shell out of middle large prefab elements. They still can be transported and they have fewer joints to be constructed. An example of very thin large precast shell elements are the elements used for the Stuttgart Federal Garden Fair shell (1977) by German engineer Jörg Schlaich. The sections consisted out of Glass Reinforced Concrete with a thickness of only *12 mm* and combined they spanned a circular area with a diameter of *26 m*. The segments are seen in Figure 4.15.

The Millau shell, seen in Figure 4.16, is a special example of a prefabricated shell. The shell near Millau consists of several prefabricated curved elements of self-compacting high strength fibre reinforced concrete with a length of *28 m* and a maximum height of *850 mm*, however with a hollow core. The skin is only *100 mm* thick. The elements are put side-by-side on temporary framework and, subsequently, the elements are pressed together by longitudinal prestressing ties. The positioning of the elements is executed using temporary scaffolding. The special part is the fact that the elements are prefabricated on site, avoiding maximum transportation sizes (except for the crane capacity).

4.6 Conclusions

Shells are predominantly constructed using conventional timber formwork as mould. In conventional timber formwork the spatial curvature is achieved by curved glued-laminated beams supported by trestles or metal frames and timber boards. The timber formwork allows for almost every possible shell shape to be constructed. For highly double curved sections, the timber formwork can be replaced by foamed plastic (polystyrene) formwork fit into shape with a CNC milling cutter. The main disadvantages of conventional formwork are the high costs involved, in particular, labour costs. Therefore, prefabricated moulds, airform techniques and by spraying concrete on stressed membranes have been developed. Furthermore, shells assembled from prefabricated elements are developed to save on costs. However, for several reasons (e.g. lack of repetition for prefabrication or lack of architectural freedom when airforms are involved), only minor success has been reached on replacing the timber moulds.

The choice for a particular formwork may not only influence the design of the shell, but also puts restrictions on the placement and design of the reinforcement and the concrete mixture. The placement of reinforcement on double curved surfaces follows ordinary principles, however, for airform construction methods the reinforcement may be asked to autoposition itself. The placement of concrete is either by skip of sprayed. Conventional timber moulds are mainly filled using a skip and compacted by flat vibrating plates and poker vibrators for the thicker parts. Unusual techniques involve the vibration of the reinforcement mesh or the framework. Concrete placed by skip needs heavy retardation and plasticizers to permit a drier mix which does not flow down the slope. When the concrete is sprayed onto the formwork, accelerators are indispensable for fast hardening when the mix is deposited. Spraying bounds the grain size and fibres may be required to control shrinkage and thermal cracking. During placement the bounce back of particles must be closely examined and modified by adapting the air pressure.

After hydratation of the concrete possible prestressing ties can be activated and the concrete surface may be finished by, e.g. cement paint or complete claddings. However, generally, the concrete can be left untreated and maintenance can be limited to occasionally whitewashing.

part II

Theory

5 Theory of Shells

The introduction to the 'classical shell theory' in Chapter 3 remained restricted to a short historical perception. Following Chapter 3, this Chapter will give a concise description of the theory of elasticity, an explanation of the linear equations concerning the relation between loads, stresses, strains and deformations of (shell) structures. The sequence of explanation may in short be named as bar, plate, shell. Hence, it is logical and comprehensive to develop the theoretical considerations in stages, each time stepping up one dimension.

The theory of elasticity is an idealisation of the nonlinear reality and uses linear elastic laws to describe the structural behaviour. Similar to any other theory in continuum mechanics, the classical shell theory is based on three sets of basic equations; the kinematic equations, the constitutive equations and the equilibrium equations. The three basic equations are based on observed intensities of infinitesimal elements. They connect the deformations to the external applied load (external work) by relating them to the stresses and strains of the deformed structure (internal work). Boundary conditions conclude the mathematical description of the problem.

To be able to use the theory in hand calculation, the relations are simplified by restricting them to small deformations and slender cross-sections. It is, thus, impossible to analyse large deformation (nonlinear) problems. Regarding slender cross-sections, it is assumed that stress or strain in normal direction is of no significance to the solution. Aforementioned in Chapter 3, this so-called thin shell assumption is the most important hypothesis of the classical shell theory of Love and reduced the original three-dimensional problem to a surface deformation problem.

To perform a solution, use can be made of direct and indirect methods. Directs methods are closely related to the formulation of the basic relations. They solve the problem in a so-called direct manner, by the use of relationships based on observed intensities. Indirect methods are energy based methods and solve the problem by stating that the energy has to be stationary. The application of energy principles are the basis of computational numerical software such as the finite element method as they offer the possibility to generate approximated solutions and are also valid in the plastic range. This is discussed in Chapter 11.

In this Chapter, the application of the theory of elasticity on the bar, plate and shell is limited to types of loads that lead to both membrane straining and flexural deformation.

5.1 General

5.1.1 History

Most of the twentieth century shell structures rely on the progress made in the theory of elasticity from the late 19th century by mathematicians as Cauchy, Kirchhoff and Love. Elasticity always attracted the attention of the greatest minds in mathematical science. From the study of Galileo, the physical investigations of Hooke and Young, the theories by Euler and Bernoulli, the research of Navier and Saint Venant and the researches of Poisson, Cauchy, Kirchhoff, Lamé, the generalisations of Green, the papers of Stokes and Lord Rayleigh. The great merit of the theory of elasticity is that via an analytical approach 'exact' solutions could be obtained for problems of mechanics, long before numerical methods were developed, Milne [61].

Founded by Augustus Edward Hough Love in 1888, the classical shell theory was the first theory which enabled engineers to calculate the stresses in shells assuming linear elastic behaviour. The theory was an extension of the plate theory to structures with surface-like geometries using the same assumptions as the Kirchhoffean theory of plates. Thus, the theory is a low order theory and does not include shear deformation. The classical shell theory from Love is often referred to as Love's first approximation, Milne [61].

Love identified that the load carrying behaviour of shells consisted of a membrane effect in combination with bending action. The most important of his theory was, however, the reduction of the three-dimensional problem to two dimensions, the description of a surface deformation. His classical shell theory, therefore, is a 'thin shell' theory. The assumption that the thickness of the shell is much smaller than the radius of curvature yields that the flexural rigidity is much smaller than the extensional rigidity. Hence, the shell produces mainly in-plane membrane forces, resultants of the in-plane normal and shear stresses. The bending solution will arise in regions were the membrane solution is insufficient, for example at the supports where the membrane displacements are suppressed. The bending moments are often referred to as compatibility moments as they do not carry any load but only compensate the shortcomings of the membrane behaviour. The bending moments can be calculated separately and superimposed on the membrane solution as discovered in 1912 by H. Reissner, Hoogenboom [49].

The years following Love's formulation of linear elastic shell behaviour, scientist as Geckeler, Flügge and Byrne questioned Love's theory and formulated their own expressions. In particular the equations that Flügge derived in 1934 often serve as theoretical background in literature. The main reason it that the theory as presented by Flügge is based on the exact formulation and, thus, is valid for non-shallow shells as well. Independently from each other, Sanders and Koiter removed the inconsistencies of the different theories and concluded that there was only little difference between their accuracies. Therefore, sometimes is referred to the Sanders-Koiter equations, Hoogenboom [49].

5.1.2 Basic Relations

The behaviour of structures can be determined by three sets of *basic relations*; the *kinematic relation*, the *constitutive relation* and the *equilibrium relation*. The connection between the relations is seen in Figure 5.1. To complete the mathematical description, the *boundary conditions* of the particular problem must be introduced.

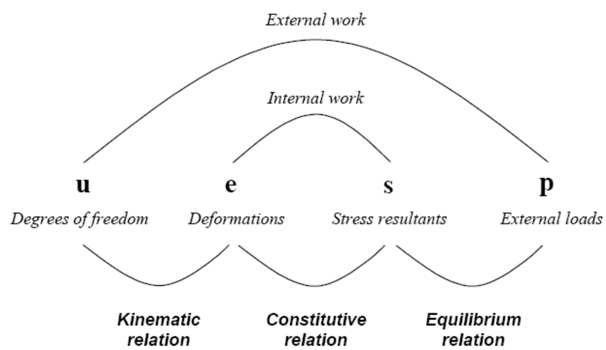

Figure 5.1. Relations of continuum mechanics, Hoefakker and Blaauwendraad 2003

The three basic relations between the degrees of freedom, deformations, stress resultants and external loads for an arbitrary structure can, in short, be described as

$$\begin{aligned} &\mathbf{e} = \mathbf{Bu} && \text{kinematic relation} \\ &\mathbf{s} = \mathbf{De} && \text{constitutive relation} \\ &\mathbf{p} = \mathbf{B}^T\mathbf{s} && \text{equilibrium relation} \end{aligned} \tag{5.1}$$

In the relations, ***u*** and ***p*** represent respectively the *deformation* and *load vector*, and ***e*** and ***s*** the *strain* and *stress resultant tensor*, see Chapter 11.1. A three-dimensional body can be completely described by:

$$\begin{aligned} \mathbf{u} &= \begin{bmatrix} \mathrm{u_x} & \mathrm{u_y} & \mathrm{u_z} \end{bmatrix}^T \\ \mathbf{e} &= \begin{bmatrix} \varepsilon_{xx} & \varepsilon_{yy} & \varepsilon_{zz} & \gamma_{xy} & \gamma_{yz} & \gamma_{zx} & \kappa_{xx} & \kappa_{yy} & \kappa_{zz} & \rho_{xy} & \rho_{yz} & \rho_{zx} \end{bmatrix}^T \\ \mathbf{s} &= \begin{bmatrix} n_{xx} & n_{yy} & n_{zz} & \mathrm{n_{xy}} & \mathrm{n_{yz}} & \mathrm{n_{zx}} & \mathrm{m_{xx}} & \mathrm{m_{yy}} & \mathrm{m_{zz}} & \mathrm{m_{xy}} & \mathrm{m_{yz}} & \mathrm{m_{zx}} \end{bmatrix}^T \\ \mathbf{p} &= \begin{bmatrix} \mathrm{p_x} & \mathrm{p_y} & \mathrm{p_z} \end{bmatrix}^T \end{aligned} \tag{5.2}$$

Furthermore, in the three basic relations, ***B*** is the *kinematic matrix*, ***D*** the *stiffness matrix* and ***B^T*** the *equilibrium matrix*. One presumably will notice the remarkable similarity in notation between the equilibrium matrix and the kinematic matrix. The equilibrium matrix ***B^T*** is the adjoint matrix of the kinematic matrix ***B***, in which the adjoint matrix is, in this context, defined as the transpose of a matrix where the uneven derivatives do change sign and the even or zero-order derivatives do not, Hoefakker and Blaauwendraad [45]. The similarity between the kinematic and equilibrium matrices can be simply explained with the *virtual work equation* as is done later in Paragraph 5.5.

5.1.3 Assumptions

By determining the matrices relating the displacements to the strains, the strains to the stress resultants and the stress resultants to the external loads a few assumptions are done to obtain simplified equations usable for hand calculation. They are valid for as well the bar and plate as the shell equations, being all slender structures with small deformations.

a. All points lying on a normal of the middle surface before deformation remain on that normal, which remains a normal of the deformed middle surface.
b. For all kinematic relations it is assumed that the distance z of a point from the middle surface remains unaltered by the deformation.
c. The stress component σ_{zz} normal to the middle surface is considered to be very small in comparison to the other stress components and is therefore neglected.
d. All displacements are so small that they are negligible in comparison to the radii of curvature of the middle surface. Consequently, their higher powers can be neglected and the first derivatives of the lateral displacement u_z, the slopes, are negligible compared to unity.

Assumption *a* is in the beam theory known as the *Bernoulli hypothesis*, deformations due to transverse shearing stresses are neglected. Assumptions *b* and *c* are the so-called thin shell assumptions. Stresses or strains in normal direction are of no significance to the solution, reducing the three-dimensional problem to a two dimensional surface deformation problem. The last assumption *d* is done to keep the equations linear, discarding possible nonlinear behaviour, Hoefakker and Blaauwendraad [45].

Applying the assumptions to the general vectors of (5.2) yields a reduced vector scheme:

$$\begin{aligned}
\mathbf{u} &= \left[\mathrm{u_x}\ \mathrm{u_y}\ \mathrm{u_z}\right]^T \\
\mathbf{e} &= \left[\varepsilon_{\mathrm{xx}}\ \varepsilon_{\mathrm{yy}}\ \gamma_{\mathrm{xy}}\ \kappa_{\mathrm{xx}}\ \kappa_{\mathrm{yy}}\ \rho_{\mathrm{xy}}\right]^T \\
\mathbf{s} &= \left[n_{\mathrm{xx}}\ n_{\mathrm{yy}}\ \mathrm{n_{xy}}\ \mathrm{m_{xx}}\ \mathrm{m_{yy}}\ \mathrm{m_{xy}}\right]^T \\
\mathbf{p} &= \left[\mathrm{p_x}\ \mathrm{p_y}\ \mathrm{p_z}\right]^T
\end{aligned} \tag{5.3}$$

Or, represented in a relation scheme it reads:

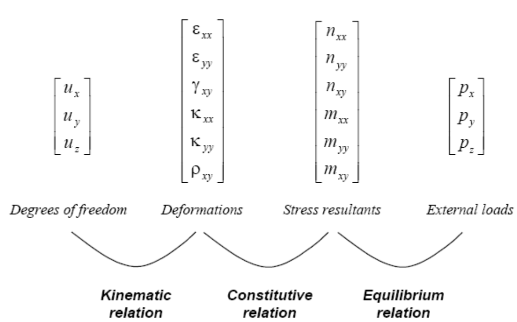

Figure 5.2. The vector scheme used for thin shells, Hoefakker and Blaauwendraad 2003

Note that the longitudinal shear terms are represented by only one parameter (n_{xy}) as the moment equilibrium with respect to the *z-axis* implies that the in-plane terms must be equal.

5.2 Theory of Bars

Because of its relative simplicity, the straight slender bar will serve as starting point for a simple application of formulating the basic relations. The three basic relations are derived for a one-dimensional bar in extension and, separately, a bar in bending. This means that the vectors of (5.3) further reduce, leaving only terms in *x*- and *z-direction*.

$$\mathbf{u} = [\mathrm{u}_x \ \mathrm{u}_z]^T \qquad \mathbf{s} = [N \ M]^T$$

$$\mathbf{e} = [\varepsilon \ \kappa]^T \qquad \mathbf{p} = [\mathrm{p}_x \ \mathrm{p}_z]^T \tag{5.4}$$

Because of the fact that the quantities of *n* and *m* have the dimension of force and moment, respectively, they are indicated by a capital.

5.2.1. Extension

Equilibrium Relations

For the one-dimensional problem of a bar loaded in extension, for example a column, the quantities that play a role are the displacement $u_x(x)$, the strain $\varepsilon(x)$, the stress resultant $N(x)$ and the external applied force $p_x(x)$, see Figure 5.3.

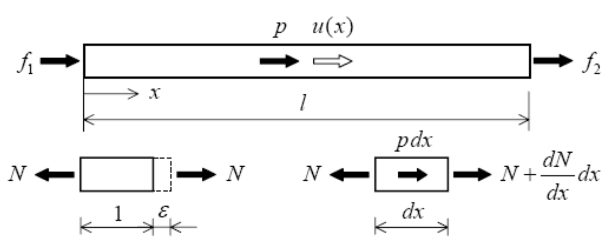

Figure 5.3. The bar subjected to extension with relevant quantities, Blaauwendraad 2004

The relations between the quantities can be determined by examining an infinitesimal element of the bar with length *dx*. For the equilibrium relations, the sum of the applied external force $p_x(x)$ and the normal force $N(x)$ must hold equilibrium. On an infinitesimal element the applied external force is $\mathrm{p}_x(x)dx$ and the change in normal force is $-N + \mathrm{N} + \frac{dN}{dx}dx = \frac{dN}{dx}dx$, as can be seen in Figure 5.3. This yields the equilibrium relation between the stress resultant gradient and the applied external force:

$$\frac{dN}{dx} + p = 0 \qquad\qquad \mathbf{B}^{\mathrm{T}}\mathbf{s} + \mathbf{p} = \mathbf{0} \tag{5.5}$$

Constitutive Relations

The internal normal force $N(x)$ causes straining of the bar. The strain $\varepsilon(x)$ is calculated using Hooke's law for the stress-strain relation of linear elastic structures. By dividing the normal force through a stiffness term EA, the axial stiffness of the bar, the strain is found. The stiffness term is the product of Young's modulus E, representing the linear stress-strain relation of Hooke, and the cross-sectional area A over which the force acts. Thus, the constitutive relation is:

$$\varepsilon = \frac{N}{EA} \qquad \text{(flexibility formulation)} \qquad \mathbf{e} = \mathbf{Cs}$$

$$\text{or} \quad \mathrm{N} = \mathrm{EA}\varepsilon \qquad \text{(stiffness formulation)} \qquad \mathbf{s} = \mathbf{De} \tag{5.6}$$

Kinematic Relations

The strain $\varepsilon(x)$ of the bar gives rise to extensional deformation. The strain can be determined by dividing an infinitesimal extension du_x through the original length dx, see Figure 5.3. Therefore, the kinematic relation can be described as:

$$\varepsilon = \frac{du_x}{dx} \qquad \mathbf{e} = \mathbf{Bu} \tag{5.7}$$

The kinematic, constitutive and equilibrium relations (respectively 5.5, 5.6 and 5.7), in combination with the particular boundary conditions of a certain problem, can be solved with *direct* or *indirect methods*, discussed in Paragraph 5.5.

The one-dimensional bar in extension is a very simple, statically determined problem. However, the same analogy holds for less trivial, statically indeterminate problems, where there are more quantities that play a role. Various examples can be found in literature.

5.2.2 Bending

When the one-dimensional bar of section 5.2.1 is loaded eccentrically, or perpendicular to the bar axis, for example by a distributed load in *z-direction*, bending occurs. Bending in a bar causes curvature. Thus, when considering a bar loaded by a distributed load in *z-direction*, the quantities that play a role are the displacement $u_z(x)$ *(or $w(x)$)* in *z-direction*, the curvature $\kappa(x)$, a moment $M(x)$ and the distributed load $p_z(x)$.

It must be said that, because of the slender beam assumption, the quantities concerning shear rotation, shear deformation, shear force and torsion are not included in the vector scheme of (5.4). However, in the following they will be mentioned to obtain an understandable derivation of the equations.

Equilibrium Relations

The distributed load *p(x)* perpendicular to the bar axis generates a shear force *V(x)* in the same direction. To ensure equilibrium of an infinitesimal element of the bar, bending moments arise. The equilibrium behaviour, thus, can be divided into two parts, seen in Figure 5.4.

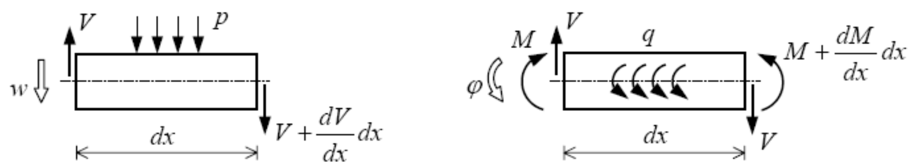

Figure 5.4. Equilibrium of a bar loaded in z-direction, Blaauwendraad 2004

In Figure 5.4 the equilibrium of the external load with the internal shear force V and the internal moment M can be seen. Aforementioned in the introduction of the chapter, the torsion load q is set equal to zero.

The equilibrium relations become:

$$\frac{dV}{dx} + p = 0 \qquad \text{in } z\text{-direction}$$

$$\frac{dM}{dx} - V = 0 \qquad \text{in } x\text{-direction} \tag{5.8}$$

By substitution of the second equilibrium relation into the first relation the shear force V is eliminated and the basic equation for equilibrium is obtained:

$$\frac{d^2M}{dx^2} + p = 0 \qquad \mathbf{B}^T\mathbf{s} + \mathbf{p} = \mathbf{0} \tag{5.9}$$

Note that, by setting the torsion load equal to zero, the shear force is the derivative of the bending moment, which is well-known to engineers.

Constitutive Relations

The constitutive relation between the curvature κ and the bending moment M can be determined by dividing the bending moment through the bending stiffness of the bar EI, the product of the Young's modulus and the moment of inertia I. The equation shows similarities with equation (5.6).

$$\kappa = \frac{M}{EI} \qquad \text{(flexibility formulation)} \qquad \mathbf{s} = \mathbf{De}$$

or

$M = EI\kappa$ (stiffness formulation) $\mathbf{e} = \mathbf{Cs}$ (5.10)

Kinematic Relations

The kinematic relation couples the curvature κ to a displacement u_z *(or $w(x)$)*. If an infinitesimal element of length dx deforms du_z, then the rotation φ of the element can be described as:

$$\varphi = -\frac{du_z}{dx} \tag{5.11}$$

The minus sign enters the equation due to the fact that a positive displacement u_z is related to a negative rotation of the cross-section, see Figure 5.5. This can be explained by examining a shear deformation γ. Figure 5.5 also shows the definition of shear deformation. The deformation can be calculated with the equation $\gamma = \varphi + \frac{du_z}{dx}$.

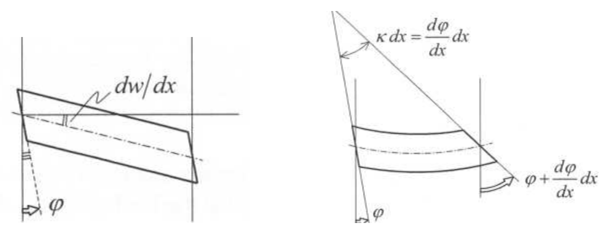

Figure 5.5. The definition of shear deformation (left) and curvature (right), Blaauwendraad 2004

Due to the fact that the shear deformation is set equal to zero, the rotation φ can be determined with equation (5.11).

It can also be seen in the Figure 5.5, that the curvature of the same element is the described by the increase of the rotation φ over the element length dx.

The situation in Figure 5.5 can be formulated as:

$\kappa = \frac{d\varphi}{dx} = -\frac{d^2u_z}{dx^2}$ $\mathbf{e} = \mathbf{Bu}$ (5.12)

The latter is the kinematic relation of a bar in bending and completes the description of a bar in bending.

Looking at equation (5.9) and (5.12) it can be concluded that the quantities concerning shear are eliminated and neglected. However, it must be pointed out that, this is only possible because the calculation remains restricted to slender bars. This assumption is applicable when the slenderness ratio of the depth of the bar to the span is smaller than *1/5*. Then, the shear contribution is smaller than *10%*. There is referred to the Euler-Bernoulli or Navier beam solution. When the beam cannot be regarded as slender, shear deformation must be included in the calculation. Engineers will recognise this as the Timoshenko beam solution.

5.2.3 Combined Extension and Bending

Finally, the extensional and bending relations can be combined in the slender beam equations:

Kinematic Relations

$$\begin{bmatrix} \varepsilon \\ \kappa \end{bmatrix} = \begin{bmatrix} \dfrac{d}{dx} & 0 \\ 0 & -\dfrac{d^2}{dx^2} \end{bmatrix} \begin{bmatrix} u_x \\ u_z \end{bmatrix}$$

Constitutive Relations

$$\begin{bmatrix} N \\ M \end{bmatrix} = \begin{bmatrix} EA & 0 \\ 0 & EI \end{bmatrix} \begin{bmatrix} \varepsilon \\ \kappa \end{bmatrix} \tag{5.13}$$

Equilibrium Relations

$$\begin{bmatrix} -\dfrac{d}{dx} & 0 \\ 0 & -\dfrac{d^2}{dx^2} \end{bmatrix} \begin{bmatrix} N \\ M \end{bmatrix} = \begin{bmatrix} p_x \\ p_z \end{bmatrix}$$

From the relations it can be seen that, in case of a linear beam, extension and bending are not coupled and, thus, can take place independently from each other (theoretically). Furthermore, it can be seen that the kinematic matrix **B** indeed is the adjoint of the equilibrium matrix $\mathbf{B}^T$.

The beam equations, complemented with the boundary conditions, can be solved with *direct-* or *indirect methods* as discussed in Paragraph 5.5.

5.3 Theory of Plates

Following the preceding discussion of the theory of bars, this paragraph contains the derivation of the plate theory. Plates are two-dimensional structures which can be loaded in-plane (plates) or perpendicular of their plane (slabs). They can be divided into thick and thin plates. For flat plates loaded in their plane, there is a plane stress situation. A plate can be seen as a generalisation of bars and therefore, equations derived in Paragraph 5.2 are valuable for the derivation of the theory of plates as well. Stepping up one dimension from the bar to the plate, the vector scheme of (5.4) expands with terms of the *y-direction*. By that, the general vector scheme of (5.3) is reached. Recapitulate from Paragraph 5.1.2:

$$\mathbf{u} = \left[\mathrm{u_x} \ \mathrm{u_y} \ \mathrm{u_z} \right]^T$$

$$\mathbf{e} = \left[\varepsilon_{\mathrm{xx}} \ \varepsilon_{\mathrm{yy}} \ \gamma_{\mathrm{xy}} \ \kappa_{\mathrm{xx}} \ \kappa_{\mathrm{yy}} \ \rho_{\mathrm{xy}} \right]^T$$

$$\mathbf{s} = \left[n_{\mathrm{xx}} \ n_{\mathrm{yy}} \ \mathrm{n_{xy}} \ \mathrm{m_{xx}} \ \mathrm{m_{yy}} \ \mathrm{m_{xy}} \right]^T \tag{5.3}$$

$$\mathbf{p} = \left[\mathrm{p_x} \ \mathrm{p_y} \ \mathrm{p_z} \right]^T$$

Because the forces and moments are now expressed per unit of length, the quantities are written down without a capital.

5.3.1 Extension

Kinematic Relations

Like the derivation of the arch bending equations, for plates (and later also for shells) at first the kinematic equations are deduced. For the kinematic relations of a two-dimensional plate loaded in-plane an infinitesimal small part of a plate is considered of dimensions *dx dy*. The plate part can deform in *x-direction* and *y-direction*, therefore equation (5.7) must be extended to a two-dimensional situation. The strains in both directions become:

$$\varepsilon_{xx} = \frac{\partial u_x}{\partial x} \quad \text{and} \quad \varepsilon_{yy} = \frac{\partial u_y}{\partial y} \tag{5.14}$$

Note that *d* is substituted a curved ∂, indicating the equation is a partial differential equation.

Moreover, the plate can also experience a shear deformation γ_{xy}, which changes the shape of the plate. This possible shear deformation γ_{xy}, is graphically shown in Figure 5.6.

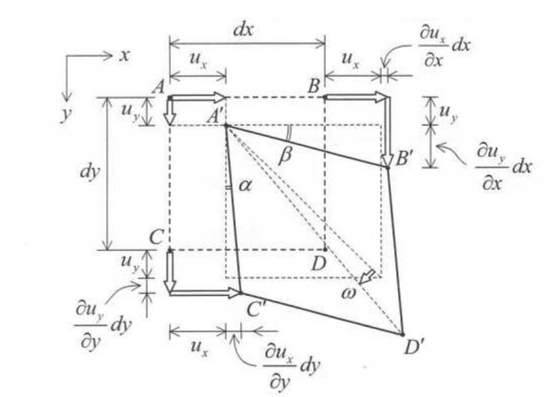

Figure 5.6. Deformations of a plate part, Blaauwendraad 2004

The shear deformation can be determined by adding the rotations $\alpha \left(= \frac{\partial u_x}{\partial y}\right)$ and $\beta \left(= \frac{\partial u_y}{\partial x}\right)$:

$$\gamma_{xy} = \frac{\partial u_x}{\partial y} + \frac{\partial u_y}{\partial x} \tag{5.15}$$

The kinematic relations are, thus, described as:

$$\begin{bmatrix} \varepsilon_{xx} \\ \varepsilon_{yy} \\ \gamma_{xy} \end{bmatrix} = \begin{bmatrix} \frac{\partial}{\partial x} & 0 \\ 0 & \frac{\partial}{\partial y} \\ \frac{\partial}{\partial y} & \frac{\partial}{\partial x} \end{bmatrix} \begin{bmatrix} u_x \\ u_y \end{bmatrix} \qquad \mathbf{e = Bu} \tag{5.16}$$

Constitutive Relations

The constitutive relations provide the relation between the stresses and the strains according Hooke's law. For a two-dimensional stress state the three strains need to be related to the three internal forces; n_{xx}, n_{yy} and n_{xy} for the shear stress belonging to the shear deformation γ_{xy}. The three internal forces are also called extensional forces or membrane forces and are determined by multiplying the three strains ε_{xx}, ε_{yy} en γ_{xy} by the stiffness parameter. For thin plates the stiffness parameter is determined by multiplication of the Young's modulus E with the thickness of the plate t (yields the stiffness per square unit plate).

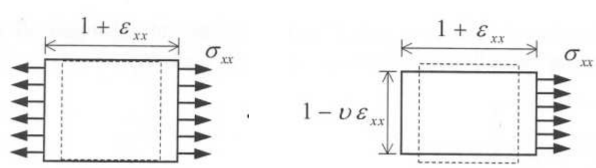

Figure 5.7. Plate without (left) and with (right) lateral contraction, Blaauwendraad 2004

In addition to the relations found for a one-dimensional bar (equation 5.6) a two-dimensional plate part under extension in one direction experiences lateral contraction in the perpendicular direction, see Figure 5.7. Lateral contraction is the phenomenon of decreasing width in one direction while pulling in another direction, e.g. seen when stressing an elastic band. In the relation the lateral contraction coefficient or Poisson's ratio ν appears.

The constitutive relation of a plate part in flexibility formulation then becomes:

$$\begin{bmatrix} \varepsilon_{xx} \\ \varepsilon_{yy} \\ \gamma_{xy} \end{bmatrix} = \frac{1}{Et} \begin{bmatrix} 1 & -\nu & 0 \\ -\nu & 1 & 0 \\ 0 & 0 & 2(1+\nu) \end{bmatrix} \begin{bmatrix} n_{xx} \\ n_{yy} \\ n_{xy} \end{bmatrix} \qquad \mathbf{e = C\,s}$$

By inverting the stiffness formulation is found:

$$\begin{bmatrix} n_{xx} \\ n_{yy} \\ n_{xy} \end{bmatrix} = \frac{E\,t}{1-\nu^2}\begin{bmatrix} 1 & \nu & 0 \\ \nu & 1 & 0 \\ 0 & 0 & \dfrac{(1-\nu)}{2} \end{bmatrix}\begin{bmatrix} \varepsilon_{xx} \\ \varepsilon_{yy} \\ \gamma_{xy} \end{bmatrix} \qquad \mathbf{s} = \mathbf{D\,e} \tag{5.17}$$

For a more general formulation the terms in the rigidity matrix may be replaced by stiffness terms such as D_{xx}, D_{yy} and D_{xy}.

Equilibrium Relations

The final relation completing the basic equations for a plate in extension is the equilibrium relation between the membrane forces and the external applied loads. In the figure below a plate part *dx dy* is projected with the equilibrium quantities.

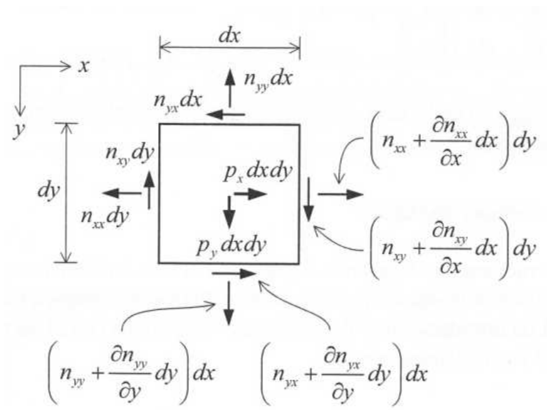

Figure 5.8. Equilibrium of a 2D plate part, Blaauwendraad 2004

As is seen in Figure 5.8, both the *x-directional* and *y-directional* part of load *p* must be in equilibrium with the membrane forces. The total equation in *x-direction* becomes:

$$-n_{xx}dy + n_{xx}dy + \frac{\partial n_{xx}}{\partial x}dxdy - n_{yx}dx + n_{yx}dx + \frac{\partial n_{yx}}{\partial y}dydx + p_x dxdy = \frac{\partial n_{xx}}{\partial x} + \frac{\partial n_{yx}}{\partial y} + p_x = 0$$

and in *y-direction:*

$$-n_{yy}dx + n_{yy}dx + \frac{\partial n_{yy}}{\partial y}dydx - n_{xy}dy + n_{xy}dy + \frac{\partial n_{xy}}{\partial x}dxdy + p_y dxdy = \frac{\partial n_{yy}}{\partial y} + \frac{\partial n_{xy}}{\partial x} + p_y = 0 \tag{5.18}$$

Due to the moment equilibrium with respect to the out-of-plane z-axis, the two longitudinal shearing stress resultants must be equal: $n_{xy} = n_{yx}$. The equilibrium relation in matrix notation is then

$$\begin{bmatrix} -\frac{\partial}{\partial x} & 0 & -\frac{\partial}{\partial y} \\ 0 & -\frac{\partial}{\partial y} & -\frac{\partial}{\partial x} \end{bmatrix} \begin{bmatrix} n_{xx} \\ n_{yy} \\ n_{xy} \end{bmatrix} = \begin{bmatrix} p_x \\ p_y \end{bmatrix} \qquad \mathbf{B}^T\mathbf{s} = \mathbf{p} \qquad (5.19)$$

The basic equations for a plate in extension are now determined.

5.3.2 Bending

Plates loaded perpendicular to their plane (slabs) experience bending behaviour. Again, the plate or slab can be seen as a generalisation of bars which span in two directions. By loading the slab, bending moments and shear deformation can be expected. As with the bar, the slenderness of the slab is decisive for possible neglecting the shear deformation. For thin plates it also holds that if the thickness to span ratio is smaller than *1/5*, Blaauwendraad [8].

Kinematic Relations

The kinematic relation between the displacement u_z perpendicular to the plate surface and the curvature κ of a plate part *dx dy* shows equalities with the bar in bending. From Chapter 5.2.2 it can be read that the curvature (in *x-direction*) is equal to minus the second derivative of the displacement u_z:

$$\kappa = \frac{d\varphi}{dx} = -\frac{d^2 u_z}{dx^2} \qquad (5.12)$$

For thin plates, the same expression holds for curvature in *x-direction*. Additional, in a *2D* plate part, there is also a curvature in *y-direction*. Both curvatures are:

$$\kappa_{xx} = \frac{\partial \varphi_x}{\partial x} = -\frac{\partial^2 u_z}{\partial x^2}$$

$$\kappa_{yy} = -\frac{\partial^2 u_z}{\partial y^2} \qquad (5.20)$$

The third curvature in a *2D* plate part is the curvature due to possible torsional moments m_{xy} and m_{yx}:

$$\rho_{xy} = \frac{\partial \varphi_x}{\partial y} + \frac{\partial \varphi_y}{\partial x} = -2\frac{\partial^2 u_z}{\partial x \partial y} \qquad (5.21)$$

The three curvatures can be seen in Figure 5.9.

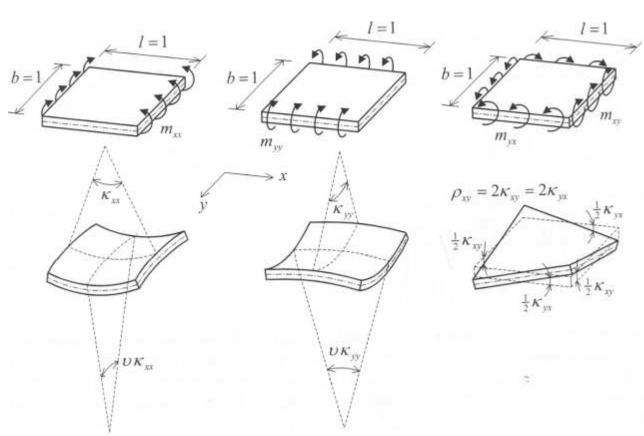

Figure 5.9. Stress resultants and curvatures of a plate in bending with lateral contraction, Blaauwendraad 2004

Subsequently, the kinematic relations for a plate in bending can be described as:

$$\begin{bmatrix} \kappa_{xx} \\ \kappa_{yy} \\ \rho_{xy} \end{bmatrix} = \begin{bmatrix} -\frac{\partial^2}{\partial x^2} \\ -\frac{\partial^2}{\partial y^2} \\ -2\frac{\partial^2}{\partial x \partial y} \end{bmatrix} [u_z] \qquad \mathbf{e = Bu} \qquad (5.22)$$

Constitutive Relations

The quantities that play a role in the constitutive relations can also be seen in Figure 5.9. Again, the bending moment can be determined by multiplying the curvature with the bending stiffness. For the plate relation the general bending stiffness D_b is used. Like the plate in extension, the lateral contraction ν enters the constitutive relation.

$$\begin{bmatrix} m_{xx} \\ m_{yy} \\ m_{xy} \end{bmatrix} = \begin{bmatrix} D_b & \nu D_b & 0 \\ \nu D_b & D_b & 0 \\ 0 & 0 & D_b\left(\frac{1-\nu}{2}\right) \end{bmatrix} \begin{bmatrix} \kappa_{xx} \\ \kappa_{yy} \\ \rho_{xy} \end{bmatrix} \qquad \mathbf{s = D\,e} \qquad (5.23)$$

For a thin plate, the expression for the bending stiffness can be described as $D_b = \frac{Et^3}{12(1-\nu^2)}$.

Equilibrium Relations

The equilibrium relation for a thin plate can easily be obtained by extending the equilibrium relations for a bar in bending with the *y-direction*. Hence, the equilibrium in *z-direction* becomes:

$$\frac{\partial v_x}{\partial x} + \frac{\partial v_y}{\partial y} + p_z = 0 \qquad (5.24)$$

Analogous to the bar equations, the out-of-plane shear is eliminated by setting-up the equilibrium of moments with respect to the *x-direction* and *y-direction* and therefore, the first two terms of the equilibrium relation can be replaced by terms which contain bending moments:

$$\frac{\partial m_{xx}}{\partial x} + \frac{\partial m_{yx}}{\partial y} - v_x = 0$$
$$\frac{\partial m_{yy}}{\partial y} + \frac{\partial m_{xy}}{\partial x} - v_y = 0 \qquad (5.25)$$

The equilibrium relation, thus, becomes:

$$\begin{bmatrix} -\frac{\partial^2}{\partial x^2} & -\frac{\partial^2}{\partial y^2} & -2\frac{\partial^2}{\partial x \partial y} \end{bmatrix} \begin{bmatrix} m_{xx} \\ m_{yy} \\ m_{xy} \end{bmatrix} = [p] \qquad \mathbf{B}^{\mathrm{T}}\mathbf{s} = \mathbf{p} \qquad (5.26)$$

Note that, when the kinematic relation is substituted into the constitutive relation and the equilibrium relation, a partial differential equation in u_z is derived:

$$D_b\left(\frac{\partial^4}{\partial x^4} + 2\frac{\partial^4}{\partial x^2 \partial y^2} + \frac{\partial^4}{\partial y^4}\right)u_z = p \qquad (5.27)$$

By replacing the term $\frac{\partial^2}{\partial x^2} + \frac{\partial^2}{\partial y^2}$ by the Laplace operator ∇^2 (or Δ) the well known biharmonic plate equation is found, derived for the first time by Lagrange in 1811:

$$D_b \nabla^2 \nabla^2 w = p \qquad (5.28)$$

To perform a solution to the biharmonic equation at the free edge, the Kirchhoff or 'modified shear' boundary condition is introduced along with the prescribed (zero) stress resultants and moments. Kirchhoff stated that the transverse shearing stress summed up with the derivative of the torsional moment is equal to zero (this also leads to the well-known corner forces of plates). There is referred to the Kirchhoff thin plate theory. As denoted by Zienkiewicz and Taylor [87], Kirchhoff formulated his thin plate theory in 1850, though, an early version was presented by Sophie Germain in 1811. A modification of the thin plate theory was made by Reissner in 1945 and, slightly different, by Mindlin in 1951 (they are similar for a Poisson's ratio equal to zero). These modified theories, including shear deformation like the Timoshenko beam, extend the field of application of the theory to thick plates.

5.3.3 Combined Extension and Bending

Finally, the extensional and bending relations can be combined in the thin plate equations:

Kinematic Relations

$$\begin{bmatrix} \varepsilon_{xx} \\ \varepsilon_{yy} \\ \gamma_{xy} \\ \kappa_{xx} \\ \kappa_{yy} \\ \rho_{xy} \end{bmatrix} = \begin{bmatrix} \frac{\partial}{\partial x} & 0 & 0 \\ 0 & \frac{\partial}{\partial y} & 0 \\ \frac{\partial}{\partial y} & \frac{\partial}{\partial x} & 0 \\ 0 & 0 & -\frac{\partial^2}{\partial x^2} \\ 0 & 0 & -\frac{\partial^2}{\partial y^2} \\ 0 & 0 & -2\frac{\partial^2}{\partial x \partial y} \end{bmatrix} \begin{bmatrix} u_x \\ u_y \\ u_z \end{bmatrix}$$

Constitutive Relations

$$\begin{bmatrix} n_{xx} \\ n_{yy} \\ n_{xy} \\ m_{xx} \\ m_{yy} \\ m_{xy} \end{bmatrix} = \begin{bmatrix} D_m & \nu D_m & 0 & 0 & 0 & 0 \\ \nu D_m & D_m & 0 & 0 & 0 & 0 \\ 0 & 0 & D_m\left(\frac{1-\nu}{2}\right) & 0 & 0 & 0 \\ 0 & 0 & 0 & D_b & \nu D_b & 0 \\ 0 & 0 & 0 & \nu D_b & D_b & 0 \\ 0 & 0 & 0 & 0 & 0 & D_b\left(\frac{1-\nu}{2}\right) \end{bmatrix} \begin{bmatrix} \varepsilon_{xx} \\ \varepsilon_{yy} \\ \gamma_{xy} \\ \kappa_{xx} \\ \kappa_{yy} \\ \rho_{xy} \end{bmatrix}$$

Equilibrium Relations

$$\begin{bmatrix} -\frac{\partial}{\partial x} & 0 & -\frac{\partial}{\partial y} & 0 & 0 & 0 \\ 0 & -\frac{\partial}{\partial y} & -\frac{\partial}{\partial x} & 0 & 0 & 0 \\ 0 & 0 & 0 & -\frac{\partial^2}{\partial x^2} & -\frac{\partial^2}{\partial y^2} & -2\frac{\partial^2}{\partial x \partial y} \end{bmatrix} \begin{bmatrix} n_{xx} \\ n_{yy} \\ n_{xy} \\ m_{xx} \\ m_{yy} \\ m_{xy} \end{bmatrix} = \begin{bmatrix} p_x \\ p_y \\ p_z \end{bmatrix} \tag{5.29}$$

From the relations it can be seen that, similar to the straight bar, for the plate extension and bending are not coupled.

All basic relations, for a plate in extension as well for a plate in bending are known. To solve the relations the use of *direct-* or *indirect methods* is necessary together with the boundary conditions of the particular problem.

5.4 Theory of Shells

Last, but not least, formulas for extensional shells and shells with bending are provided in this paragraph. A shell is a three-dimensional curved surface. They are essentially curved plates, a combination of a plate in extension and a plate in bending. The theory that deals with the extension of shells is called the membrane theory. The membrane theory describes the shell in an idealised pure membrane action: there are only normal and longitudinal shearing stresses produced, uniformly distributed through the thickness. Thus, in the case of extension the middle surface of the thin shell remains free of bending and twisting moments as well as transverse shear forces. This is possible due to correcting circumferential stresses, as described in Chapter 3. The membrane force field, therefore, causes the stretching or contraction of the shell, as a membrane, without producing any bending and/or local curvature changes. However, in many shell problems the presence of moments and shear forces is necessary to accept the type of loading and to satisfy the shell boundary conditions. For example, bending eventually occurs due to (restricted) deformations of the shell causing curvature and thus bending. Aforementioned bending moments do not carry load and, therefore, they are referred to as compatibility moments. The need for a shell theory which combines membrane behaviour with bending has led to, a more comprehensive shell theory including bending. The describing relations will be derived here.

The vector scheme of (5.3) is used. Recapitulate from Paragraph 5.1.2:

$$\mathbf{u} = \left[u_x \ u_y \ u_z \right]^T$$
$$\mathbf{e} = \left[\varepsilon_{xx} \ \varepsilon_{yy} \ \gamma_{xy} \ \kappa_{xx} \ \kappa_{yy} \ \rho_{xy} \right]^T$$
$$\mathbf{s} = \left[n_{xx} \ n_{yy} \ n_{xy} \ m_{xx} \ m_{yy} \ m_{xy} \right]^T \tag{5.3}$$
$$\mathbf{p} = \left[p_x \ p_y \ p_z \right]^T$$

5.4.1 Extension

Aforementioned, the structural behaviour of a thin shell in extension is described by the membrane theory dealing with membrane forces. Membrane forces are actually resultants of the normal stresses and the in-plane shear stresses that are uniformly distributed over the thickness. A shell is in pure membrane action when bending stress actions are not developed. Thus, the membrane theory is based on the assumption that bending stress resultants can be neglected and that the transverse shearing stress resultants are correspondingly equal to zero. Therefore, all bending actions and transverse shearing stress resultants are not of interest in this Chapter. They will be deal with in Paragraph 5.4.2.

Kinematic relations

Due to the assumptions made in Paragraph 5.1.2 the deformation is the shell surface is only dependent of translations of the middle surface. Because there is no bending, rotations of the surface are of no interest.

For a shell, the kinematic relation between the strain ε and the displacement u can be found by describing the displacement of the middle surface. For simplicity, a polar coordinate system is used in which the curvature and length of a ring segment are expressed in terms of radius r and angle $d\theta$. Hence, the terms can be converted back to a global coordinate system with the relation $dx = rd\theta$.

Considering an infinitesimal ring segment of length $ds_\theta = rd\theta$ as is shown in the left of Figure 5.10, the strain corresponding to the elongation of the ring segment by Δds_θ is defined by $\varepsilon_{\theta\theta} = \dfrac{\Delta ds_\theta}{ds_\theta}$

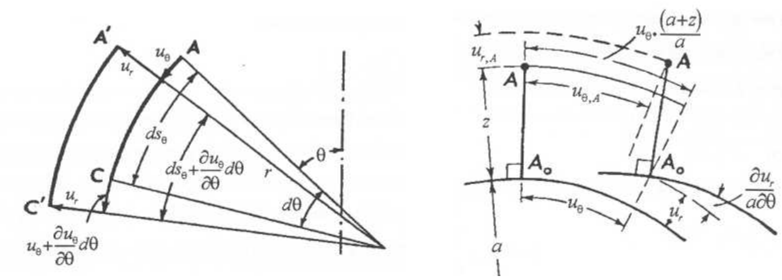

Figure 5.10. Ring segment before and after deformation, Hoefakker and Blaauwendraad 2003

Further in Figure 5.10, the elongation of the segment without a radial displacement u_r is equal to $\frac{du_\theta}{d\theta}d\theta$. The radial displacement u_r results in additional elongation. The radius r increases to $r + u_r$ and therefore the length of the segment increases proportionally to $\left(ds_\theta + \frac{du_\theta}{d\theta}d\theta\right)\frac{r+u_r}{r}$. The elongation of a segment is defined by $\Delta ds_\theta = \left(ds_\theta + \frac{du_\theta}{d\theta}d\theta\right)\frac{r+u_r}{r} - ds_\theta = \frac{du_\theta}{d\theta}d\theta + \frac{u_r}{r}ds_\theta$. Hereby, the strain for all fibres in the ring segment becomes:

$$\varepsilon_\theta = \frac{1}{r}\left(\frac{du_\theta}{d\theta} + u_r\right) \tag{5.30}$$

Herein the initial curvature k of the arch is represented by the term $1/r$.

However, for a shell of arbitrary curvature it is convenient to stay within the general coordinate system. When the relation is converted back to the global coordinate system, the kinematic equation reads:

$$\varepsilon_{xx} = \frac{\partial u_x}{\partial x} + \frac{1}{r_x}u_z \tag{5.31}$$

And in the *y-direction*:

$$\varepsilon_{yy} = \frac{\partial u_y}{\partial y} + \frac{1}{r_y}u_z \tag{5.32}$$

The curvatures are $|k_x| = 1/r_x$ and $|k_y| = 1/r_y$. Hence, the curvature for shells is positive when the centre of curvature lies on the positive part of the normal of the middle surface.

Similar to the bar-to-plate transformation, additional shear rotation is necessary for a correct description of the surface deformation.

When placing the general coordinate system parallel to the principal curvatures, the formula describing the shell shear deformation is equal to the plate shear deformation. Recapitulate from Paragraph 5.3.1:

$$\gamma_{xy} = \frac{\partial u_x}{\partial y} + \frac{\partial u_y}{\partial x} \tag{5.15}$$

Substitution of the three kinematic equations yields the kinematic relation for a coordinate system placed in principal direction:

$$\begin{bmatrix} \varepsilon_{xx} \\ \varepsilon_{yy} \\ \gamma_{xy} \end{bmatrix} = \begin{bmatrix} \frac{\partial}{\partial x} & 0 & -k_x \\ 0 & \frac{\partial}{\partial y} & -k_y \\ \frac{\partial}{\partial y} & \frac{\partial}{\partial x} & 0 \end{bmatrix} \begin{bmatrix} u_x \\ u_y \\ u_z \end{bmatrix} \qquad \mathbf{e} = \mathbf{B}\mathbf{u}$$

For an arbitrary placed coordinate system the relation changes into:

$$\begin{bmatrix} \varepsilon_{xx} \\ \varepsilon_{yy} \\ \gamma_{xy} \end{bmatrix} = \begin{bmatrix} \frac{\partial}{\partial x} & 0 & -k_x \\ 0 & \frac{\partial}{\partial y} & -k_y \\ \frac{\partial}{\partial y} & \frac{\partial}{\partial x} & -2k_{xy} \end{bmatrix} \begin{bmatrix} u_x \\ u_y \\ u_z \end{bmatrix} \qquad \mathbf{e} = \mathbf{B}\mathbf{u} \tag{5.33}$$

The similarity with the kinematic relation for the plate part is evident; it is the curvature that makes the difference.

Constitutive relations

For the constitutive relations the shell is assumed to behave according to Hooke's law. The stresses and strains are uniformly distributed over the thickness due to the assumption that the shell is in pure membrane behaviour with no bending actions. As mentioned, the moment equilibrium around the *z-axis* implies equal longitudinal shearing stresses and, therefore, the deformation of the middle surface is described by the normal strains ε_{xx}, ε_{yy}, and shear strain γ_{xy}.

Hooke's law for the stress-strain relation for the linear elastic shell is described by

$$\begin{bmatrix} \sigma_{xx} \\ \sigma_{yy} \\ \sigma_{xy} \end{bmatrix} = \frac{E}{1 - \nu^2} \begin{bmatrix} 1 & \nu & 0 \\ \nu & 1 & 0 \\ 0 & 0 & \frac{1-\nu}{2} \end{bmatrix} \begin{bmatrix} \varepsilon_{xx} \\ \varepsilon_{yy} \\ \gamma_{xy} \end{bmatrix}$$

The stress resultants can be determined from the strains by multiplication with the thickness *t*.

$$\begin{bmatrix} n_{xx} \\ n_{yy} \\ n_{xy} \end{bmatrix} = \frac{Et}{1-\nu^2}\begin{bmatrix} 1 & \nu & 0 \\ \nu & 1 & 0 \\ 0 & 0 & \frac{1-\nu}{2} \end{bmatrix}\begin{bmatrix} \varepsilon_{xx} \\ \varepsilon_{yy} \\ \gamma_{xy} \end{bmatrix} \qquad \mathbf{s} = \mathbf{D}\,\mathbf{e} \qquad (5.34)$$

Hence, the constitutive relation of the shell is equal to the constitutive relation of the plate part derived in section 5.3.1.

Equilibrium relations

The stress resultants on a shell element, with thickness t, are shown in Figure 5.11. The coordinate system is placed in the direction of the principal curvatures.

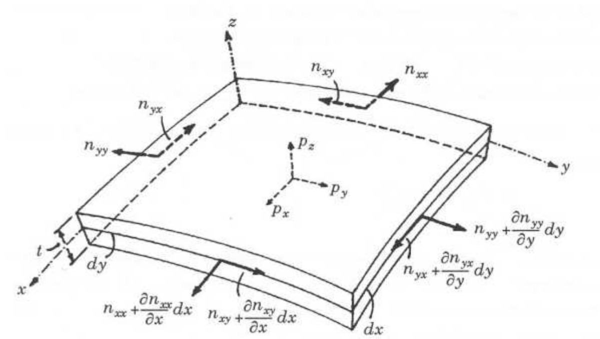

Figure 5.11. Stress resultants and load components on a shell element, Hoefakker and Blaauwendraad 2003

Considering an infinitesimal element of the shell with length *dx* and *dy*, the equilibrium in *x*- and *y-direction* can be described as:

$$-n_{xx}dy + n_{xx}dy + \frac{\partial n_{xx}}{\partial x}dxdy - n_{yx}dx + n_{yx}dx + \frac{\partial n_{yx}}{\partial y}dydx + p_x dxdy = \frac{\partial n_{xx}}{\partial x} + \frac{\partial n_{yx}}{\partial y} + p_x = 0$$

And

$$-n_{yy}dx + n_{yy}dx + \frac{\partial n_{yy}}{\partial y}dydx - n_{xy}dy + n_{xy}dy + \frac{\partial n_{xy}}{\partial x}dxdy + p_y dxdy = \frac{\partial n_{yy}}{\partial y} + \frac{\partial n_{xy}}{\partial x} + p_y = 0 \qquad (5.35)$$

Hereby, as mentioned, the two longitudinal shearing stress resultants must n_{xy} and n_{yx} are equal.

Equation (5.35) is equal to the equilibrium relations found for the *2D* plate part in extension in Section 5.3.1.

Because of the curvature of the shell element, there is also equilibrium in *z-direction*. For the equilibrium in *z-direction* the principal curvatures $|k_x| = 1/r_x$ and $|k_y| = 1/r_y$ must be determined.

Figure 5.12 shows a ring segment of the shell surface in the *x-direction* with the normal load component p_z in the *z-direction* and the stress resultant n_{xx}. The segment has a (negative) curvature k_x.

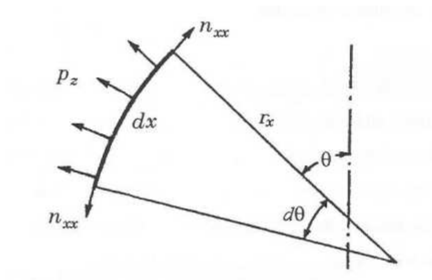

Figure 5.12. Normal load p_z and stress resultant n_{xx}, , Hoefakker and Blaauwendraad 2003

A simple equilibrium for the *x-direction* segment can be described as

$$-n_{xx}d\theta + p_z \cdot r_x d\theta = k_x n_{xx} + p_z = 0 \tag{5.36}$$

(Note that the equation is independent of the sign of the curvature)

When the *y-direction* is also included in the equation, the final equation for the equilibrium of p_z can be described as

$$k_x n_{xx} + k_y n_{yy} + p_z = 0 \tag{5.37}$$

Substitution of equations (5.35) and (5.37) yields the equilibrium relation for a coordinate system placed in principal direction:

$$\begin{bmatrix} -\frac{\partial}{\partial x} & 0 & -\frac{\partial}{\partial y} \\ 0 & -\frac{\partial}{\partial y} & -\frac{\partial}{\partial x} \\ -k_x & -k_y & 0 \end{bmatrix} \begin{bmatrix} n_{xx} \\ n_{yy} \\ n_{xy} \end{bmatrix} = \begin{bmatrix} p_x \\ p_y \\ p_z \end{bmatrix} \qquad \mathbf{B^T s = p}$$

For an arbitrary placed coordinate system the shear stress resultants also takes part in the equilibrium in *z-direction* and the relation changes into:

$$\begin{bmatrix} -\frac{\partial}{\partial x} & 0 & -\frac{\partial}{\partial y} \\ 0 & -\frac{\partial}{\partial y} & -\frac{\partial}{\partial x} \\ -k_x & -k_y & -2k_{xy} \end{bmatrix} \begin{bmatrix} n_{xx} \\ n_{yy} \\ n_{xy} \end{bmatrix} = \begin{bmatrix} p_x \\ p_y \\ p_z \end{bmatrix} \qquad \mathbf{B^T s = p} \tag{5.38}$$

It can be seen that the equilibrium relation is equal to the equilibrium relation of a 2D plate part with the addition of the initial shell curvatures.

5.4.2 Bending

Aforementioned in the introduction of the paragraph, the classical shell theory consists of a membrane field and a moment field. Because of the high extensional rigidity in compare to the flexural rigidity, the shell mainly produces membrane stresses, described by the membrane theory. The membrane theory is, however, only sufficient if the membrane stress field is not disturbed. If not, for example in the case of deformation constrains, compatibility moments are required to compensate the shortcomings of the membrane theory (and, thus, not for carrying load). The compatibility or bending force field consists of bending moments, twisting couples and transverse shear forces. The theory for calculating the shell bending moments is derived in this paragraph. For that, the hypothesis which states that the shell in bending can be described with the shell membrane theory in combination with the plate bending theory is used.

Recapitulate from Chapter 3, it can be stated that bending moments arise at:

1. Deformation constrains and some boundary conditions which are incompatible with the requirements of a pure membrane field
2. Application of concentrated forces, and change in the shell geometry and/or sudden change of curvature

Kinematic relations

The kinematic relation for the bending of shells can be derived using the thin shell assumptions as for a shell the cross-sectional thickness is small in compare to the radius of curvature. For the derivation of kinematic relations of a shell, first a ring segment is considered. For the kinematic relation for the ring segment in bending, the extension of the middle surface is extended with a description for the strain at an arbitrary point in the cross-section, seen in the right picture of Figure 5.10. By using the relation $r = a + z$ for a certain point A at distance z from the middle surface and an additional rotation of the gradient $\frac{du_r}{ad\theta}$ that produces a displacement $-z\frac{du_r}{ad\theta}$, the displacement of point A is described by:

$$u_{\theta A} = \frac{a+z}{a}u_\theta - \frac{z}{a}\frac{du_r}{d\theta} = u_\theta + \frac{z}{a}\left(u_\theta - \frac{du_r}{d\theta}\right) = u_\theta + z\,\varphi_\theta \quad \text{where} \quad \varphi_\theta = \frac{1}{a}\left(u_\theta - \frac{du_r}{d\theta}\right).$$

The strain distribution at an arbitrary point related to the displacement and the rotation of the middle surface is hereby:

$$\varepsilon_\theta(z) = \frac{1}{a+z}\left(\frac{du_\theta}{d\theta} + u_r + z\frac{d\varphi_\theta}{d\theta}\right)$$

Or, after substitution of the rotation:

$$\varepsilon_\theta(z) = \frac{1}{a}\frac{du_\theta}{d\theta} + \frac{u_r}{a+z} - \frac{z}{a(a+z)}\frac{d^2u_r}{d\theta^2} \tag{5.39}$$

Equation (5.39) represents the exact strain distribution across the thickness expressed by the displacement of the middle surface. Setting the distance z is equal to zero (middle surface), an identical expression as equation (5.30) in Paragraph 5.4.1 is obtained.

An important step is the introduction of the assumptions b and c of Paragraph 5.1.2, the thin shell assumptions. For a thin shell, it holds that $z \ll a$, and therefore the approximation $a + z \approx a$ is used. Consequently, equation (5.39) changes into:

$$\varepsilon_\theta(z) = \frac{1}{a}\frac{du_\theta}{d\theta} + \frac{u_r}{a} - \frac{z}{a^2}\frac{d^2u_r}{d\theta^2} = \varepsilon_\theta + z\kappa_\theta \tag{5.40}$$

Hence, the thin shell assumption leads to the approximated expression for the deformation curvature:

$$\kappa_\theta = -\frac{1}{a^2}\frac{d^2u_r}{d\theta^2} \tag{5.41}$$

The latter is the kinematic relation for a ring segment in bending and shows similarity with the kinematic relation for the bar in bending. Actually, when the result is converted to a global coordinate system using the relation $dx = rd\theta$, the exact same relation is found:

$$\kappa_x = -\frac{d^2u_z}{dx^2} \qquad \mathbf{e} = \mathbf{Bu} \tag{5.42}$$

It can be concluded that the strain distribution at an arbitrary point in the cross-section of a ring segment in extension and bending can be described by the strain of the middle surface added with the curvature due to bending of a straight bar.

By simply combining the ring segment equations with additional *y-direction* and twisting curvature ρ_{xy} (similar to the bar-to-plate extension of section 5.5.2) the kinematic relation for a shell in bending is found:

$$\begin{bmatrix} \kappa_{xx} \\ \kappa_{yy} \\ \rho_{xy} \end{bmatrix} = \begin{bmatrix} -\dfrac{\partial^2}{\partial x^2} \\ -\dfrac{\partial^2}{\partial y^2} \\ -2\dfrac{\partial^2}{\partial x \partial y} \end{bmatrix} [u_z] \qquad \mathbf{e} = \mathbf{Bu} \tag{5.43}$$

This is exact the same relation as (5.22).

Constitutive relations

Similar to the plate in bending, the constitutive relation between the curvatures and bending moments is described by the bending stiffness and a term for the lateral contraction. As the shell is a two-dimensional surface structure the constitutive law is equal to the plate bending constitutive law, even though the shell is in a three-dimensional space. The constitutive relations are:

$$\begin{bmatrix} m_{xx} \\ m_{yy} \\ m_{xy} \end{bmatrix} = \begin{bmatrix} D_b & \nu D_b & 0 \\ \nu D_b & D_b & 0 \\ 0 & 0 & D_b\left(\frac{1-\nu}{2}\right) \end{bmatrix} \begin{bmatrix} \kappa_{xx} \\ \kappa_{yy} \\ \rho_{xy} \end{bmatrix} \qquad \mathbf{s} = \mathbf{D}\,\mathbf{e} \tag{5.44}$$

with $D_b = \dfrac{Et^3}{12(1-\nu^2)}$ as the bending stiffness.

Equilibrium relations

The equilibrium relations involve the equilibrium between the moments, out-of-plane shear stresses and the external applied load. The out-of-plane shear, neglected for the extensional behaviour, is generated by the applied load, analogous to the beam and plate in bending. Therefore, the equilibrium is satisfied if:

$$\frac{\partial v_x}{\partial x} + \frac{\partial v_y}{\partial y} + p_z = 0 \tag{5.45}$$

As with the plate equations, the out-of-plane shear is eliminated by setting-up the equilibrium of moments with respect to the *x-direction* and *y-direction*:

$$\frac{\partial m_{xx}}{\partial x} + \frac{\partial m_{yx}}{\partial y} - v_x = 0$$

$$\frac{\partial m_{yy}}{\partial y} + \frac{\partial m_{xy}}{\partial x} - v_y = 0 \tag{5.46}$$

The first to terms of the equilibrium relation (5.45), the out-of-plane shears, can be replaced by the moment equilibrium relations (5.46). The total equilibrium relation of a shell in membrane and bending action can thus be described as:

$$\begin{bmatrix} -\frac{\partial^2}{\partial x^2} & -\frac{\partial^2}{\partial y^2} & -2\frac{\partial^2}{\partial x \partial y} \end{bmatrix} \begin{bmatrix} m_{xx} \\ m_{yy} \\ m_{xy} \end{bmatrix} = \begin{bmatrix} p_z \end{bmatrix} \qquad \mathbf{B}^{\mathbf{T}}\mathbf{s} = \mathbf{p} \tag{5.47}$$

Thus, it can be concluded that the bending equations of a shell are similar to the plate in bending.

5.4.3 Combined Extension and Bending

Finally, the extensional and bending relations can be combined in the thin shell equations:

Equilibrium Relations

$$\begin{bmatrix} -\frac{\partial}{\partial x} & 0 & -\frac{\partial}{\partial y} & 0 & 0 & 0 \\ 0 & -\frac{\partial}{\partial y} & -\frac{\partial}{\partial x} & 0 & 0 & 0 \\ -k_x & -k_y & -2k_{xy} & -\frac{\partial^2}{\partial x^2} & -\frac{\partial^2}{\partial y^2} & -2\frac{\partial^2}{\partial x \partial y} \end{bmatrix} \begin{bmatrix} n_{xx} \\ n_{yy} \\ n_{xy} \\ m_{xx} \\ m_{yy} \\ m_{xy} \end{bmatrix} = \begin{bmatrix} p_x \\ p_y \\ p_z \end{bmatrix}$$

Constitutive Relations

$$\begin{bmatrix} n_{xx} \\ n_{yy} \\ n_{xy} \\ m_{xx} \\ m_{yy} \\ m_{xy} \end{bmatrix} = \begin{bmatrix} D_m & \nu D_m & 0 & 0 & 0 & 0 \\ \nu D_m & D_m & 0 & 0 & 0 & 0 \\ 0 & 0 & D_m\left(\frac{1-\nu}{2}\right) & 0 & 0 & 0 \\ 0 & 0 & 0 & D_b & \nu D_b & 0 \\ 0 & 0 & 0 & \nu D_b & D_b & 0 \\ 0 & 0 & 0 & 0 & 0 & D_b\left(\frac{1-\nu}{2}\right) \end{bmatrix} \begin{bmatrix} \varepsilon_{xx} \\ \varepsilon_{yy} \\ \gamma_{xy} \\ \kappa_{xx} \\ \kappa_{yy} \\ \rho_{xy} \end{bmatrix} \tag{5.48}$$

with $D_m = \dfrac{Et}{(1-\nu^2)}$ and $D_b = \dfrac{Et^3}{12(1-\nu^2)}$

Kinematic Relations

$$\begin{bmatrix} \varepsilon_{xx} \\ \varepsilon_{yy} \\ \gamma_{xy} \\ \kappa_{xx} \\ \kappa_{yy} \\ \rho_{xy} \end{bmatrix} = \begin{bmatrix} \frac{\partial}{\partial x} & 0 & -k_x \\ 0 & \frac{\partial}{\partial y} & -k_y \\ \frac{\partial}{\partial y} & \frac{\partial}{\partial x} & -2k_{xy} \\ 0 & 0 & -\frac{\partial^2}{\partial x^2} \\ 0 & 0 & -\frac{\partial^2}{\partial y^2} \\ 0 & 0 & -2\frac{\partial^2}{\partial x \partial y} \end{bmatrix} \begin{bmatrix} u_x \\ u_y \\ u_z \end{bmatrix}$$

The classical shell theory is now derived. In the deduced basic relations, the similarity with the plate equations (5.29) is clear. Only the kinematic and equilibrium membrane relations have additional parameters due to the initial geometric curvatures of the shell. Two important conclusions that can be drawn following the equalities and differences between the basic relations of a plate and a shell is that (1) the initial curvature of the shell indicates that, unlike plates, the in-plane and the flexural problem are coupled, even for the linear case, and (2) the combined stretching and bending behaviour of a shell can be described by the extension behaviour of the shell (including the initial curvature) in combination with the bending behaviour of a plate. Thus, the shell behaviour can be approximated by superposition of shell membrane stresses and the plate bending moments. This hypothesis, first discovered by H. Reissner in 1912, enabled simple hand calculation of stresses in shells.

To solve the classical shell relations the use of *direct-* or *indirect methods* is necessary together with the boundary conditions of the particular problem. This will be discussed in the next paragraph.

5.5 Solve Methods

5.5.1 Direct Methods

The three relations including additional boundary conditions can be solved by direct methods or by indirect methods. Direct Methods solve the problem by the use of relationships based on observed intensities. They can be divided into the force method and the displacement or stiffness method. The indirect methods are discussed in the next paragraph.

Force Method

The force method evaluates the three basic equations in opposite order. First, the equilibrium relations, than the constitutive relations (flexibility formulation) and finally the kinematic relations. When the equations contain only one unknown, direct solution by integration and substitution of the boundary conditions is allowed. If not, the equilibrium equations are used to express the stresses in one or more redundants which guarantees an equilibrium system of stresses. Subsequently, the deformations are expressed in the redundants after substitution of the equilibrium system into the constitutive equations. Finally, the kinematic relations are evaluated by eliminating the degrees of freedom which results in one or more relations between the deformations and the compatibility conditions. Combining the steps leads to a differential equation with respect to the redundants. While following the force method, attention must be paid to the construction of a stress field, with redundants, which satisfies the equilibrium equations and the derivation of suitable compatibility equations by elimination of the displacements. The equations of the force method have similarities with classical graphical methods. The associated equilibrium equation is actually the mathematical description of the graphical method involving the drawing of the Cremona diagrams and the kinematic relation corresponds with the mathematical formulation of the graphical displacement diagram or Williot diagram (1877), Blaauwendraad [10]. The force method is extensively used in historical mathematics.

Displacement Method

In the displacement method the kinematic and constitutive relations are substituted into the equilibrium relations without any modifications. The constitutive relations are used in stiffness formulation. The result of the displacement method is a set of one or more differential equations with respect to the degrees of freedom. Increasing use of the displacement method came with the invention of the computer. The method appeared to be the more suitable for computer analysis as the computer is unable to choose proper redundants.

5.5.2 Indirect Methods

The principle of minimum potential energy and the principle of minimum complementary energy are indirect methods. Indirect or *variational* methods are energy based methods. They solve the problem by the use of a differential equation which is determined by minimising the potential or complementary energy with respect to variations in displacements or stresses respectively. For both methods the equation of virtual work serves as base. The main reason for discussing variational methods is that the computer has only minor application of classical calculation procedures but more and more on energy based principles, such as the solution procedures of the finite element method, Blaauwendraad [11].

Principle of Minimum Potential Energy

Potential energy can be described as the energy which is accumulated in a material; it represents the area under the *σ-ε diagram*. The potential energy can be determined by adding the amount of energy which is needed for a small deformation of a certain volume, the deformation (or strain) energy, and the energy from the position of the external loads. When implemented in the virtual work equation it results in a differential equation for unknown displacements; the equation of *virtual work for potential energy*. By minimising the potential energy a stationary value with respect to variations of displacements is determined, which provides the equilibrium relation between the external and internal forces. Therefore, the principle of minimum potential energy is related to the direct displacement method.

Principle of Minimum Complementary Energy

The principle of minimum complementary energy is related to the direct force method, it provides in a differential equation for unknown stresses; the equation of *virtual work for complementary energy.* Complementary energy represents the area above the *σ-ε diagram* and relates, for elastic materials, to potential energy by the equation $E'_c = \sigma\varepsilon - E'_s(\varepsilon)$. It is hard to give a physical interpretation. By minimising the complementary energy a stationary value with respect to variations of stresses is found. The equation which follows describes the relation between the strains and displacements.

Virtual Work Equation

The equation of virtual work relates the internal energy to the external energy. The internal energy is formed by the stresses and strains. They are related according to the constitutive relations. The external energy deals with as well the volume loads and displacements as the ones on the edge. The equation can be obtained by setting-up the energy equilibrium for any admissible displacement field. Such a field is admissible if it corresponds with prescribed displacements and satisfies the kinematic relations in the volume of the body. Without any further derivation (done in Chapter 11), the equation of virtual work is given below:

$$\iiint_V \sigma\delta\varepsilon dV - \iint_V P\delta u dV - \iint_S p\delta u dS = 0 \tag{5.49}$$

As mentioned in Paragraph 5.1.2 the equation of virtual work can be used to explain the similarity between the two matrices of the kinematic and equilibrium relation. As reported by Hoefakker and Blaauwendraad [45], the equation of virtual work (5.49) can be rewritten, leaving out possible load applied in the volume.

$$\iiint_V \sigma\delta\varepsilon dV = \iint_S p\delta u dS \tag{5.50}$$

By integration over the thickness t the stresses are transformed to the stress resultant and the volume integral changes to a surface integral. This is, however, only valid for slender cross-sections. Furthermore, rewriting the equation by using the vector notation of Paragraph 5.1, the virtual work equation changes to:

$$\iint_S \delta\boldsymbol{e}^T \boldsymbol{s} dS = \iint_S \delta\boldsymbol{u}^T \boldsymbol{p} dS \tag{5.51}$$

To obtain equilibrium between the stress resultant vector and the load vector, the variations of the strains are expressed in variations of the displacements using the kinematic relation (5.1):

$$\iint_S \delta(\boldsymbol{Bu})^T \boldsymbol{s} dS = \iint_S \delta\boldsymbol{u}^T \boldsymbol{p} dS \tag{5.52}$$

According the rules of matrix calculation $(\boldsymbol{Bu})^T = \boldsymbol{u}^T\boldsymbol{B}^T$ equation (5.50) can be rewritten:

$$\iint_S \delta\boldsymbol{u}^T \boldsymbol{B}^T \boldsymbol{s} dS = \iint_S \delta\boldsymbol{u}^T \boldsymbol{p} dS \tag{5.53}$$

Which means that $\boldsymbol{B}^T\boldsymbol{s} = \boldsymbol{p}$.

Hence, the differential operator matrix $\mathbf{B}^T$ of the equilibrium relation must be the transpose matrix $\mathbf{B}$ of the kinematic relation. Furthermore, by the fact that the matrix transformation $(\boldsymbol{Bu})^T = \boldsymbol{u}^T\boldsymbol{B}^T$ is performed within the area integrals $dS = dx\,dy$, the integration by parts rule must be used. The rule reads:

$$\int\left(\frac{df}{dx}g\right)dx = [f \cdot g]_{x_1}^{x_2} - \int\left(f\frac{dg}{dx}\right)dx$$

As the constant term $[f \cdot g]_{x_1}^{x_2}$ is used for the boundary conditions, it is not of interest for the equilibrium equation. Leaving out the constant term, yields:

$$\int\left(\frac{df}{dx}g\right)dx = \int\left(-f\frac{dg}{dx}\right)dx \tag{5.54}$$

Or by integration twice:

$$\iint\left(\frac{d^2f}{dx^2}g\right)dxdx = \iint\left(f\frac{d^2g}{dx^2}\right)dxdx \tag{5.65}$$

Equations (5.52) and (5.53) give answer to the question why the even terms do not change sign and the uneven do. Therefore, in Section 5.1.1 the similarity between the matrices is not regarded as being the transpose of each other, but is referred to as being their adjoint matrices.

6 Structural Failure

In Chapter 5 the classical shell theory of elasticity is discussed. Equally important is to know how the shell fails. In this Chapter the structural failure of shells is discussed. Aforementioned in Chapter 3, shells may fail either due to large deformations or because of material degradation or by a combination of both. The first failure mechanism is referred to as buckling instability and the second is a so-called strength failure, Ramm [66]. The distinction between both failure mechanisms can be seen in Figure 6.1.

For thin shells, the stresses are normally so low that the strength criteria are satisfied and the safety against buckling is dominant, although intensified by inelastic material behaviour (inelastic buckling). For sure in case of shells made of high strength materials, the stability behaviour often dictates the structural dimensions. As a buckling failure can be sudden and catastrophic, sufficient factors of safety must ensure that it will not occur. The buckling phenomenon is extensively discussed in Section 6.2 to 6.9.

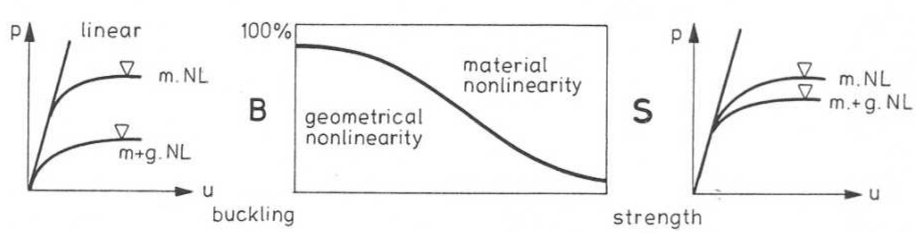

Figure 6.1. Structural failure due to buckling or strength, Ramm 1987

When significant compressive stresses or tensile stresses arise (e.g. in the lower part of hemispherical caps) the material degradation may become critical. In particular, the highly nonlinear behaviour of concrete in tension causing cracking and rebar yielding considerably lowers the load carrying capacity. Strength failure is discussed first in Section 6.1.

6.1 Strength Failure

A strength failure is a failure for which the load causing plastic flow of the material is lower than the critical (buckling) load causing large deformations. Thus, a strength failure is caused by tensile cracking or compressive crushing of concrete while the deformations of the shell are small. In case of reinforced concrete, a third failure mechanism is yielding of rebars or continuous frictional pull-out of fibres.

A strength failure is purely material orientated. Therefore the behaviour of material surpassing the elastic branch up to plastic failure is captured in Chapter 8. Subsequently, a simple example is outlined in Chapter 10 and the modelling of the material properties in a so-called material model which enables finite element programs to determine whether a material failure or buckling failure will occur, follows in Chapter 15.

6.2 Buckling Failure

Under certain conditions structures may fail not on account of high stresses surpassing the strength of material, but due to insufficient stability. A special mode of instability of equilibrium is buckling. All structures that are subjected to loads which cause in-plane compressive forces are subject to buckling. Buckling instability can be characterised as a premature failure mechanism caused by eccentricity of compression forces, initiated by deformations or initial geometric imperfections. Consequently, the critical buckling load causing the structure to be in an unstable state of equilibrium can be found by introducing an eccentricity of normal forces in the equation of equilibrium that produces a moment. The form of the equation for buckling of structural elements is linear and homogeneous. The study of the solutions of such equations is in the branch of mathematics known as the eigenvalue theory.

The phenomenon of buckling is closely related to the name of 18th century mathematician Leonhard Euler. Euler derived a formula which gives the maximum axial load that a long, slender ideal column can carry without buckling in 1744 (even before Navier formulated the general theory of elasticity in 1821). He presented his solution in the first paper on structural stability in which he described the behaviour of a bar under axial load before and after the buckling load was exceeded. This so-called postbuckling behaviour was captured in a nonlinear formulation and solved by Lagrange in 1867. It took about one century and a half before an extension into the domain of plates was formulated by Bryan in 1891, and only in the 20th century the investigation of the stability of shells took place. Earliest solutions for buckling of axially compressed cylinders were obtained by Lorenz in 1908, Timoshenko in 1910 and Southwell in 1914, Popov and Medwadowski [62]. On the basis of the linear theory Zoëlly developed in 1915 his buckling formula for a spherical dome under radial pressure.

For some *200* years after the basic paper of Euler, the underlying theory of buckling was thought to be completed. The critical load of a structure was found by assuming an infinitesimal deviation from the prebuckling position and subsequently determine the load at which the structure remained in equilibrium in the perturbed position. For as far as columns and plates are considered the analytical results are in fair agreement with experiments. In 1928, however, Robertson indicated a significant discrepancy between theory and experiment while axial compressed thin cylindrical shells, Seide [70].

The question to which caused the great discrepancy was not answered until Von Karman and Tsien discovered the answer to lie within the nonlinear behaviour in 1941. Von Karman and Tsien discovered that for shells, contrary to columns and plates, the equilibrium path after the bifurcation point falls-down, showing decreasing load carrying capacity. Strangely enough, they did not recognise the role of the initial imperfections causing the bifurcation point never to be reached as demonstrated in experiments, Kollar and Dulacska [54]. The paper that can be said to have the most influence on the understanding of the buckling process and indicating that the postbuckling behaviour determines the sensitivity to initial imperfections is the basic paper of Koiter published in 1945. Since the first version was in Dutch, it did not gain international attention before the English translation in 1963, Seide [70]. The Koiter initial postbuckling theory, later improved by the so-called special theory of Koiter which was more accurate (Kollar and Dulacska [54]), handed a simple linearised formulation for finding the postbuckling path in the vicinity of the bifurcation point and proved that even small imperfections lead to significant decrease in buckling capacity. According to Popov and Medwadowski [62] it seems fair to say that the Koiter initial post-buckling theory represents one of the most important contributions in the field of stability of elastic systems since the initial investigations of Euler and Lagrange.

Throughout the twentieth century, the buckling was expanded to inelastic behaviour where loss of stability and material failure are intertwined due to plastic behaviour and creep. Furthermore, the negative effects of fracture propagation and finite strain effects on stability gained attention. Contemporary advancement is mostly by nonlinear finite element analysis, allowing the calculation of bifurcation loads of perfect shells and collapse loads of imperfect shells.

In the following, the previously mentioned buckling phenomena are explained. As the curvature, which is an obvious distinguishing feature of the shell, introduces mathematical complexities, the relative simple bar is considered first. Similar to Chapter 5 the sequence can in short be named as bar-plate-shell. For each structural element the linear critical load is determined. These values are important to ally with the first research question as to find the so-called knock-down factor which indicates the difference between the linear and actual critical load taking into account geometrical and physical nonlinearity. Furthermore, the nonlinear behaviour (caused by large deformations) is described and subsequently the influence of initial geometric imperfections. In the end, the influence of inelastic material behaviour on buckling is discussed. But first the basic terms are explained.

In the subsequent buckling survey the literature is not completely processed, nor is the theory discussed in every detail. But the most important phenomena are to make known and clearly described serving the reader with sufficient knowledge for the analyses in the following Chapters.

6.2.1 Stability and Instability

An effective starting point in the buckling investigation is to explain the terms of stability and instability. Therefore, there is referred to the state of a system, which is the collection of values of the system parameters at any instant of time. The state of a system is stable if relatively small changes in system parameter (for shells e.g. geometrical and material properties) and/or environmental conditions (e.g. applied forces and thermal conditions) would bring relatively small changes in the existing state of the system, at any instant time. Analogously, the state of a system in unstable if relatively small changes in system parameter and/or environmental conditions cause major changes in the existing state, at any instant time.

In case of buckling there is referred to the stability and instability of the equilibrium state of a system. Buckling is a mode of instability of equilibrium. The equilibrium state of a system is stable if small perturbations, caused by effects such as load changes, would confine to vicinity of the existing equilibrium state whereas slight changes in an unstable equilibrium state of a system force the system away from that equilibrium configuration. The unstable system finds other equilibrium states which may be close to the initial state or far away, Farshad [34]. In terms of energy, the state of equilibrium can said to be stable if the potential energy is a minimum. For any small displacement from the equilibrium position the potential energy increases. Hence, for unstable equilibrium the potential energy is a maximum.

Buckling occurs in deformable bodies subjected to compressive loadings. Hereby, the loading causing instability of equilibrium can be classified as conservative or non-conservative loading. Conservative loads, such as the dead weight of a shell, are time independent loads whereas non-conservative loads are generally time dependent or depend on the state of the system. Bodies subjected to conservative loading may suffer buckling type loss of equilibrium stability and find other equilibrated configurations. Bodies subjected to non-conservative loading may become dynamically unstable which cause oscillations with increasing amplitude, Farshad [34]. This instability mode is known as flutter. Buckling in structural problems, as considered, alters the initial state of equilibrium due to loss of stability and finds a new equilibrium state (which also may be a total collapse) under the influence of conservative load. Hence, buckling is also referred to as static instability.

6.2.2 Forms of Buckling

According to Popov and Medwadowski [62], it can be said that there are five types of loss of stability due to buckling; (1) bifurcation buckling and (2) limitation buckling in the elastic branch expanded with (3) inelastic buckling, (4) creep buckling and (5) dynamic buckling. They will be discussed in the following.

Bifurcation Buckling

The process of buckling can be divided into a prebuckling, buckling and postbuckling stage. The path up to the critical buckling load is often named the primary path, while the secondary path represents the postbuckling portion. Bifurcation of equilibrium refers to a situation in which a body subjected to increased loading will have, at the point of buckling, two possible paths of equilibrium: the primary path which becomes unstable after buckling (a small perturbation leads to large deflection) and the (adjacent) stable secondary path, represented in Figure 6.2. In reality the structure chooses the path that yields the minimum energy of the system. Both paths intersect at the buckling point, or so-called bifurcation point as in that point two states of equilibrium can exists for the same load, Farshad [34].

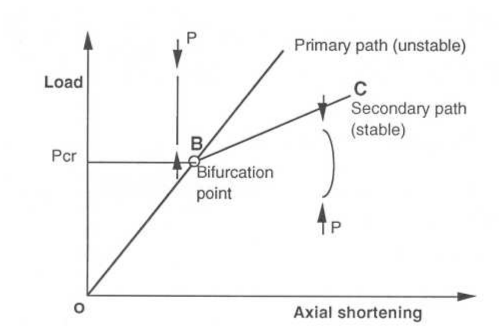

Figure 6.2. Bifurcation buckling of an axially compressed column, Farshad 1992

The existence of two equilibrium paths and the fact that the structure chooses its own buckled shape beyond the bifurcation point is characteristic for the bifurcation of equilibrium. Bifurcation buckling is often referred to as classical buckling: in a classical linear (Euler) stability analysis the existence of a bifurcation point and an adjacent equilibrium state are assumed, Farshad [34].

Limitation Buckling

Structures that carry transverse load mainly by axial compressive forces, such as shallow shells, typically may suffer loss of stability by limitation of equilibrium. Instability due to limitation of equilibrium is characterised by a continuous load-deformation curve without a bifurcation point. The curve has stationary maximum and minimum points in which one of them represents the critical load or limit point. The limit point is the intersection of the prebuckling and postbuckling path. In limitation buckling the structure may show a smooth transition from prebuckling to postbuckling or may show a sudden snap-through towards a non-adjacent equilibrium point caused by an unstable region after the limit point. Snap-through buckling is visualised in Figure 6.3.

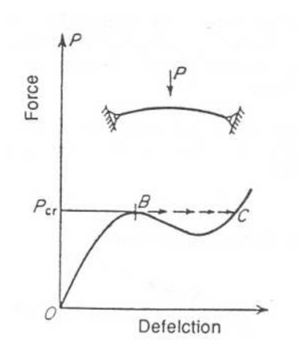

Figure 6.3. Snap-through buckling, Farshad 1992

Unfortunately, whether a structure experiences bifurcation buckling or limitation buckling cannot be determined in advance. The buckling mode of spherical shells under external pressure may be as well bifurcation as snap-through buckling, depending on the geometry of the shell.

Inelastic Buckling

Previous modes of buckling failure may also be addressed as elastic instability failures. However, shells are mostly built of materials for which the assumption of elastic behaviour does not apply. Thus, in addition to the elastic buckling, inelasticity must be considered, Popov and Medwadowski [62], Reinforced concrete shells experience nonlinear material behaviour almost from the beginning of the loading process. If the material behaviour becomes plastic the critical load will be less than given by the elastic theory. The amount of decrease due to inelasticity it is not known and has to be determined by computational analysis or experimental tests. Inelastic buckling is discussed later in Section 6.6.

Creep Buckling

So far, in the discussion, no time effect is assumed. However, most materials develop deformations that not only depend on stresses but also on time. In other words, the initial elastic deformation increases in time, even with constant stress. This so-called creep effect may become important for buckling as creep causes flattening and therefore loss of curvature. In case of a sound reinforced concrete structure, the process tends to an asymptote as the compressive reinforcement enables the composite to reach equilibrium. However, even sound designed structure can show load-carrying capacities depending on the length of time a load is sustained. Thus, the longer the structure is subjected to load, the lower the collapse load.

For an analytical calculation it appears that a sufficiently accurate approach consists of the introduction of a creep modulus of elasticity into the critical load formulae, together with a somewhat larger factor of safety to overcome its uncertainties. The creep modulus is approximately one-third the value of the Young's modulus. For reasons of simplicity, the effect is often taken into consideration with a critical time, although not correct (critical load is normative). More accurate is to idealise creep based on the concepts of linear visco-elasticity using a (chain spring-dashpot) Maxwell model, a (parallel spring-dashpot) Kelvin model or a Burger model (combination of both). The solutions based on linear visco-elasticity appear to be satisfactory for reinforced concrete, Popov and Medwadowski [62].

Although creep may lead to a significant lower critical load, approximately one third of the short time test as found in experiments, Billington and Harris [6], it is not treated in this thesis.

Dynamic Buckling

Dynamic buckling refers to a situation in which buckling is caused by rapidly varying or transient loads. In rare circumstances that such loading occurs, the mechanical properties of materials are significantly increased and, due to the inertia effect, the same holds for the critical buckling load. The dynamic critical load may be up to *3* times as high as the normal critical load, as shown by Volmir (1967). Hence, it appears that dynamic buckling is only of minor importance and therefore not taken into account here.

6.2.3 Koiter Initial Postbuckling Theory

The main question of the buckling phenomena is the shape of the postbuckling path of equilibrium. The axially compressed column, seen in Figure 6.2, shows increasing load carrying capacity after the bifurcation point, independent on the chosen path of equilibrium. The question is, however, if this is true for all columns, or even in general, for all structures. As mentioned, the importance of postbuckling research was stressed when it was examined that shells may experience a significant reduction in load carrying capacity.

To determine the shape of the secondary path it is not possible to use the linear theory, which was sufficient to calculate the critical buckling load. As the postbuckling stage involves large deformations, in general, it demands a nonlinear formulation and solution. Such solutions are very complex and have been obtained for just a few simple shell geometries, Popov and Medwadowski [62].

A significant step to determine the postbuckling behaviour of a structure in the vicinity of its bifurcation point is taken by Koiter; the Koiter initial postbuckling theory. In his dissertation Koiter provides in a study to the slope and curvature of the secondary path in the immediate vicinity of the bifurcation point. Instead of using a nonlinear formulation he approached the secondary path on the basis of linearised formulation in such a way that the buckling shape(s) are expanded into power series of displacements measured from the prebuckling state. Consequently, it is only exact at the point of bifurcation, Popov and Medwadowski [62]. By adding as many terms as the computing possibilities allow, the actual postbuckling behaviour is approached, Kollar and Dulacska [54].

Koiter concluded that the shape of the secondary path can be divided into three possible types of bifurcation of equilibrium: (I) stable symmetrical bifurcation, (II) labile symmetrical bifurcation and (III) labile unsymmetrical bifurcation, represented in Figure 6.4. Labile unsymmetrical bifurcation is characteristic for structures in which the postbuckling behaviour can only occur in a preferred direction. In case of an imperfect structure, also seen in Figure 6.4, the primary and secondary paths of equilibrium often show a fluent transition. More important, imperfect structures do not show a clear bifurcation point and they may fail before the linear critical buckling load is reached (limit point buckling). Such imperfection buckling is discussed later.

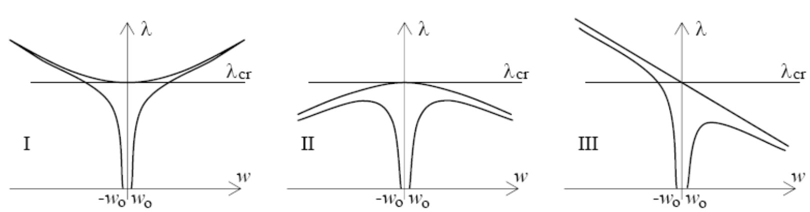

Figure 6.4. Possible paths of equilibrium according to the Koiter theory, Hoogenboom 2006

Using the theory of Koiter, for different type of buckling behaviour the paths of equilibrium can be defined. As the equilibrium of a perfect system can be described by:

$$\lambda = \lambda_{cr}\left(1 - c_1 w - c_2 w^2\right)$$

Herein, the load factor λ depends on the imperfection amplitude w and the characteristic constants c dependent on the structural shape.

For type II and type III behaviour, Koiter developed the so-called power laws:

Two-third Power Law: $$\lambda_{max} = \lambda_{cr}\left(1 - 3\left(w_0 \tfrac{1}{2} \rho \sqrt{c_2}\right)^{\frac{2}{3}}\right) \quad (6.1)$$

Half Power Law: $$\lambda_{max} = \lambda_{cr}\left(1 - 2\left(w_0 \rho c_1\right)^{\frac{1}{2}}\right) \quad (6.2)$$

Using the power laws and a correct description of the constants which depends on the type of structure (c) and the imperfection shape (ρ) and magnitude (w_o) the structural behaviour of an imperfect structure can be computed.

6.2.4 Paths of Equilibrium

The buckling behaviour of various structures is extensively investigated. According to Kollar and Dulacska [54], these investigations show that way in which most structures find a new equilibrium state is according to one of the diagrams presented below in Figure 6.5. Figure 6.5 shows the load P plotted against the buckling deformation w for different types of buckling behaviour. Kollar and Dulacska [54], describe the following situations:

When the equilibrium of a certain structure becomes indifferent after buckling, the path of equilibrium is similar to the one presented in Figure 6.5.a. The load bearing capacity of this type of structures remains constant and initial imperfections increase the deformations, but finally approach the linear critical load. Structures which behave according to this diagram are, thus, insensitive to imperfections. For shells, the behaviour seldom occurs, however, the graph reasonably accurately describes the behaviour of bar structures.

The diagram of Figure 6.5.b shows increasing load carrying capacity in the postbuckling range. Consequently, structures that fit into this type of behaviour are insensitive to imperfections. Without initial imperfections these structures demonstrate bifurcation buckling, but with eccentricity of compression forces, the buckling behaviour shows a smooth transition between prebuckling and postbuckling equilibrium. Furthermore, the diagram is symmetrical, in other words, it makes no difference whether the imperfection is in positive of negative direction. Examples of such structures are plates and shells with negative Gaussian curvature. Hence, the latter are not of interest for the investigation to shell buckling.

Figure 6.5.c also shows symmetrical buckling behaviour as imperfections in both direction cause decrease in load carrying capacity. If disturbances are present, either geometrical imperfections or initial bending moments (e.g. at boundary conditions or point loads), the maximum load is a limit point after which the structure transforms to a new (non-adjacent) equilibrium shape. Obviously, these structures cannot be designed on the basis of the linear critical buckling load as they are very sensitive to imperfections.

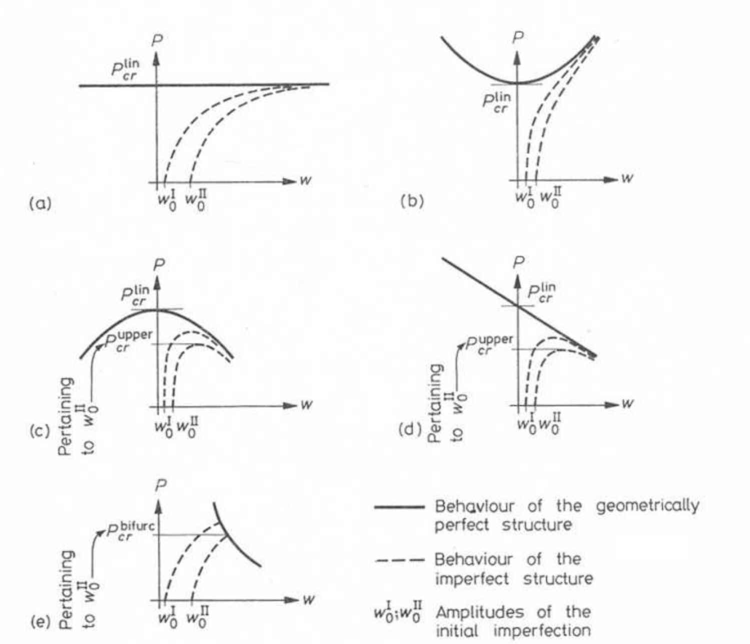

Figure 6.5. Characteristic cases of postbuckling load bearing behaviour plotted against the buckling deformation, Kollar and Dulacska 1984

Figure 6.5.d represents structures which have asymmetrical buckling behaviour with respect to the direction of the initial imperfection. The physical explanation of this asymmetric behaviour is that the structure stiffens during buckling deformation in one direction, while in the other it unstiffens. An example is an axially compressed circular cylindrical shell, in which outward buckles increase the curvature and thus stiffen the shell while inward buckles unstiffen, see Figure 6.6. In practice only the declining branch is of interest as it shows decreasing load behaviour similar to diagram *c*. However, this time, the decrease in load is more sudden.

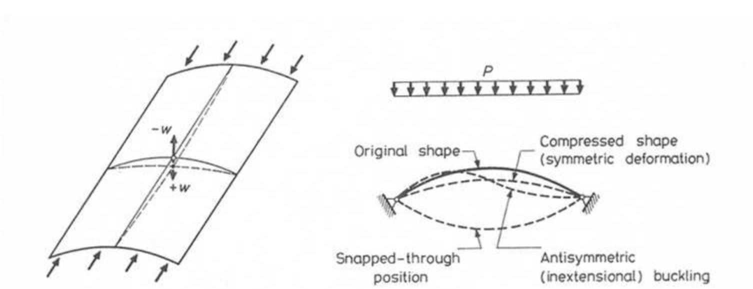

Figure 6.6. Asymmetric post-critical behaviour (left) and different types of arch buckling, Kollar and Dulacska 1984

Figure 6.5.e is a special type of buckling behaviour. The structure deforms according to the shape of a certain imperfection, however, before snap-through, a bifurcation occurs as the structure finds a new adjacent equilibrium shape. This kind of behaviour is referred to as a composite behaviour. A simple example of such composite behaviour is the flat arch of Figure 6.6. After the arch is brought into compression the arch may snap-through downwards or can buckle by bifurcation into an antisymmetric shape with in-extensional deformation, depending on the geometrical proportions.

Finally, multimode (or compound) buckling must be mentioned, a mode in which several buckling modes are associated with the same critical buckling load. Within the frame of the linear theory, these buckling modes are orthogonal to each other. However, in the nonlinear frame, the modes interact resulting in a dramatic fall-back in postbuckling load carrying capacity. Hence, this kind of buckling is highly uninvited. Unfortunately, as will become clear in the following, the spherical shell under external pressure experiences this kind of behaviour. Furthermore, compound buckling may also be associated with initial imperfections causing further decrease in load bearing behaviour.

Hence, aforementioned in the introduction of this chapter, it can be concluded that the postbuckling behaviour of a shell determines the sensitivity to initial imperfections.

6.3 Elastic Column Buckling

Analogous to the previous Chapter, the buckling phenomenon is discussed considering a sequence which in short may be named bar, plate and shell. The bar serves as starting point while the plate and shell are discussed in the following paragraphs.

6.3.1 Ideal Linear Elastic Column

The buckling phenomenon can be introduced by an example of a simple column subjected to a concentric compressive load. By gradually increase of the compressive load, at first, the column remains straight and experiences only a small shortening. However, at a certain load, the column may also experience a lateral displacement, which increases significant without a corresponding change in the compression load. By then, the column is said to be buckled and the value of the load at which the buckling occurred is the so-called the critical buckling load, Popov and Medwadowski [62].

To determine the critical buckling load of a column, an ideal elastic column under increasing axial compression force P is considered. The column is assumed to be simply supported (pinned) at both ends. Recapitulate from Chapter 5.2 the kinematic and constitutive relations for a bar in compression:

$$\varepsilon = \frac{du_x}{dx} \tag{5.7}$$

$$N = EA\varepsilon \tag{5.6}$$

$$\kappa = -\frac{d^2w}{dx^2} \tag{5.12}$$

$$M = EI\kappa \tag{5.10}$$

By assuming small deflections and negligible shear force in *z-direction*, the equilibrium relations of the deformed column can be described as:

$$\left.\frac{dN}{dx} = o\right\} \text{ in-plane equilibrium}$$

And

$$\left.EI\frac{d^4w}{dx^4} - N\frac{d^2w}{dx^2} = o\right\} \text{ out-of-plane equilibrium} \tag{6.3}$$

Here, w is the lateral displacement as seen in Figure 6.7.

The system of differential equations (6.3) is nonlinear as there are two unknowns which appear as a product in the second equation. Fortunately, equation one can be solved and the solution can be substituted into the second equation. For the second equation, it holds that the internal axial compression N equals minus the external compression force P. This is based on reasoning that at the bifurcation point the pre-buckling load and internal forces are in equilibrium. The second equation evolves to a general solution:

$$EI\frac{d^4w}{dx^4} + P\frac{d^2w}{dx^2} = o \tag{6.4}$$

The equilibrium relation is valid for any value of P in case of zero lateral displacement. From a physical point of view, the trivial solution corresponds to the pre-buckled configuration. However, at a certain point, the bifurcation point, there is another equilibrium state in which w is nontrivial. Thus, the force P must be determined in such a way that it allows the solution for w to be nontrivial.

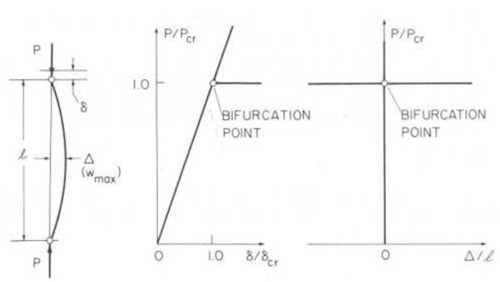

Figure 6.7. Buckling of an ideal elastic column, Popov and Medwadowski 1981

This stability problem, described by this general equation, is mathematically an eigenvalue problem. An eigenvalue problem is a problem which has only trivial solution unless the existing free parameter acquires certain values. With those values, the homogeneous problem has a nontrivial solution. The special parameter values are called the eigenvalues or synonymously the characteristic values; the corresponding nonzero solutions are called the eigenfunctions or characteristic functions. The eigenvalues are the values of critical buckling loads and the buckling modes are the eigenfunctions of the problem.

As can be seen in Figure 6.7, the bending moment M can be described as the compression force times the lateral displacement. By using the relations (5.12) and (5.10), the general equation of (6.4) can be transformed to the well-known differential equation for a column with static boundary conditions:

$$\frac{\partial^2 w}{\partial x^2} + k^2 w = 0 \quad where \quad k^2 = \frac{P}{EI} \tag{6.5}$$

The general solution to this differential equation is:

$$w = A \sin kx + B \cos kx \tag{6.6}$$

To satisfy the boundary conditions at the bottom support of Figure 1 ($x = 0$) the value of B in relation (6.6) is equal to zero, which means that the shape of the lateral displacement over the length of the column equals a sinus-wave. Obviously, the lowest critical load is obtained with the least amount of sinus-waves; for the column in Figure 6.7 a one-sinus-wave is normative. The boundary conditions at the lower support ($x = 0$) are satisfied for any value of k. The top support ($x = l$) boundary conditions are fulfilled if $k = \frac{\pi}{l}$.

Hence, equation (6.5) is satisfied and the critical load is equal to:

$$P_{cr} = \frac{\pi^2 EI}{l^2} \tag{6.7}$$

Engineers will recognise expression (6.7) as the Euler buckling equation of a column in axial compression.

The solution to equation (6.4) can be plotted in load-displacement graphs as is done in Figure 6.7. Clearly, the column is an example of bifurcation buckling as at the buckling point the path of equilibrium splits into two. Note that the magnitude of the lateral displacement remains indefinite.

6.3.2 Ideal Nonlinear Elastic Column

The weakness of equation (6.4) lies in the fact that it is linearly derived and, therefore, unable to predict the magnitude of the lateral displacement Δ or provide in information about the slope and shape of the secondary path after the bifurcation point. Evidently, the solution to this problem lies in a nonlinear formulation of the column equations.

The nonlinear formulation and solution was first obtained by Lagrange in 1867, based on the exact expressions of the strain and curvature, Popov and Medwadowski [62]. The solution predicted a critical load equally to the one as found with the linear Euler theory. In contrast with the linear solution, the nonlinear postbuckling path of the column, Figure 6.8 showed an increase in load carrying capacity, while being in a bent position. This is visualised in Figure 6.8. Referring back to Section 6.2.3, the column is, thus, an example of stable symmetrical bifurcation. However, so far as the structural problem is concerned, it must be mentioned that the lateral deflection may become so large that the column is unacceptable to serve as proper structural element.

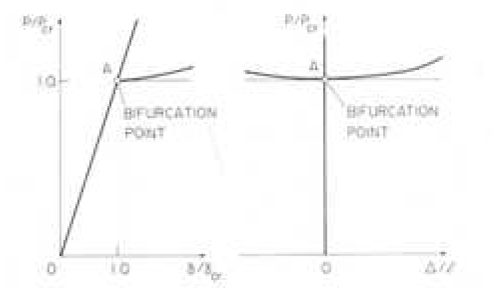

Figure 6.8. Buckling behaviour of ideal elastic column according to the nonlinear theory, Popov and Medwadowski 1981

The observation that the nonlinear critical load is equal to the linear critical load raised the thought that the nonlinearity has only minor influence on the postbuckling behaviour in the vicinity of the bifurcation point, Popov and Medwadowski [62]. This turns out to be true and the simplest nonlinear strain formulation including fairly large rotations leads to:

$$\varepsilon = \frac{du}{dx} + \frac{1}{2}\left(\frac{dw}{dx}\right)^2 \tag{6.8}$$

For columns, this relation may be of little practical use as the exact solution is already offered by Lagrange. However, relation (6.8) will proof worthy later in the equivalent discussion of plates and shells.

When equation (6.8) is implemented into the equilibrium relation, this leads to a factor between the linear critical buckling load and a nonlinear critical buckling load equal to:

$$\lambda = 1 + 0.125\pi^2\left(\frac{A}{l}\right)^2$$

From the above relation, the increase in load carrying capacity becomes clear. The increase is, however, rather small. For a substantial deflection of $w = 0.2 \cdot l$ the carrying capacity is only 3% higher, Vrouwenvelder [81].

6.3.3 Imperfect Elastic Column

Since ideal straight columns are almost unachievable in practice, it is important to investigate the effect of an initial lateral displacement w_o, a so-called initial geometrical imperfection, on the path of equilibrium. The effect is illustrated in Figure 6.9. The influence of the initial imperfection according to the linear theory as described in equation (6.4) is plotted in the left graph. In the graph it is seen that initial lateral displacements cause a departure from the linear path of equilibrium to a nonlinear equilibrium path. As the initial imperfection increases the deviation of the ideal line becomes larger and larger.

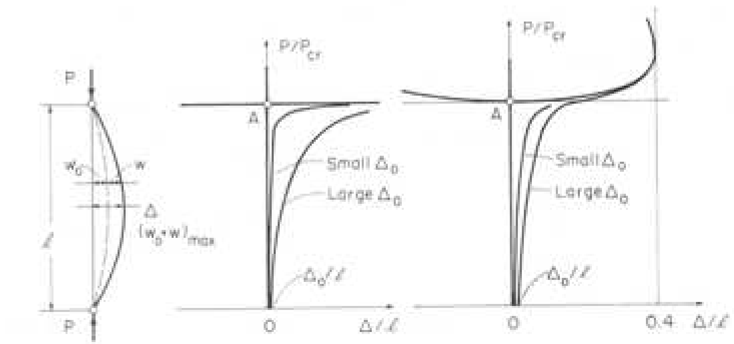

Figure 6.9. Linear and nonlinear buckling behaviour of initial imperfect elastic column, Popov and Medwadowski 1981

However, regardless the magnitude of the imperfection, the critical load as obtained by Euler serves as an asymptote. When the initial lateral deflection becomes so large that the linear theory is not suitable anymore, the nonlinear solution provides in a more accurate approximation. The nonlinear result is plotted in the right graph of Figure 6.9.

Aforementioned in the previous paragraph, it must be emphasised that the solutions as illustrated in Figure 6.9 are bounded by practical considerations. The nonlinear path of equilibrium suggests the possibility of very large lateral displacements to a value of *0.4* times the original length of the column. For a pin-ended column this means that the column is almost a complete circle, which obviously is unacceptable for a structural element.

Finally, it must be mentioned that the buckling of a column is by no means restricted to the phenomenon described above. Dependent of the character of the applied load, buckling also appears in other ways such as torsional buckling or lateral buckling.

6.3.4 Imperfections (I)

The previous example of an imperfect column shows that initial imperfections cause the buckling path of equilibrium to be nonlinear from the beginning. This nonlinearity implies large lateral displacements to reach up for the asymptotic linear critical load. Concerning structural elements, this may result in a lower allowable load than follows from the linear theory as the lateral displacement is often bounded by practical considerations. Hence, the magnitude of the imperfection that must be taken into account is often prescribed in national building codes.

The column is an example of a structural element that shows stable symmetrical bifurcation of equilibrium according to Koiter, seen in the outer left graph of Figure 6.5.b. I.e. the influence of imperfections does not result in a decrease in load carrying capacity.

6.4 Elastic Plate Buckling

6.4.1 Ideal Linear Elastic Plate

The elastic theory of a thin plate is outlined in Chapter 5.3. It was found that the thin plate can be idealised as a two-dimensional structure which can be described by three in-plane forces, three bending moments and two transverse shear terms which vanish in case of zero torsional moment. Recapitulate from Chapter 5, the kinematic relations (replacing u_x, u_y and u_z by u, v and w):

$$\varepsilon_{xx} = \frac{\partial u}{\partial x} \quad \text{and} \quad \varepsilon_{yy} = \frac{\partial v}{\partial y} \tag{5.14}$$

$$\gamma_{xy} = \frac{\partial u}{\partial y} + \frac{\partial v}{\partial x} \tag{5.15}$$

$$\kappa_{xx} = -\frac{\partial^2 w}{\partial x^2} \quad \text{and} \quad \kappa_{yy} = -\frac{\partial^2 w}{\partial y^2} \tag{5.20}$$

$$\rho_{xy} = -2\frac{\partial^2 w}{\partial x \partial y} \tag{5.21}$$

And the constitutive relations:

$$\begin{bmatrix} n_{xx} \\ n_{yy} \\ n_{xy} \end{bmatrix} = \begin{bmatrix} D_m & \nu D_m & 0 \\ \nu D_m & D_m & 0 \\ 0 & 0 & D_m\left(\frac{1-\nu}{2}\right) \end{bmatrix} \begin{bmatrix} \varepsilon_{xx} \\ \varepsilon_{yy} \\ \gamma_{xy} \end{bmatrix} \tag{5.17}$$

$$\begin{bmatrix} m_{xx} \\ m_{yy} \\ m_{xy} \end{bmatrix} = \begin{bmatrix} D_b & \nu D_b & 0 \\ \nu D_b & D_b & 0 \\ 0 & 0 & D_b\left(\frac{1-\nu}{2}\right) \end{bmatrix} \begin{bmatrix} \kappa_{xx} \\ \kappa_{yy} \\ \rho_{xy} \end{bmatrix} \tag{5.23}$$

Where $D_m = \frac{Et}{1-\nu^2}$ and $D_b = \frac{Et^3}{12(1-\nu^2)}$.

Analogous to the ideal elastic column, the equilibrium equations for a slightly deformed plate are:

$$\left.\begin{aligned} \frac{\partial n_{xx}}{\partial x} + \frac{\partial n_{yx}}{\partial y} &= 0 \\ \frac{\partial n_{yy}}{\partial y} + \frac{\partial n_{xy}}{\partial x} &= 0 \end{aligned}\right\} \text{ in-plane equilibrium}$$

$$\left. D_b \nabla^2 \nabla^2 w - \left(n_{xx}\frac{\partial^2 w}{\partial x^2} + 2n_{xy}\frac{\partial^2 w}{\partial x \partial y} + n_{yy}\frac{\partial^2 w}{\partial y^2} \right) = 0 \right\} \text{ out-of-plane equilibrium} \tag{6.9}$$

In which the biharmonic plate equation as derived by Lagrange (5.28) is rewritten, replacing the load p_z by the in-plane stresses that arise due to the initial displacement w perpendicular to the plate surface. Note that the third equation becomes equal to the column equation (6.4) if the plate becomes a column and the terms in *y-direction* vanish.

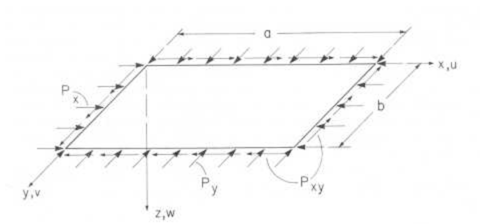

Figure 6.10. Rectangular edge loaded plate, Popov and Medwadowski 1981

When an edge loaded plate as seen in Figure 6.10 is assumed, for small deformations the in-plane forces are constant throughout the plate. Assuming compression forces in only one-direction, the third relation of (6.9) changes to a differential equation in w of the fourth order which can be solved easily using simply (pinned) supported plate edges similar to those of the column. For one-directional compression, equation (6.9) changes to:

$$\nabla^2\nabla^2 w = \frac{n_{xx}}{D_b}\frac{\partial^2 w}{\partial x^2} \tag{6.10}$$

For a rectangular plate of length a and width b the trail solution to this equation is:

$$w = W sin\left(\frac{n\,\pi\,x}{a}\right) sin\left(\frac{m\,\pi\,y}{b}\right) \tag{6.11}$$

Where n and m are the number of half-waves in the x- and *y-direction* respectively

Equation (6.11) satisfies the boundary conditions if:

$$w = \frac{\partial^2 w}{\partial x^2} = 0 \; for \; x = 0$$

$$w = \frac{\partial^2 w}{\partial x^2} = 0 \; for \; x = a$$

$$w = \frac{\partial^2 w}{\partial y^2} = 0 \; for \; y = 0$$

$$w = \frac{\partial^2 w}{\partial y^2} = 0 \; for \; y = b$$

Substituting the general solution (6.11) in equation (6.10) gives the expression:

$$n_{xx} = \frac{\pi^2 a^2 D_b}{n^2}\left(\frac{n^2}{a^2} + \frac{m^2}{b^2}\right)^2 \tag{6.12}$$

The smallest value of n_{xx}, and therefore the critical load, is found when m is taken equal to one. The plate buckles in such a way that there can be several half-waves in the direction of compression but only one half-wave in the perpendicular direction. By introducing parameter k and the expression for D_b equation (6.12) simplifies to:

$$n_{xx,cr} = k\frac{\pi^2 E t^3}{12\left(1 - \nu^2\right)b^2} \tag{6.13}$$

Where $k = \left(\frac{a}{nb} + \frac{nb}{a}\right)^2$ and n the number of half-waves buckles in the compression direction

Finally, the general expression for the buckling stress of an ideal elastic rectangular plate of length a and width b can be obtained;

$$\sigma_{cr} = k\frac{\pi^2 E}{12\left(1 - \nu^2\right)}\left(\frac{t}{b}\right)^2 \tag{6.14}$$

This solution was first obtained by Bryan in 1891. Therefore, there is sometimes referred to the Bryan critical buckling load, Popov and Medwadowski [62]. Note that when k is equal to one and the stress is equal to the critical load divided by the area, equation (6.14) is similar to the Euler critical buckling load.

If the number of half-waves in the compression direction is equal to one, k in equation (6.14) reaches its minimum for a square plate *(k = 4)*. Similarly, if the plate buckles in two half-waves, k acquires its minimum when the plate length is twice the plate width. The relationship between k and the plate dimensions is represented in Figure 6.11.

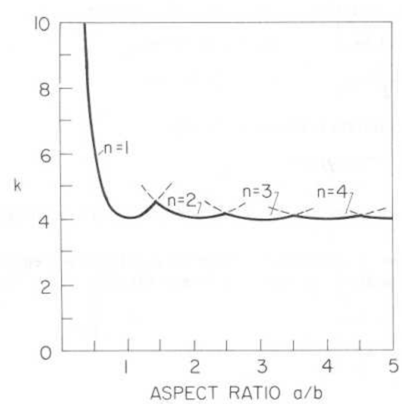

Figure 6.11. Buckling coefficient k for axially compressed simply supported plates, Popov and Medwadowski 1981

As an example, the half-wave buckling pattern of a plate in which the length is three times the width which is only simply supported along the loaded boundaries is seen in Figure 6.12.

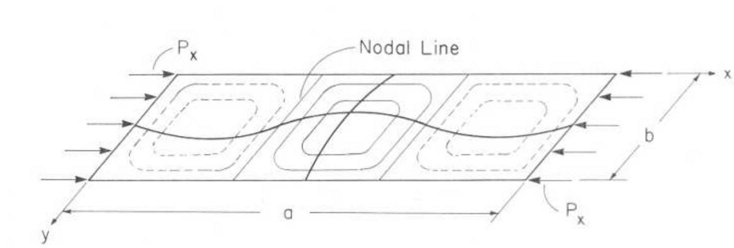

Figure 6.12. Buckling shape of a simply supported plate panel, Popov and Medwadowski 1981

The plate as seen in Figure 6.12 can also buckle in several other shapes. In fact plates exhibit many buckling modes, similar to shells as will be seen later. However, unlike shells, the corresponding critical loads are far apart, so that compound buckling (see Section 6.2.4) will not occur.

Finally, it must be said that, in general, the critical buckling load is very sensitive to the way in which the plate is supported.

6.4.2 Ideal Nonlinear Elastic Plate

As with the column, the linear theory is insufficient to predict the slope and shape of the postbuckling path. To find the postbuckling behaviour in the immediate vicinity of the bifurcation point, again, the simplest nonlinear formulation is assumed to be sufficient. I.e. considering the squares of the greatest displacement component w, perpendicular to the surface, is good enough to describe the behaviour of the buckled shape up to displacements several times the thickness of the plate. Equivalent to equation (6.8), the strains become:

$$\begin{aligned} \varepsilon_{xx} &= \frac{\partial u}{\partial x} + \frac{1}{2}\left(\frac{\partial w}{\partial x}\right)^2 \\ \varepsilon_{yy} &= \frac{\partial v}{\partial y} + \frac{1}{2}\left(\frac{\partial w}{\partial y}\right)^2 \\ \gamma_{xy} &= \frac{\partial u}{\partial y}\frac{\partial v}{\partial x} + \frac{\partial w}{\partial x}\frac{\partial w}{\partial y} \end{aligned} \tag{6.15}$$

Hence, the effect of transverse deflections on in-plane strains is approximated.

From these expressions and the linear elastic constitutive relations found earlier, the resulting governing system of differential equations can be derived. For reasons of simplicity, the *stress function of Airy Φ* is introduced defined by:

$$\frac{\partial^2\Phi}{\partial y^2} = n_{xx}$$

$$\frac{\partial^2\Phi}{\partial x^2} = n_{yy} \qquad (6.16)$$

$$\frac{\partial^2\Phi}{\partial x \partial y} = -n_{xy}$$

With simple equating the system of differential equation describing equilibrium (6.9) changes to:

$$\left.\nabla^2\nabla^2\Phi - E\,h\left(\left(\frac{\partial^2 w}{\partial x \partial y}\right)^2 - \frac{\partial^2 w}{\partial x^2}\frac{\partial^2 w}{\partial y^2}\right) = 0\right\} \text{ in-plane equilibrium}$$

$$\left.D_b\nabla^2\nabla^2 w - \left(\frac{\partial^2\Phi}{\partial y^2}\frac{\partial^2 w}{\partial x^2} + 2\frac{\partial^2\Phi}{\partial x \partial y}\frac{\partial^2 w}{\partial x \partial y} + \frac{\partial^2\Phi}{\partial x^2}\frac{\partial^2 w}{\partial y^2}\right) = 0\right\} \text{ out-of-plane equilibrium} \qquad (6.17)$$

The nonlinear theory as described above was first proposed by Von Karman in 1910. It is by no means simple to find a solution which satisfies the equilibrium. Therefore, the solution is only examined with respect to the distribution of in-plane forces and the corresponding path of equilibrium, as described in the paper of Popov and Medwadowski [62].

The nonlinear postbuckling stress distribution of a simply supported buckled plate is illustrated in Figure 6.13. Obviously, the difference with the linear stress distribution is the fact that the unloaded *y-directional* sides are not free of stress anymore. The buckling pattern develops lateral compressive stresses at both of the loaded edges and pulling stresses in the midheight part. Furthermore, the buckled plate has lower vertical stresses in the middle of the plate, which might be expected by engineers intuitively. The corresponding path of equilibrium that belongs to the nonlinear stress distribution is shown in the Figure 6.14.a.

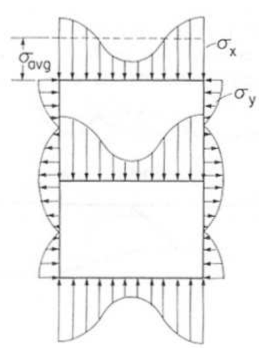

Figure 6.13. Postbuckling in-plane stresses in a pinned plate with uniform end shortening, Popov and Medwadowski 1981

In Figure 6.14.a point *A* is the bifurcation point as derived by the linear theory in the previous paragraph. It can be seen that after the bifurcation point the load carrying capacity continuous to increase along the stable path of equilibrium.

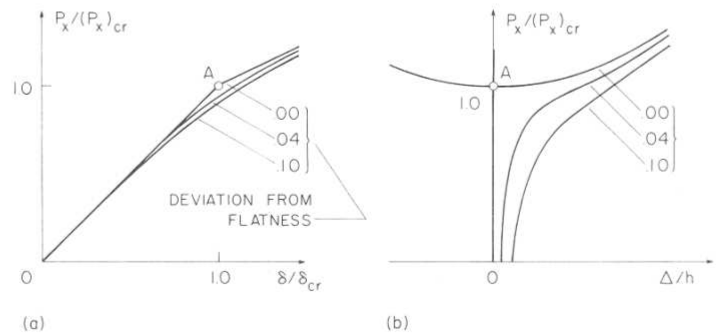

Figure 6.14. Postbuckling behaviour of perfect and imperfect elastic plates, Popov and Medwadowski 1981

6.4.3 Imperfect Elastic Plate

Similar to the column buckling, it seldom occurs that an ideal straight plate is formed. Therefore, the influence of initial geometrical imperfections to the buckling behaviour is investigated. They are plotted in Figure 6.14. It is seen that for each initial imperfection, a separate path of equilibrium is found similar to the column example. With increasing imperfection, the deviation from the linear path and ideal nonlinear path also increases. The plate is, like the column, an example of stable symmetrical bifurcation of equilibrium. In general, the buckling behaviour of unrestrained (only supported along the loaded edges) plates, tends toward columns. Restrained plates however show significant increase in load carrying capacity after the bifurcation point, which in turn means that the factor of safety can be lower. The same holds for biaxial loaded plates with one load tension and the perpendicular load compression. Logically, the tension load stiffens the plate.

6.4.4 Imperfections (II)

As the plate shows stable symmetrical bifurcation of equilibrium, the imperfections show no decrease in critical load after a certain amount of deflection. Hereby it is important to mention that the horizontal scale of Figure 6.14.b is smaller by a factor of approximately ten than the scale of Figure 6.9. In other words, the influence of initial imperfections on the plate buckling behaviour is confined to the vicinity of the bifurcation point. Plates are a good example of structures insensitive to imperfections as the postbuckling load intensity increases. Also note the symmetrical behaviour as the direction of the imperfection makes no difference.

6.5 Elastic Shell Buckling

Shell buckling shows some major differences with the cases described before. As it is probably accurate to say that the origin of the current understanding of the problem lies in the widespread studies towards as well spheres as circular cylindrical shells, in this section two basic cases are discussed: an axially compressed circular cylindrical shell and a spherical shell under external pressure. In this way the main characteristics of shell buckling behaviour will come out.

The text below is based on Popov and Medwadowski [62], Kollar and Dulacska [54] and Hoefakker and Blaauwendraad [45].

6.5.1 General Buckling Equation

In Chapter 5.4 the linear theory of shells with arbitrary curvature is discussed. It was illustrated the structural behaviour of shells is described by three in-plane forces, three bending moments and two transverse shear terms that, analogous to the plate example, vanish in case of zero torsional moment. Recapitulate from Chapter 5.4 the kinematic, constitutive and equilibrium relations (replacing u_x, u_y and u_z by u, v and w):

Kinematic relations:

$$\varepsilon_{xx} = \frac{\partial u}{\partial x} + k_x w \quad \text{and} \quad \varepsilon_{yy} = \frac{\partial v}{\partial y} + k_y w$$

$$\gamma_{xy} = \frac{\partial u}{\partial y} + \frac{\partial v}{\partial x} - 2k_{xy} w \tag{5.33}$$

$$\kappa_{xx} = -\frac{\partial^2 w}{\partial x^2} \quad \text{and} \quad \kappa_{yy} = -\frac{\partial^2 w}{\partial y^2}$$

$$\rho_{xy} = -2\frac{\partial^2 w}{\partial x \partial y} \tag{5.43}$$

Constitutive relations:

$$\begin{bmatrix} n_{xx} \\ n_{yy} \\ n_{xy} \end{bmatrix} = \begin{bmatrix} D_m & \nu D_m & 0 \\ \nu D_m & D_m & 0 \\ 0 & 0 & D_m\left(\frac{1-\nu}{2}\right) \end{bmatrix} \begin{bmatrix} \varepsilon_{xx} \\ \varepsilon_{yy} \\ \gamma_{xy} \end{bmatrix} \tag{5.34}$$

$$\begin{bmatrix} m_{xx} \\ m_{yy} \\ m_{xy} \end{bmatrix} = \begin{bmatrix} D_b & \nu D_b & 0 \\ \nu D_b & D_b & 0 \\ 0 & 0 & D_b\left(\frac{1-\nu}{2}\right) \end{bmatrix} \begin{bmatrix} \kappa_{xx} \\ \kappa_{yy} \\ \rho_{xy} \end{bmatrix} \tag{5.44}$$

Where $D_m = \frac{Et}{1-\nu^2}$ and $D_b = \frac{Et^3}{12(1-\nu^2)}$.

The equilibrium relations derived in Chapter 5.4 are:

$$\left.\begin{aligned}\frac{\partial n_{xx}}{\partial x} + \frac{\partial n_{yx}}{\partial y} + p_x &= 0\\ \frac{\partial n_{yy}}{\partial y} + \frac{\partial n_{xy}}{\partial x} + p_y &= 0\end{aligned}\right\}\text{ in-plane equilibrium}$$

$$\left.\frac{\partial^2 m_{xx}}{\partial x^2} + 2\frac{\partial^2 m_{xy}}{\partial x \partial y} + \frac{\partial^2 m_{yy}}{\partial y^2} + k_x n_{xx} + k_y n_{yy} + 2k_{xy} n_{xy} + p_z = 0\right\}\text{ out-of-plane equilibrium} \tag{5.48}$$

From these equations the differential equation for a lateral displacement w perpendicular to the shell surface can be derived. Therefore, the stress functions of Airy Φ (with additional load terms) are introduced, replacing the membrane stress resultants:

$$\begin{aligned}\frac{\partial^2 \Phi}{\partial y^2} &= n_{xx} + \int p_x dx\\ \frac{\partial^2 \Phi}{\partial x^2} &= n_{yy} + \int p_y dy\\ \frac{\partial^2 \Phi}{\partial x \partial y} &= -n_{xy}\end{aligned} \tag{6.18}$$

The Airy stress function satisfies the in-plane equilibrium (first two equilibrium relations) and the out-of-plane equilibrium can be described with:

$$-k_x \frac{\partial^2 \Phi}{\partial y^2} + 2k_{xy}\frac{\partial^2 \Phi}{\partial x \partial y} - k_y \frac{\partial^2 \Phi}{\partial x^2} - \left(\frac{\partial^2 m_{xx}}{\partial x^2} + 2\frac{\partial^2 m_{xy}}{\partial x \partial y} + \frac{\partial^2 m_{yy}}{\partial y^2}\right) = p_z - k_x \int p_x dx - k_y \int p_y dy \tag{6.19}$$

By substituting the kinematic relations for a shell in bending in the constitutive relations and subsequently in the out-of-plane equilibrium relation (6.19) the relation changes into:

$$-k_x \frac{\partial^2 \Phi}{\partial y^2} + 2k_{xy}\frac{\partial^2 \Phi}{\partial x \partial y} - k_y \frac{\partial^2 \Phi}{\partial x^2} + D_b\left(\frac{\partial^4 w}{\partial x^4} + 2\frac{\partial^4 w}{\partial x^2 \partial y^2} + \frac{\partial^4 w}{\partial y^4}\right) = p_z - k_x \int p_x dx - k_y \int p_y dy \tag{6.20}$$

The notation is simplified by introducing the *shell differential operator* Γ (or *Pucher operator*) and the *Laplace operator* ∇^2 defined as:

$$\begin{aligned}\Gamma(\ ) &= k_x \frac{\partial^2 (\ )}{\partial y^2} - 2k_{xy}\frac{\partial^2 (\ )}{\partial x \partial y} + k_y \frac{\partial^2 (\ )}{\partial x^2}\\ \nabla^2 (\ ) &= \frac{\partial^2 (\ )}{\partial x^2} + \frac{\partial^2 (\ )}{\partial y^2}\end{aligned} \tag{6.21}$$

The out-of-plane equilibrium equation is then:

$$-\Gamma\Phi + D_b \nabla^2 \nabla^2 w = p_z - k_x \int p_x dx - k_y \int p_y dy \tag{6.22}$$

Note that the latter equation shows similarity with the *biharmonic plate equation* (5.28), however extended with a term covering the membrane stress field, the reason why shells have such a preferable stress distribution in compare to plates.

To solve equation (6.22) for the unknown w another differential equation for the displacement w is derived from the kinematic relations of a shell in bending. Therefore, first, the in-plane displacements u and v are eliminated by differentiate the normal strains and shear strain of the middle surface.

Differentiated normal strain equilibrium:

$$\frac{\partial^2 \varepsilon_{xx}}{\partial y^2} + \frac{\partial^2 \varepsilon_{yy}}{\partial x^2} = \frac{\partial^3 u}{\partial x \partial y^2} + \frac{\partial^3 v}{\partial x^2 \partial y} - k_x \frac{\partial^2 w}{\partial y^2} - k_y \frac{\partial^2 w}{\partial x^2} \tag{6.23}$$

Differentiated shear strain equilibrium:

$$\frac{\partial^2 \gamma_{xy}}{\partial x \partial y} = \frac{\partial^3 u}{\partial x \partial y^2} + \frac{\partial^3 v}{\partial x^2 \partial y} - 2k_{xy} \frac{\partial^2 w}{\partial x \partial y} \tag{6.24}$$

The difference of the two equations results in the compatibility requirement for thin shells. The compatibility requirement thus relates the change of curvature to the deformation of the middle surface by:

$$\frac{\partial^2 \varepsilon_{xx}}{\partial y^2} - \frac{\partial^2 \gamma_{xy}}{\partial x \partial y} + \frac{\partial^2 \varepsilon_{yy}}{\partial x^2} = -k_x \frac{\partial^2 w}{\partial y^2} + 2k_{xy} \frac{\partial^2 w}{\partial x \partial y} - k_y \frac{\partial^2 w}{\partial x^2} \tag{6.25}$$

By introducing the constitutive relations into the latter equation and replacing the membrane stress resultants by the stress function of Airy, the differential equation reads:

$$\frac{\partial^4 \Phi}{\partial x^4} + 2\frac{\partial^4 \Phi}{\partial x^2 \partial y^2} + \frac{\partial^4 \Phi}{\partial y^4} + D_m(1 - \nu^2)\left(k_x \frac{\partial^2 w}{\partial y^2} + 2k_{xy} \frac{\partial^2 w}{\partial x \partial y} + k_y \frac{\partial^2 w}{\partial x^2}\right) = \frac{\partial^2}{\partial y^2}\int p_x dx + \frac{\partial^2}{\partial x^2}\int p_y dy - \nu\frac{\partial p_x}{\partial x} - \nu\frac{\partial p_y}{\partial y} \tag{6.26}$$

Which can be simplified to the equation for the in-plane equilibrium of a shell:

$$\nabla^2\nabla^2\Phi + D_m(1 - \nu^2)\,\Gamma w = \frac{\partial^2}{\partial y^2}\int p_x dx + \frac{\partial^2}{\partial x^2}\int p_y dy - \nu\frac{\partial p_x}{\partial x} - \nu\frac{\partial p_y}{\partial y} \tag{6.27}$$

If the shell differential operator has constant coefficients, the relation between the shell differential operator and the Laplace operator becomes:

$$\nabla^2\Gamma(\;) = \Gamma\nabla^2(\;) \tag{6.28}$$

The differential equation for a lateral displacement w is achieved by multiplying equation (6.22) by $\nabla^2\nabla^2$ and equation (6.27) by Γ and subsequently eliminating the stress function of Airy:

$$D_b\nabla^2\nabla^2\nabla^2\nabla^2 w + D_m(1-\nu^2)\,\Gamma^2 w = \nabla^2\nabla^2 p_z - \nabla^2\nabla^2\left(k_x\int p_x dx + k_y\int p_y dy\right)$$
$$+\Gamma\left(\frac{\partial^2}{\partial y^2}\int p_x dx + \frac{\partial^2}{\partial x^2}\int p_y dy\right) - \nu\left(\frac{\partial p_x}{\partial x} + \frac{\partial p_y}{\partial y}\right) \qquad (6.29)$$

The latter equation is an eight order differential equation for one displacement. The equation is sometimes referred to as the Sanders-Koiter equation and is of general validity, Hoogenboom [49].

For the case in which only the load component perpendicular to the shell surface is present, equation (6.29) simplifies to:

$$D_b\nabla^2\nabla^2\nabla^2\nabla^2 w + D_m(1-\nu^2)\,\Gamma^2 w = \nabla^2\nabla^2 p_z \qquad (6.30)$$

As buckling instability is caused by eccentricity of compressive forces, the general buckling equation for the linear critical buckling load of a shell is derived by introducing an incremental radial load $\overline{p}_z$ whereas the pre-buckling load and the internal forces (being in equilibrium) are omitted. The increment radial load is the product of the eccentric compressive forces n_{xx}, n_{yy}, and n_{xy} and the change of curvature due to the buckling deformation w perpendicular to the shell surface. Indeed, this was previously done without mentioning in the bar and plate examples. The general buckling equation becomes:

$$D_b\nabla^2\nabla^2\nabla^2\nabla^2 w + D_m(1-\nu^2)\,\Gamma^2 w = \nabla^2\nabla^2 \overline{p}_z \qquad (6.31)$$

Where $\overline{p}_z = \left(n_{xx}\dfrac{\partial^2 w}{\partial x^2} + n_{xy}\dfrac{\partial^2 w}{\partial x\partial y} + n_{yy}\dfrac{\partial^2 w}{\partial y^2}\right)$

Similar to the bar and plate examples, the attained equation (6.31) actually represents an eigenvalue problem: the stresses n_{xx}, n_{yy} and n_{xy} must be determined in such a way that they allow the solution for w to be nontrivial.

Note that the general buckling equation is only valid if the buckle takes place in the shell surface, as is assumed. In other cases the stability of the combined shell-edge member system must be considered.

6.5.2 Axially Compressed Circular Cylindrical Shells

Perfect Linear Shell

The general buckling equation can be transformed to an expression for circular cylindrical shells in axial compression. Then, the smallest characteristic value represents the critical buckling load for an axially compressed cylindrical shell. Previously, the critical buckling load of a plate was found using the following general solution:

$$w = W sin\left(\frac{n\,\pi\,x}{a}\right) sin\left(\frac{m\,\pi\,y}{b}\right) \tag{6.11}$$

Here, n and m represented the number of half-waves and a and b the plate dimensions. In case of shells, however, the type of buckling expected is different: according to experiments local buckling occurs rather than global buckling. For developing the critical buckling load, the fact that one buckle extends over a small area only, as observed in the experiments, in which the shell can be regarded as shallow, is used. This means that the dimension terms a and b for shells represent the area of a single buckle. When assuming a buckled area of πa, πb and initial deformation W, which logically has a one half-wave in each direction, equation (6.11) changes to:

$$w = W sin\left(\frac{x}{a}\right) sin\left(\frac{y}{b}\right) \tag{6.32}$$

Subsequently the shell differential operator Γ and the Laplace operator ∇^2 change to:

$$\Gamma(\,) = \left(\frac{1}{R_y a^2} + \frac{1}{R_x b^2}\right) \qquad \text{and} \qquad \nabla^2(\,) = \left(\frac{1}{a^2} + \frac{1}{b^2}\right) \tag{6.33}$$

When the coordinate system is placed in the direction of the principal stresses, the shear terms vanish:

$$\overline{p}_z = \left(n_{xx}\frac{\partial^2 w}{\partial x^2} + n_{yy}\frac{\partial^2 w}{\partial y^2}\right) \tag{6.34}$$

Equation (6.31) furnishes the general expression for the calculation of the linear critical buckling load:

$$D_b\left(\frac{1}{a^2} + \frac{1}{b^2}\right)^4 + D_m\left(1 - \nu^2\right)\left(\frac{1}{a^2 R_y} + \frac{1}{b^2 R_x}\right)^2 = \left(\frac{n_{xx}}{a^2} + \frac{n_{yy}}{b^2}\right)\left(\frac{1}{a^2} + \frac{1}{b^2}\right)^2 \tag{6.35}$$

Note that equation (6.35) for the linear critical buckling load is of general validity and, thus, can be used for several structural elements. For example, by putting both radii and the variable b to infinity, the well-known expression of the Euler buckling load for a bar in compression is reached if the buckle dimension is chosen equal to the length of the beam divided by π, which obviously makes sense. Furthermore, the equation for plate buckling can be determined by putting both radii to infinity and then finding the minimum value for the first buckling load.

To find the buckling load of the cylindrical shell due to axial compression, the stress n_{yy} and the terms containing R_x vanish. By that, the load increment is given by the prebuckling internal force n_{xx} multiplied by the change in curvature during buckling which is equal to $1/a^2$ as was proven in equation (6.33). Subsequently, relation (6.35) changes to:

$$D_b\left(\frac{1}{a^2}+\frac{1}{b^2}\right)^4 + D_m\left(1-\nu^2\right)\left(\frac{1}{a^2 R_y}\right)^2 = \left(\frac{n_{xx}}{a^2}\right)\left(\frac{1}{a^2}+\frac{1}{b^2}\right)^2 \tag{6.36}$$

This can simply be rewritten to:

$$n_{xx} = a^2 D_b\left(\frac{1}{a^2}+\frac{1}{b^2}\right)^2 + \frac{D_m\left(1-\nu^2\right)}{a^2 R_y^2}\frac{1}{\left(\frac{1}{a^2}+\frac{1}{b^2}\right)^2} \tag{6.37}$$

By introduction of $K = a^2 R_y\sqrt{\frac{D_b}{D_m}}\left(\frac{1}{a^2}+\frac{1}{b^2}\right)^2$ the latter equation becomes:

$$n_{xx} = \frac{\sqrt{D_b D_m\left(1-\nu^2\right)}}{R_y}\left(K+\frac{1}{K}\right) \tag{6.38}$$

It can be shown that the expression $\left(K+\frac{1}{K}\right)$ has a minimum of *2* and because of the fact that buckling occurs at the lowest possible value the equation changes into:

$$n_{\sigma,xx}^{lin} = \frac{2\sqrt{D_b D_m}}{R_y} = \frac{2\sqrt{\left(\frac{Et^3}{12\left(1-\nu^2\right)}\right)\left(\frac{Et}{\left(1-\nu\right)^2}\right)\left(1-\nu^2\right)}}{R_y} = \frac{2\sqrt{\frac{E^2t^4}{12\left(1-\nu\right)^2}}}{R_y} \tag{6.39}$$

Simplified:

$$n_{\sigma,xx}^{lin} = \frac{Et^2}{R_y\sqrt{3\left(1-\nu^2\right)}} \tag{6.40}$$

The latter equation is the linear critical buckling load which is similar to the one that Donnell, Mushtari and Vlasov found for the critical load that belongs to their simple shell theory: the so-called DMV theory. Remarkable: the buckled shape does not take part in the buckling equation (6.40). This means that, despite the fact that it is known the buckle is local; the shape of the buckling mode is not defined. As indicated by Popov and Medwadowski [62], subsequent investigations show that the equation holds for as well axisymmetric as asymmetric buckling modes.

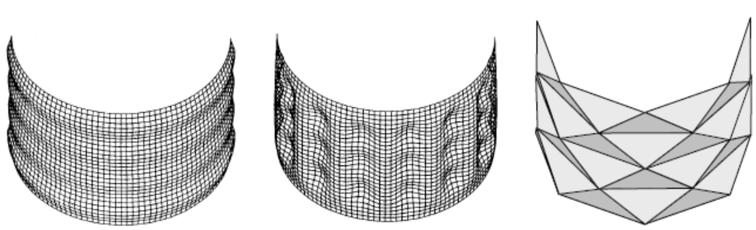

Figure 6.15. A ring and square buckling pattern and a Yoshimura pattern of an axially compressed cylindrical shell, Bažant and Cedolin 1991

As denoted by Farshad [34], from experiments follows that the buckled shape that belongs to equation (6.40) is either a local ring buckling mode or a local square (chess-board) buckling mode, illustrated by the two left pictures in Figure 6.15 (the right *Yoshimura pattern* is discussed later). Whether the cylindrical shell buckles in the ring mode or square mode depends on the shell proportions.

Despite the fact that equation (6.40) is derived from the general buckling equation, there are some restrictions to its usage. First shown by Batdorf (1947), the assumed shallowness of the shell surface cause the expression to be valid only for cylindrical shells larger than $L > 1.72\sqrt{Rt}$ (this is actually quite obvious as it is the length of the longitudinal buckle). Shorter shells need a modification due to the influence of edge effects (membrane disturbance by bending moments). They buckle as wide flat plates. Furthermore, when the length becomes very large, the total shell may experience global buckling, like a column with circular tube-like cross-Section, instead of local buckling as assumed in the above derivation, Farshad [34]. Clearly, global buckling behaviour is not predicted correctly as equation (6.40) is derived for small deformations. Buckling equations based on the non-shallow shell theory of Flügge (1932) do predict column-like buckling correct. Kollar and Dulacska [54], denote that the three buckling phenomena as mentioned above can be found in the diagram of Flügge (1962), seen in Figure 6.16.

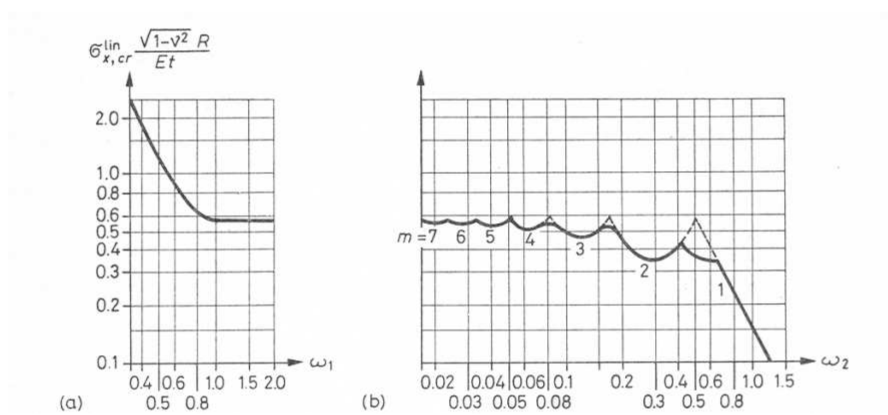

Figure 6.16. Exact diagram for the axial linear critical stress of the cylinder for short shells (a) and long shells (b), Kollar and Dulacska 1984

Herein, the geometric parameters ω_1 and ω_2 are:

$$\omega_1 = \frac{\sqrt[4]{12\left(1-\nu^2\right)}}{\pi}\frac{L}{\sqrt{Rt}} \tag{6.41}$$

And

$$\omega_2 = \frac{1}{\pi\sqrt[4]{12\left(1-\nu^2\right)}}\frac{L}{R}\sqrt{\frac{t}{R}} \tag{6.42}$$

In the left diagram of Figure 6.16 the ascending part represents plate-like buckling while the descending branch of the right Figure is column-like buckling. The more or less horizontal branch is the actual shell buckling with local buckling pattern described in equation (6.40), Kollar and Dulacska [54].

Unfortunately, test results of axially compressed circular cylindrical shells yielded only about *15* to *60%* of the linear critical stress derived before, seen in Figure 6.17. Note that the fall-back in load bearing capacity increases with increasing *R/t ratio*, a phenomenon prescribed to the decreasing bending stiffness of the relatively thinner shells as they are more vulnerable to imperfections during construction. Furthermore, one may notice the Figure represents *R/t ratios* much larger than possible for concrete shell structures (which are currently limited to *R/t ratios* of about *1000*).

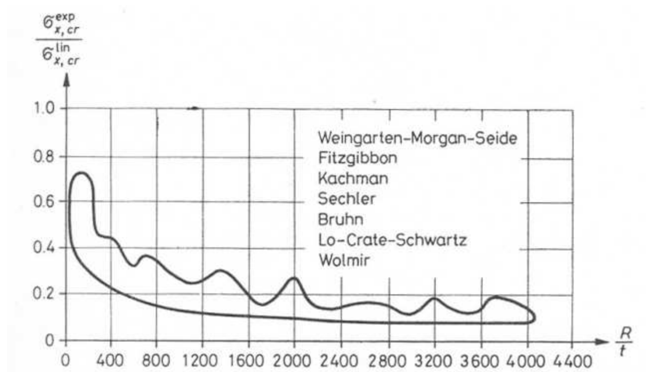

Figure 6.17. Experimental results on axially compressed cylindrical shells, Kollar and Dulacska 1984

The explanation of the great discrepancy between the theoretical and experimental results led to extensive studies to the effects of boundary conditions and prebuckling rotations and the effects of nonlinearity and initial imperfections, Kollar and Dulacska [54]. Hoff and Soong (1965) solved the buckling equations for axially compressed cylinders for several boundary conditions. Their results, later confirmed by Thielemann and Esslinger (1964), showed that the boundary conditions indeed may lead to lower critical stresses. For example, for a cylinder with the edges free to move circumferentially, the critical load is half the value of equation (6.38) and for simply supported edges (not constrained in circumferential direction) the value is even lower. Furthermore, for shells, as a rule, pre-buckling rotations will occur due to restraint supports and are relative big. The inclusion of the prebuckling deformations, caused by radial expansion (nonzero Poisson's ratio) which cannot be followed by the supports, is actually an inclusion of initial deformations. This so-called consistent theory (it applies similar boundary conditions to both the buckled and unbuckled shell) also yielded a value *8* to *15%* lower than equation (6.38), Kollar and Dulacska [54].

However, the most important step towards the experimental obtained buckling values is the introduction of large deformations (the nonlinear theory discussed below) and initial geometrical imperfections (discussed thereafter).

Perfect Nonlinear Shell

As the linear solution gives no information about the postbuckling behaviour, a nonlinear solution is required. Analogous to the column and plate a simple approximation is done by adding the first nonlinear terms. Equation (5.43) changes to:

$$\varepsilon_{xx} = \frac{\partial u}{\partial x} + \frac{1}{2}\left(\frac{\partial w}{\partial x}\right)^2 \quad \text{and} \quad \varepsilon_{yy} = \frac{\partial v}{\partial y} + k_y w + \frac{1}{2}\left(\frac{\partial w}{\partial y}\right)^2$$

$$\gamma_{xy} = \frac{\partial u}{\partial y} + \frac{\partial v}{\partial x} + \left(\frac{\partial w}{\partial x}\frac{\partial w}{\partial y}\right) \tag{6.43}$$

Note the fact that the curvature is left out of the strain in *x-direction* as the cylinder only has curvature in *y-direction*. The nonlinear formulation of (6.43) was first set-up by Donnell (1934).

As the curvature terms and constitutive law remains, the in-plane and out-of-plane equilibrium equations, respectively (6.29) and (6.24), transform to:

$$\nabla^2\nabla^2\Phi + D_m(1-\nu^2)\,\Gamma w - Et\left(\left(\frac{\partial^2 w}{\partial x\partial y}\right) - \frac{\partial^2 w}{\partial x^2}\frac{\partial^2 w}{\partial y^2}\right) = \frac{\partial^2}{\partial y^2}\int p_x dx + \frac{\partial^2}{\partial x^2}\int p_y dy - \nu\frac{\partial p_x}{\partial x} - \nu\frac{\partial p_y}{\partial y} \tag{6.44}$$

$$-\Gamma\Phi + D_b\nabla^2\nabla^2 w - \left(\frac{\partial^2\Phi}{\partial y^2}\frac{\partial^2 w}{\partial x^2} - 2\frac{\partial^2\Phi}{\partial x\partial y}\frac{\partial^2 w}{\partial x\partial y} + \frac{\partial^2\Phi}{\partial x^2}\frac{\partial^2 w}{\partial y^2}\right) = p_z - k_x\int p_x dx - k_y\int p_y dy \tag{6.45}$$

Solving the latter system of differential equations truly is a formidable task. A suitable method to solve the equations is the energy method. By writing down the total potential energy of the system and subsequently minimise it, it can replace the equilibrium relation. The more terms of buckling deformation w taken into account, the more exact the obtained solution, Popov and Medwadowski [62]. Von Karman and Tsien (1941) were the first to obtain a confident solution, taken into account two coefficients. The results of Von Karman and Tsien are shown in Figure 6.18.a. Von Karman and Tsien found that, contrary to plates, there are several buckling modes associated with the same critical load. Therefore, the shell experiences the phenomenon of multimode or compound buckling. Within the linear range, the buckling modes are orthogonal to each other, but in the case of nonlinear post-buckling deformations, they interact resulting in a significant decrease in post-buckling load-bearing capacity.

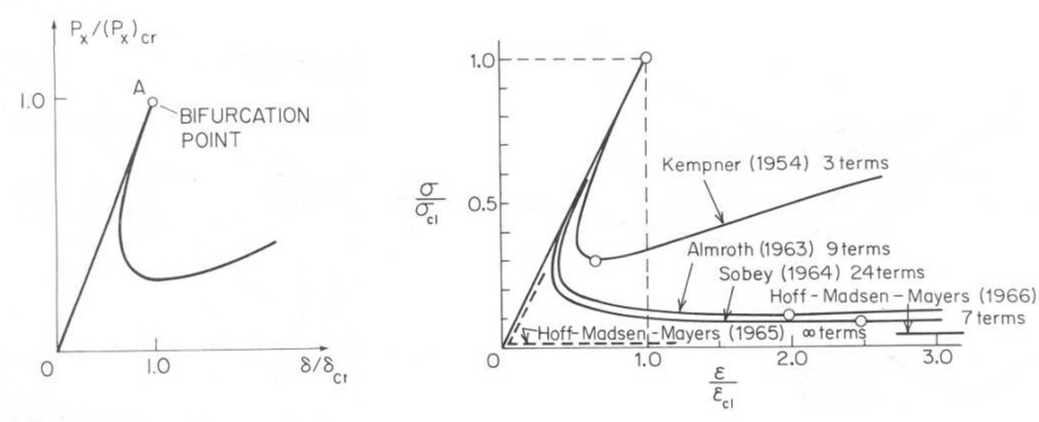

Figure 6.18.a. Postbuckling path of equilibrium for an Ideal Axially Compressed Cylinder, Popov and Medwadowski 1981 and b. Increasingly accurate postbuckling curves for axially compressed cylinders, Seide 1981

Later, the solution of Von Karman and Tsien was improved by mathematicians such as Kempner (1954) and Almroth (1963) taken into account more and more free parameters, Figure 6.18.b. However, it did not change the shape of the postbuckling branch, its lowest point further dropped. The buckling pattern that belongs to the lowest point is the so-called Yoshimura pattern, shown previously in Figure 6.15.c. The Yoshimura pattern is the limit buckling pattern and clearly shows the tendency of axially compressed shells to 'snapping'. The Yoshimura pattern is an in-extensional mapping of the cylindrical surface. However, for practical geometrical reasons, the shell first has to deform extensional. This explains the 'snapping' phenomenon: the Yoshimura pattern represents a smaller resistance than the preceding stage leading to it, Kollar and Dulacska [54]. The diamond shape of the Yoshimura pattern may be described as a combination of the axisymmetric and reticulated (chess-board) shape and yields the same linear critical buckling load.

Remarkable, Hoff, Madsen and Mayers (1965) found that, when increasing the number of terms considered, the lowest point in the end tends to zero, see Figure 6.18.b. The explanation for this can be found in the fact that several simplifications in the formulation lead to demands which are practically nonsense. An example is the fact that the method also requires the minimisation of the potential energy with respect to the number of waves in circumferential direction, resulting in less than two waves, which is obviously impossible for geometric reasons, Kollar and Dulacska [54]. Eventually, these observations leaded to the energy criterion as proposed by Tsien (1941) to be put aside, in favour of the Koiter initial postbuckling theory.

Imperfect Shell

The solution of the nonlinear buckling equations for axially compressed cylindrical shells by Von Karman and Tsien (1941), served as basis for further research to the discrepancies between the critical buckling loads as obtained by experimental tests and the theoretical ones. The answer was found in the extreme sensitivity of buckling behaviour to geometrical imperfections. As described in the paper of Popov and Medwadowski [62], Donnell and Wan (1950) investigated the influence of geometrical imperfections by assuming a shape similar to the deflected surface with an increasing unevenness factor *U*, taking into account five free parameters. Although this buckling configuration assumption is theoretically wrong (the buckle varies in during the buckling process) it was assumed to be the worst one, Popov and Medwadowski [62]. The influence of the non-dimensional factor *UR/h*, which is the unevenness factor times the radius divided by the shell thickness, is shown in Figure 6.19.

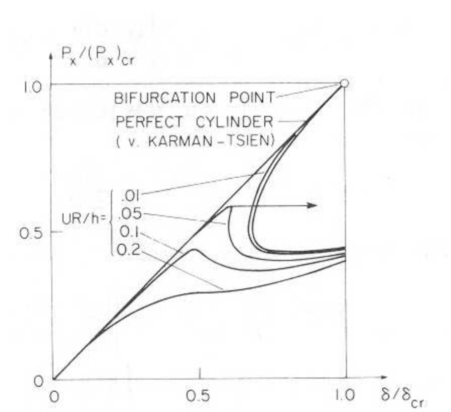

Figure 6.19. The effect of imperfections according to Donnell and Wan, Popov and Medwadowski 1981

In Figure 6.19 the pre-buckling path and the postbuckling path of equilibrium as determined by Von Karman and Tsien are seen. Furthermore, the results as obtained by Donnell and Wan show the effect of initial geometrical imperfections. It can be seen that the imperfections drastically decrease the load carrying capacity introducing limitation of equilibrium buckling. Even small imperfections already have a significant influence on the critical buckling load, up to less than *50%* of the ideal shell. Moreover, imperfections cause the stability problem to be nonlinear from the beginning as the primary path smoothly approaches the secondary path of the perfect shell. The investigations of Donnell and Wan also introduce the phenomenon of snap-through. In Figure 6.19 it is seen that for the case of *UR/h = 0.05*, the shell experiences a snap-through, a sudden jump from the prebuckled shape to a non-adjacent equilibrium configuration (not seen in the figure). Clearly, whether the structure experiences snap-through or a smooth transition to the secondary path depends on geometrical parameters, such as the size of the imperfection. Unfortunately, it cannot be determined in advance which structural behaviour will appear.

Due the complexity of the approach of Donnell and Wan, only solutions of an approximate nature were obtained. The initial postbuckling theory of Koiter (1945) provided in a simpler and faster approach and, with this method, Budiansky (1969), Hutchinson (1968) and others performed many studies on the critical load degradation due to imperfections for a variety of shell structures. As denoted by Kollar and Dulacska [54], using the general theory of Koiter (1945) makes possible a qualitative investigation to the influence of several imperfections (axisymmetric, asymmetric, reticulated or combined) and buckling modes on the critical load. Koiter selects the linear modes which in the nonlinear frame interact and thereby yield the minimum value of the critical load. Kollar and Dulacska [54] argue that the investigations of Koiter show that, as far as shells are considered, it is not necessarily true that the imperfections shaped similar to the buckling modes prove to be the most onerous ones. They referred to Figure 6.5.e where the shell begins to deform according to an initial imperfection but bifurcates before the limit point. According to Kollar and Dulacska [54] the latter approach yields that axisymmetric imperfections provide in the lowest critical load as the structure jumps over into another buckling mode similar to the diagram presented in Figure 6.5.e. It must be noted, however, that others find the reasoning of the hypothesis of Kollar and Dulacska far-fetched and doubt whether this is true. They presume the imperfection shaped similar to the buckling mode to be the most onerous.

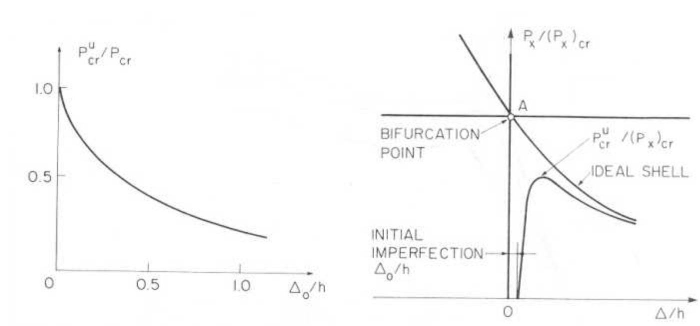

Figure 6.20. Approximate dependence of the buckling load of an axially compressed cylinder to initial imperfections (left) and the path of equilibrium of an imperfect and ideal cylindrical shell, Popov and Medwadowski 1981

The analytical results described above show great similarity with the experimental obtained values. The fall-back in load carrying capacity can be, in case of buckling, almost totally ascribed to the sensitivity to geometrical imperfections of axially compressed cylinders. The amount of sensitivity is illustrated in Figure 6.20, which can be constructed from a graph such as illustrated in Figure 6.19. It can be seen that the largest fall-back in load carrying capacity occurs for small imperfections. Besides the dependence to imperfections Figure 6.20 also shows the path of equilibrium of an imperfect and perfect cylindrical shell.

An attempt to bring into account the initial imperfections and nonlinear behaviour in a so-called knock-down factor *C* which bridges the cap between the linear critical load and the experiments (Figure 6.17) can be found in the paper of Seide [70]. The experimentally obtained relation is a lower bound solution:

$$C = \frac{P_{cr}}{P_{cr}^{lin}} = 1 - 0.9\left(1 - e^{-\frac{1}{16}\sqrt{\frac{R}{t}}}\right) \tag{6.46}$$

Valid for cylinder dimensions equal to:

$$0.5 < \frac{L}{R} < 5$$

$$100 < \frac{R}{t} < 3000 \tag{6.47}$$

Finally, the predominant effect of initial imperfections can be clarified by observing experimental test on nearly-perfect circular cylindrical shells in axial compression. The models are constructed using highly accurate fabrication methods (such as electroforming) and testing equipment. The results are seen in Figure 6.21 and clearly show that the critical values approach the linear critical buckling load. With that, the circle is completed.

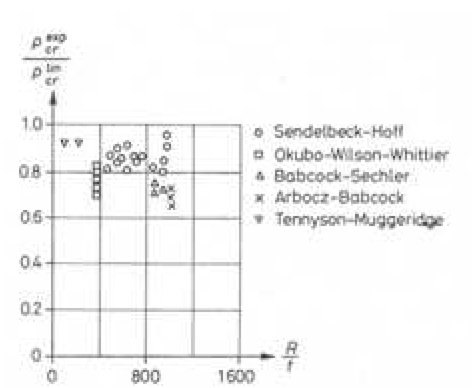

Figure 6.21. Near-perfect models of axially compressed cylindrical shells, Kollar and Dulacska 1984

A final remark on cylindrical shells may be that, besides axial compression, the circular cylindrical shell under circumferential compression and torsion are also extensively investigated. As illustrated by Popov and Medwadowski [62] and Seide [70], these investigations show much less decrease in the load carrying capacity in the postbuckling range than for axially compressed cylinders. According to Kollar and Dulacska [54], it can be concluded that a cylinder is most sensitive to initial imperfections if subjected to axial compression. Less sensitive in case of circumferential compression and, in case of torsion, the influence of initial imperfections is very small.

6.5.3 Spherical Shells under External Pressure

Perfect Linear Shell

The general buckling equation can also be transformed to an expression for spherical shells under external pressure. Similar to the cylindrical shell, the spherical dome is simply to treat mathematically due to the fact that the geometry can be described by a single curvature. Again, the derivation is facilitated by assuming the shell shallow in the buckled region, known from the exact derivation using Legendre functions, Kollar and Dulacska [54], and from experiments that have demonstrated that the buckled shape for a spherical dome under uniform pressure is a circular area extending over only a comparatively small portion of the area of the shell, Billington and Harris [6].

Similar to the circular cylindrical shell a buckling pattern with a buckled area of πa, πb and initial deformation W is assumed, described by equation (6.32):

$$w = W\sin\left(\frac{x}{a}\right)\sin\left(\frac{y}{b}\right) \tag{6.32}$$

And, with the coordinate system parallel to the meridian and circumferential stresses (the principal stresses of the spherical dome), once more equation (6.35) appears:

$$D_b\left(\frac{1}{a^2}+\frac{1}{b^2}\right)^4 + D_m\left(1-\nu^2\right)\left(\frac{1}{a^2R_y}+\frac{1}{b^2R_x}\right)^2 = \left(\frac{n_{xx}}{a^2}+\frac{n_{yy}}{b^2}\right)\left(\frac{1}{a^2}+\frac{1}{b^2}\right)^2 \tag{6.35}$$

Now, the geometric expressions corresponding to the sphere can be substituted into equation (6.35). For a sphere it holds that the curvature in both directions can be described by:

$$\frac{\partial^2 z}{\partial x^2} = \frac{\partial^2 z}{\partial y^2} = \frac{1}{R} \tag{6.48}$$

By neglecting the in-plane shear stress and the load component in x- and y-*direction*, the internal forces from equation (5.38) of the pre-buckling state can be described as:

$$n_{xx} = n_{yy} = -\frac{pR}{2} \tag{6.49}$$

Substituting the internal forces and the geometric expressions into equation (6.35) the differential equation for a spherical shell is derived:

$$D_b\left(\frac{1}{a^2}+\frac{1}{b^2}\right)^4+D_m\left(1-\nu^2\right)\frac{1}{R^2}\left(\frac{1}{a^2}+\frac{1}{b^2}\right)^2=\frac{pR}{2}\left(\frac{1}{a^2}+\frac{1}{b^2}\right)\left(\frac{1}{a^2}+\frac{1}{b^2}\right)^2 \tag{6.50}$$

By introduction of $K=R\sqrt{\frac{D_b}{D_m}}\left(\frac{1}{a^2}+\frac{1}{b^2}\right)$ the latter equation becomes:

$$p=\frac{2}{R^2}\sqrt{D_bD_m\left(1-\nu^2\right)}\left(K+\frac{1}{K}\right) \tag{6.51}$$

Using the previously statement that $K+\frac{1}{K}$ has a minimum of 2, equation (6.51) changes into:

$$p=\frac{4}{R^2}\sqrt{D_bD_m\left(1-\nu^2\right)} \tag{6.52}$$

Filling in the terms for the bending stiffness and membrane stiffness, the latter yields the classical linear critical buckling load for a perfect elastic sphere under uniform radial pressure load:

$$P_{cr}^{lin}=\frac{2E}{\sqrt{3(1-\nu^2)}}\left(\frac{t}{R}\right)^2 \tag{6.53}$$

Note that, similar to equation (6.40), the buckling pattern has disappeared, the critical load being independent of the buckling shape. Therefore, again, several buckling modes are associated with the same critical load and the shell experiences the phenomenon of multimode or compound buckling.

The equation for the classical linear critical buckling load for a perfect elastic sphere under uniform radial pressure was derived first by Zoëlly (1915). However, Zoëlly derived the critical pressure assuming an axisymmetric buckling pattern (disregarding experimental results) and using exact equations (non-shallow equations), solving them with Legendre polynomials. Later it was proved by Van der Neut (1932) that the same critical pressure also yields for an asymmetric buckling pattern, Popov and Medwadowski [62].

According to Simitses and Cole (1968), the type of uniform loading (spherical, uniform load over the horizontal projection or uniform load over the shell) does not appear to change the linear critical buckling load drastically. As contrasted with the cylindrical shell under external pressure. The reason for this may be due to the fact that spherical shells always buckle in small, local, shallow waves, Kollar and Dulacska [54]. However, this is only valid if buckling occurs in the upper part of the shell. Furthermore, as denoted by Scordelis [69], Klöppel and Roos (1956) have shown that the critical pressure load for a partially loaded sphere is close to that for a load over the total shell surface.

Unfortunately, similar to the cylindrical shell (Figure 6.17), the experimental buckling values are significant lower than the linear critical buckling load. Again, the most important step towards the explanation of the lack of correlation between theoretical and experimental obtained results was the introduction of large deformations.

Perfect Nonlinear Shell

Von Karman and Tsien (1939) were the first to formulate a nonlinear theory, based on similar additions as proposed for cylindrical shells (equation (6.43)), that is, taken into account for the second powers of the first derivatives. Although the derivation contained some errors of principle, as denoted by Friedrichs (1941) and Mushtari and Surkin (1955): in Kollar and Dulacska [54], their result was convincing and it was found that in as well the nonlinear behaviour as the sensitivity to initial imperfections the spherical shell acts qualitatively identical to axially compressed cylindrical shells. Their result is shown in Figure 6.22. In Figure 6.22 the load ratio is plotted against the ratio of the average postbuckling displacement f over the linear buckling displacement f_{cr}^{lin} which is similar to the ratio of the change in postbuckling volume to the change in linear buckling volume.

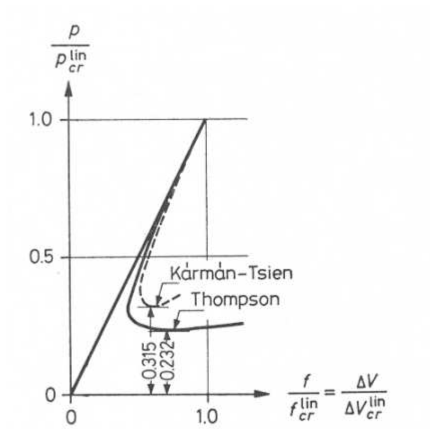

Figure 6.22. Postcritical behaviour of the perfect spherical shell, Kollar and Dulacska 1984

Similar to the previous shell examples, the decrease in load carrying capacity indicates that the shell experiences multimode or compound buckling and the interacting linear buckling modes in the postbuckling can said to be responsible.

As seen in Figure 6.22, Von Karman and Tsien determined the lowest point of the postbuckling path of equilibrium being equal to (zero Poisson's ratio):

$$P_{cr} = 0.365\, E\left(\frac{t}{R}\right)^2 \tag{6.54}$$

The latter being optimised (improving the accuracy of the calculation) by Tsien in 1942:

$$P_{cr} = 0.312\, E\left(\frac{t}{R}\right)^2 \tag{6.55}$$

The expressions of Von Karman and Tsien and Tsien were later improved by other investigators such as Mushtari (1950) and Feodosjew (1954), arriving at respectively:

$$P_{cr} = 0.34\, E\left(\frac{t}{R}\right)^2 \quad \text{and} \quad P_{cr} = 0.32\, E\left(\frac{t}{R}\right)^2 \tag{6.56}$$

The results obtained by Thompson (1962) must be mentioned. Thompson was able to show that the shape and size of the bucklevary during snapping-through, as he assumed four free parameters, see Figure 6.23.

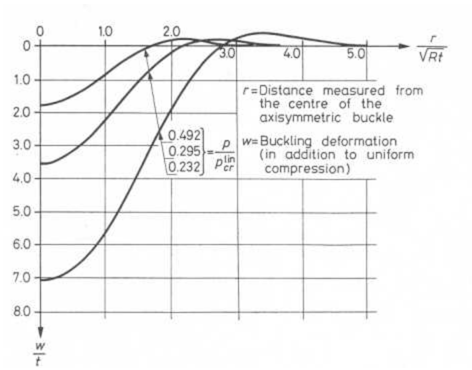

Figure 6.23. Variation of the buckling shape during the buckling process as found by Thompson, Kollar and Dulacska 1984

According to Thompson, the lowest point of Figure 6.23 is determined by:

$$P_{cr} = 0.268\, E\left(\frac{t}{R}\right)^2 \tag{6.57}$$

Supplementary investigations on a similar basis show an even further decrease of the lowest nonlinear buckling point. Dostanowa and Raiser (1973) found:

$$P_{cr} = 0.126\, E\left(\frac{t}{R}\right)^2 \tag{6.58}$$

And Del Pozo and Del Pozo (1979) arrived at:

$$P_{cr} = 0.228\, E\left(\frac{t}{R}\right)^2 \tag{6.59}$$

Further research on spherical buckling was based on Koiter's method. Using the Koiter initial postbuckling theory and Koiter's special theory Hutchinson (1967) found an even steeper postbuckling branch than Thompson, although he did not determine the corresponding lower point.

Imperfect Shell

Similar to axially compressed circular cylindrical shells, spherical shells are extremely sensitive to initial geometrical imperfections. A rapid reduction in the maximum critical load and a transition from bifurcation buckling to limit point buckling is observed with increasing imperfection amplitude. The phenomenon is sketched in Figure 6.24.

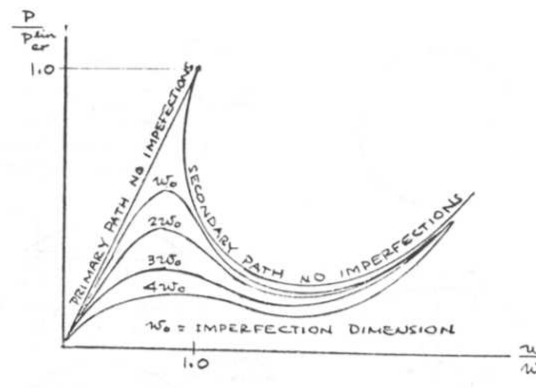

Figure 6.24. Influence of increasing imperfection amplitude on the load carrying capacity, Scordelis 1981

In his research on imperfect shells, Hutchinson discovered that the sphere behaves according to Figure 6.5.e, if initial imperfections are present. Hutchinson plotted the lower bifurcation load against the amplitude of the initial imperfection, as seen in Figure 6.25.

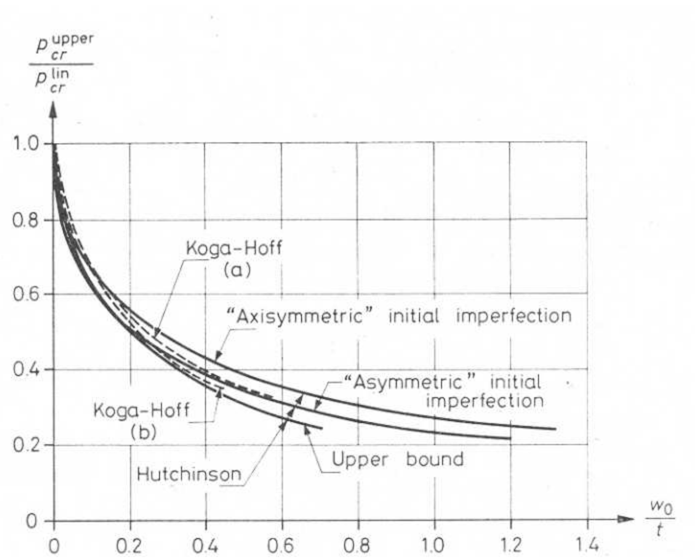

Figure 6.25. Influence of the initial imperfection amplitude on the upper critical load of spherical shells, Kollar and Dulacska 1984

In Figure 6.25 it can be seen that Hutchinson investigation integrated the most onerous combination of axisymmetric and asymmetric buckling modes caused by both axisymmetric and asymmetric initial imperfections, with the latter producing the lowest curve. Furthermore, Hutchinson used the special theory of Koiter to produce a more accurate solution for larger imperfection amplitudes, yielding the upper bound curve, Kollar and Dulacska [54].

From the results of Hutchinson as illustrated in Figure 6.25, it can be concluded that the critical load of a spherical shell loaded in external pressure, in contrast to the cylindrical shell, is practically the same whether symmetric imperfection and buckling deformation or asymmetric imperfection and deformation are taken into account. Subsequent research on axisymmetric imperfections and buckling shapes by Bushnell (1967) and Koga and Hoff (1969), based on an exact formulation, underlines this hypothesis, Kollar and Dulacska [54]. The results of Koga and Hoff are also plotted in Figure 6.25, and consist of two graphs, referring to two types of imperfection shapes. Both shapes *(a)* and *(b)* are seen in Figure 6.26 below.

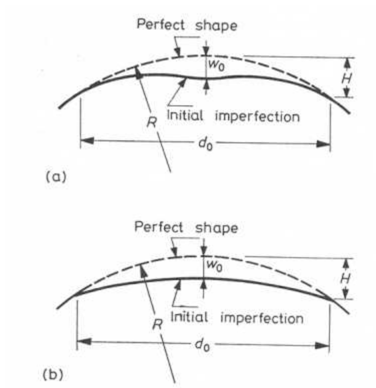

Figure 6.26. Assumed initial imperfections by Koga and Hoff (1969), Kollar and Dulacska 1984

As both graphs of Koga and Hoff lie close to each other, it can be concluded that, for practical purposes, the initial imperfections can be characterised by their amplitude only.

Similar to the axially compressed cylindrical shell, extensive research has been done to the influence of boundary conditions and prebuckling rotations. To investigation to the effects of boundary conditions, different types of supports are introduced, see Figure 6.27.

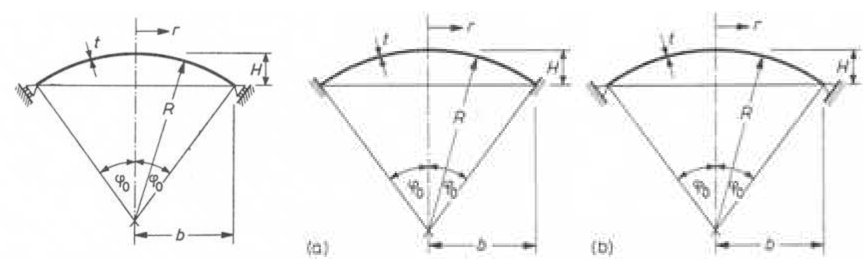

Figure 6.27. Roller supported, clamped supported, and hinged supported spherical caps, Kollar and Dulacska 1984

The roller supported spherical cap undergoes compression without bending when subjected to external pressure. Hence, there is referred to a 'membrane' support. In as well the clamped as hinged supported situation bending moments arise, even in the perfect shell, causing prebuckling rotations. This means that the shell behaves according to the imperfect equilibrium path illustrated in Figure 6.5.d. It was found that the bending deformation caused by the bending moments can be either of the same character as the buckling deformations or of opposite character, depending on a geometrical parameter. This geometrical parameter is a characteristic of a spherical cap, and is defined as:

$$\lambda = 2\sqrt[4]{3\left(1 - \nu^2\right)}\sqrt{\frac{H}{t}} \tag{6.60}$$

Using the latter geometrical parameter, the change of slope of the bending and buckling deformation can be plotted side by side as is done in Figure 6.28.

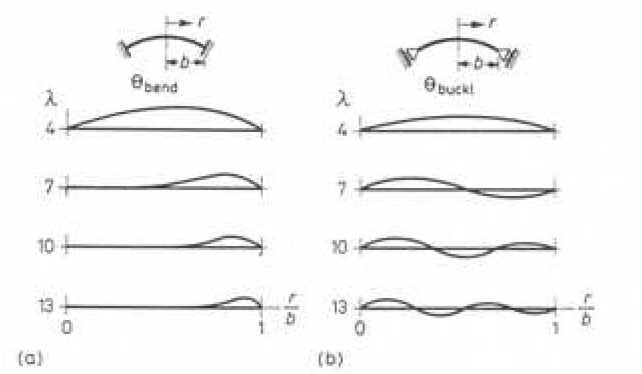

Figure 6.28. Change in slope of the bending (left) and buckling deformations (right), Kollar and Dulacska 1984

Clearly, depending on the geometrical parameter, the prebuckling rotations caused by restrained deformation at the supports amplify or reduce the buckling deformations. By varying the geometrical parameter, a graph can be found which indicates the influence of the geometrical parameter on the buckling load, see Figure 6.29.

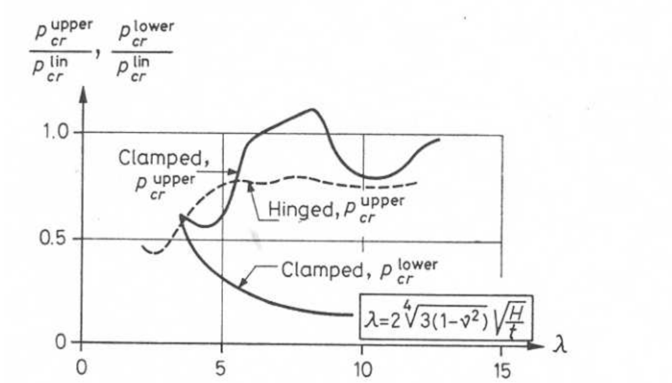

Figure 6.29. Snapping load of the perfect spherical cap assuming axisymmetric buckling shape, Kollar and Dulacska 1984

In Figure 6.29 it can be seen that the upper critical load of the clamped shell oscillates about the line of the upper critical load being similar to the linear critical load. This can be explained by comparing the values of λ in Figure 6.29 to Figure 6.28. For example, when the bending deformation counteracts the buckling deformation, the buckling load is greater than the linear critical load. That this phenomenon does not occur in reality, as demonstrated by many experiments, can be contributed to initial imperfections in the shell surface. Hence, Figure 6.29 is only valid for a perfect shell. When, next to the bending deformations, axisymmetric initial imperfections are introduced in the shell surface, Figure 6.29 changes to the graphs as illustrated in Figure 6.30 (with n the number of circumferential full-waves of the asymmetric mode).

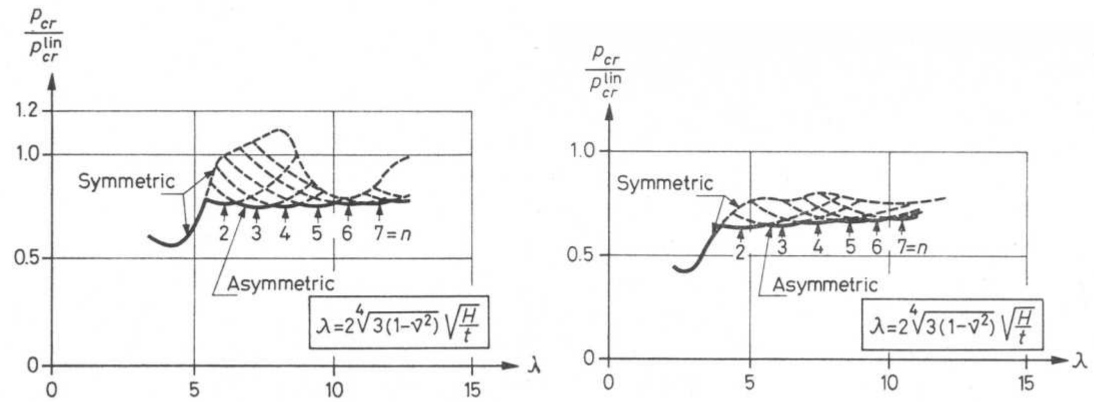

Figure 6.30. Critical load pertaining to the asymmetric buckling which bifurcates from the axisymmetric deformation of the (left) clamped perfect spherical cap and (right) hinged spherical cap, Kollar and Dulacska 1984

The graphs in Figure 6.30 are proposed by Weinitschke (1965). Weinitschke, and independently Huang (1964), solved the performance of the spherical cap with initial imperfections and different types of supports according to the behaviour which corresponds to Figure 6.5.e. Assuming an initial axisymmetric initial imperfection, Huang and Weinitschke determined the point in Figure 6.5.e at which the axisymmetric deformation (described by the nonlinear theory) bifurcates into an asymmetric mode, a phenomenon discovered by careful observation of high-speed motion-picture recordings of the buckling process. They solved the lower bifurcation problem by the linear theory, combining a linear eigenvalue problem with a nonlinear axisymmetric deformation. Based on the graphs of Figure 6.30 it can be concluded that deep caps ($\lambda >> 10$) bifurcate before limitation of equilibrium.

As reported by Kollar and Dulacska [54], a further improvement of Weinitschke and Huang is the incorporation of asymmetric initial imperfections as is done by Kao and Perrone (1971) and Kao (1972). They found that, taking into account an asymmetrical initial imperfection extending over a quarter of the shell (see Figure 6.31) the critical load further decreases, as shown in Figure 6.32. Furthermore, Kao and Perrone found that, when the asymmetric initial imperfection is extended over one-eight of the shell, this does not change the snapping load significantly.

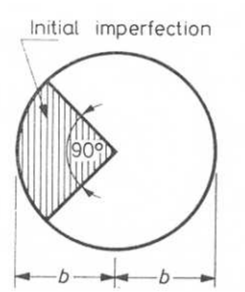

Figure 6.31. Ground plan of the assumed asymmetric initial imperfection, Kollar and Dulacska 1984

With the imperfection of Figure 6.31, Kao obtained the greatest reduction so far. However, the extremely onerous imperfection is rather unlikely to occur in practice. Therefore, the results of Kao are often only partly taken into account, for example in the IASS Recommendations, discussed later in Section 6.9.

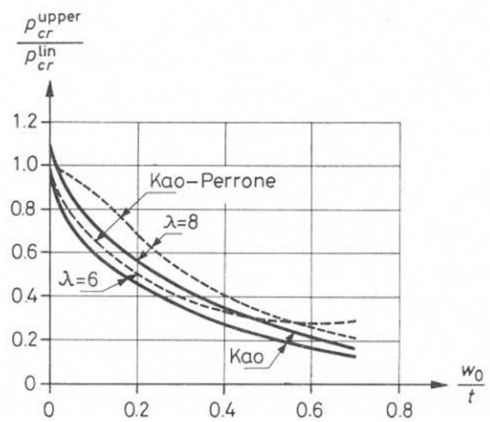

Figure 6.32. Influence of the asymmetric imperfection on the snapping load of the clamped spherical cap, Kollar and Dulacska 1984

A final remark on the influence of boundary conditions on the buckling behaviour of spherical shells may be that if, contrary to what is assumed here, the boundary conditions are not stiff enough (or weaker than that provided by an imaginary adjacent part of the shell as being a complete sphere), the shell buckles prior to the critical load of a complete sphere. Shells with a ground plan sliced to a rectangle and supported by diaphragms belong to this group, Kollar and Dulacska [54]. Here, the investigations of Van Koten and Haas [41] must be mentioned as they formulated to problem on the basis of a comparison between the rigidities of the boundary with the missing part of the shell. Although, according to Scordelis [69], the relations as proposed by Van Koten and Haas give rather low buckling load as compared to the experimental results. Later, Bushnell (1967) improved the relations of Van Koten and Haas by incorporating the extensional rigidity (which was neglected by Van Koten and Haas). The results of Bushnell showed more resemblance with the experiments and consequently showed that the edge rotational rigidity is, with respect to buckling, highly inferior to its extensional rigidity, effective against displacement.

6.5.4 Imperfections (III)

Contrary to the previously discussed columns and plates, it is found that shells are extremely sensitive to initial imperfections. Only small initial imperfections may already cause the load carrying capacity of the shell to decrease drastically. Furthermore, in the foregoing it was found that, not only geometric imperfections lower the critical load, but also the restrained boundary conditions introduced uninvited bending moments, acting like imperfections. Most sensitive to initial imperfections is the spherical shell subjected to radial pressure load as it contains areas of compression in both principal directions. Hence, it is logic to investigate the spherical buckling behaviour more closely as done in Chapter 13, 14 and 15. For a further discussion on imperfections, there is referred to Chapter 6.7.

6.6 Inelastic Shell Buckling

In the previous paragraph, the buckling description is restricted to elastic structures. However, as far as reinforced concrete shells are considered, material inelasticity (plasticity) must be taken into account as the shell contains inelastic properties. Unfortunately, the inclusion of inelasticity gives a further reduction of the buckling load found for an elastic homogeneous shell.

The most trivial solution is to introduce inelasticity in the calculation by the tangent (Engesser (1899)) or reduced modulus theories (Jasiński (1894) and Considère (1899)), Popov and Medwadowski [62].The tangent modulus is defined as the slope of a line tangent to the stress-strain curve at a point of interest. The tangent modulus is always equal (in the elastic path) or less (in the plastic path) than the Young's modulus. The reduced modulus theory is based on the observation that in a buckling mode a purely elastic strain reversal will occur, while in the remaining part, plastic loading will continue. The reduced modulus theory recognises this elastic unloading branch and it defines a reduced Young's modulus to compensate for the underestimation given by the tangent modulus. Hence, the reduced modulus theory is sometimes referred to as the double modulus theory, Popov and Medwadowski [62].

By simply replacing the original Young's modulus by the tangent modulus, the critical buckling load of ideal inelastic columns can be found with reasonable correlation to experimental results. The reduced modulus theory approximately yields the same result. For imperfect columns, as proposed by Von Karman (1910), the entire path of equilibrium belonging to an initial imperfection can be found by carrying out a series of equilibrium solutions for different bend configurations which corresponds to a given force, hereby, taking into account for (idealised) elasto-plastic behaviour, Popov and Medwadowski [62].

Also for plates and shells it appears that good correlation with experimental values is achieved by assuming isotropic behaviour based on the tangent modulus in both directions. However, for plates and shells with initial imperfections the problem is vastly more complicated. Kollar and Dulacska [54] developed, on the basis ideal elasto-plastic behaviour, a method for determining the inelastic buckling load while assuming that during buckling plastic flow develops simultaneously in both directions. Their resulting graph is seen in Figure 6.33. Without any further introduction, the value of the abbreviations γ is given by:

$$\gamma = \frac{n_{yield}}{n_{cr}^{lin}} < H_o \tag{6.61}$$

In which n_{yield} is the central compressive stress causing yield stress in an entire cross-Section and n_{cr}^{lin} the linear elastic buckling stress resultant. The value of H_o is approximately equal to 4 in case of axially compressed isotropic cylinders and 2 for radially compressed spheres.

The graph of Figure 6.33 shows decreasing influence of inelasticity as the buckling approaches to elastic buckling ($\gamma > H_o$). Obviously, this makes sense. Furthermore, it can be seen that initial imperfections reduce the difference between the elastic and inelastic critical stress.

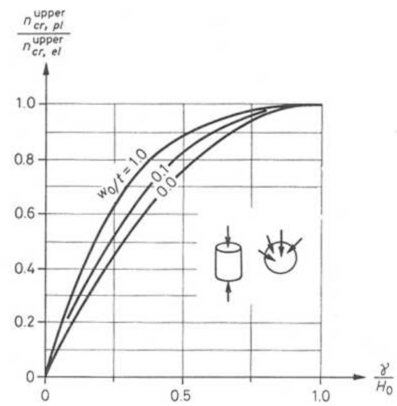

Figure 6.33. The plastic critical loads of axially compressed cylindrical and of radially compressed spherical shells, Kollar and Dulacska 1984

Since the finite element era, much progress in the analysis of inelastic imperfect shells has been obtained. The actual structural behaviour can be approached more accurately by replacing the idealised elasto-plastic behaviour by more exact material models. In Chapter 15, the influence of inelastic material effects is further investigated using a finite element approach.

6.7 Initial Geometrical Imperfections

To investigate the effect of initial geometrical imperfections on a spherical shell, the question is what reasonable dimensions of imperfections are. As imperfection dimensions do not appear in the critical buckling load equations, this question has not been answered yet. In general, it can be said that imperfections in concrete shells arise due to imperfections of the formwork, due to removal of the formwork after concrete hardening or by external effects such as concentrated loads. The size of the imperfections depends on practical considerations such as the shape and proportions of the shell, the type of construction material, the construction technique, etc.

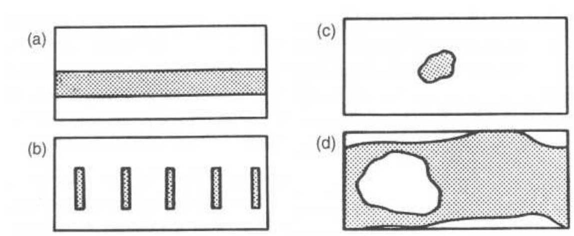

Figure 6.34. Space distribution of imperfections, Godoy 1996

According to Godoy [38], initial imperfections can be classified by several criteria. Godoy gives three possible classifications, based on (1) the relation between an imperfection and the loading process, (2) the space distribution of imperfections and (3) whether the source of the imperfections is found in intrinsic (constitutive) or geometric parameters. As far as initial geometric imperfections are considered, the second category is most useful as in Section 6.5.3 it is shown by Kao and Perrone (1971) and Kao (1972) that the position of the imperfection does influence the decrease in load carrying capacity. Godoy suggests a subdivision in axisymmetric imperfections, imperfections with a repeated pattern, a localised imperfection and a global imperfection, see Figure 6.34. For a logic and comprehensive investigation, the influences of each imperfection pattern must be determined.

As yet the shape, size and amplitude of the local imperfection are left to be determined. For the shape of the imperfection, Godoy suggests cosine or polynomial curves. Aforementioned, as concluded by Koga and Hoff (1969), initial imperfections can be characterised by their amplitude only.

The shape of the imperfection depends on practical considerations and, hence, cannot be given a geometric description in advance. Therefore, several investigators searched for a shape which produces the most uninvited situation. A proper choice may be to shape the imperfection according to the linear buckling shape, although, aforementioned in Section 6.5.3, others argue that it is not always an initial imperfection similar to the buckling shape that is most detrimental. According to Scordelis [69] many experiments demonstrated that the buckled shape for a spherical dome under uniform external pressure usually consists of a circular area over a portion of the dome snapping through. The theoretical diameter of the buckled area can be defined as:

$$\phi_{imp} = 2.5\sqrt{Rt} \tag{6.62}$$

According to Scordelis, the buckled area for other double curvature shells is found to be much similar: a roughly circular portion. Though, as denoted by Godoy [38], Ballesteros (1978) found an elliptical shape when investigating the collapse of a concrete elliptical paraboloidal shell (elpar). Nevertheless the choice for a circular area can be considered appropriate as in the extensive experimental tests of Vandepitte in 1967 and 1976 all ninety spherical shells failed due to snapping of a nearly circular disc with a diameter corresponding to equation (6.62), Billington and Harris [6].

The magnitude of the amplitude of the imperfection, as found in literature (Farshad [34], Popov and Medwadowski [62], Scordelis [69], Seide [79]), varies from 0 to 1.0 times the shell thickness for average thicknesses (concrete shells) and up to *1.5* and higher for very thin thicknesses (steel, plastics). Godoy [38] reports that Ballesteros (1978) found the amplitude of deviation from the mid-surface between *1* and *1.5* times the thickness, however, these values may be considered as extremely high as concrete shells normally are as thick as *60* to *80 mm* (Chapter 3).

The influence of initial geometrical imperfections is investigated in Chapter 14 and 15. Here, the imperfection is limited to a local imperfection, as it is most likely to occur, located at the top of the shell. The size is chosen equal to the theoretical buckled area of Scordelis and the imperfection amplitude ranges from *0.0* to *1.0* times the shell thickness.

6.8 Knock-Down Factor Approach

In the previous Chapters it is seen that there is a large discrepancy between the linear critical buckling load and the experimental obtained one. Although the difference can be explained, from a design standpoint, the basic question to be answered for a given reinforced concrete shell is what is the factor of safety against structural failure. As the structural engineer prefers general methods of calculation with a limited amount of computational work, there is searched for simple design formulae to determine the failure load. Hereby, it is assumed that the effects causing the fall-back in load bearing behaviour can be incorporated into the designing process by applying an empirical factor, the so-called knock-down factor, to the linearly established buckling values. Hence, the linear buckling theory needs not to be totally discounted.

Aforementioned in Chapter 1, finding the knock-down factor by making a comparison between the linear critical buckling load and the actual critical buckling load, is one of the main purposes of this thesis. Ideally, the knock-down factor handles the engineer a simple tool to determine the actual buckling load of a typical shell structure by multiplication of the knock-down factor with the linear critical buckling load, which in turn can be found by hand calculation or simple analysis.

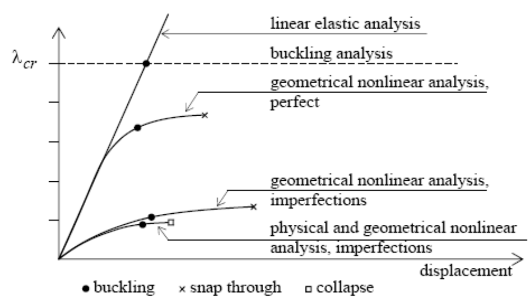

Figure 6.35. The fall-back in load carrying capacity due to several negative effects, Samuelson and Eggwertz 1992

In the foregoing, it is explained that the load bearing capacity of synclastic shells decreases when taking into account for geometrical nonlinearity, initial imperfections and inelastic effects. Consequently, the total knock-down factor can be seen as a summation of the individual knock-down factors that belong to these effects. This is illustrated in Figure 6.35 for a simply supported shallow spherical dome.

To find the actual buckling load, the influence of each of the individual effects must be determined. Referring back to the introduction of this chapter, these individual effects also clarify if the shell fails due to buckling (the geometrical nonlinearity knock-down factor is much larger than the one belonging to physical nonlinearity) or due to surpassing the material strength (vice versa). To determine each of the individual effects can hardly be done without computational software such as finite element programs. This is further discussed in Chapter 14 and 15.

6.9 Buckling Recommendations

Aforementioned in Chapter 3, there are two design codes that contain recommendations for the analysis of buckling of concrete shells. However, the ACI Standard is known to be of little practical use as it gives almost no information of use to a shell designer, Popov and Medwadowski [62]. Therefore, only the IASS recommendation is discussed here. The IASS recommendation includes a buckling paragraph largely based on Kollar and Dulacska [54] (and in particular on Chapter 9) which gives a practical application of the stability theory with respect to shells fabricated from reinforced concrete, timber, synthetics and metal. The method as proposed by Kollar and Dulacska is a practical semi-empirical (analytical formulas adapted to test results), but rational, approach. The method tries to overcome the differences in linear critical buckling load and the actual buckling load by considering influences of initial imperfections and nonlinear geometrical and physical behaviour. The procedure followed in the IASS recommendations is discussed below in five steps (Paragraph 6.9.1 to 6.9.5). In paragraph 6.9.6 the total reduction factor and safety factor are derived. In the final paragraph some conclusions are drawn.

6.9.1 Linear Buckling Load

The first step is to determine the linear critical buckling load for an ideal shell. For simple shell geometries with external normal pressure, the formulas derived by Zoëlly, van der Neut and Flügge may be applied to calculate the linear buckling load. This is already extensively described in the previous chapter. The linear buckling load of more advanced shell geometries may be determined using computational software, for example DIANA. An example and some critical comments are given in Chapter 13.

6.9.2 Postbuckling Category

As explained in the previous chapter, different types of shells experience different types of post-buckling behaviour. For shells which experience increasing capacity in the post-buckling range, such as some anticlastic shells (hypars), no reduction is necessary and simply applying the safety factor over the linear critical buckling load is sufficient for a safe shell structure. For shells with decreasing capacity in the post-buckling regime, however, the load bearing capacity decreases significantly. An important step is therefore to ascertain in which category the shell problem falls with respect to its post-buckling behaviour.

Depending on the shell geometry this may be more or less apparent. In case of uncertainty, the categorisation can be done on the basis of established analytical or experimental results which conclusively show whether the shell experiences a reduction in the buckling load or not. If the shell problem does not fall in the category of increasing load bearing capacity in the post-buckling range, the initial linear buckling load is presumed to decrease after the buckling point. To determine the allowable load the IASS recommendations lower the linear critical buckling load with several reduction parameters. The reduction parameters are related to effects which have significant influence on the buckling behaviour. Aforementioned in this Chapter, there is referred to large deflections, geometrical imperfections, and material parameters as creep, cracking and inelastic behaviour. They will be dealt with in the following paragraphs.

6.9.3 Modification for Large Deflections and Geometric Imperfections

The first modification is for large deflections. The reduction factor can be obtained from the graph of Figure 6.36 after computing the linear deflection w_o' and the deflection to thickness ratio w_o'/h. The curves shown are calculated analytically using a large deformation theory. For other geometries similar graphs can be found in literature. In case that there is no solution available, the lowest possible value of Figure 6.36 must be used.

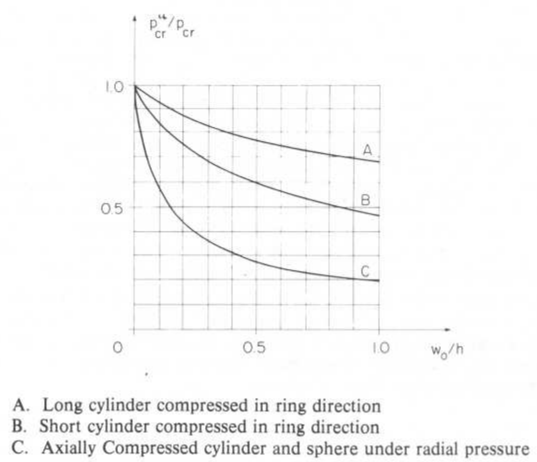

Figure 6.36. Reduction in critical load due to postbuckling behaviour and initial imperfections, Popov and Medwadowski 1981

A second modification concerns geometric imperfections. As explained in the previous Chapter, geometric imperfections cause a significant decrease in load bearing capacity even before the linear buckling load is reached. The IASS recommendations suggest to calculate or assume an additional deflection w_o'' as shape imperfection. The calculation of the additional deflection is based on Chapter 9.2.2 of Kollar and Dulacska [54]. The proposed equations are listed below.

The additional deflection w_o'' is in Kollar and Dulacska [54] denoted as the accidental imperfection due to inaccuracies of erection. By analytical equating the following expression is found:

$$w_{0,accid} = \frac{R}{3500} \tag{6.63}$$

The latter expression showed acceptable results in compare to measurements on carefully fabricated cylinders. However, a shortcoming is that it disregards the fact that the imperfection also depends on the thickness as denoted in Chapter 3 and that it cannot become infinitely large. Furthermore, when the erection method results in greater imperfections such as reinforced concrete shells erected with a sliding formwork, it may be reasonable to assume larger imperfections. Therefore, by evaluating measurements on cooling tower shells, Kollar and Dulacska propose the empirical formula:

$$w_{0,accid} = 0.05h + \frac{R}{2000}\frac{a}{\frac{R/h}{1000} + \frac{1000}{R/h}} \tag{6.64}$$

Where a stands for the influence of the accuracy of the erection method. For reinforced concrete shells with conventional (rigid) formwork the value of a can be set equal to 1, while for sliding formwork the value can be taken equal to 6.

Independent of the chosen equation, the total deflection according to the IASS recommendations becomes:

$$w_0 = w_0^{'} + w_0^{''} \tag{6.65}$$

Again, the (total) deflection to thickness ratio must be determined in order to obtain the reduction factor from the graph of Figure 6.36 as previously explained in Section 6.9.3.

Kollar and Dulacska [54] state that it is rather improbable that the maximum values of both imperfections coincide. Therefore, by the rules of probability theory, they take the largest value of:

$$w_0 \geq \begin{cases} w_0^{'} + 0.8 w_0^{''} \\ w_0^{''} \end{cases} \tag{6.66}$$

However, this hypothesis is not borrowed by the IASS recommendations.

6.9.4 Modification for Material Properties

The final step is to include material modification factors for creep, reinforcement and cracking and the effect of inelastic behaviour of reinforced concrete.

Effect of Creep

To allow for creep influences a reduced value of the modulus of elasticity is introduced according to the equation:

$$E_{cr} = \frac{E_c}{1 + C_u} \qquad where \quad C_u = 4 - 2\log f_c \tag{6.67}$$

In which E_c is the modulus of elasticity of concrete and f_c is the strength of concrete in *MPa*. Furthermore C_u represents the ultimate creep coefficient for the concrete.

The previously found critical load p^u_{cr} must be reduced in the same proportion as the reduction of the value of E_c.

Effect of Reinforcement and Cracking

In accordance with an empirical approach as proposed by Kollar and Dulacska [54], the effect of reinforcement and concrete cracking on the modulus of elasticity is related to the product of the modular ratio and the steel ratio:

$$\frac{E_s}{E_{cr}} \cdot \frac{A_s}{A_c} \tag{6.68}$$

The quantity of equation (6.78) is used to determine the value of coefficient ψ in Figure 6.37.a.

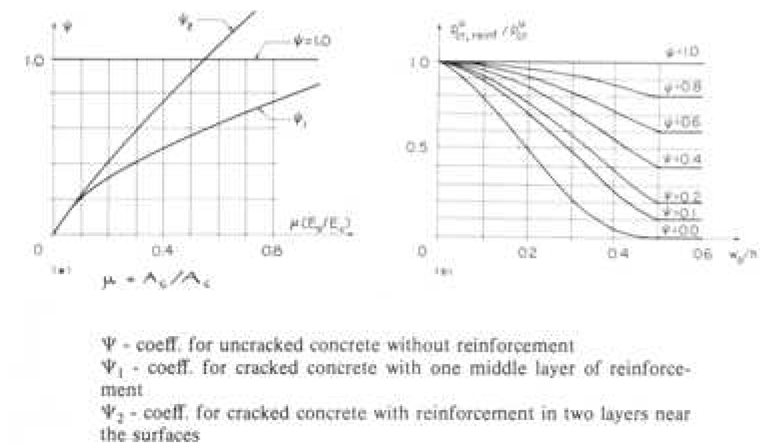

Figure 6.37.(a) Modification of critical load due to reinforcement and cracking and (b) Reduction of buckling capacity, Popov and Medwadowski 1981

Consequently, the coefficient ψ and the deflection to thickness ratio w_o/h are used in Figure 6.37.b. to determine the ratio between the upper critical buckling load and the value of $p^u_{cr,reinf}$.

Effect of Inelasticity of Concrete

Due to the nonlinear behaviour of concrete the critical buckling load further reduces. The critical load due to inelasticity of concrete can be determined according to the semi-quadratic interaction formula:

$$\left(\frac{p_{cr}^{plast}}{p_{plast}}\right)^2 + \left(\frac{p_{cr}^{plast}}{p_{cr,reinf}^{u}}\right) = 1 \tag{6.69}$$

Where p_{plast} is the load bearing capacity of a shell as governed by the ultimate strength of the reinforced concrete shell cross-Section, independent of any buckling consideration.

The IASS recommendations suggest reducing the thickness of shells thinner than *80 mm* with *10 mm* to allow for possible inaccuracies of construction resulting in a thinner shell than designed. This is based on extensive measurements on a series of erected reinforced concrete slabs, conducted by the Institute of Quality Control of the Building Industry in Budapest.

6.9.5 Total Reduction Factor and Safety Factor

Summarising the steps taken in the paragraphs 6.9.3 and 6.9.4 a reduced buckling load can be found in terms of the linear critical buckling load with the following equation:

$$p_{cr}^{reduced} = \alpha_1\ \alpha_2\ \alpha_3\ \alpha_4\ p_{cr}^{lin} = \alpha\ p_{cr}^{lin} \tag{6.70}$$

In which α_1 to α_4 are the reduction factors from paragraph 6.9.3 to 6.9.5 and α is the single product of the individual reduction factors.

α_1 = Large deformation and imperfection factor
α_2 = Creep factor
α_3 = Crack factor
α_4 = Material nonlinearity factor

Finally, the allowable load on the shell is determined by dividing the reduced critical load through a factor of safety γ:

$$p_{allow} = \frac{p_{cr}^{red}}{\gamma} \tag{6.71}$$

The IASS recommends value of *1.75* for shells which experience an increase in load bearing capacity of the point of linear buckling and a value of *3.5* for shells with decreasing capacities in the post-buckling range.

6.9.6 Conclusion IASS Recommendations

Basically, the IASS recommendations provide in a reduced factor approach which shows similarities with the searched knock-down factor which determines the fallback in load bearing capacity between the linear critical buckling load and the actual buckling load. Hence, the thesis research can be extended with the question whether the reducing factor as proposed by the IASS fits with the observations made in this thesis or not. Furthermore, it must be mentioned that the design approach as proposed in the recommendations assumes that the boundaries of the shell are well supported so that the buckling instability occurs within the shell surface. In a different situation additional analytical and/or experimental studies are necessary.

6.10 Conclusions

The aforementioned survey on the buckling of circular cylindrical shells and spherical shells have revealed that close agreement between theoretical and experimental results may exist when the effect of imperfections, geometrical and physical nonlinearity and the boundary conditions are taken into consideration. The strengths are in particular sensitive to the amplitude of the initial imperfections in the shell surface. To bring into account for these negative effects on the critical load, a design procedure is proposed using a knock-down factor which represents the discrepancy between the idealised linear elastic theory and the actual nonlinear inelastic reality. However, it is difficult to give a general expression for the knock-down factor since it is very dependent on the shell geometry and boundary conditions, the shape of imperfection, the shell theory used, and the approximations made. In Chapter 15 it is tried to give a complete description of the knock-down factor for spherical shells.

The buckling discussion is by far not complete. For a more comprehensive review on shell buckling one could read the following books and papers. A general review of the buckling phenomenon is found in the books of Bažant and Cedolin (1991), Brush and Almroth (1975), Timoshenko and Gere (1961) [72], Kollar and Dulacska (1984) [54] and Hutchinson and Koiter (1970). Additionally, for thin concrete shells, one may read the review of existing knowledge paper of Bradshaw (1963) and the books of Ramaswamy (1968), Budiansky and Hutchinson (1979) and Popov and Medwadowski (1981) [62] and the paper of Haas and Van Koten (1970) [41].

part III

Case Study

7 Zeiss Planetarium

The lack of theoretical knowledge on postbuckling behaviour and decreasing load carrying capacity caused by imperfection sensitivity and concrete cracking, as discussed in the previous chapter, is one of the main objectives of this thesis. In order to obtain qualitative and quantitative information about the structural response up to structural failure a base shell is introduced. The shell used is the first thin concrete shell of the modern era, the Zeiss planetarium in the city of Jena. The shell is seen in Figure 7.1.

Figure 7.1. The 1925 Zeiss planetarium in Jena, Germany, www.structurae.co.uk

The choice for the Zeiss planetarium can be explained by the fact that the shell has a simple geometrical hemispherical shape, easily described by a radius of curvature and an angle. Due to its relative simplicity the linear elastic behaviour is widely discussed in literature. Furthermore, the buckling and postbuckling behaviour of a (hemi) sphere is extensively investigated, which results in several theoretical formulae and benchmark tests to validate the thesis' results.

7.1 Geometry

The Zeiss planetarium is a hemispherical cap situated on a circular base. Part of the shell is concealed behind an entrance building. On top of the hemisphere, an extension is built. Later, both the entrance building and the top extension are disregarded in the shell modelling phase. The hemispherical geometry dimensions of the Zeiss planetarium are tabulated below in table 7.1.

Geometry	Dimension
Total height of building	*17000 mm*
Span	*25000 mm*
Radius of Curvature	*12500 mm*
Thickness	*60 mm*
Shell surface area	*981.75* m^2
R/t	*200*

Table 7.1. Geometrical dimensions of the Zeiss planetarium

7.2 Material

The Zeiss planetarium is a thin reinforced concrete shell. There is no information about the concrete quality or the reinforcement in the shell. Therefore, the material proportions of the shell must be guessed. As the shell is completed in the early *20*th *century*, a relative low quality of concrete is chosen for the analysis. Chosen is for a *C20/25* mixture. Furthermore, the quality of the reinforcement is chosen rather low selecting *FeB220*. The reinforcement of the shell is a single layer geodesic *Zeiss-Dywidag* triangular mesh, seen in Figure 2.5. The reinforcement is located in the middle of the shell cross-section. In general, shells are low reinforced structures, thus, the percentage of reinforcement is chosen to be between *0.15* and *0.40 volume %* (Chapter 3). The material properties and characteristics are further discussed in Chapter 8.

7.3 Support

However not seen in Figure 7.1, the base of the Zeiss planetarium is stiffened by a tension ring with a depth of *800 mm*, which rest on the circular base building, Fernandez Ordonez and Navarro Vera [35]. The ring ensures a continuous clamped support at the base of the shell.

7.4 Loading

The loading on the shell consists out of the dead weight and variable loads such as wind and snow. As is seen in Figure 7.1, today the shell surface is cladded by sheet metal. However, the cladding is assumed to be negligible when determining the dead weight of the structure. For the variable loading it is important to know the environmental conditions. The Zeiss planetarium is built in the city of Jena, in the east of Germany on the river Saale. Jena lies at a height of *155 m* above sea level in a slightly hilly country. The surrounding area of the shell shows regular cover of vegetation and buildings. The loading is determined in Chapter 9.

8 Material Properties

To obtain an answer to the question whether high strength concrete can contribute to more slender shells or not, the thesis' shells are analysed using two different types of concrete mixtures. A reference conventional concrete mixture and a high strength fibre reinforced concrete mixture are selected for analyses. Both mixtures and their characteristics are discussed in this chapter.

The shell analysed in Chapter 10 and 12 to 15 is the Zeiss planetarium in Jena in the east of Germany, discussed in the previous chapter. The shell is completed in 1925. Therefore, the conventional concrete employed is a low quality mixture to ally with the early *20th* century concrete technology. Chosen is for a C20/25 mixture according to the *Eurocode 2*. The high strength mixture originates from late developments in concrete technology. They find extensional application by the engineering profession at the present day. Recently, the first high strength concrete shell structures are realised in Canada and France. The shell in Calgary is a station cap for a light rail concept constructed in 2003. The double curved individual cast shell elements are only *20 mm* thick and span an area of *5.5 × 6.1 m*. The shell is constructed using a Ductal mixture with compression strength of *151 MPa* and a flexural strength of *25 MPa*. Typically, there is no conventional reinforcement in the shell. This also holds for the 2005 tollgates in front of the Millau viaduct in France. Architect Michel Herbert designed a *98 × 28 m* twisted shell with spans of *28-26-28 m*. Longitudinal prestressing ties bring the shell into compression. The shell is *850 mm* thick; however, it includes a hollow core as can be seen in Figure 4.16. The skin is only *100 mm* thick. It is constructed using a BSI-Céracem self-compacting mixture with average compression strength of *200 MPa*. The mixture contains *3.5 volume %* synthetic fibres, Walraven [83]. Both structures are seen in Figure 8.1.

Figure 8.1. Shawnessy LRT Station in Calgary and the Tollgates near Millau, structurae.co.uk

It must be mentioned that all material properties used in this thesis are mean values. Hence, the real structural response can be approximated as closely as possible. In practice, design values must be used.

8.1 Conventional Concrete

Conventional (reinforced) concrete does not need much of introduction. The compressive and tensile behaviour of conventional reinforced concrete according to the *Eurocode 2* is outlined in the following. The constitutive behaviour of concrete is characterised by *compressive crushing* and *tensile cracking*. For reinforced concrete, a third failure mechanism is the *yielding of rebars*. Time-dependent material behaviour such as *creep, shrinkage* and ambient influences like temperature are not considered, although they might be of significant influence on the shell structural behaviour (Chapter 3).

8.1.1 Compressive Behaviour

The nonlinear compressive behaviour of conventional concrete is characterised by a linear branch followed by nonlinear branch with strain hardening and strain softening up to compressive crushing. The presence and propagation of micro cracks in the cement matrix cause the stress-strain curve to be 'rounded' near the point of maximum compression strength. The height of the diagram depends on the concrete quality, the loading time and the amount of confinement. Confinement results in a modification of the stress-strain law, higher strength and higher critical strains are achieved. The uniaxial stress-strain relation can be modelled in several ways. For relatively low compression strengths (< *40 MPa*) a *parabola* is applicable and the approximation of *Thorenfeldt* et al. Furthermore, the Eurocode provides in a relation for short term uniaxial loading for nonlinear structural analysis.

The mean value of the cylinder compression strength f_{cm}, used in the analyses, can be determined from the *5%* characteristic value of the cylinder compression strength f_{ck} obtained according to EN 206-1 by:

$$f_{cm} = f_{ck} + 8\,(MPa) \tag{8.1}$$

Furthermore, according to Table3.1 of Eurocode EN 1992-1-1 [33], the strain at the peak stress is:

$$\varepsilon_{c1}(‰) = 0.7 \cdot f_{cm}^{\;0.31} < 2.8 \tag{8.2}$$

Subsequently, the stress-strain diagram can be defined using the mean value of the compression strength and the expression for the strain at peak stress.

The parabola is described by:

$$\sigma_c = f_{cm}\left(2\frac{\varepsilon_c}{\varepsilon_{c1}} - \left(\frac{\varepsilon_c}{\varepsilon_{c1}}\right)^2\right) \tag{8.3}$$

The Thorenfeldt curve, a modification to the *Popovics* compression curve as the slope of the descending curve is increased by a factor *k*, is described by:

$$\sigma_c = -f_{cm}\frac{\varepsilon_c}{\varepsilon_{c1}}\left(\frac{n}{n-1+\left(\frac{\varepsilon_c}{\varepsilon_{c1}}\right)^{nk}}\right) \tag{8.4}$$

where $n = 0.80 + \frac{f_{cm}}{17}$

$$k = \begin{cases} 1 & \text{if } \varepsilon_c \leq \varepsilon_{c1} \\ 0.67 + \frac{f_{cm}}{62} & \text{if } \varepsilon_{c1} < \varepsilon_c < 0 \end{cases}$$

The Eurocode 2 (art. 3.1.5) relation for short term uniaxial loading is described by:

$$\frac{\sigma_c}{f_{cm}} = \frac{k\eta - \eta^2}{1 + (k-2)\eta} \tag{8.5}$$

where $\eta = \frac{\varepsilon_c}{\varepsilon_{c1}}$ with ε_{c1} the strain at peak stress and $k = 1.05\, E_{cm}\frac{|\varepsilon_{c1}|}{f_{cm}}$ which is only valid for $0 < |\varepsilon_{c1}| < |\varepsilon_{cu1}|$ with ε_{cu1} the nominal ultimate strain

Relation (8.5) is schematically presented in Figure 8.2 below:

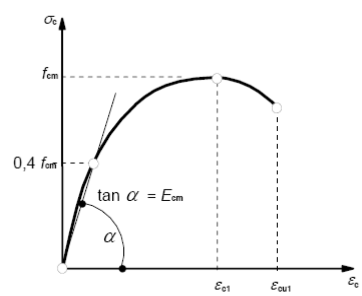

Figure 8.2. Schematic representation of stress-strain curve for structural analyses, Eurocode 2 EN 1992-1-1 2001

(The value of $0,4\, f_{cm}$ for the definition of the secant modulus of elasticity E_{cm} in Figure 8.2 is approximate, depending on the moduli of elasticity of the mixture components.)

The compressive behaviour of concrete is often simplified to a parabolic or a bi-linear diagram, both with yield plateau.

8.1.2 Tensile Behaviour

Typically, conventional concrete shows relatively high compressive strength while it cannot resist much of tensile stress. Therefore, the shells that are commonly built are reinforced by one or two layers of steel reinforcement to absorb tension forces in the post-cracking stage. Hence, the tensile behaviour of conventional concrete is largely influenced by the amount of reinforcement in the structure. The tensile behaviour is characterised by concrete cracking and rebar yielding. Prior to cracking the tensile behaviour is assumed to be linear up to the tensile strength of the concrete mixture. Characteristically, the tensile behaviour can be divided into *axial* tensile behaviour and *flexural* tensile behaviour.

The axial tensile strength of the plain concrete, thus, without reinforcement, can be found in Table 3.1 of the Eurocode 2 EN 1992-1-1. The axial tensile strength is, for strength classes below *C50/60*, determined according to the relation:

$$f_{ctm} = 0.3 \cdot f_{ck}^{(2/3)} \tag{8.6}$$

Where, f_{ck} is the characteristic (*5%*) value of the cylinder compression strength according to EN 206-1.

The mean value of the flexural tensile strength can be determined from the axial tensile strength by the relation (3.23) in Eurocode EN 1992-1-1 [33], which is defined as:

$$f_{ctm,fl} = max\{(1.6 - h/1000)\, f_{ctm}; f_{ctm}\} \tag{8.7}$$

With h the height of the cross-section in *mm* and f_{ctm} is the mean value of the axial tensile strength in *MPa*.

For the steel reinforcement the strength is chosen equal to the characteristic yield strength or *0.2%* strain value. The steel will deform according to the typical stress-strain diagrams for steel as seen in Figure 8.3. In practice they are often approximated by a simplified bi-linear law in which the horizontal branch is maximised by the yield strength.

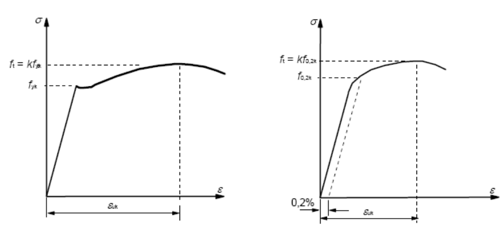

Figure 8.3. Typical stress-strain diagrams for hot rolled steel (left) and cold worked steel (right), Eurocode 2 EN 1992-1-1 2001

When the tensile strength of the plain concrete is surpassed, cracks initiate and the reinforcement is activated. The tensile behaviour after cracking is a complex phenomenon. Two post-cracking phenomena can be distinguished. First, the tensile stresses in the concrete are zero at a crack; however, they are introduced into the concrete between cracks by bonded reinforcement. Secondly, the stresses in the reinforcement fully absorb the tensile stresses at the crack but decrease in the concrete in between which causes the total strain being smaller when compared to single steel rebars in tension, Walraven [82]. Crack development and redistribution of tensile stresses from concrete to reinforcement due to bond between the rebars and the concrete is called tension stiffening. The largest problem of the post-cracking behaviour is the occurrence of a few wide cracks. This non-isotropic behaviour makes it impossible to capture the structural behaviour of reinforced concrete into a constitutive law. The exact post-cracking behaviour of the combined phenomena depends on the concrete and reinforcement proportions in a cross-section. Assuming that the reinforcement satisfies the minimum and maximum percentages to prevent sudden failure and has good bonding strength, the composite structure in tension will, in the end, fail due to yielding of rebars; however, at that stage the serviceability of the shell is often far in violation.

8.1.3 C20/25 Mixture Design

Aforementioned in the introduction, there is chosen for a relative low quality C20/25 concrete mixture according to the Eurocode to associate with the early *20th* century Zeiss planetarium shell. Using the equations (8.1), (8.2), (8.6) and (8.7), the properties of the C20/25 mixture are tabulated in Table 8.1.

C20/25			
Mean value of cylinder compressive strength	f_{cm}	-28	MPa
Yield compressive strain	ε_{c1}	-2.0	‰
Ultimate compressive strain	ε_{cu}	-3.5	‰
Mean value of axial tensile strength	f_{ctm}	+2,2	MPa
Mean value of flexural tensile strength (h=60 mm)	$f_{ctm,fl}$	+3,4	MPa
Young's modulus	E_c	30	GPa
Specific weight	ρ_c	2500	kg/m³

Table 8.1. Material properties of a C20/25 concrete mixture

The quantities of Table 8.1 can be combined with the expressions for the compression stress-strain law of Section 8.1.1. The two approximation methods are presented in the graph of Figure 8.4 for C20/25 concrete.

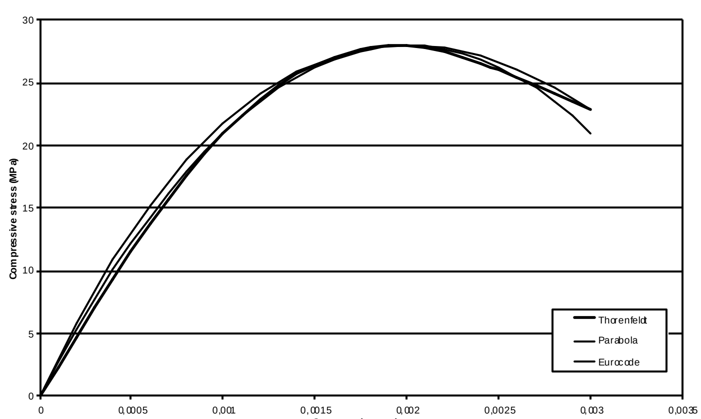

Figure 8.4. Uniaxial compressive stress-strain curves for C20/25 concrete

In addition to the C20/25 mixture, the choice is made to apply a relative low quality of steel reinforcement FeB220. For the chosen reinforcement there is referred to FeB220 HWL in which the latter stands for weldable hot rolled steel (cold worked steel is addressed by the addition of HK). The constitutive law is depicted in the left of Figure 8.3. For FeB220 HWL the following values are prescribed in the Dutch codes:

FeB220 HWL Steel Reinforcement			
Yield strength	f_{yk}	220	MPa
Strain at maximum load	ε_{uk}	5	%
Young's modulus	E_s	200	GPa
Specific weight	ρ_s	7850	kg/m³

Table 8.2. Properties of FeB220 steel reinforcement according to the Dutch code

The data of Table 8.1, 8.2 and 7.1 can be used to determine the behaviour in axial tension and flexural bending of a flat plate with similar cross-sectional dimensions as the Zeiss shell. The characteristic stress-strain relations for the flat plate (or shell) in axial tension and flexural bending can be seen in Figure 8.5.

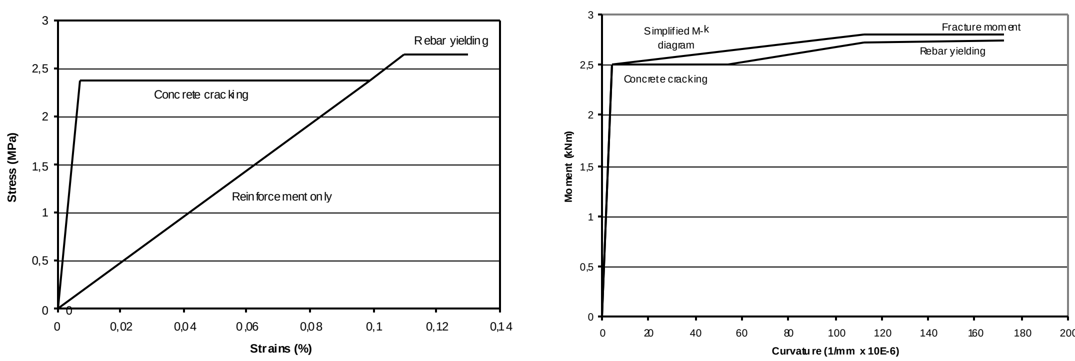

Figure 8.5. Typical stress-strain relationship in axial tension (left) and flexural bending (right) for a low reinforced beam with one layer of reinforcement located in the middle of the cross-section

Both relationships seen in Figure 8.5 are typical stress-strain diagrams for low reinforced concrete structures as shells with a low quality of steel located in the middle of the cross-section. In the left Figure, this can be seen by the relative long horizontal stage, which represents crack propagation. The low peak stress of rebar yielding is caused by the low quality of steel. In the right Figure as well as the low quality, as the low percentage of reinforcement, is responsible for a minimal increase of bending moment by increasing curvature. Furthermore, in the right Figure the reinforcement is assumed to be located in the middle of the concrete cross-section, which results in a relative long path of increasing moment during the cracking process (curvature causes the cross-section to open). This can be explained simply as the cross-section needs to develop large curvature before the reinforcement in the middle is activated. Hence, shells with a double layer of reinforcement will experience less cracking and reduced crack opening. Both graphs in Figure 8.5 end rather abruptly, which is caused by the brittle failure of the steel reinforcement. However, not at this stage already as both graphs are cut-off for clarity.

8.2 High Strength Fibre Reinforced Concrete

8.2.1 High Compression Strength

Recent developments in concrete technology have lead to concrete mixtures with high compressive strength. During the *1980s* research was done to concrete mixtures with a higher early strength, requested by contractors to speed up the building process. When the new developed concrete mixture hardened, it showed higher compression strength than usual. The newly achieved knowledge in concrete technology, fillers and additives contributed to a substantial advancement in the concrete industry and the development of high strength concrete. The new material was captured in regulations for the first time in France in 2002. Today, these codes are still the main codes of practice.

According to Den Hollander [47] high strength concrete can be classified as concrete with a characteristic cube compressive strength above *95 MPa*. Within the high strength range further classification is made in normal high strength concrete ranging from *95* to *155 MPa*, ultra high strength concrete from *155* to *250 MPa* and super high strength concrete with compression strengths over *250 MPa*. However, various other classifications may be found in literature.

The higher compressive strength of concrete is reached by optimising the mixture composition. The mixture composition can be subdivided into aggregate, cement and the interface between the aggregate and cement. Optimisation of the three components to a more homogeneous mixture with higher internal bond lowers tensile stresses perpendicular to the compression direction, see Figure 8.6.a. By reducing the largest particle size to a prescribed maximum value the homogeneity of the concrete becomes more favourable and the stress variation decreases. Additionally, an optimal (or higher) packing density yields higher compression strength as more particles contribute to the bearing capacity and weak voids are reduced, see Figure 8.7.b.

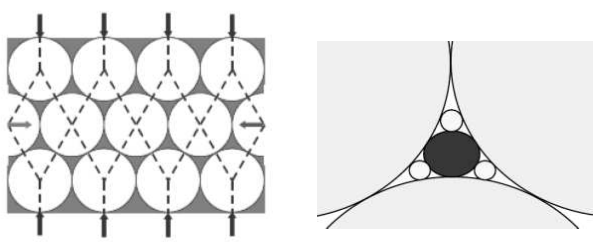

Figure 8.6.a. The force transmission in the concrete and b. an increased packing density, Den Hollander 2006

To optimise the interface between the aggregate and the cement silica fume is added to the mixture. Silica fume, which is highly reactive, contributes to a better bond between the aggregate and cement particles by the forming of secondary calcium-silicate crystals which grow through the primary crystals formed at the surface of the cement particles, see Figure 8.7. Furthermore, silica fume reduces the voids filled with water and air, Den Hollander [47].

Contrasting with the conventional concrete reflection that there must be enough water to react all cement particles, for high strength concrete the amount of water is not sufficient. Cement particles that do not react are assumed to strengthen the cement matrix as fillers. Superplasticizers enable the lowering of the water/cement ratio without reducing the workability. Possible hardening at higher temperature and/or at higher atmospheric pressure improves the microstructure, however, is of less practical use.

Figure 8.7. The hydration of concrete with and without silica fume, Den Hollander 2006

An optimal mixture can give compression strength of *200 MPa* and higher, theoretically up to about *800 MPa*. Not only the compression strength enhances, the mixture can also be classified as more durable with low permeability and favourable creep and shrinkage characteristics, Den Hollander [47]. Also the fatigue behaviour, however experiments show high scatter, is profoundable in compare to conventional concrete, Lappa [56]. Additionally, designing with high strength concrete has ecological advantages such as low material consumption.

For some differences between normal *C45* concrete and *C200* ultra high performance concrete the mixture components are shown in Table 8.3 from Den Hollander [47].

Component [kg/m^3]	C45	C200
Cement	360	1075
Silica fume	-	165
Sand	790	1030
Gravel	1110	-
Steel fibres	-	235
Superplasticizers	0.5	39
Water	145	200
Specific mass	2405	2810
Water/cement ratio	0.40	0.19

Table 8.3. Mixture components plain concrete and UHPFRC, Den Hollander 2006

8.2.2 Fibre Reinforcement

The properties of high strength concrete before cracking are similar to the properties of plain concrete. However, experiments show that when the cracking process initiates, the high strength concrete fails almost instantly, being a highly brittle material. In general: the higher the concrete strength the more brittle the concrete behaviour, Den Hollander [47]. To counteract the brittleness, fibres are added during the mixing process, which can be seen in Table 8.3.

The addition of fibres can be explained by examining the cracking behaviour of (high strength) concrete. Cracking appears on micro level and macro level, see Figure 8.8. Micro cracks appear in the interface layer due to the imposed deformation of the cement matrix by stiff aggregates during hydratation. In a loading situation micro cracks grow until they become visual as macro cracks. Fibres added to the mixture act as well on micro level, as reinforcement of the cement matrix, as on macro level, as reinforcement of the structure. The reduction of micro cracking by fibres is achieved by the takeover of the tension stresses around a crack and thereby reducing the tension stresses in the cement matrix. On macro level the fibre tends to span the crack and prevent enlarging. By local pull-out behaviour the post-cracking ductility is significantly improved as fibres provide in the most advantageous low-level post cracking plateau, Markovic [57].

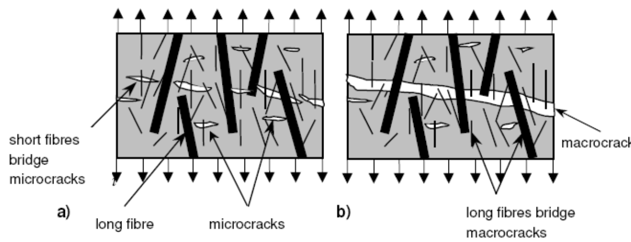

Figure 8.8 Micro-cracking and macro-cracking, Markovic 2006

Fibres do not necessarily lead to an increase in tensile strength; however, it is possible to increase the tensile strength through the addition of fibres with different dimensions (fibre mixture). The micro cracking can be decreased with the smaller fibres and with that the elastic behaviour extended while in case of macro cracking the longer fibres become active, Markovic [57]. Though, fibres are added to improve ductility, they can reduce the amount of reinforcement or even totally substitute the reinforcement.

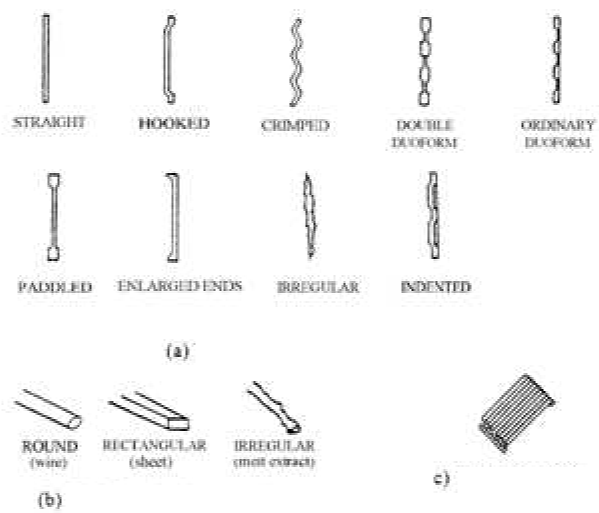

Figure 8.9. Different types of (a) shapes, (b) transverse sections and (c) glued steel fibres, Burgers 2006

Fibres are needle shaped elements manufactured from different materials such as steel or plastics. Fibres are available in all shorts of shapes and lengths, see Figure 8.9. Fibre lengths vary from *7* to *75 mm* with a diameter ranging from *0.15* to *2 mm*. In general they are in between *25* to *60 mm* with a diameter of *0.4* to *0.8 mm*. Fibre geometry is classified according their aspect ratio, which is qualified as the fibre length divided by the fibre diameter (L_f/d_f). Hence, the general aspect ratio is in between *40* to *80*. In structures, the amount of fibres starts at *35 kg/m3*, or *0.45 volume %*. Hereby the fibres are additional to conventional steel bar reinforcement. In traditional fibre reinforced concrete the volume amount is smaller than *2 %*, though, fibre volumes over *2 %* are becoming more and more accepted. Hereby the fibres totally substitute the original reinforcement which is referred to as high performance material, recognised by an increasing plastic strain (strain hardening) and multiple cracking. They may be applied up to an amount of *15 volume %,* e.g. the SIFCON (slurry infiltrated fibre concrete) mixtures, Kooiman [55]. Fibres have a ductile plastic stress strain relation and show only minor shrinkage. The strength of steel fibres ranges from *900* to *3000 MPa*. Plastic fibres have even higher strengths up to *4000 MPa* and more. Plastic fibres are more expensive and therefore find less application, Bouquet and Braam [17].

Fibres added to the concrete mixture can be considered as coarse aggregates. Fibres cannot just be added, they must be able to take position without disturbing the mixture composition, Figure 8.10. For an optimal mixture the addition thus leads to adjustment of the original components. An increase of the cement weight of approximately *10 %* compensates the larger amount of internal surface. Hence, to ensure workability, the amount of water must be increased or replaced by superplasticizers. The aggregates must be properly chosen for a sufficient fibre distribution in the mixture, Grünewald [39].

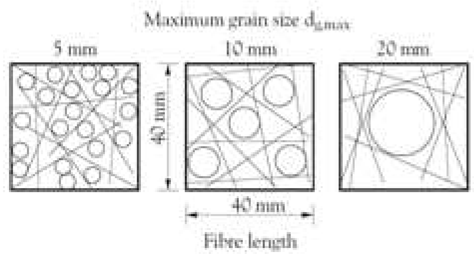

Figure 8.10. Effect of maximum grain size on fibre distribution and orientation, Kooiman 2000

Limiting the maximum grain size to half the fibre length is recommended for satisfying fibre distribution and favourable for workability and preventing so-called fibre balling. As fibres are needle shaped elements in a mixture of spherical elements, they tend to decrease the workability considerable. Furthermore, refining the ratio of fine particles to total volume of the aggregate contributes to a higher packing density which is negatively influenced by the addition of fibres, as is illustrated in Figure 8.11. According the American Concrete Institute (ACI) Committee 544, 1993, depending on the fibre volume, an optimal packing density is reached by a ratio of fine particles to total volume between *40* and *60 %*, Den Hollander [47].

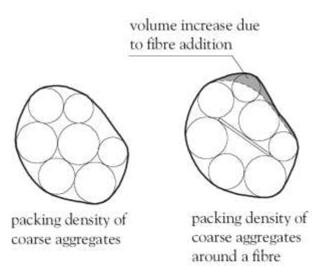

Figure 8.11. Effect fibres on packing density, Kooiman 2000

The influence of the type of fibres in the mixture is often presented referring to the aforementioned fibre aspect ratio. For example, in Table 8.4, the limitations to the fibre volume in relation to the maximum grain size are shown with respect to the fibre aspect ratio. The values are obtained by Kooiman [55] for hooked-end fibres in dry mixtures.

d_{max} (mm)	$L_f/d_f = 60$	$L_f/d_f = 75$	$L_f/d_f = 100$
4	2.0 %	1.6 %	1.2 %
8	1.5 %	1.3 %	0.9 %
16	1.0 %	0.9 %	0.7 %
32	0.6 %	0.5 %	0.4 %

Table 8.4. Maximum fibre volume for different maximum grain size and different aspect ratio, Kooiman [55]

Some restrictions to the mixture components due to application of fibres are determined by the ACI Committee 544, 1993. Table 8.5 provides ranges for mixture components for different fibre aspect ratios. Though, effects of additives as superplasticizers are not mentioned.

Component	$L_f/d_f = 60$	$L_f/d_f = 75$	$L_f/d_f = 100$	
Water/cement ratio	0.35 – 0.45	0.35 – 0.50	0.35 – 0.55	-
Cement	360 – 600	300 – 540	280 – 420	kg/m³
Fine/total aggregates	45 – 60	45 – 55	40 – 55	%
Air volume	4- 8	4 – 6	4 – 5	%
V_f straight fibres	0.8 – 2.0	0.6 – 1.6	0.4 – 1.4	%
V_f deformed fibres	0.4 – 1.0	0.3 – 0.8	0.2 – 0.7	%

Table 8.5. ACI guideline for SFRC mixtures, Den Hollander [47]

When the fibres are added to the mixture, the tensile behaviour, and in particular the post-cracking tensile behaviour, of the composite mixture must be determined. To provide information about the expected post-cracking behaviour, pullout test on a simple fibre out of a block of matrix material is widely accepted as one of the basic tests. The pullout behaviour is dependent of the fibre characteristics, the quality of the cement matrix and the fibre orientation. Figure 8.12 shows a close-up of the pullout behaviour of a straight fibre as determined by Naaman 1999, as reported by Kooiman [55].

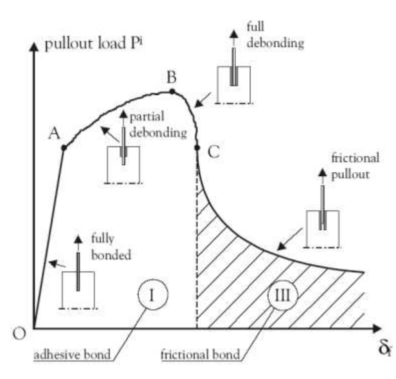

Figure 8.12. Close-up of a typical pullout versus end-slip relationship for a straight fibre, Kooiman 2000

The fully bonded stage *OA* is of significance influence to stabilise micro cracks in the early stage of loading. The graph path *AB* indicates the debonding stage until full debonding occurs in *BC*. The frictional stage is decaying out due to the increasing slip of the progressing pulled out fibre. The debonding stage and frictional pullout stage are of importance for the total amount of cracking energy consummated by the fibre, the so-called fracture energy. The area under the curve denotes a value for the ductility, Kooiman [55]. The complete pullout versus end-slip relationship is seen in Figure 8.13 for straight and hooked-end fibres. The influence of a higher bonding of the fibre on the pullout load can be seen.

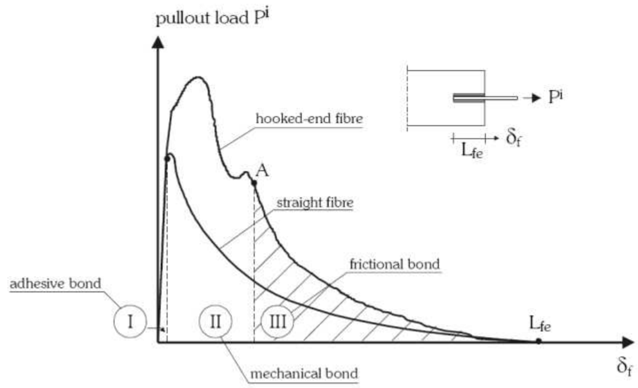

Figure 8.13. Typical pullout versus end-slip relationship for a straight and hooked-ended fibre, Kooiman 2000

Due to the random distribution of the fibres in the cross-section, the results of the pullout test of a single fibre can not be directly translated to the behaviour of a fibre reinforced concrete structure. Because of the efficiency of a single fibre is related to the orientation of the fibre with respect to the pullout load, the so-called inclination angle, there is a difference in efficiency between a single fibre and a group of fibres, which must be taken into account. The orientation of the fibres is included in the structural design method by the orientation factor $1/K$ that deals with randomly distributed fibres and the so-called wall-effect (fibres align with the wall). Furthermore, the orientation factor depends on the dimensions of the structural element and on the placement technique, Den Hollander [47]. For plates and shells the orientation of fibres is not negatively influenced by the wall effect and, thus, the factor can be set equal to the minimum value of one.

Variations in fibre material, shape, size and quantity cause differences in the mechanical behaviour as found for single fibre pullout tests. The stiffness of the fibre is a measure for the resistance to micro cracking, with the higher stiffnesses causing lesser micro cracks. On the other hand the fibre contributes to enlargement of the tension stiffness of the cement matrix as soon as the fibre goes through the micro crack. Hereby the bonding and aspect ratio of the fibre are essential. This can be explained by the observation that fibres, although they stiffen the cement matrix, still need a certain amount of cracking before they are activated, Bouquet and Braam [17].

In case of macro cracking, the fibre must ensure a ductile post-cracking behaviour. When the cracking stage initiates, there are three mechanisms which can occur. At first, the composite can have brittle failure when the fibres are unable to resist the tensile force in the composite after cracking. Secondly, the composite can fail due to consecutively pulled out fibres and, at last, the composite can have increasing tension strength due to a large amount of fibres in combination with high bonding capacity before it fails due to fibre pullout. In such cases, attention must be paid to prevent the possibility of brittle failure of the compression zone. Hence, when appropriately applied, the use of fibres to reinforce the concrete changes the third mechanism of plain concrete, being the yielding of rebars, to pull-out failure of fibres. As the first mechanism is highly uninvited, the pull-out failure mechanisms are to be obtained. Therefore the fibre must contain enough tensile and bonding strength. By increasing the fibre tensile and bonding strength, the fracture energy, and thus the toughness of the concrete can be enlarged. Furthermore, a larger amount of fibres, increased aspect ratio and a better orientation of the fibres (higher effectiveness of the fibre) also increase the ductility. However, attention must be paid to the possible occurrence of brittle failure. To high bonding strength leads to brittle failure of fibres or the compression zone, Bouquet and Braam [17].

The problem is, however, the contrary fibre demands in case of micro or macro cracking. At micro level a high bonding is profound while at macro level a to large bonding strength results in uninvited brittle behaviour of the fibres or the compression zone. It can be concluded, that there is an optimal relation between the fibre tension strength and the bonding capacity, the critical fibre length, Burgers [20].

Avoiding fibre rupture, the fibre bridging stress must be smaller than the fibre tensile stress which, in turn, is a function of the embedded fibre length, the maximum bond stress at the fibre to the matrix interface and the fibre diameter. If the length is smaller, the fibre is not loaded to its full capacity. The fibre will be pulled out of the matrix. When larger, there is brittle failure. If the length of the fibre is critical, theoretically, the fibre and cement matrix fail at the same time. In practice the fibre must be pulled out, but as close to the critical value as possible for higher toughness. Therefore, the fibre length is sub critical, Kooiman [55]. Hence, the basic idea of fibre reinforcement is fundamentally different to the application of conventional steel bar reinforcement that must fit tight in the concrete and start yielding before brittle cracking of the compression zone occurs.

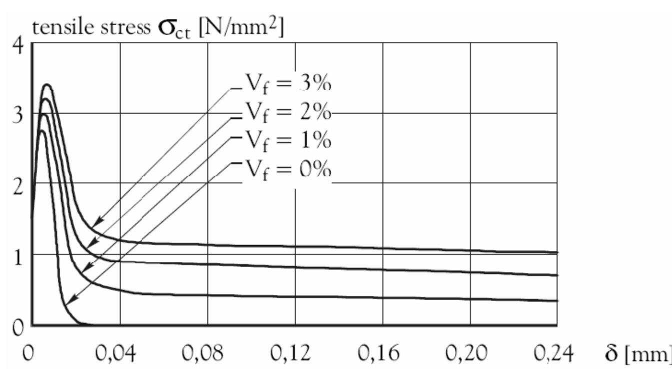

Figure 8.14. Typical stress-strain opening displacement relations for FRC and plain concrete, Kooiman 2000

In the final UHPFRC mixture design, the total amount of cracking energy consummated by the fibres by continuous frictional pullout is the cause for the most advantageous property of fibre reinforced concrete in contrast to plain concrete, namely the low level post-cracking plateau, seen in Figure 8.14. Figure 8.14 shows a typical stress-crack opening displacement relation for plain concrete and fibre reinforced concrete in case of uni-axial tensile stress. The low level post-cracking plateau due to the addition of fibres leads to a higher toughness and more ductile failure behaviour. Besides the advantageous low level post-cracking plateau, also a slightly higher tensile peak stress is seen.

8.2.3 UHPFRC in Practice

Different types of mixtures of high strength concrete are available on the market. However, basically there are only three which are commonly used. The Ductal mixture, patented by French cooperation Lafarge, Bouygues and Rhodia, the BSI / Céracem product by French company Eiffage and the CRC (Compact Reinforced Composite) mixture developed by Aalborg Portland A/S and marketed by CRC Technology. Both the Ductal and BSI mixture contain only (steel) fibres, the CRC mixture combines fibres with closely spaced reinforcement bars. A shell constructed with such a mixture is the l'Oceanografic shell in Valencia, seen in Figure 3.25. The material properties of the three mixtures are captured in Table 8.6. More information concerning the latter mixtures is available on the internet, e.g. BSI Eiffage [92].

Property	Ductal	BSI	CRC	
Specific weight	2500	2800	3200	Kg/m³
Characteristic compressive strength	200 (HT)*	180	140	MPa
Tensile strength	8.0	10.0	7.0	MPa
Flexural bending strength	42.0	45.0	25.0	MPa
Young's modulus	58000	65000	46000	MPa
Poisson's ratio	0.2	0.2	?	-

* HT = Heat treatment

Table 8.6. Material properties of Ductal, BSI and CRC

8.2.4 Compressive Behaviour

Like conventional concrete, the compressive behaviour of UHPFRC is characterised by a nonlinear stress-strain curve. After the linear branch the aforementioned micro cracks that occur in the cement matrix at relatively low stress levels cause a 'rounded' compression curve with strain hardening and strain softening up to compressive crushing. Though, fibres act as reinforcement of the cement matrix and reduce the micro cracking, several researchers such as Maidl, König & Kützing, Sato found that the contribution of fibres to the compression strength is negligible, Den Hollander [47]. Furthermore, the contribution of the steel fibres to the modulus of elasticity is rather small and therefore neglected. Hence, the compression curve is only determined by the concrete properties.

To describe the uniaxial stress-strain relation of high strength concrete in compression, the approximation of Thorenfeldt et al. is used, described by relation (8.4). For higher compressive strength the Thorenfeldt curve gives a better approximation than the parabola expressed in relation (8.3), Burgers [20]. The relation as presented by the Eurocode 2 (equation (8.5)) is not applicable for such high strengths.

According to the French codes, the compressive behaviour of high strength concrete can be approximated with a bi-linear constitutive law defined by the concrete strength and the Young's modulus. The strain hardening/softening is neglected as there is a yield plateau up to failure due to crushing, illustrated in Figure 8.15. In general, the higher the concrete compression strength, the more linear the stress-strain relation is up to the peak load. Hence, for UHPFRC the bi-linear law makes sense.

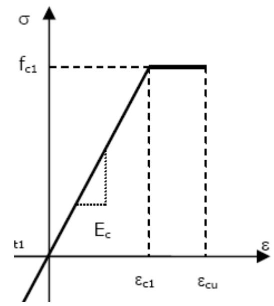

Figure 8.15. The compressive behaviour of high strength concrete according to the French codes, Den Hollander 2006

The characteristic points of the bi-linear law are defined in the French codes. The yield plateau initiates at *60%* of the characteristic compression strength f_{ck} at a strain of *-1.75 ‰*. Crushing is assumed to occur at a strain of *-3.0 ‰*.

8.2.5 Tensile Behaviour

The tensile behaviour of UHPFRC depends on the proportions of conventional reinforcement, fibres and concrete and on the concrete quality. Here, the tensile behaviour of a UHPFRC mixture in which fibres totally substitute the conventional reinforcement is examined. The tensile behaviour is characterised by a linear stage, limited by the tensile strength of the cement matrix, and a nonlinear post-cracking stage with low-level post-cracking plateau.

A big advantage of fibre reinforced concrete in tension is the occurrence of a large amount of small cracks instead of a few wide cracks which were seen in conventional reinforced structures. Due to the addition of fibres, the composite mixture loaded in tension will behave more like an isotropic material, which means that the structural behaviour can be observed with a constitutive law instead of a stress-crack relation. Thus, especially the mathematical part simplifies.

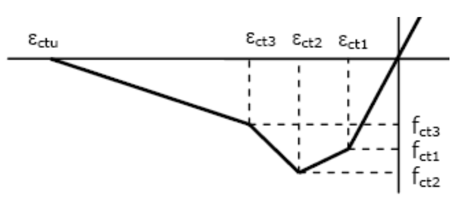

Figure 8.16. The tensile behaviour of UHPFRC, Den Hollander 2006

According to the French codes, the tensile stress-strain relation of UHPFRC may be modelled with a multi-linear stress-strain diagram with either strain softening (reduction in load bearing capacity accompanied by increasing deformation) or strain hardening (increasing deformation and increasing load bearing capacity) in the plastic stage. Strain hardening is visualised in Figure 8.16 as, in general, UHPFRC mixtures allow for further load increase after the first cracking load. The characteristic point of the tensile strengths of Figure 8.16 must be determined by experimental tests. The French codes provide in the following relations for the multi-linear strain hardening/softening tension curve:

$$\varepsilon_{ct1} = \frac{f_{ct1}}{\gamma_c E_c} \tag{8.8}$$

Where the material factor γ_c is set equal to *1*.

$$\varepsilon_{ct2} = \frac{w_2}{l_c} + \varepsilon_{ct1} \tag{8.9}$$

Where w_2 is the crackwidth at t_2

$$\varepsilon_{ct3} = \frac{w_3}{l_c} + \varepsilon_{ct1} \tag{8.10}$$

With w_3 the crackwidth at point t_3

$$\varepsilon_{ctu} = \frac{l_f}{4 l_c} \leq 1\ \% \tag{8.11}$$

Where l_c is the characteristic length and l_f the fibre length.

The characteristic length is a quantity to change the stress-crackwidth relation resulting from the pull-out tests to a constitutive stress-strain law needed in the analyses. For a rectangular shaped cross-section the value equals *2/3* times the height, Den Hollander [47].

8.2.6 C180/210 Mixture Design

For the thesis' shell analyses a high strength concrete mixture BSI C180/210 according to Redaelli and Muttoni [67] is chosen with *2.4 volume %* steel fibres and no conventional reinforcement. The fibres are *20 mm* long and have a diameter of *0.16 mm*. The mixture has a characteristic value of the cylinder compressive strength of *180 MPa* and a Young's modulus of *60 GPa*. The compressive behaviour is captured in Table 8.7.

BSI C180/210			
Mean value of cylinder compressive strength	f_{cm}	-190	MPa
Yield compressive strain	ε_{c1}	-1.75	‰
Ultimate compressive strain	ε_{c1}	-3	‰
Young's modulus	E_c	60	GPa
Specific weight	ρ_c	2800	kg/m³

Table 8.7. Material properties of the applied high strength concrete mixture from Redaelli and Muttoni [67]

The compressive stress-strain curve of C180/210 UHPFRC is approximated by the Thorenfeldt rule (relation (8.4)) and the parabola (relation (8.3)). In addition the compression curve according to Popovics is determined. The approximation methods are presented in the graph of Figure 8.17. In particular the Thorenfeldt curve shows high brittleness after the point of peak stress/strain.

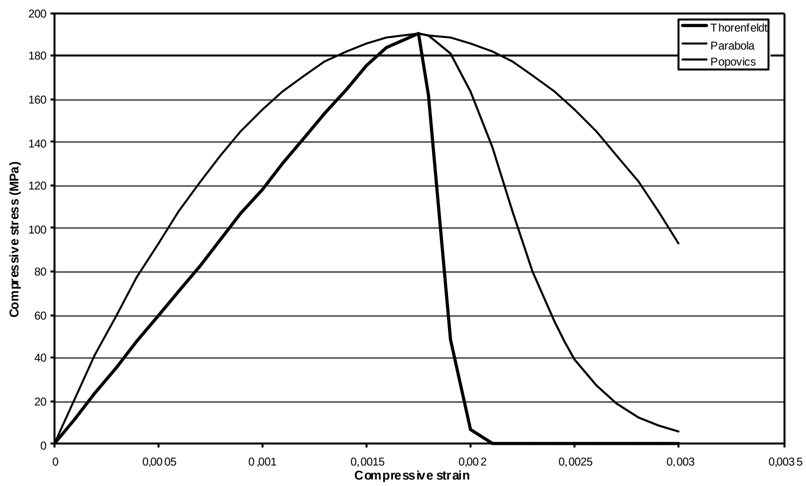

Figure 8.17. Compressive stress-strain curves for C180/210 UHPFRC

The tensile behaviour is based on the values as found by Redaelli and Muttoni [67]. They are represented in the Figure 8.20. In the figure it can be seen that the strain hardening branch is introduced by adding a linear branch beyond the elastic branch in the stress-strain relation. After hardening phase, the strain softening initiates and the relation changes to a stress-crackwidth relation.

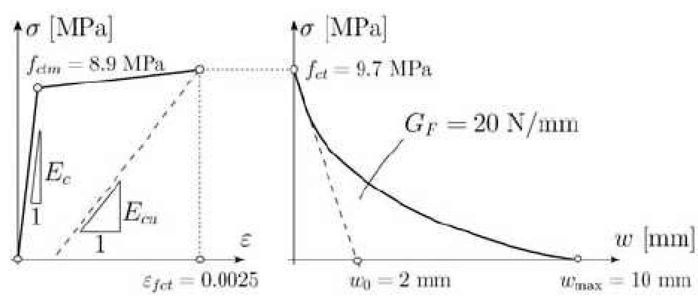

Figure 8.18. Axial tensile behaviour of a BSI C180/210 mixture, Redaelli and Muttoni 2007

The material behaviour as seen in Figures 8.17 and 8.18 is simplified in accordance with the French codes to a multi-linear stress-strain relation, a combination of Figure 8.15 and 8.16. The characteristic points of the compressive branch are tabulated in Table 8.7. For the tensile regime the values as seen in Figure 8.20 are used. The strain softening branch seen in Figure 8.18, caused by continuous pullout of fibres, is approximated with a bi-linear law. The value of the tensile strength at the point of *2 mm* crackwidth is determined using the fracture energy as denoted in Figure 8.18.

The values obtained from Figure 8.18 are captured in Table 8.8.

Component			
Characteristic tensile strength at point t1	f_{ct1}	+8.9	MPa
Characteristic tensile strength at point t2	f_{ct2}	+9.7	MPa
Characteristic tensile strength at point t3	f_{ct3}	+2.0	MPa
Tensile strain at point t1	ε_{ct1}	0.148	‰
Tensile strain at point t2	ε_{ct2}	2.5	‰
Crack opening at point t3	w_0	2	mm
Ultimate crack opening	w_{max}	10	mm

Table 8.8. Characteristic axial tensile strengths from Redaelli and Muttoni [67]

For the flexural tensile strength of UHPFRC, the values of Table 8.8 may also be converted using relation (8.7). However, doing so, the obtained values are significant lower than the values found at the material properties of Ductal and BSI on the internet. The main reason is that the flexural strengths obtained by both French companies are misleading. They assumed that the advantageous low-level post-cracking plateau, which allows for much larger cross-sectional rotations, can be introduced in the calculation by increasing the pre-cracking material flexural tensile strength. In other words, they propose to add cracked properties to uncracked properties. The graphical explanation of their method is seen in Figure 8.19.

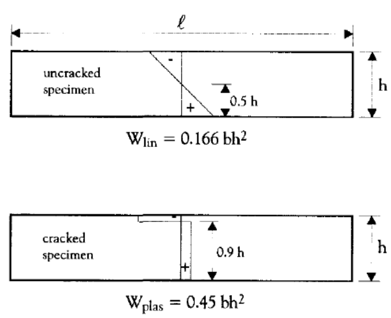

$$f_{fct,plas} = \frac{0.166\ bh^2}{0.45\ bh^2} \cdot f_{fct,lin} = 0.37 \cdot f_{fct,lin}$$

Figure 8.19. Section modulus in cracked and uncracked state, Kooiman 2000

In Figure 8.19 it is seen that the translation from plastic to elastic deformation is based on the assumption that the depth of the compression zone is approximately *1/10* of the beam depth or structural thickness. Thus, the equivalent linear-elastic flexural tensile stress can be determined by multiplying the plastic flexural tensile stress with *1/0.37 = 2.7*.

Though, they reached reasonable agreement with their experimental tests as they have chosen their specimen dimensions such that the factor which results from equation (8.7) is almost at maximum. Obviously, such low cross-sectional heights are not representative for structures that appear in practice. Hence, the extremely high flexural tensile strengths can be questioned and are of little practical value.

8.3 Conclusions

To obtain an answer to the question whether high strength fibre reinforced concrete can contribute to more slender shells in this chapter two mixtures are designed. A reference conventional concrete mixture with a relatively low quality is selected to ally with concrete technology available at the time the Zeiss planetarium was constructed and an ultra high performance fibre reinforced mixture. The conventional concrete mixture selected is a C20/25 mixture (cylindrical compression strength/cube compression strength) which is characterised by a rounded compression curve with, after a linear branch, strain hardening, strain softening and finally compressive crushing, respectively. The behaviour in compression can, for example, be described by a Thorenfeldt, parabola or Eurocode 2 curve. The tensile behaviour is characterised by concrete cracking and rebar yielding and determined by the axial concrete tensile strength and the amount of reinforcement in the cross-section. The interaction between the cracked concrete and bonded reinforcement is complicated and non-isotropic and impossible to capture within a single constitutive law. The material properties of the C20/25 mixture and FeB220 HWL steel reinforcement can be found in table 8.1 and 8.2.

High strength fibre reinforced concrete is a relative new development in concrete technology and still subject to many researches. An optimised mixture composition allows for much higher strengths than conventional concrete compositions. The selected high strength mixture is a C180/210 mixture for which the compression curve can, for example, be described by a Thorenfeldt curve or a bi-linear law according to the French codes. Opposite to the profoundable high compression strength, the material is highly brittle in tension. To counteract the brittleness, fibres are added, needle shaped elements manufactured from materials such as steel or plastics. Fibres work both on micro-level, as reinforcement of the cement matrix, as on macro-level as reinforcement of the structure providing in an advantageous low-level post-cracking plateau. Therefore, fibres can reduce the amount of reinforcement or even totally substitute the reinforcement as in the selected C180/210 mixture. Opposite to conventional steel rebars, fibre addition allows for the modelling of the tensile behaviour within one constitutive law, e.g. the multi-linear law as defined in the French codes, as a fibre reinforced concrete behaves more like an isotropic material with a large amount of small cracks. The fibres have only minor influence on the compressive behaviour and, hence, the compression curve is only determined by the concrete properties. The material properties of the C180/210 mixture can be found in table 8.7 and 8.8.

9 Loading

Before going into analysis, the loads on the shell must be determined. As it is not known on forehand which load, or combination of loads, will challenge the shell to the limit, several loads are defined here. Loads can be classified by their variation in time into *permanent*, *variable*, *accidental* and *time dependent* loads. Aforementioned in Chapter 3, time dependent effects such as *creep*, *shrinkage* and *temperature gradients* are not considered, although they might have severe influence on the structural failure of a shell. The loads that are discussed are referred to as *static* loads as they do not change in time.

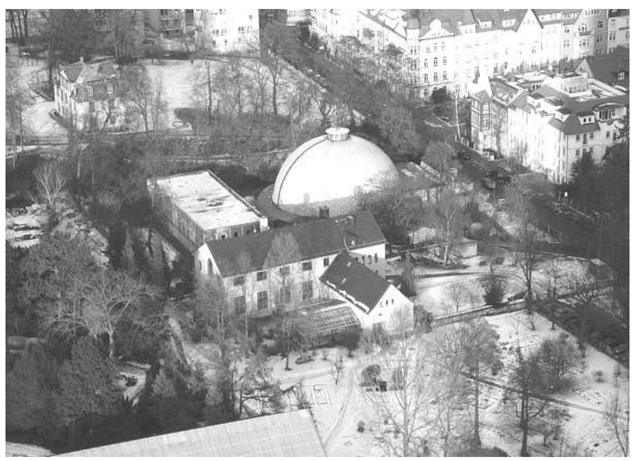

Figure 9.1. The Zeiss planetarium in Jena, Germany

When determining (static) loads on a structure, the basic parameters include the magnitude of the load, the direction of the load and the location of the load. These parameters are determined according to the Eurocode 2. To provide in a proper explanation the loads are determined for the Zeiss planetarium in Jena, described in Chapter 7. Similar to Chapter 8, no safety factors are applied in order to approach the real behaviour of the structure as closely as possible.

9.1 Permanent Loads

The permanent load is assumed to act vertically over the shell surface. In general, the load consists out of the dead weight of the shell and possible finishing such as insulation or cladding. However, it is assumed that the shell does not contain any finishing, thus, the permanent load only consists out of the dead weight. The dead weight is determined by multiplying the shell area times the thickness times the specific weight. The values for the specific weight are obtained from the previous chapter. The conventional concrete has a specific weight of *2500 kg/m³* and the UHPC has a specific weight of *2800 kg/m³*. The values include the additional weight of reinforcement.

Zeiss Planetarium	Specific weight (kN/m^2)
C20/25	1.50
UHPC	1.68

Table 9.1. Specific weight of concrete

The shell covering the Zeiss planetarium has a thickness of *60 mm*, as can be seen in Table 7.1. Depending on the type of concrete, the dead weight of the shell can be seen in Table 9.1.

9.2 Variable Loads

The variable loading on the shell is covered by wind load and snow load. They are discussed in the following.

9.2.1 Wind Load

Wind action is represented by a simplified set of pressures whose effects are equivalent to the extreme effects of the turbulent wind. Wind load is an example of a non-axisymmetric load. In shell structures subjected to loading which is not axisymmetric, the meridional curves and parallel circles do no longer present the *principal directions* of the internal stresses as there is a nonzero membrane shear force field, as well as normal membrane forces. Thus, the so-called *stress trajectories* transform under the influence of wind load. Other examples of non-axisymmetric loadings are earthquake effects and temperature gradients.

The wind load is determined according to the Eurocode 2 EN 1991-1.4. Wind loads act, by definition, perpendicular to the shell surface. Depending on the wind direction, some areas of the shell structure are subjected to wind pressure or wind suction. The basis for calculation is a basic wind velocity depending on the wind climate. The basic values are characteristic values having annual probabilities of exceedence of *0.02*, which is equivalent to a *mean return period* of *50* years. To determine the effect of wind on a structure, the basic wind velocity is transformed to a wind pressure acting on the external surfaces while taking into account for size, shape and dynamic properties as well as landscape effects like terrain roughness and orography.

Peak Velocity Pressure

As is recommended by the Eurocode 2 EN 1991-1.4, Chapter 4.2, the basic wind velocity v_b depends on the fundamental value of the basic wind velocity $v_{b,o}$. The fundamental value is, however, unknown for the city of Jena in the east of Germany. There is chosen for a wind speed of *27 m/s* which corresponds to a wind speed of a *10* Beaufort storm. This value is similar to the value as proposed by the Dutch codes for wind region *2* (e.g. coastal areas near Delft) with a return period of *50* years. Hence, the wind speed is considered to be a save choice. According to the Eurocode basic wind velocity is:

$$v_b = c_{dir} \cdot c_{season} \cdot v_{b,o} \tag{9.1}$$

To determine the peak velocity pressure, Eurocode 2 EN 1991-4.5 suggests the relation:

$$q_p(z) = c_e \cdot \tfrac{1}{2} \cdot \rho \cdot v_b^2 \tag{9.2}$$

In which ρ represents the air density, recommended equal to $1.25\ kg/m^3$, and c_e is the exposure factor depending on the height and terrain roughness, determined according to Figure 9.2.

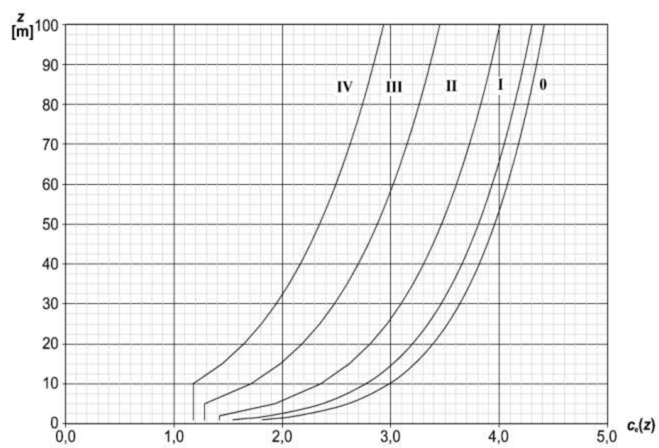

Figure 9.2. The exposure factor c_e according to figure 4.2 of Eurocode 2 EN 1991-1.4

For the city of Jena, in the east of Germany, there is chosen for terrain category III, which refers to areas with regular cover of vegetation or building. With a height of *17 m* the exposure factor is approximately equal to *2.2*. When implemented in equation (9.2) the peak velocity pressure becomes:

$$q_p(z) = 2.2 \cdot \tfrac{1}{2} \cdot 1.25 \cdot 27^2 = 1002\ kg/ms^2 = 1\ kN/m^2$$

Wind Pressure on Surfaces

The final step is to determine the wind pressures on the structure. Wind actions are determined taking into account of both external and internal actions. However, as the inside of the Zeiss planetarium shell is not accessible to wind, the internal part is neglected. Chapter 5 of the Eurocode 2 EN 1991-1.4 suggest the following relation for the external wind pressure:

$$w_e = q_p(z_e) \cdot c_{pe} \tag{9.3}$$

Here, $q_p(z_e)$ is the peak velocity pressure at reference height z_e and c_{pe} is the pressure coefficient for the external pressure. The reference height is set equal to the maximum height of the shell.

For the external pressure coefficient, the Eurocode provides in various values depending on the geometrical shape of the structure. For domes with circular base the values of c_{pe} can be determined using Figure 9.3. In the figure the coefficient is denoted as $c_{pe,10}$ which refers to the fact that the pressure coefficient depends on the size of the loaded area A, which is the area of the structure, that produces the wind action in the section to be calculated. The external pressure coefficient is given for loaded areas A of $1\ m^2$ (local, denoted by $c_{pe,1}$) and $10\ m^2$ (global, denoted by $c_{pe,10}$).

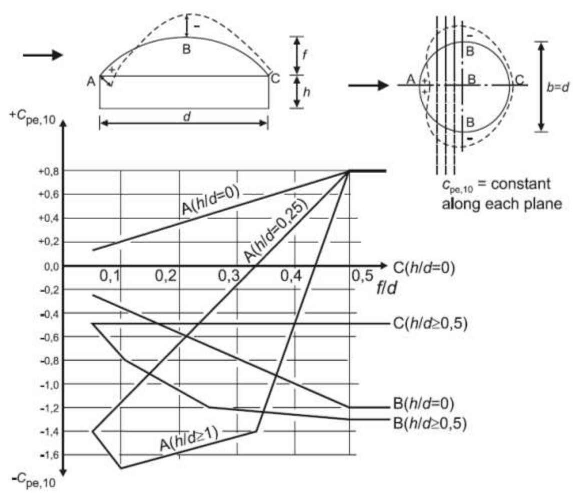

Figure 9.3. The external pressure coefficient $c_{pe,10}$ according to figure 7.12 of Eurocode 2 EN 1991-1.4

For the shell over the Zeiss planetarium, the value of f/d is equal to 0.5. Depending on the location on the shell surface, the external pressure coefficient becomes:

Region	$C_{pe,10}$	w_e (kN/m²)
A	+0.8	+0.8
B	-1.2	-1.2
C	0.0	0.0

Table 9.2. External pressure coefficient

The regions A, B and C on the shell surface are still to be located. As the Eurocode does not give any recommendations for domes, the distribution as suggested for *vaulted roofs* is used, see Figure 9.4.a, however, projected on a hemispherical cap. This means that turning point of wind pressure to wind suction is located at one fourth of the dome at *45 degrees*, Figure 9.4.b. Note that the wind load of Figure 9.4.b. shows a stepwise transition between region A and B.

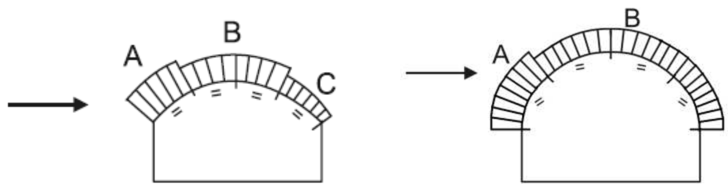

Figure 9.4.a. The distribution suggested for vaulted roofs and b. the distribution on the Zeiss planetarium

For the circumferential distribution of the wind load, there is chosen for an opening angle of *30 degrees* on each side, thus, a total angle of *60 degrees*, see Figure 9.5. The transition between wind pressure and wind suction is smooth, however, a stepwise transition is assumed for simplicity.

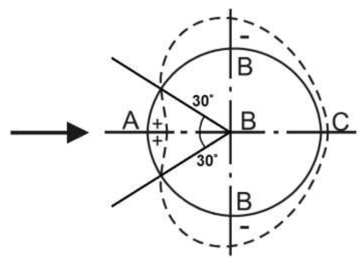

Figure 9.5. Wind distribution in circumferential direction

The wind load on the Zeiss planetarium shell is defined.

9.2.2 Snow load

Snow load is assumed to act vertically and refers to a horizontal projection of the roof area. Whether the snow is distributed over the total surface of the shell or not, depends on the curvature of the shell and possible drift of the snow. The load situation after the snow has been moved from one location to another (drift), e.g. by the action of the wind, can be highly onerous. The magnitude of the snow load largely depends on the location of the shell. The Eurocode recognises *8 climatic regions* throughout entire Europe. The largest snow loads are found in the Alpine region. Furthermore, the magnitude of the load depends on the bulk weight density of the snow as it varies with the duration of the snow cover and possible rainfalls with consecutive melting and freezing. The snow load is determined according to the Eurocode 2 EN 1991-1.3.

Characteristic Value

To determine the snow load on a structure, first the characteristic snow load on the ground must be determined. The characteristic value of snow on the ground at the relevant site follows from *Annex C* in the

Eurocode EN 1991-1.3. The value is the result of scientific work carried out by a specially formed research group. The characteristic values of ground snow loads given are referred to *mean recurrence interval* (MRI) equal to *50 years* (also based on annual probability of exceedence of *0.02*).

In *Annex C* a relation for the characteristic value of snow on the ground is recommended for each of the *8* climatic regions. The city of Jena falls under the climate region '*Central East*' and subsequently, the characteristic value is described by:

$$s_k = (0.264\,Z - 0.002)\left[1 + \left(\frac{A}{256}\right)^2\right] \tag{9.4}$$

Here, *Z* is a zone number from Figure *C.3* of *Annex C* and *A* stands for the attitude above sea level. The city of Jena lies in zone number *2* on *155 m* above sea level. The characteristic value becomes:

$$s_k = (0.264 \cdot 2 - 0.002)\left[1 + \left(\frac{155}{256}\right)^2\right] = 0.72\ kN/m^2$$

According to the table in *Annex E* of the Eurocode EN 1991-1.3, the bulk weight density increases with the duration of the snow cover, represented in Table 9.3. When the characteristic value is compared to the bulk weight density, there may be a snow layer of *720 mm* fresh snow on top of the shell.

Type of snow	Bulk weight density [kN/m³]
Fresh	1,0
Settled (several hours or days after its fall)	2,0
Old (several weeks or months after its fall)	2,5 – 3,5
Wet	4,0

Table 9.3. Mean bulk weight density of snow according to Annex E of the Eurocode EN 1991-1.3

Snow Loads on Surfaces

The snow load on the shell depends, besides the characteristic value, on the arrangement of the snow over the surface. Snow load can be deposited on a roof in many different patterns. Hereby, there is referred to *undrifted* snow load (*Case I*) and *drifted* snow load (*Case II*), both represented in Figure 9.6. In particular situations this can lead to a combination of exceptional snow falls and drifts which consequently lead to areas with exceptional snow load. For the hemispherical cap the latter is, however, not of interest.

The snow load on a surface can be determined by:

$$s_k = \mu_i \cdot C_e \cdot C_t \cdot s_k \tag{9.5}$$

Where, μ_i is the roof shape coefficient, C_e the exposure coefficient, C_t the thermal coefficient and s_k the previously defined characteristic value of the snow load on the ground.

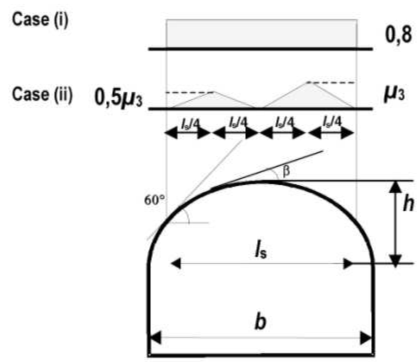

Figure 9.6. Snow load shape coefficients for cylindrical roof, figure 5.6 of Eurocode 2 EN 1991-1.3.
As a reference, according to the Dutch codes, the snow must be applied at regions up to *30 degrees*.
From *30* to *60 degrees*, the snow load may decrease linearly to zero.

The recommended value for the exposure coefficient C_e following from table 5.1 EN 1991-1.3 for normal topography equals *1.0*. Moreover, the value of the thermal coefficient C_t also equals to *1.0* as the thermal transmittance of concrete is lower than $1\ W/m^2K$. Thus, relation (9.5) simplifies to:

$$s_k = \mu_i \cdot s_k \tag{9.6}$$

The roof shape coefficient is defined for different shapes. For cylindrical shaped roofs, the value of μ is equal to *0.8* for the undrifted case (Case I), while for the drifted case the value is equal to:

For $\beta > 60°$, $\mu_3 = 0$
For $\beta \leq 60°$, $\mu_3 = 0.2 + 20\, h/b$

An upper value of $\mu_3 = 2$ is recommended for rise to span ratios larger than *0.18* (see Figure 9.7).

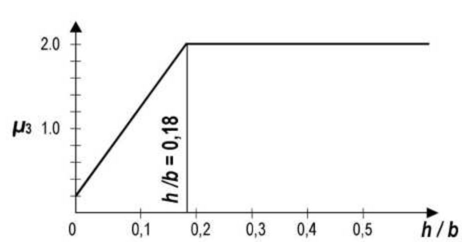

Figure 9.7. Snow load shape coefficient for cylindrical roofs (for β ≤ 60°) of figure 5.5 of Eurocode 2 EN 1991-1.3

For the Zeiss hemisphere, with a rise to span ratio of 0.5, μ_3 is equal to 2. In Table 9.4 the resulting snow loads on the shell are tabulated.

Load case	Magnitude [kN/m²]
Case I (Undrifted)	0.58
Case II (Drifted)	1.44 (max)
	0.72 (min)

Table 9.4. Snow loads on the Zeiss planetarium shell

9.3 Accidental Loads

Accidental loads may cause highly uninvited stresses and bending moments in the shell. Though, they are not considered here. The effect of accidental loading, in particular accidental loading that appears like a point load on the shell surface, is, however, included in the analysis by the introduction of *initial geometrical imperfections*. They are discussed in Chapter 10 and 12.

9.4 Load Cases

The loading scheme of the shell covering the Zeiss planetarium is illustrated in Table 9.5 in which the loads as defined in this chapter are combined in several *load combinations*. The load combinations follow from reasonable thinking, e.g. because there is little chance that wind and snow load have their maximum at the same time, they are divided into different load cases. The loads are not multiplied with a safety factor to approximate the structural behaviour as close as possible.

LC	Dead weight	Wind	Undrifted Snow	Drifted Snow
1	x			
2	x	x		
3	x		x	
4	x			x

Table 9.5. Load cases for the analysis of the Zeiss planetarium shell

9.5 Conclusions

In the foregoing the permanent dead weight load and variable wind and snow load are determined for the Zeiss planetarium in Jena constructed out of conventional and UHPFRC (see Chapter 8). Furthermore, the loads are combined into four basic load combinations. Comparing the load intensities, it can already be concluded that the dead weight of the shell is the main load, pointing in vertical direction.

10 Hemispherical Example

The Zeiss planetarium shell as discussed in Chapter 7 is used to apply the linear elastic theory as described in Chapter 5 and the buckling theory as discussed in Chapter 6 in this chapter in a numeric example. Therefore, in this chapter several computations are performed on the Zeiss' hemispherical shell shape. The results serve as benchmark for the finite element results discussed in Chapter 12.

Aforementioned, the Zeiss planetarium is a hemispherical shell and the hemispherical shape is extensively discussed in literature. The fact that the hemisphere is widely discussed can simply be explained. Usually *10* stress resultants are considered to act on the shell element. Membrane stress resultants remain as shown in Figure 5.11, while non-membrane stress resultants are the out-of-plane shear stresses and bending moments, similar to the plate bending problem. Because there are only *6* equilibrium equations, the shell in bending is statically indeterminate. However, if the loads are axisymmetric, the twisting moments, in-plane shear forces, and the transverse shear forces on the meridional planes are zero. The shell turns into a statically determined problem.

For the numeric example the original design of the Zeiss planetarium is modelled in different ways. The linear elastic theory is applied on a shell subjected to a uniformly distributed vertical load with varying support conditions to investigate the effect of the so-called edge disturbances. The sequence of supports may in short be named as roller supports, inclined-roller supports and a hinged and clamped supports. The different models are numbered *Zeiss 1* to *4*, respectively, and the same numbering will return in Chapter 12 to 15. Opposite to the vertical 'civil engineering' load, e.g. the dead weight of the shell, a uniformly distributed spherical load is used for the calculation of the linear critical buckling load. The spherical load is applied in combination with an inclined-roller support, as if the shell is a complete sphere, as almost all of the buckling investigations are directed towards spheres and radial pressure loads (originating from the aeroplane industry)

Thus, in this chapter the linear stresses, strains and displacements are determined for a vertically loaded shell with varying support conditions and the linear critical buckling is determined for a shell under radial pressure load, restricted to an inclined-roller support condition. Moreover, the spherically loaded inclined-roller supported shell also serves as basis for a nonlinear buckling discussion.

10.1 Shell Parameters

10.1.1 Geometry

Recapitulate from Chapter 7; the shell covering the Zeiss planetarium in Jena has a radius of *12500 mm*, a thickness of *60 mm*.

10.1.2 Material

The numeric example is elastic based. Hence, the material is modelled as infinite elastic and the only material parameters that have to be defined are the Young's modulus of elasticity, the Poisson's ratio and the specific weight. Recapitulate from Chapter 8, for the conventional C20/25 mixture the Young's modulus is *30 GPa* whereas the C180/210 mixture has a Young's modulus of *60 GPa*. The specific weights are *2500* kg/m^3 and *2800* kg/m^3, respectively. For simplicity, the Poisson's ratio is equal to zero.

10.1.3 Support

The shell of the Zeiss planetarium is, aforementioned in Chapter 7, assumed to be based on a continuous clamped support. To illustrate characteristic shell behaviour, or in case of the buckling analysis, to ally with the experiments, the shell behaviour will be determined with different types of supports also, namely, a roller support, inclined-roller support, a pinned support and a clamped support.

10.1.4 Loading

The loading is previously derived in Chapter 9. For the hand calculation, the load on the structure is simplified to an equally distributed vertical load over the total shell surface with the magnitude of the dead weight of the shell and the undrifted snow load. Except for the buckling analysis, where the load is an equally distributed spherical load with a dummy magnitude equal to *1.0 MPa*.

Load	Magnitude (kN/m^2)
Specific weight C20/25	1.5
Undrifted snow load	0.58
Total	2.08

Table 10.1. Load on the shell as used in hand calculation

10.2 Analysis Scheme

The various linear analyses done are described in Table 10.2. The Zeiss 2 shells appears twice as it is first considered subjected to vertical load for the stresses, strains and displacements, while later is loaded by a spherical compression load to determine the linear critical buckling load.

Name	Loading Conditions	Supporting Conditions	Type of Analysis
Zeiss 1	Vertical load	Roller	Linear Elastic
Zeiss 2	Vertical load	Inclined-roller	Linear Elastic
Zeiss 3	Vertical load	Hinged	Linear Elastic
Zeiss 4	Vertical load	Clamped	Linear Elastic
Zeiss 2	Spherical load	Inclined-roller	Linear Buckling

Table 10.2. Analysis scheme

10.3 Linear Analysis

The theoretical solution is based on the relations found in Chapter 5. The relations are for shells with arbitrary curvature which are described using a global coordinate system. A spherical shell can be described as non-shallow and is a thin shell of revolution; it is generated by rotating a curve (meridian) over a vertical axis of revolution. For simplification the general coordinate system is changed to a local polar coordinate system when the membrane stress field is to be determined. In the local polar coordinate system the *z-axis* points outward of the shell surface, the *x-axis* is the meridian direction and the *y-axis* the circumferential direction. In the description the x and y terms are replaced by ϕ and θ respectively, see Figure 10.1. As mentioned in Chapter 5, the total solution to the behaviour of the shell consists out of the membrane solution and the bending solution. For performing a solution to the shell in bending the global coordinate system is more convenient. As only in the bending solution the influence of different support conditions will be seen, the membrane solution is valid for all Zeiss shell types.

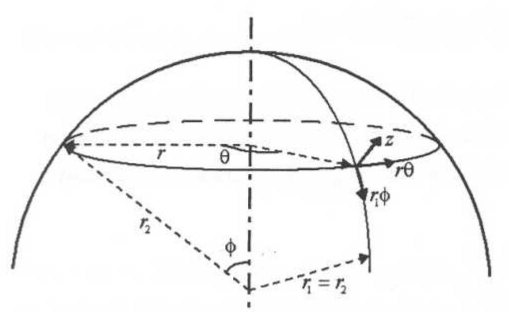

Figure 10.1. Geometry and coordinate system of a spherical shell of revolution, Hoefakker and Blaauwendraad 2003

10.3.1 Membrane Behaviour

For the membrane behaviour, first the general relations for a thin shell of arbitrary curvature are recapitulated from Chapter 5. As explained, the general relations with global coordinate system are rewritten for a shell of revolution with local polar coordinate system. Comparing the new coordinate system with the conventional system, it is observed that $dx = r_1 d\phi$ and $dy = rd\theta$. Since the edges of the shell of revolution are often in the θr-plane, an extra displacement u_r is introduced, perpendicular to the axis of revolution (Figure 10.2). Because of axisymmetry, displacement and rotational terms in the *θ-direction* become zero and, therefore, are left out of the relation. For the same reason, the load component p_θ, the derivative $\partial / \partial\theta$ and the longitudinal shearing stress resultant $n_{\phi\theta}$ are set equal to zero.

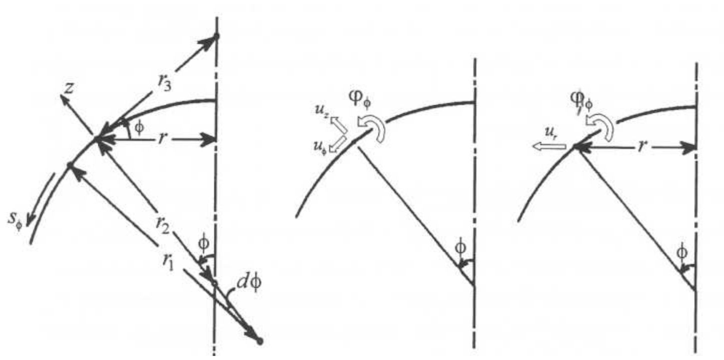

Figure 10.2. Geometry of the meridian and positive directions of the displacements, Hoefakker and Blaauwendraad 2003

The meridional strain of a small part of a shell of revolution is dependent on the elongation of an element due to the tangential displacement u_ϕ and the normal displacement u_z. The elongation of the element due to the difference in the normal displacement u_z at each end of the element is of second order and, therefore, negligible. The meridional strain becomes:

$$\varepsilon_{\phi\phi} = \frac{1}{r_1}\left(\frac{\partial u_\phi}{\partial \phi} + u_z\right) \tag{10.1}$$

Which is equal to the strain relation (5.30) found in Chapter 5 for a shell in extension.

The strain in *θ-direction* is, due to the axisymmetry, also determined by the tangential and normal displacement only. The tangential displacement causes an elongation of the horizontal radius r in circumferential direction. The strain contribution can thus be calculated by dividing the elongation $dr = u_\phi \cos\phi$ by the original radius $r = a \sin\phi$. The circumferential strain becomes:

$$\varepsilon_{\theta\theta} = \frac{1}{r_2}\left(u_\phi \cot\phi + u_z\right) \tag{10.2}$$

Combining equation (10.1) and (10.2) and setting $r_3 = r_2 \tan\phi$ yields the kinematic relation for a shell of revolution in polar coordinates:

$$\begin{bmatrix} \varepsilon_{\phi\phi} \\ \varepsilon_{\theta\theta} \end{bmatrix} = \begin{bmatrix} \frac{1}{r_1}\frac{\partial}{\partial\phi} & \frac{1}{r_1} \\ \frac{1}{r_3} & \frac{1}{r_2} \end{bmatrix} \begin{bmatrix} u_\phi \\ u_z \end{bmatrix} \tag{10.3}$$

The constitutive relations are equal to the relations derived in Chapter 5 omitting the shear terms, thus:

$$\begin{bmatrix} n_{\phi\phi} \\ n_{\theta\theta} \end{bmatrix} = \frac{Et}{1 - \nu^2} \begin{bmatrix} 1 & \nu \\ \nu & 1 \end{bmatrix} \begin{bmatrix} \varepsilon_{\phi\phi} \\ \varepsilon_{\theta\theta} \end{bmatrix} \tag{10.4}$$

And

$$\begin{bmatrix} \varepsilon_{\phi\phi} \\ \varepsilon_{\theta\theta} \end{bmatrix} = \frac{1}{Et} \begin{bmatrix} 1 & -\nu \\ -\nu & 1 \end{bmatrix} \begin{bmatrix} n_{\phi\phi} \\ n_{\theta\theta} \end{bmatrix} \tag{10.5}$$

Finally, the equilibrium relations can be obtained from Figure 10.3. The load component p_z and p_ϕ must be in equilibrium with the constant circumferential stress resultants $n_{\theta\theta}$ and the meridional stress resultants $n_{\phi\phi}$. Additional, the meridional load component p_ϕ must be in equilibrium with the increase of the meridional stress resultant $\frac{dn_{\phi\phi}}{d\phi} d\phi$. Because the load component in circumferential direction is equal to zero and the equilibrium of forces in the circumferential direction needs not to be investigated due to the constant stress resultant $n_{\theta\theta}$, the equilibrium relations simplify to a statically determinate system with two unknown stress resultants and two load components.

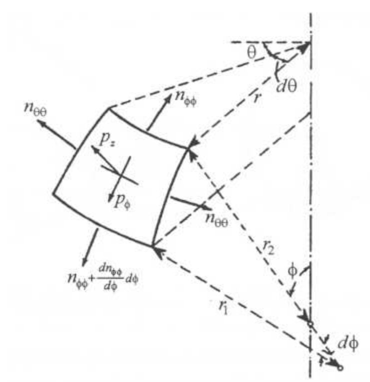

Figure 10.3 Load components and stress resultants on an infinitesimal element, Hoefakker and Blaauwendraad 2003

The equations of equilibrium for an infinitesimal shell element become:

$$\frac{d(n_{\phi\phi} r)}{d\phi} - n_{\theta\theta} r_1 cos\phi + p_\phi r r_1 = 0 \qquad \text{and}$$

$$-\frac{n_{\phi\phi}}{r_1} - \frac{n_{\theta\theta}}{r_2} + p_z r = 0 \tag{10.6}$$

The equations can also be written in matrix notation:

$$\begin{bmatrix} -\frac{1}{r_1}\frac{d}{d\phi} & \frac{1}{r_3} \\ \frac{1}{r_1} & \frac{1}{r_2} \end{bmatrix} \begin{bmatrix} n_{\phi\phi} r \\ n_{\theta\theta} r \end{bmatrix} = \begin{bmatrix} p_\phi r \\ p_z r \end{bmatrix} \tag{10.7}$$

Relation (10.7) could also have been obtained directly by determining the adjoint matrix from the kinematic relation (10.3).

10.3.2 Membrane Stress Resultants

Because of the statically determinate system, the stress resultants can be derived directly from the equilibrium equations. By eliminating the circumferential stress resultant in the equation (10.6) after multiplying the first equation by $sin\phi$ and the second with $cos\phi$, the vertical equilibrium for a shell part limited by two adjacent parallel circles with radius r at distance $d\phi$ from each other is found.

$$\frac{d\left(n_{\phi\phi} r\right)}{d\phi} \sin\phi + n_{\phi\phi} r \cos\phi = \frac{d\left(n_{\phi\phi} r \sin\phi\right)}{d\phi} = \left(p_z \cos\phi - p_\phi \sin\phi\right) r r_1 \tag{10.8}$$

The meridional stress resultant is found by integration of equation (10.8).

$$n_{\phi\phi} = \frac{1}{r \sin\phi} \int \left(p_z \cos\phi - p_\phi \sin\phi\right) r r_1 \, d\phi \tag{10.9}$$

Consequently, the circumferential stress resultant can be obtained by substitution of expression for $n_{\phi\phi}$ in equation (10.6).

$$n_{\theta\theta} = p_z \, r_2 - \frac{1}{r_1 \sin^2\phi} \int \left(p_z \cos\phi - p_\phi \sin\phi\right) r r_1 \, d\phi \tag{10.10}$$

The membrane solution is hereby obtained.

For a spherical shell of revolution under uniform vertical load over the shell surface the exact values of the stress resultants can be obtained. The geometry of a spherical shell can be described with only one radius:

$$r_1 = r_2 = a$$
$$r = a \sin\phi$$

Furthermore, the load components of the vertical load read:

$$p_z = -p \cos\phi$$
$$p_\phi = p \sin\phi$$

Hence, the expressions for the internal forces, (10.9) and (10.10) can be rewritten and integrated to:

$$n_{\phi\phi} = pa\left(\frac{\cos\phi - 1}{\sin^2\phi}\right) + \frac{C}{a \sin^2\phi}$$

$$n_{\theta\theta} = -pa\cos\phi - pa\left(\frac{\cos\phi - 1}{\sin^2\phi}\right) - \frac{C}{a\sin^2\phi}$$

Using the relation $\sin^2\phi = 1 - \cos^2\phi$ this can be rewritten to:

$$n_{\phi\phi} = -pa\frac{1}{1+\cos\phi} + \frac{C}{a\sin^2\phi}$$

$$n_{\theta\theta} = pa\left(\frac{1}{1+\cos\phi} - \cos\phi\right) - \frac{C}{a\sin^2\phi}$$

The constant term C must be equal to zero, considering that the term becomes infinite for $\phi = 0$. Thus, the equations simplify to:

$$n_{\phi\phi} = -pa\frac{1}{1+\cos\phi} \tag{10.11}$$

$$n_{\theta\theta} = pa\left(\frac{1}{1+\cos\phi} - \cos\phi\right) \tag{10.12}$$

The stress resultants for a spherical shell subjected to uniform vertical load are now derived. The meridional stress resultants are always compression stresses. The circumferential stresses, however, change from compression to tension, as is visualised in Figure 10.4.

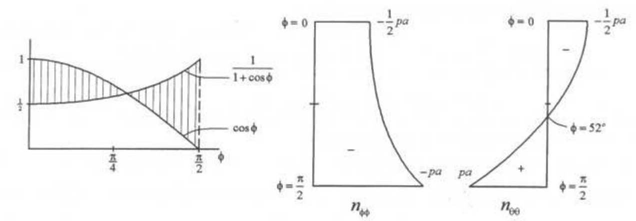

Figure 10.4. Distribution of the stress resultants for a spherical shell under vertical load, Hoefakker and Blaauwendraad 2003

Figure 10.4 shows the meridional stress resultants and the circumferential stress resultants for a spherical shell under vertical load that can move freely at its base, i.e. roller supported (Zeiss 1). At the top and base of the shell, both stress resultants give the same value, however, at the base the circumferential stress resultants are of opposite sign. It can be calculated, using equation (10.12) that the stresses change sign at 52° from the top of the shell. Thus, when the shell is constructed, reinforcement must be placed in the lower part of the shell structure. It can be concluded, that when the shell stops at 52° the shell is completely in compression. Then, theoretically, no reinforcement is necessary.

The membrane stress resultants of the Zeiss planetarium shell, caused by the load of section 10.1.4, become:

Stress resultants	$\phi = 0$ (top)	$\phi = 90$ (base)	
$n_{\phi\phi}$	-13	-26	N/mm'
$n_{\theta\theta}$	-13	+26	N/mm'

Table 10.3. Membrane stress resultants for spherical shell with vertical load

Assuming an equally distributed stress over the thickness of the shell, the stresses become:

Stresses	$\phi = 0$ (top)	$\phi = 90$ (base)	
$\sigma_{\phi\phi}$	-0.217	-0.433	N/mm²
$\sigma_{\theta\theta}$	-0.217	+0.433	N/mm²

Table 10.4. Membrane stresses for spherical shell with vertical load

As can be seen, the membrane stresses with conventional load are extremely low. The stresses even do not violate the tensile strength of the plain concrete; hence, there is no structural need for reinforcement at all.

10.3.3 Membrane Strains

Using relation (10.5), the expressions for the membrane strains become:

$$\varepsilon_{\phi\phi} = \frac{1}{Et}\left(n_{\phi\phi} - \nu n_{\theta\theta}\right) \tag{10.13}$$

$$\varepsilon_{\theta\theta} = \frac{1}{Et}\left(n_{\theta\theta} - \nu n_{\phi\phi}\right) \tag{10.14}$$

The strains can easily be obtained with the values of the stress resultants from Table 10.4.

Strains	$\phi = 0$ (top)	$\phi = 90$ (base)	
$\varepsilon_{\phi\phi}$	-0.00722	-0.0144	‰
$\varepsilon_{\theta\theta}$	-0.00722	+0.0144	‰

Table 10.5. Membrane meridional- and circumferential strains for spherical shell with vertical load

These strains are also extremely low values and the shell will almost experience no extension or contraction.

10.3.4 Membrane Displacements

The linear translational and rotational displacements of the shell of revolution are seen in Figure 10.2. The quantities of highest interest are the displacements at the top and the displacement and rotation at the base radius of the shell.

From equation (10.1) and (10.2) can be derived that the equation for the displacement u_z at the top of the shell reads:

$$u_{z,top} = \varepsilon_{\phi\phi} r_1 + \varepsilon_{\theta\theta} r_2 \tag{10.15}$$

It can be shown that after filling in the expressions for the radii of curvature and the integrated strain energy in both directions, and subsequently setting Poisson's ratio equal to zero, the equation becomes:

$$u_{z,top} = 2\frac{pa^2}{Et} \tag{10.16}$$

The translation u_r can be calculated multiplying the strain in circumferential direction with the radius r. Because $r = r_3\, cos\phi = r_2\, sin\phi$ the translation u_r can be described by:

$$u_r = \varepsilon_{\theta\theta} r = u_\phi\, cos\phi + u_z sin\phi \tag{10.17}$$

For axisymmetric loading only the rotation φ_ϕ in the ϕr-*plane* needs to be derived. The rotation is dependent of the meridional displacement u_ϕ and the normal displacement u_z. The rotation due to the meridional displacement is a positive rotation of the tangent, being u_ϕ / r_1. The uniform normal displacement does not contribute to the rotation, however, the additional normal displacement does. The additional displacement $\frac{du_z}{d\phi} d\phi$ divided by the length of a surface element $r_1 d\phi$ yields a negative rotation. Thus rotation φ_ϕ, becomes:

$$\varphi_\phi = \frac{1}{r_1}\left(u_\phi - \frac{du_z}{d\phi}\right) \tag{10.18}$$

Equation (10.18) describes the displacement of the spherical shell. However, it provides in a relation where the meridional and normal displacement must be known. A more useful expression for the rotation can be obtained by direct derivation from the strains. Therefore, the displacement u_z is eliminated from the equations (10.1) and (10.2) and, subsequently, the relations are multiplied by $cot\phi$ which results in the expression:

$$\frac{du_\phi}{d\phi} cot\phi - u_\phi cot^2\phi = cot\phi\left(\varepsilon_{\phi\phi} r_1 - \varepsilon_{\theta\theta} r_2\right) \tag{10.19}$$

Differentiating (10.19) for $\left(u_\phi cot\phi + u_z\right)$, eliminating the term $\frac{du_\phi}{d\phi} cot\phi$ by adding the differentiated result to (10.19) and subsequently dividing by the radius of curvature r_1 yields:

$$\frac{1}{r_1}\left(u_\phi - \frac{du_z}{d\phi}\right) = \varepsilon_{\phi\phi} cot\phi - \frac{1}{r_1}\left[\frac{d}{d\phi}\left(\varepsilon_{\theta\theta}\frac{r}{sin\phi} + \left(\varepsilon_{\theta\theta} r\right)\frac{cos\phi}{sin^2\phi}\right)\right]$$

The rotation φ_ϕ, (10.18) can easily be recognised in this expression, thus

$$\varphi_\phi = \varepsilon_{\phi\phi} cot\phi - \frac{1}{r_1 sin\phi}\frac{d(\varepsilon_{\theta\theta} r)}{d\phi} \qquad (10.20)$$

To calculate the membrane rotation at the base the strain equations (10.13), (10.14) are introduced and the Poisson's ratio is equal to zero. Equation (10.20) changes into

$$\varphi_\phi = \frac{pa\ cot\phi}{Et\ (1+cos\phi)} - \frac{pa}{Et sin\phi}\left(\frac{sin\phi}{(1+cos\phi)^2} + sin\phi\right) \qquad (10.21)$$

The membrane displacements of the Zeiss planetarium shell under vertical load can now be calculated using equation (10.16), (10.17) and (10.21) and the values of Table 10.6. The rotations are tabulated in Table 10.7.

Displacements	$\phi = 0$ (top)	$\phi = 90$ (base)	
u_z	-0.181	0	mm
u_r	0	0.181	mm
φ_ϕ	0	-0.0000288	mm/mm

Table 10.7 Membrane displacements for a spherical shell with vertical load

10.3.5 Bending Behaviour

The total solution for the shell behaviour is obtained by adding the bending solution to the membrane solution which is thus taken as the inhomogeneous solution. With the bending solution the influence of the different support conditions will be defined; the bending solution makes sure the final solution satisfies the boundary conditions. For the description of the bending behaviour of shell of revolution, use is made of a local coordinate system, in which the x and y terms remain and the *z-axis* is always perpendicular to the shell surface. Identical to the membrane behaviour it is observed that $dx = r_1 d\phi$ and $dy = rd\theta$ and due to axisymmetry, displacement and rotational terms in the *θ-direction*, the load component p_y and the derivative $\frac{\partial(\ )}{r\partial\theta} = \frac{\partial(\ )}{\partial y}$ are zero. Also the longitudinal shearing stress resultants are equal to zero.

Recapitulating from Chapter 5.4 the general relations for a shell of arbitrary curvature are rewritten to the new local coordinate system, leaving out the zero parts. The kinematic relation thus becomes

$$\begin{bmatrix} \varepsilon_{xx} \\ \varepsilon_{yy} \\ \kappa_{xx} \\ \kappa_{yy} \end{bmatrix} = \begin{bmatrix} \frac{d}{dx} & -\frac{1}{r_x} \\ 0 & -\frac{1}{r_y} \\ 0 & -\frac{d^2}{dx^2} \\ 0 & 0 \end{bmatrix} \begin{bmatrix} u_x \\ u_z \end{bmatrix} \qquad (10.20)$$

Hence, due to the zero derivate $\frac{\partial(\ )}{r\partial\theta} = \frac{\partial(\ )}{\partial y}$ the change of curvature in circumferential κ_{yy} is zero.

The constitutive relation remains unchanged, apart from the zero terms, thus

$$\begin{bmatrix} n_{xx} \\ n_{yy} \\ m_{xx} \\ m_{yy} \end{bmatrix} = \begin{bmatrix} D_m & \nu D_m & 0 & 0 \\ \nu D_m & D_m & 0 & 0 \\ 0 & 0 & D_b & \nu D_b \\ 0 & 0 & \nu D_b & D_b \end{bmatrix} \begin{bmatrix} \varepsilon_{xx} \\ \varepsilon_{yy} \\ \kappa_{xx} \\ \kappa_{yy} \end{bmatrix} \tag{10.21}$$

Where, the extensional and bending rigidity are already defined in Chapter 5.4.

$$D_m = \frac{Et}{(1-\nu^2)}$$

$$D_b = \frac{Et^3}{12(1-\nu^2)}$$

To complete the description for the bending behaviour of a shell of revolution, the equilibrium relations must be derived. Rewriting the equilibrium equations for a shell of revolution yields:

$$\frac{dn_{xx}}{dx} + p_x = 0$$

$$\frac{dv_x}{dx} + \frac{n_{xx}}{r_x} + \frac{n_{yy}}{r_y} + p_z = 0$$

From the bending action of a flat plate, described in Chapter 5.3, is known that the derivative of the moment stress resultant is equal to the transverse shearing stress resultant. Thus, eliminating v_x out of the latter equation, yields

$$\frac{dn_{xx}}{dx} + p_x = 0 \tag{10.22}$$

$$\frac{d^2 m_{xx}}{dx^2} + \frac{n_{xx}}{r_x} + \frac{n_{yy}}{r_y} + p_z = 0 \tag{10.23}$$

And, written down in matrix notation, reads

$$\begin{bmatrix} -\frac{d}{dx} & 0 & 0 & 0 \\ -\frac{1}{r_x} & -\frac{1}{r_y} & -\frac{d^2}{dx^2} & 0 \end{bmatrix} \begin{bmatrix} n_{xx} \\ n_{yy} \\ m_{xx} \\ m_{yy} \end{bmatrix} = \begin{bmatrix} p_x \\ p_z \end{bmatrix} \tag{10.24}$$

Conform the earlier examples; the equation that is derived is equal to the adjoint matrix of equation (10.20).

10.3.6 Bending Solution

From the bending relations, the single differential equation for the displacement u_z can be obtained, similar to the procedure followed in Chapter 5.3. However, because the stress resultant n_{xx} can directly derived from the first equilibrium condition, the differential equation can be found in a simpler way.

The stress resultant can be determined by integrating equation (10.22)

$$n_{xx} = -\int p_x dx \qquad (10.25)$$

Substituting the stress resultant in equation (10.23) yields

$$-\frac{n_{yy}}{r_y} - \frac{d^2 m_{xx}}{dx^2} = p_z - \frac{1}{r_x}\int p_x dx \qquad (10.26)$$

Using the constitutive relations (10.21) and kinematic relations (10.20) in combination with equation (10.26) the normal stress resultant n_{yy} can be completely expressed by the displacement u_z

$$n_{yy} = -D_m\left(1 - \nu^2\right)k_y u_z - \nu\int p_x dx \qquad (10.27)$$

Again, using the constitutive relations (10.21) and kinematic relations (10.20), the bending stress resultants can be expressed in the displacement u_z.

$$m_{xx} = -D_b\frac{d^2 u_z}{dx^2}$$

$$m_{yy} = -\nu D_b\frac{d^2 u_z}{dx^2} = \nu m_{xx} \qquad (10.28)$$

Substituting the equations (10.25), (10.27) and (10.28) in (10.24) yields the differential equation for the displacement u_z

$$D_b\frac{d^4 u_z}{dx^4} + D_m\left(1 - \nu^2\right)k_y^2 u_z = p_z - \left(k_x + \nu k_y\right)\int p_x dx \qquad (10.29)$$

By setting the curvature k_y equal to zero, the radius r_y is constant and the bending behaviour of the shell of revolution is equal to the bending behaviour of a circular cylinder under axisymmetric loading.

The inhomogeneous solution to the differential equation corresponds with the membrane solution. Therefore, to obtain the bending solution, the homogeneous solution to the differential equation (10.29) must be determined:

$$D_b \frac{d^4 u_z}{dx^4} + D_m\left(1 - \nu^2\right) k_y^2 u_z = 0$$

To simplify the equation, a parameter μ is introduced: $\mu^4 = \dfrac{D_m\left(1-\nu^2\right)k_y^2}{4D_b} = \dfrac{3\left(1-\nu^2\right)}{\left(r_y t\right)^2}$

The differential equation then simplifies to

$$\frac{d^4 u_z}{dx^4} + 4\mu^4 u_z = 0 \tag{10.30}$$

Obviously, the similarity with a differential equation for a beam on an elastic foundation is clear. The general solution to the fourth order differential equation with constant coefficients consist of four terms of the form

$$u_z(x) = Ce^{rx}$$

When the solution is substituted into the equation (10.30) the differential equation reads

$$r^4 + 4\mu^4 = 0$$

The four solutions to the differential equation are:

$$r = \pm\left(1 \pm i\right)\mu$$

The solution describes two pairs of conjugate complex functions. Because the sum and the difference of the functions of each pair are purely real or purely imaginary and constitute another set of four independent homogeneous solutions, the solution can be written as

$$u_z(x) = e^{-\mu x}\left[C_1 \cos \mu x + C_2 \sin \mu x\right] + e^{\mu x}\left[C_3 \cos \mu x + C_4 \sin \mu x\right] \tag{10.31}$$

The terms which are multiplied with $e^{\pm\mu x}$ have an influence length of:

$$l_i = \frac{\pi}{\mu} = \frac{\pi\sqrt{r_y t}}{\sqrt[4]{3(1-\upsilon^2)}} \tag{10.32}$$

Neglecting the effect of Poisson's ratio, the influence length of the bending behaviour on the shell of revolution can be determined:

$$l_i = 2.4\sqrt{r_y t} \tag{10.33}$$

The influence length is illustrated in Figure 10.5.

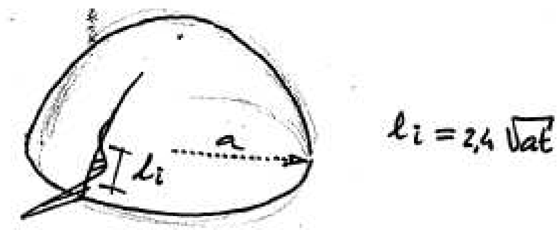

Figure 10.5. Influence length of a spherical shell under external pressure, Hoogenboom 2006

From equation (10.33) it can be concluded that the influence of an edge disturbance becomes smaller with decreasing thickness. Thus, thinner shells have increasing preference for membrane-dominant behaviour.

For determining the constants the equation (10.31) must be transformed. The term of equation (10.31) multiplied with the constants C_3 and C_4, damped oscillations which decrease exponentially for decreasing x, is rewritten using an ordinate x' which is positive in the negative *x-direction*.

$$u_z(x) = e^{-\mu x}\left[A_1 \cos \mu x + A_2 \sin \mu x\right] + e^{-\mu x'}\left[B_1 \cos \mu x' + B_2 \sin \mu x'\right]$$

By introduction of free constants C_1 and C_2 and phase angles ψ_1 and ψ_2 the equation transforms to:

$$u_z(x,x') = C_1 e^{-\mu x} sin\left(\mu x + \psi_1\right) + C_2 e^{-\mu x'} sin\left(\mu x' + \psi_2\right) \tag{10.33}$$

Where:

$$C_1^2 = A_1^2 + A_2^2 \quad ; \quad tan\psi_1 = \frac{A_1}{A_2}$$

$$C_2^2 = B_1^2 + B_2^2 \quad ; \quad tan\psi_2 = \frac{B_1}{B_2}$$

By substitution of equation (10.33) in the relations (10.20), (10.25), (10.26), (10.27) and (10.28), the quantities of interest become:

$$u_z = C_1 e^{-\mu x} sin\left(\mu x + \psi_1\right) + C_2 e^{-\mu x'} sin\left(\mu x' + \psi_2\right)$$

$$u_x = -\frac{\left(k_x + \nu k_y\right)}{\mu\sqrt{2}}\left[C_1 e^{-\mu x} sin\left(\mu x + \psi_1 + \frac{\pi}{4}\right) - C_2 e^{-\mu x'} sin\left(\mu x' + \psi_2 + \frac{\pi}{4}\right)\right]$$

$$\varphi_x = \mu\sqrt{2}\left(C_1 e^{-\mu x} sin\left(\mu x + \psi_1 - \frac{\pi}{4}\right) - C_2 e^{-\mu x'} sin\left(\mu x' + \psi_2 - \frac{\pi}{4}\right)\right)$$

$$n_{yy} = -D_m\left(1 - \nu^2\right)k_y\left(C_1 e^{-\mu x} sin\left(\mu x + \psi_1\right) + C_2 e^{-\mu x'} sin\left(\mu x' + \psi_2\right)\right)$$

$$m_{xx} = -2D_b\mu^2\left(C_1e^{-\mu x}sin\left(\mu x + \psi_1 - \frac{\pi}{2}\right) + C_2e^{-\mu x'}sin\left(\mu x' + \psi_2 - \frac{\pi}{2}\right)\right)$$

$$v_x = 2\sqrt{2}D_b\mu^3\left(C_1e^{-\mu x}sin\left(\mu x + \psi_1 - \frac{3\pi}{4}\right) - C_2e^{-\mu x'}sin\left(\mu x' + \psi_2 - \frac{3\pi}{4}\right)\right) \tag{10.34}$$

From equation (10.32) it can be seen that the influence length of an edge disturbance, as a result of the exponential damping of the wave, for a thin shell is small *(t « r)* in comparison to the distance between two edges. In that case, the term which determines the bending behaviour at one edge, is negligible at the other edge. Therefore, the constants in the equations (10.33) can be derived independently from each other with the aid of the boundary conditions at $x = 0$ and $x' = 0$.

To determine the free constants C_1 and C_2 and phase angles ψ_1 and ψ_2 the boundary conditions of the shell are divided into two elementary cases: a first case in which the shell undergoes a displacement u_r due to an edge load f_r and a second case in which the shell undergoes an rotation φ_x due to an edge torque t_x.

$$\left.\begin{aligned} u_r &= u_z \sin\phi_0 \\ \varphi_x &= \varphi_x \end{aligned}\right\} \left\{\begin{aligned} f_z &= f_r \sin\phi_0 \\ t_x &= t_x \end{aligned}\right.$$

The homogeneous boundary condition for the edge load is

$$v_{x(x'=0)} = f_z \qquad ; \qquad m_{xx(x'=0)} = t_x = 0$$

From these boundary conditions and the equations (10.34), the phase angle ψ_2 and the constant C_2 can be derived directly

$$\psi_2 = \frac{\pi}{2} \qquad ; \qquad C_2 = \frac{f_r}{2D_b\mu^3}$$

For the second case, the edge torque, the same procedure can be followed, however, this time the shear component is equal to zero and the moment is equal to the torque. The phase angle and constant can be described as

$$\psi_2 = \frac{3\pi}{4} \qquad ; \qquad C_2 = \frac{-t_x}{\sqrt{2}D_b\mu^2}$$

Combining the two elementary cases yields the relation

$$\frac{1}{D_b}\begin{bmatrix} \frac{1}{2\mu^3} & -\frac{1}{2\mu^2} \\ -\frac{1}{2\mu^2} & \frac{1}{\mu} \end{bmatrix}\begin{bmatrix} f_z \\ t_x \end{bmatrix} = \begin{bmatrix} u_z \\ \varphi_x \end{bmatrix}$$

Or written in *r-direction*

$$\frac{1}{D_b}\begin{bmatrix} \frac{1}{2\mu^3}\sin^2\varphi_o & -\frac{1}{2\mu^2}\sin\varphi_o \\ -\frac{1}{2\mu^2}\sin\varphi_o & \frac{1}{\mu} \end{bmatrix}\begin{bmatrix} f_r \\ t_x \end{bmatrix} = \begin{bmatrix} u_r \\ \varphi_x \end{bmatrix} \tag{10.35}$$

The inverse relation is

$$\begin{bmatrix} f_r \\ t_x \end{bmatrix} = D_b\begin{bmatrix} \frac{4\mu^3}{\sin^2\phi_o} & \frac{2\mu^2}{\sin\phi_o} \\ \frac{2\mu^2}{\sin\phi_o} & 2\mu \end{bmatrix}\begin{bmatrix} u_r \\ \varphi_x \end{bmatrix} \tag{10.36}$$

Obviously, for the spherical shell of revolution, at the base, the *z-direction* equals the *r-direction*.

The solutions to the bending behaviour of the shell can now be determined in combination with the results of the membrane behaviour and the boundary conditions of each of the shells as denoted in Table 10.3.

10.3.7 Total Solution

The total solution is the bending solution added to the membrane solution. As mentioned the membrane solution will yield over the majority of the shell. The bending solution occurs only locally near the supports. Therefore, for the total solution, only the displacement, rotation and moment distribution of the lower part of the shell (near the supports) are determined. Recapitulating the membrane results at the base radius of each Zeiss shell, obtained with the equations (10.11), (10.12), (10.13), (10.14), (10.17), (10.21) yields:

Displacements	$\phi = 0$ (top)	$\phi = 90$ (base)	
u_r	0	0.181	mm
φ_ϕ	0	-0.0000288	mm/mm

Table 10.8 Membrane displacements for a spherical shell with vertical load

Zeiss 1

The Zeiss 1 shell is roller supported and, thus, neither displacements nor rotations are restrained. Consequently no edge disturbance occurs. Therefore, the membrane solution is the total solution.

Zeiss 2

The shell has inclined-roller supports which mean that the shell is not allowed to rotate near the supports but is free to move outward. The boundary conditions thus yields a zero rotation $\varphi_{x,total}$ and zero edge force f_r, thus:

$\varphi_{x,total} = \varphi_{x,m} + \varphi_{x,b} = 0$ and $v_{x(x'=0)} = f_r = 0$

Using the boundary conditions and equation (10.36) yields the quantities of the edge loads:

Edgeloads	*ϕ = 90 (base)*	
f_r	0	N/mm'
t_x	23.707	Nmm/mm'

Table 10.9 Bending solution at the base radius for a spherical shell with vertical load and inclined-roller support

On the principle of superposition, the membrane and bending behaviour can be added to achieve the total displacements of the shell. As a check, they must satisfy the boundary conditions.

Displacements	*Membrane*	*Bending*	*Total*	
u_r	0.181	-0.00951	0.171	mm
φ_ϕ	-0.0000288	0.0000288	0	mm/mm

Table 10.10 Total solution for a spherical shell with vertical load and inclined-roller support

Zeiss 3

For the Zeiss 3 shell, the base radius is supported with hinged supports which suppresses the circumferential displacement $u_{r,total}$ and cannot develop a torsion edge load t_x, thus:

$u_{r,total} = u_{r,m} + u_{r,b} = 0$ and $m_{xx} = t_x = 0$.

The bending solution becomes:

Edgeloads	*ϕ = 90 (base)*	
f_r	-0.684	N/mm'
t_x	0	Nmm/mm'

Table 10.11 Bending solution at the base radius for a spherical shell with vertical load and pinned support

The total displacements of the shell at the base radius become:

Displacements	Membrane	Bending	Total	
u_r	0.181	-0.181	0	mm
φ_ϕ	-0.0000288	0.000274	0.000245	mm/mm

Table 10.12 Total solution for a spherical shell with vertical load and pinned support

Zeiss 4

Finally, the bending solution for the clamped Zeiss 4 shell, the most realistic model of the actual shell, must be determined. The boundary conditions at the base circle of the shell are:

$u_{r,total} = u_{r,m} + u_{r,b} = 0$ and $\varphi_{x,total} = \varphi_{x,m} + \varphi_{x,b} = 0$

Using equation (10.36) this results in the following expressions for the edge loads:

Edge loads	$\phi = 90$ (base)	
f_r	-1.297	N/mm'
t_x	402,92	Nmm/mm'

Table 10.13 Bending solution at the base radius for a spherical shell with vertical load and clamped support

The total displacement solution must satisfy the boundary conditions:

Displacements	Membrane	Bending	Total	
u_r	0.181	-0.181	0	mm
φ_ϕ	-0.0000288	0.0000288	0	mm/mm

Table 10.14 Total solution for a spherical shell with vertical load and clamped support

From the above results it can be observed that the calculated values of maximal stresses and displacements are remarkably low for such a structure. In particular, the maximum tensile hoop stress is very small and can be carried by weak materials such as various masonry products. This is generally true for most shell structures and the many historical masonry shells which still remain after many centuries demonstrates this unique feature of shells.

10.4 Geometrical and Material Influences

10.4.1 Geometrical Influences

As the hemispherical shell is the basic shape of this thesis, the shell thickness is the only parameter to vary. In the membrane situation, if additional snow load is left out of scope, a smaller thickness lowers the shell dead weight and the stress resultants while it increases the stresses, strains and displacements with the same amount. The governing effect is, thus, zero. For the bending solution, a twice as thin shell reduces the bending moments *26%*. Aforementioned, the influence of an edge disturbance becomes smaller with decreasing thickness. Thus, thinner shells have increasing preference for membrane-dominant behaviour.

10.4.2 Material Influences

In linear elastic analysis, the material is characterised by the Young's modulus and Poisson's ratio only. Moreover, fibre additions and higher packing density increases the specific weight of the UHPFRC concrete and the dead weight of the shell increases. Therefore, when the UHPFRC mixture is applied, the stress resultants increase and the strains decrease according to the equations described above. A non-zero Poisson's ratio means that the membrane displacements slightly increase at the supports (compression/tension) while the top displacement decreases (biaxial compression). Still, the resulting effect may be that of an increasing top displacement (see Chapter 12).

10.5 Linear (Euler) Buckling Analysis

The next step is to calculate the linear critical buckling load for the Zeiss planetarium shell. Buckling causes premature instability failure caused by eccentricity of compressive forces. The phenomenon is discussed in Chapter 6. Here, the general equation of Zoëlly for shells as obtained in Chapter 6 is used to determine the critical load of the Zeiss planetarium.

In Chapter 6 the expression for the linear critical buckling load of a sphere under external pressure load (equation (6.53)) is derived. When Poisson's ratio is set equal to zero the equation changes to:

$$P_{cr}^{lin} = 1.16E\left(\frac{t}{R}\right)^2 \tag{10.46}$$

For the given parameters the critical load for the Zeiss shell under radial pressure load becomes:

$$P_{cr}^{lin} = 1.16 \cdot 30000\left(\frac{60}{12500}\right)^2 = 0.802\ MPa = 802\ kN/m^2$$

This is an extremely large load in compare to the load as determined in Chapter 9. Moreover, the linear critical buckling load is so high that the shell fails on surpassing the concrete compression strength ($P_{cr}^{plast} = 2\frac{f_{cm} \cdot t}{R} = 2\frac{28 \cdot 60}{12500} = 0.268\ MPa$) rather than failure due to buckling instability (crushing load is 33*.4%* of buckling load). The critical crushing load can simply be calculated from the uniaxial compression stresses (the shell is in complete compression). For the C180/210 UHPFRC mixture with mean cylinder compression strength of *190 MPa*, however, it can be computed that buckling occurs before concrete crushing is reached.

The above paragraph is interesting as the question arises if, for a shell constructed with conventional C20/25, the buckling load will prevail over the crushing load when the shell thickness decreases. Therefore, in Figure 10.6 the maximum spherical load corresponding to the linear critical buckling load and the concrete crushing load is plotted against an increasing radius to thickness ratio. In Figure 10.6 it can be seen that with increasing *R/t ratio*, the critical buckling load eventually will be lower than the crushing load. In other words, when the *R/t ratio* becomes larger than approximately *600*, buckling will occur before crushing. For UHPFRC the linear critical buckling load is lower for all *R/t ratios*.

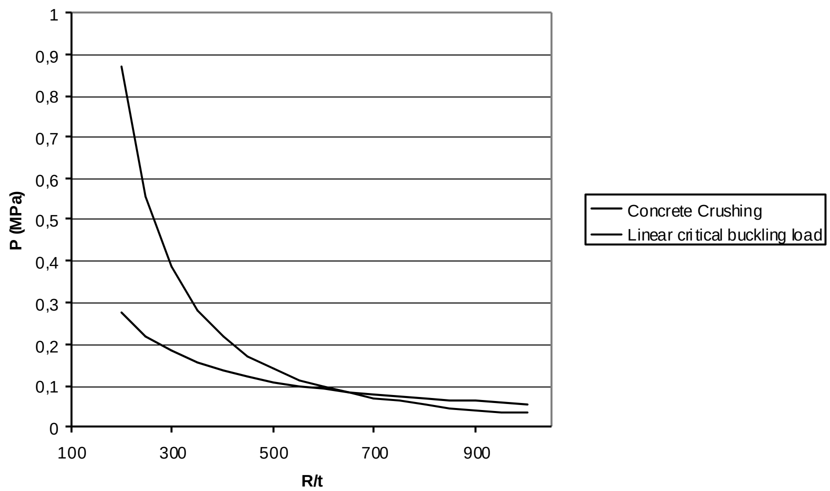

Figure 10.6. Decisive failure mechanism at increasing thickness to radius ratio for C20/25

The fact that the shell fabricated from conventional C20/25 concrete does not fail by buckling for all *R/t ratios* means that in the search to the knock-down factor the shell behaves different for various thicknesses. For lower *R/t ratios* the shell fails by surpassing the material strength whereas for higher *R/t ratios* the shell fails by buckling instability. Later, in Chapter 14 and 15, imperfections and material nonlinearities move the buckling curve downwards and the turning point moves towards the left, i.e. buckling may also prevail for lower *R/t ratios* than *600*.

10.6 Postbuckling Analysis

The next step in this numeric example is to determine the lowest postbuckling load. As explained in Chapter 6 the shell experiences a significant decrease in load-carrying capacity after the bifurcation point. The maximum decrease in load carrying capacity in the postbuckling range, as illustrated in Figure 6.22, can be computed using the analytical relations as obtained by Von Karman and Tsien, Tsien, Thompson and Del Pozo and Del Pozo. Their research has resulted in various analytical relations for obtained the lowest point for a spherical shell subjected to radial pressure load (from Chapter 6):

Classical theory by Zoëlly: $P_{cr}^{lin} = 1.16E\left(\frac{t}{R}\right)^2 = 0.802\ MPa$

Von Karman and Tsien: $P_{cr} = 0.365E\left(\frac{t}{R}\right)^2 = 0.252\ MPa$

Thompson: $P_{cr} = 0.283E\left(\frac{t}{R}\right)^2 = 0.196\ MPa$

Del Pozo and Del Pozo: $P_{cr} = 0.228E\left(\frac{t}{R}\right)^2 = 0.158\ MPa$

Dostanowa and Raiser: $P_{cr} = 0.126E\left(\frac{t}{R}\right)^2 = 0.087\ MPa$

The values of the lowest postbuckling load range from *0.252* to *0.087 MPa*. The lowest value as proposed by Del Pozo and Del Pozo shows a decrease in load carrying capacity of almost *90%*. Although, the lowest postbuckling load is far greater than the external applied load as determined according to the Eurocode in Chapter 9 (= *0.0021 MPa*), the load is lower than the load needed for compressive crushing of the concrete. This means that the original Zeiss shell (with *R/t ratio 200* and conventional concrete) with imperfections may fail due to buckling rather than to compressive crushing after all, if, however, the imperfection is large enough.

10.7 Inelastic Buckling Analysis on Imperfect Shells

To determine the load-carrying capacity of an inelastic imperfect shell, the relations as proposed by the IASS recommendations have been introduced in Chapter 6. Basically, the IASS recommendations determine a reduced load by multiplying the linear critical buckling load by a factor which takes into account for imperfections and material nonlinearities. The relation proposed in Chapter 6 is:

$$p_{cr}^{reduced} = \alpha_1\ \alpha_2\ \alpha_3\ \alpha_4\ p_{cr}^{lin} = \alpha\ p_{cr}^{lin} \qquad (6.70)$$

Herein:
α_1 = Large deformation and imperfection factor
α_2 = Creep factor
α_3 = Crack factor
α_4 = Material nonlinearity factor

If the maximum imperfection is taken equal to the shell thickness, α_1 is equal to *0.2* (see Figure 6.36).

For the creep factor the mean value of cylinder compression strength and the Young's modulus of Table 8.1 are used into equation (6.67):

$$\left.\begin{aligned} C_u &= 4 - 2\log 28 = 1.11 \\ E_{cr} &= \frac{30000}{1 + 1.11} = 14247 \end{aligned}\right\} \alpha_2 = \frac{14247}{30000} = 0.475$$

For the crack factor a reinforcement percentage of *0.4%* is assumed (see Chapter 3) and the properties of reinforcement are taken from Table 8.2. Using equation (6.68) and Figure 6.37 the crack factor becomes:

$$\left.\begin{array}{l} n\rho = \dfrac{E_s}{E_{cr}} \cdot \dfrac{A_s}{A_c} = \dfrac{200\,GPa}{14247\ MPa} \cdot 0.004 = 0.06 \\ \psi_1 = 0.2 \end{array}\right\} \alpha_3 = 0.2$$

Finally, the material nonlinearity factor is determined using equation (6.69):

$$\alpha_4 = \frac{p_{cr}^{plast}}{p_{cr}^{lin} \cdot \alpha_1 \cdot \alpha_2 \cdot \alpha_3} \approx \frac{0.015}{0.015} \approx 1.0$$

The reduced critical load, thus, becomes:

$$p_{cr}^{reduced} = \alpha_1\ \alpha_2\ \alpha_3\ \alpha_4\ p_{cr}^{lin} = 0.2 \cdot 0.475 \cdot 0.2 \cdot 1 \cdot 0.7981 = 0.015$$

Applying the safety factor of 3.5, described in Section 6.9.5, the allowable load is equal to:

$$p_{allow} = \frac{p_{cr}^{reduced}}{3.5} = \frac{0.015}{3.5} = 0.00433\ MPa = 4.33\ kN/m^2$$

Hereby, the total reducing factor is approximately *184.3*. However, aforementioned, creep is not taken into account in the finite element analysis. Hence, the allowable load is assumed to be equal to:

$$p_{allow} = \frac{0.2 \cdot 0.2 \cdot 1 \cdot 0.7981}{3.5} = 0.00912\ MPa = 9.12\ kN/m^2$$ (Total reducing factor is equal to *87.5*)

The allowable loads are close to the external applied loads as determined in Chapter 9 and used in the numeric example described above. However, it must be mentioned that the IASS procedure followed is rather unclear and the author's confidence in the correctness of this procedure is not very high.

10.8 Conclusions

In this chapter a linear solution to the Zeiss planetarium is performed for different types of support conditions. The stresses, strains and deformations of a shell in membrane action are determined in combination with the influence of edge disturbances caused by restrained deformation at the supports. For the chosen dimensions and material and loading parameters the stresses, strains, and displacements appear to be very low, i.e. in reality they may not be noticed at all. When the thickness of the shell is decreased, the dead weight and membrane stress resultants lower, however, the stresses, strains and displacements increase with the same amount. The governing effect is, thus, zero. For the bending solution, a twice as thin shell reduces the bending moments *26%*. Moreover, the influence of an edge disturbance becomes smaller with decreasing thickness. Thus, thinner shells have increasing preference for membrane-dominant behaviour. The linear solution changes linearly with changes in material parameters, if variations in specific weight are not taken into account.

Besides the linear solution, the linear (Euler) buckling load, the (lowest) postbuckling load and the inelastic imperfect buckling load are determined. The linear buckling load yields extreme high values in compare to the expected external loads and concrete crushing may prevail over buckling instability for low qualities of concrete. This may change when the radius to thickness ratio or the quality of the concrete is increased. After the bifurcation point the maximum decrease in load carrying capacity in the postbuckling branch is determined with the various equations as proposed by mathematicians such as Von Karman and Tsien, Del Pozo and Del Pozo and Dostanowa and Raiser. The maximum load carrying capacity decreases up to more than *80%*. Finally, inelastic buckling of imperfect shells is considered using an approach suggested by the IASS Recommendations. The procedure, however, is rather unclear and the author's confidence in the correctness of the procedure is not very high.

part IV

Finite Element Analysis

11 Finite Element Method

From the preceding discussion on shells and their sensitivity to initial imperfections it is clear that the behaviour of a shell structure must be closely investigated. However, analytic solutions to the structural behaviour of many shell structures are almost unattainable due to the importance of nonlinear features such as large deformations and material nonlinearities.

As denoted by Schnobrich [68], the arrival of the computer made possible a rational approach to the analysis of structures by the use of numerical methods. In particular the finite element method, basically a numerical approximation method, has revolutionised numerical computer analysis and is widely available in advanced software. The finite element method that is the most convenient for the majority of the problems is the displacement approach which uses displacements as basic variables. The general procedure involves the construction and solution of a matrix system from partial differential equations describing the equilibrium of an idealised structure by transferring it to an equivalent weak form, a reduced order problem, which has a relaxing effect. Instead of finding an exact solution everywhere, there is searched for a solution that satisfies the equilibrium 'on average' over the domain allowing an approximated displacement field for which the structure is discretised into finite elements. In the elements a displacement field is described by nodal parameters, and stretched over the element by shape functions. The discrete set of unknown displacement coefficients are related by a stiffness matrix to the external applied load. The problem is solved by evaluating the stiffness matrix by numerical integration over the elements and subsequently performing a solution to the unknown displacements. The strains and stresses can successively be computed from there.

To analyse a structure using the finite element method, the analyst must make a model which correctly describes the structural behaviour. Basically, the finite element model consists out of the discretized geometry of the structure by a mesh, the physical properties and the loading and boundary conditions such as supports. The implementation of the model in computational software is often aided by pre-processors offered in combination with the finite element program which e.g. offer design tools and mesh generation algorithms. A postprocessor can be used to present the analysis result by graphical methods such as a contour plots. For analysis the program DIANA is used equipped with iDIANA as pre- and postprocessor.

The aim of this chapter is to introduce the reader into finite element procedures and to familiar the reader with the most important aspects so that more advanced literature such as Bathe [3], Crisfield [25], Hughes [51] or Zienkiewicz and Taylor [87], [88] can be understood.

11.1 Mathematical Fundamentals

Throughout Chapter 5 reference was made to matrices and vectors, e.g. in the notation of the basic quantities, related to each other by the kinematic, constitutive and equilibrium matrices. In this chapter vectors, matrices and tensors are used to express the finite element procedure in a compact manner, similar to the relations in Chapter 5. For the benefit of the reader the fundamentals of vectors, tensors and matrices will be presented. Obviously, the discussed is rather limited considering only those aspects which are important in finite element analysis. Straight formulations of the definitions can e.g. be found in Bathe [3].

11.1.1 Matrices and Vectors

Basically, a *matrix* is a two-dimensional array of *scalars* (physical quantities that have the same value, irrespective of the choice of reference frame, Wells [85]. A matrix is said to have m rows and n columns, which do not have to be equal, and denoted by capital bold characters. In general, a matrix represents the relation between a set of variables and often it has a physical meaning, such as a system stiffness matrix. An example from Zienkiewicz and Taylor [88] shows the definition of a matrix:

A linear relationship between a set of variables x and b, e.g.:

$$\begin{aligned}
a_{11}x_1 + a_{12}x_2 + a_{13}x_3 + a_{14}x_4 &= b_1 \\
a_{21}x_1 + a_{22}x_2 + a_{23}x_3 + a_{24}x_4 &= b_2 \\
a_{31}x_1 + a_{32}x_2 + a_{33}x_3 + a_{34}x_4 &= b_3
\end{aligned}$$

Can be written shortly as $[A][x] = [b]$ or $\boldsymbol{Ax} = \boldsymbol{b}$. Where the matrix $\boldsymbol{A}$ is defined as:

$$\boldsymbol{A} \equiv [A] = \begin{bmatrix} a_{11} & a_{12} & a_{13} & a_{14} \\ a_{21} & a_{22} & a_{23} & a_{24} \\ a_{31} & a_{32} & a_{33} & a_{34} \end{bmatrix} \text{ and the variables are presented by } \boldsymbol{x} \equiv [x] = \begin{bmatrix} x_1 \\ x_2 \\ x_3 \\ x_4 \end{bmatrix} \text{ and } \boldsymbol{b} \equiv [b] = \begin{bmatrix} b_1 \\ b_2 \\ b_3 \end{bmatrix}$$

The particular column matrix presentation of the variables is often referred to as a *vector*. A vector is a one-dimensional array of scalars which is said to have m entities (in an m-dimensional space) and denoted by normal bold characters. As seen in Chapter 5, in structural mechanics quantities such as forces and displacements can be listed as a vector.

Besides the definition of a matrix and a vector, the example shows the multiplication process of two matrices. In general, multiplication is not commutative like ordinary algebra, i.e. $\boldsymbol{AX} \neq \boldsymbol{XA}$. Addition and subtraction of matrices is based on the addition and subtraction of individual terms of the array and follows the ordinary rules. Addition and subtraction is only possible if the matrices are of identical size.

Two important matrix operations are the calculation of the transpose and inverse of a matrix. The *transpose* of a matrix is a definition for simple reordering of the terms in an array in the following manner:

$$\begin{bmatrix} a_{11} & a_{21} \\ a_{12} & a_{22} \\ a_{13} & a_{23} \end{bmatrix} = \begin{bmatrix} a_{11} & a_{12} & a_{13} \\ a_{21} & a_{22} & a_{23} \end{bmatrix}^T$$

The transpose vector is indicated by the addition of a capital *T*. In case of a vector, the transpose vector simply means that the scalars are written down as a row. An operation that often occurs is to take the transpose of a matrix product, which follows by the rule $(\boldsymbol{AB})^T = \boldsymbol{B}^T\boldsymbol{A}^T$. Furthermore, the transpose becomes useful as, by the rule of matrix multiplication, the product of two vectors is written as $\boldsymbol{f}^T\boldsymbol{a} = \boldsymbol{a}^T\boldsymbol{f}$. Previously, these multiplications were done in Chapter 5, e.g. the virtual work equation.

Taking the *inverse* of a matrix may be required to solve a system of equations. The inverse of a matrix is a matrix $\boldsymbol{A}^{-1}$ such that $\boldsymbol{A}^{-1}\boldsymbol{A} = \boldsymbol{I} = \boldsymbol{AA}^{-1}$, where $\boldsymbol{I}$ represents the *identity* matrix with only unity terms on the diagonal and zero terms in off-diagonal positions. The inverse of a matrix is only possible for square matrices with the additional requirement of a non-zero *determinant*. A matrix possessing an inverse is called *nonsingular* or *invertible*. Nonsingular matrices are sometimes also called *regular* matrices. If the matrix in the example of Zienkiewicz and Taylor is square, it is possible to solve for the unknowns in terms of the known coefficients *b*. The solution can be written as $\boldsymbol{x} = \boldsymbol{A}^{-1}\boldsymbol{b}$ which can be obtained by multiplying each side with the inverse matrix $\boldsymbol{A}^{-1}$. Taking the inverse of a matrix is previously executed in Chapter 5, e.g. rewriting the flexibility formulation of the constitutive relation to the stiffness formulation.

Special properties of matrices appearing in structural problems are *symmetry* and *sparseness*. Symmetry simply means that for all terms in the array it holds $a_{ij} = a_{ji}$ or $\boldsymbol{A} = \boldsymbol{A}^T$. A symmetric matrix, thus, always is a square matrix. Furthermore, in case of symmetry, it can be shown that $\boldsymbol{A}^{-1} = (\boldsymbol{A}^{-1})^T \equiv \boldsymbol{A}^{-T}$. Matrices with a high percentage of zero entries are called sparse.

Finally, a very important matrix operation involves the determination of the *eigenvalues* of a matrix. Eigenvalues are a special set of scalars which arises in common applications such as stability analysis. An eigenvalue of a symmetric matrix $\boldsymbol{A}$ is a scalar λ_i which allows the solution of $(\boldsymbol{A} - \lambda_i\boldsymbol{I})\boldsymbol{\varphi}_i = 0$ and $det|\boldsymbol{A} - \lambda_i\boldsymbol{I}| = 0$, Zienkiewicz and Taylor [88]. Herein, $\boldsymbol{\varphi}_i$ is called the *eigenvector* which is paired with a corresponding eigenvalue. For a symmetric matrix $\boldsymbol{A}$ of size *n* x *n* there are *n* such *eigenpairs*. The eigenvectors can be shown to be orthogonal; $\boldsymbol{\varphi}_i^T\boldsymbol{\varphi}_j = \delta_{ij} = (1\ for\ i = j\ and\ 0\ for\ i \neq j)$ where δ_{ij} is known as the *Kronecker delta*. For symmetric matrices all eigenvalues are real. The matrix is said to be *positive-definite* if all eigenvalues are not only real, but also positive and, as a consequence, the inverse of the matrix exists and has a unique solution. Furthermore, the *condition* of a matrix is defined as the largest eigenvalue divided over the smallest eigenvalue. If this operation results in a large value, the matrix is said to be *ill-conditioned*. For a singular matrix the smallest eigenvalue is zero, and thus, it is ill-conditioned. Unfortunately, ill-conditioning is often the case for beam, plate and shell elements, Bathe [3]. Ill-conditioning of the stiffness matrix may also be caused by improper or few boundary conditions.

11.1.2 Tensors

A more general way to express scalars, vectors and matrices is the *tensor*. In fact, all calculations described above are based on tensor calculus. A tensor is said to have an n-th rank in an m-dimensional space. Tensors are generalisations of scalars (ero-order tensor), vectors (first-order tensor) and matrices (second-order tensor) to an arbitrary number of indices. A tensor is a multi-dimensional array relative to a choice of basis of the particular space on which it is defined. A tensor is independent of any chosen frame of reference, and hence, provides in a natural and concise mathematical framework. In structural problems stresses and strains are referred to as tensors, although they are actually *tensor fields*, a tensor valued function defined on a geometric or topological space. In this context the tensor field is a generalisation of the idea of a vector field which can be thought of as a 'vector that varies from point to point', Bathe [3].

11.2 Generalised Finite Element Procedure

Aforementioned in Chapter 5, any problem in continuum mechanics is based on three basic relations; the *kinematic relation*, the *constitutive relation* and the *equilibrium relation*. The three basic relations serve as starting point for the derivation of the finite element formulation. Recapitulate from Chapter 5, the three basic relations between the displacements $\boldsymbol{u}$, the strains $\boldsymbol{e}$, the stresses $\boldsymbol{s}$ and the external loads $\boldsymbol{p}$:

$$\begin{aligned} \boldsymbol{e} &= \boldsymbol{Bu} \\ \boldsymbol{s} &= \boldsymbol{De} \\ \boldsymbol{p} &= \boldsymbol{B}^T \boldsymbol{s} \end{aligned} \tag{5.1}$$

By stating that the system stiffness matrix is defined as $\boldsymbol{K} = \boldsymbol{B}^T \boldsymbol{DB}$, the basic relations can be combined to:

$$\boldsymbol{Ku} = \boldsymbol{p} \tag{11.1}$$

Equation (11.1) is the *governing equilibrium relation* that has to be solved. In general, the problem is identified by known external applied forces and unknown displacements. Basically, the finite element method involves performing a solution to the system of equations by the composition of the system stiffness matrix and successive solution of the unknown displacement vector.

11.2.1 Global Formulation

An arbitrary three-dimensional body is subjected to external applied loads and experiences unknown displacements $\boldsymbol{u}$. The arbitrary three-dimensional body is denoted V and seen in Figure 11.1. The body is subjected to known body forces per unit volume $\boldsymbol{g}$. Furthermore, external forces such as concentrated forces and known tractions $\boldsymbol{t}$ are applied on the boundary part S_t and the displacements are specified as known values $\bar{\boldsymbol{u}}$ on the boundary part S_u. The known tractions $\boldsymbol{t}$ on S_t are called the *natural* or *Neumann* boundary conditions whereas the prescribed displacements $\bar{\boldsymbol{u}}$ on S_u are referred to as *essential* or *Dirichlet* boundary conditions, Wells [85]. In Figure 11.1 a vector $\boldsymbol{n}$ is visualised as being a component of the unit outward pointing normal to the surface. To find the unknown displacements $\boldsymbol{u}$, a finite element procedure is used.

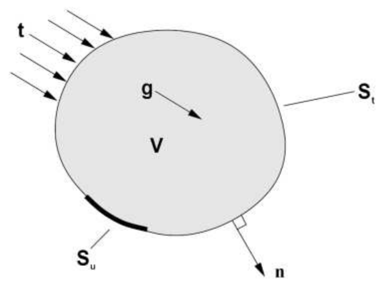

Figure 11.1. Continuous body with forces and boundary conditions, Wells 2004

Aforementioned in the introduction, using the finite element method means looking for an approximate solution of the displacement field $\boldsymbol{u}$ that satisfies the partial differential equations describing the equilibrium of the body V and the boundary conditions. In that process, the discretisation procedure in which the body V is divided into a finite number of elements connected at a finite number of nodes plays a major part.

11.2.2 Displacements

Spatial Discretisation by Finite Elements

The discretisation procedure leads to an approximation of the body V as an assemblage of finite elements connected by nodes. The geometric arrangement of elements and nodes is called a mesh and the elements and nodes of the mesh are used in describing the unknown displacement field.

Shape Functions

The finite element method describes the displacement field in the nodes, as the nodes represent points at which displacements and rotations occur. For that, each node has 6 degrees of freedom, 3 translational and 3 rotational (and each degree of freedom is associated with a corresponding load vector).To generate a solution for the approximated displacement field of a structure it is assumed that the nodal displacements are somehow known. To determine the value of a displacement at an arbitrary point so-called *trail* or *shape functions* are introduced which describe a reasonable displacement path between the nodes.

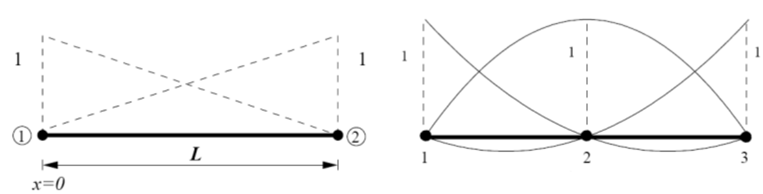

Figure 11.2. Linear (left) and quadratic shape functions, Wells 2004

Generally, shape functions are associated with a single node and they are presented by typical piecewise continuous polynomial functions with compact support, i.e. they equal unity at their node and they are only non-zero close to their node and zero at all others. Typically, the finite element method uses linear or quadratic polynomial shape functions for *C⁰ continuity* between elements, Wells [85]. Shape functions must ensure continuity up to a certain degree in order to let the solution converge to the exact solution if the mesh is refined. Continuity is, as a consequence, a common topic in finite element analysis and refers to whether or not the derivatives of a function are continuous. Most common are C^0 functions, Wells [85], which means that the functions are continuous but their first derivatives are not and second (and higher) derivatives do not exists. Two types of shape functions for a two and three noded line element are illustrated in Figure 11.2.

Compatibility and Isoparametric Mapping

The shape functions between neighbouring elements must satisfy the compatibility demands, see Figure 11.3. Compatibility demands refer to the continuity of corresponding element boundaries without openings of overlap, both in the undistorted as the deformed state, Wells [85]. By adaptation of the finite element method, the shape of the element is fixed in the original coordinates of the nodes of the elements in the undistorted state. If the nodal displacements are known, the deformed shape of the element is known. Like the undistorted element boundaries, the deformed boundaries also must meet the compatibility requirement that they have coinciding boundary lines. The shape of the undistorted and deformed element boundaries, therefore, must be determined by the original coordinates to be sure that they are compatible.

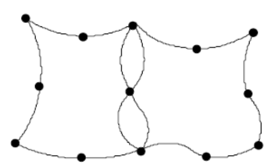

Figure 11.3. Non-compatible (left) and compatible elements, Wells 2004

To simplify the compatibility problems between neighbouring elements with interpolation functions of higher order, isoparametric mapping is introduced. Elements with higher order interpolation functions can have deformed boundaries with unknown curvature and, hence, it becomes impossible to achieve compatibility. The problem is solved by the introduction of a base element of unit length, convenient origin and sides aligned with the coordinate system. Both, the undistorted and the deformed element, are seen as a transformed base element and the transformation is called *isoparametric mapping*, see Figure 11.3.

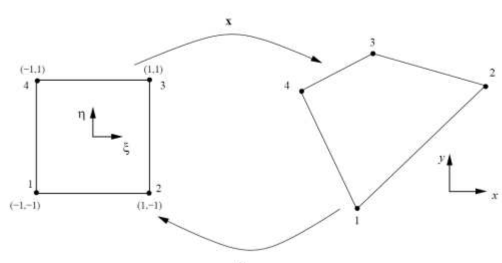

Figure 11.3. The basic element (left) and the real (undistorted or distorted) element, Wells 2004

When isoparametric mapping is used, the independent parameters are the base element ξ- and η-*coordinates* instead of the *x*- and *y-coordinates*. The mapping of the isoparametric element to the real element is done by a matrix with transfer functions. For both mapping operations the same transfer functions can be used. Hence, there is referred to 'isoparametric'. An important finding is that the shape functions used earlier, can be used for the mapping as well, significantly reduce coding, Wells [85]. In addition, isoparametric mapping is numerical advantageous. Because the shape functions are formed for simple elements it requires the programming of only one shape function to evaluate the shape functions of a type of element, irrespective of the exact shape of the element. It also allows for simple application of numerical integration (discussed later).

Discretised Displacement Equations

In order to solve the problem of equation (11.1) the displacements $\boldsymbol{u}$ are, thus, approximated by nodal point variables (such as components of displacements and rotations) and shape functions, clustered in an interpolation matrix $\boldsymbol{N}$. The displacements of a particular point *(x,y,z)* are assumed to be continuous functions expressed in terms of discretised variables at the nodal points and are approximated as:

$$\boldsymbol{u_c}(x,y,z) \approx \tilde{\boldsymbol{u}}(x,y,z) = \boldsymbol{N}(x,y,z)\boldsymbol{u} \tag{11.2}$$

Obviously, the approximated displacement field must satisfy the essential boundary conditions:

$$\boldsymbol{u} = \bar{\boldsymbol{u}} \quad on\ S_u \tag{11.3}$$

Within each element the displacement of an arbitrary point (x,y,z) can be defined in a convenient local *Cartesian* coordinate system and approximated by the shape functions and the element nodal displacement (*degrees of freedom*) vector $\boldsymbol{u}_e$. The displacements of an arbitrary point are then described as:

$$\boldsymbol{u}_c(x,y,z) = \boldsymbol{N}\boldsymbol{u}_e \tag{11.4}$$

Using the element transformation matrix $\boldsymbol{T}_e$ the element displacement vector can be composed from the nodal variables of the system degrees of freedom vector by:

$$\boldsymbol{u}_e = \boldsymbol{T_e}\boldsymbol{u} \tag{11.5}$$

11.2.3 Strains and Stresses

The strains at any point in the discretised structure can be determined from the element displacements $\boldsymbol{u}_e$. In combination with the approximated displacement field, the strain field can be written as the derivative of the vector $\boldsymbol{u}_e$ by:

$$\boldsymbol{\varepsilon} = \boldsymbol{L}\boldsymbol{N}\boldsymbol{u}_e = \boldsymbol{B}\boldsymbol{u}_e \tag{11.6}$$

In which $\boldsymbol{L}$ is a differential operator matrix and $\boldsymbol{B}$ the kinematic relation for a particular point and is called the *differential matrix*. Hence, the displacements $\boldsymbol{u}_e$ has to satisfy differentiability to a necessary degree.

The relationship between the strains and stresses is either *linear* or *nonlinear*. For now, there is no constitutive relation ascribed and the relation is simply formulated using the stress-strain constitutive relation matrix $\boldsymbol{D}$. In this way, the procedure will be valid for as well linear as nonlinear material behaviour.

$$\boldsymbol{\sigma} = \boldsymbol{D}\boldsymbol{\varepsilon} \tag{11.7}$$

11.2.4 Equilibrium Relations

The third basic relation of (5.1) can be rewritten to the equilibrium between the stress vector $\boldsymbol{\sigma}$ and the vector of the known body forces $\boldsymbol{g}$ which hold for every point in the structural domain:

$$\boldsymbol{L}^T\boldsymbol{\sigma} + \boldsymbol{g} = 0 \quad in\ V \tag{11.8}$$

(Note that, in the case of a dynamical problem, the right hand side vector of equation (11.8) is not equal to zero but contains a term which describes the acceleration.)

Furthermore, the stress vector needs to satisfy the natural boundary conditions on S_t:

$$\boldsymbol{L}_n^T\boldsymbol{\sigma} = \boldsymbol{t} \quad on\ S_t \tag{11.9}$$

Equation (11.8) and (11.9) represent the governing equilibrium equations of the structural body V in which equation (11.8) is identified as the *strong form* of the equilibrium. The strong form serves, in combination with the finite element discretisation of the previous paragraph, as basis for the derivation of a column of nodal displacements of a 3D continuum. However, to find a displacement field $\boldsymbol{u}$ that satisfies the partial differential equilibrium condition and the boundary conditions is (almost) impossible. This certainly is true for shells, as the equilibrium relation results in an 8th order partial differential equation. An important step in finite element analysis is, therefore, to transform the strong form to its equivalent *weak form*.

11.2.5 Strong form – Weak form

Constructing the governing equilibrium equation or strong form and transferring it to the corresponding weak form is an essential step in the finite element method, Wells [85]. The strong form represents the original partial differential equation with the particular boundary conditions of the problem which appeared to be (almost) impossible to solve. Fortunately, the original governing equation is proven to be equivalent to an integral weak form statement of the problem, an equation of reduced order, suitable for numerical solution. The weak form has a relaxing effect on the problem, as it allows for solutions which hold 'in average'. Though, it may be surprising that the weak form often is more realistic physically than the original differential equation which implied an excessive 'smoothness' of the true solution, Zienkiewicz and Taylor

[87]. In general, the transformation of the strong form to the weak form is either based on the *method of weighted residuals*, on *global physical statements* such as *virtual work* or on *variational principles*.

Weighted Residual Method (Galerkin Procedure)

The transformation of the strong form to the weak form by the method of weighted residuals is done by multiplication with continuous *weight functions* and consecutive *integration by parts*. A weight function can be defined as an arbitrary chosen function which comes from a predefined space $\mathcal{V}$ and must satisfy the essential boundary conditions. If the structural domain is assumed to be divided into finite elements, the strong form (equation (11.8)) can be transferred to the weak form by multiplication with a column of arbitrary weight functions $\boldsymbol{w}$:

$$\int_{V_e} \boldsymbol{w}^T \left(\boldsymbol{L}^T\boldsymbol{\sigma} + \boldsymbol{g}\right) dV = 0 \quad \forall \boldsymbol{w} \in \mathcal{V} \tag{11.10}$$

It can be noted that the term between the brackets represents the *residual* or *error* obtained by the substitution of the approximated displacement field $\boldsymbol{Nu}$ into the differential equation. Thus, equation (11.10) is a *weighted integral of such residuals*. Applying Gauss' theorem to transfer the volume integral to a surface integral by partial integration in more dimensions, the weighted equilibrium can be rewritten to a part that holds inside the volume which needs to be equal to a part that holds on the surface. Equation (11.10) transforms to:

$$\int_{V_e} \left(\boldsymbol{w}^T \left(\boldsymbol{L}^T\boldsymbol{\sigma}\right) + \left(\boldsymbol{L}\boldsymbol{w}\right)^T \boldsymbol{\sigma}\right) dV = \int_{S_t} \boldsymbol{w}^T \left(\boldsymbol{L}_n^T\boldsymbol{\sigma}\right) dS \tag{11.11}$$

When applied into equation (11.10) the weak form of the governing equilibrium relations is found:

$$\int_{V_e} \left(\boldsymbol{L}\boldsymbol{w}\right)^T \boldsymbol{\sigma}\, dV = \int_{V_e} \boldsymbol{w}^T\boldsymbol{g}\, dV + \int_{S_t} \boldsymbol{w}^T\boldsymbol{L}_n^T\boldsymbol{\sigma} dS \quad \forall \boldsymbol{w} \in \mathcal{V} \tag{11.12}$$

Note that, equation (11.12) is equivalent to equation (11.8) as the weight function is any arbitrary function. Subsequently, after introduction of the Neumann boundary condition $\left(\boldsymbol{L}_n^T\boldsymbol{\sigma} = \boldsymbol{t} \text{ on } S_t\right)$ this changes to:

$$\int_{V_e} \left(\boldsymbol{L}\boldsymbol{w}\right)^T \boldsymbol{\sigma}\, dV = \int_{V_e} \boldsymbol{w}^T\boldsymbol{g} dV + \int_{S_t} \boldsymbol{w}^T\boldsymbol{t} dS \quad \forall \boldsymbol{w} \in \mathcal{V} \tag{11.13}$$

The latter equation is the weak form of the governing equilibrium relation.

Aforementioned, miscellaneous weight functions are to be chosen to complete the weak form formulation. However, one weight function may give better results than another. Hence, to find the best possible solution to the weak form involves the selection of proper weight functions. Common choices are called *point collocation* (impulse functions selected as weight functions, Burden and Faires [19]), *subdomain collocation* (each weight function equal unity over a specific region, Burden and Faires [19]) and, in particular, the *Galerkin method*. Basically, the (*Bubnov-*)Galerkin method chooses the shape functions as weight functions: $\boldsymbol{w}_j = \boldsymbol{N}_j$. The Galerkin method is beneficial as it provides some numerical advantages. I.e. the weight functions are already there, the stiffness matrix often ends up symmetric and the method gives good approximations (*Galerkin orthogonality*). It can be proven that the Galerkin method is optimal in strain energy terms, Bathe [3].

Virtual Work

When applied for structures in the continuum mechanics, the finite element procedure is closely related to the concepts of energy and virtual work. In fact, the principle of virtual work is a simpler way of introducing the equilibrium relations (11.8) and (11.9). The exact solution of the equations (11.8) and (11.9) is found if for every variation δ of the *virtual displacement* $\boldsymbol{u}$ the following relation is satisfied:

$$\int_V \left(\boldsymbol{L}^T\boldsymbol{\sigma} + \boldsymbol{g}\right)\delta\boldsymbol{u}^T \, dV + \int_{S_t} \delta\boldsymbol{u}^T \left(\boldsymbol{L}_n^T\boldsymbol{\sigma} - \boldsymbol{t}\right) dS = 0 \tag{11.14}$$

Applying Gauss' theorem for partial integration in more dimensions to transform the internal equilibrium of equation (11.14) to a volume integral and a surface integral, yields after some equating:

$$\int_V (\delta\boldsymbol{\varepsilon})^T \boldsymbol{\sigma} \, dV = \int_V \delta\boldsymbol{u}^T\boldsymbol{g} dV + \int_{S_t} \delta\boldsymbol{u}^T\boldsymbol{t} dS \tag{11.15}$$

The latter equation is the well-known *equation of virtual work*. Note that, when the weight functions of the weighted residual method are considered to be a variation of the virtual displacement ($\boldsymbol{w} = \delta\boldsymbol{u}$) and the virtual strains are described by $\delta\boldsymbol{\varepsilon} = \boldsymbol{L}\delta\boldsymbol{u}$ equation (11.13) is equivalent to the virtual work equation. Thus, the virtual work equation represents the weak form of the governing equilibrium relations (11.8) and (11.9). In general, it can be stated that, there is a close relation between weak forms and virtual work for a wide range of problems.

Variational Principles

The variational approach of establishing the governing equilibrium equations is based on the calculation of the total potential Π of the system and to invoke *stationarity*, i.e. $\delta\Pi = 0$. The total potential can be defined by an integral form (which e.g. represents the equilibrium of a continuum problem):

$$\Pi = \int_{V_e} \boldsymbol{F}\left(\boldsymbol{u}, \frac{\partial \boldsymbol{u}}{\partial x}, \ldots\right) dV + \int_{S_t} \boldsymbol{E}\left(\boldsymbol{u}, \frac{\partial \boldsymbol{u}}{\partial x}, \ldots\right) dS \tag{11.16}$$

Herein, $\boldsymbol{u}$ is the unknown displacement function and $\boldsymbol{F}$ and $\boldsymbol{E}$ are specified differential operators.

The solution to equation (11.16) is a function $\boldsymbol{u}$ which makes Π stationary with respect to small changes $\delta \boldsymbol{u}$. Substituting the approximate displacement field defined by equation (11.4) into equation (11.16) yields:

$$\delta\Pi = \frac{\partial \Pi}{\partial \boldsymbol{u}_1}\delta \boldsymbol{u}_1 + \frac{\partial \Pi}{\partial \boldsymbol{u}_2}\delta \boldsymbol{u}_2 + \ldots.. + \frac{\partial \Pi}{\partial \boldsymbol{u}_n}\delta \boldsymbol{u}_n = 0 \tag{11.17}$$

This being true for any variations $\delta \boldsymbol{u}$ yields a set of equations:

$$\frac{\partial \Pi}{\partial \boldsymbol{u}} = \begin{bmatrix} \dfrac{\partial \Pi}{\partial \boldsymbol{u}_1} \\ \ldots \\ \dfrac{\partial \Pi}{\partial \boldsymbol{u}_n} \end{bmatrix} = 0 \tag{11.18}$$

From equation (11.18) the parameters $\boldsymbol{u}_i$ are found. The process of finding stationarity with respect to the trial functions $\boldsymbol{u}$ is called the *Rayleigh-Ritz method*, Burden and Faires [19].

The equations listed above need to be of an integral form necessary for the finite element approximation as Π is given in terms of volume and boundary integrals. Hence, if Π is a *quadratic form* (a scalar, quadratic function of a vector), equation (11.18) reduces to a linear form similar to equation (11.1), thus:

$$\frac{\partial \Pi}{\partial \boldsymbol{u}} \equiv \boldsymbol{K}\boldsymbol{u} + \boldsymbol{p} = 0 \tag{11.19}$$

Generally, two types of variational principles can be distinguished; *natural* and *contrived* variational principles. Natural variational principles refer to situations in which the physical aspects of the problem, such as minimisation of total potential energy to achieve equilibrium, can be stated directly in a variational principle form. In the latter case natural variational principles are closely related to the Galerkin method and the method of virtual work. Hence, the weak form can also be addressed as a variational form. Unfortunately, natural variations do not exist for all continuum problems. Contrived variational principles refer to situations in which natural variations do not exist. A variational principle can, however, still be constructed for any differentially specified problem either by extending the number of unknown functions $\boldsymbol{u}$ by additional variables known as *Lagrange multipliers* or, alternatively, by procedures such as using *Penalty functions* (force a function to stay inside a region determined by a constrained equation, while minimising the total potential, Bathe [3]) or the *Least Square method* (minimises a new error term defined as the volume integral of the squared residual, Burden and Faires [19]) which, opposite to Lagrange multipliers, do not posses the drawback of increasing the total number of unknowns, Zienkiewicz and Taylor [88]. Least Square approximations can also be used to minimise an error term based on the residual of the weighted residual approach.

The finite element procedure, discussed so far, is summarised in Figure 11.4, by Zienkiewicz and Taylor [87].

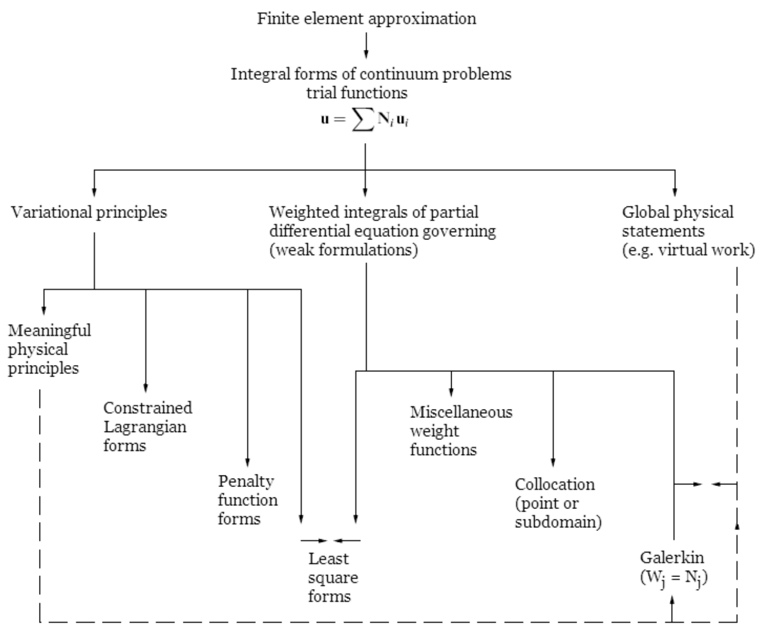

Figure 11.4. Finite element approximation, Zienkiewicz and Taylor 2000

In the Figure the dotted lines indicate a close relationship between the methods. The result at the end of each procedure is the weak form of equilibrium ready to solve.

11.2.6 Numerical Integration

To solve the weak form of equilibrium still involves the construction of the right hand side vector (discussed later) and the stiffness matrix by applying numerical integration over the elements. Basically, *numerical integration* is the approximate computation of a definite integral, e.g. an area under a graph or a volume under a surface. In the case of structural finite element analysis, the graph or volume represents the material properties of an element and integration leads to the element stiffness matrix.

Within the elements the stiffness integrand is determined with respect to a number of specific *integration points*, part of an *integration scheme*, and then weighted and summed to obtain the volume total value. The weight function is dependent on the chosen integration scheme as each integration point represents a certain ascribed, weighted, volume part of the total element volume. Depending on the number of integration points, the position of the integration points and the appropriate corresponding volumes, the integration is more or less accurate. Obviously, it is a trivial demand that the integration points are equally scattered over the element. Two schemes which frequently arise in finite element analysis are *Newton-Cotes* and *Gauss integration*. The system stiffness matrix is computed by looping over each element and within each element looping over the individual integration points.

With respect to the chosen integration scheme, the concept of *reduced integration* is introduced. Until now, there was referred to full integration as the stiffness matrix was assumed to be integrated exactly. However, the displacement formulation of finite element analysis produces a strain energy lower than the exact strain energy of the model considered, which means that the system stiffness is overestimated. Countering the overly stiff behaviour (caused by the finite element discretisation) the idea is to not evaluate the stiffness matrix exactly in the numerical integration but to use less integration points than needed to soften the element, Zienkiewicz and Taylor [88]. This so-called reduced integration causes higher order polynomial terms to vanish at the low-order Gaussian points so that they do not make any contribution to the strain energy. The application of reduced integration also has the advantageous property of lowering computational time and is effective in overcoming numerical difficulties such as *locking* (discussed later).

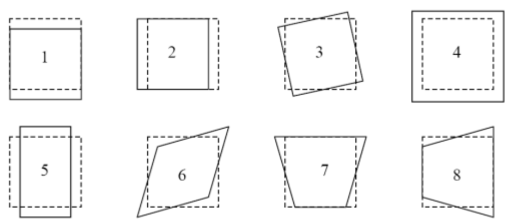

Figure 11.5. Deformation modes of an element

Disadvantageous of reduced integration is the danger that *spurious modes* or *hourglass modes* may arise, Bathe [3]. A spurious mode is an instability mode of an element, referring to a nodal displacement vector that is not a rigid-body motion but nevertheless produces zero strain energy. Hence, there is also referred to *zero-energy modes*. Using reduced 1-point Gauss integration, mode *1*, *2* and *3* of Figure 11.5 are rigid body motions, *4*, *5* and *6* are non-zero energy modes, but *7* and *8* are zero-energy modes as the single Gaussian point does not notice the deformation modes (normal strains and the shear strain are zero in the centre of the element). Using full 4-point Gauss integration, the zero-energy modes disappear. Spurious modes indicate that the solution of the problem is not unique, and the global stiffness is singular or nearly singular. A test for the spurious modes is to calculate the eigenvalues of the stiffness matrix. The number of zero eigenvalues indicates the number of rigid body modes, modes which do not contribute to the energy. If there are more zero eigenvalues than there should be on the basis of the number of translations and rotations, there are spurious modes. A more practical test is to observe the mesh of the deformed structure.

11.2.7 System Stiffness Matrix

The stiffness matrix which results from the finite element approximation has a rank equal to the total number of unknown nodal degrees of freedom. The matrix is in general a sparse banded matrix with, caused by the spatial connectivity of the elements and the compact support of the shape functions, an irregular cluster of non-zero elements near the diagonal. A graphical representation is illustrated in Figure 11.6. As rigid body motions of the structural domain are assumed to be suppressed, the matrix is stated to be regular.

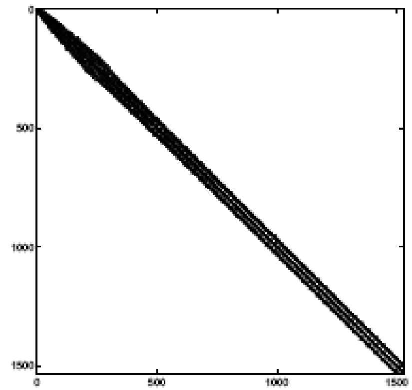

Figure 11.6. Graphical representation of a stiffness matrix, Wells 2004

The special properties of the stiffness matrix of a linear elastic problem offer a number of advantages in the solution process. Because the matrix is a sparse banded matrix, computational time (and storage requirements) can be saved by storing only the diagonal non-zero elements. Furthermore, as the matrix is symmetric, storing only the terms at the diagonal and above the diagonal is sufficient.

11.2.8 Right Hand Side Vector

Besides the stiffness matrix, the external force column, or right hand side (RHS) vector, consisting of element loads and external nodal forces, must be determined. Element loads refer to the contribution of the element body forces, the element surface tractions, and element initial stress and strain contributions, DIANA User's Manual [29]. In general, all the element loads are transferred to equivalent nodal forces and subsequently assembled and added to the nodal force column. Therefore, the body forces are determined by numerical integration over the elements. The surface tractions result from external boundary loading, known at the places where the natural boundary conditions are prescribed. The surface tractions received from neighbouring elements are eliminated because of the third law of Newton.

11.3 Linear Finite Element Procedure

Linear analysis is the most elementary finite element procedure. In linear analysis the relation between a force vector and a displacement vector is linear, an idealisation of the nonlinear reality. Using the finite element method, the displacement vector is discretised and represented by nodal variables and shape functions. The linear analysis involves the calculation of the discretised displacement vector that equilibrates the internal and external forces.

11.3.1 Virtual Work Formulation

The linear finite element procedure can be formulated using the principle of virtual work, which represents the weak form of the equilibrium relations. Aforementioned, the principle of virtual work states that an elastic structure is in equilibrium if for any virtual displacement $\delta\boldsymbol{u}$ the virtual work is equal to the virtual strain energy:

$$\int_V (\delta\boldsymbol{\varepsilon})^T \boldsymbol{\sigma}\, dV = \int_V \delta\boldsymbol{u}^T \boldsymbol{g} dV + \int_{S_t} \delta\boldsymbol{u}^T \boldsymbol{t} dS \tag{11.20}$$

Or, written as a summation over n_e elements:

$$\sum_{e=1}^{n_e} \int_{V_e} \delta\boldsymbol{\varepsilon}^T \boldsymbol{\sigma}\, dV = \sum_{e=1}^{n_e} \int_{V_e} \boldsymbol{u}^T \boldsymbol{g}_e dV + \sum_{e=1}^{n_e} \int_{S_t} \boldsymbol{u}^T \boldsymbol{t}_e dS \tag{11.21}$$

Opposite to equation (11.20), the discretised equation (11.21) imposes some restrictions on the displacement functions. This can be explained by examining element equilibrium of the equations (11.8) and (11.9) for every variation δ of the virtual displacement $\boldsymbol{u}$:

$$\int_{V_e} \delta\boldsymbol{u}^T \left(\boldsymbol{L}^T\boldsymbol{\sigma} + \boldsymbol{g}_e\right) dV - \int_{S_e} \left(\boldsymbol{L}_n^T\boldsymbol{\sigma} - \boldsymbol{t}_e\right) dS = 0 \tag{11.22}$$

Equation (11.22) is only valid if all derivatives of $\boldsymbol{u}$ and $\boldsymbol{\sigma}$ are finite through V. In general, the stresses do not achieve continuity across element interfaces, however, if the shape functions are such that they provide in matching nodal displacements at the interface of neighbouring elements, then continuity of stresses *in the mean* is met, DIANA User's Manual [29]:

$$\int_{S_{e_{i+j}}} \delta\boldsymbol{u}^T \left(\boldsymbol{L}_n^T\boldsymbol{\sigma}_i - \boldsymbol{L}_n^T\boldsymbol{\sigma}_j - \bar{\boldsymbol{t}}_e\right) dS = 0 \tag{11.23}$$

Herein, $\bar{\boldsymbol{t}}_e$ is the contribution of the external applied loads. Equation (11.23) is another approximate expression of satisfying equilibrium, and therefore, equation (11.21) is valid only within a single element up to its boundaries. If the displacements satisfy equation (11.21) the integrations can be performed over the element volumes and surfaces safely. Introducing relation (11.4) and (11.6) into (11.22) yields for an individual element:

$$\delta\boldsymbol{u}_e^T \int_{V_e} \boldsymbol{B}^T\boldsymbol{\sigma}\, dV = \delta\boldsymbol{u}_e^T \int_{V_e} \boldsymbol{N}^T\boldsymbol{g}_e\, dV + \delta\boldsymbol{u}_e^T \int_{S_e} \boldsymbol{N}^T\boldsymbol{t}_e\, dS \tag{11.24}$$

If the integral of the element boundary tractions is replaced by a kinematically equivalent nodal force vector $\boldsymbol{r}_e$ which corresponds to $\boldsymbol{u}_e$, reordering of (11.24) leads to:

$$\delta\boldsymbol{u}_e^T \left(\int_{V_e} \boldsymbol{B}^T\boldsymbol{\sigma}\, dV - \int_{V_e} \boldsymbol{N}^T\boldsymbol{g}_e\, dV \right) = \delta\boldsymbol{u}_e^T \boldsymbol{r}_e \tag{11.25}$$

As equation (11.25) must be valid for all virtual displacements, the equilibrium can be rewritten to:

$$\int_{V_e} \boldsymbol{B}^T \boldsymbol{\sigma} \, dV \; - \; \int_{V_e} \boldsymbol{N}^T \boldsymbol{g}_e \, dV \; = \boldsymbol{r}_e \tag{11.26}$$

Note that, equation (11.26) is valid for any stress-strain relation (linear and nonlinear).

11.3.2 Stiffness Matrix Formulation

If the stress-strain relation is linear, i.e. $\boldsymbol{\sigma} = \boldsymbol{D}(\boldsymbol{\varepsilon} - \boldsymbol{\varepsilon}_o) + \boldsymbol{\sigma}_o$ equation (11.26) is equal to:

$$\boldsymbol{K}_e \boldsymbol{u}_e + \boldsymbol{p}_e = \boldsymbol{r}_e \tag{11.27}$$

Herein, the element stiffness is defined as $\boldsymbol{K}_e = \int_{V_e} \boldsymbol{B}^T \boldsymbol{D} \boldsymbol{B} \, dV$ and the element contribution to the force vector is equal to $\boldsymbol{p}_e = \int_{V_e} \boldsymbol{N}^T \boldsymbol{g}_e \, dV - \int_{V_e} \boldsymbol{B}^T \boldsymbol{D} \boldsymbol{\varepsilon}_o \, dV + \int_{V_e} \boldsymbol{B}^T \boldsymbol{\sigma}_o \, dV$.

If the displacement approximate relation (11.4) and the discrete strain-displacement relation (11.6) are substituted into equation (11.21) a similar expression can be found as summation over the elements, thus:

$$\sum_{e=1}^{n_e} \delta \boldsymbol{u}_e^T \left(\int_{V_e} \boldsymbol{B}^T \boldsymbol{D} \boldsymbol{B} \, dV \right) \boldsymbol{u}_e = \sum_{e=1}^{n_e} \delta \boldsymbol{u}_e^T \int_{V_e} \boldsymbol{N}^T \boldsymbol{g}_e dV + \sum_{e=1}^{n_e} \delta \boldsymbol{u}_e^T \int_{S_t} \boldsymbol{N}^T \boldsymbol{t}_e dS + \sum_{e=1}^{n_e} \delta \boldsymbol{u}_e^T \left(\int_{V_e} \boldsymbol{B}^T \boldsymbol{D} \boldsymbol{\varepsilon}_o \, dV - \int_{V_e} \boldsymbol{B}^T \boldsymbol{\sigma}_o \, dV \right) \tag{11.28}$$

Then, the system stiffness matrix can be defined as:

$$\boldsymbol{K} = \sum_{e=1}^{n_e} \boldsymbol{T}_e^T \boldsymbol{K}_e \boldsymbol{T}_e \tag{11.29}$$

Herein, the element stiffness matrix is defined as $\boldsymbol{K}_e = \int_{V_e} \boldsymbol{B}^T \boldsymbol{D} \boldsymbol{B} \, dV$ and the matrix $\boldsymbol{T}$ transforms the element stiffness from local (element) to global coordinates.

11.3.3 Assembling RHS Vector

The right hand side vector is composed out of element loads and the contribution of the external nodal forces $\boldsymbol{p}_c$. The element loads are added to the external nodal force vector after integration over the elements. In the DIANA User's Manual [29], they are defined as:

$\boldsymbol{p}_g = \sum_{e=1}^{n_e} \boldsymbol{T}_e^T \int_{V_e} \boldsymbol{N}^T \boldsymbol{g}_e \, dV$ *Contribution of the element body forces*

$\boldsymbol{p}_t = \sum_{e=1}^{n_e} \boldsymbol{T}_e^T \int_{S_e} \boldsymbol{N}^T \boldsymbol{t}_e \, dS$ *Contribution of the element surface tractions*

$$\boldsymbol{p}_{\varepsilon_o} = \sum_{e=1}^{n_e} \boldsymbol{T}_e^T \int_{V_e} \boldsymbol{B}^T \boldsymbol{D} \boldsymbol{\varepsilon}_e \, dV \qquad \textit{Contribution of the element initial strains}$$

$$\boldsymbol{p}_{\sigma_o} = \sum_{e=1}^{n_e} \boldsymbol{T}_e^T \int_{V_e} \boldsymbol{B}^T \boldsymbol{\sigma}_e \, dV \qquad \textit{Contribution of the element initial stresses}$$

The right hand side vector can, thus, be expressed as:

$$\boldsymbol{p} = \boldsymbol{p_g} + \boldsymbol{p_t} + \boldsymbol{p}_{\varepsilon_o} - \boldsymbol{p}_{\sigma_o} + \boldsymbol{p_c} \tag{11.30}$$

11.3.4 Equilibrium

After applying the theorem of virtual displacement the weak equilibrium equations of the element assemblage are:

$$\boldsymbol{K}\boldsymbol{u} = \boldsymbol{p} \tag{11.31}$$

Herein, $\boldsymbol{p}$ is described by equation (11.30) and the stiffness matrix $\boldsymbol{K}$ by equation (11.29). Finite element programs approximate the displacements $\boldsymbol{u}$ either direct of iteratively. This is discussed in section 11.4.

11.4 Nonlinear Finite Element Procedure

In practice, the range of linear structural response is rather limited and the *physical* (e.g. plasticity, creep, viscoelasticity) and *geometrical* (large deformations, large strains) behaviour may become nonlinear. Moreover, *boundary* nonlinearity (contact, nonlinear supports or opening/closing of gaps) may occur (however, not further discussed here). For a realistic assessment of the structural behaviour these nonlinear effects must be incorporated. In particular in situations such as research, the assessing of existing structures or to establish the cause of a structural failure. Hence, there is a need for finite element procedures which are able to bring into account for nonlinearities.

In nonlinear finite element analysis the relation become nonlinear and the displacements often depend on the displacement at earlier stages. Similar to the linear analysis, in nonlinear analysis a displacement vector is to be found that equilibrates the internal and external forces. However, in nonlinear analysis the solution vector cannot be calculated right away. To determine the state of equilibrium the problem is not only made discrete in place (with finite elements) but also in time (with increments). Hence, the nonlinear problem can be formulated as to find a displacement increment (step) such that there is equilibrium of external and internal forces in the increment.

Thus, the objective is to calculate a displacement vector which satisfies equilibrium between the internal and external force vectors, satisfying the essential boundary conditions:

$$\boldsymbol{p}_{int} = \boldsymbol{p}_{ext} \tag{11.32}$$

$$\boldsymbol{u}_i = \boldsymbol{u}_i^0 \quad (i\ prescribed) \tag{11.33}$$

In nonlinear analysis the internal force vector depends nonlinearly on the displacements (nonlinear elasticity) or on the displacements in the history (plasticity). The external force vector can also be dependent of the displacements, e.g. in case of the magnitude or direction of loading being depending on the displacements, DIANA User's Manual [29]. Therefore, relation (11.32) must be rewritten to:

$$\boldsymbol{p}_{int}(\boldsymbol{u}, history) = \boldsymbol{p}_{ext}(\boldsymbol{u}) \tag{11.34}$$

To solve the above relation, the system must be discretised in space (the finite elements) and in time. Starting at time t with a corresponding approximated solution ${}^t u$, a solution ${}^{t+\Delta t}u$ is searched that complies with equation (11.34). For each time increment, only the displacements at the beginning and at the end are known. The internal force vector of equation (11.34) is calculated from the situation at time t, the time increment Δt and the displacement increment Δu. The external forces are determined by the current geometry. For one time step, equilibrium only depends on the displacement increment Δu. Thus, the nonlinear problem involves the search for Δu such that:

$${}^{t+\Delta t}\boldsymbol{u} = {}^t\boldsymbol{u} + \Delta\boldsymbol{u} \tag{11.35}$$

Thus, equation (11.32) transforms to:

$$\boldsymbol{g}(\Delta\boldsymbol{u}) = \boldsymbol{p}_{ext}(\Delta\boldsymbol{u}) - \boldsymbol{p}_{int}(\Delta\boldsymbol{u}) = \boldsymbol{o} \tag{11.36}$$

Herein $\boldsymbol{g}(\Delta u)$ stand for the *residual force vector* or *out-of-balance force vector* which has to be zero for the exact solution. Starting at time t we can increment the time with a number of increment until the desired end value t is reached.

To achieve equilibrium at the end of the increment, we can use an iterative solution algorithm; the combination is called an incremental-iterative solution procedure. This is discussed in Section 11.5.

11.4.1 Physical Nonlinearity

Physical nonlinearity refers to nonlinear material behaviour, i.e. the constitutive relationship between the stresses and strains is nonlinear. Physical nonlinear behaviour can be categorised by its variation in time. Time independent physical behaviour refers to effects such as *cracking*, *plasticity* and *nonlinear elasticity* whereas time dependent behaviour deals with *creep*, *shrinkage*, *viscoelasticity* and *viscoplasticity*. In finite element programs the physical nonlinear behaviour is modelled in so-called material models. They are discussed later in Section 11.11.

11.4.2 Geometrical Nonlinearity

In a geometrical nonlinear analysis large deformations and rotations are accounted for. Two convenient types of geometrical nonlinear descriptions are a *Total Lagrange* and an *Updated Lagrange* description. Basically, both descriptions are conceptually identical but they use different type of reference geometry for their stress and strain measures. In a Total Lagrange description the stress and strain measures are defined with reference to the undeformed geometry. According to Crisfield [25], a Total Lagrange description is useful if rotations and displacements are large and strains are small, and is even obligatory for large strain hyper-elastic (rubber) material behaviour. Opposed to the Total Lagrange description, an Updated Lagrange description uses an updated reference geometry (e.g. last known equilibrium state). An Updated Lagrange description can be used advantageously in case of large plastic deformations, Crisfield [25].

It must be pointed out that, the choice of geometrical nonlinear description determines the stress and strain measures that will be used. In order to correctly describe large deformations and rotations in a Total Lagrange description, the small strain formulation used in Chapter 5 is insufficient and the strains must be determined according to the Green-Lagrange formulation. The *Green-Lagrange strain* tensor (or short, Green strain tensor) gives deformations exact for any size deformation independent of rigid body motions. The Green strain tensor $\boldsymbol{E}$ is defined as:

$$ {}_0^t\boldsymbol{E} = \tfrac{1}{2}\left({}_0^t\boldsymbol{F}^T \cdot {}_0^t\boldsymbol{F} - \boldsymbol{I} \right) \tag{11.37} $$

Herein $\boldsymbol{F}$ represents the deformation-gradient matrix and $\boldsymbol{I}$ the identity matrix.

Just as new strains are needed, new stress measures are needed; the small-stress definition ‘force over area’ is not unique in geometrical nonlinear analysis as the area may change in magnitude and/or direction. The stress measure that is energy conjugate to the Green strain tensor is the *second Piola-Kirchhoff* stress tensor. In very simple terms it can be said that the second Piola-Kirchhoff stress is force of original area and is related to the original configuration. Hence, a Total Lagrange description requires second Piola-Kirchhoff stress representation. Contrary, Updated Lagrangian formulations strictly require *Cauchy* stress formulation, which can be defined as force over final area and is related to the deformed configuration. The energy conjugate of the Cauchy stress is the linearised strain. With respect to the Updated Lagrange description, it must be mentioned that, although large displacements, rotations and strain are described correctly, still a constitutive relation appropriate for large strain behaviour has to be used, DIANA User’s Manual [29].

As denoted by Bathe [3], second Piola-Kirchhoff stresses have little physical meaning and, in practice, Cauchy stresses must be calculated. The second Piola-Kirchhoff stress tensor $\boldsymbol{S}$ is related to the Cauchy stresses $\boldsymbol{\sigma}$ by:

$$ {}_0^t\boldsymbol{S} = det\, {}_0^t\boldsymbol{F} \cdot {}_0^t\boldsymbol{F}^{-1} \cdot {}_t^t\boldsymbol{\sigma} \cdot {}_0^t\boldsymbol{F}^{-1} \tag{11.38} $$

Generally, the finite element program will execute the transformation and the user may ask for Cauchy stresses independent from the chosen formulation.

11.5 Solution Procedures for Static Linear Analysis

To obtain the approximated displacements, stresses and strains a solution to the linear system of equations needs to be performed. The solution of this system of equations is usually the most computation intensive part in the finite element analysis and the overall effectiveness largely depends on the numerical procedures used. Basically, there are two different classes of methods for the solution. In a *direct solution method* the equations are solved using a number of steps and operations that are predetermined in an exact manner, whereas iteration is used when an *iterative solution method* is employed. At present, direct techniques are employed in most cases, but for very large systems iterative methods can be more effective, Bathe [3].

11.5.1 Direct Procedures

Direct solvers obtain the exact solution of the displacement vector in a known number of steps (floating point operations), subject only to roundoff error. The most effective direct solution methods currently used are essentially applications of *Gauss elimination*, Bathe [3]. The basic procedure of Gauss elimination is to reduce the equations to an upper triangular coefficient matrix from which the unknowns can be calculated by back-substitution. A commonly used Gaussian' method, however, under the guise of a matrix factorisation, is *LDU-decomposition*. The LDU-decomposition divides the stiffness matrix into three matrices, the lower triangular matrix $\boldsymbol{L}$, the upper triangular matrix $\boldsymbol{U}$ and the diagonal matrix $\boldsymbol{D}$, from which the product is equal to the original matrix. The advantage of LDU-decomposition (or $\boldsymbol{LDL}^T$ in case of a positive-definite symmetric matrix) is that the triangular matrices can be solved apart from each other by simple and fast successive forward and backward-substitution. For specific (e.g. sparse, symmetric and positive-definite such as for linear elastic problems) systems the direct solver algorithm can be modified. Examples are the *Generalised Element method*, based on a combined wavefront (active rows during the elimination of the *i*-th equation)-super-element technique, and the *(Sparse) Cholesky decomposition method*. The Cholesky method (DIANA default) is optimised for cache based memory access and is superior to all other methods; however, it needs more primary memory, DIANA User's Manual [29].

The efficiency of solving large systems of equations with direct methods is governed by the pattern of nonzero elements in the matrix. Therefore, *ordering techniques* have been developed to reorder the equations so as to increase the effectiveness of the numerical solution process. Ordering techniques refer to row-column interchanging in the matrix (*pivoting*) in order to limit the bandwidth and minimise fill-in elements (elements that originally are zero but become nonzero, Bathe [3]). Especially when a sparse solver (not operating on elements that remain zero throughout the solution) is involved, ordering algorithms play a major role to decrease the number of fill-ins. Ordering is also used to minimise effects of roundoff error between large and small terms on the diagonal. When dealing with symmetric positive-definite matrices, Gauss elimination can be done without row interchanges. Moreover, the computations are stable with respect to the growth of roundoff errors.

11.5.2 Iterative Procedures

Disadvantageous of the 'robust' direct solvers are the long computational time needed for solving very large problems and the amount of storage required. Therefore, alternatively, iterative solvers can be used which require less storage as only the nonzero matrix elements are stored and operated on, Bathe [3]. The basic idea behind iterative solvers is to create a sequence of initial approximations to the displacement vector and, from there, approach to the exact solution by successive iteration:

$$\boldsymbol{u}_{i+1} = \boldsymbol{u}_i + \gamma_i(\boldsymbol{p} - \boldsymbol{K}\boldsymbol{u}_i) \tag{11.39}$$

Herein, $\boldsymbol{p} - \boldsymbol{K}\boldsymbol{u}_i = \boldsymbol{r}_i$ represents the residual which must converge to zero (or the desired accuracy).

Historically, iterative solvers have been employed during initial developments of the finite element method, though abandoned in the *60s* and *70s* as the number of steps to achieve convergence is impossible to calculate in advance, Bathe [3]. Besides that, ill-conditioned matrices, which often occur in structural mechanics, show slow convergence.

Examples of iterative solvers are the *Gauss-Seidel method* (not offered by DIANA), the *Conjugate Gradient method* and *Generalised Minimal Residual algorithm*. The iterative methods differ in the way the iteration parameters γ_i are computed, DIANA User's Manual [29].

The Conjugate Gradient (CG) method is the most popular method used today. It is the best method involving systems with a symmetric positive-definite matrix, significantly reducing the number of iterations in compare to the other methods, DIANA User's Manual [29]. The CG method is based on the variational principle idea that the solution of **Ku** = **p** minimises the total potential. Recapitulate, the linear total potential is a quadratic form defined as $\Pi = \frac{1}{2}\boldsymbol{u}^T\boldsymbol{K}\boldsymbol{u} - \boldsymbol{u}^T\boldsymbol{p}$. If $\boldsymbol{K}$ is symmetric and positive-definite, Π is described by a paraboloid bowl and is minimal at the solution of $\boldsymbol{K}\boldsymbol{u} = \boldsymbol{p}$. Hence, when the gradient of Π is zero, the solution is found. The CG algorithm iterates to the zero gradient by selecting a set of *K-conjugate* (or *K-orthogonal*) search directions $\boldsymbol{d}_i$ ($\boldsymbol{d}_i^T\boldsymbol{K}\boldsymbol{d}_j = 0$) for which each search direction is orthogonal to all previous ones (in the *n x n* dimensional space of the matrix). If each step is orthogonal to all previous ones, the next step represents the orthogonal residual of all previous ($\boldsymbol{d}_i^T\boldsymbol{r}_{i+1} = 0$). In fact, if the residual is orthogonal to all previous search directions, it is also orthogonal to all previous residuals ($\boldsymbol{r}_i^T\boldsymbol{r}_j = 0$). Storing all previous residuals is, however, costly. By making clever use of the symmetry of $\boldsymbol{K}$ the CG algorithm uses only the residuals of the two previous iterations obtaining the same result. The new displacement can be defined as $\boldsymbol{u}_{i+1} = \boldsymbol{u}_i + \boldsymbol{\alpha}_i\boldsymbol{d}_i$ wherein $\boldsymbol{\alpha}_i = \boldsymbol{r}_i^T\boldsymbol{r}_i / \boldsymbol{d}_i^T\boldsymbol{K}\boldsymbol{d}_i$. For optimal use, preconditioners must be used to improve the condition number of the stiffness matrix. If the stiffness matrix is not positive-definite (e.g. non-symmetry) the Conjugate Gradient method need not converge, DIANA User's Manual [29].

For non-symmetric systems other iterative schemes like the more generally applicable Generalised Minimal Residual (GMRES) method have been developed. In the GMRES method the iteration parameters are computer by orthogonalising the residual explicitly against all previous residuals. Disadvantageous is the fact that all previous residuals must be stored and that the number of iterations increases per iteration, similar to the CG method. GMRES differs from the CG method in the way that the iteration is restarted after a fixed number of iterations is added to the basis instead of only the two previous ones, DIANA User's Manual [29].

The key to effective iterative solvers is to reach convergence within a reasonable number of iterations. Of major importance in the iterative scheme are precondition procedures to speed up the rate of convergence when slow convergence is observed. Basically, the rate of convergence depends on the matrix condition and preconditioners provide in a more favourable eigenvalue distribution. Various preconditioners have been proposed, but particularly effective is the use of some *incomplete Cholesky factors of* $\boldsymbol{K}$ (or the more general *Incomplete LU-decomposition* or *ILU preconditioning*) or *Jacobi preconditioning*. Incomplete LDU-decomposition only factorises non-zero elements larger than a given threshold parameter and, thus, approximates $\boldsymbol{K}$ by the product of incomplete upper and lower diagonal matrices. Jacobi preconditioning refers to a scale process of the stiffness matrix with its own diagonal matrix for problems with a diagonally dominant stiffness matrix. Hence, the resulting matrix is equal to the inverse of the diagonal of the original matrix and good-conditioned. In the preconditioning process it is not necessary to reorder the stiffness matrix as preconditioning does not depend on the ordering of the equations.

11.5.3 General Remarks

It is observed that ill-conditioned matrices show slow convergence in case of iterative solution procedures. Aforementioned, this is often the case for beam, plate and shell elements. An ill-conditioned linear system is also susceptible to rounding errors which may ruin the solution. This is the case for as well iterative as direct solvers, but more hidden for direct and therefore even more dangerous.

11.6 Solution Procedures for Static Nonlinear Analysis

Nonlinear problems are successfully solved using an *incremental-iterative* solution procedure as a purely incremental procedure (explicit process) only leads to accurate solutions with very small step sizes. The combination with an iterative procedure, which is implicit, allows for larger steps sizes as it effectively reduces errors. Basically, the incremental-iterative solution procedure for a nonlinear problem involves the solution of a linear set of equations at every iteration with a 'reasonable' stiffness matrix. Both the incremental and the iterative procedures can be discussed separately.

11.6.1 Iterative Procedures

Essentially, the general procedure for all iteration processes is the same as it involves the adaptation of the total displacement $\Delta\boldsymbol{u}$ iteratively by iterative increments $\delta\boldsymbol{u}$ until convergence is reached up to the desired degree. Thus, the incremental displacement at iteration $i+1$ is defined as:

$$\Delta \boldsymbol{u}_{i+1} = \Delta \boldsymbol{u}_i + \delta \boldsymbol{u}_{i+1} \tag{11.40}$$

Each iteration procedure differs in the way the iterative increment is computed. The iterative increment is calculated from a stiffness matrix and the out-of-balance force vector $\boldsymbol{g}_i$ at the start of the iteration *i*:

$$\delta \boldsymbol{u}_i = \boldsymbol{K}_i^{-1} \boldsymbol{g}_i \tag{11.41}$$

The stiffness matrix represents a linearised form of the equilibrium relation between the internal and external force vector. The way in which the stiffness matrix is derived categorises the different schemes. Well-known iteration schemes are *Constant* and *Linear Stiffness* and *Regular* and *Modified Newton-Raphson*.

Iteration Schemes

To illustrate the iteration procedure Regular Newton-Raphson and Modified Newton-Raphson are illustrated in Figure 11.7. The Regular Newton-Raphson iteration evaluates a tangential stiffness matrix at every iteration. Thus, the stiffness matrix in equation (11.41) is based on the last known situation which may be a non-equilibrium situation. Regular Newton-Raphson has the advantage of fast, quadratic, convergence, however, is less efficient as it repetitively needs to set-up and decompose (only when using a direct solver) the stiffness matrix at every iteration. Hence, the iterations becomes relatively time consuming.

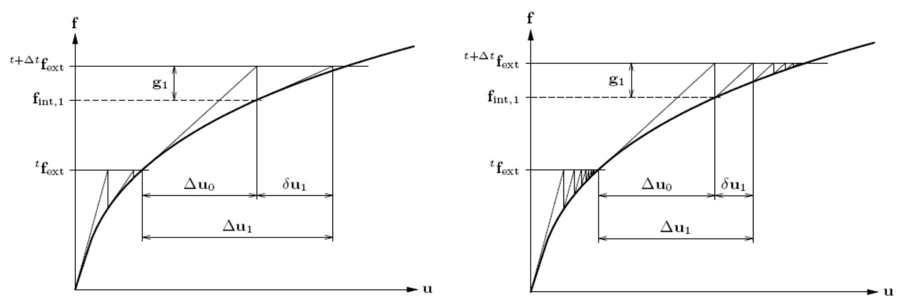

Figure 11.7. Regular (left) and Modified Newton-Raphson iteration, DIANA User's Manual 2005

Modified Newton Raphson only derives the tangent stiffness matrix every increment which consequently results in a larger number of iterations. Each iteration can be performed faster as it is not necessary to repeat the costly decomposition. Modified Newton-Raphson may still converge in situations where the Regular Newton-Raphson method does not, DIANA User's Manual [29].

Some other schemes offered by DIANA may in short be characterised by the way they evaluate the stiffness matrix. Linear Stiffness uses the linear stiffness matrix at every iteration, resulting in a very robust but slow convergence scheme. Constant stiffness uses the same stiffness matrix as results from the previous increment, which may be one of the methods described above. *Continuation* schemes use the displacements of the previous increment as a first prediction for the current increment and *Quasi-Newton* (or *Secant* method) determines the stiffness from known positions at the equilibrium path. Note that, if the Quasi-Newton scheme is used for a system with more than one degree of freedom, the secant stiffness is not unique and the stiffness matrix must be computed using methods such as *Broyden*, *BFGS* (Broyden, Fletcher, Goldfarb and Shanno) and *Crisfield*. These methods use the previous secant stiffness and so-called update vectors to determine the inverse of the new (unique) stiffness matrix (via the *Sherman-Morrison* formula which computes the sum of a regular matrix and a dyadic product of a column and row vector). In combination with the global selected iteration method, *Line Search* algorithms may be applied to stabilise the convergence (Line Search ensures a 'reasonable' prediction close to the equilibrium path) or increase the speed. Basically, the Line Search algorithm reads the out-of-balance force and checks whether a better solution can be found by a try solution of small interpolated displacement steps.

Convergence Criteria

Similar to linear iteration procedures, the number of iterations depends on the desired accuracy of the final solution. To stop the iteration there are several convergence criteria. The iteration is also stopped at a specified number of maximum iterations or when divergence occurs. The convergence criteria are force, displacement or energy based and illustrated in Figure 11.8. The force norm checks the out-of-balance force norm of the current iteration against the out-of-balance force norm of the previous iteration. The displacement norm compares the norm of the current displacement with the norm of the displacement increments in the first prediction of the increment. The energy norm checks the ratio between the current and previous energy norm, composed out of the internal forces and relative displacements. The force norm immediately knows whether divergence or convergence occurs, all other require one additional iteration.

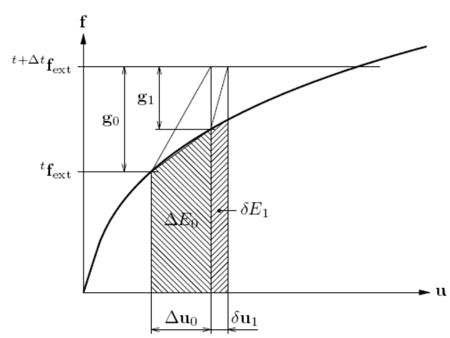

Figure 11.8. Norm items, DIANA User's Manual 2005

The question of which convergence criteria is the best option for a particular problem cannot be answered directly. In general, it is the best option to select a norm in which the reference value (ratio denominator) is not close to zero, DIANA User's Manual [29]. It is important to put the convergence criteria strict enough, i.e. the discrepancy between the iterated and actual equilibrium point is passed on to the next increment.

11.6.2 Incremental Procedures

The iterative part is combined with an incremental procedure. Most typical incremental procedures are the *Load* and *Displacement controlled* methods, discussed first. A more powerful method is the *Arc-length* method, capable of handling heavy nonlinear material behaviour.

Load and Displacement Control

The Load and Displacement Control are the most basic incremental procedures. The iteration processes discussed in Section 11.6.1 are an example of load controlled methods as at the start of an increment, the external load vector is directly increased. Besides load controlled incremental methods there are displacement controlled methods which were introduced to overcome difficulties with *limit points*. At the start of an increment, the displacement is prescribed. Both methods are illustrated in Figure 11.9.

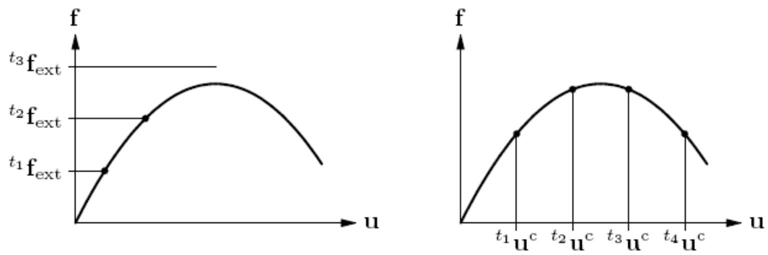

Figure 11.9. Load control (left) and displacement control, DIANA User's Manual 2005

In load control the load is kept constant during a load step and in the displacement control the displacement is kept constant during increment.

Arc-length Control

For structural systems which experience *limit point snap-through* or *snap-back* behaviour, see Figure 11.10, both the load control and the displacement control lead to error. E.g. the tangent stiffness becomes singular in limit points. To overcome these problems the arc-length method, originally developed by Riks (1972; 1979) and Wempner (1971) and later modified by others, can be used. The arc-length method modifies the load-factor at each iteration so that the solution follows some specified path until convergence is achieved. All iteration schemes described above may be combined with the arc-length control method.

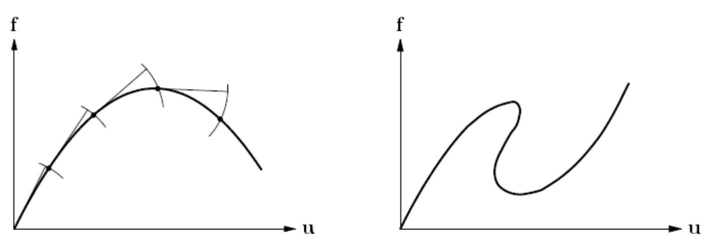

Figure 11.10. Arc-length control on snap-through (left) and snap-back, DIANA User's Manual 2005

In the arc-length method a variable load-factor is introduced in the equilibrium equation of a nonlinear system. Then the method is aimed to find the intersection of the new equilibrium equation with constant Δl termed as the arc-length. Arc-length methods that have been developed differ in the way the iterations are banded and the way the tangential stiffness matrix is used, i.e. the way in which the tangent stiffness matrix is derived and whether or not the tangential stiffness matrix is updated each iteration.

DIANA offers *updated normal plane* and *spherical path* arc-length control. Originally, the work of Riks and Wempner include an iterative change orthogonal to the predictor solution. Each iteration is banded by this so-called normal plane which is updated every new step, Crisfield [25]. Hence, the method is referred to as the Updated Normal Plane arc-length method. The method is seen in Figure 11.11. Crisfield (1981, 1983; 1984) developed a method in which a constraint equation is introduced which forms a circular constraint. The proposed technique is termed as cylindrical path arc-length method for one-dimensional problems and was later modified to the spherical path arc-length method for higher-dimensional problems. Hence, the spherical path arc-length is sometimes referred to as the *Arc-length Crisfield* method, Memon et al. [60]. The spherical constrained arc-length method is also seen in Figure 11.11.

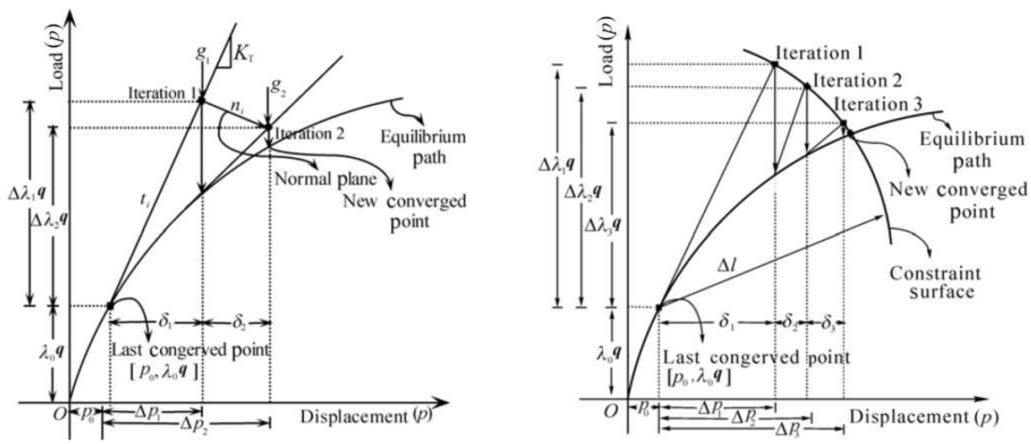

Figure 11.11. Updated normal plane (left) and spherical path (right) arc-length method

The either spherical (quadratic terms included) or updated normal plane (only linear terms) constraint approximately yield the same result. More important is the choice for the value of the arc-length. Generally, for the first increment the trail load-factor is assumed to be 1/5 or 1/10 of the total load. Further increments determine the load-factor according to the rate of convergence of the solution process, Memon et al. [60]. The arc-length method shows faster convergence when combined with Line Searches as proven by Foster (1992), Memon et al. [60]. Moreover, the arc-length method is particularly useful if combined with adaptive load incrementation (discussed later). The arc-length method fails if convergence is not obtained within the maximum number of iterations or by numerical instabilities.

In case of a local collapse mechanism, De Borst and Rots (1987) introduced an indirect displacement control option. In the iterations of the standard arc-length method the load increment (or decrement) is scaled as a function of all nodal displacements. When localisation of deformation occurs, the standard method may fail and a selection of a limited number of displacements near the localisation in a reduced displacement increment vector to scale the load increment or decrement can yield better results. This is indirect displacement control. It differs from the standard method in that it involves a constraint equation based on a few dominant displacement parameters. Another option is CMOD (Crack Mouth Opening Displacement) control which uses a vector formed with new degrees of freedom that can e.g. simulate the difference in nodal displacements at a crack, DIANA User's Manual [29].

Adaptive Loading

Besides the choice for an incremental step control method, the incremental process also involves the choice for the initial step size. An optimal choice for the increment sizes is not known and cannot be fixed in advance. Therefore, *adaptive loading* is introduced which uses increment sizes dependent of previous results. In DIANA, adaptive loading can either be *iteration based* (all types of loading) or *energy based* (only for arc-length methods). Iteration based refers to a method which adapts the increment by a desired number of iterations, using the results of the previous increment for the increment prediction. The energy based method determines a load increment such that the vector product of the load increment and the displacement increment (the work increment) in the first prediction equals the final work increment of the previous step. Furthermore, adaptive loading also refers to the choice between load increments or decrements (loading-unloading). A simple way is to choose based on the appearance of *negative pivots* in the global system of equations as negative pivots often indicate unstable structural behaviour related with some type of snap-through, DIANA User's Manual [29].

11.6.3 General Remarks

In nonlinear analysis it is observed that, generally, over stiff stiffness matrices lead to a slow convergence but are stable. Matrices which are too soft, however, will lead to divergence. Furthermore, exact tangent stiffnesses will lead to a fast (quadratic) convergence but might become unstable.

For nonlinear analysis additional substructuring can be used. Substructuring is a standard technique in finite element analysis and refers to group treatment of elements as they are a single substructure. For example when in non-linear analysis many elements behave linearly, these elements can be put in a substructure. The internal degrees of freedom are then removed and the calculation goes faster.

11.7 Stability Analysis

Aforementioned, a property of matrices is the existence of a set of scalars which, when multiplied with the identity matrix, allow for the solution of $(\boldsymbol{A} - \lambda_i \boldsymbol{I})\boldsymbol{\varphi}_i = 0$ and $det|\boldsymbol{A} - \lambda_i \boldsymbol{I}| = 0$. Here, $\boldsymbol{\varphi}_i$ is a corresponding mode shape vector. The set of scalars are called *eigenvalues* and the corresponding mode shape vectors are called the *eigenvectors*. The determination of eigenvalues and eigenvectors of a matrix is mathematically known as an *eigenvalue problem*.

Eigenvalue problems arise in common applications such as *stability analysis*. In case of a stability analysis the eigenvalues represent critical buckling loads and the buckling shapes are defined by the eigenvectors. In a stability analysis a critical displacement (or *stability point*) $\boldsymbol{u}_{crit}$ is searched such that the internal force vector $\boldsymbol{r}(\boldsymbol{u})$ equilibrates the external force vector $\boldsymbol{p}(\boldsymbol{u})$ and that incremental variations $\delta\boldsymbol{u}$ to the solution exist such that the equilibrium remains satisfied, DIANA User's Manual [29]. Thus:

$$\boldsymbol{r}(\boldsymbol{u}_{crit}) = \boldsymbol{p}(\boldsymbol{u}_{crit}) \tag{11.42}$$

$$\boldsymbol{r}(\boldsymbol{u}_{crit} + \delta\boldsymbol{u}) = \boldsymbol{p}(\boldsymbol{u}_{crit} + \delta\boldsymbol{u}) \tag{11.43}$$

Assuming $\delta\boldsymbol{u}$ close to $\boldsymbol{u}_{crit}$ equation (11.43) can be linearised as:

$$\boldsymbol{r}(\boldsymbol{u}_{crit}) + \left(\frac{\partial \boldsymbol{r}}{\partial \boldsymbol{u}}\right)_{crit} \delta\boldsymbol{u} \approx \boldsymbol{p}(\boldsymbol{u}_{crit}) + \left(\frac{\partial \boldsymbol{p}}{\partial \boldsymbol{u}}\right)_{crit} \delta\boldsymbol{u} \tag{11.44}$$

Subtracting equation (11.42) from equation (11.44), introducing a tangent stiffness matrix $\boldsymbol{K} = \left(\frac{\partial \boldsymbol{r}}{\partial \boldsymbol{u}}\right)_{crit}$ and assuming *conservative loading* (load not dependent of displacement) the equation can be simplified to:

$$\boldsymbol{K}\delta\boldsymbol{u} \approx 0 \tag{11.45}$$

The latter equation is the instability condition.

11.7.1 Euler Stability (Linear Buckling)

The *Euler stability analysis* verifies whether the solutions from linear elastic analysis are stable or whether small disturbances exist, requiring no extra external energy. An Euler stability analysis partly takes into account for geometrical nonlinear effects. Therefore, the tangent stiffness matrix is presented by a linear and a nonlinear part $\boldsymbol{K} = \boldsymbol{K}_L + \boldsymbol{K}_{NL}$ which can be described as:

$$\boldsymbol{K}_L = \int_V \boldsymbol{B}_L^T \boldsymbol{D} \boldsymbol{B}_L \, dV \qquad \text{with} \qquad \boldsymbol{B}_L = \boldsymbol{B}_{L0} + \boldsymbol{B}_{L1}$$

$$\boldsymbol{K}_{NL} = \int_V \boldsymbol{B}_{NL}^T \boldsymbol{\tau} \boldsymbol{B}_{NL} \, dV \tag{11.46}$$

The kinematic differential matrix $\boldsymbol{B}$ is subdivided into a zero displacement effect ($\boldsymbol{B}_{L0}$) and an initial displacement effect ($\boldsymbol{B}_{L1}$). Both the linear and the nonlinear matrix have up to second-order displacement contributions. The Euler stability analysis is, however, a linear buckling analysis and, thus, only first order displacement terms are of interest. Suppose that $\boldsymbol{u}_{lin}$ is known from the linearised equilibrium between the internal force vector $\boldsymbol{r}(\boldsymbol{u})$ and the external force vector $\boldsymbol{p}(\boldsymbol{u})$:

$$\boldsymbol{K}_{L0} = \left(\int_V \boldsymbol{B}_{L0}^T \boldsymbol{D} \boldsymbol{B}_{L0} \, dV\right) \boldsymbol{u}_{lin} = \boldsymbol{p} \tag{11.47}$$

The question is then if there is a critical displacement satisfying equation (11.42) and (11.45) such that:

$$\boldsymbol{u}_{crit} = \lambda_{crit} \boldsymbol{u}_{lin} \tag{11.48}$$

Which results from a loading $\boldsymbol{p}_{crit} = \lambda_{crit}\boldsymbol{p}$, as can be shown by multiplying equation (11.47) with λ_{crit}:

$$\lambda_{crit}\boldsymbol{K}_{L0}\boldsymbol{u}_{lin} = \lambda_{crit}\boldsymbol{p} \tag{11.49}$$

Taking into account only first-order displacement terms, stored in $\boldsymbol{K}_{LL} = \int_V \left(\boldsymbol{B}_{L1}^T\boldsymbol{D}\boldsymbol{B}_{L0} + \boldsymbol{B}_{L0}^T\boldsymbol{D}\boldsymbol{B}_{L1}\right)dV$ and linearising the second Piola-Kirchhoff stresses by $\boldsymbol{\tau} \approx \lambda_{crit}\boldsymbol{\sigma}_{lin}$ leads to the approximation solution:

$$\left(\boldsymbol{K}_{L0} + \lambda_{crit}\left(\boldsymbol{K}_{LL}(\boldsymbol{u}_{lin}) + \boldsymbol{K}_G(\boldsymbol{u}_{lin})\right)\right)\delta\boldsymbol{u} = 0 \tag{11.50}$$

Where $\boldsymbol{K}_G(\boldsymbol{u}_{lin}) = \int_V \boldsymbol{B}_{NL}^T\boldsymbol{\sigma}_{lin}\boldsymbol{B}_{NL}dV$ and $\boldsymbol{K}_{L0} = \int_V \boldsymbol{B}_{L0}^T\boldsymbol{D}\boldsymbol{B}_{L0}dV$.

Hence, equation (11.50) is satisfied for any incremental variation $\delta\boldsymbol{u}$ if:

$$det\left(\boldsymbol{K}_{L0} + \lambda_{crit}\left(\boldsymbol{K}_{LL}(\boldsymbol{u}_{lin}) + \boldsymbol{K}_G(\boldsymbol{u}_{lin})\right)\right) = 0 \tag{11.51}$$

In linear stability analysis, the general stability conditions of equation (11.42) and (11.43) are replaced by equation (11.49) and (11.51). Equation (11.51) can be written as:

$$\boldsymbol{K}_{L0}\boldsymbol{\varphi}_i = -\lambda_{i\,crit}\left(\boldsymbol{K}_{LL}(\boldsymbol{u}_{lin}) + \boldsymbol{K}_G(\boldsymbol{u}_{lin})\right)\boldsymbol{\varphi}_i \tag{11.52}$$

Where $\boldsymbol{\varphi}_i$ is the i-th buckling mode and λ_i is the corresponding buckling value. Note that the Euler stability analysis is a linearised stability analysis and, thus, is an upper bound solution as it neglects displacement terms of a higher order than one.

11.7.2 Generalised Eigenproblem

Equation (11.52) is solved as a *generalised eigenproblem*. The generalised eigenproblem is defined by the equation:

$$\boldsymbol{K}\boldsymbol{\varphi} = \omega^2\boldsymbol{M}\boldsymbol{\varphi} \tag{11.53}$$

Where, $\boldsymbol{M}$ is the mass matrix and ω is the circular natural frequency in radians per second. In stability analysis the generalised equation changes to the linearised problem described by:

$$\boldsymbol{K}\boldsymbol{\varphi} = \lambda\boldsymbol{K}_G\boldsymbol{\varphi} \tag{11.54}$$

Where, $\boldsymbol{K}_G$ is the geometric stress-stiffness matrix. Obviously, equation (11.54) is closely related to equation (11.52). Solution procedures to the generalised eigenproblem are discussed in section 11.8.

11.7.3 Shifting

An important operation involving the solution of a generalised eigenproblem is *shifting*. Shifting refers to a shift factor μ applied on the stiffness matrix which provides the eigenvalues and eigenmodes close to -μ first:

$$\widehat{\boldsymbol{K}}\boldsymbol{\varphi} = \widehat{\omega}^2 \boldsymbol{M}\boldsymbol{\varphi} \tag{11.55}$$

Where $\widehat{\boldsymbol{K}} = \boldsymbol{K} + \mu\boldsymbol{M}$ and $\widehat{\omega}^2 = \omega^2 + \mu$. Then, the actual eigenvalues are corrected by $\lambda = \left(\widehat{\omega}^2 + \mu\right)$. Note that a negative shift factor is equivalent to a positive shift.

Shifting may be applied to overcome difficulties with zero or negative eigenvalues, in case of softening material behaviour (when the tangent stiffness is obtained by a physical nonlinear analysis) where only the first negative eigenvalue is of interest. Furthermore, shifting may be effective in a perturbation analysis where the nonlinear interaction of eigenmodes is considered (discussed hereafter) to improve the accuracy of the interacting eigenvalues and modes, DIANA User's Manual [29].

11.7.4 Postbuckling Analysis

If the postbuckling behaviour needs to be investigated, the Euler stability analysis must be followed by a *perturbation analysis* and a *continuation analysis*, the finite element presentation of the Koiter initial postbuckling theory (see Chapter 6). The analyses describe the static initial postbuckling path in the vicinity of the bifurcation point by an asymptotic expansion of the displacement field around the bifurcation point. In fact, the analyses represent a nonlinear analysis; however, instead of a large set of nonlinear equations in full nonlinear analysis, the calculation is done with a reduced number of equations.

Perturbation Analysis

In the perturbation, or *reduced*, analysis the nonlinear interaction of a (small) selection of buckling modes is considered which were orthogonal within the linear scheme. Basically, the perturbation analysis involves the calculation of a postbuckling displacement $\boldsymbol{u}_{pb}$ satisfying $\boldsymbol{r}(\boldsymbol{u}_{pb}) = \boldsymbol{p}(\boldsymbol{u}_{pb})$ but different from the primary path described by $\boldsymbol{u} = \lambda\ \boldsymbol{u}_{lin}$ with λ the load parameter. Assuming M coinciding or nearly interacting buckling modes, denoted by $\boldsymbol{\varphi}_k$ with $k = 1, \ldots, M$, the (mode interacted) initial postbuckling displacement field is defined as:

$$\boldsymbol{u}_{pb} = \lambda\boldsymbol{u}_{lin} + a_i\phi_i + a_i a_j \boldsymbol{u}_{ij} \tag{11.56}$$

Where $\boldsymbol{u}_{ij}$ is the second-order displacement vector and a_i the amplitude of the respective mode. It is shown by Koiter that $\boldsymbol{u}_{ij}$ must be calculated by solving the system:

$$\left(\boldsymbol{K}_{L0} + \lambda_p\lambda_1\boldsymbol{K}_G\left(\boldsymbol{u}_{lin}\right)\right)\boldsymbol{u}_{ij} = \boldsymbol{p}_{ij} \tag{11.57}$$

Herein, $\lambda_p \neq 1$ is a user specified factor. Applying the orthogonality conditions

$$\boldsymbol{\varphi}_k^T \boldsymbol{K}_{L0} \boldsymbol{u}_{ij} = 0 \qquad \text{with } k = 1, \ldots, M \tag{11.58}$$

Where, $\boldsymbol{p}_{ij}$ is defined as the mode interaction load vector:

$$\boldsymbol{p}_{ij} = \int_V \left(\boldsymbol{B}_{L0}^T \boldsymbol{\sigma}_{ij} + \boldsymbol{B}_{NL}^T (\boldsymbol{\varphi}_i) \boldsymbol{\sigma}_j + \boldsymbol{B}_{NL}^T (\boldsymbol{\varphi}_j) \boldsymbol{\sigma}_i \right) dV \tag{11.59}$$

Where $\boldsymbol{\sigma}_{ij}$ is the stress related to interaction of modes i and j and $\boldsymbol{\sigma}_i$ is the stress related to mode i. Further, the potential can be written as a function of the load parameter λ and the mode amplitudes a_i:

$$P(a_i \lambda) = \tfrac{1}{2} \sum_{I=1}^{M} \left(1 - \frac{\lambda}{\lambda_I} \right) a_I a_I + A_{ijk} a_i a_j a_k + A_{ijkl} a_i a_j a_k a_l \tag{11.60}$$

Wherein $A_{ijk} = \tfrac{1}{2} \int_V \boldsymbol{\sigma}_{ij} \boldsymbol{\varepsilon}_k dV$ and $A_{ijkl} = \tfrac{1}{8} \int_V \boldsymbol{\sigma}_{ij} \boldsymbol{\varepsilon}_{kl} dV - \tfrac{1}{2} \boldsymbol{u}_{ij} \boldsymbol{p}_{kl}$ are the third- and fourth-order potential terms.

Hence, the perturbation analysis yields a potential energy function expressed in terms of amplitudes of modes determined by a linear stability analysis, DIANA User's Manual [29].

Continuation Analysis

The potential function (11.60) is the basis for the calculation of the initial postbuckling nonlinear equilibrium equations in a stepwise approach, the continuation analysis. The equilibrium points of the initial postbuckling path are indicated by terms of a_i and λ. The postbuckling displacement field $\boldsymbol{u}_{pb}$ can be derived using equation (11.56) using a stepwise generalised Newton-Raphson scheme.

11.8 Solution Methods for Eigenproblems

The solution of an eigenproblem involves the calculation of the eigenpairs (eigenvalues and eigenvectors) for a given matrix. For a symmetric matrix $\boldsymbol{K}$ of size n x n there are n eigenpairs. The solution for p eigenpairs (used specified number) can be written as $\boldsymbol{K\Phi} = \boldsymbol{\Phi\Lambda}$ where $\boldsymbol{\Phi}_{n \times p}$ is the matrix with eigenvectors and $\boldsymbol{\Lambda}_{p \times p}$ is a diagonal matrix with the corresponding eigenvalues.

In general, all solution methods for eigenproblems are iterative. Basically, solving the eigenproblem $\boldsymbol{K\varphi} = \lambda \boldsymbol{M\varphi}$ is equivalent to calculating the roots of the polynomial $p(\lambda)$, which has order equal to the order of $\boldsymbol{K}$ and $\boldsymbol{M}$. Since there are for the general case no explicit formulas available for the calculation of the roots of $p(\lambda)$ when the order of p is larger than 4, an iterative solution method has to be used, Bathe [3]. Once one member of the eigenpair is known the other member can be obtained without further iteration. Hence, a basic question is whether first to solve the eigenvalue or the eigenvector. Another option is to solve them simultaneously. The best choice depends on the solution requirements and the properties of the matrices involved, i.e. number of eigenpairs requested, order of the matrices, bandwidth and bandedness. The effectiveness of a chosen solution procedure depends largely on the reliability of the procedure and the computational effort determined by the number of high-speed storage operations and an efficient use of backup storage devices. With respect to reliability one must be aware of the fact that numerical stability is by no means mechanical instability.

The iterative solution methods can be divided into four basic procedures; *Vector Iteration Methods*, *Transformation Methods*, *Polynomial Iterations* and *Sturm Sequence Techniques*. In finite element programs, however, the solution procedures offered are often a combination these techniques.

The basic relation of Vector Iteration algorithm can be described as $\boldsymbol{K\varphi}_i = \lambda_i \boldsymbol{M\varphi}_i$. The aim of the method is to satisfy the basic relation by directly operating on it, Bathe [3]. Thus, introducing an arbitrary vector $\boldsymbol{x}_1$ for $\boldsymbol{\varphi}_i$ and setting λ = 1 the basic relation changes to $\boldsymbol{R}_1 = \boldsymbol{Mx}_1$ and $\boldsymbol{Kx}_2 = \boldsymbol{R}_1$. Assuming $\boldsymbol{x}_2$ an approximation more closely to the eigenvector than $\boldsymbol{x}_1$ it is possible to iterate to a better approximation. Some vector iteration methods are the *Inverse Iteration*, *Forward Iteration* and the *Rayleigh Quotient Iteration*.

Transformation Methods have basic properties described by $\boldsymbol{\Phi}^T \boldsymbol{K\Phi} = \boldsymbol{\Lambda}$ and $\boldsymbol{\Phi}^T \boldsymbol{M\Phi} = \boldsymbol{I}$. Where, $\boldsymbol{\Phi} = [\boldsymbol{\varphi}_1, ..., \boldsymbol{\varphi}_n]$ and $\boldsymbol{\Lambda} = diag(\lambda_i),\ i = 1,...,n$. Basically, the unique matrix $\boldsymbol{\Phi}$ diagonalises $\boldsymbol{K}$ and $\boldsymbol{M}$ and is computed by multiplication of $\boldsymbol{K}$ and $\boldsymbol{M}$ by a matrix $\boldsymbol{P}_k$ which diagonals $\boldsymbol{K}$ and $\boldsymbol{M}$ more closely each iteration. Thus, $\boldsymbol{K}_{k+1} \to \boldsymbol{\Lambda}$ and $\boldsymbol{M}_{k+1} \to \boldsymbol{I}$ as $k \to \infty$. At the last iteration l the eigenvector matrix is then $\boldsymbol{\Phi} = [\boldsymbol{P}_1 \boldsymbol{P}_2 ... \boldsymbol{P}_l]$. In practice $\boldsymbol{K}$ and $\boldsymbol{M}$ only need to converge to the diagonal form, thus, $\boldsymbol{K}_{k+1} \to diag(\boldsymbol{K}_r)$ and $\boldsymbol{M}_{k+1} \to diag(\boldsymbol{M}_r)$. The most effective Transformation Methods are the *Jacobi Method, Generalised Jacobi Method* and the *Householder QR Inverse Iteration Method* (HQRI), Bathe [3].

Polynomial and Sturm Sequence Iteration methods have a close relationship as they both use the characteristic polynomials and can be employed in one solution scheme. The important property of the eigenvalues of the generalised eigenproblem, i.e. that they are the roots of the characteristic polynomial, is the basic property of polynomial iteration. Thus, polynomial iteration methods operate on $p(\lambda_i) = 0$ (either explicit or implicit) where $p(\lambda) = det(\boldsymbol{K} - \lambda \boldsymbol{M})$. In combination with a polynomial iteration, it is natural and can be effective to use Sturm Sequence Techniques. Sturm Sequence (or *chain*) is a symbolic procedure to determine the number of unique roots of a polynomial. It finds all the eigenpairs in a given range. The basic property is described as $p(\lambda) = det(\boldsymbol{K} - \lambda \boldsymbol{M})$ and $p^{(r)}\left(\lambda^{(r)}\right) = det\left(\boldsymbol{K}^{(r)} - \lambda^{(r)} \boldsymbol{M}^{(r)}\right);\ \ r = 1,....,n-1$ where $p^{(r)}\left(\lambda^{(r)}\right)$ is the characteristic polynomial of the r-th associated constraint problem corresponding to $\boldsymbol{K}\phi = \lambda \boldsymbol{M}\phi$, Bathe [3].

Aforementioned, finite element programs offer methods which are a combination of the basic properties. Well-known algorithms are the *Lanczos Method,* the *Arnoldi Method* and the *Subspace Iteration Method.*

The Lanczos method transforms the generalised eigenproblem into a standard form with a *tridiagonal* (almost a diagonal) coefficient matrix which is real and symmetric. It is particular effective if only a few eigenpairs need to be calculated. The Arnoldi Method is analogous to the Lanczos Method, however, also applies to *non-Hermitian* matrices. Subspace Iteration is the most widely used due to its robustness and simplicity. It is particular effective for calculating a few eigenpairs of very large systems, Bathe [3].

11.9 Finite Element Software

The finite element procedure is widely available in computer software programs such as ABAQUS, ANSYS, ADINA and DIANA. Typically, finite element software architecture is based on the general finite element procedure, i.e. pre-process, analysis and post-process. Therefore, finite element software consists of a pre-processor, an analysis frame and a post-processor which is often combined with the pre-processor. The pre-process involves the description of the physical problem, which, in general, depends on the response to be predicted. It can be divided into three major parts; modelling the structure, i.e. the geometrical modelling, material modelling, boundary conditions, defining the nature of the problem to be solved, i.e. linear analysis, nonlinear analysis, stability analysis, and the modelling of external actions such as imposed displacements, environmental conditions and loading. The analysis part solves the physical problem and in the post-process the response of the structure can be viewed.

Considerable concern may arise on the reliability of the finite element programs. Therefore, important for finite element programs are the so-called Benchmark tests. Benchmark tests are developed to validate the solution and solution accuracy of finite element programs by comparing results to references, Hoogenboom [48]. Since 1983 the finite element benchmark tests are set and maintained by the National Agency for Finite Element Methods and Standards (NAFEMS), an independent non-profit organisation 'to promote the safe and reliable use of finite element and related technology', NAFEMS [95].

The finite element program DIANA is used for the thesis' analyses. DIANA is a software package for finite element analysis of structures and fluids, developed by TNO in Delft, the Netherlands since 1972. DIANA is FORTRAN coded, a code especially developed for technological programs, Burden and Faires [19]. The finite element code is based on the displacement approach using displacements as basic variables. Most appealing capabilities of DIANA are soil and concrete calculations. For the pre- and post-processing the iDIANA user's interface is used which works with two databases called FemGV (Fem generation and Fem view) which both comprise an index file and a data file in binary format. FemG is the design environment and FemV the results environment. The geometrical and physical modelling and the mesh generator are included in the iDIANA design environment. DIANA offers a wide variety of almost 200 elements. Using FemG the structure can be modelled and stored in a *Neutral file* format in ASCII text format (the so-called *dat*-file). The contents of the results database can also represented in a Neutral file. If the results are viewed with iDIANA, the structural response can be visualised (contour plots, stress graphs, etc) by selecting a load case, attribute and component of analysis results for assessment. Results may be viewed as values at the nodes for averaged nodal results, element wise at the nodes of each element if discontinuities at the element boundaries are to be examined, or as values at integration points within the elements or as a single value per element.

11.10 Geometrical Modelling

The implementation of a structural domain into a finite element program starts with the definition and discretization of the geometry in the design environment. The primary objective of a model is to realistically replicate the important parameters and features of the real model, thus, the geometrical modelling must approach the geometry of a designed (or realised) shape in the most optimal way. Mesh generation is part of geometrical modelling and the discretisation of the geometry must result in a correctly described structural response to external loads.

To define the geometry the user must be familiar with computer aided design. For the discretization the user needs knowledge of applied mechanics and finite elements in particular. This section contains some of the knowledge needed to create an appropriate geometrical model. However, as geometrical modelling (or modelling in general) gives access to an extremely large amount of background information, there will only be referred to the modelling as needed for thin shell structures.

11.10.1 Geometry

The geometry of a structure can be drawn in a pre-processor or imported out of computer aided design programs such as AutoCAD or MAYA. Commonly, the computer aided design programs foresee in more advanced design aids than the pre-processors of finite element programs. However, problems may arise when converting the imported model as in general the programs are based on different codes. This may lead to a situation in which (a part of) the original drawn geometry becomes useless. Finite element programs may include *repair* and *merge* options, which repairs geometry and deletes duplicated points, lines, surfaces and bodies, respectively. However, the final result is different for each particular problem.

The geometrical model is parametric as lines, surfaces and bodies can be defined from points and transforms (transformation of an original part to a new part). The nodal points of the geometry are stored in a data file in terms of a global coordinate system. To create, basic shapes can be combined by *complement* (appends the complement of two sets to another set) and *intersect* (only the intersecting part of two sets remains) operations. It must be mentioned, however, that there is no such thin as a perfect numerical model. The model always contains numerical irregularities and, thus, is imperfect.

11.10.2 Mesh Generation

The geometrical shape of the structure is discretised by a finite element mesh. To generate a mesh that correctly describes the structural behaviour is as complicated as it is important. The mesh contains all the properties that are needed in order to let the finite element analyses determine how the structure will respond. Hence, errors in the mesh formulation or too coarse meshes will lead to an insufficient solution.

Basically, the efficiency of the finite element solution depends on the *mesh fineness*, the *elements* (type and integration scheme, discussed later) and the *mesh quality*. The mesh fineness determines the exactness of the solution and must be fine enough the reach the desired solution accuracy. The mesh can be refined until it reaches the limit imposed by the amount of RAM available plus the size of the virtual memory swap file. Unfortunately, the rank of the stiffness matrix is equal to the total number of unknown nodal degrees of freedom and the matrix (and computational time) can become extremely large when applying many elements. Hence, it is important to find a compromise between the exactness of the approximation and the calculation time needed.

The mesh quality is important for the reliability of the solution as finite element programs tend to develop *mesh sensitivity* with respect to distortions. The elements of the mesh must be smooth as abrupt shape deviations between neighbouring elements are uninvited as they, for example, lead to irregular stress and strain representations. A major requirement is that the elements are not folded or degenerate any points or lines. Furthermore, the *aspect ratio* (the ratio of the length of the smallest side of the element to the length of the longest) of the elements must not be too large. A large aspect ratio leads to convergence problems and has a bad accuracy. To correctly and efficiently describe the boundary, a sufficient number of nodes must be present at the edges. To evaluate the mesh quality, finite element programs often contain a mesh *quality test*. In general, the mesh quality test evaluates the shape of the element with respect to a theoretical ideal. The criteria involved, such as element angles, warping, aspect ratio, and midnode position, depends on the selected element type. Sometimes an overall quality value is offered which averages the contribution from all other tests, with an option to add a weight factor to a quality test of personal preference.

The mesh can be generated by hand (for simple problems) or by a mesh generator. The mesh generator is often part of the pre-processor, although it is also possible to import. During the import operation, however, the same problems may occur as previously mentioned for the geometry. Once more, merging may be the key. A computer mesh generator is based on an advanced discretisation formula, which are often very complicated to meet the high standards needed for an accurate finite element solution. As denoted by Vermeij [78], in general, a mesh can be divided into three classes, a *structured mesh* and an *unstructured mesh* or a combination of both. The difference between the classes lies in the way the connectivity is stored. A structured mesh is implicitly taken into account as the nodes have a fixed relationship to each other. A structured mesh is often based on mapping as a regular flat grid is mapped to the irregular geometrical shape. The mesh is usually generated by a *differential method* which defines interior coordinate lines by performing a solution to partial differential equations which are constructed by describing the original geometry in terms of computational space coordinates. Another technique is the *algebraic method* which interpolates internal coordinates from their values on the boundaries. The differential method is more popular as it results in a smooth mesh without irregularities from discontinuous boundaries, Vermeij [78].

However, as a structured mesh has difficulties to handle complex geometries, often an unstructured (or *free*) mesh is applied as they provide in a flexible aid for the discretization. In an unstructured mesh, the connectivity must be explicitly described by a data structure. The unstructured grid is often generated by an *Octree approach*, a *Delaunay approach* or an *Advancing Front approach*, Vermeij [78]. The Octree approach is a fast meshing technique as it simply overlays a triangular of quadrilateral mesh over the structural domain and crops off the protruding elements, replacing them by triangular boundary elements. However, the mesh quality at the boundary is poor. The Delaunay approach divides a surface into triangular elements by stating that, when a circle is drawn through the vertices of the triangular element, the circle does not contain any other nodal points. The Advancing Front method generates the mesh by successive cell building, one at a time, and progress from the boundary into the volume. Independent of the chosen mesh algorithm, effective nodal point numbering is needed to cluster all nonzero terms around the diagonal of the stiffness matrix.

DIANA offers both meshing generation techniques. A structured mesh can be generated by the IJK-complex algorithm, which is based on the differential method or the *mapped option*, based on the conventional simple algebraic equations. To overcome the disadvantages of a non-smooth mesh, DIANA offers a smoothing algorithm which can be applied after the mapped mesh generation. For unstructured mesh generation, see Figure 11.12, DIANA offers the (default) *Paving algorithm* which generates a quadrilateral free mesh on any type of surface and the Delaunay approach for a triangular free mesh, both based on the Advancing Front method (like a pavior). Furthermore, a specific algorithm can be specified for a closed polygon surface which does not alter the algorithm assigned to any existing surface by the *Default Region option*. A combination of different meshing techniques is possible by simply ascribe a technique to a surface.

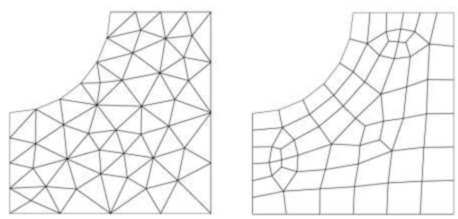

Figure 11.12. Delaunay (left) and a Paving mesh, DIANA User's Manual 2005

Before the mesh can be generated a generic element type must be chosen. A generic element only describes the shape of the element and the number of nodes. To achieve an actual finite element, the generic element types must be mapped onto elements for applied analysis program containing the mathematical description of the shape functions and integration points. Using generic elements, the density of the mesh is controlled by division of lines, surfaces and bodies or by a specified length of an element.

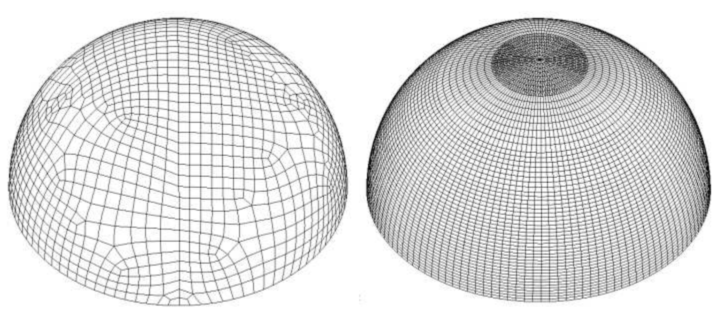

Figure 11.13. The mesh of a hemisphere by DIANA (left) or the hand regulated mesh (right)

Despite the fact that mesh generators have matured, meshing spatial curved structures may still lead to unwanted or irregular element arrangements. This can be seen below in Figure 11.13 for the case of a hemispherical shell used in the thesis' next chapters. The left picture represents the mesh as generated by

DIANA and the right picture shows the mesh as is programmed partly by hand (meridional and circumferential ribs) and partly by the mesh generator (the surface in between the ribs).

11.10.3 Element Types

For structural analysis, the element types can be divided into *line elements*, *surface elements*, *volume elements* and the *interface elements* which are used for contact boundary problems. The choice for a particular element type largely depends on the nature of the structural problem. Theoretically, for the most optimal description of a shell structure (a volume), volume elements are to be chosen. However, volume elements are of little practical use for shells as they do not only have the tendency to produce very large systems of equations, leading to exceptional long computational time. In addition it may lead to serious numerical ill-conditioning problems, Zienkiewicz [87]. Their usage is, thus, restricted to relatively small structural elements or parts of a larger structure. Fortunately, as seen in Chapter 5, the three-dimensional thin shell problem can be reduced to a two-dimensional surface problem by applying the thin shell assumptions. Hence, the shell can be modelled by using two-dimensional surface elements. Moreover, for thin shells of revolution, the model can be even further simplified by using axisymmetric curved line elements. In linear analysis the circumferential displacement of shells of revolution is equal to zero and the belonging strains and stresses are constant. Hence, a line model is sufficient to describe the meridional and out-of-plane response. For buckling or nonlinear analysis, however, the axisymmetric elements may become useless as the circumferential behaviour is not by definition constant. When a finite element program does not offer special shell elements, a simple approximation is to design a (segmented) shell by a combination of flat plate elements. However, uninvited bending will undoubtedly arise at every segment connection.

The two-dimensional surface elements offered by DIANA are based on *isoparametric degenerated-solid approach* which means that the stress component normal to the shell surface is equal to zero (*plain stress* assumption) and that a normal remains straight after deformation but not necessarily normals. The transverse shear deformation is included according to the Mindlin-Reissner hypothesis, discussed below. The elements are named after their usage. For example, the surface element QU8-CQ40S, where QU8 stands for an *8* noded *Q*uadrilateral shaped element and CQ40 specifies the belonging to a *C*urved *Q*uadrilateral with *40* degrees of freedom. The *S* at the end stands for a regular *S*hell element. The boundaries of the element are pointed out by nodes. The vertex nodes indicate the corners of the element and, depending on the type of element that is chosen, there are zero, one or more interior points at the element edge or even midnodes inside the element. Aforementioned, every node has 6 degrees of freedom, *3* translational and *3* rotational, and just as many corresponding load vectors. However, in the case of surface elements, the out-of-plane rotation is not included. Hence, there are *(5 x 8 =) 40* degrees of freedom in a QU8 element. This is seen in Figure 11.14.

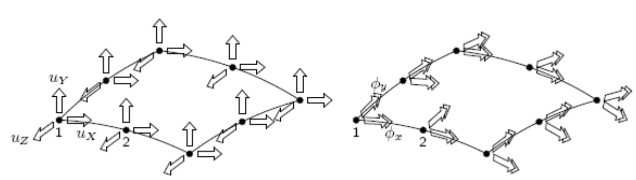

Figure 11.14. QU8-CQ40S Curved shell element and its degrees of freedom, DIANA User's Manual 2005

The number of nodes determines the order of the shape functions. Normally, 6 noded triangular or 8 noded quadrilateral elements with quadratic shape functions are appropriate for shell analysis. The polynomial terms of the shape functions of higher-order elements can be taken from a Pascal triangle. The quadratic shape functions of triangular elements are complete, they contain all polynomial terms in the triangle. Triangular elements of higher order are complete if they have one or more midnote(s). Higher-order quadrilateral elements belong to the serendipity or Lagrange family, Wells [85]. Serendipity elements have only nodes on the element boundaries. When the Pascal triangle is drawn, Figure 11.15, it can be seen that serendipity elements of second order already miss polynomials terms. For higher-order than three they are therefore not recommended. The problem can be solved by using Lagrange elements which have nodes on the element interior as well and therefore remain complete. As a consequence, serendipity elements are suboptimal on quadrilateral elements. The 9-node Lagrange element is shown to be superior to the more commonly used 8-noded serendipity element. The main advantage of serendipity elements is that since the internal nodes of the higher-order Lagrange elements do not contribute to the inter-element connectivity, the elimination of internal nodes results in reductions in the size of the element matrices, still providing the same order of convergence. Therefore, Lagrange elements are not implemented since the 1970s, Arnold [1].

$$
\begin{array}{ccccccccc}
 & & & & 1 & & & & \\
 & & & x & & y & & & \\
 & & x^2 & & xy & & y^2 & & \\
 & x^3 & & x^2y & & xy^2 & & y^3 & \\
x^4 & & x^3y & & & & xy^3 & & y^4 \\
\iddots & & \iddots & & & & \ddots & & \ddots
\end{array}
\qquad
\begin{array}{ccccccccc}
 & & & & 1 & & & & \\
 & & & x & & y & & & \\
 & & x^2 & & xy & & y^2 & & \\
 & x^3 & & x^2y & & xy^2 & & y^3 & \\
\iddots & & x^3y & & x^2y^2 & & xy^3 & & \ddots \\
 & \iddots & & x^3y^2 & & x^2y^3 & & \ddots & \\
 & & \iddots & & x^3y^3 & & \ddots & &
\end{array}
$$

Figure 11.15. The Pascal triangle for serendipity (left) and Lagrange elements, Wells 2004

The order of the shape functions, combined with the number of integration points, appear in the exactness of the derived variables (strains, stresses and the generalised moments and forces). In general, it can be said that linear interpolation and area integration yields a constant stress and strain distribution in the main direction and a linearly varying stress and strain in the perpendicular direction. Elements with quadratic interpolation and area integration, Figure 11.16, yields a linearly varying stress and strain in the main direction and a quadratically in the perpendicular direction. The same logic holds for higher-order elements. In the elements, the in-plane strains vary linearly in thickness direction. Furthermore, the transverse strain is forced to be constant, equivalent to the shear strain energy of the actual, parabolically varying, transverse shearing strain. Therefore a shear correction factor is applied. For shells, it is convenient to use elements with quadratic interpolation and area integration.

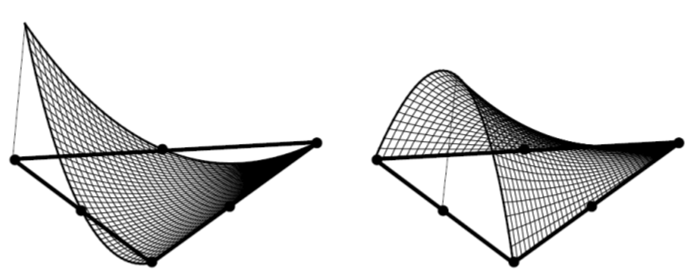

Figure 11.16. Two-dimensional shape functions of a six-noded triangular element, Wells 2004

Aforementioned in paragraph 11.2.2, typically, the finite element method uses C^0 continuous shape functions, made possible by the fact that shell elements (and plate elements) include the transverse shear deformation according to the *Mindlin-Reissner theory*. However, essentially a thick shell theory, it can be used for thin shells as well. It is used as in the formulation of shell elements according to the classic bending theory, a problem stems from the need of C^1 continuity in the shape functions. This can be explained by examining the classical thin shell equations, derived in Chapter 5. The shell equations are simplified for hand calculation by introducing the thin shell assumptions and the hypothesis that the in-plane shear deformations are negligible. Neglecting the in-plane shear deformation means that the rotation of the shell element can be calculated from the curvature (equation (5.12)), similar to the bending theory of thin plates (*Kirchhoff thin plate theory*). Consequently, the governing equilibrium equation of a shell in bending is similar to the biharmonic plate equation, a partial differential equation of the fourth order. The transfer of the fourth order strong form to the weak form yields a differential equation of the second order which needs C^1 continuous shape functions (a second derivative unequal to zero). Unfortunately, in general unstructured meshes, it is not possible to ensure C^1 continuity as it leads to inabilities to account for stress and strain discontinuities in case of properties varying discontinuously across element boundaries, and, the presence of spurious oscillations in the solution, Hughes [51]. Referring to the problems that arise, the few Kirchhoff elements that are available (DIANA offers plate bending Kirchhoff elements with prescribed moments) are *non-conforming*, which means that they do not meet C^1 continuity and thus not meet the compatibility demands, either within or across the element boundaries. The elements, often based on a sort of mixed formulation (they are not tricked Mindlin neither C^1 continuous), are tested by a patch test in order to check whether it correctly describes rigid body motions and constant strain (constant curvature). In general they are not very reliable, e.g. common rectangular elements with four nodes are not able to pass the patch test as a quadrilateral. Despite the disadvantages they might give proper solutions in some situations.

The problem of C^1 continuity is, thus, solved by using the Mindlin-Reissner theory. The difference of the Mindlin-Reissner theory to the Kirchhoff theory lies in the kinematic and constitutive model as it includes shear deformation, analogous to the *Timoshenko beam theory*. In other words, the rotation of the plate cannot be calculated from the curvature and, as a result, the equilibrium cannot be described in a single equation. In contrast to the Kirchhoff theory, the Mindlin-Reissner theory is modelled by a system of differential equations of second order and their corresponding weak forms contain derivatives no higher than order one. Thus, ironically, the simplest shell bending theory presents the most problems when using finite elements.

The major concern of Mindlin-Reissner elements is *shear-locking*. When the thickness of the shell approaches to zero, the elements show an excessively stiff behaviour in compare to the exact thin shell solution which leads to inaccurate results. The reason is that the contribution of the transverse shear deformation to the energy does not vanish. The simplest solution to prevent shear locking is to use a *reduced integration scheme* as it excludes the contribution of the transverse shear deformation to the bending energy. However, one must be aware of spurious modes. For linear elements DIANA prevent shear locking by automatically modifying the transverse shear strain fields, the so-called *assumed strain concept*. For quadratic and higher order elements DIANA uses a reduced integration scheme.

Note that, constant strains and stresses, which are calculated in the integration points, are discontinuing over the element boundaries. Graphical presentation in postprocessors may lead to misleading smoothened results, especially in areas with large gradients.

For shell analysis DIANA offers the following elements:

Triangular Curved Shell Elements

The Triangular curved shell elements have 3, 6 or 9 nodes, see Figure 11.17. The 3-node element is based on linear interpolation and area integration. For more accurate results, the 6-node element is available, based on quadratic interpolation and area integration, and the 9-node element in combination with third-order interpolation and area integration. The shape of the element may be of flat, cylindrical, spherical, conical, hyperbolic or parabolic.

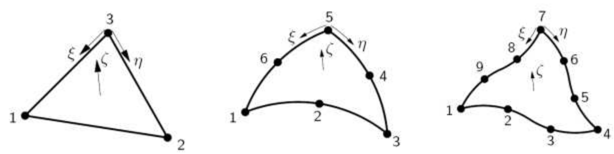

Figure 11.17. Triangular curved shell elements, DIANA User's Manual 2005

Each of the elements represented in Figure 11.17 is combined with an integration scheme. The integration schemes of triangular elements are outlined in paragraph 11.10.4. It can be stated that, triangular elements with more than 6 nodes rarely find practical application, DIANA User's Manual [29].

Quadrilateral Curved Shell Elements

The quadrilateral curved shell elements have 4, 8 or 12 nodes, distributed as in Figure 11.18. Analogously to the triangular elements, the quadrilaterals are based on linear, quadratic or third-order interpolation and area integration, respectively. The shape of the element may be of flat, cylindrical, spherical, conical, hyperbolic or parabolic.

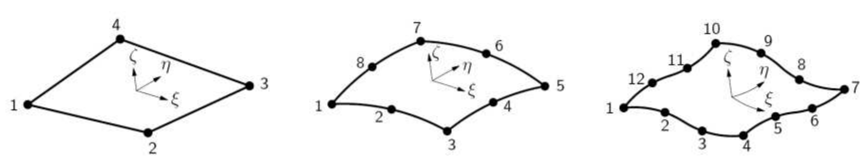

Figure 11.18. Quadrilateral curved shell elements, DIANA User's Manual 2005

Each of the elements represented in Figure 11.8 is combined with an integration scheme. The integration schemes of quadrilateral elements are outlined in paragraph 11.10.4. It can be stated that, quadrilateral elements with more than 8 nodes rarely find practical application, DIANA User's Manual [29].

Axisymmetric Curved Line Elements

The CL9AX element is an axisymmetric curved line element with similar properties as the surface elements. The element has three nodes and is based on quadratic interpolation and line integration and, thus, yields a strain and stress that varies linearly in length direction. The shape of the element may be of flat, spherical or parabolic. The element, seen in Figure 11.19, is combined with an integration scheme of in section 11.10.4.

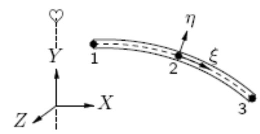

Figure 11.19. The CL9AX element and its degrees of freedom, DIANA User's Manual 2005

Note that, when ascribing a certain element to a mesh, one must be aware of the fact that the element has a default shape which may not be the same as the desired shape of the geometry. For example, the axisymmetric element has a default parabolic shape and, thus, is not compatible with a spherical line. In these situations, the shape of the elements must be mapped onto the geometrical shape manually. Furthermore, it must be mentioned that problems may be encountered with the tolerances of adjacent elements at the element assembly operation. If these problems cannot be solved by either mesh refinement or increasing the allowed tolerance, redefinition of the geometry is needed.

11.10.4 Integration schemes

The finite element is combined with an integration scheme which specifies the number and position of the integration points and the corresponding integration method. DIANA offers the *Gauss*, *Simpson*, *Newton-Cotes* and *Lobatto* integration schemes. Usually, over the surface of a curved shell element a Gauss integration scheme is used as requires the least number of integration points, DIANA User's Manual [29]. For elements with linear interpolation and area integration it is even the only possible integration method. In the thickness direction the Simpson method may be preferred over Gauss integration as it gives information about the surface strains and stresses. Standard is Simpson 3, with integration points at both outer surfaces and one in the middle. Higher order Simpson is recommended for physical nonlinear analysis where the number of integration points depends on the expected nonlinearity, Hughes [51].

The integration scheme chosen is either a full integration scheme or a reduced integration scheme. Full integration schemes integrate the stiffness matrix exactly. For higher order elements than one, a reduced scheme is recommended to prevent membrane and shear locking. Aforementioned, when reduced integration is applied, the strain and stress solution is better while the accuracy of the displacement is not affected. Off course, this is only true when spurious modes do not arise.

Questions may arise on the position of the integration points inside or at the boundary of the element. The integration points must give the most optimal approximation for the whole element. However, it is known that at certain places, the strains and stresses are obtained with a higher accuracy than at other places.

Research on this subject was done by Barlow. The *Barlow stress points* (used in DIANA) are placed in such way that they provide for the best possible approximation. For reduced integration schemes, the Gauss integral points coincide with the Barlow stress points, Barlow [2].

For the elements as presented in the previous paragraph, DIANA offers the following integration schemes:

Triangular Curved Shell Elements

Several integration schemes for the integration of the triangular elements are presented in Figure 11.20. Depending on the problem, the triangular elements may be integrated in-plane only (for two-dimensional problems, like plate bending) or combined with a Gauss or Simpson thickness integration scheme.

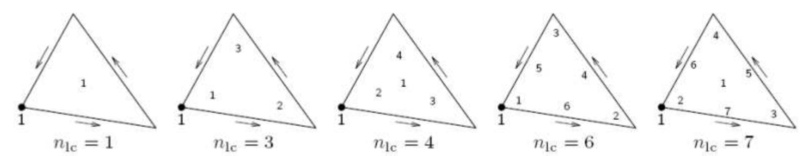

Figure 11.20. Several integration schemes for triangles, DIANA User's Manual 2005

In combination with the in-plane integration scheme is the scheme for thickness integration. The Gauss integration is 2-point integration. For more than 2-points the Simpson rule is applied, see Figure 11.21.

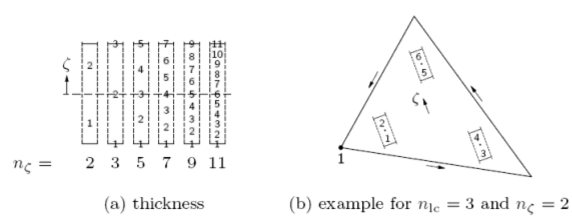

Figure 11.21. Thickness integration schemes for triangles, DIANA User's Manual 2005

Quadrilateral Curved Shell Elements

Some integration schemes for the integration of the quadrilateral elements are presented in Figure 11.22. Depending on the problem, the quadrilateral elements may be integrated in-plane only (for two-dimensional problems, like plate bending) or combined with a Gauss or Simpson thickness integration scheme.

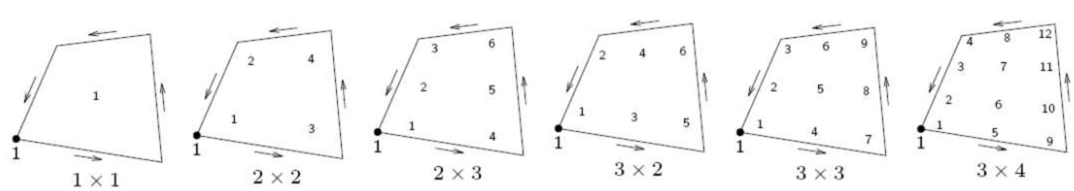

Figure 11.22. Several Gauss integration schemes for quadrilateral elements, DIANA User's Manual 2005

In combination with the in-plane integration scheme is the scheme for thickness integration. The Gauss integration is 2-point integration. For more than 2-points the Simpson rule is applied, Figure 11.23.

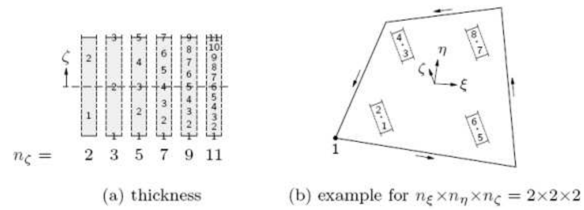

Figure 11.23. Thickness integration schemes for quadrilaterals, DIANA User's Manual 2005

Axisymmetric Curved Line Elements

For axisymmetric shell elements, DIANA offers Gauss and Simpson integration schemes, Figure 11.24. The default integration scheme is Gauss integration in the length and thickness direction. Higher order schemes in the direction of the length of the element are not recommended as the element will become extremely sensitive the shear locking, DIANA User's Manual. Possible higher order integration in thickness, Simpson integration, is only useful for surface stress-strain evaluation and nonlinear analysis.

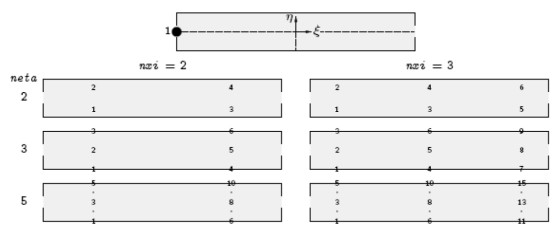

Figure 11.24. Some integration schemes for axisymmetric curved line elements, DIANA User's Manual 2005

Aforementioned, the structural behaviour is determined in the integration points and the values as determined there are the best approximated values. This means that the nodal strains and stresses are interpolated (and averaged) values. One must take into account that the interpolation operation sometimes yields largely deviating results. This is certainly true in case of irregular meshes.

11.11 Material Modelling

The response of a structure under load is evaluated within the elements using the material properties. Therefore, the actual *elastic* and *plastic* (permanent or irreversible deformations) material behaviour as determined in Chapter 8 must be implemented into a numerical *material model*. The aim of the material model is to approach the actual material behaviour in the most optimal way.

The material model for this thesis must correctly describe the properties and characteristics of the (fibre) reinforced concrete mixtures. The elastic behaviour is easily described by a constant Young's modulus and Poisson's ratio. However, when the *yield condition*, which specifies the state of stress at which the material starts to deform permanent, is violated, reinforced concrete experiences highly nonlinear plastic behaviour up to failure. For the modelling process, the user needs knowledge about the failure mechanisms which can occur in (fibre) reinforced concrete. Recapitulate from Chapter 8; the nonlinear behaviour of reinforced concrete is characterised by *direct* failure due to compressive *crushing*, tensile *cracking* and *yielding of reinforcement* and *indirect* failure due to long-term effects as *shrinkage*, *creep* and *ambient influences* like temperature and maturity. Fibre additions further contribute to the nonlinear behaviour through the continuous frictional pullout of fibres in the post-cracking stage.

To model brittle or quasi-brittle materials such as reinforced concrete with their physical nonlinear behaviour, DIANA offers several material models. Commonly, in multi-axial stress states, a crack model for tension is combined with a plasticity model which describes the crushing of the material. Regular yield models as *Tresca*, *Von Mises*, *Drucker-Prager* and *Mohr-Coulomb* are available combined with a (isotropic) plasticity formulation. Furthermore, DIANA offers the concept of *Total Strain*, that describes compression and tension within one constitutive relation, and the *Modified Maekawa Concrete* model which combines a multi-axial *damage plasticity model* for compression with a crack model based on Total Strain for tension. Damage plasticity models are similar to plasticity models with the difference that unloading does not take place elastically but that the degradation of the elastic stiffness is taken into account. The Maekawa model is in particular suitable to describe hysteresis in tensile and compression unloading/reloading loops (e.g. earthquake loading). For two-dimensional plane stress, plane strain or axisymmetric situations, the *Rankine* model, possibly combined with Von Mises or Drucker-Prager, foresees in a plasticity-based formulation for cracking. However, for three-dimensional analysis Rankine cannot be used. Finally, the modelling of so called long-term effects as relaxation and creep (not treated in this thesis) is done with viscoelastic models as the *Power law*, a *Maxwell Chain* and a *Kelvin Chain*.

11.11.1 Tensile Cracking

The tensile behaviour of reinforced concrete is characterised by a linear elastic branch up to crack initiation, followed by a nonlinear post-cracking path with *tension stiffening* (redistribution of tensile stresses from concrete to reinforcement due to bond between the rebars) or *tension softening* (reduction in tensile load capacity accompanied by increasing deformation), see Chapter 8. The crack propagation in the post-cracking stage is numerically decomposed in crack opening (*mode-I behaviour*) and crack sliding (*mode-II behaviour*). The crack process can be modelled with a discrete or smeared cracking approach.

Discrete Cracking Concept

Discrete cracking models consist of predefined cracks modelled by interface elements. Interface elements have equal located dual nodes which move away from each other after the tensile strength is violated. Before crack initiation, they have an extremely high dummy stiffness as if they are not there. The discrete cracking approach is limited to trivial situations in which the location of one dominant crack is known on forehand, such as a notched beam. Discrete cracking models are, thus, not appropriate for distributed failure and large scale analysis in which a wide variety of cracks can be expected at unknown locations such as shell analyses.

Smeared Cracking Concept

In the smeared cracking concept cracks may appear at arbitrary locations with arbitrary orientation. Opposite to the discrete cracking approach, the smeared cracking concept describes cracking within the elements. For each element in the mesh holds that, when the maximum tensile stress is violated, a crack will appear. The tension cut-off criterion specifies the initiation of cracks. In DIANA it is possible to use a constant or a linear tension cut-off, represented in Figure 11.25. The constant stress cut-off criterion neglects the positive influence of a compression stress in the other direction whereas a linear tension cut-off does not. The actual behaviour of concrete is neither constant nor linear, but somewhere in between.

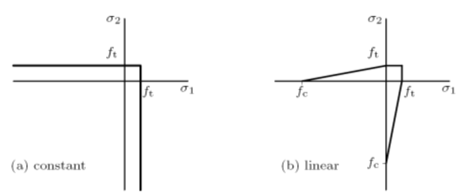

Figure 11.25. Tension cut-off in a two-dimensional stress state, DIANA User's Manual 2005

The crack propagation in an element is described by a crack model. A crack model determines the stiffness around a crack in the constitutive law. To be able to correctly express different stiffnesses in different directions, the crack model must be orthogonal and the original isotropic constitutive law is changed to an orthogonal stress-strain law. The crack relation is described within a crack orientated coordinate system *n-t*. A simplification is made by ignoring the coupling between mode-I and mode-II behaviour according to:

$$\begin{bmatrix} \sigma_{nn}^{cr} \\ \sigma_{nt}^{cr} \end{bmatrix} = \begin{bmatrix} D_{secant}^{I} & 0 \\ 0 & D_{secant}^{II} \end{bmatrix} \begin{bmatrix} \varepsilon_{nn}^{cr} \\ \gamma_{nt}^{cr} \end{bmatrix} \tag{11.61}$$

The secant stiffness terms can be determined by use of the constitutive relations of Chapter 5. When, for example, assuming a plane stress situation the linear elastic stiffness matrix reads:

$$\begin{bmatrix} \sigma_{xx} \\ \sigma_{yy} \\ \sigma_{xy} \end{bmatrix} = \frac{E}{1-\nu^2} \begin{bmatrix} 1 & \nu & 0 \\ \nu & 1 & 0 \\ 0 & 0 & \dfrac{(1-\nu)}{2} \end{bmatrix} \begin{bmatrix} \varepsilon_{xx} \\ \varepsilon_{yy} \\ \gamma_{xy} \end{bmatrix} \tag{5.34}$$

Supposed, that, relation (5.34) is transformed to the crack coordinate system and both the normal crack stiffness as the shear crack stiffness are assumed to be zero, the relation can be rewritten to:

$$\begin{bmatrix} \sigma_{nn} \\ \sigma_{tt} \\ \sigma_{nt} \end{bmatrix} = \begin{bmatrix} 0 & 0 & 0 \\ 0 & E & 0 \\ 0 & 0 & 0 \end{bmatrix} \begin{bmatrix} \varepsilon_{nn} \\ \varepsilon_{tt} \\ \gamma_{nt} \end{bmatrix} \tag{11.62}$$

To achieve a closer estimation of the reality, the normal and shear crack stiffnesses are reintroduced, equipped with tension softening behaviour and shear reduction respectively. Therefore, the parameters μ

and β are introduced. Furthermore, the reimplementation of the Poisson coupling contributes to a better approximation. Substitution of the approximations in equation (11.62) yields the orthogonal relation:

$$\begin{bmatrix} \sigma_{nn} \\ \sigma_{tt} \\ \sigma_{nt} \end{bmatrix} = \begin{bmatrix} \frac{\mu E}{1-\mu\nu^2} & \frac{\mu\nu E}{1-\mu\nu^2} & 0 \\ \frac{\mu\nu E}{1-\mu\nu^2} & \frac{E}{1-\mu\nu^2} & 0 \\ 0 & 0 & \frac{\beta E}{2(1+\nu)} \end{bmatrix} \begin{bmatrix} \varepsilon_{nn} \\ \varepsilon_{tt} \\ \gamma_{nt} \end{bmatrix} \tag{11.63}$$

In the latter, the parameters μ and β represent the coupling between the traditional and secant crack parameters. They are related to the secant stiffness by:

$$D^{I}_{secant} = \frac{\mu}{1-\mu}E \quad \text{and} \quad D^{II}_{secant} = \frac{\beta}{1-\beta}G \tag{11.64}$$

The parameter μ determines the stiffness of the material normal to the crack depending on the crack strain. Hence, the crack stress implicitly depends on the crack strain and can be written as a multiplicative relation:

$$\sigma^{cr}_{nn}\left(\varepsilon^{cr}_{nn}\right) = f_t \; y\left(\frac{\varepsilon^{cr}_{nn}}{\varepsilon^{cr}_{nn.ult}}\right) \tag{11.65}$$

Here *y(....)* represents a user specified softening function. The crack propagation in concrete is characterised by tension softening, i.e. the concrete increasingly eases up to open a crack after initiation. The type of softening behaviour can be implemented after the typical material characteristics. In equation (11.65) the softening is represented by the (linear) function *y(....)*,. DIANA offers various softening models such as linear tension softening, multi-linear tension softening, nonlinear tension softening according to Hordijk et al., etc. They are seen in Figure 11.26. The softening models determine whether the construction is in elastic stage (positive tangent modulus), cracking stage (negative tangent modulus) or fully cracked (beyond diagram).

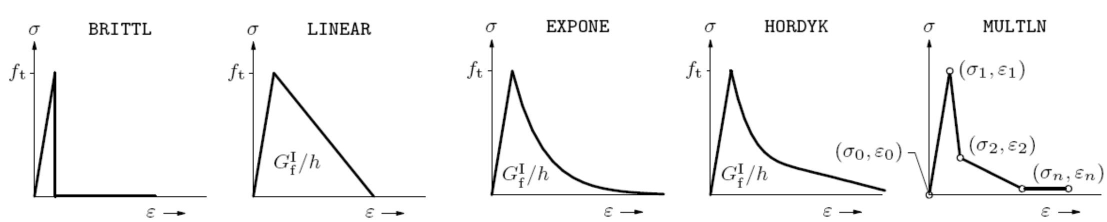

Figure 11.26. Tension softening relations, DIANA User's Manual 2005

As can be seen in the Figure, Brittle cracking is a special form of tension softening as it is distinguished by full reduction immediately after cracking and, thus, does not contain a tension softening branch. The softening relation to be chosen depends on the mode-I fracture energy of the material, e.g. measurable by means of material tests.

With respect to the fracture energy, the so-called *crack bandwidth* is introduced. Figure 11.26 shows tension softening behaviour on the constitutive level, a relation between cracking stress and strain. Hence, for the smeared crack concept, the relation between stress and crack (used in the discrete crack model) must be transformed to a relation between stress and strain. However, releasing the mode-I fracture energy in an element after the tensile strength is violated, results in a crack-width dependent of the size of the element. More practical, a larger element consumes more energy to reach the ultimate crack strain than a smaller element and, thus, the fracture energy dissipation differs with respect to the size of the element.

The simplest and general accepted solution to the problem is so-called *fracture energy regularisation*. Fracture energy regularisation is based on the assumption that each element can have only one crack (in reality cracks occur at every integration point) related to an equivalent length or crack bandwidth. In this way the crack is 'smeared' over the element. Doing so, the result is that, upon mesh refinement, the thickness of the crack region decreases while the dissipated energy remains constant. The relation between the crack width w and the crack bandwidth h can be written as:

$$\varepsilon_{nn}^{cr} = \frac{w}{h_c} \tag{11.66}$$

A crucial point is the definition of the bandwidth. Irregularity in element shapes force the use of a so-called characteristic length h_c that approximates the crack bandwidth with respect to the average element area A. For higher-order plane stress elements DIANA uses the relation $h_c = \sqrt{A}$. Hence, the ideal element is a square. In the postprocessor the above relation can be reversed to calculate the crack width.

Following the fracture energy regularisation, the mode-I fracture energy becomes related to the softening behaviour by crack bandwidth multiplication and, thus, related to the size of an element:

$$G_f^I = h\, f_t \int_{\varepsilon_{nn}^{cr}=0}^{\varepsilon_{nn}^{cr}=\infty} y\left(\frac{\varepsilon_{nn}^{cr}}{\varepsilon_{nn.ult}^{cr}}\right) d\varepsilon_{nn}^{cr} \tag{11.67}$$

Aforementioned, *y(....)* represents the softening diagram.

Unfortunately, the introduction of the crack bandwidth also has a disadvantage as it may lead to a snap-back in the constitutive model. One can probably imagine that overly large elements lead to a characteristic length so large that the integral of equation (11.67) leads to a decreasing crack strain while the crack further opens (decreasing crack stress). This so-called snap-back behaviour is highly uninvited and therefore must be solved. The simplest solution is to refine the mesh such that the crack bandwidth is smaller. Alternatively, the tensile strength can be reduced, although this implies that the material becomes more ductile.

Besides the parameter μ, the parameter β, which determines the shear behaviour, must be defined. The reducing shear stiffness during cracking is modelled with so-called shear retention. Shear retention deals with selecting a value for the parameter β between 0 and 1. DIANA offers full shear retention (β = 1) and constant shear retention (0 < β < 1).

Finally, as unloading and reloading situations may lead to closing and reopening of cracks, the behaviour during these conditions must be prescribed. The closing and reopening of cracks is done by the linear secant modulus in DIANA. This means that in the constitutive model the unloading and reloading branch goes linearly back to zero, although we might expect residual strain upon closing the crack in reality.

Strain Decomposition Concept

The principle of smeared cracking to model the tensile behaviour is offered by DIANA in two different concepts, *Strain Decomposition* and the later discussed *Total Strain* concept. Strain decomposition is based on decomposition of the total strain into an elastic and irreversible plastic (or crack) part, like a series connection of strains. The crack stresses are solely determined by the corresponding crack strain. Strain decomposition is related to the decomposed Multi-direction fixed crack model, seen in Figure 11.27.

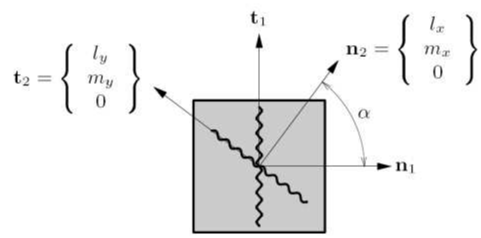

Figure 11.27. Multi-directional fixed crack model, DIANA User's Manual 2005

The Multi-direction fixed crack model determines crack stresses from the corresponding crack strains in the local *n-t* coordinate system. A fundamental feature is that the crack-strains are sub-decomposed in order to allow for several cracks occur simultaneously in one element. Therefore, in addition to the aforementioned tension cut-off, a *threshold angle* between two cracks is defined for consecutive crack initiation. The user must be aware of the possibility that the tensile stress temporarily becomes greater than three times the tensile strength while cracking does not start as the threshold is not violated yet, DIANA User's Manual [29].

The decomposition of strains also allows for the combination of a crack model in tension with a plasticity model in compression. In DIANA, the Multi-directional fixed crack model may be combined with a Tresca, Von Mises, Drucker-Prager or Mohr-Coulomb plasticity model discussed later.

Total Strain Concept

The total strain concept also describes the stress as a function of the strain; however, opposite to strain decomposition, total strain models describe the elastic and plastic strain in one constitutive relation. This is also known as hypo-elasticity, however, the DIANA formulation includes secant unloading and reloading. In the total strain concept the principal directions are uncoupled (the linear elastic stress space is a cube), cracks occur whenever the tensile strength in one direction is violated, indicated by a negative tangent modulus. Consequently, the crack stress is evaluated in a direction given by the crack direction.

The total strain concept is related to the *Total Strain Rotating Crack* model and the *Total Strain Fixed Crack* model. Basically, the total strain rotating crack model is a coaxial stress-strain concept which ensures that the crack orientated coordinate system is orthogonal to the principal stresses by rotating the crack. The model is only realistic if the crack rotation angle is small. Hence, the model is useless in case of consecutive loadcases with significant loads in different directions. The most advantageous property is its numerical uncomplicatedness as there is no shear stress which implicitly means that the shear retention factor, which often causes numerical stability problems, is not needed.

The fixed crack model does not rotate the crack with the principal stresses. When the principal stresses change in direction, the aforementioned shear retention factor will enfold for the shear stresses which appear along the crack surface. The fixed crack concept is off course closer to the nature of concrete cracking. The advantage lies in the fact that it is numerical simpler than the multi-directional fixed crack model.

11.11.2 Compressive Behaviour

The compressive behaviour of concrete is discussed in Chapter 8. It was found that the nonlinear compressive behaviour of concrete can be characterised by compression hardening and softening up to compressive crushing. This resulted in the 'rounded' stress strain curve. Hereby, the influence of (fibre) reinforcement was neglected. The compressive behaviour as observed can be modelled with a plasticity model or a constitutive curve, depending on the chosen model in tension. Therefore, the compression models are treated separately under their corresponding tension concept.

Strain Decomposition Concept

The strain decomposition concept allows for the combination of a crack model in tension with a yield model and a plasticity formulation in the compressive regime. Similar to the decomposed crack model, the compressive behaviour is decomposed in an elastic and irreversible plastic part. The yield condition specifies the state of stress at which the plastic part is initiated. The usual approach to describe the so-called *elastoplastic* behaviour is the *flow theory of plasticity*. The total stress $\boldsymbol{\sigma}$ at time t is then modelled as a function of the total strain $\boldsymbol{\varepsilon}$ at time t, but also as a function of the stress and strain history, Vrouwenvelder [80].

Typically, the stress and strain history is taken into account implicitly by an internal state parameter κ which is governed by a specific evolution law. The elastoplastic material behaviour can then by described by assuming and *elastic stress-strain relation*, a *yield condition* (specifying the state of stress at which the plastic flow is initiated), a *flow rule* (specifying the plastic strain rate vector as a function of the state of stress) and a *hardening hypothesis* (specifying the evolution of the internal state parameter κ). DIANA User's Manual [29].

The yield function f is a function of the stress vector $\boldsymbol{\sigma}$ and the internal state parameter κ:

$$f(\boldsymbol{\sigma}, \kappa) = 0 \tag{11.68}$$

Note that, if the value of the yield function is smaller than zero, the material is in elastic state and if the state of stress forces the yield function equal to zero, plastic deformation can occur. A value larger than zero is not allowed for rate-independent plasticity, DIANA User's Manual [29].

The yield function describes the *yield contour* of a *yield model*, a hypersurface in the *n*-dimensional stress space. In DIANA, the Multi-directional fixed crack model can be combined with yield models such as Tresca, Von Mises, Drucker-Prager or Mohr-Coulomb. They are illustrated in Figure 11.28 and 11.29.

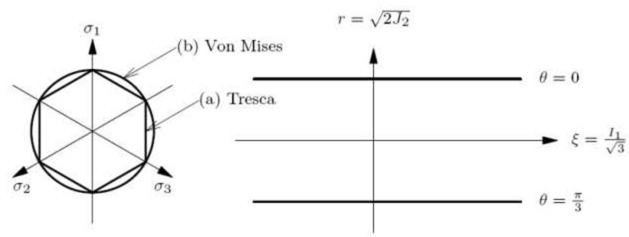

Figure 11.28. Tresca and Von Mises yield condition, DIANA User's Manual 2005

A yield model determines whether the concrete is in elastic (inside the yield surface) or plastic range (on the yield surface) in a uniaxial stress state. The yield model to be chosen alongside the Multi-directional fixed crack model depends on the type of structure, material, analysis, etc. In general, it can be said that Tresca and Von Mises are typical yield models for steel. They are based on the notion that when a material fails it does so in shear. The model of Von Mises provides in a better approximation as it does not underestimates the yield shear stress like Tresca, which is more conservative (Tresca lies inside the Von Mises yield criterion). Although in particular suited to steel, they may give proper solutions in some concrete situations.

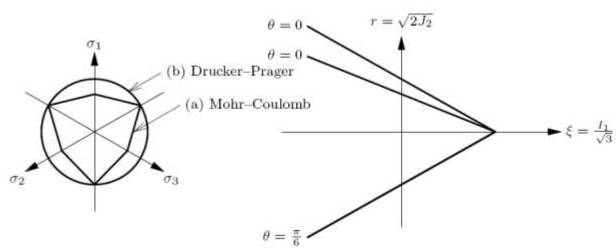

Figure 11.29. Mohr-Coulomb and Drucker-Prager yield condition, DIANA User's Manual 2005

The Mohr-Coulomb and Drucker-Prager yield conditions are especially applicable for quasi-brittle materials such as concrete. Both models better suits to the characteristic property of concrete as that there is an enormous difference in compression and tension. It is assumed that failure occurs if in an arbitrary plane the shear stress equals the maximum allowable shear stress. Hereby, the allowable shear stress depends linearly on the normal stress on the same plane. The Drucker-Prager yield model is a less conservative smooth approximation of the Mohr-Coulomb condition, as can be seen in Figure 11.29.

The yield function determines whether plastic deformation can occur. However, plastic deformations only occur when the stress point remains on the yield contour for a 'short' period, De Borst and Sluys [15]. Thus, plastic straining will occur if and only if $f(\boldsymbol{\sigma}, \kappa) = 0$ and $\dot{f}(\boldsymbol{\sigma}, \kappa) = 0$ (Prager's consistency equation).

The plastic behaviour on the yield surface is described by the flow rule and the hardening hypothesis. Aforementioned, the flow rule defines the plastic strain rate vector as a function of the stress state vector. For elastoplastic materials undergoing an infinitesimal deformation, the total strain increment is therefore decomposed in an elastic and plastic part $\dot{\varepsilon} = \dot{\varepsilon}^e + \dot{\varepsilon}^p$. By definition, the elastic deformations occur in a zero network dissipation, i.e. $\int(\boldsymbol{\sigma} - \boldsymbol{\sigma}_o)^T \dot{\varepsilon}^e dt = o$ while in case of plastic deformations $\int(\boldsymbol{\sigma} - \boldsymbol{\sigma}_o)^T \dot{\varepsilon}^p dt \geq o$. The plastic part, or so-called *plastic strain rate vector*, is described with the flow rule. The flow rule derives the plastic strain rate vector from the so-called plastic potential function g_j. The plastic potential function describes the variation in equilibrium of the energy dissipation equation. By definition the gradient of the plastic potential function is perpendicular to the yield contour (*normality rule*). The problem is however that the plastic potential is not uniquely defined and thus only the direction of the strain rate vector can be obtained. Therefore the flow rule involves a multiplication with a scale factor or *plastic multiplier*:

$$\dot{\varepsilon}^p = \sum_{j=1}^{n} \dot{\lambda}_j \frac{\partial g_j(\boldsymbol{\sigma}, \kappa)}{\partial \boldsymbol{\sigma}} \tag{11.69}$$

In which $\dot{\lambda}_i$ is the plastic multiplier.

The plastic multipliers are restricted depending on the yield function value. Considering that the plastic multiplier is nonzero only when plastic deformations occur, the loading-unloading criterion can be established via the *Kuhn-Tucker conditions* $f \leq o \;\; ; \;\; \dot{\lambda}_j \geq o \;\; ; \;\; \dot{\lambda}_j f = o$.

The final step is to use the yield function and the flow rule to define the plastic constitutive law, including the hardening hypothesis which specifies the evolution of the internal state parameter according to:

$$\dot{\kappa} = h\left(\boldsymbol{\sigma}, \dot{\varepsilon}^p\right) \tag{11.70}$$

Herein, h is the hardening function which in DIANA is either based on *strain hardening* or on *work hardening* for Tresca and Von Mises or, in case of Mohr-Coulomb or Drucker-Prager, only strain hardening.

To determine the (tangent) material stiffness matrix, first the initial tangent stiffness matrix following from the elastic branch is calculated. The initial stress rate vector can be determined from the elastic part of the strain rate vector and the material stiffness matrix $\boldsymbol{D}$ by:

$$\dot{\boldsymbol{\sigma}} = \boldsymbol{D}\left(\dot{\varepsilon} - \dot{\varepsilon}^p\right) = \boldsymbol{D}\left(\dot{\varepsilon} - \dot{\lambda}\frac{\partial g}{\partial \boldsymbol{\sigma}}\right) \tag{11.71}$$

Subsequently, the necessary expression for the scale factor can be determined from Prager's consistency condition, i.e. $\dot{f} = \frac{\partial f^T}{\partial \boldsymbol{\sigma}} \dot{\boldsymbol{\sigma}} + \frac{\partial f}{\partial \kappa}\frac{\partial \kappa}{\partial \lambda}\dot{\lambda} = 0$, which leads to the formulation:

$$\dot{\lambda} = \frac{1}{E_p}\frac{\partial f^T}{\partial \boldsymbol{\sigma}}\dot{\boldsymbol{\sigma}} \qquad \text{with} \qquad E_p = -\frac{\partial f}{\partial \kappa}\frac{\partial \kappa}{\partial \lambda} \quad \text{the plastic hardening modulus} \tag{11.72}$$

Substitution of equation (11.72) in equation (11.71) after applying the Sherman-Morrison formula (described earlier) yields the continuum tangent material stiffness matrix:

$$\dot{\boldsymbol{\sigma}} = \left[\boldsymbol{D} - \frac{\boldsymbol{D}\frac{\partial g}{\partial \boldsymbol{\sigma}}\frac{\partial f^T}{\partial \boldsymbol{\sigma}}\boldsymbol{D}}{E_p + \frac{\partial f^T}{\partial \boldsymbol{\sigma}}\boldsymbol{D}\frac{\partial g}{\partial \boldsymbol{\sigma}}}\right]\dot{\varepsilon} \tag{11.73}$$

Note that the matrix is symmetric for $f = g$, thus, as the plastic potential is equal to the yield function.

To update the constitutive equations of elastoplastic materials in a consistent manner the *Euler Backward* algorithm (accurate and stable independent of the step size) can be used within an *elastic predictor-plastic corrector* algorithm. The updated stress at the end of iteration *i+1* is used to derive the consistent tangent stiffness matrix. For increasing the performance and robustness of the iteration method used, the tangent stiffness matrix may be obtained by consistent linearisation of the stress resulting from the *return-mapping* algorithm. Using the return-mapping algorithm leads to a modification of equation (11.73) by substituting the elastic stiffness matrix $\boldsymbol{D}$ by $\boldsymbol{H}$, in which $\boldsymbol{H}$ is defined as:

$$\boldsymbol{H} = \left[\boldsymbol{I} + \Delta\lambda \boldsymbol{D}\frac{\partial^2 g}{\partial \boldsymbol{\sigma}^2}\right]^{-1}\boldsymbol{D} \tag{11.74}$$

Total Strain Concept

Aforementioned, the total strain concept describes the elastic and plastic strain in one constitutive relation. As the principal directions are uncoupled it is not possible to combine the total strain crack models with a yield model. Instead, the compression behaviour is modelled with predefined stress-strain curves. Some of the compression curves are presented in Figure 11.30, such as Thorenfeldt, parabolic curves and the multi-linear stress-strain curve which may be used to approximate the Eurocode 2 behaviour.

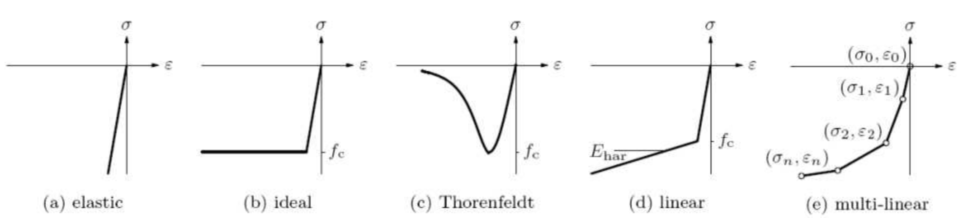

Figure 11.30. Predefined compression behaviour for Total Strain crack models, DIANA User's Manual 2005

The behaviour of compression is evaluated in a rotating coordinate system when the material is not cracked, where in case of a fixed concept the compressive behaviour is evaluated in the fixed coordinate system determined by the crack directions.

However, the cracking behaviour is based on a single stress-strain relation it may be refined to include influences of *lateral confinement* and *lateral cracking* to approach the pressure-dependent behaviour of concrete in compression more closely. Therefore, the parameters of the compressive stress-strain function, f_{cf} and ε_p are determined with a *failure function* which gives the failure compressive stress as a function of the confining stresses in the lateral direction, DIANA User's Manual [29]. The confinement relation used in DIANA is graphically presented in Figure 11.31. Clearly, the beneficial effect of increasing lateral confinement is at maximum for full triaxial loading in which failure cannot be reached and the graph is linear.

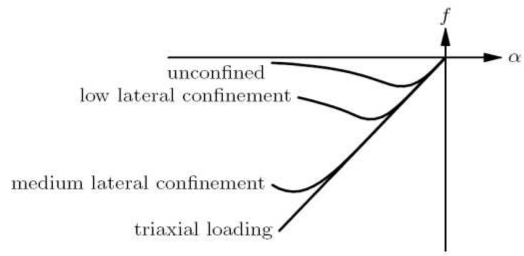

Figure 11.31. Influence of lateral confinement on compressive stress-strain curve, DIANA User's Manual 2005

For compressive behaviour with lateral cracking, the parameters of the compressive stress-strain function, f_{cf} and ε_p are determined with a failure function given by:

$$f_p = \beta_{\sigma_{cr}} \cdot f_{cf}$$
$$\alpha_p = \beta_{\varepsilon_{cr}} \cdot \varepsilon_p$$

In which α_p represents the reduced strain at the reduced ultimate stress f_p. The reduction factors $\left(\beta_{\sigma_{cr}}, \beta_{\varepsilon_{cr}}\right)$ are functions of the average lateral damage variable formulated as $\alpha_{lat} = \sqrt{\alpha_{l,1}^2 + \alpha_{l,2}^2}$ in which $\alpha_{l,i}^2$ represents the strain in perpendicular direction to the compression direction. DIANA models the reduction due to lateral cracking according to *Vecchio and Collins*. Vecchio and Collins suggested $\beta_{\varepsilon_{cr}} = 1$ and $\beta_{\sigma_{cr}} = \frac{1}{1+K_c} \leq 1$ with $K_c = 0.27\left(-\frac{\alpha_{lat}}{\varepsilon_0} - 0.37\right)$. The relation is illustrated in Figure 11.32.

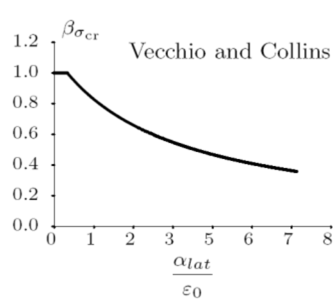

Figure 11.32. Reduction factor due to lateral cracking, DIANA User's Manual 2005

In the total strain formulation, the possible nonzero Poisson's ratio is included by a numerical trick.

11.11.3 Modelling Conclusions

From the foregoing it can be concluded that a concrete shell is best modelled using the smeared crack approach using either strain decomposition or total strain. The question of which material model is the best option for a particular problem cannot be answered in directly. Basically, the main differences refer to the way they evaluate crushing and cracking criteria for multi-axial stress states, the way in which stress rotations are treated and in the way loading and unloading is managed. Strain decomposition results in a multi-directional fixed crack model with secant unloading in tension combined with an elastoplastic yield model in compression. Total strain describes the elastic and plastic strain in tension and compression in one constitutive relation using secant unloading for both. Opposite to the strain decomposition concept the total strain cannot include creep, shrinkage, temperature and maturity effects. From a physical point of view, the strain decomposition concept is more attractive whereas total strain based models are, in general, numerical advantageous as they are much more stable.

The multi directional fixed crack model (in combination with a Drucker-Prager yield model) and total strain based crack models are compared in the report of Burgers [20]. Burgers made a compare between the results of an actual test and the results of the DIANA crack models (and a damaged plasticity model of ABAQUS) for a four point bending test on a notched beam fabricated from fibre reinforced concrete. Burgers reports on satisfying results for the total strain rotating crack model while the accurateness of the approximations of the total strain fixed crack model and the multi directional fixed crack model depends on the magnitude of the shear retention factor. Satisfying results of these models is accompanied by numerical difficulties.

11.12 Conclusions and Comments

In the foregoing the general finite element procedure is discussed. The spatial discretisation into finite elements and the formulation of the approximated displacement field using shape functions. The construction of the weak form of equilibrium which allows for approximated solutions and the stiffness matrix which is computed using numerical integration in and over the elements. Successively, the system of equations can be solved either linear, nonlinear or by performing a stability analysis using direct, iterative or incremental-iterative solution algorithms. More specific the geometrical and material modelling in DIANA is discussed, with extra attention for cracking and crushing of concrete.

Despite of the great power of the finite element method, the disadvantages must be kept in mind. The method does not necessarily reveal how the stresses are influenced by important problem variables such as material properties and geometrical features and errors in input data may produce large incorrect results that can be overlooked by the analyst. Furthermore, it should be mentioned that, for the displacement approach, the approximate solution always overestimates the total potential energy, which is the strain energy minus the work performed by the external loads. However, complied with the fact that the potential energy is negative near its minimum, the displacement based finite element method underestimates the strain or deformation energy and, therefore, the solution is often referred to as the lower bound solution. This means that the structural behaviour appears to be stiffer than the exact solution.

12 Linear Elastic FEA

In this chapter, a linear elastic finite element analysis is discussed. The theory as described before in Chapter 5 and the hemispherical example of Chapter 10, serve as background. Subsequently, in Chapter 13, the linear buckling and linearised postbuckling behaviour is discussed. Linear elastic analyses, however, may not be representative for the actual shell behaviour. Therefore, in Chapter 14 and 15, the actual shell behaviour is approached more accurately by implementation of nonlinear behaviour, i.e. a geometrically nonlinear analysis with initial imperfections in Chapter 14, and finally a geometrically and physically nonlinear analysis in Chapter 15, also taking into account for material nonlinearities.

For the linear analysis the Zeiss planetarium case study shell is used as geometry. The analyses are performed on an axisymmetric curved line model and a three-dimensional shell model consisting of two-dimensional quadrilateral and triangular curved shell elements. The axisymmetric model is the most simple shell model possible in finite element analysis. The model is, however, unable to deal with variations in circumferential direction. If these variations may occur, a three-dimensional model is required. The calculations are based on an ideal shell without any imperfections assuming infinite linear elastic material behaviour. The material properties are previously described in Chapter 8.

The results of the linear analyses are compared with the 'benchmark' results of Chapter 10. The stresses, strains and displacements are compared with the results of the classical shell theory. In addition to Chapter 10, the influence of different load conditions on the shell structural response is investigated. Therefore, wind load as derived in Chapter 9, is projected on the three-dimensional shell model.

12.1 Shell Parameters

12.1.1 Geometry

For the shell geometry, the dimensions of the Zeiss planetarium as discussed in Chapter 7 are used, i.e. a hemispherical shell with a radius of *12500 mm* and a thickness of *60 mm*.

12.1.2 Material Properties

The finite element analysis of Chapter 12 is linear elastic based. Hence, the material is modelled as infinite elastic and the only material parameters that have to be defined are the Young's modulus of elasticity and Poisson's ratio. Recapitulating from Chapter 8, for the conventional C20/25 mixture the Young's modulus is *30 GPa* whereas the C180/210 mixture is assumed to be twice as stiff with a Young's modulus of *60 GPa*. For as well the conventional C20/25 mixture as the C180/210 mixture the Poisson's ratio is set equal to zero.

12.1.3 Boundary Conditions

The shell is analysed using four types of support; a roller, inclined-roller, hinged and a clamped support. In this way the influences of boundary conditions on the structural behaviour can be investigated. The actual support of the Zeiss planetarium is a clamped support as the shell is rigidly connected (by steel reinforcement) to a tension ring which, in turn, rests on a circular base building, see Chapter 7.

12.1.4 Loading

The external applied load is equal to the (trivial) uniform vertical load consisting of the dead weight of the shell and snow load, described in Table 10.2. That is, a load $P = 0.0021\ N/mm^2$ ($2.1\ kN/m^2$). Furthermore, a spherical load with the same magnitude is considered and in Section 12.6 the structural response to wind load as defined in Chapter 9 is investigated.

12.1.5 Analysis Scheme

The different types of analyses are presented in the scheme below. As wind load varies in circumferential direction, it is not possible to combine the wind load with an axisymmetrical model.

Name	Loading Conditions	Supporting Conditions	Type of Analysis	Model
Zeiss 1	Spherical and Vertical	Roller	Linear Elastic	Axisymmetric + 3D
Zeiss 2	Spherical and Vertical	Inclined-roller	Linear Elastic	Axisymmetric + 3D
Zeiss 3	Spherical and Vertical	Pinned	Linear Elastic	Axisymmetric + 3D
Zeiss 4	Spherical and Vertical	Clamped	Linear Elastic	Axisymmetric + 3D
Zeiss 5	Wind load	Clamped	Linear Elastic	3D

Table 12.1. Analysis scheme

12.2 Axisymmetric Shell Model

The axisymmetric shell model is analysed first. The model is far less complicated and allows for much faster analyses than a three-dimensional model. The axisymmetric model is checked on support reactions, stresses, strains and displacements, respectively.

12.2.1 FE Model

The axisymmetric shell model consists of a curved line, a quarter of a circle, which presents a complete hemisphere as DIANA considers the vertical axis as axis of rotational symmetry. The line model is composed out of 92 axisymmetric curved line elements CL9AX (see Chapter 11) with in total 185 nodes. Consequently, each element has a circumferential length of approximately *213 mm*, which means that the requirement of at least 6 elements within the region of influence of a local bending moment (*2078 mm*, equation (10.32)) to ensure results of sufficient accuracy is satisfied, Hoogenboom [50]. Each element has 2 point Gauss integration over the length of the element and 3 point Simpson integration in thickness direction, which is appropriate for linear elastic analysis, DIANA User's Manual [29]. The three-point Simpson integration allows for inner, outer and middle surface stress and strain presentation. The integration polynomial of the axisymmetric elements, typically, produces stresses and strains which vary linearly over the length of the element (see Chapter 11). The shell top node is inclined-roller supported, as if it represents a complete sphere. The varying base supports are modelled by each time allowing or disallowing translation and/or rotation at the base node. The model is vertically or spherically loaded. Due to a modelling drawback of DIANA, i.e. for axisymmetrical elements it is not possible to construct a purely spherical load, the spherical load is modelled by modification of the direction of a line load; a line load is formed perpendicular to the element only at the middle node.

12.2.2 Support Reactions

The most elementary test is probably to check whether the support reactions correlate with the external applied load. For the axisymmetrical model, the support reactions resulting from the finite element analysis are illustrated by simple vectors which represent a summation of all reaction forces over the base radius. The support reactions for a vertical loaded hemisphere are presented in Table 12.2.

Name	Vertical support reaction (kN)		Horizontal support reaction (kN)	
	FEA	Theory	FEA	Theory
Zeiss 1	2060	2062	0	0
Zeiss 2	2060	2062	0	0
Zeiss 3	2060	2062	38.4	38.3
Zeiss 4	2060	2062	73.8	73.8

Table 12.2. FEA Support reactions of a shell under vertical load for different types of supports

For each shell model the total vertical support reaction (summation over the base radius) as obtained by the finite element analysis is equal to *2060 kN*. To validate the finite element result, the external applied load must be multiplied with the total shell surface area ($2.1\ kN/m^2 \cdot 981.75\ m^2 \approx 2062\ kN$). The horizontal reaction differs for each type of support. Again, the value represents a summation over the base radius of all horizontal supporting reactions. In Chapter 10, the horizontal support reactions are determined with the classical shell theory. Hence, to compare the results with the theoretical results, the values as found in Chapter 10 must be multiplied with the circumferential length.

Name	Vertical support reaction (kN)		Horizontal support reaction (kN)	
	FEA	Theory	FEA	Theory
Zeiss 1	1030	1031	0	0
Zeiss 2	1030	1031	0	0
Zeiss 3	1030	1031	-19.2	-19.2
Zeiss 4	1030	1031	-36.9	-36.9

Table 12.3. FEA Support reactions of a shell under spherical load for different types of supports

The supporting reactions of the spherical loaded shell are shown in Table 12.3. They are quite simple to validate, i.e. by definition, the vertical support reactions are equal to half the values as shown in Table 12.2 (which is, off course, also valid for the theoretical values). The same holds for the horizontal support reactions, however, they are of opposite sign. From Table 12.2 and Table 12.3 it can be concluded that the results of the finite element analysis show good correlation with the theoretical obtained results, i.e. the maximum difference is within *0.3%*.

12.2.3 Stresses

Zeiss 1

First, the axisymmetric shell model is analysed while being subjected to a uniform vertical load. The Zeiss 1 under vertical load is in a state of pure membrane action. In other words, the shell is supported in such a way that it will not disturb the membrane stress field and, consequently, there will be no bending moments in the shell. The principal meridional and circumferential stresses are presented in Figure 12.1.

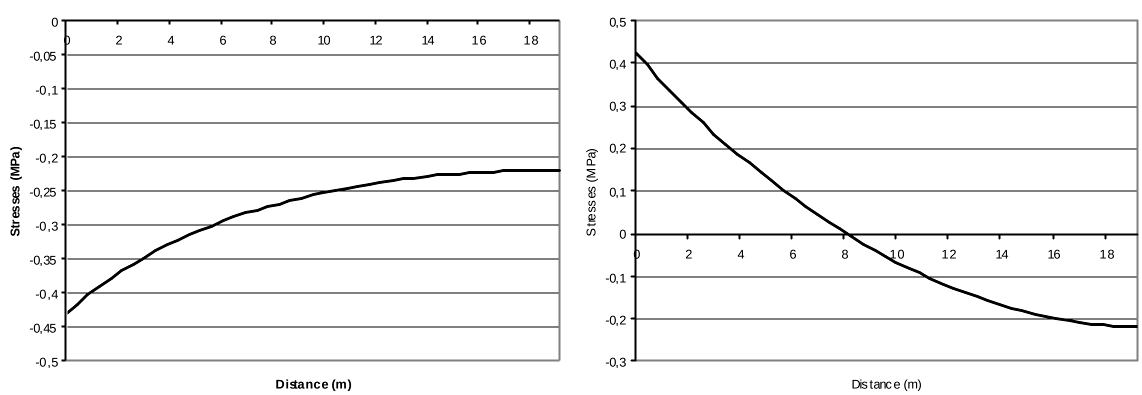

Figure 12.1. FEA membrane meridional and circumferential stresses for a shell under vertical load

On the horizontal axis of Figure 12.1 the meridional direction of the shell surface is shown from the base radius to the top node at *19635 mm* (quarter of a circle with radius *12500 mm*). The vertical axis shows the stresses from the finite element analysis. Clearly, the membrane stresses show no surprises as they have a similar distribution as Figure 10.4. Qualitatively, the stresses coincide with the values of Chapter 10.

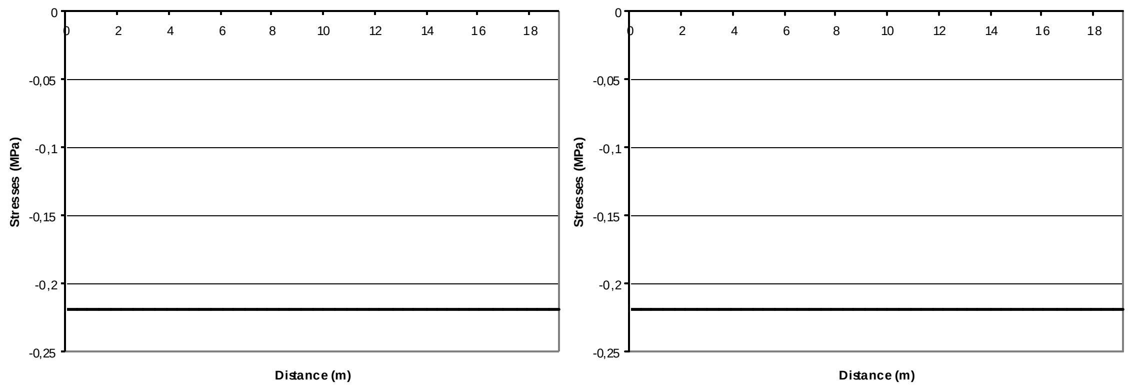

Figure 12.2. FEA meridional and circumferential stresses for a roller shell under spherical load

The roller supported Zeiss 1 shell subjected to a spherical load is a second example of a shell in a pure membrane state. The roller supports do not suppress any rotation which means that, theoretically, the shell is free from bending. Moreover, the spherical load only cause uniformly distributed radial pressing of the shell and no rotation. As can be seen in the rather trivial graphs of Figure 12.2, the principal meridional and circumferential stresses are equal to *-0.219 MPa*. Again, on the horizontal axis of the figures the meridional direction of the shell surface is shown. The vertical axis shows the stresses from the FEA.

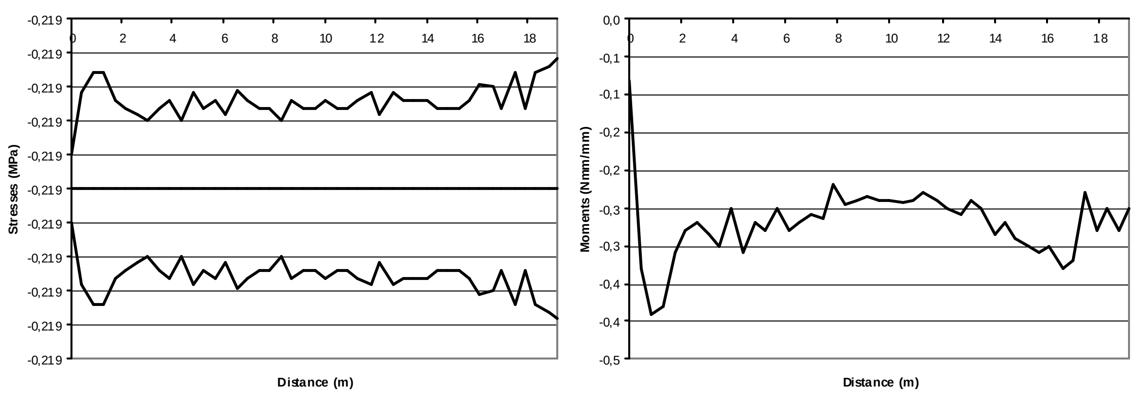

Figure 12.3. FEA uninvited meridional stress discrepancies and bending moments of a roller shell under spherical load

A closer look at the membrane stresses, however, uncovers inaccuracies in the solution. Within a very small bandwidth, between *-0.218* and *-0.219 MPa*, adjacent nodal stresses show uninvited discrepancies which lead to uninvited bending moments, both illustrated in Figure 12.3. The three different lines in the stress graph of Figure 12.3 represent the stresses in the outer, middle and inner Simpson integration points, respectively. The inaccuracies are caused by the modelling drawback of DIANA, i.e. for the axisymmetrical elements it is not possible to construct a purely spherical load. As a consequence of the aforementioned solution, small disturbances arise between adjacent nodes. These disturbances cause the stress discrepancies and bending moments. The disturbances are relatively small.

In Figure 12.3 it is also seen that the bending moments do not completely vanish at the support. Theoretically, the shell is free to rotate and thus no bending moments can be absorbed at the support. The reason for the nonzero bending moments is found in the element formulation; they do not return to zero at the support due to the fact that the mapping operation from the 'exact' integration points (which are not situated at the end of an element) to the end nodes is linear. As the actual moments experience higher order degradation, the linear mapping operation is of insufficient degree.

Zeiss 2

The Zeiss 2 shell has inclined-roller support, which means that the base radius of the shell is restrained from rotating. When the inclined-roller shell is subjected to vertical load, the supports are not membrane compatible anymore. Hence, bending moments inevitable arise and there is referred to a so-called edge disturbance. The meridional stresses and bending moments are seen in Figure 12.4. The bending moments rising from the edge disturbance do not influence the circumferential stresses, which is evident as they are in perpendicular direction. Consequently, the circumferential stresses of the inclined-roller supported shell are similar to the pure membrane situation in Figure 12.1. Due to the fact that the bending moments have a local character and decay out, reaching up to approximately *2078 mm* (equation (10.33)), both graphs of the figure are zoomed in upon the boundary layer of the shell, which is bending-dominated.

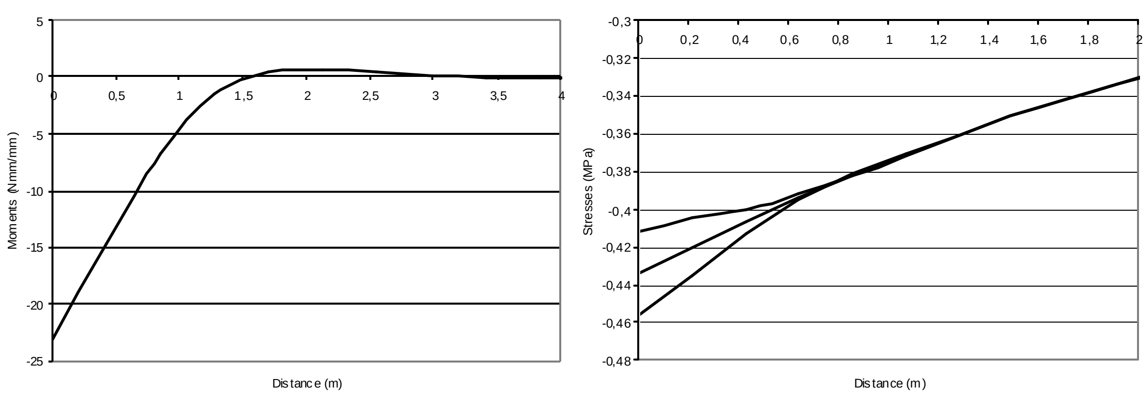

Figure 12.4. FEA bending moments and meridional stresses for a shell under vertical load with inclined-roller support

The bending moments plotted in Figure 12.4 correspond to the back curving of the shell surface for compatibility requirements. In other words, the shell flattens under the vertical load and needs to be rotated reversely at the base radius to end up straight. This is also seen in the stress graph where the meridional stresses split into three paths near the support (*-0.412*, *-0.434* and *-0.456 MPa*). As previously observed in the spherically loaded Zeiss 1 shell, these splitted lines represent the discrepancy between the both outer Simpson integration points. One line (the upper) represents the outer shell surface and experiences a release in compressive stress due to the bending moments. The other line (the lower) represents the inner shell surface and experiences an increase in compressive stress. Clearly, the line in-between is the middle surface stress.

In Figure 12.4 it can also be seen that the influence length as determined according to equation (10.33) almost coincides with the finite element result (*2078 mm* to *1700 mm*, respectively). Furthermore, Figure 12.4, shows that the maximum bending moment is only slightly lower (approximately *3%*) than the one found using the theoretical formulae. The principal middle surface stresses have good correlation with the theory. This is also seen in Table 12.4. Finally, it can be concluded from Figure 12.4 that the edge disturbance influences the meridional stresses up to roughly *1000 mm*, which means that the shell is in pure membrane action (only in-plane stresses and no bending moments) for *92%*. Hence, according to the categorisation by Farshad [34] the shell can be qualified as membrane-dominated.

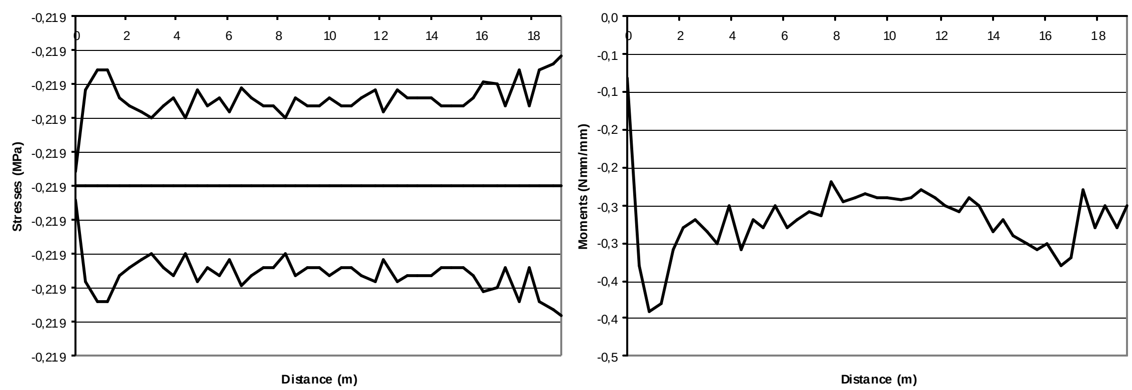

Figure 12.5. FEA uninvited meridional stresses and bending moments in an inclined-roller shell under spherical load

For a spherical load the Zeiss 2 shell remains in a pure membrane state and the principal membrane stresses are similar to the graphs of Figure 12.2. However, once more, small disturbances are present and bending moments arise. They are shown in Figure 12.5. In the figure it can be seen that the initial bending moments are smaller in compare to the previously found moments of the Zeiss 1 shell. Therefore, in the stress distribution, the inner and outer stresses reach each other more closely. Obviously, this is caused by the different compatibility requirement of the inclined-roller; no rotation allowed. Nonetheless, these disturbances should not been there at all in the first place.

Zeiss 3

The third type of support is a hinge, which means that the base radius of the shell is fixed at location while it is free to rotate. The hinge support is unable to transfer bending moments. As a consequence, the bending moments which undoubtedly will arise somewhat higher in the shell (the natural deformation is disturbed) must vanish. The bending moments from the finite element analysis are shown in Figure 12.6. From Figure 12.6 it can be observed that the results are inaccurate. Due to the fact that the integration points are not situated at the end of the elements, and the mapping operation to the end node is linear, the bending moments do not return to zero at all at the hinge support. To show the expected moment distribution, a dotted line is drawn in the same graph. Despite the inaccuracy at the end node, the influence length shows good correlation with the theoretical value. The maximum bending moment is much higher than for the inclined-roller supported Zeiss 2 shell (*145 Nmm/mm* to 23.2 *Nmm/mm*). Obviously, this may be expected; for compatibility requirements the shell must deform completely against its urge.

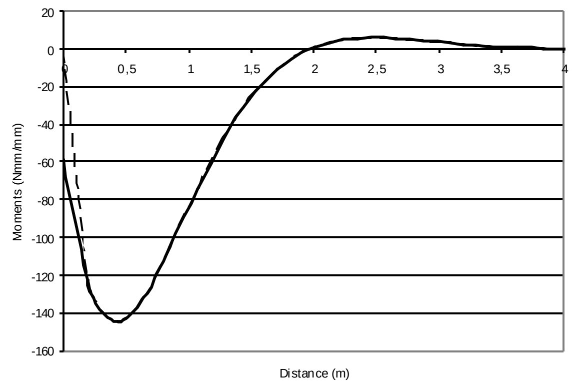

Figure 12.6. FEA and expected (dotted line) bending moments for a shell under vertical load with hinged supports

The principal meridional and circumferential stresses are plotted in Figure 12.7. Due to the nonzero bending moments at the support, the resulting graphs show a discrepancy between correct and found results, indicated by the difference in continuous and dotted lines. The dotted lines represet the correct solution. The stresses end with values of *-0.491* and *-0.377 MPa*. Also the circumferential stresses do not vanish at the support. From the figure it can be concluded that the hinged supported shell is in pure membrane action for more approximately *90%*.

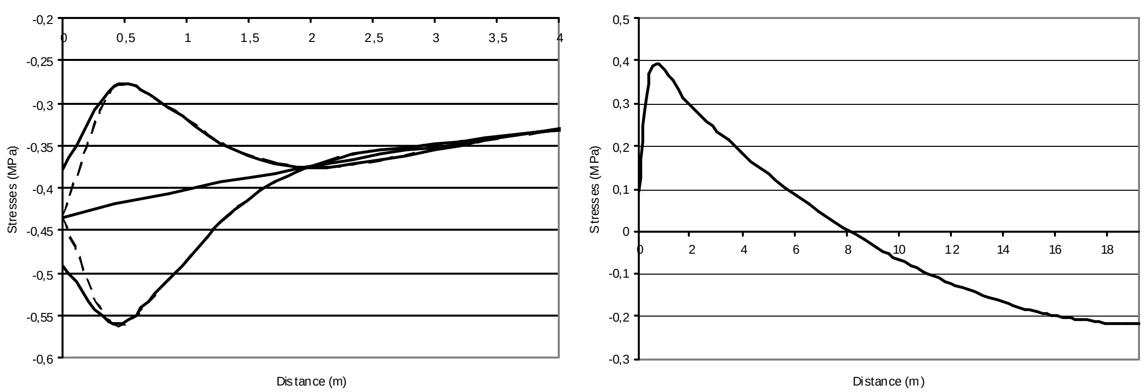

Figure 12.7. FEA meridional and circumferential stresses for a shell under vertical load with hinged supports

Also for a spherical load, a hinge supported shell is not in a pure membrane state. In fact, the stresses and bending moments of a hinged shell subjected to spherical load show great similarity with the shell under vertical load. The finite element result is plotted in Figure 12.8. Both graphs of Figure 12.8 are zoomed in upon the bending-dominated boundary layer of the shell. The bending moments are in contradiction to the theory as they do not vanish. As can be expacted based on the deformation of the shell under spherical load, the bending moments are of opposite signin compare to the bending moments of Figure 12.7. Hence, the non-vanishing meridional stresses are also of opposite sign.

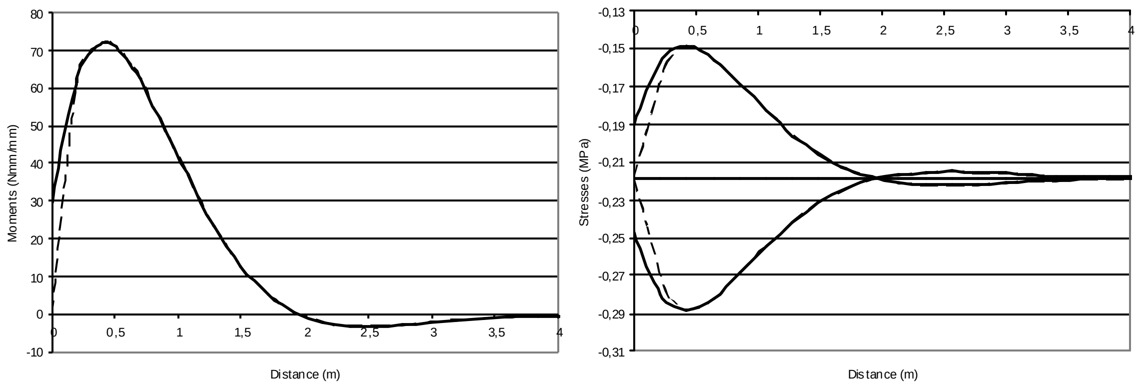

Figure 12.8. FEA meridional stresses and bending moments in a hinged supported shell under spherical load

With respect to the uninvited stresses and bending moments seen in Figure 12.3 and 12.5, it can be concluded that they become irrelevant as they are negligible in compare to the much larger stress variations caused by the edge disturbance.

Zeiss 4

The final shell support is a clamped support, no rotation and displacement allowed. For a vertically loaded clamped shell, the bending moments determined in the finite element analysis are plotted in Figure 12.9.

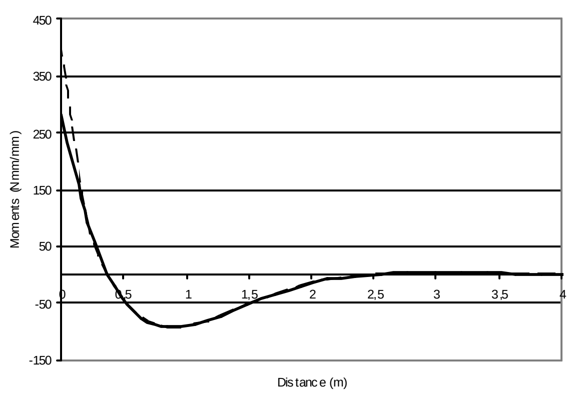

Figure 12.9. FEA and theoretical bending moments for a shell under vertical load with clamped supports

The value is significantly lower than the one found in Chapter 10 using the classical shell theory, indicated by the dotted line. The considerable disagreement is an extreme example of the factual error of the linear stress mapping within the axisymmetric elements. Counteracting the size disagreement, the influence length of the bending moment is correct and the shell behaves like a membrane for approximately *80%*, regardless of the 'severe' compatibility requirement.

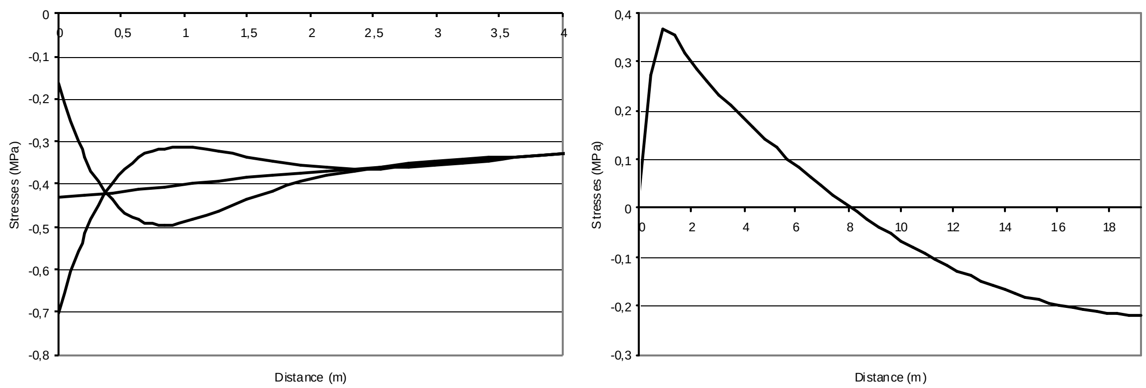

Figure 12.10. FEA meridional and circumferential stresses for a shell under vertical load with clamped supports

The resulting stresses of the vertically loaded clamped shell are illustrated in the graphs of Figure 12.10. It can be seen that, contrary to the Zeiss 3 shell, the circumferential stresses approach the actual zero stress at the base radius more closely. The meridional outer and inner surface stresses show a remarkable pattern which can be explained by curving and back curving of the shell surface near its support corresponding to the expected deformations, i.e. flattening at the top and bulging and back curving near the base. The large bending moments cause the outer surface stresses (*-0.705* and *-0.163 MPa*) to be far away from each other. Hence, as a larger moment can be expected, Figure 12.9, the actual stress dissimilarity will be even greater.

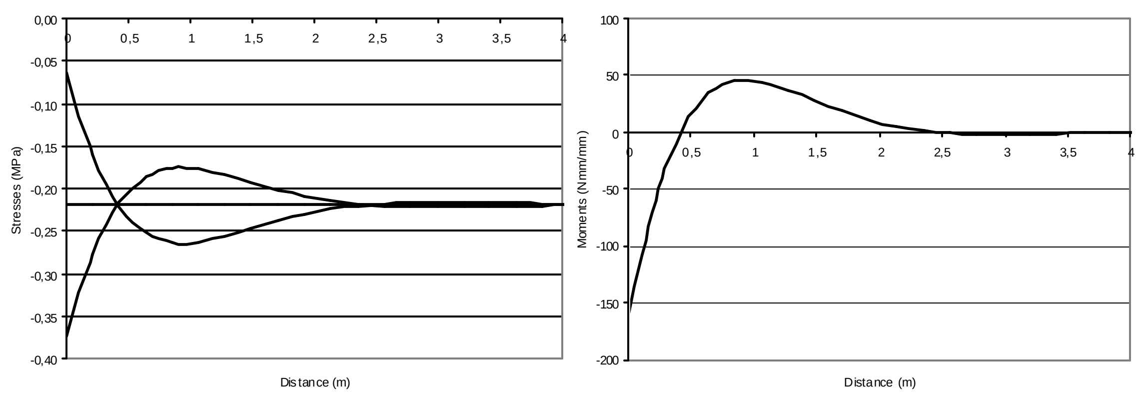

Figure 12.11. FEA meridional stresses and bending moments in a clamped supported shell under spherical load

When the clamped shell is subjected to a spherical pressure load, the bending moments and stress variation in the shell may expected to be even higher than previously found for the Zeiss 3 shell. That is, the shell does not only must preserve its initial position at the base, but also is not allowed to rotate. The results of the finite element analysis are seen in Figure 12.11. The trend of the graphs is quite similar to the graphs of Figure 12.9 and 12.10. Like the vertically loaded clamped shell, the bending moment may be underrated. Similar to the Zeiss 3 shell, the uninvited stresses and moments caused by the modelling drawback are negligible.

Name	Meridional stresses (MPa)				Circumferential stresses (MPa)			
	Top		Base		Top		Base	
	FEA	Theory	FEA	Theory	FEA	Theory	FEA	Theory
Zeiss 1	-0.219	-0.219	-0.434	-0.438	-0.219	-0.219	0.429	0.438
Zeiss 2	-0.219	-0.219	-0.434	-0.438	-0.219	-0.219	0.429	0.438
Zeiss 3	-0.219	-0.219	-0.434	-0.438	-0.219	-0.219	0.09	0
Zeiss 4	-0.219	-0.219	-0.434	-0.438	-0.219	-0.219	0.03	0

Table 12.4. Meridional and circumferential stresses for vertical loaded shells

To give a quantitative comparison between the theoretical results of Chapter 10 and the finite element results, the stresses found for vertical and spherical loaded shells are summarised in Table 12.4 and Table 12.5. In case of varying stresses over the thickness of the shell, the middle surface stresses are tabulated.

Name	Meridional stresses (MPa)				Circumferential stresses (MPa)			
	Top		Base		Top		Base	
	FEA	Theory	FEA	Theory	FEA	Theory	FEA	Theory
Zeiss 1	-0.219	-0.219	-0.219	-0.219	-0.219	-0.219	-0.219	-0.219
Zeiss 2	-0.219	-0.219	-0.219	-0.219	-0.219	-0.219	-0.219	-0.219
Zeiss 3	-0.219	-0.219	-0.219	-0.219	-0.219	-0.219	-0.049	0
Zeiss 4	-0.219	-0.219	-0.219	-0.219	-0.219	-0.219	-0.012	0

Table 12.5. Meridional and circumferential stresses for spherical loaded shells

If the supports are not membrane compatible, bending moments arise. They are quantitatively represented in Table 12.6. In the spherical (right) table, the disturbances of the load-modelling can be seen.

Name	Bending moments (Nmm/mm)			Bending moments (Nmm/mm)	
	Base			Base	
	AXI FEA	Theory		AXI FEA	Theory
Zeiss 1	0	0		-0.079	0
Zeiss 2	-23.2	-23.93		-0.049	0
Zeiss 3	-59.0	0		29.5	0
Zeiss 4	281.0	406.79		-161	-

Table 12.6. Bending moments of the vertical (left) and spherical (right) loaded shell

From Table 12.4, 12.5 and 12.6 it can be concluded that, generally, the finite element results are in reasonable agreement with the classical shell theory (within *1%*). The circumferential stresses at the base and the bending moments due to edge constraint, however, uncovers the factual error of linear stress mapping. In particular for the hinged Zeiss 3 and clamped Zeiss 4 shells the linear mapping has a significant influence on the stress distribution and bending moments. The overcome the (large) discrepancy between expected and computed results one may opt for choosing a higher order scheme in length direction with integration points at the element ends. However, aforementioned in Chapter 11, this is not recommended as the element becomes highly sensitive to shear locking. Hence, the engineer must keep in mind that these elements may yield results of insufficient accuracy. Note that, by selecting a finer mesh, the engineer is able to obtain an impression of the size of the discrepancy which he can use in the design process.

12.2.4 Strains

In linear elastic analysis the strains can directly be derived from the stresses conform the constitutive law, which is even further simplified as the Poisson's ratio is set equal to zero. Therefore, the strain graphs show a same trend as the previously plotted stresses. E.g. this is seen in Figure 12.12 for the Zeiss 1 shell.

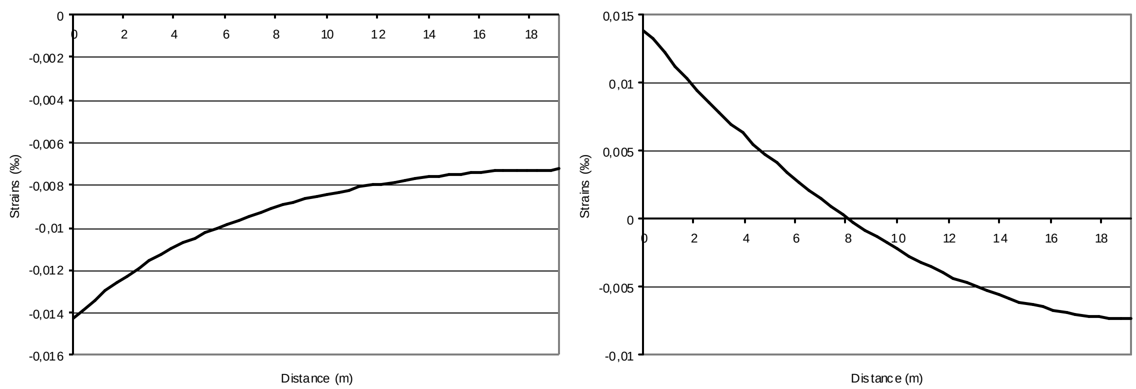

Figure 12.12. FEA meridional and circumferential strains for a shell under vertical load with roller supports

The graphs of Figure 12.12 represent the principal membrane strains for a hemispherical shell subjected to a uniform vertical load. If the boundary condition is not membrane compatible, the membrane strains will be disturbed locally (only in the boundary layer of the shell) such as the stress disturbances seen before. In those regions, the inner and outer surface strains will deviate from each other presenting the cross-sectional rotation of the shell surface. Clearly, as the strains are mapped linear over the element length, the strains violate the theory in the same manner as the stresses did. The strain results as obtained by the finite element analysis are summarised in Table 12.7.

Name	Meridional strains (‰)				Circumferential strains (‰)			
	Top		Base		Top		Base	
	FEA	Theory	FEA	Theory	FEA	Theory	FEA	Theory
Zeiss 1	-0.0073	-0.0073	-0.0145	-0.0146	-0.0073	-0.0073	0.0143	0.0146
Zeiss 2	-0.0073	-0.0073	-0.0145	-0.0146	-0.0073	-0.0073	0.0143	0.0146
Zeiss 3	-0.0073	-0.0073	-0.0145	-0.0146	-0.0073	-0.0073	0.003	0
Zeiss 4	-0.0073	-0.0073	-0.0145	-0.0146	-0.0073	-0.0073	0.0009	0

Table 12.7. Meridional and circumferential middle surface strains for a shell under vertical load

For the strains in the shells subjected to spherical pressure load, the same observations can be made. That is, their distribution is similar to the graphs seen in Figure 12.2. When the supports suppress the membrane deformation, the strains are disturbed locally and the inner and outer surface strains move away from each other. Like the stresses, the strains are not perfect and they show the same irregular pattern as seen in

Figure 12.3 and 12.5. Finally, also for the spherical strains, the linear mapping is the reason for the disagreement with the classical shell theory. The strains resulting from the finite element analysis are seen in Table 12.8.

Name	Meridional strains (‰)				Circumferential strains (‰)			
	Top		Base		Top		Base	
	FEA	Theory	FEA	Theory	FEA	Theory	FEA	Theory
Zeiss 1	-0.0073	-0.0073	-0.0073	-0.0073	-0.0073	-0.0073	-0.0073	-0.0073
Zeiss 2	-0.0073	-0.0073	-0.0073	-0.0073	-0.0073	-0.0073	-0.0073	-0.0073
Zeiss 3	-0.0073	-0.0073	-0.0073	-0.0073	-0.0073	-0.0073	0	0
Zeiss 4	-0.0073	-0.0073	-0.0073	-0.0073	-0.0073	-0.0073	0.0004	0

Table 12.8. Meridional and circumferential middle surface strains for a shell under spherical load

Analogous to the previous section, the conclusion can be drawn that the finite element results show reasonable agreement with the classical shell theory, except for the disturbed boundary regions where large bending moments are present.

12.2.5 Displacements

The shell subjected to vertical or spherical load undergoes a displacement from its initial shape. Clearly, the deformation depends on the type and magnitude of the load, the shell proportions and the boundary conditions. The deformed and undeformed vertically loaded Zeiss shells are visualised in Figure 12.13. Quantitative information concerning the deformed shells can be found in Table 12.9.

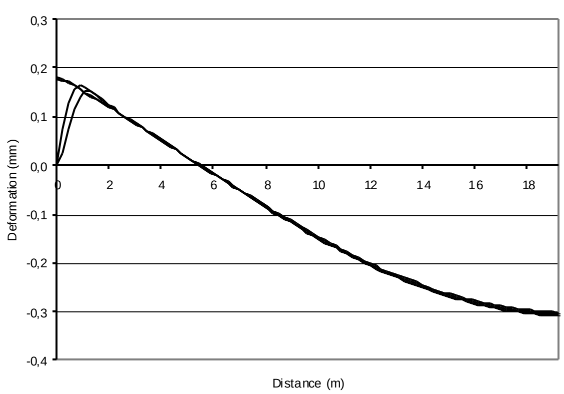

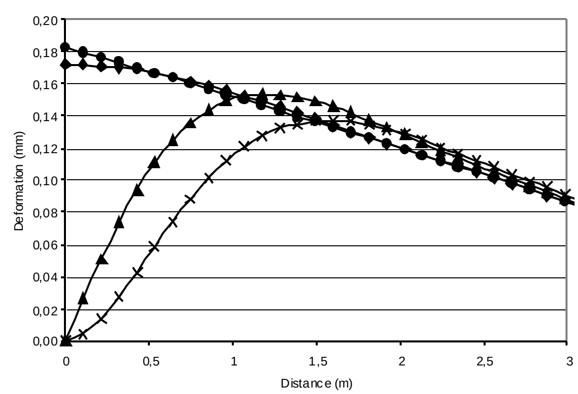

Figure 12.13. Displacements of a shell under vertical load with several support conditions

In Figure 12.13, the initial (zero line) and deformed Zeiss 1 to 4 shells are shown. The 'membrane' supported Zeiss 1 shell (dot line) can move freely, restricted by its circumferential stresses only. The largest displacement is seen at the top of the shell. At the base radius the shell moves outward and rotates slightly. Contrary to the Zeiss 1 shell, the Zeiss 2 shell (ace line) cannot rotate at the base. Hence, bending moments must bend back the shell against its membrane deformation. The support has no influence on the top displacement as it is similar to the membrane supported shell. The initial and deformed shapes of the Zeiss 3 and Zeiss 4 shell are also illustrated in Figure 12.13. The hinged support of the Zeiss 3 shell (triangular line) does not allow for any displacement at the base. Additionally, in case of the clamped supported Zeiss 4 shell (cross line), the rotation is also suppressed, causing adjacent curvatures in different directions. Both supports do not only influence the base displacement, but the top displacement as well. Due to the restraints, the top displacement is slightly less than the ones found for the Zeiss 1 and 2 shells.

Name	Displacements (mm)				Rotations (mm/mm)			
	Top		Base		Top		Base	
	FEA	Theory	FEA	Theory	FEA	Theory	FEA	Theory
Zeiss 1	-0.308	-0.365	0.182	0.182	0	0	-2.92 E-5	-2.92 E-5
Zeiss 2	-0.308	-0.365	0.170	0.173	0	0	0	0
Zeiss 3	-0.304	-0.365	0	0	0	0	0.00025	0.00025
Zeiss 4	-0.299	-0.365	0	0	0	0	0	0

Table 12.9. Displacements and rotations of the FEA and the classical shell theory

Comparing the results from the finite element analysis with the theoretical values in Table 10.8, 10.10, 10.12 and 10.14, it can be concluded that the base displacements and rotations are (nearly) similar. The top displacements, however, show considerable dissimilarities as the shell seems to act stiffer (up to *15%* and more). This discrepancy is discussed further in Section 12.3.

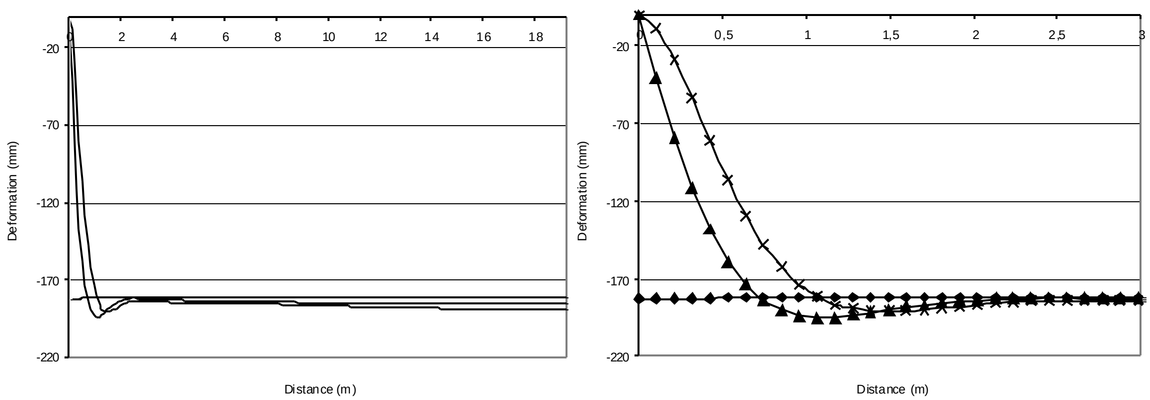

Figure 12.14. Displacements of a shell under spherical load with several supporting conditions

The deformations of the spherical loaded shell with respect to the initial (zero line) position are seen in Figure 12.14. The Zeiss 1 and Zeiss 2 shell deform very much similar and their deformation lines coincide (ace line). The corresponding deformation is presented quantitatively in Table 12.10. In Table 12.10 it is observed that the aforementioned stress and strain disturbances cause the top displacement of Zeiss 1 and 2 being different from the base displacement. Moreover, the disturbances cause both shells experience top rotation and, additionally, the Zeiss 1 shell undergoes a rotation at the base. In Figure 12.14 the deformed shapes of Zeiss 3 (triangular line) and 4 (cross line) caused by a spherical load are shown as well. It can be observed that the hinged supported shell experiences one directional curving to meet the compatibility requirement. For the clamped shell the additional requirement of zero rotation means that the shell needs two consecutive curves of opposite direction. In Figure 12.14 it can be seen that this more severe boundary condition leads to a larger disturbed region. From Figure 12.14 and Table 12.10 it can be concluded that the more severe support conditions lead to slightly higher top deformations, in contrast with the observation made for the vertical load. Aforementioned, the base displacement of Zeiss 1 and 2 and the base rotation of Zeiss 1 are misleading results caused by the stress and strain disturbances.

Name	Displacements (mm)		Rotations (mm/mm)	
	Top	Base	Top	Base
Zeiss 1	-0.0909	-0.0913	-0.478 E-7	-0.934 E-7
Zeiss 2	-0.0909	-0.0913	-0.478 E-7	0
Zeiss 3	-0.0933	0	-0.478 E-7	0.139 E-3
Zeiss 4	-0.0957	0	-0.478 E-7	0

Table 12.10. Displacements and rotations of the FEA for shell under spherical load

With respect to the differences between a shell subjected to a spherical load and a vertical load, it can be concluded that, in general, the vertical load causes higher stresses and bending moments. Consequently, the deformations caused by a spherical pressure load are far less than the deformations caused by a uniformly distributed vertical load with the same magnitude. This, however, may be expected from a simple equilibrium consideration; in the lower part of the hemisphere the vertical load does not contain a 'supporting' transverse component and, thus, the shell behaves less stiff in that region.

12.3 Three-Dimensional Model

Aforementioned in the introduction, the axisymmetric shell model is unable to produce variations in circumferential direction. However, in case of non-axisymmetric loading (wind, drifted snow), buckling, or imperfect shells the hypothesis of constant circumferential behaviour is not applicable anymore. Therefore, a three-dimensional shell model is necessary. The three-dimensional shell model is checked on support reactions, stresses, strains and displacements for each of the given supports and load conditions given in Table 12.1. However, first the 3D finite element model is discussed in detail.

12.3.1 FE Model

The three-dimensional shell model is seen in Figure 12.15. The model consists of two-dimensional curved shell elements. The model is generated by constructing several meridional and circumferential ribs which enclose rectangular and triangular surface areas. These individual areas are meshed with two-dimensional quadrilateral QU8-CQ40S curved shell and triangular TR6-CT30S curved shell elements (both discussed in Chapter 11). To ensure a pure spherical shape, the base shape of the elements is mapped onto spherical shape. Typically, the elements produce *x*- and *y-directional* stresses and strains which vary linearly in their own direction and quadratically in their perpendicular direction. For both elements a reduced integration scheme is applied to avoid membrane and shear locking. In thickness direction a 3 point Simpson integration is sufficient for linear elastic analyses, DIANA User's Manual [29]. The final model consists of *7168* elements bounded by *20609* nodes, see Figure 12.15. The requirement of at least 6 elements within the influence region of possible edge disturbance is satisfied. Similar to the axisymmetric model, the type of support is modelled by allowing or disallowing translation and/or rotation of the nodes on the base radius. The load is purely vertical or spherical.

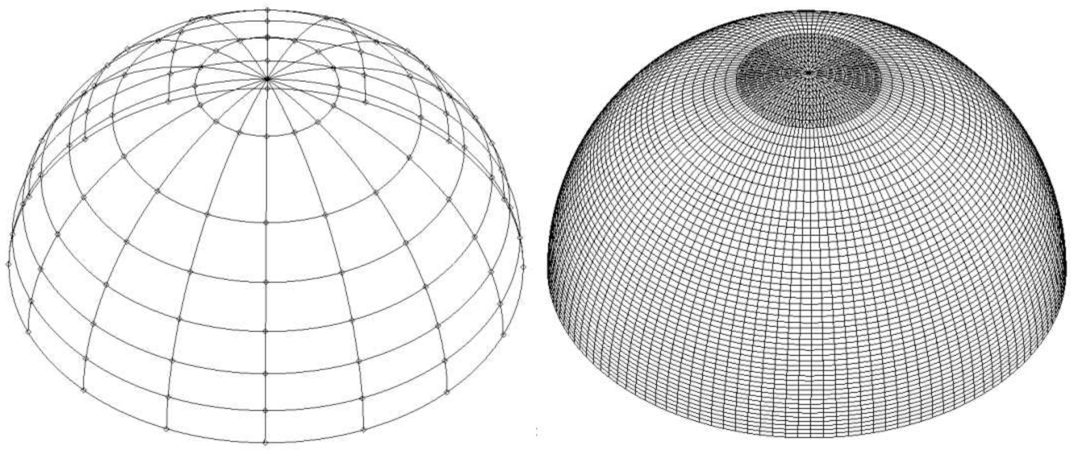

Figure 12.15. Three-dimensional shell model

Within the scheme of shell mesh generation procedures, it is also possible to let DIANA construct a mesh or to import one. The DIANA mesh, containing only quadrilateral elements, was already shown in Figure 11.13. From the figure it can be concluded that the DIANA mesh is non-smooth, showing large size deviations between neighbouring elements. This is, in fact, inherent to the generation method. To model a hemispherical cap, DIANA constructs a complete sphere which can be sliced in at least four parts (and not two). Thus, to construct a hemisphere two quarter parts of a sphere must be combined, resulting in two adjacent surfaces separated by a line of symmetry. Due to this line of symmetry two different meshes are required. Moreover, DIANA meshes the spherical shape using a paving algorithm (see Chapter 11). For a double curved shape this inevitable means that, starting at one point, at certain moment the mesh generation operation becomes entangled causing several elements of various sizes appearing next to each other. Unfortunately, the non-smoothness produces highly irregular stress and strain graphs (although they are not wrong in general). Therefore, the DIANA mesh is disregarded in favour of the manual generated mesh. Furthermore, some attempts were made to import a mesh from MAYA and RHINO. However, the import operation failed as several elements did not survive.

12.3.2 Support Reactions

The elementary support reaction test of the three-dimensional model provide in a simple and fast first check to validate the model. The finite element results for each individual support condition are summarised in Table 12.11 and 12.12. In order to be able to compare the results of the three-dimensional model with the ones previously found, the values of Table 12.2 and 12.3 are present. Similar to Table 12.2 and 12.3, the support reactions are the sum of all support reactions of the base radius.

Name	Vertical support reaction (kN)			Horizontal support reaction (kN)		
	3D	AXI	Theory	3D	AXI	Theory
Zeiss 1	2062.0	2060	2061	0	0	0
Zeiss 2	2062.4	2060	2061	0	0	0
Zeiss 3	2060.8	2060	2061	39.9	38.4	38.3
Zeiss 4	2056.8	2060	2061	74.8	73.8	73.8

Table 12.11. Support reactions for a shell under vertical load

In Table 12.11 it can be observed that there are several small differences in displacements which can be contributed to the numerical process. The differences in displacements of the three-dimensional model and the axisymmetric model are within a few percent (*4%*).

Name	Vertical support reaction (kN)			Horizontal support reaction (kN)		
	3D	AXI	Theory	3D	AXI	Theory
Zeiss 1	1030,8	1030	1031	0	0	0
Zeiss 2	1030,7	1030	1031	0	0	0
Zeiss 3	1030,9	1030	1031	-18,4	-19.2	-19.2
Zeiss 4	1031,0	1030	1031	-37,8	-36.9	-36.9

Table 12.12. Support reactions for a shell under spherical load

The support reactions corresponding to the spherical loaded shell are seen in Table 12.12. It can be concluded that the results are sufficient as the discrepancies stay within a negligible *4.2%*.

12.3.3 Stresses

Zeiss 1

The roller supported Zeiss 1 shell under vertical load is in a pure membrane state. A graphical presentation of the principal stress distribution of the three-dimensional shell analysis is plotted in Figure 12.16. In the figure, the horizontal axis represents the shell meridional direction from the base radius to the top node. The vertical axis gives the meridional (thick line) and circumferential (thin line) stresses. It can be seen that there are disturbances in the finite element solution indicated a difference in stress between the inner, middle and outer Simpson integration points near the top of the shell. As observed in the stress output, the dissimilarity between the inner, middle and outer stress varies in meridional direction, with a pattern repeating each *2000 mm*. Remarkable (or not) this is exactly the distance between to adjacent model-ribs. The explanation is found in the mapping operation of the element onto a spherical base shape. The mapping operation failed and the meshed areas between the ribs slightly deviate from an ideal sphere. In other words, the mesh lies over the ribs of the model like an unstressed fabric. The imperfectness undoubtedly leads to bending moments as there are curvature variations over the shell surface. The right graph of Figure 12.16 shows the meridional (thick) and circumferential (thin) bending moments which, in theory, would not occur.

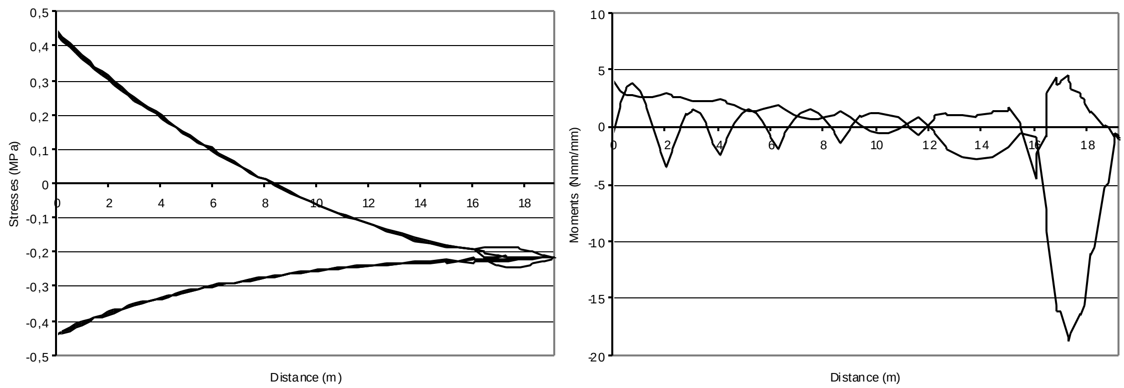

Figure 12.16. Meridional (thick) and hoop stresses and uninvited bending moments of a roller supported shell under vertical load

In Figure 12.16 it is observed that, especially in the triangular elements and in the transition zone between the quadrilateral and triangular elements, the curvature variation has large influence and the moments show 'high' peaks (up to *-18.8 Nmm/mm*). The peaks can be explained by the fact that the main shape deviations are located within the triangular zone and close to the transition zone. The average shape deviation equals *0.43 mm* with a largest value of *2.9 mm*. This is extremely high in compare to the expected discrepancy based on the number of significant digits (7) stored in the data file (there is no such thing as a perfect numerical model). As the disturbances have minor influence on the stress distribution the model is assumed to be sufficient.

A final remark on Figure 12.16 is that the bending moments do not vanish at the support. Similar to the axisymmetric shell model, this can be contributed to the stress mapping between the 'exact' integration point and the element nodes.

For the Zeiss 1 shell subjected to spherical load, the meridional (thick) and circumferential (thin) stresses are visualised in Figure 12.17. The deviating inner and outer surface stresses indicate the presence of the same disturbances as described above. The corresponding bending moments are also shown in Figure 12.17.

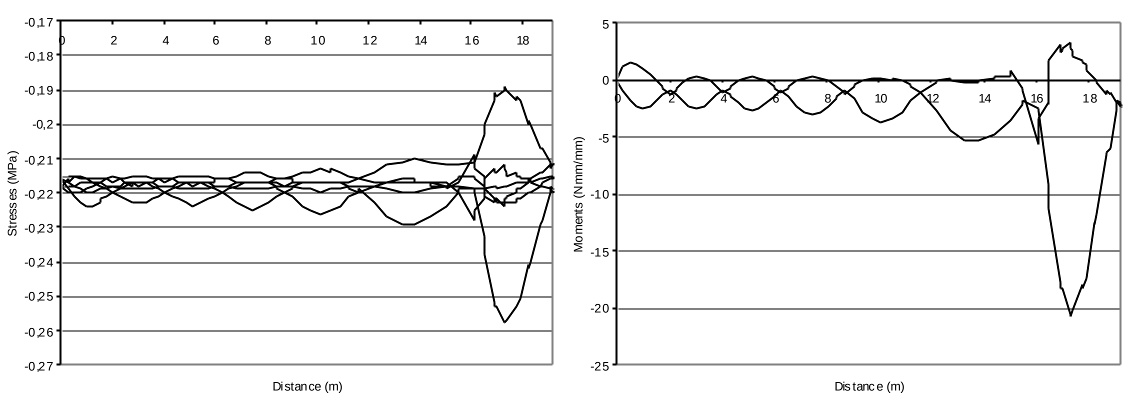

Figure 12.17. Meridional (thick) and hoop (thin) stresses and uninvited bending moments of a roller supported shell under spherical load

It can be seen that the stresses and bending moments show a repetitive pattern between the ribs. The bending moments are approximately of the same magnitude, though slightly higher, as the moments appearing in the Zeiss 1 shell under vertical load (*-20.9 Nmm/mm* to *-18.8 Nmm/mm*).

Zeiss 2

As seen before in the axisymmetric analysis, the Zeiss 2 shell is not membrane compatible when subjected to vertical load and bending moments arise. The stress distribution and bending moments along the meridian are illustrated in Figure 12.18.

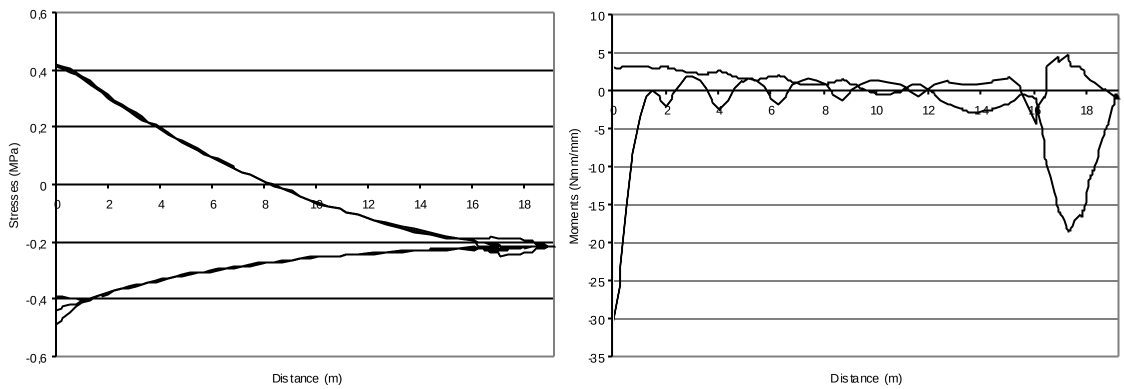

Figure 12.18. Meridional (thick) and hoop (thin) stresses and (uninvited) bending moments of an inclined-roller supported shell under vertical load

Most interesting in Figure 12.18 is the right graph presenting the moment distribution. It is observed that the uninvited moments are somewhat lower than the bending moments caused by the edge restraint.

When subjected to spherical load, the inclined-roller supported Zeiss 2 shell is still membrane compatible. Therefore, both graphs of Figure 12.19 are very much similar to the graphs of Figure 12.17. Only small differences arise in the inner and outer surface stresses and the bending moments due to the restrained deformation of the nodes at the base radius.

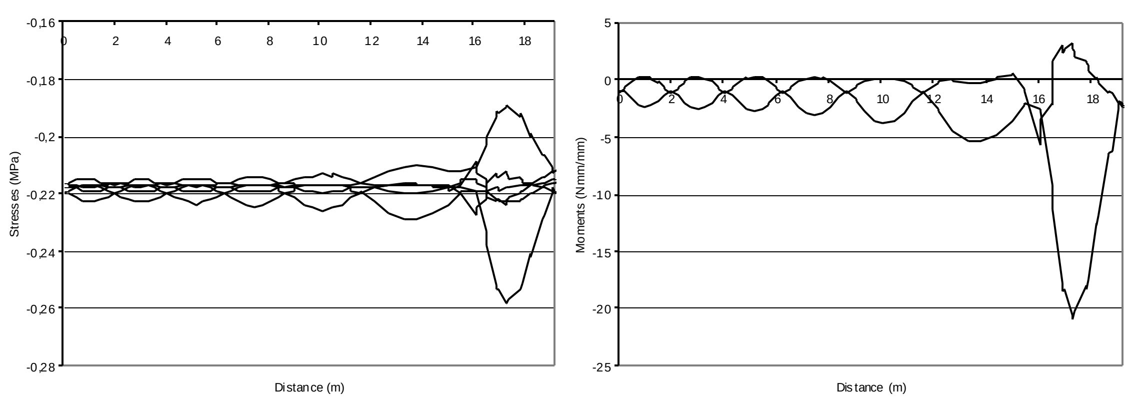

Figure 12.19. Meridional (thick) and hoop (thin) stresses and (uninvited) bending moments of an inclined-roller supported shell under spherical load

Zeiss 3

The stresses and bending moments in the hinged supported Zeiss 3 shell subjected to uniform vertical load are illustrated in Figure 12.20. It can be seen that, the influence of the bending moments caused by the numerical imperfectness is less in compare to the edge disturbance. If Figure 12.20 is compared to Figure 12.6, it can be concluded that the bending moments are almost similar. Besides, the stresses are determined more accurately by the three-dimensional model as they are in better agreement with the theory.

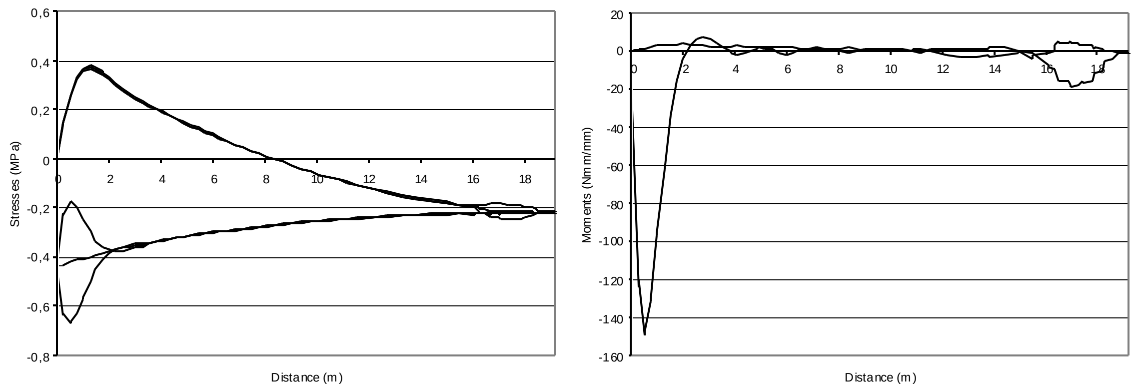

Figure 12.20. Meridional (thick) and hoop (thin) stresses and (uninvited) bending moments of a hinged supported shell under vertical load

The results of the hinged supported shell subjected to spherical load are plotted in Figure 12.21. Similar to the vertical loaded shell, it can be concluded that the three-dimensional model leads to more accurately stress and bending moment distribution at the support. The magnitude of the bending moments of both models is approximately the same.

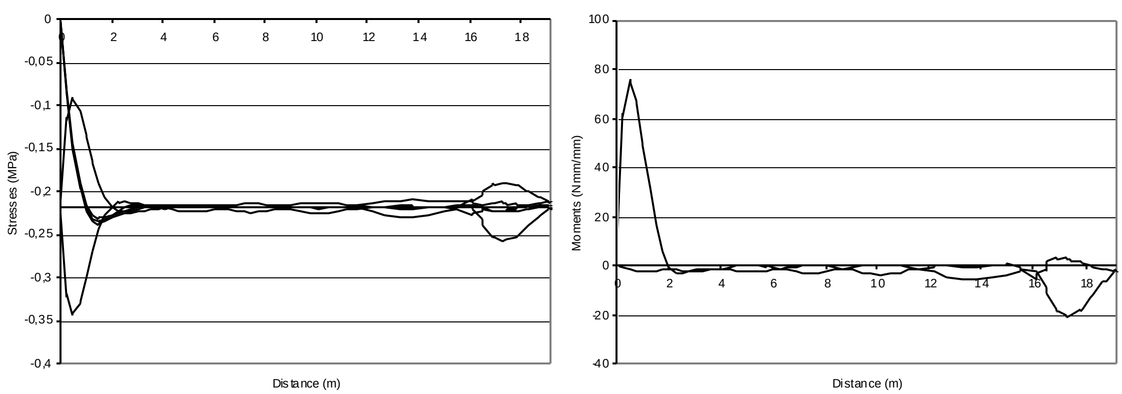

Figure 12.21. Meridional (thick) and hoop (thin) stresses and (uninvited) bending moments of a hinged supported shell under spherical load

Zeiss 4

The stress and bending moment distribution along the meridian of the clamped Zeiss 4 shell are seen in Figure 12.22. The severe edge restraint, nor any translation or rotation is allowed, leads to large bending moments and stress variations near the support. The results are in good correlation with the theory, see also Table 12.13 and 12.15, and much more accurate than the axisymmetric model, see Figure 12.9.

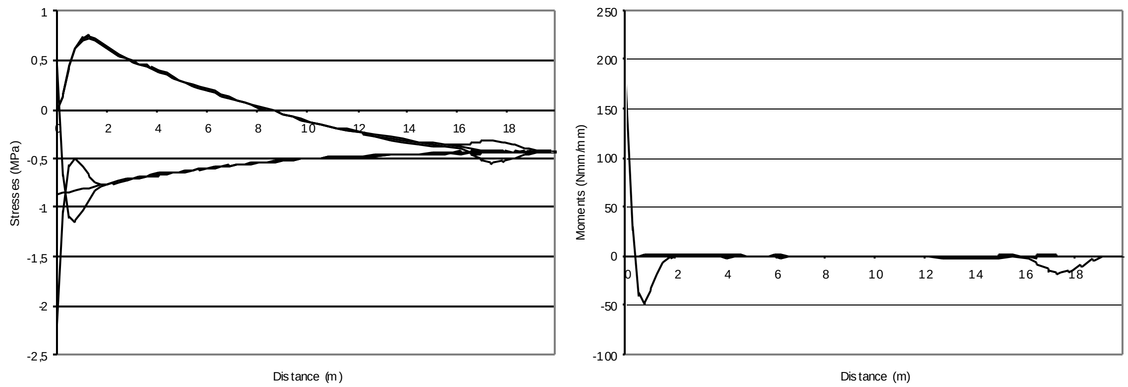

Figure 12.22. Meridional (thick) and hoop (thin) stresses and (uninvited) bending moments of a clamped supported shell under vertical load

In Figure 12.22 it can be seen that the bending moment caused by the edge disturbance is almost *400 Nmm/mm*. Due to the large bending moment, it is seen that the meridional inner surface stress even becomes positive, which means that there is not only tension in circumferential direction but also in meridional direction. Like the hinged supported Zeiss 3 shell, disturbances that result from the numerical imperfectness of the model become irrelevant as they are negligible in compare to the edge disturbance.

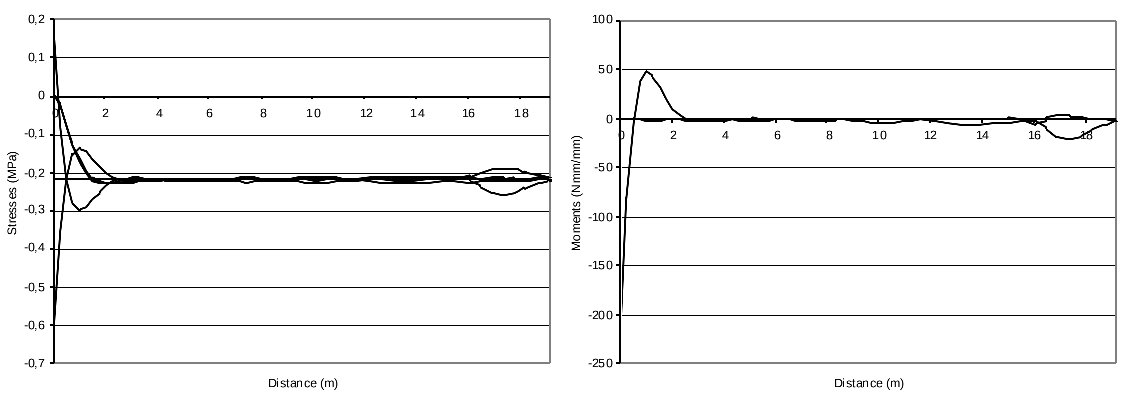

Figure 12.23. Meridional (thick) and hoop (thin) stresses and (uninvited) bending moments of a clamped supported shell under spherical load

The same observation is valid for the clamped supported shell subjected to spherical load. The results of the analysis are illustrated in Figure 12.23. Similar to the vertical loaded clamped shell, there is tension in meridional direction as the outer surface stress becomes positive under the large edge moments.

The stresses found in the three-dimensional finite element analysis are summarised in Table 12.13 and 12.14. The table shows the middle surface stresses.

Name	Meridional stresses (MPa)				Circumferential stresses (MPa)			
	Top		Base		Top		Base	
	3D FEA	Theory	3D FEA	Theory	3D FEA	Theory	3D FEA	Theory
Zeiss 1	-0.215	-0.219	-0.441	-0.438	-0.215	-0.219	0.447	0.438
Zeiss 2	-0.215	-0.219	-0.440	-0.438	-0.215	-0.219	0.424	0.438
Zeiss 3	-0.215	-0.219	-0.436	-0.438	-0.215	-0.219	0.004	0
Zeiss 4	-0.215	-0.219	-0.437	-0.438	-0.215	-0.219	-0.011	0

Table 12.13. Meridional and circumferential stress distribution for vertical loaded shells

Table 12.13 shows the stresses from the shells loaded vertically. The maximum difference is approximately *3%* whereas the average difference is about *1%*. Hence, the conclusion can be drawn that the 'average' middle surface stresses from the three-dimensional analysis are in good correlation with the classical shell theory.

In Table 12.14 the results in case of a spherical load are plotted. It can be seen that the stresses show less correlation in compare to the ones from Table 12.13. The average difference is somewhat higher and equal to *1.5%*. However, the greatest discrepancy, again found for the circumferential base stress of the roller supported shell, is less than for the vertical load.

Name	Meridional stresses (MPa)				Circumferential stresses (MPa)			
	Top		Base		Top		Base	
	3D FEA	Theory	3D FEA	Theory	3D FEA	Theory	3D FEA	Theory
Zeiss 1	-0.215	-0.219	-0.218	-0.219	-0.215	-0.219	-0.214	-0.219
Zeiss 2	-0.215	-0.219	-0.218	-0.219	-0.215	-0.219	-0.217	-0.219
Zeiss 3	-0.215	-0.219	-0.219	-0.219	-0.215	-0.219	0	0
Zeiss 4	-0.215	-0.219	-0.218	-0.219	-0.215	-0.219	0	0

Table 12.14. Meridional and circumferential stress distribution for spherical loaded shells

In Table 12.15 the bending moments are tabulated. Obviously, the bending moments arising at the roller support of the Zeiss 1 shell is the main reason for the discrepancies described above. In Table 12.15 it can be seen that the three-dimensional analysis approaches the classical shell theory bending moments more closely than the axisymmetric analysis.

Name	Bending moments (Nmm/mm)				Bending moments (Nmm/mm)		
	Base				Base		
	3D FEA	AXI FEA	Theory		3D FEA	AXI FEA	Theory
Zeiss 1	-0.851	0	0		0.23	-0.079	0
Zeiss 2	-31.0	-23.2	-23.93		1.23	-0.049	0
Zeiss 3	-9.54	-59.0	0		-4.11	29.5	0
Zeiss 4	390.0	281.0	406.79		-222	-161.0	-

Table 12.15. Bending moments of the vertical (left) and spherical (right) loaded shell

In fact, it can be concluded from Table 12.13, 12.14 and 12.15 that, in general, the three-dimensional shell model approaches the classical shell theory more closely than the axisymmetric shell model. However, in case of the given three-dimensional shell model, the stress distribution over the meridian is less smooth than the axisymmetric stress distribution.

12.3.4 Strains

For the linear elastic analysis, three-dimensional strain graphs show the same trend as the stress graphs. Therefore, the strains as obtained by the finite element analysis are not shown. They are tabulated in Table 12.16 and Table 12.17 for the vertical load and spherical load, respectively. The table shows the middle surface strains.

Name	Meridional strains (‰)				Circumferential strains (‰)			
	Top		Base		Top		Base	
	3D FEA	Theory	3D FEA	Theory	3D FEA	Theory	3D FEA	Theory
Zeiss 1	-0.0072	-0.0073	-0.0147	-0.0146	-0.0072	-0.0073	0.0149	0.0146
Zeiss 2	-0.0072	-0.0073	-0.0147	-0.0146	-0.0072	-0.0073	0.0141	0.0146
Zeiss 3	-0.0072	-0.0073	-0.0146	-0.0146	-0.0072	-0.0073	0	0
Zeiss 4	-0.0072	-0.0073	-0.0146	-0.0146	-0.0072	-0.0073	0	0

Table 12.16. Meridional and circumferential strain distribution for vertical loaded shells

Name	Meridional strains (‰)				Circumferential strains (‰)			
	Top		Base		Top		Base	
	3D FEA	Theory	3D FEA	Theory	3D FEA	Theory	3D FEA	Theory
Zeiss 1	-0.0072	-0.0073	-0.0073	-0.0073	-0.0072	-0.0073	-0.0072	-0.0073
Zeiss 2	-0.0072	-0.0073	-0.0073	-0.0073	-0.0072	-0.0073	-0.0073	-0.0073
Zeiss 3	-0.0072	-0.0073	-0.0073	-0.0073	-0.0072	-0.0073	0	0
Zeiss 4	-0.0072	-0.0073	-0.0073	-0.0073	-0.0072	-0.0073	0	0

Table 12.17. Meridional and circumferential strain distribution for spherical loaded shells

12.3.5 Displacements

The deformations of the three-dimensional shells subjected to vertical load are plotted in Figure 12.24 and Figure 12.25. In Figure 12.24, the initial undeformed and deformed shapes of the membrane supported Zeiss 1 shell are plotted against each other. Clearly, the shell can move and rotate freely at the base. Qualitatively, the deformed shape is similar to the one found before with the axisymmetric model.

In Figure 12.25 the initial and deformed shapes of the inclined-roller, hinged and clamped supported shell are plotted, respectively. The Figures are zoomed in upon the boundary layer of the shell to visualise the differences in deformation due to allowed or disallowed translations and rotations at the support. Qualitatively the shapes are similar to the axisymmetric deformed shells.

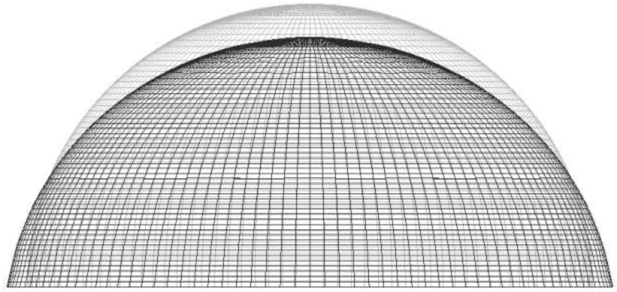

Figure 12.24. Displacement of a roller supported shell subjected to vertical load

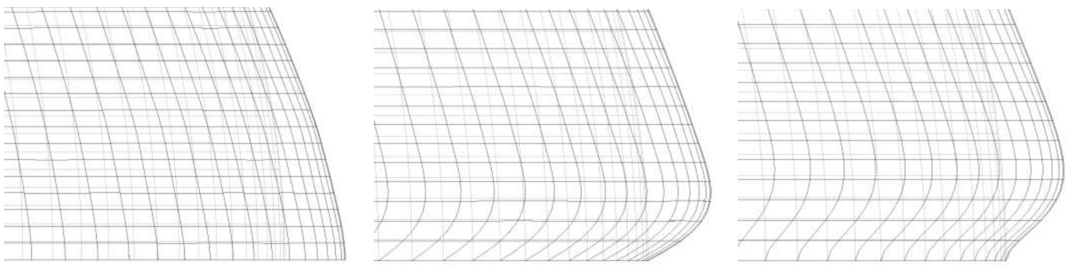

Figure 12.25. Displacement of a inclined-roller, hinged and clamped supported shell subjected to vertical load

A quantitative representation of the deformations and rotations of the top and base radius of the shell under vertical load is seen in Table 12.13. The displacements presented are the polar displacements while the rotations are examined in perpendicular direction of a node. The finite element results are compared with the values of as obtained in Chapter 10 using the classical shell theory. From Table 12.13 and Table 12.9 it can be concluded that the displacements (and the rotations) of the three-dimensional shell and the axisymmetrical shell are very much similar to each other. The top deformations of the three-dimensional model are somewhat lower whereas the base ring displacements are a little bit larger. These variations are not strange as small variations previously raised in the stresses and strains.

Name	Displacements (mm)				Rotations (mm/mm)			
	Top		Base		Top		Base	
	3D FEA	Theory	3D FEA	Theory	3D FEA	Theory	3D FEA	Theory
Zeiss 1	-0.305	-0.365	0.184	0.183	0	0	-0.352E-4	-2.92 E-5
Zeiss 2	-0.305	-0.365	0.172	0.176	0	0	0	0
Zeiss 3	-0.3	-0.365	0	0	0	0	0.00024	0.00025
Zeiss 4	-0.296	-0.365	0	0	0	0	0	0

Table 12.13. Displacements and rotations for vertical loaded shells

With respect to the top deformations, once more the conclusion can be drawn that the shell acts stiffer than predicted by the theoretical relation. Therefore, based on the finite element results, it is suggested to replace the factor of *2* in the energy based equation (10.16) by a factor of *1.7*. This factor also finds reasonable accordance with other programs; using ESA PT a value of *1.73* was found. Thus, equation (10.16) changes to:

$$u_z(\phi_o) = 1.7\,\frac{pa^2}{Et} \tag{12.1}$$

The factor also gives proper (safe-side) approximations in case of a varying *R/t ratio*.

In Figure 12.26 and 12.27 a qualitative representation of the deformations of the hemispherical shell under external spherical pressure load is shown. In Figure 12.26 the complete deformed shell is seen inside the original geometry. It is observed that the shell experiences local variations within the global radial compaction, i.e. the maximum displacement is *0.094 mm* and the minimum displacement is equal to *0.088 mm*. Therefore, the top and base displacements are quite different from the axisymmetric model, see Table 12.10 and 12.14. The average displacement is *0.091 mm* which is equal to the one previously found in the axisymmetric analysis. The variations in the nodal displacements are caused by the non-sphericalness of the three-dimensional shell surface. Hence, although not seen in Figure 12.24, the variations are present there as well. Furthermore, the numerical imperfectness causes rotations at the base radius of the shell which are in disagreement with the theory.

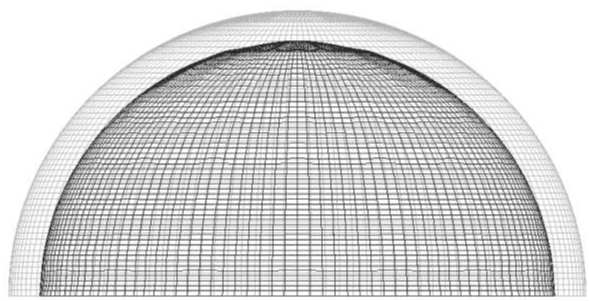

Figure 12.26. Displacement of a roller supported shell subjected to spherical load

In Figure 12.27, the inclined-roller, hinged and clamped supported shells are seen, zoomed in upon the boundary layer of the shell. The different boundary restraints are evident.

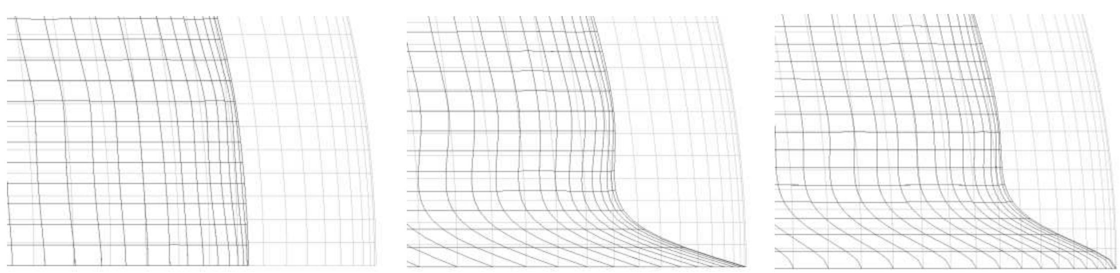

Figure 12.27. Displacement of a inclined-roller, hinged and clamped supported shell subjected to spherical load

A quantitative presentation of the deformed shell under spherical load is seen in Table 12.14. The displacements presented are the polar displacements while the rotations are the resulting values of the rotations in *x*-, *y*- and *z-direction*. It can be concluded from Table 12.14 and Table 12.10 that, due to the numerical imperfectness, the displacements of the three-dimensional shell model subjected to spherical load leads to different results than for the axisymmetric model.

Name	Displacements (mm)		Rotations (mm/mm)	
	Top	Base	Top	Base
Zeiss 1	-0.0879	-0.0895	0	-0.262 E-5
Zeiss 2	-0.0879	-0.0906	0	0
Zeiss 3	-0.0903	0	0	-0.138 E-3
Zeiss 4	-0.0927	0	0	0

Table 12.14. Displacements and rotations of the FEA for shell under spherical load

12.4 Geometrical Influences

The influence of geometrical parameters on the structural behaviour as described above must be investigated. As the hemisphere is the basic shape of this chapter, the thickness of the shell is the only parameter to investigate. The possibility of a varying shell thickness over the surface is not considered, although an increased thickness near the support is beneficial counteracting edge disturbances (Chapter 3).

In particular in case of thin shells, the linear static behaviour might be very sensitive to changes in the shell thickness. There is referred to this so-called 'highly sensitive' behaviour if a change in shell thickness causes a significant change in spatial distribution of displacement and stress response. The problem of highly sensitive behaviour is described in the paper of Bathe, Chapelle and Lee [4] which is based on the analytical studies on the asymptotic behaviour of sensitive shells with small thickness as presented by Pitkäranta and Sanchez-Palencia (1997). In general, shells can be identified into one of the categories of membrane-dominated, bending-dominated and mixed shells (Chapter 3) and their asymptotic behaviour (the *R/t ratio* reaching infinity) distinctly shows in which category the shell falls. The high sensitivity for changes in thickness, however, is characterised by the fact that the ratio of the bending energy to the total strain energy does not converge to a specific behaviour as the shell thickness decreases, but show an irregular pattern of oscillating energies. In other words, within the scheme of linear static analysis several structural responses appear for different shell thicknesses with no indication to which structural behaviour prevails.

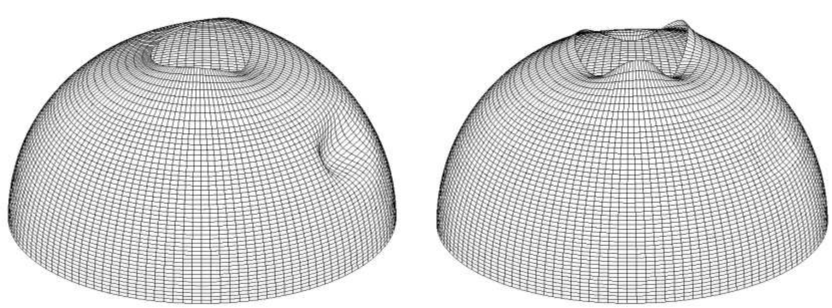

Figure 12.28. Deformed shapes as the shell thickness decreases from R/t = 100 to R/t = 1000

As an example, Bathe, Chapelle and Lee investigated the behaviour of a clamped hemispherical cap with a sliced off top under a distributed pressure load over a small part of the shell surface. For their research they used the finite element program ADINA; however, the same results are obtained in this thesis with a DIANA linear analysis. The results are seen in Figure 12.28. In the Figure the deformed shapes of two shells are illustrated for *R/t ratios* equal to 100 and 1000. The local distributed load on both shells is placed approximately halfway the shell surface (clearly seen in the left Figure, though also present in the right).

Regardless of the asymptotic behaviour; the phenomenon of high sensitivity is already observed for thicknesses reachable for thin concrete shells. Physically, the shell considered is an overly sensitive structure in the sense that the spatial distribution of displacement and stress response changes significantly with changes in the shell thickness. For higher *R/t ratios* the tendency seen in Figure 12.28 continuous, with the number of circumferential displacement waves increased each time the ratio *R/t* is multiplied with a factor of 10. However, such high ratios loose their practicability for thin concrete shells.

The question is whether the same sensitivity is seen in the Zeiss hemisphere. Therefore the analysis is done with several shell thicknesses with the *R/t ratios* varying from *200* up to *1000*. From the analysis it can be concluded that, qualitatively, the shells behaves similar. I.e. there is no change in spatial distribution of displacement and the stress distribution is equal. However, it is observed that for thinner shells, the meridional stress distribution changes slightly as it shows an increasing local peak in the region meshed by triangular elements. The peaks are the result of the failed element mapping caused by the modelling drawback of DIANA. Obviously, the thinner shell is more vulnerable to stiffness variations as the deformation is larger in compare to a thicker shell. From a quantitative examination of the results, the conclusion can be drawn that in thinner shells, the bending moments are smaller (as expected) whereas the stress variation between the integration points in thickness direction becomes larger. The stress variation becomes larger as the disturbances caused by the modelling drawback have less influence on thicker shells. The influence length of the bending moment is also smaller for thinner shells, which is in agreement with equation (10.32) and (10.33), and the statement that the preference for membrane behaviour arises by being thin (Chapter 3). In general, it can be concluded from the finite element results that the complete hemisphere is relatively insensitive to thickness variations.

12.5 Material Influences

The investigation to material influences on the stresses, strains and displacements is limited in linear elastic analysis. As the material in linear elastic analyses is modelled by the Young's modulus and the Poisson's ratio only, these are the only parameters to vary. E.g. when the shell is fabricated using the high strength mixture as proposed in Chapter 8.6.2, with a Young's modulus of *60 GPa* (twice as stiff), the stresses do not change, but the strains and displacements lower by a factor of two. Thus, in a linear elastic analysis a stiffer material is beneficial to control the displacement of the shell. This advantageous effect is slightly distressed by the increase in specific weight. The influence of a non-trivial Poisson's ratio (ν) can easily be explained with the constitutive law as determined in Chapter 5. The stresses do not change whereas the strains and displacements change by a factor related to the Poisson's ratio. For all concrete mixtures it is assumed that the actual Poisson's ratio is equal to *0.2* (Chapter 8). Thus, the new spherical displacements can be found by multiplication with a factor of *0.8* (= 1 – ν). For a vertical loaded shell it is observed that both the top displacement as the base displacement increase (in the initial direction).

12.6 Load Influences

In the analysis as presented above, the shell is loaded with a trivial uniform vertical or spherical load. Basically, the load represents the snow load summed up with the dead weight of the shell. Here, the influence of a non-axisymmetrical wind loading on the shell structural behaviour is considered. Aforementioned in Chapter 9, due to non-axisymmetrical loading the meridional curves and parallel circles do no longer present the principal directions of the internal stresses as there is a nonzero membrane shear force field, as well as normal membrane forces. Thus, the so-called stress trajectories transform under the influence of wind load. The load intensities as determined in Chapter 9 will serve as input for the analysis.

The shell is loaded by (non-axisymmetric) wind suction (*1.2 kN/m²*) and wind pressure (*0.8 kN/m²*) load, distributed according to Figure 9.4 and 9.5. Additionally, the dead weight of the shell is presented by a uniformly distributed vertical load (*1.5 kN/m²*). For reasons of simplicity, the wind load is modelled with an abrupt transition between wind suction and wind pressure. Moreover, the circumferential reduction in wind suction at the leeward side (Figure 9.5) is neglected.

The deformations of a shell subjected to dead weight only and a shell subjected to dead weight and additional wind load are illustrated in Figure 12.29. Obviously, in reality the wind load is more fluently distributed and the deformed shape is smoother. Although the shells deform significantly different, the maximum deformations are almost similar, i.e. the shell loaded by dead weight deforms *0.212 mm* at the top while the wind loaded shell deforms *0.202 mm* in the boundary layer. Hence, the effect of wind load on the maximum displacement is negligible.

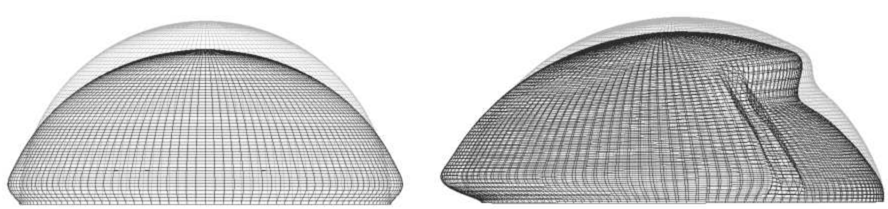

Figure 12.29. Deformation of shell loaded by dead weight (left) and a shell loaded by wind and dead weight

The stress distribution of wind load only and a combination of wind load and dead weight is shown in Figure 12.30. In Figure 12.30 the meridional stresses are indicated by the thick lines and the circumferential stresses by the thin lines. Both graphs show the stress distribution over the middle shell cross-section, parallel with the main wind direction. In the left figure it is clearly seen that the abrupt transition between wind pressure and wind suction causes large stress 'jumps', located nearby point *30 m* in the graph. The same discontinuities can be seen in the moment distribution graphs, Figure 12.31. Hence, the moments nearby *30 m* do not appear in reality.

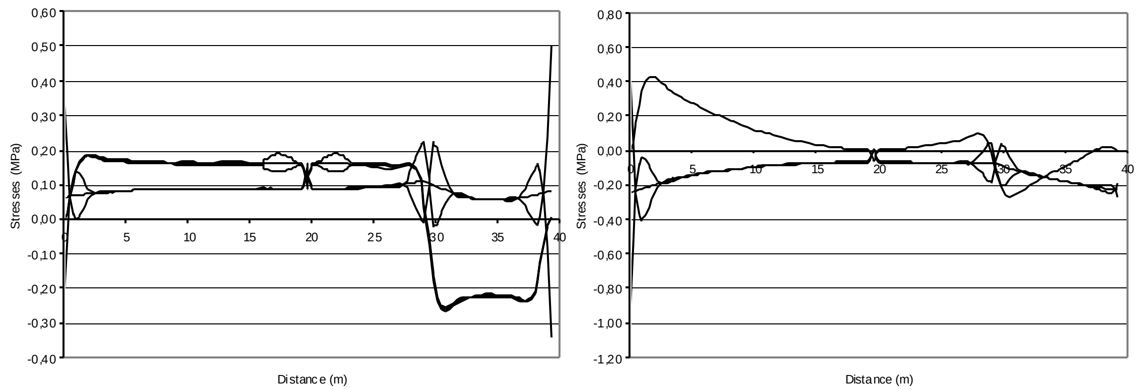

Figure 12.30. 'Wind parallel' stress distribution of a shell loaded by wind load only (left) and a shell loaded by dead weight and wind load (right)

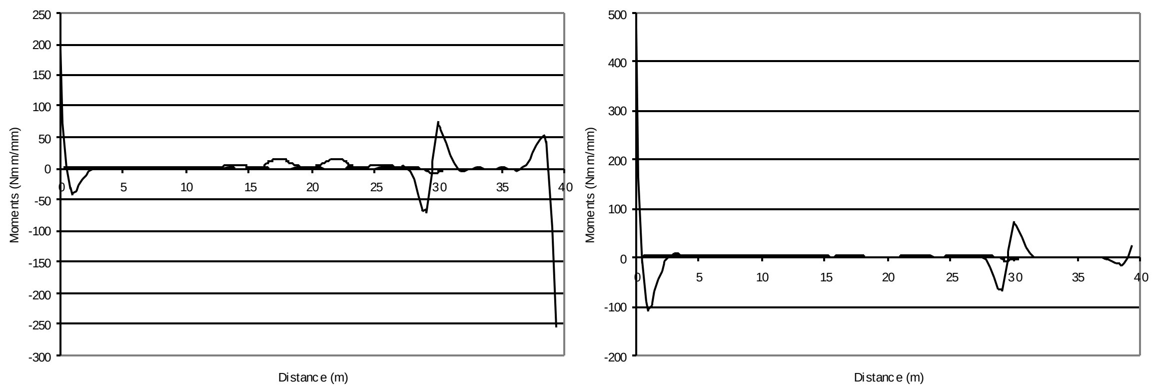

Figure 12.31. 'Wind parallel' moment distribution of a shell loaded by wind load only (left) and a shell loaded by dead weight and wind load

The stress distribution in the other direction, perpendicular to the wind direction, differs at each location in the shell. In Figure 12.32 the meridional and circumferential stresses are plotted together with the shear stresses that appear halfway of the shell. It can be seen that, at the middle section of the hemisphere, the wind load is transferred to the supports partly by meridional stresses and partly by shear.

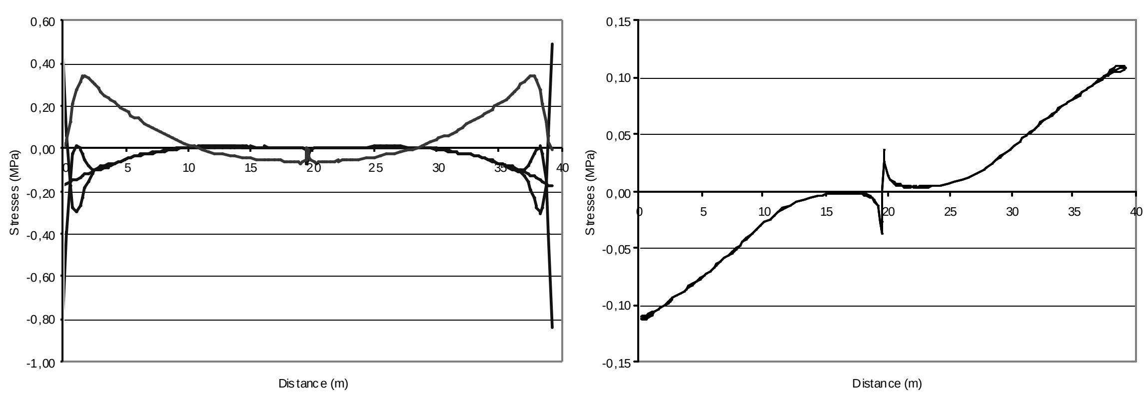

Figure 12.32. 'Wind perpendicular' stress distribution of a shell loaded by dead weight and wind load

From Figure 12.30, 12.31 and 12.32 it can be concluded that wind load significantly changes the stress and bending moment distribution over the shell. The circumferential tensile stresses, which e.g. appear in the vertical loaded shell of Figure 12.22, are compensated for at the leeward side. At the windward side, the meridional bending moment caused by the clamped support is completely compensated by the bending moments caused by the wind. Moreover, shear stresses appear which change the direction of the stress trajectories.

When the shell subjected to wind load and dead weight is compared to the shell previously examined in Section 12.3.3 (dead weight and snow load) it can be concluded that the stresses and bending moments caused by wind load do not prevail. At the leeward boundary the bending moments may be significantly higher; however, the modelling of the wind suction in that particular location is highly unrealistic, i.e. in reality the wind suction vanishes at the support, see Figure 9.3 and 9.5.

12.7 Conclusions

The linear elastic finite element analysis is performed using an axisymmetric and a three-dimensional shell model. Both models suffer numerical imperfections. In the axisymmetric line model, the spherical load could not be modelled directly, and, therefore, consists of segmented line load which introduces uninvited stress discrepancies and bending moments. The numerical imperfections in the three-dimensional model are caused by a failed mapping operation of the element base shape onto a sphere, i.e. the elements lay over a ribbed skeleton like an unstressed fabric introducing curvature variations. These curvature variations cause stress discrepancies and bending moments. However, although both models are not perfect, the general results show reasonable stress and strain distributions, bending moment localisations and displacements.

The membrane supported hemisphere subjected to spherical load is in evenly distributed compression while the membrane supported hemisphere loaded by a uniform vertical load demonstrates compression at the top and compression-tension at the bottom, analogue to the classical shell theory. When the shell support is not membrane compatible anymore, edge disturbances arise and local bending moments are introduced in the boundary layer. A clamped support is most onerous, because it introduces the largest bending moments into the shell. The shell structural behaviour is not sensitive to variations in thickness or material, i.e. the response is no other than expected. However, this is only inspected for *R/t ratios* of *200* up to *1000*. In case of a non-symmetrical wind load the axisymmetric shell model is not applicable anymore as it is unable to deal with variations in circumferential direction. From the three-dimensional finite element analysis it is observed that wind load changes the stress and bending moment distribution significantly and the meridional and circumferential directions do no longer present the principal directions of the internal stresses. Although the deformed shape is completely different, the maximum deformation caused by wind and dead weight is approximately similar to the deformation caused by dead weight only. Moreover, for the selected shell parameters, the combination of wind load and dead weight does not prevail over the combination of snow load and dead weight.

With respect to the solution accuracy, it can be concluded that the displacements, stress and strain results are almost similar to the results of Chapter 10 determined with the classical shell theory, i.e. within *3%*. For the bending moments the results are less convincing as they are significantly lower caused by the low order stress mapping between the 'exact' integration points and the element nodes. In particular the axisymmetric model is insufficient with discrepancies reaching *30%*. Hence, it can be concluded that, although the axisymmetric shell model provides in a (more) effective analysis, it is less accurate and reliable than the three-dimensional model.

13 Stability FEA

The topic of this chapter is the investigation to the linear elastic stability behaviour of a hemispherical shell. The theory of the stability behaviour of shells is discussed in Chapter 6. Here, the research is restricted to small deformations (linear) and elastic material behaviour. For these circumstances the validity of the stability relations and hypotheses of Chapter 6 are investigated.

Aforementioned in Chapter 6, in the stability behaviour of shells distinction can be made between prebuckling and postbuckling behaviour. The path up to the critical buckling point is named the prebuckling path. This path and corresponding buckling point can be determined by a linear (Euler) buckling analysis. In this type of analysis a bifurcation point is assumed and, as pointed out in Chapter 11, the finite element program solves the problem by a so-called eigenvalue analysis using an iterative solution scheme. The eigenvalues represent the critical buckling loads and the corresponding eigenfunctions determine the buckling modes.

After the bifurcation point the nonlinear postbuckling path of equilibrium initiates. For synclastic shells loaded perpendicular to their plane, the postbuckling path shows a dramatic fall in load bearing capacity. The fall-back is caused by postbuckling interaction of buckling modes, which where orthogonal within the linear scheme. Koiter found that the slope and curvature of the postbuckling path in the vicinity of the bifurcation point can be approximated closely by a linearised interaction of these buckling modes. In DIANA, the linear interaction of buckling modes is simulated by carrying out a so-called perturbation analysis. The corresponding postbuckling path of equilibrium can be found performing a continuation analysis. Hence, the successive execution of a perturbation and continuation analysis is the finite element presentation of the Koiter initial postbuckling theory.

In the following a full linear elastic stability analysis, i.e. a linear buckling analysis and a perturbation and continuation analysis, is reported. Similar to the previous chapter, the analyses concern as well the axisymmetric model as the three-dimensional model. In addition to Chapter 10, not only uniform pressure load is considered, but also the behaviour under uniform vertical load is investigated, as it shows much more resemblance with the type of load to which thin concrete shells are subjected in practice.

13.1 Shell Parameters

13.1.1 Geometry

See Chapter 12.1.1.

13.1.2 Material

See Chapter 12.1.2.

13.1.3 Boundary Conditions

See Chapter 12.1.3

13.1.4 Loading

The shell is loaded by uniform pressure or vertical load. Snow and wind load are not considered.

13.1.5 Analysis Scheme

The linear buckling calculations are presented in the analysis scheme of Table 13.1.

Name	Loading Conditions	Supporting Conditions	Type of Analysis	Model
Zeiss 1	Spherical and Vertical	Roller	Linear Stability	Axisymmetric + 3D
Zeiss 2	Spherical and Vertical	Inclined-roller	Linear Stability	Axisymmetric + 3D
Zeiss 3	Spherical and Vertical	Hinged	Linear Stability	Axisymmetric + 3D
Zeiss 4	Spherical and Vertical	Clamped	Linear Stability	Axisymmetric + 3D
Zeiss 5	Partially loaded	Clamped	Linear Stability	3D

Table13.1. Analysis scheme

13.2 Linear Buckling Analysis

The shell is modelled by axisymmetric shell elements (discussed first) and two-dimensional curved shell elements similar to the finite element models described in Chapter 12.

13.2.1 Axisymmetric Shell Model

The axisymmetrical shell model provides in a simple and fast model for buckling analysis. The spherical pressure load is analysed first. Then, the influence of a uniform vertical load is investigated. For each load the influence of several supporting conditions is considered.

Zeiss 1

The shell roller supported Zeiss 1 shell subjected to spherical load is in pure membrane action, i.e. the shell is free to move without any boundary restraint (Chapter 12). For spherical load, the buckling modes from the finite element analysis are seen in Figure 13.1. The corresponding critical loads are presented in Table 13.2.

Figure 13.1. Buckling modes 1, 2 and 3 for a roller supported axisymmetrical shell subjected to spherical load

In Figure 13.1 it can be seen that mode 1, 2 and 3 are quite different. First the shell buckles at the base radius with a corresponding buckling load which is extremely low, for sure when compared to adjacent modes (*50%* less than mode 2) or to the theoretical buckling load as derived by Zoëlly, see Table 13.2.The buckling mode seems to stands alone, which gives rise to the thought that the mode may be a premature buckling mode caused by numerical disturbances. On the other hand, the shell is considerably 'weaker' near the support as it is free to rotate. Confirmation for these thoughts will be searched later in the three-dimensional buckling analysis. From mode 2, the consecutive modes alternately show top buckling (even modes) or a global wave pattern extending over the complete shell surface (odd modes). The top buckling modes must be addressed as premature buckling modes as, according to Kollar and Dulacska [54], the shell will always buckle in small local waves distributed evenly over the shell surface. The tendency to buckle at the top stems from the basic characteristic of the model, namely, axisymmetry. The axis of axisymmetry is vertical, which means that buckling at the top corresponds to a local buckle whereas buckling in the shell surface is represented by a global buckling pattern extending in circumferential direction. The appearance of the global buckling modes can, therefore, be ascribed to the interaction of the top buckling mode with the edge mode 1.

Buckling mode	Critical buckling load (MPa)
1	0.3969
2	0.7938
3	0.8001
4	0.8106
5	0.8274
10	0.9702
Zoëlly	0.7981

Table 13.2. Linear critical buckling load for a roller axisymmetrical shell subjected to spherical load

In Table 13.2, the critical buckling loads are presented. With the exception of mode 1, it can be seen that the critical buckling loads of the axisymmetrical shell model are very close to each other (each mode differs less than *2%* and all modes between 2 and 10 are within *20%*). Aforementioned in Chapter 6, this indicates the sensitivity of the shell to multimode or compound buckling, a characteristic feature of shells where several buckling modes are associated with the same critical load. Despite the premature top buckling modes, the critical loads find good correlation (within *1%*) with the theoretical linear buckling load for a complete sphere as derived by Zoëlly (equation 6.53).

Figure 13.2. Buckling modes 1, 4 and 7 for a roller supported axisymmetrical shell subjected to vertical load

The next step is to investigate the influence of a uniformly distributed vertical load on the shell stability behaviour. The results of the finite element analysis are seen in Figure 13.2. From Figure 13.2 it immediately can be concluded that, except for mode 1, the buckling pattern is significantly different in compared to buckling caused by spherical load. Under the influence of vertical load, the buckling first stays within the boundary layer. Later, the buckling pattern extends towards the total shell. Similar to the spherical case, the critical load of mode 1 is less than *50%* of its successors. The lower based buckling is contributed to the fact that the vertical load, opposite to a spherical load, does not contain a 'supporting' transverse component in that boundary layer.

A quantitative description of the buckling behaviour is represented in Table 13.3. It can be seen that the vertical critical buckling loads approach to the spherical critical load for higher buckling modes (from *60%* at mode 2 to *20%* at mode 10). Furthermore, it can be seen that adjacent critical loads lie further away from each other (up to more than *10%*). With respect to the compound buckling, differences up to *2%* are to be expected, Hoogenboom [50], which means that the phenomenon is disqualified here.

Buckling mode	Critical buckling load (MPa)
1	0.2035
2	0.5061
3	0.5418
4	0.6048
7	0.7098
10	0.7875
Zoëlly	0.7981

Table 13.3. Linear critical buckling load for a roller axisymmetrical shell subjected to vertical load

The observation that the critical loads approach the spherical critical load when the buckling modes approach towards a global wave pattern stresses that the statement of Simitses and Cole (1968), i.e. that the type of load, radial pressure or gravity, does not appear to change the critical load drastically, is valid if and only if global buckling takes place (thus, also in the compression zone).

Zeiss 2

The 'membrane' supported inclined-roller Zeiss 2 shell model subjected to spherical load experiences only radial displacements up to buckling instability and no bending moments. Therefore, the hemispherical Zeiss 2 shell behaves as if it is a complete sphere. The results of the buckling analysis are presented in Figure 13.3 and Table 13.4.

Figure 13.3. Buckling modes 1, 5 and 10 of an inclined-roller supported axisymmetrical shell subjected to spherical load

In Figure 13.3 the buckling modes 1, 5 and 10 are shown. The first mode of the roller supported Zeiss 1 shell has disappeared as the inclined-roller support gives sufficient resistance against rotation. Moreover, the rotational disallowing releases the shell from successive appearance of local top and global modes. The buckling modes of Figure 13.3 have a global character as the wave pattern extends over the total shell, however with maximum buckling amplitude at the top due to the axisymmetry of the model. The given modes appear to be more or less similar, with only small differences in the number of half-waves (14, 12 and 20, respectively). The other computed (unplotted) buckling modes show the same tendency, i.e. the maximum buckling amplitude is unconditionally found at the top node.

Buckling mode	Critical buckling load (MPa)
1	0.7917
2	0.7959
3	0.8043
4	0.8169
5	0.8421
10	1.0017
Zoëlly	0.7981

Table 13.4. Linear critical buckling load for an inclined-roller axisymmetrical shell subjected to spherical load

It can be concluded from Table 13.4 that the critical buckling loads of the inclined-roller shell are very close to each other (compound buckling) and find good correlation (within *1%*) with the theoretical linear buckling load as derived by Zoëlly. Hence, this is encouraging as Zoëlly derived his buckling equation for a complete sphere and he already predicted the occurrence of compound buckling.

The influence of a uniform vertical load on the stability behaviour of an inclined-roller supported shell is visualised in Figure 13.4 and Table 13.5. Similar to the Zeiss 1 shell, the buckling starts at the base while it extends more and more towards the complete shell in following modes. The mode 1 which caused an extremely low buckling load is vanished, however, this time lower based buckling is intensified by the so-called edge disturbance; i.e. for a vertical load the supporting conditions are not membrane compatible anymore and bending moments undoubtedly will arise.

Figure 13.4. Buckling modes 1, 3, 6 for an inclined-roller supported axisymmetrical shell subjected to vertical load

The critical buckling loads are represented in Table 13.5. When the values of Table 13.5 are compared with the surface bucking values in Table 13.3 (neglecting mode 1), it can be concluded that the bending moments caused by the boundary conditions intensify the buckling as the critical loads are somewhat lower.

Buckling mode	Critical buckling load (MPa)
1	0.4515
2	0.5229
3	0.5754
6	0.6972
10	0.8043
Zoëlly	0.7981

Table 13.5. Linear critical buckling load for an inclined-roller supported axisymmetrical shell under vertical load

Iit can be concluded from Table 13.5 that the phenomenon of compound buckling is disqualified as adjacent critical loads vary up to *13%*. Furthermore, similar to Zeiss 1, the statement of Simitses and Cole is valid if and only if global buckling occurs.

Zeiss 3

The Zeiss 3 shell is hinged supported. The results of the finite element analysis for a hinged supported shell subjected to spherical load are illustrated in Figure 13.5. It can be observed that a hinged supported shell buckles similar to the roller Zeiss 1 shell. The lowest critical buckling load produces a local buckle in the boundary layer (though, in opposite direction to Zeiss 1 due to the 'hinged' edge disturbance) whereas adjacent buckling modes buckle locally at the top or show a global wave pattern.

Figure 13.5. Buckling modes 1, 2 and 3 for a hinged supported axisymmetrical shell subjected to spherical load

The repetitive sequence of local top buckling and global buckling in mode 2 to 10 is caused by a similar interaction or not of adjacent buckling modes as seen in Figure 13.1. Thus, the bending moments caused by the restrained support interact or not with the top buckling mode.

Buckling mode	Critical buckling load (MPa)
1	0.6405
2	0.7938
3	0.8001
10	0.9576
Zoëlly	0.7981

Table 13.6. Linear critical buckling load for a hinged supported axisymmetrical shell under spherical load

The critical loads corresponding to the buckling modes are seen in Table 13.6. Due to the hinge support the shell buckles already at a value which is approximately *80%* of the theoretical critical load for radially pressed spheres. Furthermore, a remarkable difference of approximately *20%* between the first and second critical load is seen, whereas the critical loads from mode 2 to 10 are within *12%*. This may be caused by the fact that the buckling solution is disturbed by the non-vanishing bending moments in the linear solution (see Chapter 12.2.3).

Figure 13.6. Buckling modes 1, 3 and 6 for a hinged supported axisymmetrical shell subjected to vertical load

The Zeiss 3 shell with vertical load behaves similar to the vertical loaded Zeiss 2 shell. The first buckling mode is locally, confined to the boundary layer of the shell, whereas following modes increasingly stretch towards the total shell, illustrated in Figure 13.6. The buckling modes are quantitative represented in Table 13.7. It can be concluded that the buckling load decreases to *44%* of the theoretical buckling load for radially pressed spheres (the hinge supports cause a fall back in critical load of *13%* in compare to the inclined-roller support). Moreover, there is a great discrepancy between the first and second critical load (almost 32%), whereas the other values differ more or less *7%*. Again, this can be attributed to the nonzero bending moments that appeared in the linear solution (Chapter 12.2.3).

Buckling mode	Critical buckling load (MPa)
1	0.3507
2	0.5103
3	0.5481
6	0.6825
10	0.7896
Zoëlly	0.7981

Table 13.7. Linear critical buckling load for a hinged supported axisymmetrical shell under vertical load

From the hinged supported shell it can, once more, be concluded that prebuckling rotations caused by edge disturbance bending moments amplify the buckling deformations or even may become dominant in buckling failure (e.g. Zeiss 3 spherical mode 1 in compare to Zeiss 2 spherical mode 1).

Zeiss 4

The Zeiss 4 axisymmetric shell model is clamped supported. The finite element results are plotted in Figure 13.7. In Figure 13.7 it can be seen that the restrained rotation stimulates top node buckling. Hence, the corresponding critical load, seen in Table 13.8, is almost equal to the critical load for a radially pressed sphere.

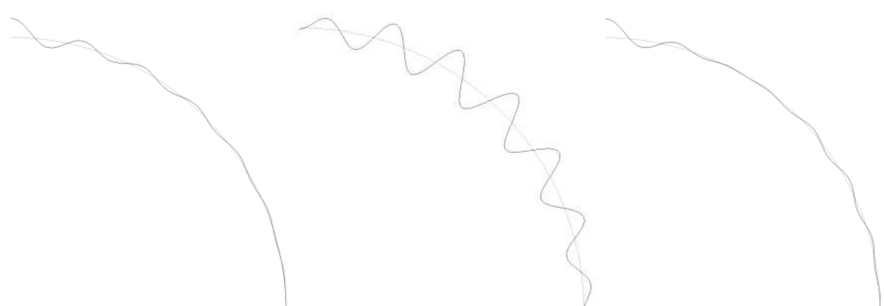

Figure 13.7. Buckling modes 1, 2 and 3 for a clamped supported axisymmetrical shell subjected to spherical load

The repetitive sequence of global and local top buckling indicates whether the critical load is spherical or based on the interaction of the spherical load with the bending moments that arise from the restraint deformation at the support. Table 13.8 shows adjacent critical loads within *2%* demonstrating the sensitivity to compound buckling.

Buckling mode	Critical buckling load (MPa)
1	0.7938
2	0.7980
3	0.8106
4	0.8211
5	0.8421
10	0.9870
Zoëlly	0.7981

Table 13.8. Linear critical buckling load for a clamped supported axisymmetrical shell under spherical load

The buckling modes of the vertically loaded clamped shell, shown in Figure 13.8, show the same tendency as seen in all previous (vertical) cases. That is, a local first buckling mode confined to the boundary layer of the shell which 'mode by mode' extends towards the complete shell. The corresponding critical buckling loads are tabulated in Table 13.9.

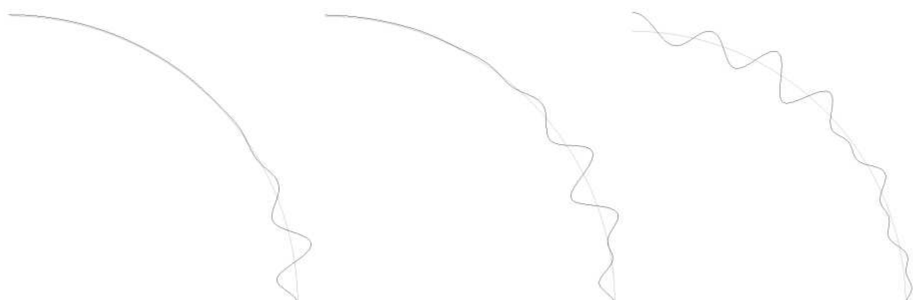

Figure 13.8. Buckling modes 1, 5 and 10 for a clamped supported axisymmetrical shell subjected to vertical load

When the values of Table 13.9 are compared to the previous cases in which vertical load is prescribed, it is observed that the clamped supported shell shows the highest critical loads. The lowest critical load at which buckling occurs is approximately *60%* of the value found by Zoëlly, and is *8%* and *28%* higher than the inclined-roller and hinged supported shell, respectively.

Buckling mode	Critical buckling load (MPa)
1	0.4977
2	0.5229
3	0.5964
4	0.6174
7	0.7371
10	0.7938
Zoëlly	0.7981

Table 13.9. Linear critical buckling load for a clamped supported axisymmetrical shell under vertical load

In particular, the fact that the clamped supported shell shows higher resistance against buckling than the inclined-supported shell is noticeable as one may expect that a more severe restraint, which introduces the highest bending moments, would be most onerous. Evidently, the resulting bending moment as obtained in the linear solution has a positive stiffening effect on the boundary layer of the shell causing the shell to be less vulnerable to buckling. This effect is, however, restricted to the first critical buckling load as the mode 2 yields a similar buckling load as the Zeiss 2 shell under vertical load.

With respect to the effect of various supporting conditions, none of them produced a positive effect on the critical buckling load as suggested in Figure 6.28 and 6.29. Thus, it can be concluded that those observations are only valid for relative low values of λ which represents shallow shells showing local snap-through behaviour.

13.2.2 Three-Dimensional Shell Model

The major deficiency of the axisymmetric model is the fact that it is unable to produce terms, and buckling modes, which vary in circumferential direction. Therefore, the stability research is extended with a three-dimensional shell model. The analysis procedure for the three-dimensional shell is similar to the axisymmetric model. The shell is first subjected to spherical load and, subsequently, the behaviour of a shell under uniform vertical load is investigated. For each load condition, the influence of the four boundary conditions is discussed.

It is observed that all three-dimensional shell models experience compound buckling up to a high level. Therefore, it is needed to compare a large number of modes and to select the ones which give good insight in the buckling behaviour. There are in total 150 modes examined for each shell. With such a high number of modes it is necessary to check whether the relative error approximately stays the same in order to ensure the correctness of the found modes. From the results in can be concluded that the relative error stays more or less equal, which means that all modes are of comparable exactness.

Zeiss 1

The first 3D buckling analysis is the roller supported shell under spherical load. The results of the analysis are seen in Figure 13.9 and Table 13.10. It is observed that the shell first buckles in the boundary layer with an axisymmetric buckling pattern, similar to the axisymmetric shell. Contrary to the axisymmetric finite element model, a lot of associative (boundary layer) modes arise which demonstrate asymmetric buckling or buckles in a large number of local circumferential waves. From mode 50 the buckling is found at the top of the shell or the buckling modes extend over a large part of the shell middle surface. The first global mode, i.e. evenly distributed buckling over the total shell surface, is mode 110.

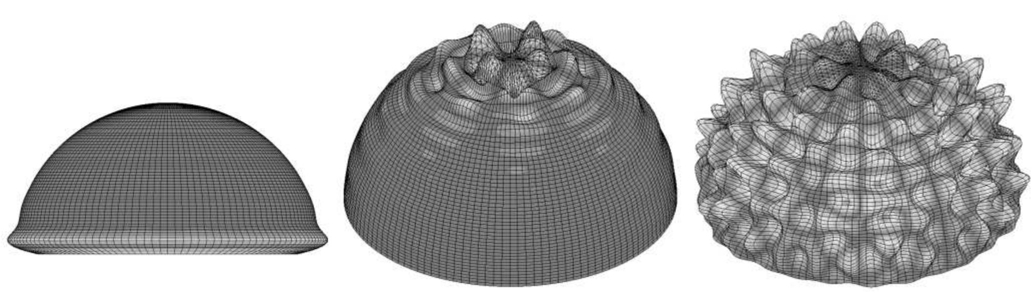

Figure 13.9. Buckling modes 1, 50 and 110 for a roller supported 3D shell subjected to spherical load

The associative critical buckling loads are presented in Table 13.10. Similar to the axisymmetric shell, mode 1 is approximately *50%* of the top buckling mode 50. Aforementioned, the shell experiences compound buckling as several buckling modes are associated with the same critical load. Furthermore, it can be seen that the global buckling mode 110 yields the same critical load as the equation found by Zoëlly for a radially pressed sphere. Combining Figure 13.9 and Table 13.10, the buckling process can be explained by the fact that the roller support is considerable 'weaker' than the shell itself. The shell is, thus, likely to buckle first in that particular area. At mode 50 the shell suddenly steps-over towards top buckling. However, the top buckling can be addressed as a premature buckling mode, similar to the top buckling that appeared in the axisymmetric model. Opposite to the axisymmetric model, not axisymmetry causes the top buckling, but the uninvited circumferential bending moments which were previously found in the linear solution of Chapter 12 (due to the numerical imperfectness of the model). The first global mode, mode 110, yields the same critical load as derived for the radially pressed sphere. In mode 110 the expected chessboard pattern is clearly seen (see Chapter 6). Hence, the shell can indeed be regarded as shallow in the region of a buckle, as previously assumed in the derivation of equation (6.53).

Buckling mode	Critical buckling load (MPa)
1	0.3969
50	0.7812
110	0.7980
Zoëlly	0.7981

Table 13.10. Linear critical buckling load for a roller 3D shell subjected to spherical load

When the three-dimensional buckling analysis results are compared to the axisymmetric buckling results it can be concluded that the three-dimensional modes gives lower values for similar buckling patterns. In fact, this phenomenon is also seen in all other analyses.

For the vertical load, the shell is membrane supported and no bending moments arise. From the buckling output file it is observed that, within the first *150* modes, the critical load does not exceed *0.6654 MPa*. This means that no global buckling patterns can be expected. The characteristic buckling modes of the analysis are seen in Figure 13.10.

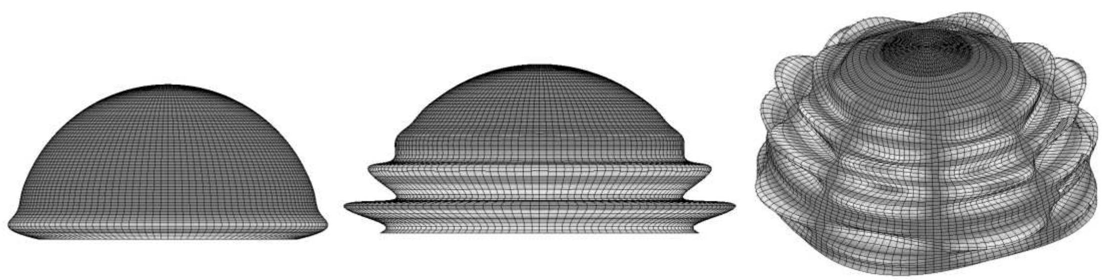

Figure 13.10. Buckling modes 1, 38 and 146 for a roller supported 3D shell subjected to vertical load

Similar to the spherical loaded Zeiss 1 shell, the first modes are restricted to the boundary layer. The buckling pattern of the vertical loaded shell stretches step-by-step towards the complete shell surface. It is observed that the buckling process evaluates each time with the same procedure, i.e. first an axisymmetrical mode occurs, followed by several asymmetrical modes with an increasing number of circumferential waves and slightly higher critical loads. The modes visualised in Figure 13.10 are mode 1, 38 and 146. Up to mode 37 the buckling is in the boundary layer. Mode 38 is the first mode in which the buckling is more stretched towards global shell buckling. Mode 146 is a mode in which the buckling pattern is maximal stretched within the 150 modes scheme. I.e. sometimes lower based modes with an extremely high number of circumferential waves interchange with modes which are stretched higher upon the shell surface.

The critical loads of Figure 13.10 are tabulated in Table 13.11. In the table it is seen that the critical loads approach the load of a radially pressed sphere more closely with higher modes. Hence, eventually, global buckling will occur similar to the spherical load confirming that the statement of Simitses and Cole (1968) is valid if and only if global buckling takes place. Furthermore, it is observed that asymmetrical modes are associated with almost the same critical load as the adjacent axisymmetrical modes (e.g. differences of *0.4%*). Thus, the statement of Van der Neut (1932), i.e. that the critical pressure corresponding to an asymmetric buckling pattern is similar to an axisymmetrical buckling pattern may assumed to be valid, however, 'within a few percent'.

Buckling mode	Critical buckling load (MPa)
1	0.2022
38	0.5028
146	0.6543
Zoëlly	0.7981

Table 13.11. Linear critical buckling load for a roller 3D shell subjected to vertical load

A remarkable observation made during the examination of the finite element results refers to the existence of negative eigenmodes which seem to arise only in case of vertical load. Negative buckling modes are numerically correct; however, physically they have no meaning for concrete shells. It simply means that the load is of opposite sign with respect to the input. These modes are, thus, numerical modes and as they are of no practical meaning they are neglected.

Comparing the results with the axisymmetric results it is seen that the first critical loads are nearly similar, however, successive critical loads are significantly lower in case of the three-dimensional shell. Encouraging is the fact that the buckling process of a step-by-step stretching towards global buckling is similar.

Zeiss 2

The inclined-roller supported shell under spherical load behaves as a complete sphere. The results of the analysis are seen in Figure 13.11. Similar to the Zeiss 1 shell (and the axisymmetric shell) premature buckling modes are observed before the expected global modes appear. Again, these modes are ascribed to the uninvited bending moments from the linear solution. It is observed that successive buckling patterns evolve rapidly towards global buckling. Within the first 12 modes, top buckling, middle shell surface buckling and global buckling takes place. Furthermore, all the global buckling modes show sign of a chessboard pattern of local buckling waves.

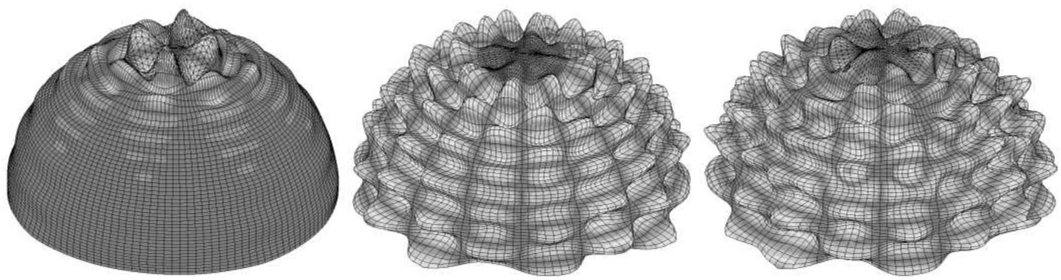

Figure 13.11. Buckling modes 1, 5 and 12 for an inclined-roller supported 3D shell subjected to spherical load

The corresponding critical loads in Table 13.12 show that all buckling values are very close (approximately *2%*) to the linear critical buckling load of a radially pressed sphere. This observation strengthens the conclusion that the finite element program delivers correct results. Furthermore, it can be concluded that the Zeiss 2 shell behaves much stiffer than the roller supported Zeiss 1 shell under spherical load, i.e. the first buckling mode is twice as high and correlates with mode 50 of the roller shell.

Buckling mode	Critical buckling load (MPa)
1	0.7811
5	0.7861
12	0.7884
Zoëlly	0.7981

Table 13.12. Linear critical buckling load for an inclined-roller 3D shell subjected to spherical load

The three-dimensional shell model shows faster global buckling with lower critical loads in compare to the axisymmetric model which seems entangled in its axisymmetry.

The vertical loaded inclined-roller shell is not membrane supported anymore and, thus, significant bending moments are present in the boundary layer. The results of the analysis are illustrated in Figure 13.12. The influence of bending moments is seen in the first buckling mode as the buckling amplitude is in opposite direction in compare to the Zeiss 1 shell. Furthermore, the bending moments cause the buckling pattern to be more stretched and it reaches global buckling faster. The procedure of reaching global buckling is analogue to the previous roller case, i.e. the buckling pattern slowly extends towards the total shell surface, hereby showing an increasing number of circumferential waves with nearly the same critical load before stepping through to a more global mode. Again, lower based modes with an extremely high number of circumferential waves interchange with modes which are stretched higher up on the shell surface.

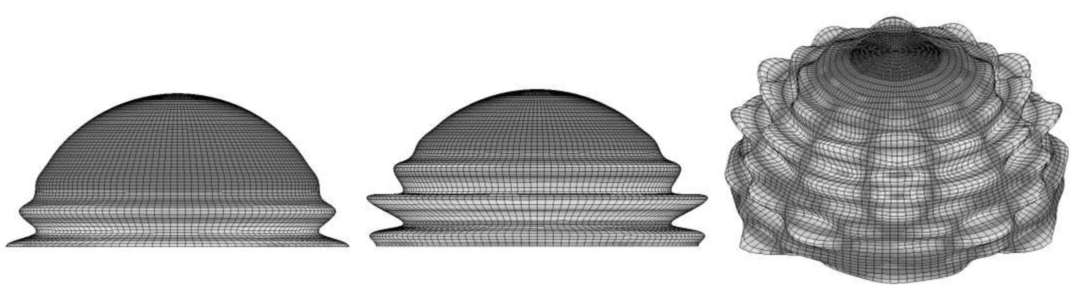

Figure 13.12. Buckling modes 1, 20 and 150 for an inclined-roller supported shell subjected to vertical load

The corresponding critical buckling loads are seen in Table 13.13. Again, it can be concluded that the shell is much stiffer that the roller supported shell as the critical load of mode *1* is approximately equal to the critical load of mode *35* of the roller shell. Clearly, from the critical load output it could already be seen that there would be no global mode as the previous analyses have shown that the critical load must be within 2% of the buckling load for a radially pressed sphere to demonstrate global buckling. The result is practically equal to the axisymmetric case.

Buckling mode	Critical buckling load (MPa)
1	0.4460
20	0.5204
150	0.7057
Zoëlly	0.7981

Table 13.13. Linear critical buckling load for an inclined-roller shell subjected to vertical load

Zeiss 3

The hinged supported Zeiss 3 shell subjected to spherical load experiences high bending moments in the boundary layer. The analysis results are shown in Figure 13.13. Parallel to the axisymmetric model, the initial three-dimensional buckling process is restricted to the boundary layer (up to mode 67). At mode 68 the buckling process suddenly moves to the top of the shell (the premature mode) followed by a series of asymmetric middle surface buckling modes. Before global buckling at mode 117, a irregular series of shell buckling patterns extending over large parts of the shell surface. The expected chessboard pattern of local buckling waves is clearly seen in the global mode.

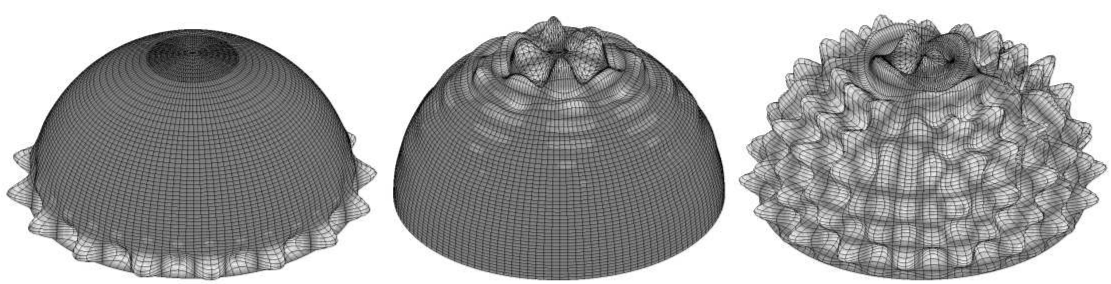

Figure 13.13. Buckling modes 1, 68 and 117 for a hinged supported shell subjected to spherical load

The critical loads are presented in Table 13.14. It can be seen that the hinged support condition provides in a stiffer support than the roller support, as one would expect from an engineering point of view. It can be seen that the shell experiences top buckling at approximately the same critical loads as previously found at Zeiss 1 and 2. Moreover, the critical load that corresponds to the global mode *117* is within *1%* of the theoretical solution for a radially pressed sphere.

Buckling mode	Critical buckling load (MPa)
1	0.5732
68	0.7812
117	0.7949
Zoëlly	0.7981

Table 13.14. Linear critical buckling load for a hinged shell subjected to spherical load

The hinged shell subjected to vertical load behaves similar to all previous vertically loaded shells. I.e. the buckling pattern initiates in the boundary layer and slowly extends towards a global buckling pattern. The results of the analysis are seen in Figure 13.14. Up to mode 31 the buckling remains in the boundary layer before its stretches further over the shell surface in mode 32. The closest mode to global buckling (within the research range) is mode 150 which is represented by four circumferential waves. The buckling modes are quite similar to the modes of the axisymmetric model.

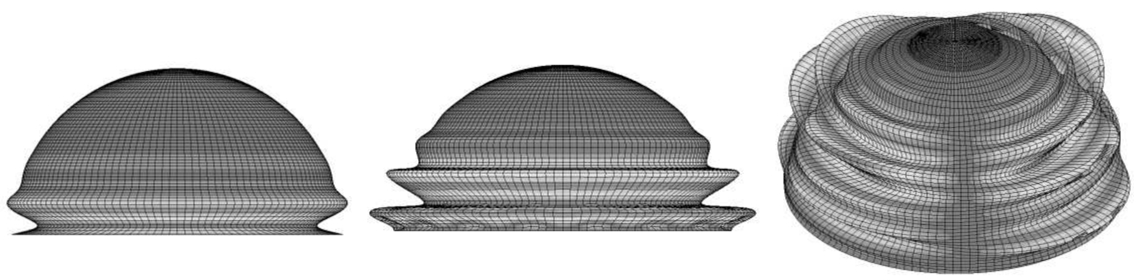

Figure 13.14. Buckling modes 1, 32 and 150 for a hinged supported shell subjected to vertical load

The corresponding buckling modes are tabulated in Table 13.15. Despite the fact that the modes look very much similar to the axisymmetric ones, the critical loads are significantly lower. In compare to the roller support, the hinged support is more severe and leads to higher critical loads.

Buckling mode	Critical buckling load (MPa)
1	0.3285
32	0.5031
150	0.6419
Zoëlly	0.7981

Table 13.15. Linear critical buckling load for a hinged shell subjected to vertical load

Zeiss 4

The result of the buckling analysis of a clamped supported Zeiss 4 shell subjected to spherical load is seen in Figure 13.15. It is observed that, opposite to the axisymmetric model, at first the bending moments caused by the clamped support cause the shell to buckle in the boundary layer. Most probably, this is caused by the much larger (but more correct) bending moments in the linear solution (Chapter 12). From mode *1*, the successive modes, however, extend more and more towards the total shell surface. At mode *39*, the shell jumps over towards premature top buckling. Adjacent modes of mode *39* buckle in the top region as well, however, after mode 46, the buckling moves away from the top. The first global modes appear at mode *41*; although large areas remain unaltered and no mode shows an equally distributed buckling pattern until mode *70*.

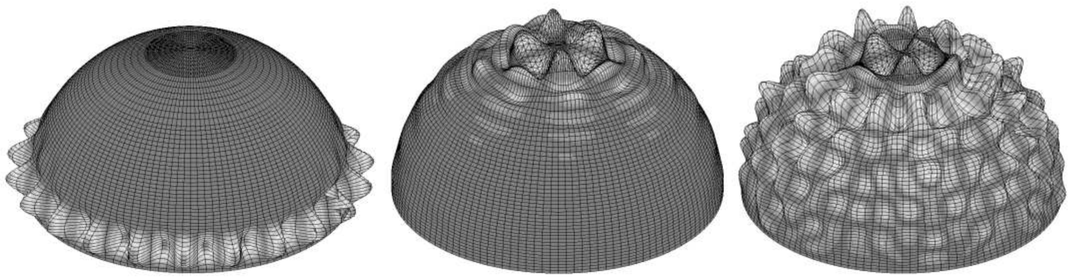

Figure 13.15. Buckling modes 1, 39 and 70 for a clamped supported shell subjected to spherical load

The corresponding critical buckling loads are seen in Table 13.16. It is seen that the clamped support yields a mode *1* critical load as close as *11%* to the critical load of a radially pressed sphere. Therefore, the clamped support is less favourable with respect to buckling than the inclined-roller support in which the shell immediately buckles inside the shell surface.

Buckling mode	Critical buckling load (MPa)
1	0.7067
39	0.7812
70	0.7926
Zoëlly	0.7981

Table 13.16. Linear critical buckling load for a clamped shell subjected to spherical load

The buckling process of a clamped shell under vertical load is visualised in Figure 13.16. Similar to all previous vertical loaded shells, the buckling initiates in the boundary layer and stretches more and more towards the total shell surface. The closest mode to global buckling is mode *148*. The chessboard pattern of local buckling waves is already visual.

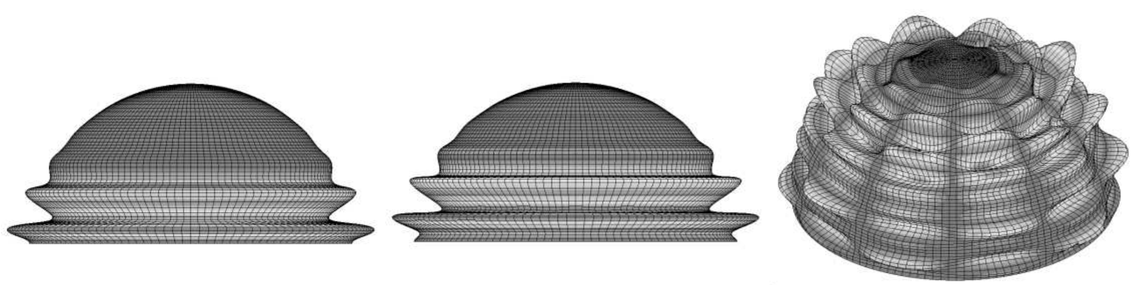

Figure 13.16. Buckling modes 1, 10 and 148 for a clamped supported shell subjected to vertical load

The critical buckling loads of the clamped shell under vertical load are seen in Table 13.17. It is seen that the critical load of mode *1* is the highest critical load in compare to all previous support conditions. The load is approximately *40%* of the critical load for radially pressed spheres. Thus, in case of a uniform vertical distributed load, the clamped support is most favourable with respect to buckling.

Buckling mode	Critical buckling load (MPa)
1	0.4874
10	0.5159
148	0.7224
Zoëlly	0.7981

Table 13.17. Linear critical buckling load for a clamped shell subjected to vertical load

Nota that, the buckling process shows large similarity with the axisymmetric buckling process.

Zeiss 5

The Zeiss 5 shell stand on its own and is introduced to validate the findings of Klöppel and Roos (1956) i.e. that the critical pressure load for a partially loaded sphere is close to that for a load over the total shell surface (Chapter 6). To investigate the validity with DIANA, an inclined-roller supported hemispherical cap is subjected to a uniform pressure load, restricted to the upper part of the shell and with a smooth transition between the loaded and unloaded part. The result of the analysis is seen in Figure 13.17.

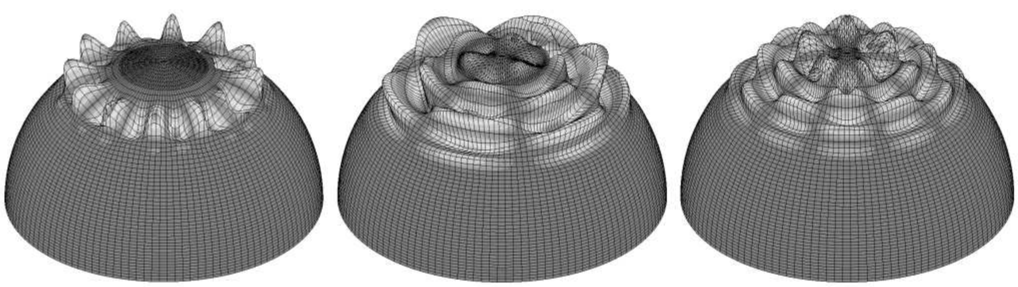

Figure 13.17. Buckling modes 1, 19 and 39 of a partially loaded sphere with inclined-roller supports

Form Figure 13.17 it can be concluded that the higher buckling modes (>*19*) show reasonable buckling patterns in which the shell buckles globally in the loaded area, with small buckling waves organised in a chessboard pattern. The critical loads of the buckling modes are presented in Table 13.18.

Buckling mode	Critical buckling load (MPa)
1	0.7126
19	0.7494
39	0.7782
Zoëlly	0.7981

Table 13.18. Critical buckling load for a partially loaded inclined-roller supported shell

In Table 13.18 it is seen that the first mode differs approximately *10%* with the buckling load for a radially pressed sphere. Higher modes show critical loads with increasing correspondence with the critical load for a radially pressed sphere, i.e. mode *19* differs *6%*, mode *39* differs *2.4%* and the difference of mode *48* is within *0.5%*. However, the corresponding modes are less convincing as the shell buckles away from the loaded region. Hence, from the observations done on the partially loaded Zeiss 5 shell, no conclusions on the validity of the theory of Klöppel and Roos can be drawn.

13.3 Geometrical Influences

Similar to Chapter 12, the influence of the thickness parameter is investigated. Previously, it was found that the linear behaviour was not sensitive to variations in shell thickness. With respect to buckling a series of shells is investigated with varying R/t ratios. The analyses are equally shifted to a percentage of the first buckling mode, counteracting the possible misleading influence of an accuracy interval.

Based on equation (6.53) it can be expected that a thinner shell will lead to a critical load which is lower by the difference in thickness squared. However, besides the logical difference in critical load, it is observed that thinner shells experience compound buckling up to a higher degree. In other words, there are more buckling modes found for thinner shells than for thicker shells when the load is equally increased. It can, for example, be seen when comparing the modes in which top buckling occurs for the first time for a shell with $R/t = 200$ and a shell with $R/t = 400$. For a roller, hinged and clamped support, the modes are *50-66*, *68-90*, *39-47*, for a $R/t = 200$ and a $R/t = 400$ shell respectively. For an inclined-roller supported shell top buckling occurs already at mode 1, however, for successive modes the same phenomenon is seen. Besides the difference in critical loads, the buckling modes of thicker shells are more distributed than the same modes for thinner shells and the number of hoop waves may be different as well.

The phenomenon described above is caused by the fact that thinner shells behave more like membranes than thicker shells. As a consequence of being thicker, bending effects have a larger influence length which means that the buckling pattern will be more stretched. Thus, more membrane dominant behaviour causes the shell to experience compound buckling up to a higher degree.

13.4 Material Influences

As is seen in Chapter 6, the modulus of elasticity appears as a constant in the buckling equation. Therefore, by changing the material, the critical buckling load changes linear with the change in Young's modulus. The critical load increases in correspondence with equation (6.53) while the relative discrepancy between the finite element result and the theory is similar. The influence of a non-trivial Poisson's ratio in the analysis is negligible.

13.5 Perturbation and Continuation Analysis

Aforementioned in the introduction, after the bifurcation point the nonlinear postbuckling path of equilibrium initiates and may demonstrate a dramatic fall-back in load carrying capacity. If the postbuckling behaviour needs to be investigated, the Euler stability analysis can be followed by a perturbation (or reduced) and continuation analysis, the finite element presentation of the Koiter initial postbuckling theory. In the perturbation and continuation analysis the postbuckling path of equilibrium is approximated by a linearised interaction of the Euler buckling modes from which the nonlinear postbuckling path is constructed. The postbuckling analysis is performed on the three-dimensional shell model only as DIANA does not offer perturbation and continuation analyses for axisymmetric elements.

For the perturbation analysis a series of buckling modes must be selected. In the foregoing, it is observed that, in particular, the inclined-roller supported shell under spherical load yielded critical loads which closely approached the theory. In order to control the computational effort, a small number of modes are used. Therefore, the first 5 modes of the inclined-roller shell subjected to radial pressure load are selected. To improve the accuracy of the interaction process, shifting is applied towards the first mode (see Chapter 11).

Perturbation Result

The result of the perturbation analysis is illustrated in Figure 13.18. In Figure 13.18 the first three interacted modes are presented. It can be seen that the modes are a combination of the first buckling modes which demonstrated top buckling, seen in Figure 13.11.

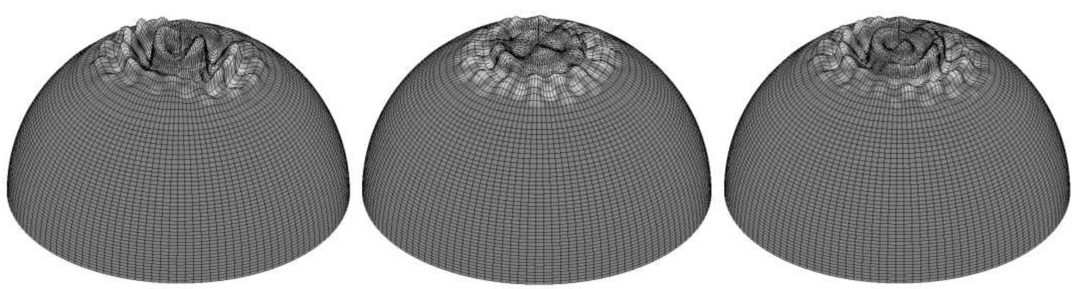

Figure 13.18. The first three perturbation modes combined from the linear buckling modes

The selection of mode 1 to 4 may seem strange as the modes were falsified as they did not show the typical shell buckling, i.e. a global buckling pattern of small local waves, organised in a chessboard pattern. This, however, is caused by the highly numerical instability of the continuation analysis which appeared to be successful only for these modes. Hence, the validity of the postbuckling analysis can be questioned.

Continuation Result

The continuation analysis appeared to be a highly numerical unstable and time consuming process. Several shell settings (different *R/t ratios*, different modes, etc) and finite element settings were implemented, but none of them proved to be successful. The results as presented below (for the 5 selected modes from the spherical loaded inclined-roller shell) took *2* days (*43* hours and *5* minutes) to complete on a 3.0 GHz Pentium 4 with 2.0 GB of RAM. Hence, this is far too long for an analysis which is assumed to provide in a fast linearised approach to the nonlinear postbuckling path.

The continuation analysis that provided the best result is shown in Figure 13.19, 13.20 and 13.21. In Figure 13.19 the top node load-displacement curve is illustrated. It can be seen that the top node experiences a decrease in load carrying capacity and deformation after the bifurcation point. The trend is similar to the trend seen in Figure 6.22. The load-displacement curves of other selected nodes are seen in Figure 13.20. Figure 13.20 represents the pre- and postbuckling behaviour of node 5163, 9551 and 10307. These nodes are selected as they are located on strategic locations in the shell. Node 10307 is found at a maximum perturbation buckling amplitude, node 5163 is located in between to maximum buckling amplitudes and node 9551 is located at the transition between triangular and quadrilateral elements, which is close the boundary of the buckles seen in Figure 13.18. It can be observed that the modes show completely different load-displacement curves.

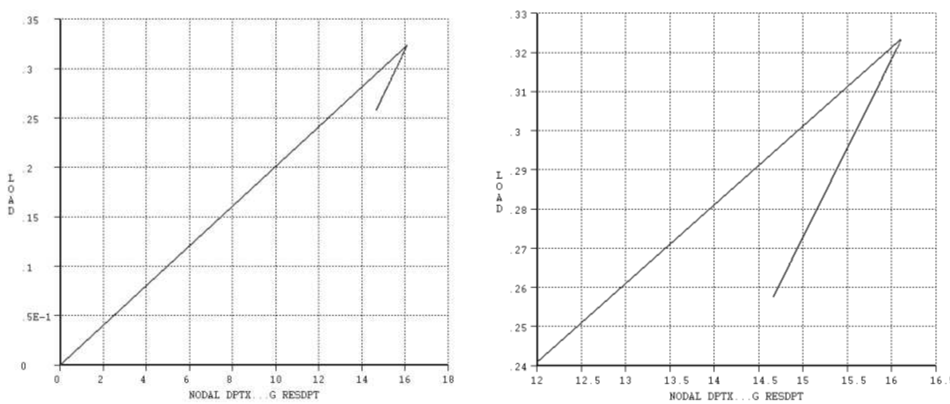

Figure 13.19. Top node load-displacement curve from FE continuation analysis for an inclined-roller supported shell under spherical load

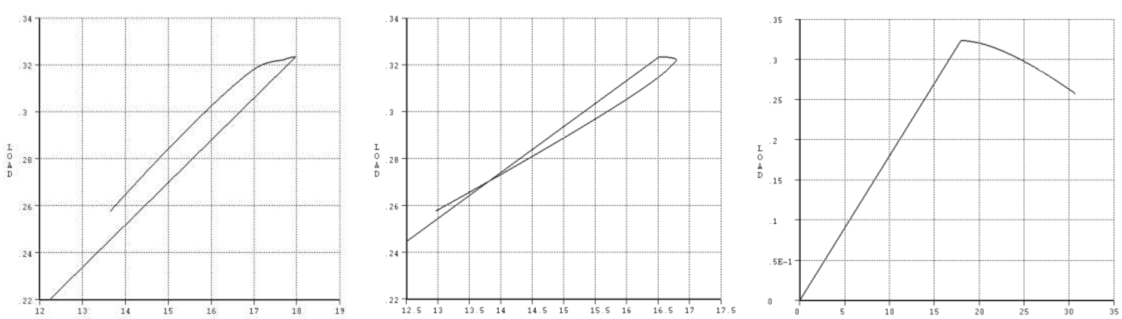

Figure 13.20. Node 5163, 9551 and 10307 load-displacement curves from FE continuation analysis for an inclined-roller supported shell under spherical load

To validate the obtained result, the load-displacement behaviour of all nodes must be determined. This is done similar to the graph of Figure 6.22, i.e. the ratio of the postbuckling load over the linear critical load is plotted against the ratio of the change of postbuckling volume over the change in linear buckling volume. The solution is presented in Figure 13.21.

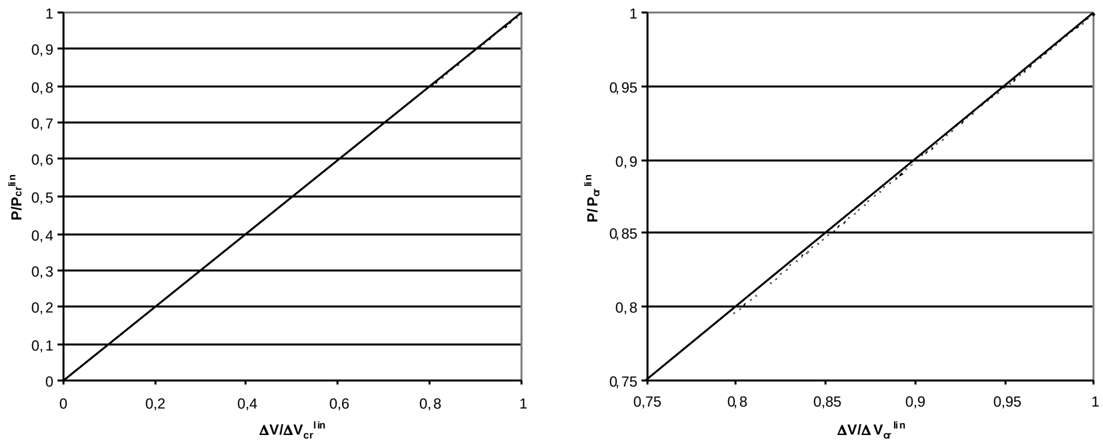

Figure 13.21. FEA initial postcritical behaviour of a perfect shell under spherical load

In Figure 13.21 the continuous line represents the prebuckling path of equilibrium and the dotted line represents the postbuckling path of equilibrium. The right graph is zoomed in upon the initial path in the vicinity of the bifurcation point. It can be seen that the results are poor. Perhaps, the best conclusion is that, at least, the results are not in contradiction with the theory.

13.6 Conclusions

In this chapter the linear elastic stability behaviour of a hemispherical shell is investigated. The prebuckling path and corresponding bifurcation point of a hemispherical shell are determined by a linear finite element (Euler) buckling analysis. The bifurcation point is computed for several support conditions and two types of external applied load, i.e. a radial pressure load and a uniformly distributed vertical load. The analyses are performed on an axisymmetric shell model and a three-dimensional shell model. Attempts were made to investigate the postbuckling behaviour by a perturbation and continuation analysis, the finite element formulation of the Koiter initial postbuckling theory. However, although the results are not in contradiction with the theory, they are poor and therefre not discussed further.

The results of the linear elastic stability analyses are summarised in Table 13.19 and 13.20.

	Axisymmetric shell model		Three-dimensional shell model	
	Spherical load (MPa)	Vertical load (MPa)	Spherical load (MPa)	Vertical load (MPa)
Roller	0.3969	0.2035	0.3969	0.2022
Inclined-roller	0.7917	0.4515	0.7811	0.4460
Hinged	0.6405	0.3507	0.5732	0.3285
Clamped	0.7938	0.4977	0.7067	0.4874

Table 13.19. Linear critical buckling loads corresponding to mode 1

The linear critical buckling loads of Table 13.19 can be compared to the theoretical linear critical buckling load as found by Zoëlly for radially pressed spheres (note that, the inclined-roller shell subjected to spherical load must approach closely this theoretical buckling load). In Table 13.20, the buckling loads from the finite element analysis are expressed in percents of the theoretical load of a radially pressed sphere.

	Axisymmetric shell model		Three-dimensional shell model	
	Spherical load (%)	Vertical load (%)	Spherical load (%)	Vertical load (%)
Roller	49.7	25.5	49.7	25.3
Inclined-roller	99.2	56.6	97.9	55.9
Hinged	80.3	43.9	71.8	41.2
Clamped	99.5	62.4	88.5	61.1

Table 13.20. Linear critical buckling loads in compare to the theoretical linear critical buckling load for a radially pressed sphere

From Table 13.19 and 13.20 it can be seen that, when compared to the linear critical buckling load of a radially pressed sphere, the buckling loads obtained by DIANA are lower. Furthermore, it can be concluded that a uniform vertical load, which by definition buckles in the boundary layer, drastically decreases the linear critical buckling loads in compare to the spherical loaded hemispheres. The roller support, which is weaker than the shell itself, is the most onerous support condition with a maximum decrease of *74.7%* of the linear critical buckling load for a radially pressed sphere. When the roller support is not considered, the hinged support is most onerous. With respect to the theory as presented in Chapter 6, the hypotheses of Van der Neut and Simitses and Cole are validated for shells confined to their compression zone or if a global buckling pattern appears.

With respect to the differences between the axisymmetric shell model and the three-dimensional shell model, it can be concluded that all buckling loads determined using the three-dimensional shell model are lower than the critical loads found using the axisymmetric model. In general the results are very much similar, however, not for the hinged and clamped supported shells subjected to spherical load. The discrepancies are *8.5%* and *11%*, respectively and is governed by the fact that for the axisymmetric shell model the bending moments in the linear solution of the hinged support do not vanish at the supports and, in case of a clamped support, the bending moments are much too low (Chapter 12). Evidently, this has a positive effect on the stability behaviour. Besides the difference in the first critical buckling load, it can be concluded that the axisymmetrical shell, as it is unable to deal with variations in circumferential direction, does not predict the effect of compound buckling correctly. Using the three-dimensional shell model it is found that compound buckling, by definition, occurs. Hence, the three-dimensional model is superior to the axisymmetric model.

Qualitatively, the conclusion can be drawn that several false buckling modes appeared in the finite element solution. The axisymmetric shell model yields false modes caused by the basic property of the model, namely, axisymmetry. The axisymmetry causes the tendency to buckle at the top of the shell as top buckling corresponds to a local buckle whereas buckling in the shell surface is accompanied by a global buckling pattern extending in circumferential direction. For the three-dimensional shell model, the uninvited bending moments which occurred in the linear solution due to the numerical imperfectness of the model (Chapter 12) appeared to be the reason for several falsified top modes as a global buckling pattern of small local waves in a chessboard pattern is expected (Chapter 6).

The buckling analyses appeared to be very sensitive to small (numerical) imperfections with several false modes arising between correct buckling modes. Therefore, the author strictly advices not only to examine the buckling loads, but also to examine the corresponding buckling shape. Only by viewing them together a good understanding of the buckling behaviour of the shell can be obtained.

14 Geometrically Nonlinear FEA

In Chapter 13 the linear critical buckling loads of a hemispherical shell with various types of loading and boundary conditions were computed. Furthermore, several attempts were made to construct the initial postbuckling path of equilibrium, but the obtained results from the perturbation and continuation analysis proved to be insufficient to confirm the theory of Chapter 6 (and in particular Figure 6.22). In experiments, however, initial geometrical imperfections in models cause the bifurcation point never to be reached. Imperfect shells suffer premature failure with a limit point dependent on the size of the imperfection (Figure 6.24). After the limit point the path of equilibrium bends downwards to the original postbuckling path of equilibrium. To bring into account for this nonlinear behaviour, geometrically nonlinear analyses need to be performed on imperfect shells.

In this chapter, the influence of geometrical nonlinearities and the influence of an initial geometrical imperfection on the shell load carrying capacity is investigated. Therefore, the shell is analysed with a geometrically nonlinear finite element analysis, thus, taking into account for large deformations, and modelled with an imperfection with increasing amplitude. The shape and implementation of the initial geometrical imperfection into the finite element model is described. Moreover, the chosen incremental-iterative solution procedure of the geometrically nonlinear analysis is explained.

To verify the finite element results, a shell with imperfection amplitude equal to zero (perfect shell) is compared to the linear critical buckling load obtained in Chapter 13. The results must be (approximately) similar. Furthermore, the results are verified by comparing the finite element output of the three-dimensional shell model with the theory of Chapter 6 and with results from the same analysis with an axisymmetric shell model.

14.1 Shell Parameters

14.1.1 Geometry

See Chapter 12.1.1.

14.1.2 Initial Geometrical Imperfections

To determine the influence of initial geometrical imperfections, the imperfections must be modelled in the original geometry of the shell. The main modelling questions refer to the amplitude of the imperfection, the size and shape of the imperfection and the location of the imperfection. Furthermore, the spatial distribution of possible several imperfections must be defined.

In this thesis the investigation to the influence of initial geometrical imperfections is restricted to a local imperfection of varying amplitudes between *0.0* and *1.0* times the shell thickness, with a step size of *0.2*. The maximum imperfection amplitude is located at the top (node) of the shell, which is assumed to be most onerous in case of buckling in the shell surface as it is in biaxial compression. At other locations, e.g. the middle of the shell meridian or near the supports, a vertical load produces one-directional compression stresses only or compression-tension stresses, respectively. Hereby, the possible interaction with an edge disturbance caused by restrained deformation at the supports is not taken into account. Thus, imperfections located near the supports may lead to a more onerous situation if they interact with the edge disturbance. For a spherical loaded shell, the location of the imperfection is not important if the shell buckles inside its surface. However, similar to the vertical loaded shell, interaction of geometrical imperfections with edge disturbances may lead to a lower load carrying capacity of the shell. The imperfections included in the finite element model are tabulated in Table 14.1.

	Location in Shell	Space distribution	Amplitude (w_o/t)	FE Model
1	Top	Local	0	(Axisymmetric +) 3D
2	Top	Local	0.2	(Axisymmetric +) 3D
3	Top	Local	0.4	(Axisymmetric +) 3D
4	Top	Local	0.6	(Axisymmetric +) 3D
5	Top	Local	0.8	(Axisymmetric +) 3D
6	Top	Local	1.0	(Axisymmetric +) 3D

Table 14.1. Imperfections in the shell

According to Koga and Hoff (1969) the imperfections can be characterised by their amplitude only. The local imperfection is modelled by a geometrically nonlinear analysis of a shell subjected to a point load at the top node. By each time increasing the point load, different imperfection amplitudes are obtained. Scordelis [69] denotes, however, that the shape of the imperfection is also important and that experiments show that the buckled shape for a spherical dome consists of a circular area of the shell snapping through (equation (6.62)), which is confirmed by the experiments of Vandepitte, as denoted by Billington and Harris [6] (Chapter 6). Although, there is discussion if the imperfection shaped according to the buckling shape is the most onerous (see Chapter 6), it is assumed here. Thus, the dimensions of the imperfection are checked upon Scordelis' theoretical buckling diameter equation (6.62). If the area is significantly different, the area is enlarged. For the investigation of the influence of an initial geometrical imperfection, the final deformed shell geometries are implemented as original imperfect geometry in the geometrically nonlinear analysis.

14.1.3 Material

See Chapter 12.1.2.

14.1.4 Boundary Conditions

See Chapter 12.1.3.

14.1.5 Loading

The shell is loaded by uniform pressure or vertical load. Hence, snow load and wind load are not considered, although asymmetrical loading in combination with asymmetrical initial geometrical imperfections may lead to situations more onerous than the one investigated here.

14.1.6 Analysis Scheme

The different types of analysis are presented in Table 14.2. Each analysis is combined with the imperfections tabulated in Table 14.1.

Name	Loading Conditions	Supporting Conditions	Type of Analysis	Model
Zeiss 1	Spherical and Vertical	Roller	Geometrically Nonlinear	(Axisymmetric +) 3D
Zeiss 2	Spherical and Vertical	Inclined-roller	Geometrically Nonlinear	(Axisymmetric +) 3D
Zeiss 3	Spherical and Vertical	Hinged	Geometrically Nonlinear	(Axisymmetric +) 3D
Zeiss 4	Spherical and Vertical	Clamped	Geometrically Nonlinear	(Axisymmetric +) 3D

Table14.2. Analysis scheme

14.1.7 FEA Settings

The geometrically nonlinear analysis is based on a Total Lagrange formulation, Green strains and Second Piola-Kirchhoff stresses (although transformed to ordinary Cauchy stresses by DIANA), see also Chapter 11. The selected incremental-iterative procedure is a Regular Newton-Raphson scheme combined with a spherical path arc-length control. The arc-length control is modified with an indirect displacement control on the top node in the negative vertical direction. The indirect displacement control ensures an increasing displacement of the top node in the vicinity and beyond the limit point. For convergence both the displacement and the force norm must be satisfied. During analyses the user specified arc-length controlled step sizes are varied in order to pass the limit point and to find as many points of the adjacent postbuckling equilibrium path as possible.

14.2 Perfect Shell

Using the geometrical nonlinear analysis only limit points can be detected; bifurcations are not taken into account. However, if the initial imperfection amplitude is equal to zero (perfect shell), the bifurcation points as determined in Chapter 13 can be approximated closely and, hence, may serve as benchmark test for the geometrical nonlinear procedure. Therefore, the geometrically nonlinear analysis is compared to the results of Chapter 13, summarised in Table 13.19 and Table 13.20.

14.2.1 Results and Findings

The geometrically nonlinear analysis on perfect three-dimensional shell models is accompanied by numerical difficulties. Convergence on postbuckling equilibrium is reached in only a very few situations and often yields non-smooth load-displacement curves. In spherical load situations, DIANA was able to construct only the linear path losing convergence just before the bifurcation point (which by definition is not found). Typical load-displacements curves of spherical shells subjected to spherical or vertical load are seen in the left graph of Figure 14.1.

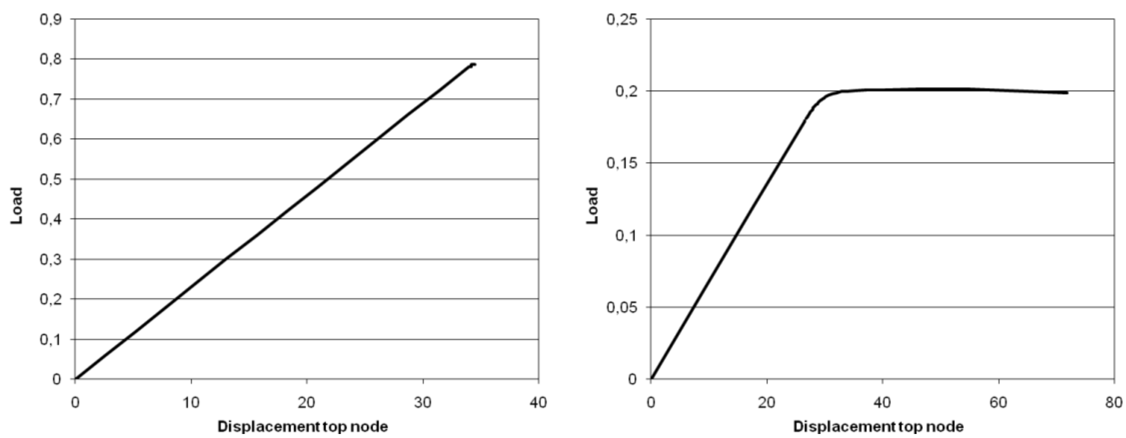

Figure 14.1. Typical load-displacement curves of a perfect membrane supported shell subjected to spherical (left) and vertical load

In Figure 14.1 it can be seen that, for a membrane supported shell subjected to spherical load (inclined-roller support), a nonlinear branch initiates just before the bifurcation point is reached. It is expected that, if convergence would have been achieved, the nonlinear branch would be the starting point of the fall-back in load carrying capacity as indicated by Figure 6.22. For a membrane supported vertical loaded shell (roller support), the finite element analysis finds convergence for an (almost) horizontal postbuckling path of equilibrium. Thus, the shell does not experience a sudden decrease in load bearing capacity. This can be explained by examining the buckling modes of Chapter 13 for vertically loaded shells. A shell subjected to vertical load, by definition, buckles in the boundary layer. I.e. the buckling does not take place inside the shell surface and, therefore, does not show the typical shell-like behaviour of Figure 6.22. The question arises if an initial geometrical imperfection at the top of the shell transforms this type of buckling behaviour to the shell-like buckling behaviour. In other words, will the imperfection become the dominant failure mechanism or not? The answer is discussed later in Section 14.3.

Quantitative results of the geometrically nonlinear analyses on perfect shells are presented in Table 14.3. The results are compared to the theoretical linear critical buckling load (equation (6.53)).

	Three-dimensional shell model			
	Spherical load		Vertical load	
	Max. Load (MPa)		Max. Load (MPa)	
Zeiss 1	0.3965	49.7 %	0.2009	25.3 %
Zeiss 2	0.7860	98.5 %	0.4447	55.7 %
Zeiss 3	0.5680	71.2 %	0.3269	41.0 %
Zeiss 4	0.6989	87.6 %	0.4840	60.6 %

Table 14.3. Comparison between geometrically nonlinear analysis on perfect shells and the theoretical buckling load

In Table 14.3 it can be seen that, however the bifurcation point by definition is not reached, the result of the inclined-roller shell subjected to spherical load is close to the theoretical load as found for a radially pressed sphere. The results from the geometrically nonlinear analysis can also be compared to the linear critical buckling loads for each support and load type, as obtained in Chapter 13. The results are expected to be approximately similar and may even be higher as the finite element linear stability analysis is solved for a discretised structure by iteration and, thus, do not yield the exact bifurcation point.

	Three-dimensional shell model	
	Spherical load	Vertical load
Zeiss 1	99.9 %	99.4 %
Zeiss 2	100.6 %	99,7 &
Zeiss 3	99.1%	99,5 %
Zeiss 4	98.9%	99.3 %

Table 14.4. Comparison between geometrically nonlinear analysis on perfect shell and buckling loads of Chapter 13

In Table 14.4 it can be seen that the expected results are obtained. The geometrically nonlinear analyses, in general, yield slightly lower results than the linear critical buckling loads as obtained in Chapter 13. Hence, it can be concluded that the graph of Figure 6.35, is misleading: the introduction of geometrical nonlinearities in the analysis only has minor influence on the maximum load that is found. With the obtained results the geometrically nonlinear analysis has passed the (author's) benchmark test.

14.2.2 Axisymmetric Comparison

The maximum loads of the axisymmetric shell model approximately yield the same result as the three-dimensional shell model. The results of the geometrical nonlnear axisymmetric model are compared to the buckling loads of the axisymmetric model as obtained in Chapter 13 in Table 14.5.

	Axisymmetric shell model	
	Spherical load	Vertical load
Zeiss 1	99.8 %	99.9 %
Zeiss 2	99.6 %	99.9 %
Zeiss 3	99.8 %	99.6 %
Zeiss 4	99.7 %	99.8 %

Table 14.5. Compare between geometrically nonlinear analysis on perfect axisymmetric shell and buckling loads of Chapter 13

14.3 Imperfect Shell

Aforementioned, experiments on (e.g.) synclastic shells loaded by a load (almost) perpendicular to their surface do not reach the bifurcation point but show premature buckling failure caused by initial geometrical imperfections in the test models. This so-called imperfection sensitivity is extremely dangerous and, hence, extensive investigations are needed to determine to load-carrying capacity of such imperfect shells.

For the investigation the initial geometrical imperfections are modelled according to Section 14.1.2, i.e. a local imperfection located at the top node with imperfection amplitude ranging from *0* to *1.0* times the shell thickness with a step size of *0.2*. First a basic shell type, the Zeiss 2 shell under radial pressure, is treated as it is widely discussed in literature. The analyses are computer with an each time increasing imperfection amplitude. Afterwards the influence on the base solution caused by different types of support and load conditions, as described in Section 14.1.4 and 14.1.5, is treated.

14.3.1 Results and Findings

The Zeiss 2 shell under radial pressure load behaves similar to a complete shell. When the shell is subjected to a geometrical nonlinear finite element analysis with increasing imperfection amplitude, the shell shows limit point buckling. At the limit point, the buckling process may show a smooth transition between the nonlinear prebuckling and postbuckling path of equilibrium, or may experience a sudden snap-through to a non-adjacent equilibrium configuration. The simplest way to examine the nonlinear buckling response is to plot the deformations of an individual load-step and compare them to adjacent load-steps. In Figure 14.2 typical adjacent deformations of the hemisphere under radial pressure with initial imperfection at the top are presented. It is observed that the shell experiences an initial smooth buckling process with adjacent modes showing ever growing buckling amplitudes at the location of the initial geometrical imperfection.

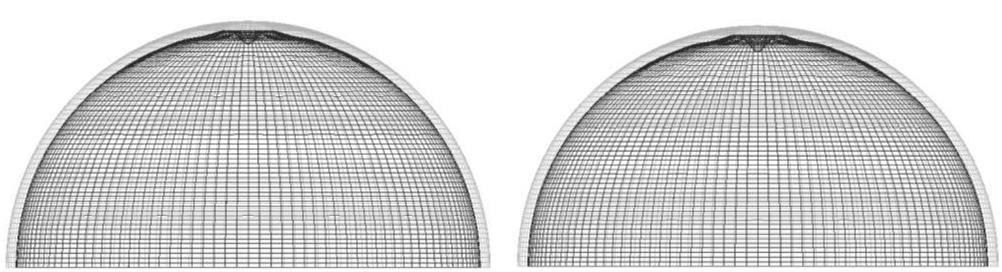

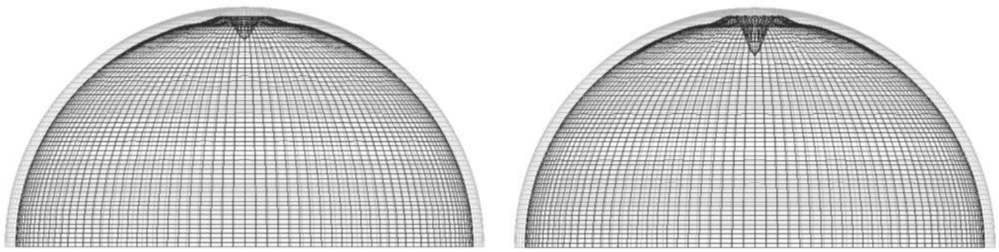

Figure 14.2. Typical smooth buckling deformation of a hemisphere under radial pressure with initial geometrical imperfection

After the smoot initial buckling process, the finite element procedure fails at finding equilibrium in the vicinity of the current position while increasing the top node deformation (indirect displacement controlled analysis). DIANA steps back a few times (the load and deformation decreases) but then snaps-through as it jumps to a non-adjacent equilibrium state. The process is illustrated in Figure 14.3.

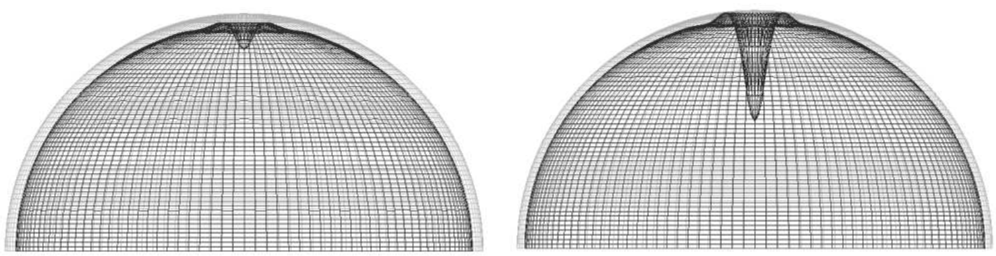

Figure 14.3. Typical snap-through buckling of a hemisphere under radial pressure with initial geometrical imperfection

The geometrically nonlinear analysis with infinite elastic material properties may also snap towards an equilibrium state with positive displacement and, thus, a spherical tensile load. These equilibrium states are not considered as they have no practical value.

A convenient way to plot the hemisphere buckling behaviour is to plot a load-displacement curve. Figure 14.4 represents a typical load-displacement curve of a hemisphere under radial pressure with an initial geometrical top imperfection (equal to $w_o/t = 0.2$ in the figure). The left curve of Figure 14.4 is the actual finite element results whereas the right curve is a 'cleaned' curve, leaving out the sudden jumps between equilibrium states. In the left curve the smooth limit point is seen, corresponding to the buckling propagation of Figure 14.2. The snap-through behaviour illustrated in Figure 14.3 is indicated by the straight lines after the limit point. The shell jumps to an equilibrium point far away from the limit point (deformations over *120 mm*). Thus, the buckling response seen in Figure 14.2 and 14.3 can occur in succession within the same shell. It is observed that, after the snap-through (arrow number 1), the finite element method finds a smoothly curved postbuckling path of equilibrium leading back to the limit point (indicated arrows number 2). Therefore, the question may arise whether the snap-through is only a numerical phenomenon related to the finite element process or actually takes place in reality. This question cannot be answered without further tests, e.g. different finite element solvers (programs) or model tests. If the left graph of Figure 14.4 is cleared from the sudden jumps (the linear lines) the right graph is obtained. The shape of the right graph is in close relationship with the graphs plotted in Chapter 6 for imperfect shells

(Figure 6.24) and only shows the prebuckling and postbuckling equilibrium paths (the linear lines in the left figure cannot be addressed as an equilibrium path).

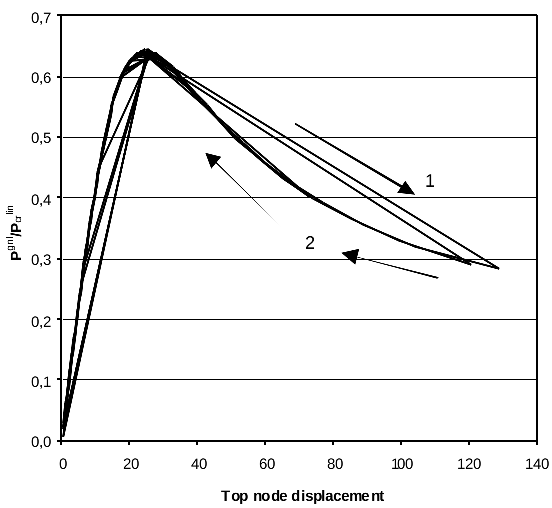

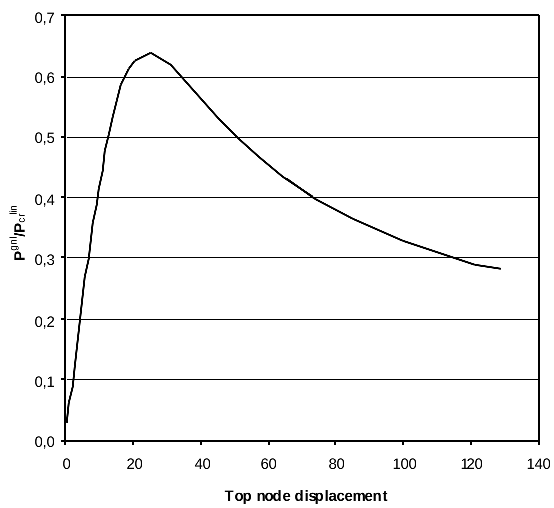

Figure 14.4. Finite element (left) and cleared load-displacement curves of limit point buckling of a hemisphere under radial pressure with an initial geometrical imperfection $w_o/t = 0.2$

The typical load-displacement curve seen in Figure 14.4, obtained by a geometrically nonlinear finite element analysis on an imperfect shell, yields a maximum load carrying capacity of approximately *64%* of the linear critical buckling load. Thus, an imperfection of *12 mm* amplitude (in case of a *60 mm* shell) already causes a fall-back in load carrying capacity of *36%*.

If the imperfection amplitude is stepwise increased up to $w_o/t = 1.0$, the load carrying capacity further decreases and the load-displacement curve has increased prebuckling nonlinearity resulting in an even smoother approach to the secondary path. Hereby it must be mentioned that numerical difficulties frequently disturbed the analysis preventing convergence on postbuckling points further away from the limit point. It is observed in the finite element results that the snapping phenomenon (physical and/or numerical?) does not disappears for larger imperfection amplitudes, although the discrepancy between the snapping branch and the equilibrium path becomes smaller. Hence, smooth buckling may be expected for a shell which includes large imperfections. If the (cleaned) load-displacement curves of a series of imperfections are plotted into one graph, the above described effects become visual. It can be seen in Figure 14.5. In Figure 14.5 all imperfection amplitudes ($w_o/t = 0.2$, *0.4, 0.6, 0.8* and *1.0*) are plotted together with the reference linear buckling solution. Obviously, the highest imperfection amplitude causes the maximum decrease in load carrying capacity. The lines which end abruptly indicate shell settings for which the finite element analysis did not find convergence.

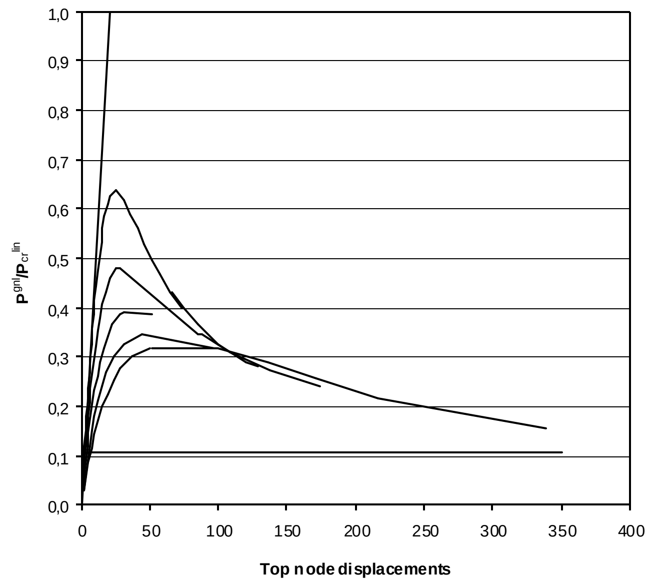

Figure 14.5. Load-displacement curves of a shell with various initial geometrical imperfection sizes

In Figure 14.5 the decrease in load-carrying capacity with increasing imperfection amplitude is clearly seen. Furthermore, it is seen that the absolute minimum of the postbuckling path as predicted by mathematicians (Chapter 6). If the minimum postbuckling load is compared to the equations of Von Karman and Tsien, Del Pozo and Del Pozo and Dostanowa and Raiser (see Chapter 6 and Chapter 10.6) it can be concluded that the load-displacement curves already violate the values of Von Karman and Tsien and Del Pozo and Del Pozo but asymptotically still may converge to the minimum load as proposed by Dostanowa and Raiser (equation (6..58)) plotted with the straight lower line. However, no real conclusions can be drawn as the finite element results are of insufficient range.

In Chapter 12 it is seen that an inclined-roller shell subjected to radial pressure load is in uniform compression, i.e. the meridional and circumferential stresses are compression stresses with the same magnitude at each location in the shell. Moreover, there are no bending moments. The geometrically imperfect shell, however, will experience stress variations and bending moments caused by the disturbed membrane field in the vicinity of the imperfection. Typical stress and bending moment distribution is plotted against the shell meridian in Figure 14.6. In the left graph the middle surface stresses and both outer surface stresses are plotted (obtained by the 3-point Simpson integration scheme). From the finite element results it is observed that the initial geometrical imperfections cause a local disturbance decaying out, e.g. similar to a point load. Furthermore, it can be seen that tensile stresses arise (which eventually may lead to concrete cracking, discussed in Chapter 15). The bending moments that appear show high peaks at the imperfection. The highest peak occurs at the eye of the imperfection which, off course, experiences the highest curvature. As the material is infinite elastic in compression and tension, the stresses and bending moments are inferior to the load-displacement curves, i.e. the maximum load is by definition determined by large deformations.

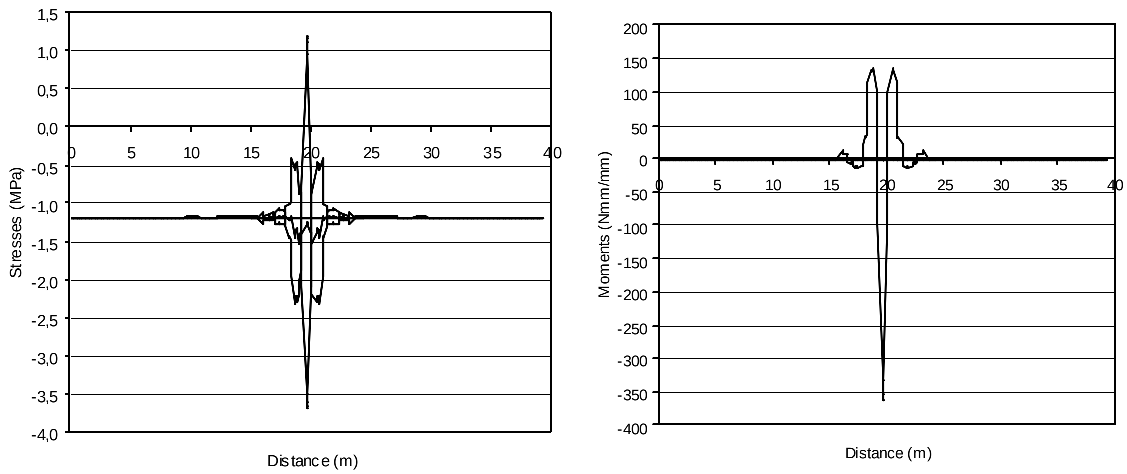

Figure 14.6. Typical stress and bending moment distribution plotted against the shell meridian

14.4 Effect of Imperfections

The inclusion of large deformations and initial geometrical imperfections indicated the shell sensitivity for imperfections; the shell experiences a fall-back in load carrying capacity. In Figure 14.5 it can be seen that this decrease in load capacity is higher for larger imperfection amplitudes. Furthermore, it can be seen in Figure 14.5 that the decrease in load carrying capacity between to imperfect shells is not linear, but seems to become less for larger imperfection amplitudes. This is also seen in Figure 14.7, where the load carrying capacity is plotted against increasing imperfection amplitude for a hemisphere under radial pressure.

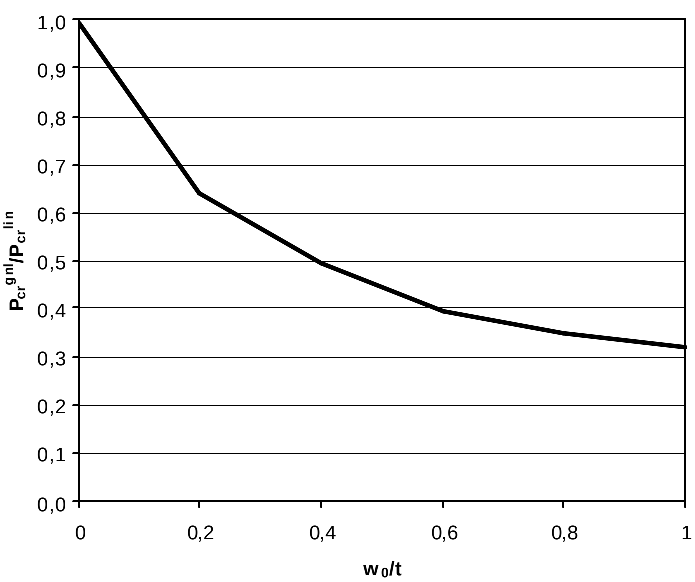

Figure 14.7. Effect of initial geometrical imperfections on load carrying capacity for a hemisphere under radial pressure

In Figure 14.7, which is valid for all *R/t ratios* investigated in this thesis, it is observed that even the smallest imperfections already have a considerable effect on the load bearing capacity. When the imperfection is equal to the shell thickness the load is as low as *32%* of the linear critical buckling load (a fall-back of *68%*). Although the graph seems to develop asymptotic behaviour, it is not likely to occur. An ever growing imperfection will lead to an ever decreasing load.

The range of application of Figure 14.7 is restricted. The graph is constructed by putting a spherical load on a shell with a local imperfection at the top. However, an imperfection at another location in the shell surface would yield the same result, provided that the buckling does not interact with edge disturbances. Therefore, the graph is valid for all situations in which a spherical load causes buckling and the buckling takes place within the shell surface. The effect of other support conditions, loads or material properties is discussed in Section 14.5 to 14.7.

14.4.1 Theoretical Comparison

The validity of the graph presented in Figure 14.7 can be checked in two ways; by comparing the results with the theory of Chapter 6 and by comparing the results with an axisymmetric shell model similar to previous chapters (Section 14.4.2).

The theory in Chapter 6 describes two methods for determined the effect of initial geometrical imperfections, i.e. the *Koiter half-power law* and the *special theory of Koiter*. The Koiter half-power law is described in equation (6.2) and corresponds to type III buckling behaviour illustrated in Figure 6.4. Type III buckling behaviour is widely accepted as the structural response of imperfect spherical shells subjected to radial pressure, Kollar and Dulacska [54]. Recapitulate from Chapter 6:

$$\lambda = \frac{p_{cr}^{upper}}{p_{cr}^{lin}} = 1 - 2\left(w_o \rho c_1\right)^{\frac{1}{2}} \tag{6.2}$$

Herein, c_1 represents type III behaviour and ρ is a coefficient depending on the imperfection shape.

The parameter ρc_1 is determined such that the Koiter half-power curve is optimal aligned with the finite element curve of Figure 14.7. Hence, the validity of the points with the largest discrepancy between the Koiter half-power curve and the curve of Figure 14.7 must be questioned. It is found that the curves coincide most optimal if the parameter ρc_1 is equal to *0.16*. The Koiter half-power curve is plotted against the finite element curve in Figure 14.8.

Using the special theory of Koiter, Hutchinson found an upper bound curve for an imperfect shell (see Figure 6.25). Kollar and Dulacska [54] used the results of Hutchinson for their graph in the IASS Recommendations, partially taking into account for the results of Kao (Figure 6.32). The IASS graph is previously presented in Figure 6.36. The graph defined by Kollar and Dulacska is also illustrated in Figure 14.8.

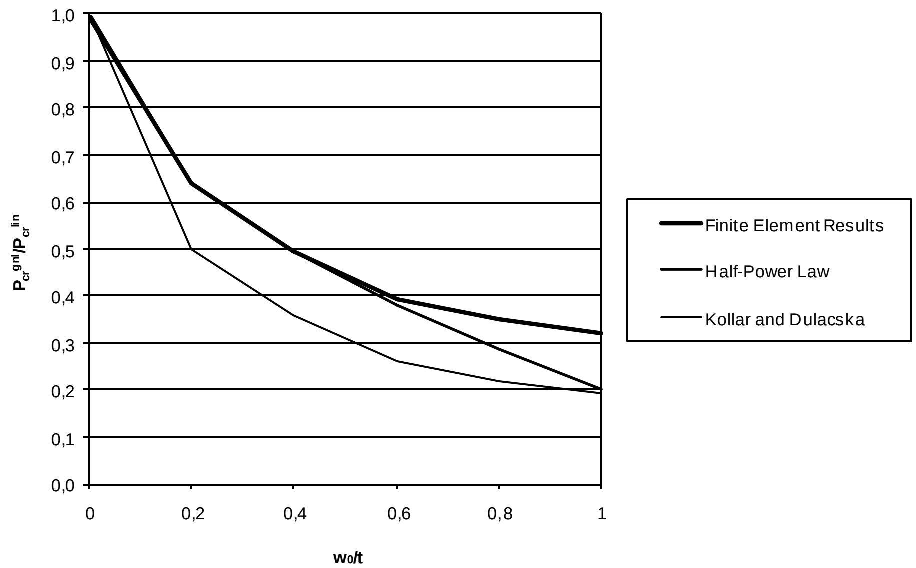

Figure 14.8. Comparison between FEA, Koiter half-power law (red) and the curve of Hutchinson/Kollar and Dulacska (blue)

From Figure 14.8 it can be concluded that the results of the finite element analysis, initially, shows good correlation with the curve of the Koiter half-power law. However, for imperfection amplitudes of $w_o/t > 0.6$ the similarity is less convincing. Hereby, it must be mentioned that the Koiter half-power law is the less exact the greater the buckling deformations are (which, in turn, are related to the size of the imperfection). For imperfections of $0.6 > w_o/t = 1.0$ the curve has approximately the same inclination as the curve of Hutchinson and Kollar and Dulacska (for which no mathematical formulation was found). Therefore, it can be concluded that reasonable correspondence is found.

14.4.2 Axisymmetric Comparison

A second check is related to the axisymmetric shell model. Due to the axisymmetry, the shell appeared to have a strong preference for local top buckling (see Chapter 13). However, in case of an inclined-roller shell with spherical load and a top imperfection, the drawback is not important anymore as the shell already fails at the top. Therefore, the axisymmetric finite element results can be used to validate the three-dimensional results. It is observed from the axisymmetric finite element results that the curve almost completely coincides with the three-dimensional curve with a maximum difference of *3%*.

14.5 Support and Load Influences

In Chapter 13 it is seen that different types of support conditions lead to lower linear critical buckling loads than a spherical shell subjected to radial pressure (or an inclined-roller hemisphere subjected to radial pressure). Moreover, if the shell was subjected to a uniform vertical load the shell, by definition, buckled first in the boundary layer. Or, as described before in Section 14.1, a vertical loaded shell does not show the shell-like buckling as defined in Figure 6.22. An imperfection in the shell may transform this type of buckling behaviour back to shell buckling if the imperfection causes the shell to buckle within the shell surface.

Similar to Chapter 12 and 13, the shell support is either roller, inclined roller, hinged or clamped. Their introduction into the shell analysis changes the stress and bending moment distribution of Figure 14.6, due to an edge disturbance (disturbed membrane stresses accompanied by bending moments). This can be seen in the stress and bending moment distribution graphs of Chapter 12. An example of an adapted stress and bending moment distribution is illustrated in Figure 14.9 for a clamped supported shell subjected to spherical load. Hence, the question is if whether the edge disturbance will be decisive for buckling or the disturbance caused by the initial geometrical imperfection.

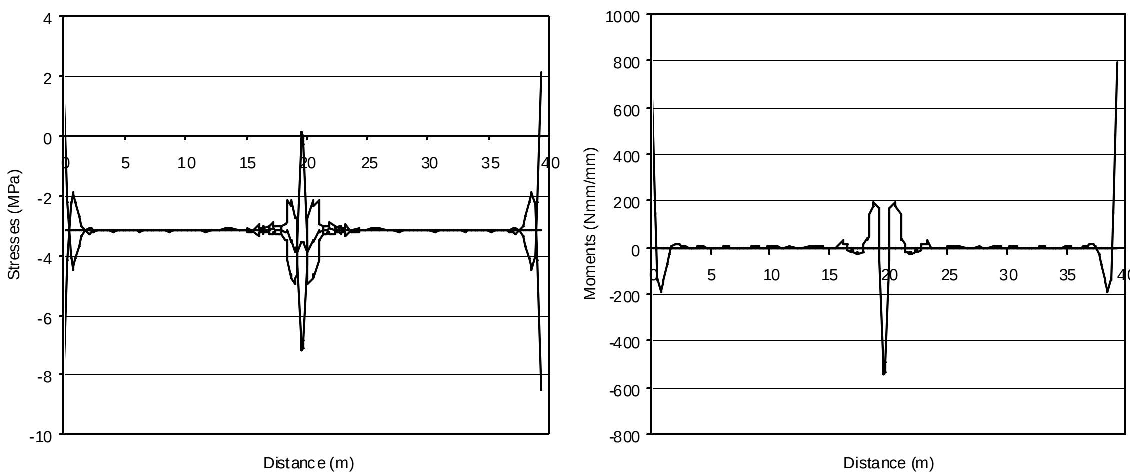

Figure 14.9. Typical stress and bending moment distribution of a clamped shell plotted against the shell meridian

From the finite element analysis it is observed that in case of a clamped shell subjected to radial pressure load the imperfection is dominant over the edge disturbance for imperfection amplitudes $w_o/t \geq 0.2$. It can be seen when the deformed shells of increasing load steps are plotted, see Figure 14.10.

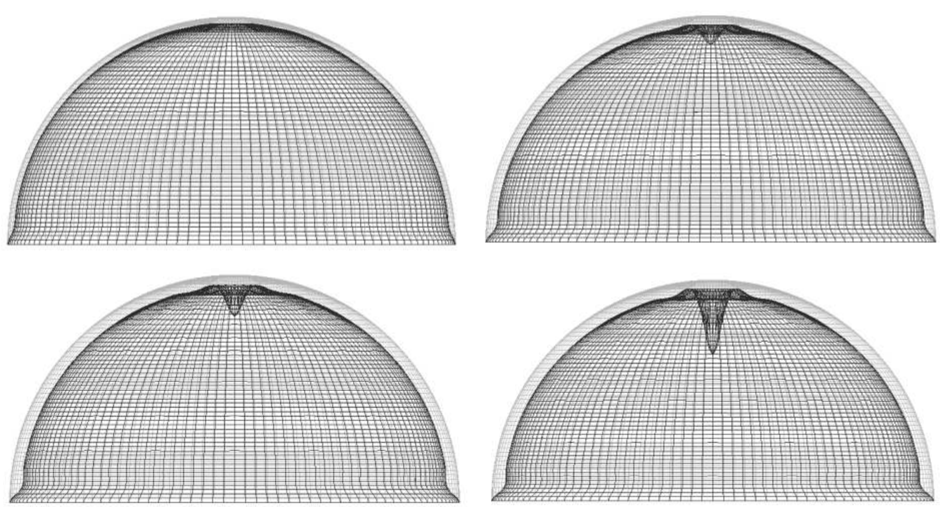

Figure 14.10. Typical deformation of a clamped shell subjected to radial pressure load with initial top imperfection dominant over edge disturbance

In case of a roller support there is no edge disturbance which means that the stress and bending moment distribution do not change. However, as the support is weaker than the shell itself, the shell is very sensitive to buckling in the boundary layer.

To investigate the influence of each of the four support conditions in combination with as well spherical load as vertical load for an imperfect shell with an each time increasing top imperfection amplitude a extensive series of analyses are performed within the range of *R/t ratios* between *200* and *1000*. From the finite element analyses it is observed that the graph of Figure 14.7 can be modified to include the aforementioned effects. The result is the graph of Figure 14.11.

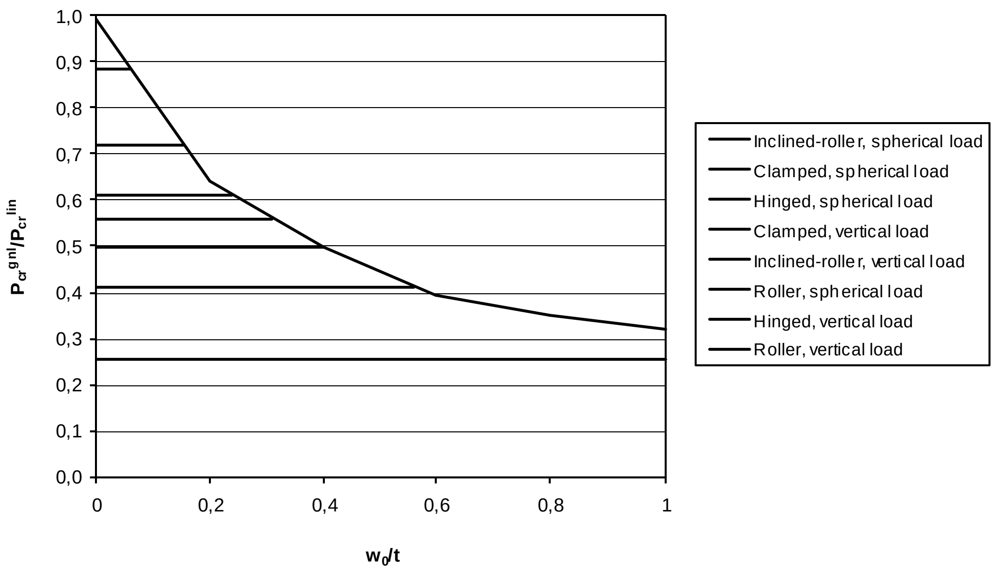

Figure 14.11. Decrease in load-carrying capacity due to boundary conditions, loads and initial geometrical imperfections at the top of the shell for R/t ratios between 200 and 1000

In the graph of Figure 14.11 the Zeiss *1* to *4* shells are plotted subjected to spherical or vertical load. At imperfection amplitude $w_o = 0.0$, the values are equal to the linear buckling loads obtained in Chapter 13. Hence, starting from the top, the lines correspond to the inclined-roller shell subjected to spherical load, the clamped shell subjected to spherical load, the hinged shell subjected to spherical load, the clamped shell subjected to vertical load, the inclined-roller shell subjected to vertical load, the roller shell subjected to spherical load, the hinged shell subjected to vertical load and the roller shell subjected to vertical load, respectively.

From Figure 14.11 it can be concluded that, except for the roller shell subjected to vertical load, imperfection buckling becomes dominant over boundary layer buckling at a certain size of imperfection amplitude. Thus, provided that the edge supports are not weaker than the shell itself, it can be seen that, for imperfection amplitudes $w_o/t \geq 0.6$ the critical load depends solely on the initial geometrical imperfections. For imperfection amplitudes $w_o/t < 0.6$ the type of buckling failure depends on the support condition and type of load. Hereby, it must be mentioned that the graph is only valid for an imperfection at the top of the shell in case of vertical load. For spherical load the graph is valid for all possible imperfection locations, provided that the buckling does not interact with possible edge disturbances. The roller shell subjected to vertical load is a special case. The shell critical load is not dependent a top imperfection, but by definition buckles in the boundary layer. However, hereby it must be mentioned that if the actual behaviour is like the graphs of Figure 14.8, eventually imperfection buckling becomes dominant, even for the roller shell under vertical load.

14.6 Geometrical Influences

The graphs as presented above are, at least, valid for all investigated *R/t ratios* between *200* up to *1000*.

14.7 Material Influences

The influence of material properties can be named 'as expected' as the Young's modulus is linearly present in the relations and analyses. The influence of a non-zero Poisson's ratio is negligible.

14.8 Knock-Down Factor Approach

Aforementioned, a structural engineer prefers general methods of calculation with a limited amount of computational work. Therefore, a procedure is proposed for which the linear critical buckling load is multiplied (which can easily be obtained from a theoretical formula or a simple linear buckling finite element analysis) with a so-called knock-down factor which incorporates the effects causing a fall-back in load carrying capacity. The knock-down factor that incorporates effects of large deformations and initial geometrical imperfections can be determined from the results presented above.

When determining the knock-down factor, the question is which imperfection amplitude must be taken into account. In Figure 14.10 it can be seen that for higher imperfection amplitudes there is little difference in maximum load carrying capacity. In the absence of imperfection measurements it seems a safe estimation to use an imperfection amplitude equal to the shell thickness. For concrete shells this leads to imperfections with a magnitude of approximately *60* to *80 mm*. Moreover, for such imperfection amplitudes the critical load is independent of boundary conditions and type of loading if the roller support is neglected (which sounds reasonable as a roller support is unlikely to occur in practice (Chapter 3)).

According to the finite element results, the knock-down factor is approximately equal to *68%* (multiplication of linear critical buckling load with *0.32*). If the knock-down factor is based on the Koiter half-power law or on the graph of Hutchinson and Kollar and Dulacska, the knock-down factor is equal to *0.2* (Figure 14.8). Obviously, the author opts for choosing *0.32*.

14.9 Conclusions

Before reading the following conclusions, one must keep in mind that they are based on shell analysis involving shells with *R/t ratios* between *200* and *1000* and a local imperfection located at the top. Furthermore, the shell is loaded by uniform pressure or vertical load. Hence, snow load and wind load are not considered, although asymmetrical loading in combination with asymmetrical initial geometrical imperfections may lead to situations more onerous than the one investigated here.

From the geometrically nonlinear analysis on imperfect shells it can be concluded that, for an imperfection equal to zero (perfect shell) the geometrically nonlinear analysis approaches the linear critical buckling load as obtained in Chapter 13 closely. In the geometrically nonlinear analysis it was found that shells experience either shell-like buckling (with decrease of load-carrying capacity in postbuckling range) or buckling with a almost horizontal postbuckling path, determined by the type of external applied load on the shell, uniform spherical or vertical load, respectively.

When imperfections are introduced the load carrying capacity falls down considerably. With increasing imperfection amplitude, the critical load becomes less and less, however, the larger the imperfection, the less difference in critical load in compare to adjacent critical loads. This can be seen in the graph of Figure 14.7. With respect to Figure 14.7 one must keep in mind that, although the graph implies asymptotic behaviour, this is not to be expected, i.e. an increasing imperfection will always lead to a lower critical load. For an inclined-roller shell subjected to spherical load, the largest decrease in load carrying capacity within the range of research (maximum imperfections equal to the shell thickness) is approximately equal to *70%* (for as well the three-dimensional shell model as the axisymmetric shell model). When the maximum decrease in load carrying capacity is compared to the Koiter half-power law or to the graph of Hutchinson and Kollar and Dulacska [54] it is observed that there is a discrepancy of approximately *10%* as they results lead to a maximum decrease of *80%*. Hence, reasonable correspondence is found.

When the influence of support conditions and load conditions are considered, it can be concluded that for imperfection amplitudes $w_o/t \geq 0.6$ the critical load depends solely on the initial geometrical imperfections, if the support is not weaker than the shell itself. I.e. a roller supported shell subjected to vertical load yields critical loads independent of any top imperfection within the range of the *R/t ratios* investigated. Hereby, it must be mentioned that with increasing *R/t ratio* eventually imperfection buckling becomes dominant, even for the roller shell under vertical load. For imperfection amplitudes $w_o/t < 0.6$ the type of buckling failure depends on the support condition and type of load.

Qualitatively the geometrically nonlinear analysis on imperfect shells shows a smooth transition from the prebuckling path of equilibrium to the postbuckling path of equilibrium, as e.g. is illustrated in Figure 14.5. However, also snap-through behaviour is observed. The question if the snap-through behaviour actually occurs in practice or only in the numerical approximation cannot be answered. Additional research may provide in the answer, e.g. using alternative finite element solution procedures or by testing small-scale models. Furthermore, with respect to the obtained postbuckling path it can be concluded that the graph seems to approach to a horizontal asymptote, the absolute minimum postbuckling point of equilibrium. If the minimum postbuckling load is compared to the equations in Section 6.5.3, proposed by mathematicians such as Von Karman and Tsien, Del Pozo and Del Pozo and Dostanowa and Raiser (see Chapter 6 and Chapter 10.6) it can be concluded that the postbuckling load-displacement curve already violates all values between Von Karman and Tsien and Del Pozo and Del Pozo, but asymptotically still may converge to the minimum load as proposed by Dostanowa and Raiser (equation (6.58)). However, no real conclusions can be drawn on the validity of the latter relation as the reach of the finite element results is insufficient.

15 Geometrically and Physically Nonlinear FEA

In Chapter 14, the influence of initial geometrical imperfections on the load-carrying capacity of a hemispherical shell subjected to uniform spherical or vertical load is investigated by performing a geometrically nonlinear analysis. However, in reality, the matter is further complicated by the highly nonlinear material characteristics of (fibre) reinforced concrete, i.e. compressive crushing, tensile cracking and yielding of reinforcement/continuous fibre pull-out. In this chapter material nonlinearity is also taken into consideration and, hence, there is referred to a geometrically and physically nonlinear finite element analysis.

Similar to Chapter 10, 12, 13 and 14, the Zeiss planetarium shell is the given hemispherical shape. To investigate the additional effect of material nonlinearity on the structural behaviour as found in Chapter 14, the previously described finite element model is modified with a so-called material model, which contains the properties and characteristics of the mixture designs defined in Chapter 8. Material models were previously discussed in Chapter 11. Based on the observations done by Burgers [20] the material is modelled using the total strain concept with a rotating crack approach. The nonlinearity of concrete is confined to crushing and cracking and (fibre) reinforcement characteristics. Long term effects as shrinkage and creep and ambient influences as temperature, concentration or maturity are not taken into consideration. In fact, these effects cannot be included into the total strain modelling concept.

The finite element analyses are restricted to the three-dimensional shell model as asymmetric behaviour may occur. To verify the finite element results, the results are compared to the theory and IASS Recommendations as described in Chapter 6.

15.1 Shell Parameters

15.1.1 Geometry

See Chapter 12.1.1.

15.1.2 Initial Geometrical Imperfections

See Chapter 14.1.2.

15.1.3 Material Modelling

Aforementioned, based on the observations done by Burgers [20] the material is modelled using the total strain concept with a rotating crack approach. Thus, the material properties and characteristics are described within one constitutive law. The modelling of the conventional mix and the UHPFRC mix is discussed separately.

UHPFRC C180/210

The properties of C180/210 are discussed in Chapter 8.2 and summarised in Table 8.7 and 8.8. Due to the addition of fibres, the composite mixture loaded in tension will behave like an isotropic material, which means that the structural behaviour can be captured in a single constitutive law. The axial tensile behaviour is presented in Figure 8.18. According to the French codes, this behaviour can be approximated by a multi-linear stress-strain law. To obtain a constitutive relation (stress-strain) from a stress-crack relation of Figure 8.18, so-called fracture energy regularisation must be used to prevent crackwidths related to the element size, previously discussed in Chapter 11. Recapitulate from Chapter 11, equation (11.66):

$$\varepsilon_{nn}^{cr} = \frac{w}{h_c} \tag{11.66}$$

For higher-order plane stress elements (as used) DIANA suggests the relation $h_c = \sqrt{A}$, with A the average element area which can simply be calculated by dividing the total shell surface area ($\frac{1}{2} \cdot 4\pi R^2 = 981.7\, m^2$) through the number of elements (7168). Doing so:

$$h_c = \sqrt{\frac{981.7 \cdot 10^6}{7168}} \approx 370$$

Thus, to obtain the crack strains from the crack width, the crack width must be divided through 370.

In the graph of Figure 8.18, the stress at crackwidth *2 mm* is not defined, however, the fracture energy of the postcracking stage is equal to *20 N/mm*. Hence, using a bilinear postcracking graph with strains determined according to fracture energy regularisation, the point can be calculated and yields *2 MPa*.

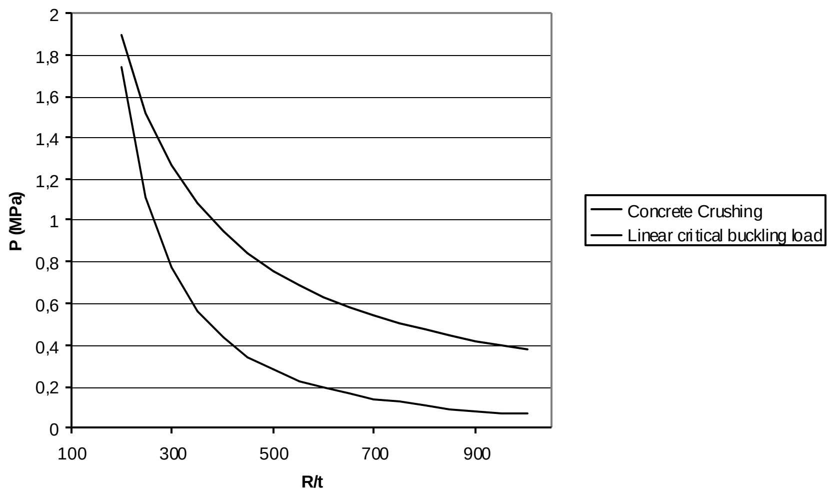

Figure 15.1. Comparison between compressive crushing of UHPFRC with a mean value cylinder strength of 190 MPa and the linear critical buckling load as obtained by Zoëlly

The compressive behaviour is illustrated in Figure 8.17. It can be seen that the Thorenfeldt curve behaves almost linear up to compressive crushing. Moreover, if the maximum applicable load is plotted against the linear critical buckling load, Figure 15.1, it can be seen that buckling prevails over crushing, at least within the range of $200 \leq R/t \geq 1000$. Hence, the crushing strength is not reached and the concrete can be modelled as infinite elastic in compression, obtaining a much simpler constitutive law.

In Figure 15.2, the complete stress-strain relationship for the UHPFRC mixture that is modelled in a total strain rotating crack model for the nonlinear finite element analysis is seen.

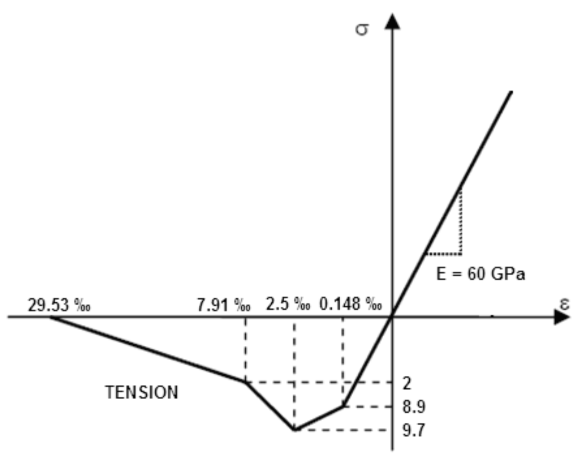

Figure 15.2. Stress-strain relationship for UHPFRC as used in the nonlinear finite element analysis

Conventional C20/25

The conventional mix properties are discussed in Chapter 8.1 and summarised in Table 8.1 and 8.2. It was argued that the non-isotropic behaviour of plain reinforced concrete in tension, caused by crack development in a few wide cracks and redistribution of tensile stresses from concrete to bonded reinforcement, makes it impossible to capture the structural behaviour in a single constitutive law. However, as shells are low reinforced structures and the quality of the rebars is assumed to be low (Table 8.2), a serviceability approach is suggested by the author.

In Figure 8.5 it can be seen that, for axial tension, the low quality and percentage of reinforcement results in only a small increase of axial tensile forces after crack initiation. Therefore, it is proposed to neglect the effect of reinforcement and to model the axial tensile behaviour with a bilinear law. The bilinear law is defined by a linear branch up to the axial tensile strength with an inclination determined by the Young's modulus, followed by a horizontal postcracking branch. The horizontal branch is implemented into the material model with a slightly negative inclination as DIANA evaluates crack initiation when the E-modulus becomes negative (see Chapter 11). The (almost) horizontal branch extends to strains of *30‰*, which is extremely large (according to the aforementioned fracture energy regularisation approach, *30‰* corresponds to cracks equal to *11 mm*). In the finite element results the serviceability limit state bounds the solution as at a certain moment the crack size violates the maximum crack size as dictated by the codes, discussed later.

In Chapter 7 it is defined that the reinforcement is located in the middle of the shell cross-section. In case of a flexural tensile stress situation, the reinforcement is not activated until a significant amount of cracking has occurred. Therefore, it is proposed to neglect the effect of reinforcement and to model the flexural tensile behaviour as brittle. Thus, the flexural tensile behaviour is modelled by a linear branch up to the axial tensile strength (with inclination equal to the Young's modulus) and after the axial tensile strength is reached the graph instantly returns to zero. Again, in the finite element results the serviceability limit state bounds the solution as at a certain moment the crack size violates the maximum crack size as dictated by the codes. The axial and flexural tensile models are seen in Figure 15.3.

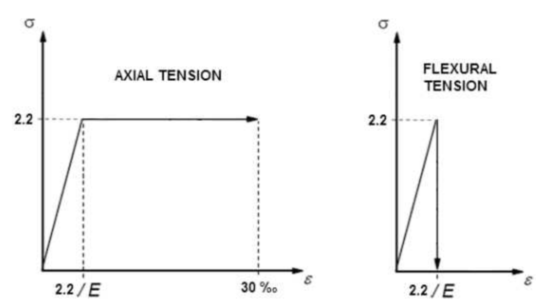

Figure 15.3. Axial and flexural tensile behaviour as implemented into the material model

Obviously, it is not possible to perform an analysis with two tensile relations implemented in the finite element model. Therefore, the decisive failure mechanism needs to be determined in advance.

The compression branch is modelled by a Thorenfeldt curve. To include effects of biaxial compression, lateral confinement is incorporated according to the relation of Selby and Vecchio (see Figure 11.31).

15.1.4 Boundary Conditions

See Chapter 12.1.3.

15.1.5 Loading

See Chapter 14.1.5.

15.1.6 Analysis Scheme

The different types of analysis are presented in Table 15.1. Each analysis is combined with the imperfections tabulated in Table 14.1.

Name	Loading Conditions	Supporting Conditions	Type of Analysis	Model
Zeiss 1	Spherical and Vertical	Roller	Geometrical and physical nonlinear	3D
Zeiss 2	Spherical and Vertical	Inclined-roller	Geometrical and physical nonlinear	3D
Zeiss 3	Spherical and Vertical	Hinged	Geometrical and physical nonlinear	3D
Zeiss 4	Spherical and Vertical	Clamped	Geometrical and physical nonlinear	3D

Table 15.1. Analysis scheme

15.1.7 FEA Settings

Similar to Chapter 14, the geometrically nonlinear analysis is based on a Total Lagrange formulation, Green strains and Second Piola-Kirchhoff stresses. Physical nonlinearities are incorporated by the restrictions and constitutive formulation described in the material model. To obtain a more accurate stress distribution in thickness direction, the number of integration points in thickness direction is changed to a *7-point* Simpson integration scheme. Similar to Chapter 14, the selected incremental-iterative procedure is a Regular Newton-Raphson scheme combined with a spherical path arc-Length control which is, in turn, modified with an indirect displacement control on the top node in the negative vertical direction. For convergence both the displacement and the force norm must be satisfied. During analyses the user specified arc-length controlled step sizes are varied in order to pass the limit point and to find as many points of the adjacent postbuckling equilibrium path as possible.

15.2 Results UHPFRC Shell under Spherical Load

Similar to Chapter 14, first the basic (sphere under radial pressure) shell type is investigated, the Zeiss 2 (inclined-roller) shell subjected to a spherical pressure load in combination with an each time increasing top imperfection amplitude. Afterwards the influence of different boundary conditions is discussed. In Section 15.3, the UHPFRC shell under uniform vertical load is discussed.

15.2.1 Zeiss 2

The C180/210 Zeiss 2 shell, subjected to spherical load with increasing top imperfection amplitude and increasing *R/t ratio* is considered first. The deformations of the shells are similar to the deformations seen in Chapter 14 (Figure 14.2 and 14.3). Hence, due to the introduction of material nonlinearities, the shell eventually will fail by surpassing the flexural tensile strength. The fully nonlinear response of the Zeiss 2 shell is illustrated by load-displacement curves, stresses and bending moments and, off course, crack plots.

Load-displacement relation

The top node load-displacement (*MPa*)-(*mm*) relation for a (cracked) inclined-roller supported C180/210 shell with *R/t ratio* equal to *400* and increasing top imperfection amplitude is presented in Figure 15.4. In the graphs, the point of crack initiation is marked with a black spot. The final step of each of the load-displacement curves is questionable as the analyses failed in finding convergence in the next step.

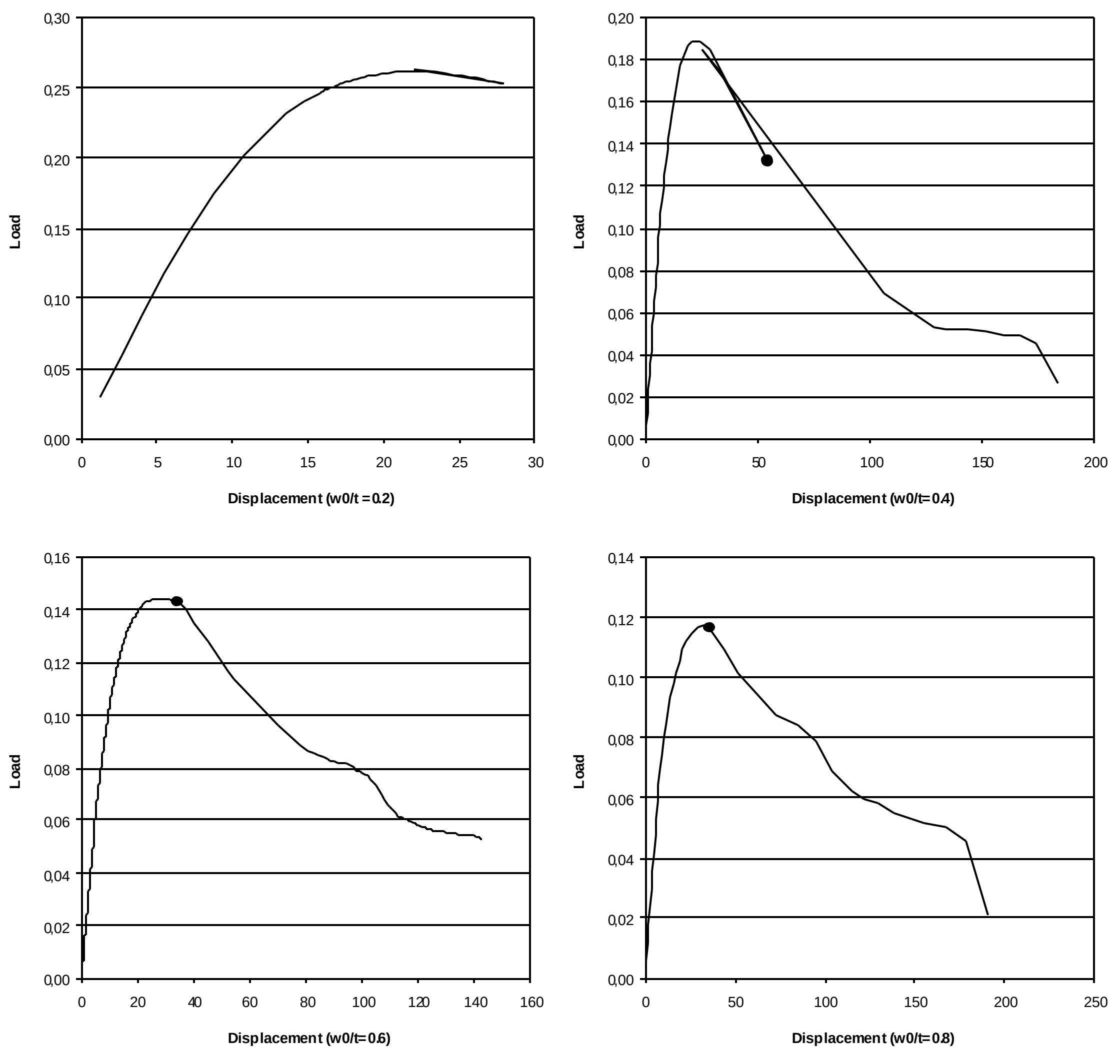

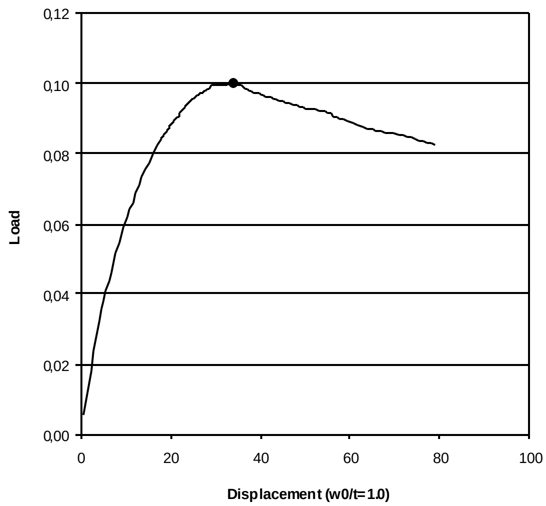

Figure 15.4. Typical top node load-displacement curves for a (cracked) inclined-roller supported C180/210 shell with an R/t ratio of 400 and increasing top imperfection amplitude ranging from 0.2 to 1.0 subjected to spherical load

From Figure 15.4 several observations can be made. First of all, it can be seen that, similar to Chapter 14, increasing imperfection amplitudes cause a further decreasing critical load, which occurs approximately at a deformation of *20* to *30 mm*. It can be seen that cracking is not present for a small imperfection amplitude of $w_o/t = 0.2$. This can be explained by the fact that the compression stresses in the shell do not allow for tensile stresses to develop (yet) and the buckling is dominant, similar to Chapter 14. Hence, the same critical load is found. When the imperfection amplitude is equal to $w_o/t = 0.4$ cracking initiates after the limit point. However, the maximum critical load is lower than obtained for the same shell in Chapter 14, caused by the fact that the C180/210 losses linearity and experiences strain hardening after the linear branch, seen in Figure 8.18. Although the material is able to stay uncracked (at least for macro cracking, see Chapter 8), the stiffness reduces significantly causing a reduced load-displacement curve. The strange forward-and-backward-step behaviour of the graph just after the limit point may be explained as a numerical self-correcting procedure caused by lack of convergence in successive steps of the first selected equilibrium direction. For imperfection amplitudes of $w_o/t = 0.6$ and *0.8,* the point of crack initiation is close to the critical load and, thus, the additional decrease in compare to Chapter 14 is caused by the loss of linearity in tension. At an imperfection equal to $w_o/t = 1.0$, the cracking coincides with the maximum critical load and a combination of buckling, softening by loss of linearity and cracking may said to be decisive; plastic buckling. With respect to the postbuckling path, it can be seen that there are 'bumps' indicating stiffness variations. The bumps are related to the crack propagation process, i.e. weakening (and redistribution) due to local loss of linearity, initiation of new cracks, closing and re-opening of old cracks, change in principal crack direction and the transition towards the low level postcracking plateau, characteristic for fibre reinforced concrete.

Effect of increasing imperfection amplitude

The influence of loss of linearity and cracking in the tensile regime on the load carrying capacity can be plotted against an increasing imperfection amplitude as is done in Figure 15.5. As a reference the curve previously obtained in Chapter 14 (Figure 14.7) is plotted in the same graph. From Figure 15.5 it can be concluded that with increasing imperfection amplitude the influence of material nonlinearity becomes larger. Obviously, this makes sense, as it was observed in Figure 15.4 that the effects of loss of linearity and cracking became more and more important with increasing top imperfection amplitude. It can also be seen that the 'cracked' shell experiences a maximum decrease in load carrying capacity up to *23%* of the linear critical buckling load. Hence, cracking leads to an additional decrease of approximately *9%* which means a cracking factor equal to *0.72* and a total knock-down factor of *0.23*. For imperfection amplitudes $w_o/t = 0.4$, *0.6* and *0.8* the differences are *2.2*, *3.4* and *5.4%*, respectively.

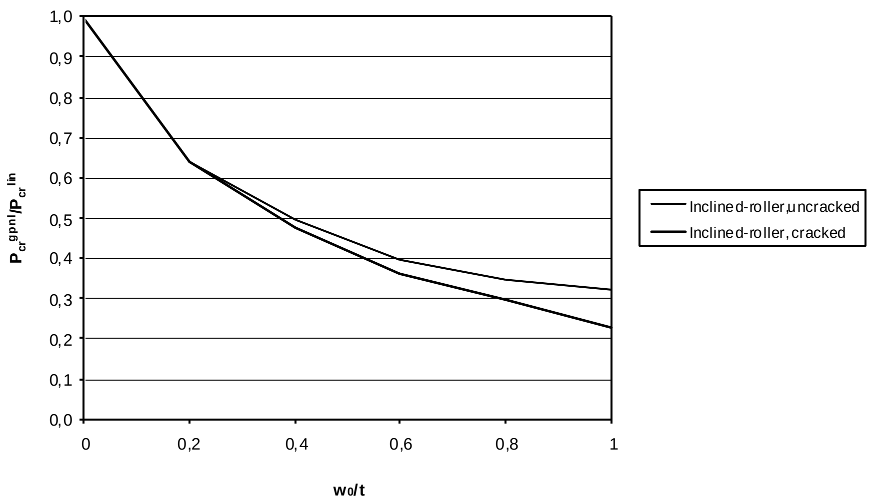

Figure 15.5. Effect of initial geometrical imperfections and cracking on the critical load for hemispherical C180/210 shell with top imperfection subjected to spherical load for an R/t ratio equal to 400

Stresses and bending moments

The stresses and bending moments of an imperfect shell subjected to radial pressure load are seen in Figure 14.6. Opposite to the results of Chapter 14, this time the tensile and compressive stresses are bounded by crushing and cracking.

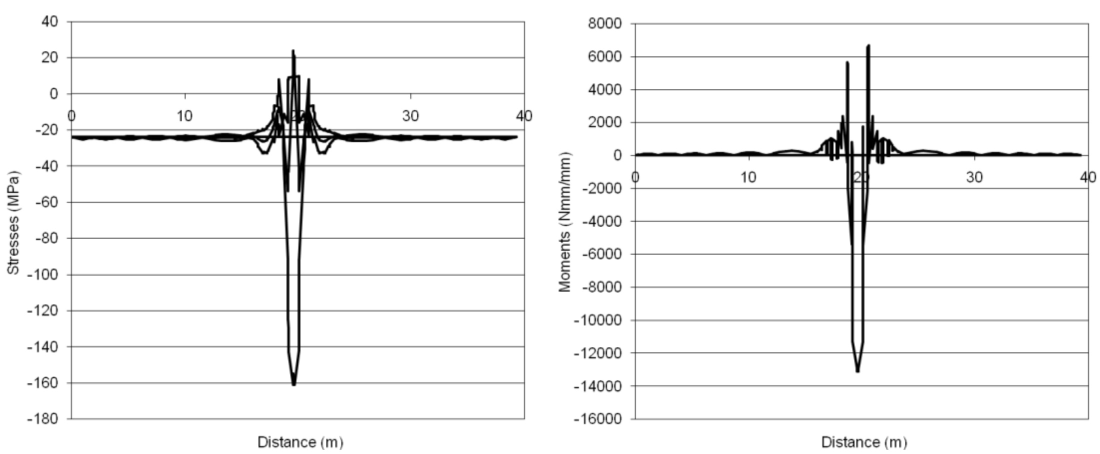

Figure 15.6. Typical nodal stress and bending moment distributions in a hemispherical shell subjected to radial pressure at the point of crack initiation for a shell with R/t = 400 and w_o/t =0.8

In Figure 15.6 typical stress and bending moment distributions at the point of crack initiation are shown for a C180/210 hemispherical shell with inclined-roller support subjected to radial pressure load. They are much similar to the distribution graphs of Chapter 14, although the tensile stress peak is cut-off and the compressive stresses are approximately *8* times higher than the tensile stresses. Hence, a nonlinear stress distribution appears over the shell cross-section, similar to Figure 8.19. It can be seen that the compressive crushing strength of the C180/210 mixture for the given shell is not violated, as assumed before when modelling the structural behaviour of the UHPFRC mixture. Furthermore, it can be seen that crack initiation is accompanied by maximum nodal tensile stresses equal to *23.4 MPa*. The averaged stress is *11.7 MPa* and the maximum stress in the integration points is *9.7 MPa*, which indicates the difference that is introduced by stress mapping from the integration points to the nodes. Based on the tensile stresses, it can be concluded that the high flexural strengths claimed by the companies of Ductal and BSI are not reached (see Chapter 8).

Cracking

Typical crack initiation and crack propagation for a hemispherical shell under radial pressure load with a local top imperfection is seen in Figure 15.7 and 15.8. In Figure 15.7 the cracking development for the inner surface is illustrated by an arbitrary series of crack patterns. In Figure 15.8 the cracks that appear in the outer surface of the shell are shown.

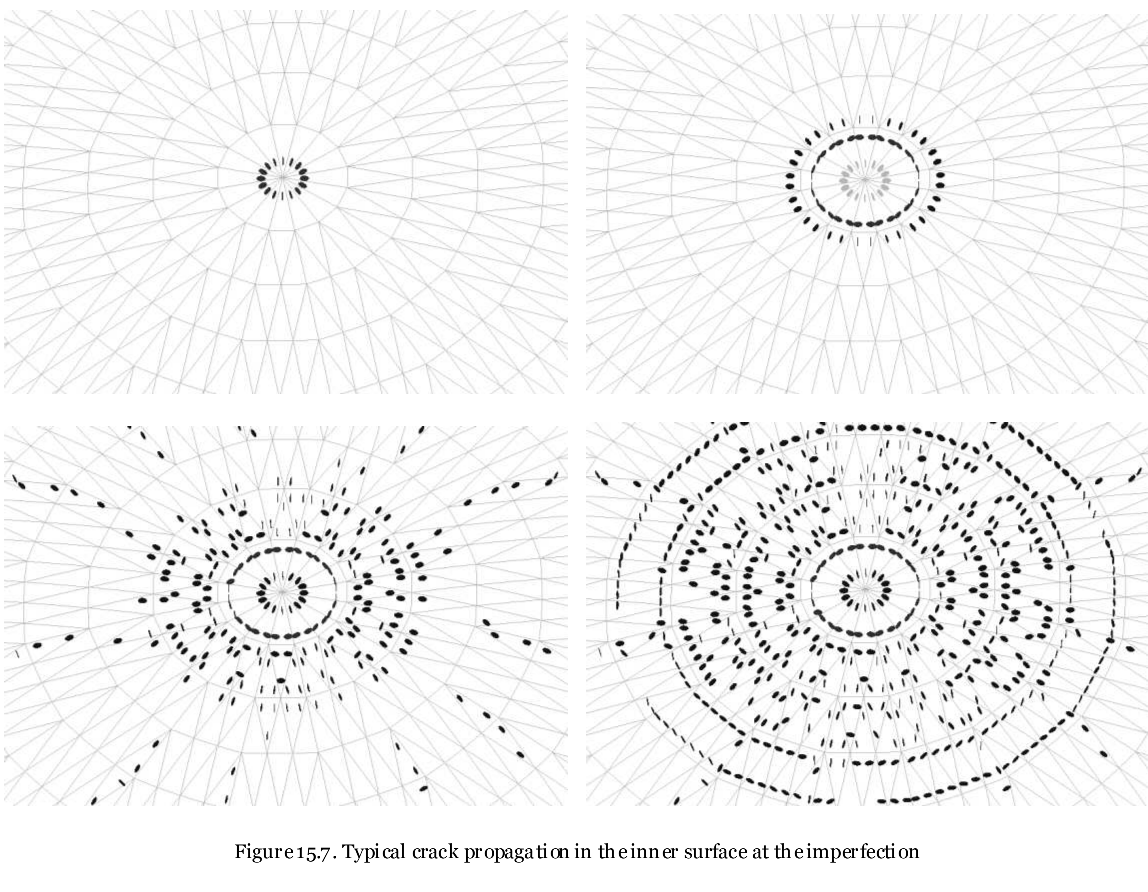

Figure 15.7. Typical crack propagation in the inner surface at the imperfection

In Figure 15.7 the crack pattern at steps *21*, *28*, *49* and *59* of a particular analysis are presented. More important are the corresponding sizes of the cracks that appear. The crackwidth can be determined by examination of the crack strain and transform them to crackwidths by reversing relation (11.66), thus using the average element size. The maximum crack strains (red discs) that correspond to the steps presented in Figure 15.7 are *0.00284*, *0.0135*, *0.0928* and *0.404*, respectively. The corresponding maximum crackwidths are *1.1 mm*, *5.0 mm*, *34.3 mm* and *149.5 mm*. Obviously, these cracks far exceed the stress-strain diagram and serviceability limits.

During buckling the shell does not only crack at the inner surface, but also on the outer surface. The outer surface cracks at step 28, 34 and 51 are presented in Figure 15.8. Thus, the left crack pattern of Figure 15.8 corresponds to the upper right crack pattern of Figure 15.7. The correlating crackwidths are *0.97 mm*, *1.57 mm* and *39.22 mm*. The latter cracks are so large that the structure is disqualified on serviceability demands.

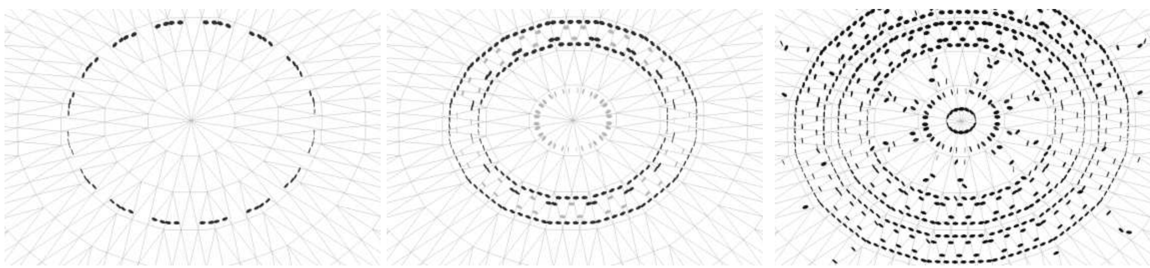

Figure 15.8. Typical crack propagation in the outer surface in the region of the imperfection

After a close inspection of the crack patterns, one may notice that some cracks (discs) change direction in successive crack steps. Apparently, this is originated in the selected total strain rotating crack concept.

Different R/t ratios

The load-displacement curves as presented in Figure 15.4 and the effect of initial imperfections and cracking as illustrated in Figure 15.5 are valid for spherical loaded inclined-roller supported hemispherical shells with an *R/t ratio* equal to *400*. For other *R/t ratios* the effect of cracking may be different as the point of crack initiation varies depending on the ratio of membrane over bending behaviour (i.e. is the shell closer to membrane dominant behaviour or bending dominant behaviour). Aforementioned in Chapter 3, the preference for membrane or bending behaviour is governed by the radius to thickness ratio of the shell. Thinner shells behave more like membranes than thicker shells. Consequently, for thicker shells than the one of Figure 15.4 (*R/t = 400*) the point of crack initiation moves to the prebuckling stage while for thinner shells the effect of cracking becomes less important for the maximum critical load as the point of cracking moves further away from the limit point. This phenomenon is illustrated in Figure 15.9, the load-displacement curves of the top node. Due to the point of cracking (and the point of loss of linearity in the tension relation) the critical load varies. For an *R/t ratio* of *400*, *600*, *800* and *1000*, the maximum critical load at maximum imperfection amplitude is as low as *23%*, *24%*, *25%* and *33%* of the linear critical buckling load, respectively. For the *R/t ratio* equal to *1000*, the maximum critical load is similar to the one found in Chapter 14. Hence, the possible occurrence of cracking does not influence the maximum load carrying capacity which is solely determined by buckling instability. This may also lead to the conclusion that the critical load of even thinner shells (*R/t ratios > 1000*) is not influenced by possible cracking.

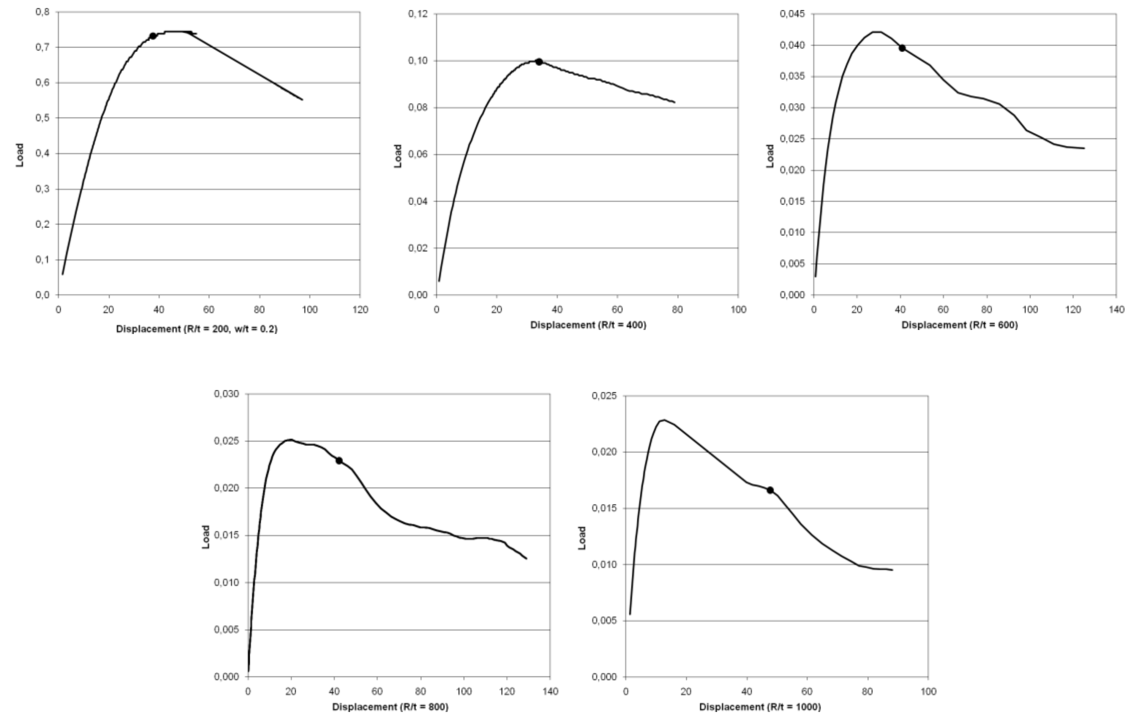

Figure 15.9. The effect of the R/t ratio on the maximum critical load and cracking behaviour in a typical top node load-displacement curve of a hemispherel loaded by radial pressure with a local top imperfection equal to 0.4 the shell thickness (for R/t = 200) or equal to the thickness of the shell

For the shell with an *R/t ratio* of *200*, no analyses could be made for imperfection amplitudes $w_o/t > 0.4$ as modelling errors were encountered (out-of-tolerance radius errors between adjacent nodes). Therefore, in Figure 15.9, imperfection amplitude $w_o/t = 0.4$ is plotted for the shell with an *R/t ratio* equal to *200*. However, the phenomenon still can be seen if the graph is compared to the graph of Figure 15.4 for the same imperfection amplitude. In can be seen that, opposite to the *R/t = 400* shell, in which the point of crack initiation was far from the limit point, the point of cracking in the *R/t = 200* shell is before the limit point and, thus, has major influence on the maximum critical load. The cracking causes the graph of Figure 15.5 to lower approximately *2%* at the imperfection amplitude $w_o/t = 0.4$. When the graphs of *R/t = 400* and *R/t = 800* (shell thickness is twice as thin) are compared an increase of *2%* is observed. If the same difference occurs between the *R/t = 400* and *R/t = 200* shell, the maximum critical load may approach *19-21%* of the linear critical buckling load.In Figure 15.10 the influence of a local initial geometrical imperfection at the top of the shell on the load carrying capacity is illustrated for several *R/t ratios*. The order of the curves follows the order of the list right of the figure. Hereby, the curve for *R/t = 1000* coincides with the uncracked curve as the shell does not experience an additional decrease due to material nonlinearity. It can be seen that the curves are very close to each other, indicating the small effect of cracking in compare to the effect of buckling in combination with an initial imperfection. The curve for *R/t = 200* stops at $w_o/t = 0.4$. Aforementioned, further results could not be obtained due to out-of-tolerance errors of the finite element model.

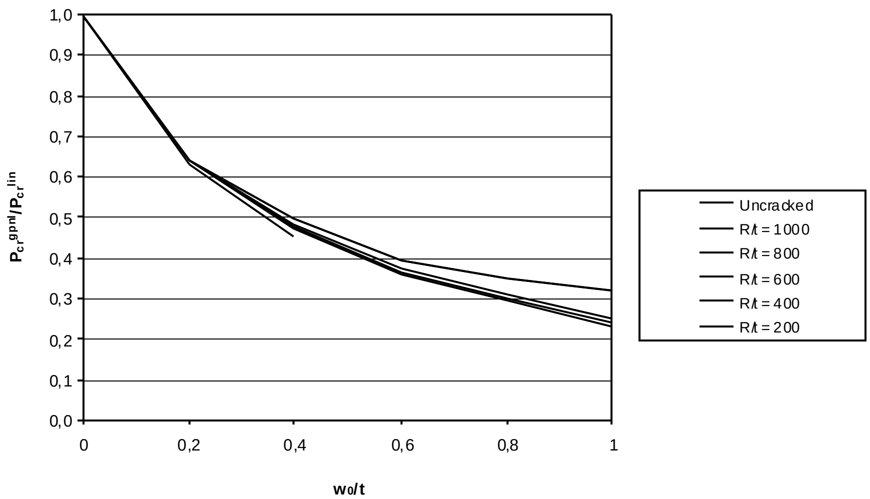

Figure 15.10. Influence of increasing imperfection amplitude on a cracked C180/210 hemispherical shell with inclined-roller support and top imperfection subjected to spherical load for several R/t ratios

15.2.2 Zeiss 1, 3 and 4

Similar to Chapter 14, the influence of different types of support is investigated. Besides the inclined-roller support (Section 15.2.1) the shell is also modelled with a roller, hinged and clamped support. Because there is only referred to a spherical load on a hemispherical shell, the expected result can simply be obtained from Figure 14.11. In Figure 15.11 the influence of various support conditions for a hemisphere subjected to radial pressure load with increasing top imperfection amplitude is visualised.

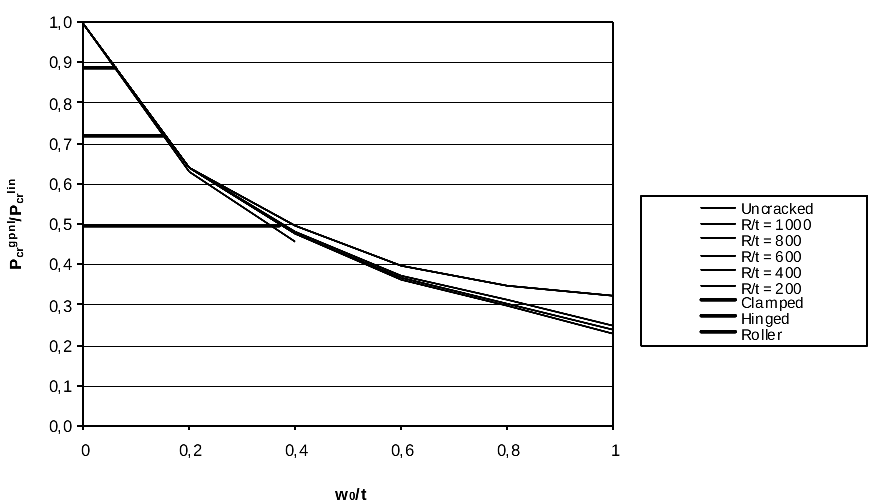

Figure 15.11. Effect of initial geometrical imperfections and cracking on the critical load for hemispherical C180/210 shell with top imperfection subjected to spherical load for several R/t ratios and support conditions

From Figure 15.11 it can be concluded that the boundary conditions only have influence on the critical load for imperfection amplitudes $w_o/t < 0.4$. In that region the edge disturbances caused by restrain deformation at the support are dominant over the effects of a local top imperfection. For imperfection amplitudes $w_o/t \geq 0.4$ buckling takes place inside the shell surface independent of the boundary conditions.

15.3 Results UHPFRC Shell under Vertical Load

In Chapter 14 it was discovered that the UHPFRC shell under vertical load may experience shell-like postbuckling behaviour or a buckling behaviour without a sudden decrease in load carrying capacity after the bifurcation point, depending on the imperfection amplitude. It can be seen in Figure 14.11 that for $w_o/t \geq 0.6$ the shell experiences shell-like buckling, except for the vertical loaded shell with roller support which appeared to be insensitive to any local top imperfection (at least within the range of the research). If cracking is introduced, the vertical loaded shell may fail due to surpassing the axial tensile strength or, in case of shell-like buckling in the shell surface, due to surpassing the flexural tensile strength.

15.3.1 Zeiss 1, 2, 3 and 4

Similar to Section 15.2, the fully nonlinear response of the vertical loaded shells is illustrated by load-displacement curves, stresses and bending moments and crack plots.

Load-displacement relation

To determine whether the shell experiences shell-like buckling, the analyses involving vertical loaded shells are performed for all support conditions with maximum imperfection amplitude. From the analyses it can be concluded that the shell, by definition, fails due to surpassing the axial tensile stress of the C180/210 in the boundary layer (major part) after which buckling occurs, as can be seen in Figure 15.12.

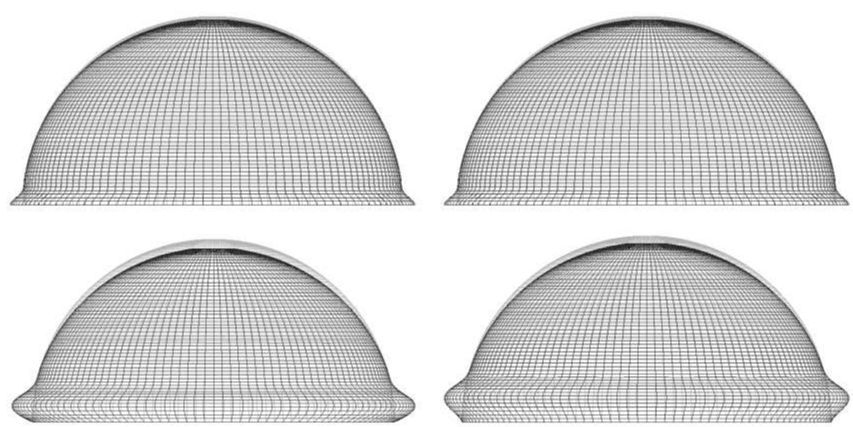

Figure 15.12. Typical deformed shapes of cracked hemispherical shells with varying support condition subjected to vertical load

The resulting load-displacement (*MPa*)-(*mm*) relations of the top node for a cracked C180/210 shell with *R/t ratio* equal to *400* and varying supports are presented in Figure 15.13. Crack initiation is marked with a black spot. From the load-displacement curves in Figure 15.13 it can be seen that the finite element analysis encounters difficulties in finding convergence when the shell starts to crack. By definition, the final step of each load-displacement curve is questionable as the analyses fails in finding convergence in the next step. The results of an analysis on a roller supported shell show a load-displacement curve which experiences a fall-back after which cracks appear. The process is reversed for the inclined-roller shell. For the hinged and clamped supported shell, the finite element procedure was unable to find any convergence after crack initiation. Obviously, the step size is rather large and better results may be obtained with smaller steps. Based on Figure 15.12 and 15.13, it can be concluded that the shell experiences the same type of buckling as illustrated in the right graph of Figure 14.1. Hence, the results of the roller graph are misleading.

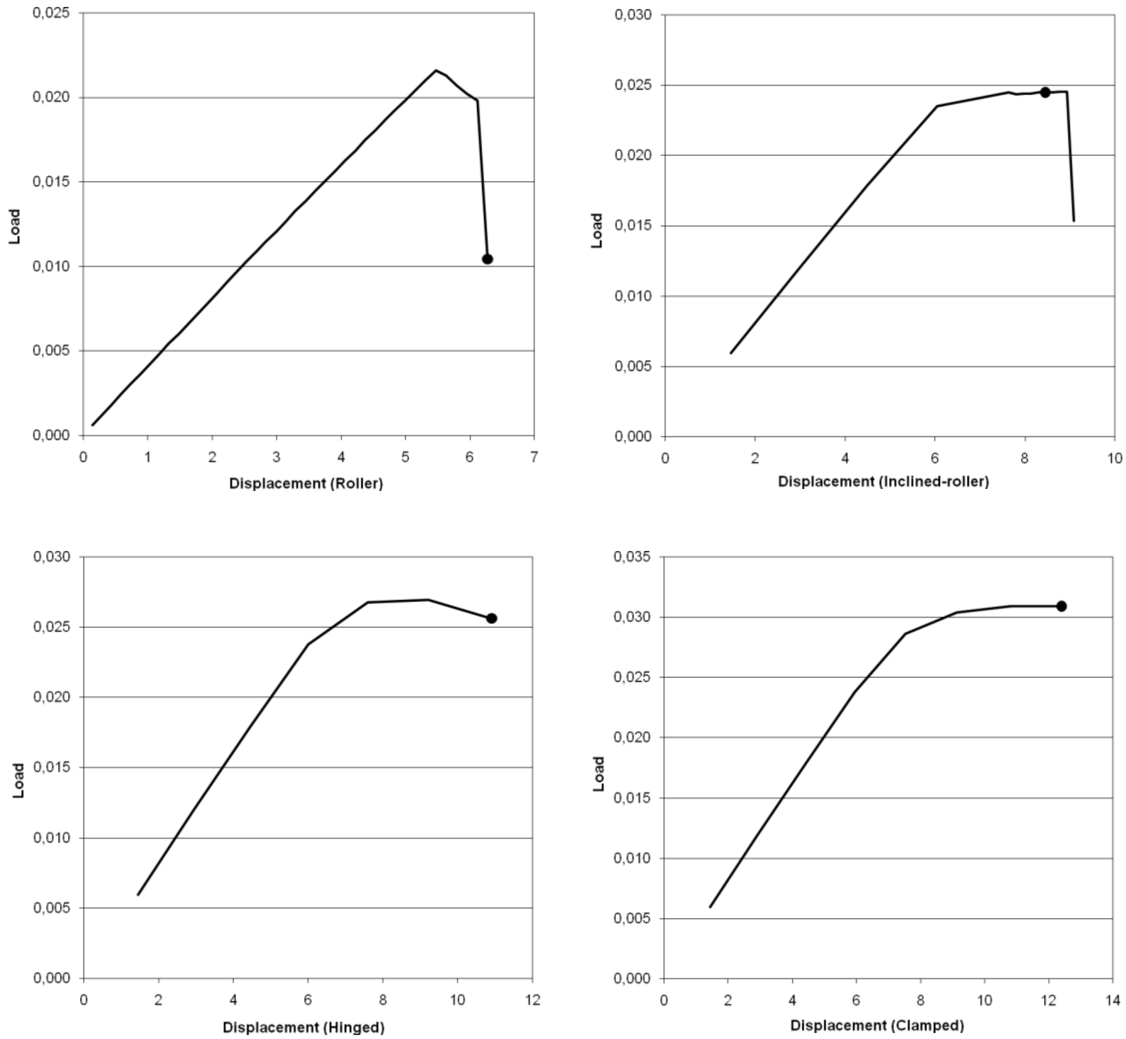

Figure 15.13. Typical top node load-displacement curves for several support conditions for a hemisphere subjected to uniform vertical load with an R/t ratio equal to 400 and a local top imperfection amplitude equal to the shell thickness

In Figure 15.13 it can be seen that the shells with different types of supports approximately fail at the same magnitude of external applied vertical load. The deformations at the point of maximum critical load are significantly different. The roller supported shell fails already at a deformation of *5.5 mm*, the inclined-roller and hinged shell fail approximately at *8 mm* and the clamped shell fails at *12 mm*.

The critical loads are tabulated in Table 15.2. As expected, based on the linear stress distribution of the circumferential stresses as seen in the figures of Chapter 12, the clamped support yields the maximum allowable load equal to *0.0309 MPa (= 30.9 kN/m²)*.

Name	P_{cr}^{gpnl} (MPa)
Zeiss 1	0.0216
Zeiss 2	0.0245
Zeiss 3	0.0269
Zeiss 4	0.0309

Table 15.2. Critical load for hemispherical C180/210 shell with R/t = 400 subjected to uniform vertical load

The load-carrying capacity is compared to the linear critical buckling load of a spherical shell under radial pressure as defined in Chapter 6 in Table 15.3. Moreover, in Table 15.3, the results are compared to the buckling loads found in Chapter 13 for the same shells (for which buckling did occur due to the assumption of linear elastic material behaviour). When compared to the results of Chapter 6 and Chapter 13, it can be said that the introduction of cracking lowers the critical load drastically.

Name	$P_{cr}^{gpnl}/P_{cr}^{lin,\ equation\ (6.63)}$	$P_{cr}^{gpnl}/P_{cr}^{lin,\ chapter\ 13}$
Zeiss 1	5.4%	21.4%
Zeiss 2	6.2%	11.0%
Zeiss 3	6.8%	16.4%
Zeiss 4	7.7%	12.7%

Table 15.3. Critical load for hemispherical C180/210 shell with R/t = 400 subjected to uniform vertical load

From Table 15.3 it can be observed that for hemispherical shells subjected to uniform vertical load, the introduction of material nonlinearities, which cause strength failure rather than buckling failure, lead to critical loads which are as low as *11%* of their linear critical buckling load and *5.4%* of the linear critical buckling load for spherical shell under radial pressure load.

Stresses and bending moments

In the stress distribution, the effect of reaching the axial tensile stress can be seen. When the stresses reach the axial tensile strength, the stresses are bounded and a horizontal plateau develops due to redistribution. The phenomenon is seen in Figure 15.14.

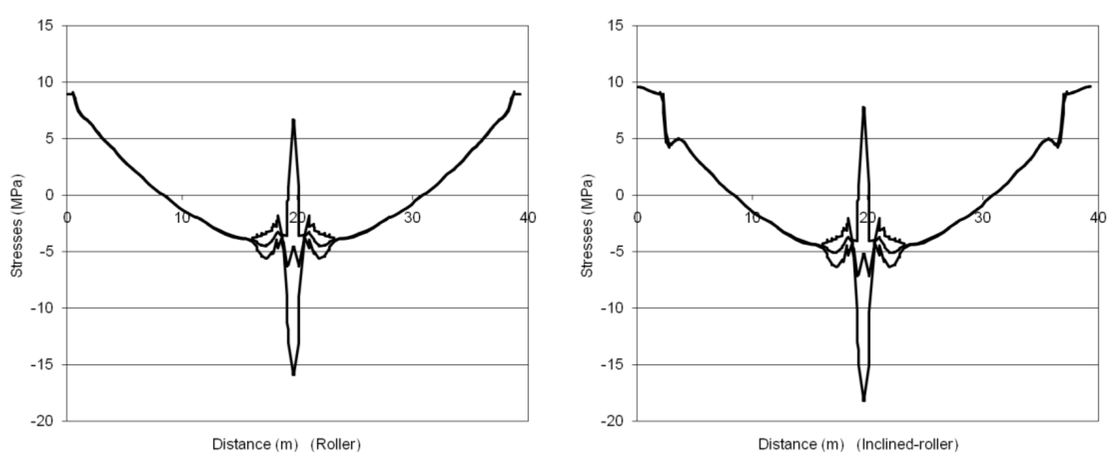

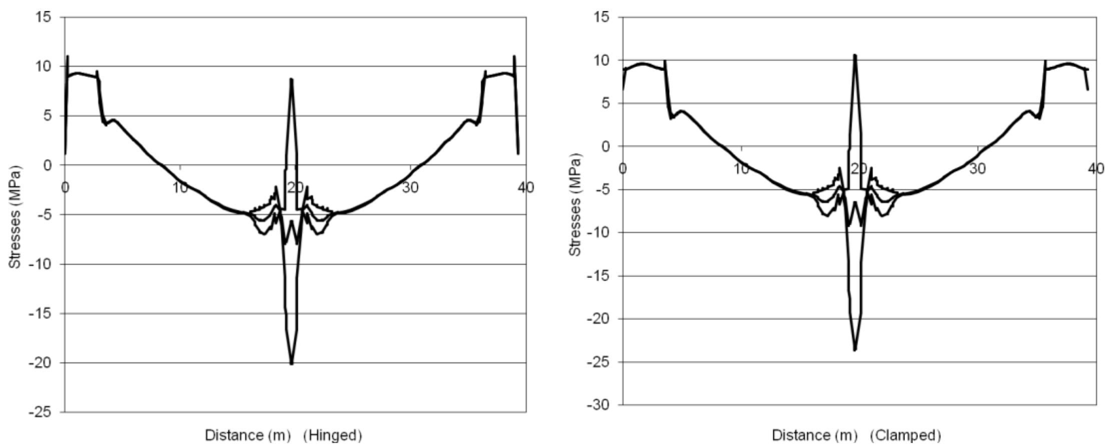

Figure 15.14. Stress distribution at crack initiation of a hemisphere with $R/t = 400$ under vertical load for several supports

Figure 15.14 presents the stress distribution at the point of crack initiation of a hemisphere with $R/t = 400$ subjected to uniform vertical load for all types of support conditions. In the figure it is observed that the axial tensile stresses slightly violate the axial tensile strength of $9.7\ MPa$ (Chapter 8). This is caused by the stress mapping. Furthermore, in Figure 15.14, the effect of the initial geometrical imperfection, which is equal to $w_0/t = 1.0$, is clearly seen given by the disturbances at the top of the shell. As the stress distribution over the cross-section at the imperfection is practically linear (tensile and compressive stresses show peaks of the equal size), there is no plastic deformation (cracking).

With respect to the bending moments, although not shown, it can be said that the distribution is (almost) similar to Figure 15.6. This is caused by the fact that the bending moments at the imperfection are far higher than the bending moments resulting from the so-called edge disturbance.

Cracking

For the vertical loaded shells, two types of crack patterns are observed, illustrated in Figure 15.15 and 15.16. In figure 15.15 two successive symmetrical crack scatters are shown, typical for the isotropic type of behaviour one would expect from fibre reinforced concrete. However, in the analysis of the Zeiss 2 shell another crack pattern appeared which demonstrates a few wide cracks (more like the behaviour of conventional reinforced structures), shown in Figure 15.16.

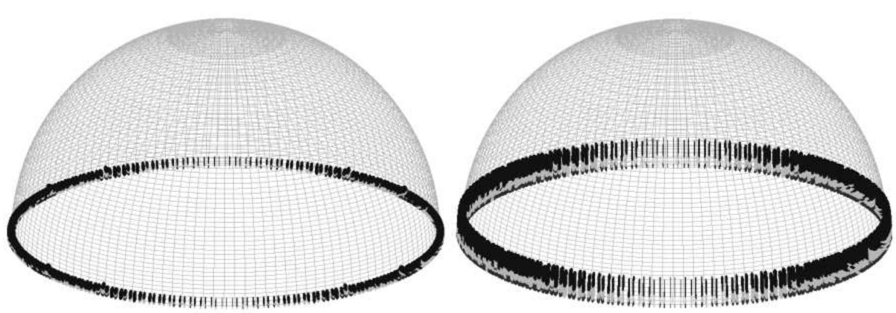

Figure 15.15. Typical crack scatter propagation in hemispherical shells subjected to vertical load

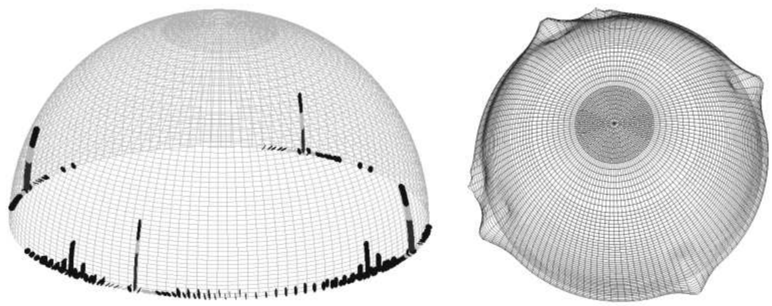

Figure 15.16. Inexplicable cracking with few wide cracks and corresponding deformed shell in hemispherical shell subjected to vertical load

In Figure 15.16 the occurrence of a few wide cracks is clear. Also the corresponding deformation of the shell is illustrated. The occurrence of a few wide cracks cannot be explained via the material model and, hence, must be originated in numerical disturbances.

Different R/t ratios

The observed structural behaviour appeared to be independent of *R/t ratios* between *200* and *1000*. However, it is seen that for a shell with *R/t = 1000*, the shell also cracks at the location of maximum imperfection amplitude, although, the largest crack strains and deformations are still located near the supports. The expectation is that for a certain (higher) *R/t ratio* the shell may fail by buckling inside the shell surface instead of failure by surpassing the axial tensile strength near the base radius. Based on the observation that the thickness appears linearly in the axial tensile strength equation but quadratically in the linear buckling equation the turning point may be more or less *R/t = 2333* (for the chosen material properties and the expectation that the critical load is approximately *32%* of the linear critical buckling load for *R/t ratios > 1000*, thus $R/t = 0.32 \cdot p_{cr}^{lin} \cdot (R/t)^2 / f_{ct2}$)

15.4 Results C20/25 Shell under Spherical Load

Similar to Section 15.2, first the basic shell type is investigated, the Zeiss 2 shell subjected to a spherical pressure load in combination with an each time increasing imperfection amplitude. Afterwards the influence of different boundary conditions is discussed. In Section 15.5, the C20/25 shell under uniform vertical load is discussed. In Section 15.2 it is found that the shell under spherical load fails due to surpassing the flexural tensile strength in the region of the local top imperfection. Therefore, the conventional reinforced concrete is modelled according to the right brittle relation of Figure 15.3.

15.4.1 Zeiss 2

The C20/25 Zeiss 2 shell, subjected to spherical load with increasing local top imperfection amplitude and increasing R/t ratio is considered first. The deformations of the shells are similar to the deformations seen in

Chapter 14 (Figure 14.2 and 14.3). The fully nonlinear response of the Zeiss 2 shell is illustrated by load-displacement curves, stresses and bending moments and crack plots.

Load-displacement relations

In Figure 15.17 the typical load-displacement curves for an inclined-roller C20/25 hemispherical shell with $R/t = 400$ subjected to spherical load are plotted for imperfection amplitudes ranging from $w_o/t = 0.2$ to $w_o/t = 1.0$. Crack initiation is marked with a black spot and, additionally, the point of compressive crushing is marked with a black square. Due to the low quality of concrete, concrete compressive crushing may be dominant for the maximum applicable load. The final step of the load-displacement curves is questionable as the analyses failed in finding convergence in the next step.

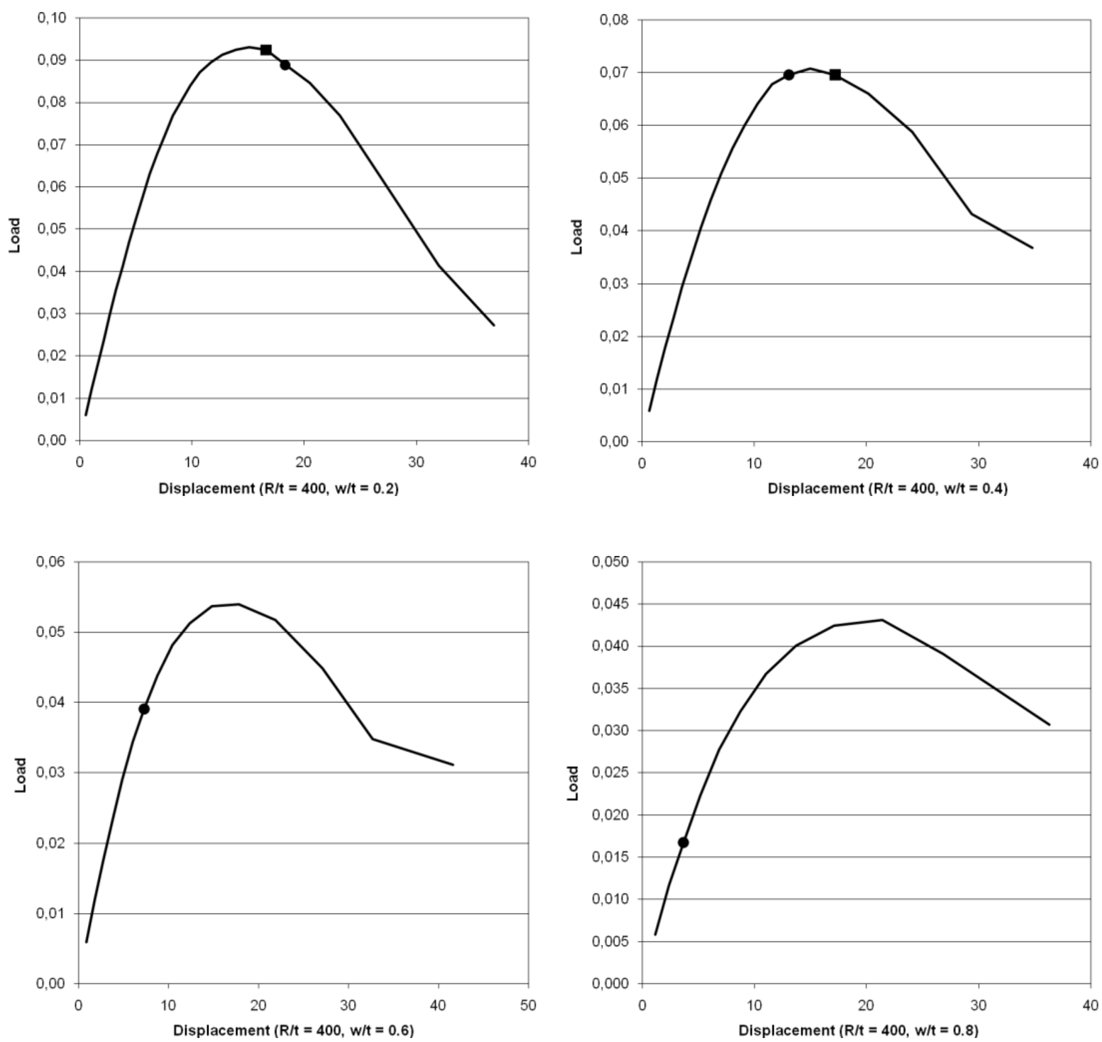

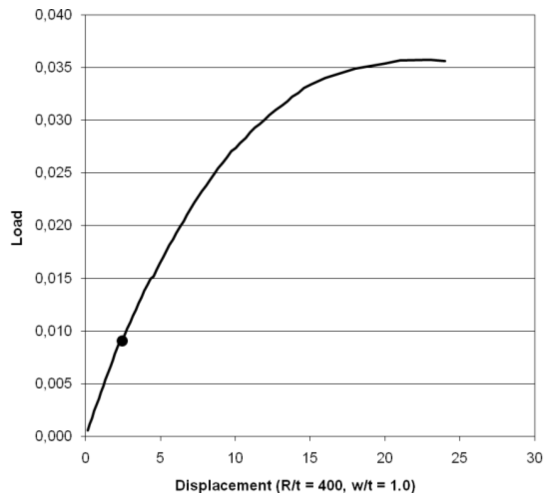

Figure 15.17. Typical top node load-displacement curves for a (cracked) inclined-roller supported C20/25 shell with an R/t ratio of 400 and increasing top imperfection amplitude ranging from 0.2 to 1.0 subjected to spherical load

It is found that for the given shell (*R/t = 400*) the effect of compressive crushing dominates over tensile cracking for an imperfection amplitude $w_o/t = 0.2$. This is seen in the upper left graph of Figure 15.17. Although the crushing initiates after the limit point, the maximum load is lower than the load of Chapter 14 as the Thorenfeldt compression curve shows a rounded stress-strain curve near the point of maximum compression strength (see Figure 8.4) and thereby contributes to the (dominating) effect of large deformations. For the given shell with *R/t = 400* and $w_o/t = 0.2$, the maximum load carrying capacity is approximately *46.6%* of the linear critical buckling load for a sphere subjected to radial pressure. This is significantly (*17.4%*) lower than the load which follows from Figure 14.7.

For an imperfection amplitude $w_o/t = 0.4$ the effects of cracking and crushing are reversed, although crushing still contribute to the decrease in load carrying capacity due to the aforementioned rounded Thorenfeldt curve. For imperfection amplitudes $w_o/t > 0.4$ the concrete crushing strength is not reached. With increasing imperfection amplitude, cracking initiates earlier in the load-displacement graph. Due to the phenomenon of redistribution the shell still experiences an increase in load carrying capacity after the first crack. Obviously the points of cracking and crushing are restricted for hemispherical shells with *R/t = 400*.

Stresses and bending moments

Typical nodal stress and bending moment distribution of an inclined-roller hemispherical C20/25 shell subjected to spherical load and a top imperfection $w_o/t = 0.2$ at the point of crushing and the point of cracking are visualised in Figure 15.18. When compared to Figure 15.6, it immediately can be seen that the stresses and bending moments are significantly lower, caused by the tensile and compressive limitations of the low quality concrete. Both upper graphs indicate the point of crushing. It can be seen that the maximum nodal compressive stresses are approximately *-36 MPa*, while the tensile stresses slightly exceed *5 MPa*. The averaged stresses are equal to *-28.0 MPa* and *4.1 MPa*. Hence, the positive effect of lateral confinement (incorporated according to the relation of Selby and Vecchio, Figure 11.31) seems negligible. Furthermore, it is observed that the axial tensile stress is violated but no cracking occurs. This can be contributed to the stress mapping operation from the integration points towards the nodes. Obviously, the stresses in the integration points do not violate the axial tensile strength.

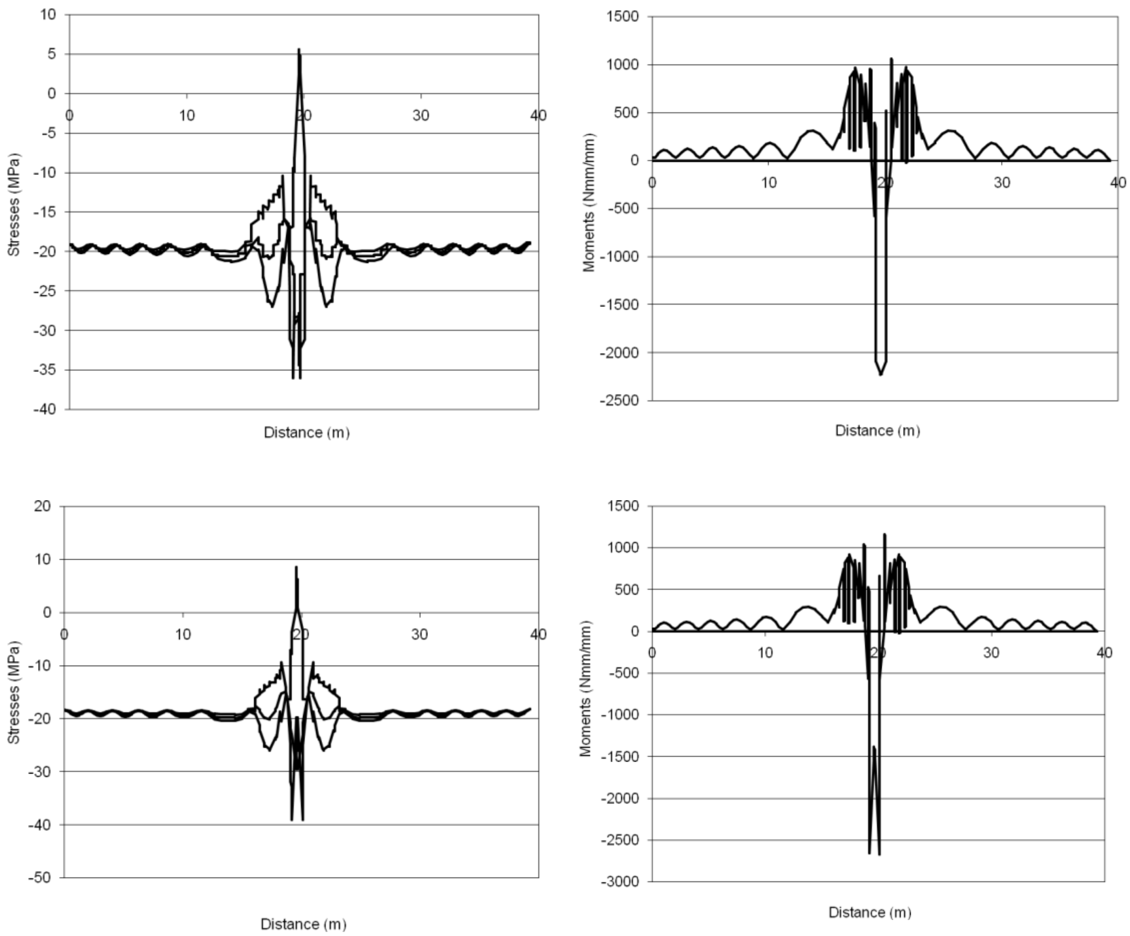

Figure 15.18. Typical nodal stress and bending moment distributions in a hemispherical shell subjected to radial pressure at the point of crushing (upper) and crack initiation (lower) for a shell with $R/t = 400$ and $w_o/t = 0.2$

The lower graphs of Figure 15.18 illustrate the point of crack initiation. It can be seen that the maximum nodal tensile stresses further increase to approximately *8.5 MPa* whereas the nodal compressive stresses increase up to almost *40 MPa*. The averaged stresses are, however, approximately *5.19 MPa* and *28.5 MPa*.

Effect of increasing imperfection amplitude

Similar to Section 15.2 the decrease in load carrying capacity can be plotted against the effect of increasing top imperfection amplitude. The result is seen in Figure 15.19. It can be seen that the effect of cracking leads to a significantly lower critical load which, additionally, is bounded by the crushing strength for imperfection amplitudes $w_o/t < 0.2$. The initial crushing path is a dotted line, as lateral confinement may lead to a higher crushing strength and, thus, a higher allowable critical load. Quantitatively, the decrease in load carrying capacity for $w_o/t > 0.2$ can in short be written as *46.6%, 35.5%, 27.1%, 21.6%* and *17.8%*. Hence, the difference at the maximum imperfection amplitude is equal to *14.2%* which means that the linear critical buckling load needs to be multiplied with a factor *0.556* to include the effects of tensile cracking. The total knock-down factor (large deformations, imperfections and cracking) for this particular shell with maximum imperfection amplitude, thus, becomes $0.556 \times 0.32 = 0.178$.

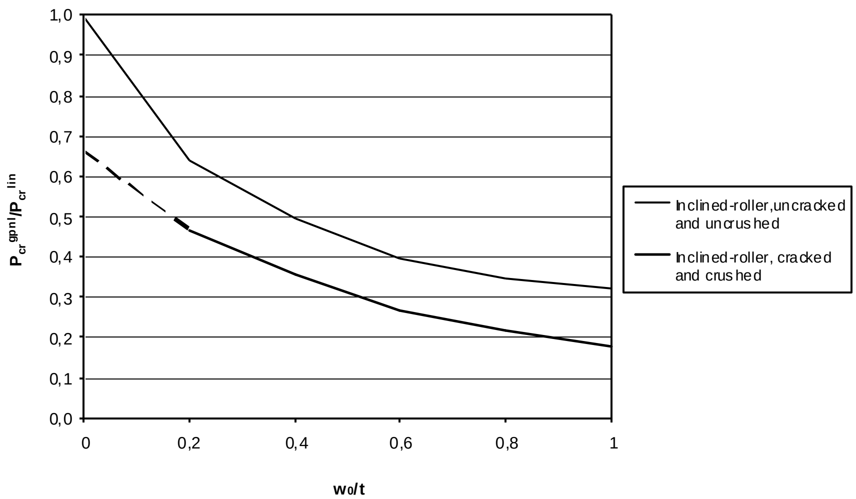

Figure 15.19. Effect of initial geometrical imperfections, cracking and crushing on the critical load for hemispherical C20/25 shell with top imperfection subjected to spherical load for an R/t ratio equal to 400

For the graph of Figure 15.19, it is assumed that the crushing strength limits the graph to a load which is equal to *66%* of the linear critical buckling load. For the given shell ($R/t = 400$, $E = 30$ *GPa* and $v = 0.2$) this equals the compressive strength of the shell (*-28 MPa*). Strangely enough the effect of cracking for higher imperfection amplitudes, which occurs more earlier in the load-displacement graph every time the imperfection is increased, does not has significant influence on the decrease in load-carrying capacity (stays approximately *13-14%*). Apparently, the effect of cracking, partly compensated for by the increase of internal lever arm, takes over the combined effect of loss of linearity and crushing in compression, leading to a maximum critical load caused by a combination of cracking and buckling.

Cracking

The cracks that appear in the C20/25 hemisphere show similar scatter as the cracks presented in Figure 15.7 and 15.8. Obviously, the crack strains are different. The crack strains are discussed later in Section 15.6.

Different R/t ratios

For thicker shells the point of cracking as well the point of crushing moves towards the prebuckling path and will become dominant for the load carrying capacity at a certain point. Thinner shells ($R/t > 600$) do not experience crushing at all, as can be seen in Figure 10.6, and the effect of cracking is much smaller. However, all shells fail due to buckling and crushing or due to buckling and cracking, opposite to Section 15.2 for which the thinnest shell ($R/t = 1000$) did not experienced a further decrease in critical load due to cracking. The load carrying capacity of different *R/t ratios* is visualised in Figure 15.20.

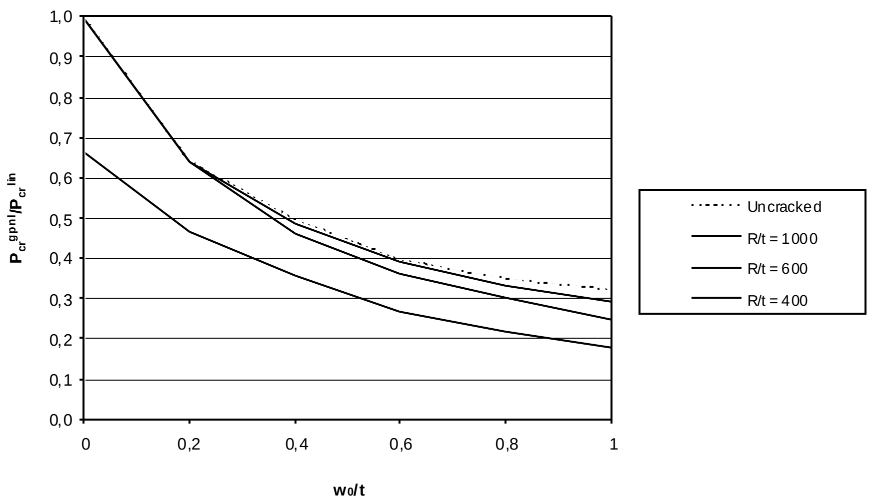

Figure 15.20. Influence of increasing imperfection amplitude on a cracked or crushed (for R/t = 400, w_o/t = 0.0) C20/25 hemispherical shell with inclined-roller support and top imperfection subjected to spherical load for several R/t ratios

In Figure 15.20 it can be seen that the critical loads at maximum imperfection amplitude are equal to *17.8%* (*R/t = 400*), *24.8%* (*600*), *27.0%* (*800*) and *29.3%* (*1000*). Aforementioned, the shell with *R/t ratio* equal to *400* experiences crushing for small imperfection amplitudes ($w_o/t < 0.2$) and, thus, does not reach the linear critical buckling load.

15.4.2 Zeiss 1, 3 and 4

The results above correspond to the inclined-roller supported Zeiss 2 shell. The influence of a roller, hinged or clamped support is illustrated in Figure 15.21.

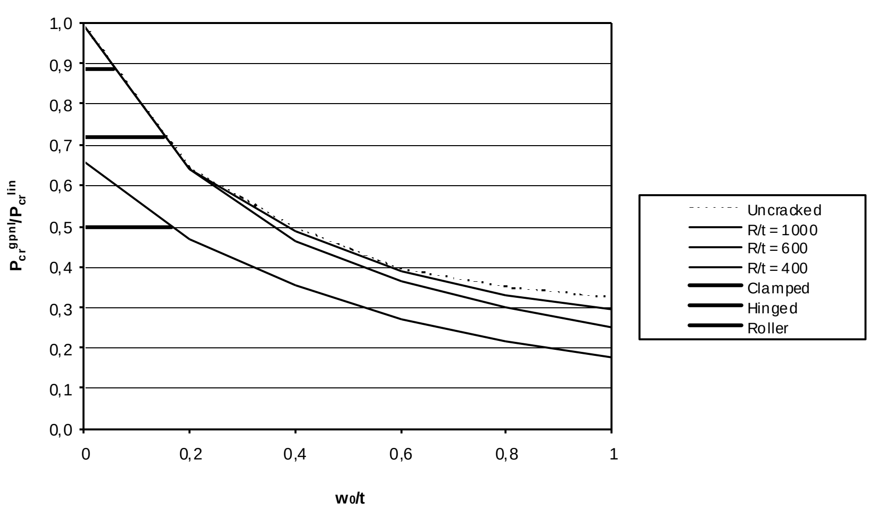

Figure 15.21. Effect of initial geometrical imperfections and cracking on the critical load for hemispherical C20/25 shell with top imperfection subjected to spherical load for several R/t ratios and support conditions

In Figure 15.21 it can be seen that only the roller supported shell influences the curves as obtained for the Zeiss 2 shell without confinement. As the linear critical buckling load is lower, the roller shell under spherical pressure load fails due to buckling with axial tension in the boundary layer if the imperfection amplitude $w_o/t < 0.2$. The lines of the clamped and hinged supported shells are not important for a shell with $R/t < 400$. Their linear critical buckling loads are so high that they show premature failure on compressive crushing. Hence, they follow the line of the inclined-roller shell. It can be concluded that for imperfection amplitudes $w_o/t \geq 0.2$ the shell fails independent of the type of support.

With respect to other *R/t ratios* it is observed that, for an *R/t ratio* equal to *200*, the roller support linear critical load coincides with the crushing load and boundary conditions do not influence the load carrying capacity at all. Aforementioned, for *R/t ratios* equal to *600* (turning point, see Figure 10.6), *800* and *1000*, the crushing load is not important anymore as the shell fails by a combination of large deformations and cracking. Hence, the curve of an inclined-roller shell starts, by definition, at *1.0* for $w_o/t = 0.0$ and the influence of the supports can be plotted similar to Figure 15.10. Obviously, the curves are bounded by a different line for the cracked inclined-roller shell as there is referred to the C20/25 shell here.

15.5 Results C20/25 Shell under Vertical Load

In Section 15.3 it is discovered that the UHPFRC shell under vertical load, by definition, fails mainly due to surpassing the axial tensile stress of the C180/210 in the boundary layer after which buckling occurs, as can be seen in Figure 15.11. Hence, the shell constructed from the low quality concrete C20/25, with an even lower axial tensile strength, experiences a similar failure mode. As a consequence, an initial geometrical imperfection at the top of the shell can be neglected and, moreover, the conventional reinforced concrete must be modelled according to the left bilinear relation of Figure 15.3.

15.5.1 Zeiss 1, 2, 3 and 4

Similar to Section 15.3, the fully nonlinear response of the vertical loaded C20/25 shells is illustrated by load-displacement curves, stresses and bending moments and crack plots.

Load-displacement relations

The deformation of a vertical loaded C20/25 shell is similar the deformation of a C180/210 shell subjected to vertical load, seen in Figure 15.11. The load-displacement curves for a cracked C20/25 shell with *R/t ratio* equal to *400* and varying supports are presented in Figure 15.22. Crack initiation is marked with a black spot. The final step of each load-displacement curve is questionable as the analysis failed in finding convergence in the next step.

From the load-displacement curves it can be seen that the shell fails by cracking as the tensile strength of the material is violated and buckling as the curves show similar trend as seen in the right graph of Figure 14.1. As the stress-strain relation is modelled as a bilinear diagram, the cracking suddenly appears in the linear load-displacement curve. In reality a more rounded curve may be expected. Furthermore, it is observed in the load-displacement curves that, after crack initiation, the point of maximum critical load is not significantly higher as 'meridional based' buckling immediately initiates after the circumferential crack process. Hence, safety with respect to the ultimate limit state may be dominant over the maximum allowable crackwidth, although it is argued in Section 15.1 that the finite element solution must be bounded by the maximum crackwidth as dictated by the serviceability limit state. This is discussed further in Section 15.6.

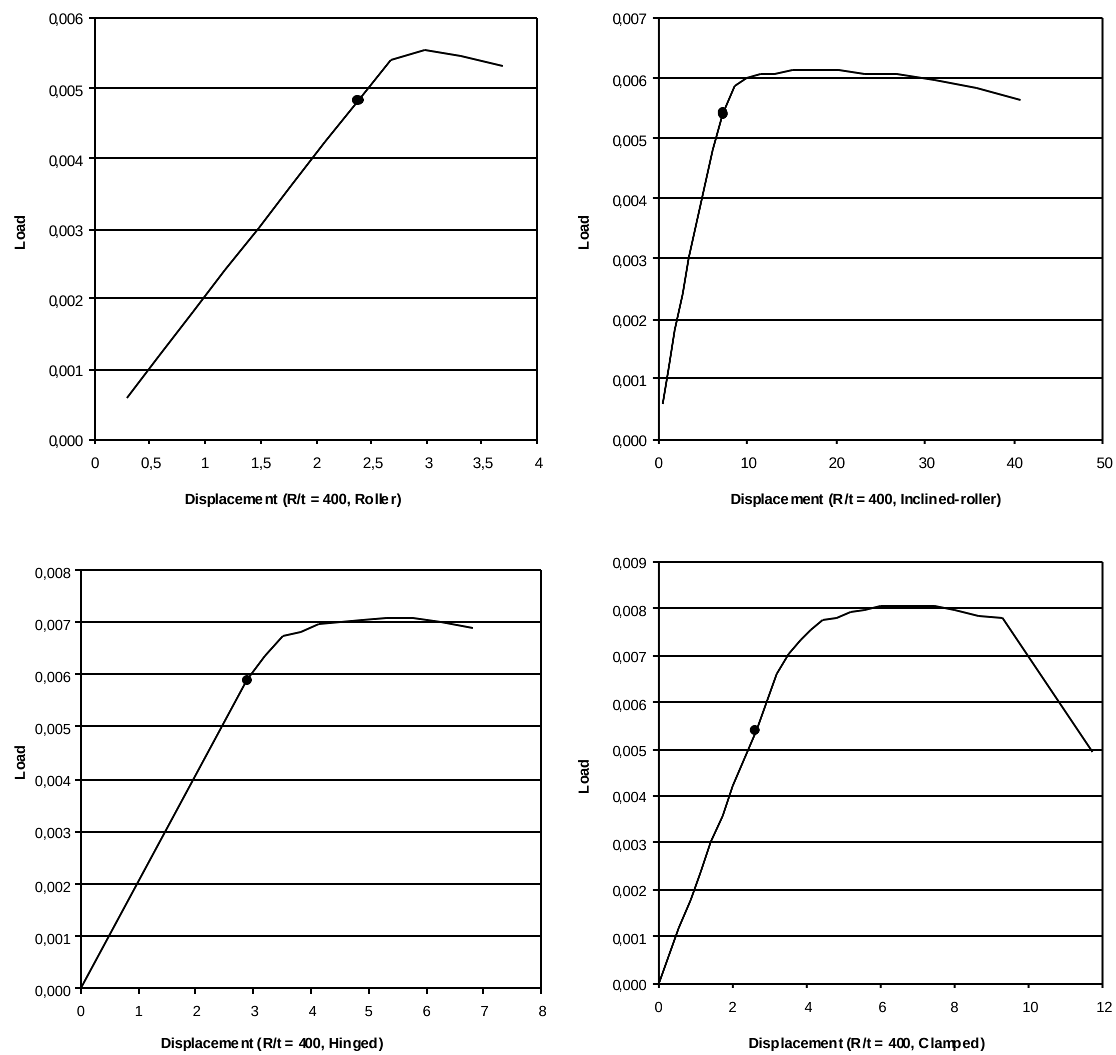

Figure 15.22. Typical top node load-displacement curves for several support conditions for a C20/25 hemispherical shell subjected to uniform vertical load with an R/t ratio equal to 400

The maximum load as obtained from the finite element analysis are summarised in Table 15.4. It can be seen that, similar to the results of Section 15.3, the shell fails approximately at the same magnitude of external applied load for each type of support. As one would expect, based on the linear stress distribution of the circumferential stresses as seen in the figures of Chapter 12, the clamped support yields the maximum allowable load, although it is only *0.00804 MPa (8.0 kN/m²)*.

Name	P_{cr}^{gpnl} (MPa)
Zeiss 1	0.00554
Zeiss 2	0.00612
Zeiss 3	0.00708
Zeiss 4	0.00804

Table 15.4. Critical load for hemispherical C20/25 shell with R/t = 400 subjected to uniform vertical load

When the results of Table 15.4 are compared to the critical load of Table 15.2, it can be concluded that the critical loads are approximately *4* times lower. Remarkable (or not) this is more or less the difference in axial tensile strength between the UHPFRC and conventional concrete mixture. Hence, the given shell under vertical load can be approximately *4* times thinner if the shell is fabricated using C180/210. For the given hemispherical shell geometry (*R = 12500 mm, t = 60 mm*), this means that the thickness (theoretically) can be reduced to just *15 mm*.

The results of the cracking and buckling failure can be compared to the linear critical buckling load of a spherical shell under radial pressure as defined in Chapter 6. Moreover, the results can be compared to the buckling loads found in Chapter 13 assuming linear elastic material behaviour. When compared to the results of Chapter 6 and Chapter 13, it can be said that the introduction of cracking lowers the critical load drastically. The decrease in load carrying capacity is seen in Table 15.5.

Name	$P_{cr}^{gpnl}/P_{cr}^{lin,\ equation\ (6.63)}$	$P_{cr}^{gpnl}/P_{cr}^{lin,\ chapter\ 13}$
Zeiss 1	2.8 %	10.8 %
Zeiss 2	3.1 %	5.5 %
Zeiss 3	3.5 %	8.6 %
Zeiss 4	3.9 %	6.3 %

Table 15.5. Critical load for hemispherical C20/25 shell with R/t = 400 subjected to uniform vertical load

It can be observed that for hemispherical shells subjected to uniform vertical load, the introduction of material nonlinearities, which cause strength failure rather than buckling failure, lead to critical loads which are as low as *5.5%* of their linear critical buckling load and *2.8%* of the linear critical buckling load for spherical shell under radial pressure load.

Stresses and bending moments

In Figure 15.20 the stress distribution at the point of crack initiation of a C20/25 hemisphere with *R/t = 400* subjected to uniform vertical load is presented, for all considered support conditions. In the stress distribution, the effect of reaching the axial tensile stress of *2.2 MPa* can be seen. Similar to Section 15.3, in case of an increasing external load, stress redistribution cause a horizontal plateau to develop, with a magnitude equal to the tensile strength. Clearly the effect of the initial geometrical imperfection, which is equal to $w_0/t = 1.0$, causes the disturbances at the top of the shell, however does not influence the maximum critical load. When the graphs of Figure 15.20 are compared to the graphs of Figure 15.13, it can be seen that the tensile stresses are approximately *4* times lower.

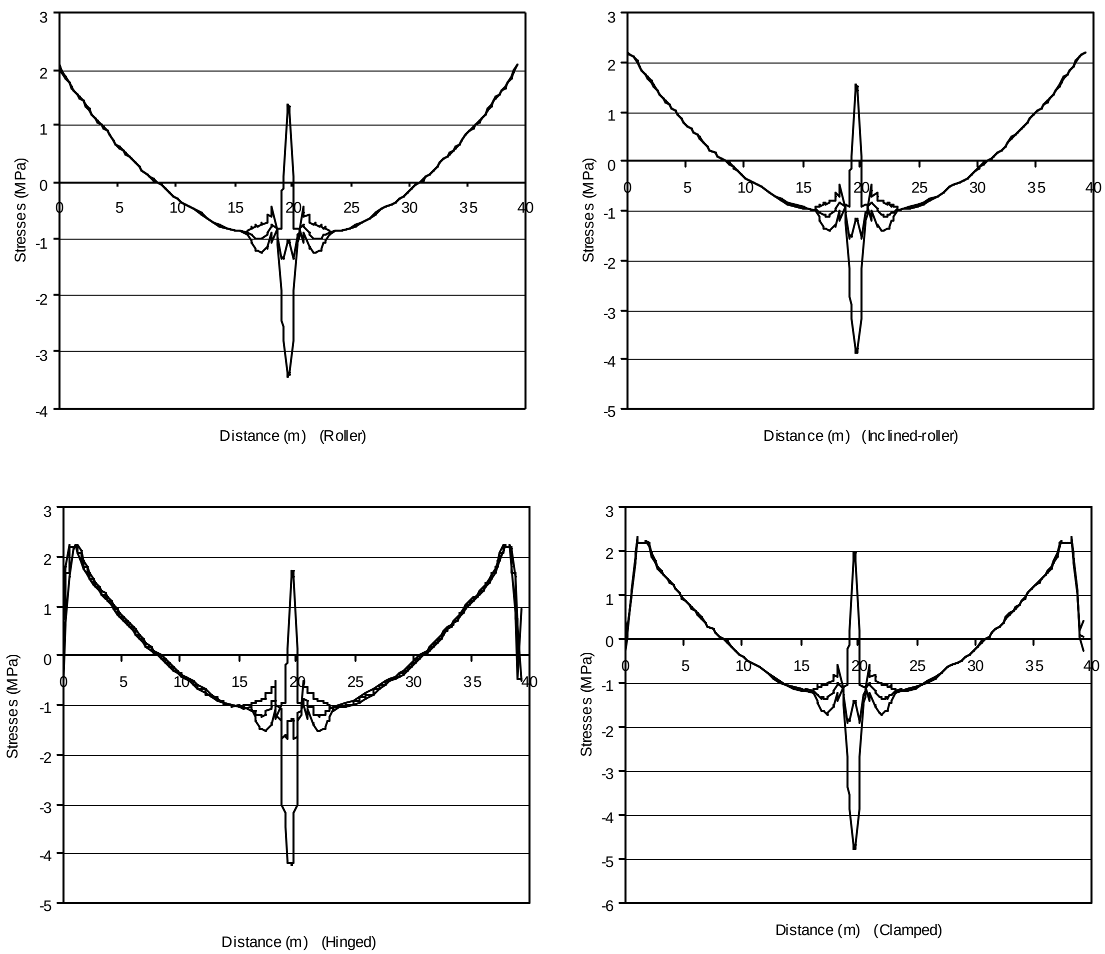

Figure 15.23. Stress distribution at crack initiation of a C20/25 hemisphere with $R/t = 400$ under vertical load for several supports

The bending moment distribution is not shown as it has a similar to Figure 15.6. This is caused by the fact that the bending moments at the imperfection are far higher than the bending moments resulting from the so-called edge disturbance.

Cracking

The cracks that appear in the C20/25 hemisphere subjected to vertical load show similar scatter as the cracks presented in Figure 15.15. A crack scatter is shown in Figure 15.24.

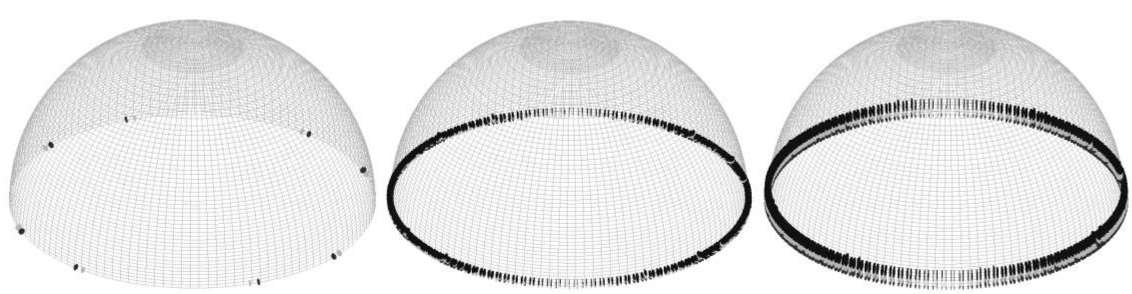

Figure 15.24. Typical finite element crack scatter propagation in hemispherical shells subjected to vertical load

Typically, cracked reinforced concrete demonstrates a few wide cracks rather than a large amount of small cracks. However, as the reinforced concrete is modelled with a bilinear law this does not occur (the cracks in the left shell are very small and immediately transform to a distributed crack pattern in the next load step).

Different R/t ratios

For the C20/25 low quality of concrete (with low quality and percentage of reinforcement), the structural failure due to surpassing the axial tensile strength is independent of *R/t ratios* between *200* and *1000*.

15.6 Practical Considerations

In the previous sections the load-displacement curves are evaluated by their maximum load-carrying capacity. However, as cracking initiates before the maximum load is reached, the shell may be disqualified by the maximum crackwidth as dictated by the serviceability limit state. Especially for the conventional concrete mixture the serviceability may be dominant, e.g. the axial tensile behaviour is modelled with a long horizontal branch in the bilinear stress-strain relation allowing cracks up to *11 mm*.

To obtain a quantitative boundary for the crackwidth, in Table 15.6 a series of crackwidths are summarised together with their corresponding crack strains (determined by reversing equation (11.66)). For an environmental class 5 (aggressive conditions), the maximum allowable crackwidth is equal to *0.2*.

Crack width (mm)	Crack strain (‰)
0.1	0.27
0.2	**0. 54**
0.3	0.81
0.4	1.08

Table 15.6. Crack width – crack strain relationship based on fracture energy regularisation

For a maximum allowable crackwidth equal to *0.2 mm* and no safety factors applied, the following observations can be made. For C180/210 shells, the maximum load carrying capacity is determined by the ultimate limit state. Thus the maximum critical load can be derived from the load-displacement curves. The maxima are bounded by (a combination of) buckling and nonlinearity of concrete in tension (loss of linearity when the hardening branch initiates and cracking). Also for C20/25 shells subjected to vertical load the ultimate limit state is dominant. The maximum critical load, determined by significant cracking after which buckling occurs, is bounded by the ultimate limit state as the critical load does not significantly increases after crack initiation. The serviceability limit state only determines the maximum allowable displacement (when the crackwidth violates the norm). For C20/25 shells subjected to spherical load, the serviceability is decisive if cracking occurs far before the limit point. In all other situations the ultimate limit state prevails and the maximum critical load is bounded by (a combination of) buckling, nonlinearity of concrete in compression (loss of linearity and crushing) and nonlinearity of concrete in tension (cracking). E.g. applying a maximum allowable crackwidth 0.2, the critical load of the last three graphs of Figure 15.16 decreases significantly to *0.0513 MPa*, *0.0323 MPa* and *0.0244 MPa*, respectively.

15.7 Material Comparison

From the foregoing it can be seen that UHPFRC shells are able to carry much higher loads than their conventional concrete equivalents. In case of vertical load, for a given shell *(R/t = 400)* the maximum critical load of the C20/25 shell is approximately *25%* of the C180/210 shell. Remarkable (or not) the factor of *4* is approximately the difference between the axial tensile strength of both mixtures. Consequently, the C180/210 shell can be *4* times thinner than a shell constructed from C20/25 concrete. This happens to be true for all *R/t ratios* (*200 – 1000*) included in this research. Hence, for vertical loaded shells, the axial tensile strength of the UHPFRC in compare to conventional concrete governs the difference in maximum critical load.

In case of a shell *R/t* = 400 subjected to spherical load, with inclined-roller support and initial geometrical top imperfection, the difference in maximum critical load between C180/210 and C20/25 is summarised in Table 15.6. The values denoted with * are values bounded by the maximum crackwidth of *0.2 mm* (see Section 15.6).

w_0/t	UHPFRC Load (MPa)	C20/25 Load (MPa)	Difference	C/UHPFRC (%)
0.2	0.262	0.0888	0.173	33.9
0.4	0.189	0.0708	0.118	37.5
0.6	0.144	0.0513*	0.093	35.6
0.8	0.118	0.0323*	0.086	27.4
1.0	0.100	0.0244*	0.076	24.4

Table 15.6. Difference in maximum allowable critical load based on a maximum crackwidth of 0.2 mm for an inclined-roller supported hemisphere with R/t = 400 and an initial geometrical imperfection at the top subjected to spherical load

In Table 15.6 it can be seen that the maximum difference is *24.4%* (*7.6* kN/m^2), in case of an imperfection $w_0/t = 1.0$. This means that the shell made from the C20/25 is able to carry only one quarter of the load of the shell made from the C180/210 mixture. For larger imperfections, it may be expected that the difference will be even larger; however, this is counteracted by the fact that cracking of the C180/210 starts to influence the maximum point in the load-displacement curve (see Figure 15.4).

The given shell with maximum imperfection, however, cannot be four times thinner when using the chosen C180/210 over C20/25. This is caused by the fact that the thickness of the shell appears quadratically in the buckling relation. Moreover, the effect of loss on linearity and cracking is different for different *R/t ratios*. As an example, the given shell *R/t = 400* with given material properties can be reduced to *R/t = 700,* based on the maximum critical load as found in by DIANA, while the shell can be reduced to *R/t = 800* when the maximum allowable crackwidth (Table 15.6) is taken into account.

For small imperfections ($w_o/t < 0.2$) in combination with a low quality of concrete and a relative thick shell (*R/t ratio* between *200* and *400*), it is found that compressive crushing is decisive above buckling failure (strength failure). E.g., for a shell *R/t = 400* crushing leads to a load which is *34%* lower than the elastic theory while for a shell *R/t = 200* the load is just *50%* of the elastic theory. Using the given C180/210 the *R/t ratios* can be increased to *700* and *400*, respectively. Hence, the use of UHPFRC is advantageous to prevent the negative effect of compressive crushing on the load carrying capacity

15.8 Knock-Down Factor Approach

In Chapter 14, the knock-down factor that incorporated effects of large deformations and initial geometrical imperfections was defined at a value of *68%*, thus the decrease in load carrying capacity is determined by multiplication with *0.32*. It is observed in the results described above that cracking and crushing lead to a further decrease in load carrying capacity, except for the thinnest C180/210 shell. In fact, for vertical loaded shells, cracking appeared to be dominant after which buckling occurs. Hence, for vertical loaded shells, the knock-down factor is superfluous as the failure load can be determined simply by computing the circumferential stresses. This is not the case for shells subjected to spherical load. However, opposite to the general influence of large deformations and initial geometrical imperfections, the general effects of crushing and cracking (both accompanied by loss of linearity) on spherical loaded shells cannot be reduced to a simple graph or equation. A different shell thickness, imperfection, boundary condition and material property leads to an enormous scatter of results. Therefore, it is not possible to formulate a general expression for the knock-down factor which determines the decrease in load-carrying capacity for a hemispherical shell under spherical load. However, as can be seen in the results reported above, it is possible to determine the fall-back in load carrying capacity for a specific case by introducing initial geometrical imperfections and material nonlinearities in a geometrically and physically nonlinear finite element analysis.

Based on the observation that it is possible to find the knock-down factor of a specific case, valuable conclusions can be drawn by determining the knock-down factor for the most onerous situation. In Figure 15.19 it can be seen that for a *R/t 400* shell subjected to spherical load with an imperfection amplitude equal to the shell thickness leads to a knock-down factor of *82.2%* (multiplication by *0.178*), independent of the boundary conditions. Hence, for thinner shells, a higher quality of concrete or a higher percentage of reinforcement, the decrease in load carrying capacity will be less. If the additional cracking multiplication factor (*0.556*) is compared to the one found in Chapter 10, using the IASS Recommendations (*0.2*), it is observed that the latter leads to a load capacity which is significantly lower. Most likely, the large discrepancy may be explained by the conservative approach of the IASS Recommendations. The recommendations provide in a crack parameter based on reinforcement percentages and (reduced) material stiffness and does not take into account for geometrical influences such as the point of crack initiation in case of a varying *R/t ratio*. Furthermore, the crack parameter of the IASS Recommendations is based on the hypothesis of a so-called second state of reinforced concrete structures, i.e. assuming a cracked tensile zone but still linearly elastic behaviour over the cross-section of the shell. The DIANA results yield a nonlinear stress distribution over the cross-section which, as can be seen in Figure 8.19, may lead to a large discrepancy between elastic and plastic behaviour.

15.9 Conclusions

Before reading the following conclusions, one must keep in mind that they are based on shell analysis involving shells with *R/t ratios* between *200* and *1000* and a local imperfection at the top of the shell. Furthermore, the shell is loaded by uniform pressure or vertical load. The results are based on a geometrically and physically nonlinear finite element analysis. The material behaviour is implemented in a so-called total strain rotating crack model according to Section 15.1.3. I.e. a multi-linear tensile relation and an infinite linear elastic compressive relation for the UHPFRC and a compressive behaviour according to the Thorenfeldt curve for the conventional concrete combined with either a bilinear or brittle tensile relation, depending on the type of failure (axial tensile or flexural tensile failure, respectively).

Hemispherical shells subjected to uniform spherical load (or shells confined to their compression zone such that the vertical load can be approximated by a spherical load):

From the results obtained by a geometrically and physically nonlinear analysis on hemispherical shells subjected to uniform spherical load, it can be concluded that spherical load leads to flexural tensile failure or compressive crushing in the region of the initial geometrical imperfection. For a spherical load the results are independent of the location of the imperfection if and only if the imperfection does not interact with (possible) edge disturbances. Depending on the *R/t ratio*, the imperfection size and the properties of the concrete, the maximum critical load is determined by cracking, crushing, buckling or a combination. The effects of cracking and crushing are accompanied by reduced material stiffness due to loss of linearity; at the initiation of the hardening branch in the C180/210 tensile relation and due to the 'rounded' Thorenfeldt curve used to model the compressive behaviour of the C20/25 mixture (Chapter 8). Thus, besides the cracking and crushing, an additional decrease in load carrying capacity is caused by this loss of linearity.

In general, for thicker shells cracking and loss of linearity in tension are more prevalent than for thinner shells, governed by the fact that thicker shells experience bending up to a higher degree. Very thin shells of high quality concrete may not experience any negative influence of cracking at all. Then, the critical load is exclusively determined by buckling, as observed for the thinnest C180/210 shell ($R/t = 1000$). The increasing influence of cracking is clearly seen in the load-displacement curves as the point of crack initiation moves further and further towards the origin of the graph as the shell becomes thicker (Figure 15.9). The same phenomenon occurs in case of an increasing imperfection amplitude (Figure 15.4). As an increasing imperfection causes substantial higher bending moments and stresses, the point of crack initiates moves towards the origin of the load-displacement curve which, consequently, leads to an increased discrepancy between the theoretical critical load and the critical load as obtained by DIANA. An increasing imperfection also leads to a critical load independent of the boundary conditions if $w_o/t > 0.4$. For smaller imperfections, $w_o/t < 0.4$, boundary conditions cannot be neglected and lead to considerable lower loads than found for the 'membrane' inclined-roller supported shell which provides in an upper bound solution. I.e. a roller support leads to a maximum critical load of approximately *50%* of the critical load for an inclined-roller supported shell. Moreover, small imperfections in combination with a low quality of concrete may lead to a failure by compressive crushing, as observed for the C20/25 shell with a load *34%* lower than the elastic shell.

In case of a spherical loaded hemispherical shell, the expectation that UHPFRC can contribute to more slender shells may said to be confirmed. In case of a failure due to surpassing the flexural tensile strength, the UHPFRC shell can carry significant higher loads than the same shell fabricated from a low quality of concrete, mainly due to the higher axial tensile strength and Young's modulus. Therefore, UHPFRC may lead to a thinner shell; however, the possibilities are counteracted by the importance of the thickness parameter in the buckling process. Furthermore, the effect is less then expected due to the fact that the advantageous postcracking plateau of UHPFRC has no influence on the maximum critical load and is only related to the inclination of the postbuckling path. I.e. the inclination of the decreasing postbuckling path is much less in compare to conventional concrete without fibre addition and only one layer of reinforcement. This might be caused by the buckling which occurs simultaneously with significant cracking. Quantitatively, for the given concrete mixtures and a maximum imperfection amplitude $w_0/t = 1.0$, cracking leads to a critical load as low as *23%* ($R/t = 400$), *24%* (*600*), *25%* (*800*) and *33%* (*1000*) in case of a C180/210 shell and *18%* (*400*), *25%* (*600*) and *29%* (*1000*) in case of a C20/25 shell of the theoretical linear critical buckling load of a sphere under spherical load. Based on the critical load and cracking influence as found by DIANA, the C20/25 shell $R/t = 400$ can be reduced to $R/t = 700$ when using C180/210.

Besides the high flexural tensile strength and Young's modulus, the use of UHPFRC can be advantageous with respect to compressive crushing. Aforementioned, for small imperfections and a low quality of concrete, crushing may be decisive for failure. In case of a sufficient UHPFRC mixture crushing does not occur (and, hence, the material can be modelled as infinite elastic in compression). As an example: for a C20/25 shell $R/t = 400$ crushing leads to a load which is *34%* lower than the elastic theory while for a C20/25 shell $R/t = 200$ the load is just *50%* of the elastic theory. Using C180/210 the *R/t ratios* can be increased to *700* and *400*, respectively.

From the obtained results it is impossible to formulate a general expression which defines the knock-down factor for an arbitrary shell structure. However, it is observed that it is possible to determine (within the scheme of a master thesis) the fall-back in load carrying capacity for a specific case by introduction of initial geometrical imperfections and material nonlinearities in a geometrically and physically nonlinear analysis. Thus, although the analysis involving shells may not be reduced to a simple expression (and may never be), contemporary finite element procedures allows the engineer to find answers to questions within days (based on current status of the author) were it took historical mathematicians years, decades or even centuries. Based on the observation that it is possible to find the knock-down factor of a specific case, valuable conclusions can be drawn by determining the knock-down factor for the most onerous situation. In this thesis, the most onerous situation (*R/t 400, C20/25,* $w_0/t = 1.0$) a knock-down factor of 82.2% (multiplication by *0.178*) is found, independent of the boundary conditions. Herein, the additional effect of cracking yields a multiplication factor of *0.556*. Previously, in Chapter 10, a cracking factor equal to *0.2* was found using the IASS Recommendations. The large discrepancy may be explained by the conservative approach of the IASS Recommendations, i.e. neglecting the influence of the *R/t ratio* on the point of crack initiation and assuming a cracked tensile zone but still linearly elastic behaviour.

With respect to the numerical process it must be mentioned that the analyses were numerically more stable in case of a multi-linear tensile diagram as used to model fibre reinforced C180/210, than when using the brittle behaviour describing the tension relation of C20/25 with one layer of reinforcement.

Hemispherical shells subjected to uniform vertical load:

From the results obtained by a geometrically and physically nonlinear analysis on hemispherical shells subjected to uniform vertical load, it can be concluded that the shell, by definition, fails due to surpassing the axial tensile strength in circumferential direction after which buckling occurs in meridional direction. As the material degradation is responsible for the major part of the fall-back in load carrying capacity, the failure load can approximated by determining the membrane stresses and calculate the failure load by simple equating using the axial tensile strength of the material. Thus, the knock-down factor is superfluous, however, based on the observation that the thickness appears quadratically in the buckling equation, it can be expected that for a given *R/t ratio* buckling becomes dominant. Due to the failure in the boundary layer, the maximum critical load is not influenced by a local top imperfection. Consequently, the cross-sectional stress distribution at the imperfection stays linear. With respect to the support conditions, it can be concluded that the type of support does not change the maximum critical load significantly. Within a small range the roller support provides in the lowest critical load, followed by the inclined-roller, hinged and clamped support. This observation is in fair agreement with the magnitude of circumferential tensile stresses found in Chapter 12.

With respect to the concrete quality, also for vertical loaded shells the expectation that UHPFRC can contribute to more slender shells may said to be confirmed. The difference in maximum allowable load is mainly governed by the difference in axial tensile strength of the given materials. Consequently, the UHPFRC shell can be thinner by the ratio of UHPFRC axial tensile strength over conventional concrete axial tensile strength. For the given concrete mixtures, this results in a shell which can be approximately *4* times thinner. Qualitatively, due to the multi-linear tensile relation of UHPFRC with strain hardening branch (Figure 15.2), the corresponding load-displacement curve show sudden appearing cracks and lead to solutions with bad convergence. The bilinear approach of the conventional mixture is much more numerically stable and cracking ends the linear branch of the load-displacement curve (which obviously makes sense).

16 Conclusions

The conclusions reported in the following, summarise the most important conclusions of the individual chapters. A more extensive conclusion can be found at the end of each chapter. The conclusions are ordered corresponding to their occurrence in the thesis, i.e. conclusions with respect to Part I: Background, Part II: Theory, Part III: Case Study and Part IV: Finite Element Analysis. In the end, the general conclusions are discussed point wise. The figures in this chapter correspond to figures of previous chapters and are indicated by the same subscription.

16.1 Part I Conclusions

Shell structures have been constructed since ancient times. Early examples are the Roman Pantheon and the Hagia Sophia. In the 18th and 19th century, however, the art of designing shells seemed to be forgotten. Guided by German designers Franz Dischinger and Ulrich Finsterwalder, the shell made a comeback in the early 20th century. The modern era of shell started in 1925 with the completion of the Zeiss planetarium shell in Jena. The modern era is recognised by the trend towards greater spans and thinner shells. Besides Dischinger and Finsterwalder, Pier Luigi Nervi, Eduardo Torroja and Anton Tedesko were among the first shell builders. In fact, their specific design approach has lead to three prominent design schools; the German school, the Italian school and the Spanish school. Up to the Second World War shells gained more and more interest to cover medium to large spans economically and aesthetically. After the Second World War, the low labour costs and steel being in short supply created exactly those conditions needed for flourishing shell construction, leading to a blooming period of widespread shell construction between 1950 and 1970. The blooming period was further stimulated by the work of Felix Candela which attracted the attention of architects. The involvement of architects leaded to more luxury shapes with less emphasis on the force flow. The blooming period ended abruptly, mainly caused by the high costs in compare to other structural systems. Still, Swiss engineer Heinz Isler was able to continue designing shells by innovative reusable formwork. Isler may also said to be the founder of free-form shells, designed by using form-finding techniques such as hanging membranes. Hence, it seems fair to add the Swiss school as the fourth prominent design school. Late 20th century shell development leaded to pioneering formwork techniques and several new shell-like structures such as grid shells. Today, there seemed to be a renewed interest in shells, stimulated by the desire to built landmark structures and by the fascination to new construction materials such as ultra high performance concrete.

Shells typically show membrane behaviour with bending effects to satisfy specific equilibrium or deformation requirements. The stresses in shells can be determined by hand, e.g. using the classical shell theory or by computer, e.g. using finite element software. Furthermore, model tests provide in a very practical and convenient method to determine the structural response. They are classified according to their Gaussian curvature and generated by mathematical functions or form-finding techniques. To design a sound shell structure, the designer must prevent in-extensional deformation, allow for membrane stresses to develop, add sufficient curvature everywhere, and take care of edge effects. Subsequently, the designer should optimise the shape and thickness of the shell for buckling and membrane dominant behaviour (minimising strain energy). Shells are low reinforced structures and prestressing may be applied to balance the outward thrust or to ensure compression in the shell surface. Effects of crushing, cracking, creep and shrinkage of concrete and the effect of temperature gradients significantly influence the structural response and must be included in the design process.

Shells are predominantly constructed by pouring concrete on a conventional timber formwork. The timber formwork allows for almost every possible shell shape to be constructed. For highly double curved sections, the timber formwork can be replaced by foamed plastic (polystyrene) formwork fit into shape with a CNC milling cutter. The main disadvantages of conventional formwork are the high costs involved. Therefore, prefabricated moulds, airform techniques and stressed membranes have been developed to serve as formwork. Furthermore, shells may be assembled from prefabricated elements to save on costs. However, for several reasons, none of them gained widespread use. The choice for a particular formwork may not only influence the design of the shell, but also puts restrictions on the placement and design of the reinforcement and the concrete mixture. The placement of reinforcement on double curved surfaces follows ordinary principles, however, for airform construction methods the reinforcement may be asked to autoposition itself. The placement of concrete is either by skip of sprayed. Generally, after hydratation, the concrete is left untreated and maintenance is limited to occasionally whitewashing.

16.2 Part II Conclusions

The classical shell theory can be used to determine the stresses, strains and deformations in an idealised linear elastic shell. The theory is a thin shell theory, an extension of the Kirchhoffean plate theory. The assumption that the thickness of the shell is much smaller than the radius of curvature yields that the flexural rigidity is much smaller than the extensional rigidity which is the reason that shells mainly carry their load by in-plane normal and shear stresses. Stresses or strains in normal direction are of no significance to the solution, reducing the three-dimensional problem to a surface deformation problem. Bending moments only compensate for the shortcomings of the membrane field and do not carry loads. As shells are essentially curved plates, the extensional and flexural problem are coupled, even for the linear case. The combined stretching and bending can be described by the membrane theory in combination with plate bending behaviour which can be calculated separately and superimposed.

Shells fail by a buckling or by strength. Strength failure refers to cracking or crushing being the dominant failure mechanism and is governed by the material properties. If the shell mainly fails by large deformations, the shell is said to be buckled. Buckling can be characterised as a premature failure mechanism caused by eccentricity of compression forces, initiated by deformations or initial geometrical imperfections. The buckling behaviour of shells is a complicated phenomenon. Opposite to columns and plates, shells experience a sudden decrease in load carrying capacity after the bifurcation point. The fall-back is caused by the phenomenon of compound buckling which refers to several buckling modes associated with the same critical load. In the postbuckling range the modes, which were orthogonal in the linear prebuckling range, start to interact resulting in a significantly reduced load carrying capacity. The major problem of the shell buckling behaviour is the accompanied imperfection sensitivity. Initial geometrical imperfections in the shell cause the bifurcation point never to be reached and lead to limit point buckling at a considerably lower load. The size of the imperfections determines the limit load at which the shell fails.

16.3 Part III Conclusions

To obtain an answer to the research questions, the Zeiss planetarium shell is subject of a case study. The stresses, strains and displacements in the shell are determined using the aforementioned classical shell theory for two types of concrete and two types of external applied load. The first concrete mixture is a low quality C20/25 concrete mixture with a single layer of low quality reinforcement to ally with the early 20th century concrete technology. Typically, the compressive behaviour can be modelled by a Thorenfeldt curve. Due to the low quality of reinforcement, the axial tensile relation is mainly determined by the axial tensile strength of the concrete. Also in case of bending, the flexural tensile strength mainly depends on the concrete flexural tensile strength as the single layer of reinforcement is activated not before significant cracking has occurred. The second concrete mixture is a high strength fibre reinforced concrete mixture. The selected mixture is a so-called ultra high performance concrete which refers to compressive strengths between *155* and *250 MPa*. The higher compressive strength originates from an optimised mixture composition. The major deficiency is the highly brittle behaviour which is counteracted by the addition of fibres. The fibres work as well on micro-level, as reinforcement of the cement matrix, as on macro-level, as reinforcement of the structure. They do not necessarily lead to a higher tensile strength, although it is possible to increase the tensile strength through the addition of fibres with different dimensions. Most advantageous is the low-level postcracking plateau that leads to a higher toughness and more ductile failure behaviour. The Zeiss planetarium shell is loaded by dead weight in combination with either wind load or snow, determined according to the Eurocode 2. The results of the classical shell theory show the profound structural behaviour of shells as they experience very small stresses, strains and deformations. I.e. the stresses are *-0.217 MPa* at the top and ±*0.433 MPa* at the base, the corresponding strains are *-0.00722 ‰* and ±*0.0144 ‰* and the maximum deformation is equal to *0.181 mm*. Furthermore, it can be seen that the restrained deformation at the supports leads to local edge disturbances reaching up to approximately *2 m*, with a maximum bending moment of *403 Nmm/mm'* in case of a clamped support. This means that *90%* of the shell is free from bending. When the shell thickness is reduced, the shell behaves more like a membrane and the influence of the edge disturbances is even less. The buckling load of the Zeiss planetarium is $802\ kN/m^2$. In case of the C20/25 concrete this means that crushing occurs before buckling. To determine the load carrying capacity in case of an imperfect concrete shell, the procedure as proposed by the IASS is followed. According to the IASS Recommendations, the maximum allowable load, including safety factors, equals $4.33\ kN/m^2$.

16.4 Part IV Conclusions

All following findings and conclusions are restricted to hemispherical shells with *R/t 200 – 1000* subjected to uniform vertical or spherical load. The shell is modelled with an axisymmetric curved line model and a three-dimensional model consisting of two-dimensional quadrilateral and triangular curved shell elements. For the geometrically nonlinear analysis a local top imperfection with an amplitude varying between *0 – 1.0* times the shell thickness is introduced. For the geometrically and physically nonlinear analysis the material behaviour is implemented in a so-called total strain rotating crack model. The C180/210 UHPFRC is modelled with a multi-linear tensile relation and an infinite linear elastic compressive relation. The C20/25 is modelled by a compressive behaviour according to the Thorenfeldt curve combined with either a bilinear or brittle tensile relation, depending on the type of failure expected (axial tensile or flexural tensile failure, respectively).

16.4.1 Linear Elastic Analysis

The linear elastic analysis proved to be in fair agreement with the (benchmark) analytical results, except for the bending moments that appear in the boundary layer due to restrained deformation at the supports. In particular the axisymmetric shell model yielded bending moments with high discrepancy in compare to the theory (up to *30%)*. This is caused by insufficient stress mapping between the 'exact' integration points and the end nodes. Therefore, the axisymmetric shell model is less accurate and reliable in compare to the three-dimensional model. In addition to the case study of Part III, a non-symmetrical wind load is considered in combination with dead weight. It is observed that wind load changes the direction of the principal stresses and is transferred to the supports partly by meridional stresses and partly by shear. The deformed shape, although different, yields approximately similar deformations as caused by dead weight only as they partly compensate for each other. In the linear elastic results of the three-dimensional shell model disturbances in the stress and bending moment distribution were observed, due to the numerical imperfectness of the model. In particular in the top region of the shell relative large inconsistencies were found. The imperfectness of the model does not disturb the linear results considerably.

16.4.2 Stability Analysis

The disturbances are more apparent in the linear elastic stability analysis, as the analysis proved to be very sensitive to small numerical disturbances. The numerical disturbances cause premature buckling modes preceding the actual shell buckling shape; a global scatter of small local waves in a chessboard pattern. Remarkable, the corresponding critical buckling loads of these premature modes may be nearly similar to the theoretical critical buckling load. Additionally, several false modes were observed between the correct buckling modes. Hence, to obtain a good understanding of the buckling behaviour of a shell, it is necessary to examine both the critical buckling loads as well as their corresponding buckling modes. It is observed that adjacent buckling loads are very close to each other, revealing the occurrence of compound buckling. In general, thinner shells experience compound buckling up to a higher degree than thicker shells.

The critical buckling load is significantly lower for membrane incompatible support conditions. This is caused by the edge disturbances or, in case of a roller support, due to the fact that the support is weaker than the shell itself. Shells subjected to vertical load, by definition, buckle in the boundary layer, accompanied by a much lower bifurcation load. Higher modes advance to global buckling modes similar to the global buckling behaviour of a radial pressed spherical shell. Simultaneously, the corresponding critical buckling load approaches the theoretical load of the sphere subjected to radial pressure. The results of the axisymmetric shell model are poor, as compound buckling is not predicted correctly. Moreover, the axisymmetry causes the tendency to buckle at the top and the buckling loads are disturbed by the incorrect bending moments in case of a hinged and clamped support.

Attempts were made to investigate the postbuckling behaviour by a Koiter theory based perturbation and continuation analysis; however, although the results are not in contradiction with the theory, the results are poor and no conclusions can be drawn.

16.4.3 Geometrically Nonlinear Analysis

A geometrically nonlinear analysis on a perfect shell, finds the buckling bifurcation load. It is observed that perfect shells experience either shell-like buckling with decrease of load-carrying capacity in postbuckling range or buckling with an almost horizontal postbuckling path. The type of external applied load on the shell, i.e. uniform spherical or uniform vertical load, determines the type of buckling. For inclined-roller supported shells subjected to spherical load, the introduction of initial geometrical imperfections leads to premature limit point failure, as the bifurcation point is never reached. The corresponding load-displacement relation shows a smooth transition between the nonlinear prebuckling and postbuckling path of equilibrium, or may experience a sudden snap-through to a non-adjacent equilibrium configuration. Most likely, the snap-through is a numerical related process and does not occur in reality. The amount of decrease in load-carrying capacity is governed by the size of the initial geometrical imperfection. This can be seen in Figure 14.5, which is valid for an inclined-roller supported hemispherical shell subjected to spherical load. The graph is valid for all *R/t ratios*.

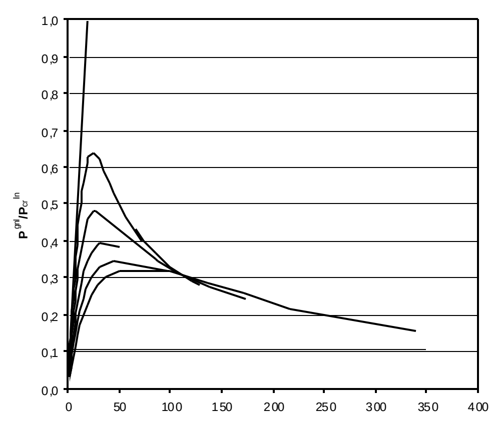

Figure 14.5. Load-displacement curves of a shell with various initial geometrical imperfection sizes (0, 0.2, 0.4, 0.6, 0.8 and 1.0) and the minimum postbuckling load as proposed by Dostanowa and Raiser

In Figure 14.8 it can be seen that an initial imperfection equal to the shell thickness causes a fall-back of approximately *70%*. It is observed that the influence of an initial geometrical imperfection on the load-carrying capacity depends on the size of the imperfection, as can be seen in Figure 14.8. To validate, the finite element results are be compared to the Koiter half-power law and the graph as proposed by the IASS Recommendations. It can be concluded that there is reasonable correlation.

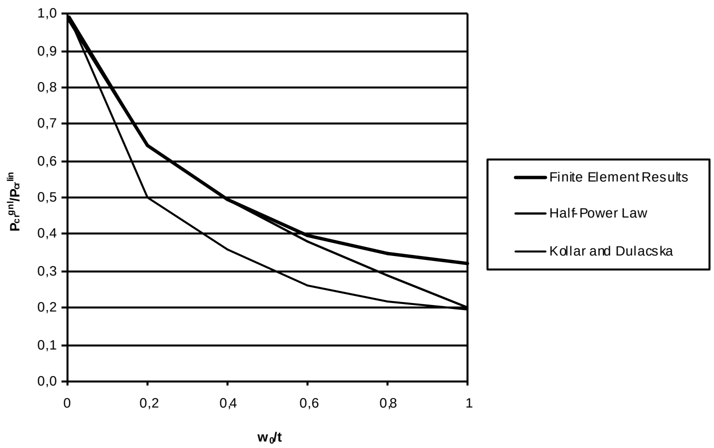

Figure 14.8. Comparison between FEA, Koiter half-power law (red) and the curve of Hutchinson/Kollar and Dulacska (blue)

The influence of a different type of load, e.g. uniform vertical load replacing the uniform spherical load, and different types of support can be incorporated in the graph of Figure 14.8 as illustrated in Figure 14.11.

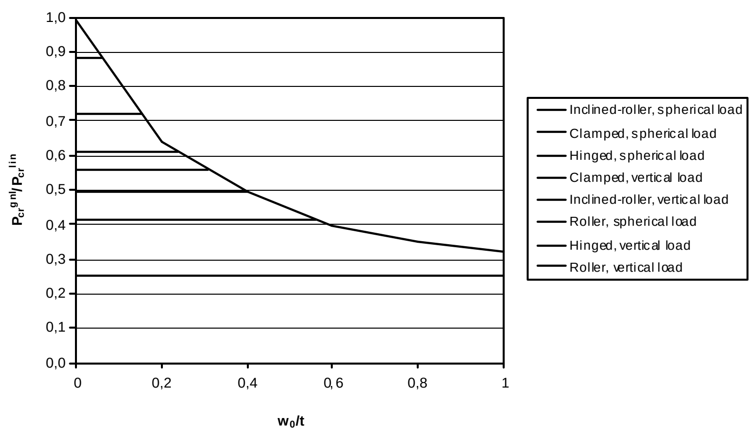

Figure 14.11. Decrease in load-carrying capacity due to boundary conditions, loads and initial geometrical imperfections at the top of the shell for R/t ratios between 200 and 1000

From Figure 14.11 it can be concluded that the inclined-roller supported shell subjected to spherical, which buckles by definition in the shell surface, is an upper bound solution. Furthermore, it can be seen that a roller supported shell subjected to vertical load yields a critical load independent of any top imperfection (within the range of the *R/t ratios* investigated). If the roller support it neglected, the shell buckles in the shell surface when $w_o/t > 0.6$. For imperfection amplitudes $w_o/t < 0.6$ the type of buckling failure depends on the support condition and type of load.

16.4.4 Geometrically and Physically Nonlinear Analysis

The introduction of material nonlinearity leads to two major effects: (1) the further reduction of the load-carrying capacity due to cracking and/or crushing (accompanied by loss of linearity) and (2) the transformation to a strength failure rather than a buckling failure in case of shells subjected to uniform vertical load. Shells subjected to vertical load mainly fail by violation of the axial tensile strength due to circumferential tensile stresses at (or near) the base radius of the shell (depending on the type of support). After significant cracking has occurred, responsible for the major part of the knock-down factor, buckling eventually occurs. As the strength failure is governed by the axial tensile strength of the (fibre) reinforced concrete, the shell can be thinner as much as the difference in axial tensile strength. For the given concrete mixtures this means that the C180/210 can be *4* times thinner than the C20/25 shell.

Spherical loaded shells, or shells confined to their compression zone such that the vertical load can be approximated by a spherical load, fail in the region of the imperfection by surpassing the flexural tensile strength, by compressive crushing, by buckling or a combination. Whether cracking, crushing or buckling occurs first and to which amount depends on the size of the imperfection, the material properties and on the thickness of the shell. The C20/25 shell failed due to compressive crushing for small imperfections ($w_o/t \leq 0.2$) combined with a relative thick shell ($200 < R/t \leq 400$). The occurrence of crushing lowered the load carrying capacity up to *50%*, for $R/t = 200$ and $w_o/t \geq 0.0$). For C180/210 crushing did not occur and, hence, UHPFRC is advantageous. For thinner shells ($R/t \geq 600$), crushing does not occur as buckling prevails.

In case of imperfection amplitudes $w_o/t > 0.2$, crushing is not decisive or does not occur at all and the shell fails by cracking and buckling. The influence of cracking increases for larger imperfection amplitudes and thicker shells (governed by the fact that thicker shells experience bending up to a higher degree). Thus, the point of crack initiation moves further and further towards to origin of the load-displacement curve if the imperfection amplifies or the shell thickness increases. Consequently, for a given imperfection amplitude and *R/t ratio*, cracking initiates before, at or after the maximum load carrying capacity. In the latter case, the maximum load carrying capacity may be influenced by the loss of linearity preceding crack initiation or is exclusively determined by initial geometrical imperfections and buckling (no influence of cracking at all).

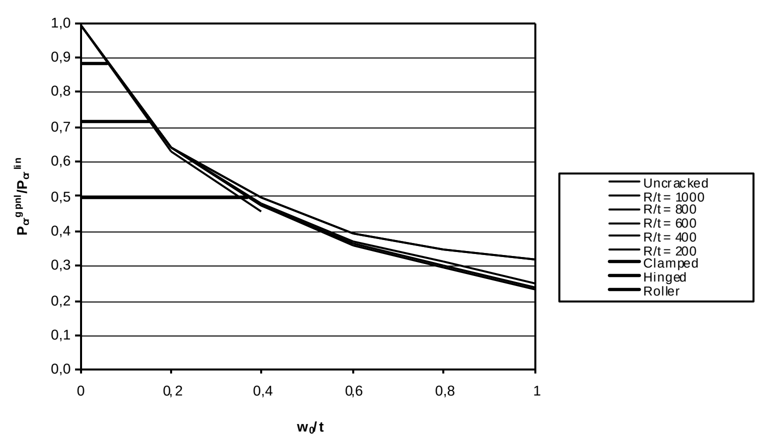

Figure 15.11. Effect of initial geometrical imperfections and cracking on the critical load for hemispherical C180/210 shell with top imperfection subjected to spherical load for several R/t ratios and support conditions

The influence of buckling, cracking and crushing on the load carrying capacity of the hemispherical shell can be plotted in a graph for various *R/t ratios* and support conditions. In Figure 15.11 the influence of cracking and imperfection buckling can be seen for various R/t ratios for a shell constructed from C180/210 fibre reinforced ultra high performance concrete. Each line represents an *R/t ratio* ordered similar as the legend. It can be concluded that the shell with $R/t = 1000$ does not experience cracking as it coincides with the uncracked line. The results of the shell with $R/t = 200$ are limited, as modelling errors were encountered. The inclined-roller shell provides an upper bound solution. Edge disturbances or the support being weaker than the shell itself (roller) cause premature failure in the boundary layer for imperfection sizes $w_o/t < 0.4$. In case of imperfection amplitudes $w_o/t \geq 0.4$ the shell fails by surpassing the flexural tensile strength and/or by buckling in the region of the imperfection, independent of the support conditions. It can be seen that the influence of cracking leads to a maximum knock-down factor equal to *77%* in case of a hemispherical shell with $R/t = 400$. Thus, the additional effect of cracking on the load capacity equals *9%*.

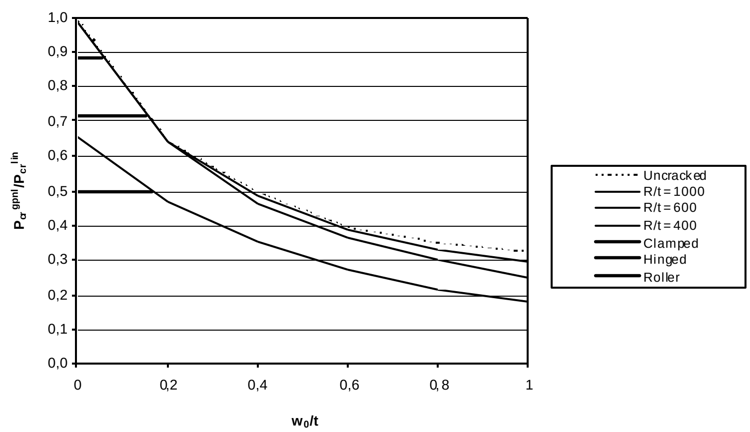

Figure 15.21. Effect of initial geometrical imperfections and cracking on the critical load for hemispherical C20/25 shell with top imperfection subjected to spherical load for several R/t ratios and support conditions

In Figure 15.21 the influence of cracking, crushing and imperfection buckling can be seen for various R/t ratios for a shell constructed from C20/25 reinforced concrete. Each line represents an *R/t ratio* ordered similar as the legend. Note that not all *R/t ratios* are included due to missing results. It can be seen that the influence of cracking is restricted to the shell with $R/t = 400$. Crushing lowers the load carrying capacity by *34%*. Therefore, the influence of boundary conditions is limited to small imperfection sizes. However, if crushing not occurs (for thinner shells), the roller support influences the failure up to $w_o/t = 0.4$. Similar to the C180/210 shell, for imperfection amplitudes $w_o/t \geq 0.4$ the shell fails by surpassing the flexural tensile strength and/or by buckling in the region of the imperfection, independent of the support conditions. It can be concluded from Figure 15.21 that the difference between the lines of $R/t = 400$ and $R/t = 600$ is significantly larger than for a shell constructed from C180/210. This is caused by the much greater influence of cracking in case of a shell constructed from a low quality concrete with a single layer of reinforcement. For a shell $R/t = 400$, it can be concluded that the influence of initial geometrical imperfections, buckling and material nonlinearity leads to a maximum knock-down factor equal to *82%*. Herein the cracking parameter lowers the linear critical buckling load by *14%*.

From the results it can be concluded that the thickness reduction possible due to the use of C180/210 is not governed by a single parameter but depends on the shell geometry (*R/t ratio*), the material properties and the size of the initial geometrical imperfection. For spherical loaded shells, which fail by surpassing the flexural tensile strength, by compressive crushing, by buckling or by a combination, the advantageous higher axial tensile strength and Young's modulus are counteract by the importance of the thickness parameter in the buckling process. As an example: from the obtained results it can be concluded that a C20/25 shell with *R/t = 400* and one layer of reinforcement can be reduced to *R/t = 700* in case of a C180/210 concrete, based on the maximum load carrying capacity. Besides, the shell can be reduced to *R/t = 800* when the maximum allowable crackwidth of *0.2 mm* is taken into consideration.

The finite element results clearly show that cracking, crushing and buckling strongly interact, depending on the *R/t ratio*, material properties and initial geometrical imperfections. Hence, it can be concluded that it is impossible to find a general expression for the knock-down factor, unless high factors of uncertainty are taken into consideration. In this thesis, the most onerous situation (*R/t 400, C20/25,* $w_o/t = 1.0$) yields a knock-down factor of *82.2%*, leading to a maximum load carrying capacity of *0.178* times the linear critical buckling load of a radially pressed sphere. Herein, the additional effect of cracking is a factor of *0.556*. Using the IASS Recommendations, a cracking factor equal to *0.2* is found. The large discrepancy can indeed be explained by the very conservative approach of the IASS Recommendations, i.e. neglecting the influence of the *R/t ratio* on the point of crack initiation and assuming a cracked tensile zone but still linearly elastic behaviour.

16.5 Principal Conclusions

1) Contemporary finite element software makes possible to determine the structural behaviour of an imperfect shell and to compute its fall-back in load carrying capacity conveniently within a small amount of time by performing a geometrically and physically nonlinear analysis. The reliability and accuracy is proved by the performed checks. In fact, it is this conclusion that is the most salient.

2) For the considered hemispherical shell the knock-down factor is much smaller than the knock-down factor as derived using the IASS Recommendations, which apparently are very conservative.

3) Concrete shells with traditional steel reinforcing bars are practically limited to thicknesses not thinner than *60 mm* or *80 mm*, for one or two layers of reinforcement, respectively. Using high strength fibre reinforced concrete the shell thickness can be much less.

4) High strength fibre reinforced concrete can contribute to the trend towards greater spans and thinner shells. In particular the higher axial tensile strength and modulus of elasticity give the engineer opportunities to design thinner shells. Furthermore, high strength concrete is advantageous in compression as it excludes premature compressive crushing failure before the critical buckling load is reached. Opposite to fibre reinforced beams in bending, the significant ductility (postcracking plateau) of high strength fibre reinforced concrete does not influence the ultimate load carrying capacity of hemispherical shells. This might be caused by the buckling which occurs simultaneously with significant cracking.

5) In the considered hemispherical shells cracking, crushing and buckling interact strongly before and during failure. This is influenced by loading, shell thickness, material properties and geometrical imperfections. Therefore, it is impossible to formulate a general expression for the knock-down factor without significant concession on the accuracy.

6) High strength fibre reinforced concrete can be modelled straightforward in a finite element program as the isotropic-like behaviour with a large amount of small cracks allow for the modelling within one constitutive law. The modelling of traditional reinforcing bars is far more complicated due to the interaction between the cracked concrete and bonded reinforcement. The thesis' approximation by a simple bilinear and brittle law, neglecting the (small) influence of the reinforcement, makes the results difficult to interpret.

17 Recommendations

The recommendations reported in the following are ordered corresponding to their occurrence in the thesis, i.e. recommendations with respect to Part I: Background, Part II: Theory, Part III: Case Study and Part IV: Finite Element Analysis. The recommendations are discussed point wise.

17.1 Part I Recommendations

1) More research is needed on shell history in Asia, in particular Japan, and Russia

2) More research is needed on computational shell modelling and (computational) shell optimisation. There is a wide field of possibilities still to discover in designing shells and optimise shells using the computer.

3) Further research is needed on shell construction with stressed membrane formwork.

4) Further research is needed on shell construction by the use of prefabrication.

17.2 Part II Recommendations

1) Research is needed into the shape deficiency, sizes and amplitudes of imperfections that occur in practice, e.g. by making measurements on all kinds of realised shells.

2) Research is needed on the parameters used in the Koiter power laws for other types of shell structures.

17.3 Part III Recommendations

1) Research is needed towards possibilities to further increase the axial and flexural tensile strength of high strength fibre reinforced concrete as specifically these properties lead to opportunities for thinner shells.

2) Extension of shell loading towards accidental load, foundation settlement and seismic load.

17.4 Part IV Recommendations

1) Research is needed to include more effective meshing algorithms for double curved surfaces.

2) Research is needed on the influence of variations in size, location, number and distribution of initial geometrical imperfections on the fall-back in load carrying capacity.

3) Research is needed towards the inclusion of time-dependent material behaviour such as creep, shrinkage and ambient influences like temperature into the analysis. To incorporate the effects of creep, shrinkage and temperature a different material model is required as it is not possible to include these effects in the total strain concept.

4) Research is needed to a more optimal concrete mixture for a given shell structure, i.e. hemispherical shells need a concrete mixture with high axial and flexural tensile strength, whereas shallow shells need concrete which is able to give high resistance against creep.

5) Extension of the research field to a variety of shell shapes.

6) Research is needed to the effectiveness of other finite element solution procedures on finding convergence in the postbuckling regime.

References

Literature

[1] Arnold, D.N. (2002). *Approximation by quadrilateral finite elements.* Minneapolis: Institute of Mathematics and its Applications, University of Minnesota.

[2] Barlow, J. (1974). Optimal stress locations in finite element models. *International Journal for Numerical Methods in Engineering, Vol. 10, Issue 2,* 243-251.

[3] Bathe, K.J. (1996). *Finite Element Procedures.* New York: Prentice Hall.

[4] Bathe, K.J., Chappelle, D. and Lee, P.S. (2003) A Shell Problem 'Highly Sensitive' to Thickness Changes. *International Journal for Numerical Methods in Engineering, No 57,* 1039-1052.

[5] Bechthold, M. (2002). On Shells and Blobs. *ARQ Lecturas Readings, No 7,* 30-35.

[6] Billington, D.P. and Harris, H.G. (1981). Test Methods for Concrete Shell Buckling. In: Popov, E.P. and Medwadowski, S.J. (Eds) *Concrete Shell Buckling* (pp. 187-231). Detroit: Publication American Concrete Institute.

[7] Billington, D.P. (1983). *The Tower and the Bridge: The New Art of Structural Engineering.* Princeton: Princeton University Press.

[8] Blaauwendraad, J. (2003). *Plates and Slabs: Volume 1, Theory.* Delft: Delft University of Technology.

[9] Blaauwendraad, J. (2004). *Plates and Slabs: Volume 2, Numerical Methods.* Delft: Delft University of Technology.

[10] Blaauwendraad, J. (2002). *Theory of Elasticity: Direct Methods.* Delft: Delft University of Technology.

[11] Blaauwendraad, J. (2002). *Theory of Elasticity: Energy Principles and Variational Methods.* Delft: Delft University of Technology.

[12] Bletzinger, K.U. and Ramm, E. (1993). Form Finding of Shells by Structural Optimisation. *Engineering with Computers, No 9*, 27-35.

[13] Bogart, A. (2007). *The relationship between form and force of curved surfaces: A graphical solution*. Delft: Delft University of Technology.

[14] Bogart, A. (2007). *The relationship between form and force of curved surfaces: The Rain Flow analysis*. Delft: Delft University of Technology.

[15] Borst, R. de. Sluys, L.J. (2007). *Computational Methods in Non-linear Solid Mechanics*. Delft: Delft University of Technology.

[16] Bosch, I. (2006). Siebenfussler und andere Naturformen. *Tec21, No 22*, 14-20.

[17] Bouquet, G.Chr. and Braam, C.R. (2006). Vezels in beton. *Cement, No 5*, 31-35.

[18] Bradshaw, R., Campbell, D., Gargari, M., Mirmiran, A. and Tripeny, P. (2002). Special Structures: Past, Present, and Future. *Journal of Structural Engineering, June*, 691-709.

[19] Burden, R.L. and Faires, J.D. (2001). *Numerical Analysis*. Pacific Grove: Brooks/Cole.

[20] Burgers, R.A. (2006). *Non-linear FEM modelling of steel fibre reinforced concrete for the analysis of tunnel segments in the thrust jack phase*. Delft: Delft University of Technology.

[21] Caquot, A. (1974). *Nicolas Esquillan: Cinquante ans a l'avant-garde de genie civil*. Paris: Syndicat National de Beton Arme et des Techniques industrialisees.

[22] Chilton, J. (2000). *Heinz Isler: The Engineer's Contribution to Contemporary Architecture*. London: Thomas Telford Publishing.

[23] Colin, F. (1963). *Candela: The Shell Builder*. New York: Reinhold.

[24] Corts, K. (2006). Muthers Freilichtmuseum. *Tec21, No 22*, 5-11.

[25] Crisfield, M.A. (2001). *Non-linear Finite Element Analysis of Solids and Structures, Volume 1: Essentials*. New York: John Wiley and Sons.

[26] Croci, G. (2006). Seismic Behaviour of Masonry Domes and Vaults Hagia Sophia in Istanbul and St. Francis in Assisi. *Proceedings of the First European Conference on Earthquake Engineering and Seismology* (paper number: K8). Geneva.

[27] Dechau, W. (2000). *Kuhne Solitare: Ulrich Muther, Schalenbaumeister der DDR*. Stuttgart: Deutsche Verlags-Anstalt.

[28] Desideri, P. (1982). *Pier Luigi Nervi*. Zurich: Artemis.

[29] DIANA (2005). *User's manual: Release 9*. Delft: TNO DIANA BV.

[30] Dicleli, C. (2006). Ulrich Finsterwalder, Ingenieur aus Leidenschaft. *Design Report, No 10*, 76-80.

[31] Dingsté, A. and Boer, M, de. (2008). Landschap als organisatiestructuur. *Cement, No 1,* 24-33.

[32] Espion, B., Halleux, P. and Schiffmann, J.I. (2003). Contribution of Andre Paduart to the art of thin concrete shell vaulting. In: Huerta, S. (Ed). *Proceedings of the First International Congress on Construction History* (pp. 829-838). Madrid: Instituto Juan de Herrera, Escuela Técnica Superior de Arquitectura.

[33] European Committee for Standardization (2002), Eurocode 2, European Standard.

[34] Farshad, M. (1992). *Design and Analysis of Shell Structures*. Dordrecht: Kluwer Academic Publishers.

[35] Fernandez Ordonez, J.A. and Navarro Vera, J.R. (1999). *Eduardo Torroja: Engineer*. Madrid: Pronaos Publishers.

[36] Flury, P. (2002). Die Such nach der perfekte Schale. *Tec21, No 49-50*, 13-17.

[37] Garcia, R. (2006). *Concrete folded plates in The Netherlands*. Cambridge: Cambridge University.

[38] Godoy, L.A. (1996). *Thin-Walled Structures with Structural Imperfections: Analysis and Behavior*. Oxford: Elsevier Science Ltd.

[39] Grünewald, S. (2004). *Performance-based design of self-compacting fibre reinforced concrete*. Delft: Delft University Press.

[40] Günschel, G. (1996). *Große Konstrukteure 1: Freyssinet, Maillart, Dischinger, Finsterwalder*. Berlin: Verlag Ullstein.

[41] Haas, A.M. and Koten, H. van. (1970). The Stability of doubly curved shells having a positive curvature index. *HERON Vol. 17, No 4*, 9-48.

[42] Haas, A.M. (1962). *Design of Thin Concrete Shells: Vol. 1 Positive Curvature Index*. London: John Wiley and Sons.

[43] Haas, A.M. (1961). Overzicht Nederlandse Schaalconstructies. *Cement, No 8*, 423-504.

[44] Hanselaar, H. (2003). *Indoor Sneeuwskibaan.* Delft: Delft University of Technology.

[45] Hoefakker, J.H. and Blaauwendraad, J. (2003). *Theory of Shells*. Delft: Delft University of Technology.

[46] Holgate, A. (1997). *The Work of Jorg Schlaich and his Team*. London: Axel Menges.

[47] Hollander, J. den. (2006). *Technical Feasibility Study of a UHPC Tied Arch Bridge*. Delft: Delft University of Technology.

[48] Hoogenboom, P.C.J. (2006). *Finite Element Benchmarks*. Delft: Delft University of Technology.

[49] Hoogenboom, P.C.J. (2006). *Shell Equations*. Delft: Delft University of Technology.

[50] Hoogenboom, P.C.J. (2006). *Stability of Shells*. Delft: Delft University of Technology.

[51] Hughes, T.J.R. (2000). *The Finite Element Method: Linear Static and Dynamic Finite Element Analysis*. New York: Dover Publishers.

[52] Joedicke, J. (1962). *Schalenbau.* Hilversum: Uitgeverij G van Saane.

[53] Kilian, A. and Ochsendorf, J. (2005). Particle-Spring Systems for Structural Form Finding. *IASS Journal, No 6*, 139-147.

[54] Kollar, L. and Dulacska, E. (1984). *Buckling of Shells for Engineers*. New York: John Wiley and Sons.

[55] Kooiman, A.G. (2000). *Modelling Steel Fibre Reinforced Concrete for Structural Design*. Delft: Delft University Press.

[56] Lappa, E.S. (2007). *High Strength Fibre Reinforced Concrete Static and fatigue behaviour in bending*. Delft: Delft University Press.

[57] Markovic, I. (2006). *High-Performance Hybrid-Fibre Concrete: Development and Utilisation*. Delft: Delft University Press.

[58] Maute, K. and Ramm, E. (1995). Adaptive topology optimisation. *Structural Optimisation, No 10*, 100-112.

[59] Maute, K. Schwarz, S. and Ramm, E. (1998). Adaptive topology optimisation for elastoplastic structures. *Structural Optimisation, No 15*, 81-91.

[60] Memon, B.A. and Su. X. (2004). Arc-length technique for nonlinear finite element analysis. *Journal of Zhejiang University SCIENCE, No 5*, 618-628.

[61] Milne, E.A. (1941). *Augustus Edward Hough Love: 1863-1940*. Oxford: Oxford University Press.

[62] Popov, E.P. and Medwadowski, S.J. (1981). Stability of Reinforced Concrete Shells: State-of-the-Art Overview. In: Popov, E.P. and Medwadowski, S.J. (Eds). *Concrete Shell Buckling* (pp. 1-41). Detroit: Publication American Concrete Institute.

[63] Pronk, A.D.C., Houtman, R., Hanselaar, H. and Bogart, A. (2003). *A Fluid Pavillion by Rigidizing a Membrane*. Delft: Delft University of Technology.

[64] Pronk, A.D.C. (2006). Spuitbeton op voorgespannen membranen. *Cement, No 5*, 40-42.

[65] Ramm, E. and Wall, W.A. (2002). *Shell Structures: A Sensitive Interrelation between Physics and Numerics*. Stuttgart: University of Stuttgart.

[66] Ramm, E. (1987). Ultimate Load and Stability Analysis of Reinforced Concrete Shells. In: IABSE CCMCS. (Eds). *Colloquium on Computational Mechanics of Concrete Structures - Advances and Applications* (pp. 145-159). Delft: Delft University Press.

[67] Redaelli, D. and Muttoni, A. (2007). Tensile Behaviour of Reinforced Ultra-High Performance Fiber Reinforced Concrete Elements. In: Radic, J. (Ed). *Proceedings Concrete Structures - Stimulators of Development* (pp. 267-274). Zagreb: FIB Croatian Member Group & Croatian Society of Structural Engineers.

[68] Schnobrich, W.C. (1981). Analytical and Numerical Evaluation of the Buckling Strength of Reinforced Concrete Shells. In: Popov, E.P. and Medwadowski, S.J. (Eds). *Concrete Shell Buckling* (pp. 161-186). Detroit: Publication American Concrete Institute.

[69] Scordelis, A. (1981). Stability of Reinforced Concrete Domes and Hyperbolic Paraboloid Shells. In: Popov, E.P. and Medwadowski, S.J. (Eds). *Concrete Shell Buckling* (pp. 63-110). Detroit: Publication American Concrete Institute.

[70] Seide, P. (1981). Stability of Cylindrical Reinforced Concrete Shells. In: Popov, E.P. and Medwadowski, S.J. (Eds). *Concrete Shell Buckling* (pp. 42-62). Detroit: Publication American Concrete Institute.

[71] Speelman, N. (2006). Hoge capaciteit spuitbeton. *Cement, No 5, 36-39*.

[72] Timoshenko, S. and Gere, J.M. (1961). *Theory of Elastic Stability*. London: McGraw-Hill Book Company.

[73] Timoshenko, S. and Woinowsky-Krieger, S. (1959). *Theory of Plates and Shells*. London: McGraw-Hill Book Company.

[74] Timoshenko, S. and Young, D.H. (1945). *Theory of Structures*. London: McGraw-Hill Book Company.

[75] Underwood, David. (1994). *Oscar Niemeyer and Brazilian free-form modernism*. New York: Braziller.

[76] Vambersky, J.N.J.A. Wagemans, L.A.G. and Coenders, J.L. (2006). *Structural Design: Special Structures*. Delft: Delft University of Technology.

[77] Veenendaal, D. (2008). *Evolutionary Optimisation of Fabric Formed Structural Elements*. Delft: Delft University of Technology.

[78] Vermeij, P.Th. (2006). *Parametric Associative Design for Free Form Architecture*. Delft: Delft University of Technology.

[79] Vree, J.H.P. de. (2002). *Eindige Elementen Methode*. Eindhoven: Eindhoven University of Technology.

[80] Vrouwenvelder, A.C.W.M. (2003). *Plasticity: The Plastic Behaviour and the Calculation of Beams and Frames Subjected to Bending*. Delft: Delft University of Technology.

[81] Vrouwenvelder, A.C.W.M. (2003). *Structural Stability*. Delft: Delft University of Technology.

[82] Walraven, J.C. (2002). *Gewapend beton*. Delft: Delft University of Technology.

[83] Walraven, J.C. (2006). Ultra-hogesterktebeton: een materiaal in ontwikkeling. *Cement, No 5*, 57-61.

[84] Weingardt, R.G. (2007). Anton Tedesko: Father of Thin-Shell Concrete Construction in America. *Structure Magazine, No 4*, 69-71.

[85] Wells, G.N. (2004). *The Finite Element Method: An Introduction*. Delft: Delft University of Technology.

[86] Wilde, R.E. (2003). *American Concrete Institute: A Century of Progress*. Detroit: Publication American Concrete Institute.

[87] Zienkiewicz, O.C. and Taylor, R.L. (2000). *Finite Element Method: The Basis, volume 1*. Boston: Butterworth Heinemann.

[88] Zienkiewicz, O.C. and Taylor, R.L. (2000). *Finite Element Method: Solid Mechanics, volume 2*. Boston: Butterworth Heinemann.

[89] Zutven, R. van. and Vogels, F. (2003). Bekisting voor complexe betonvormen. *Cement*, *No 2, 34-37*.

Internet

[90] BINI Shell, www.bini.com

[91] Bösiger, www.boesiger-ag.ch

[92] BSI, www.bsi-eiffage.com

[93] IASS, www.iass-structures.org

[94] Monolithic Dome, www.monolithicdome.com

[95] NAFEMS, www.nafems.org

[96] Structurae, www.structurae.uk